

**On the promotion effect of trivalent cations on zinc oxide
and their influence on catalyst activity**

Dissertation

**Zur Erlangung des akademischen Grades eines Doktors der
Naturwissenschaften**

- Dr. rer. nat. -

vorgelegt von

Benjamin Mockenhaupt

Geboren in Siegen

Fakultät für Chemie

der

Universität Duisburg-Essen

September 2023

DuEPublico

Duisburg-Essen Publications online

UNIVERSITÄT
DUISBURG
ESSEN

Offen im Denken

ub | universitäts
bibliothek

Diese Dissertation wird via DuEPublico, dem Dokumenten- und Publikationsserver der Universität Duisburg-Essen, zur Verfügung gestellt und liegt auch als Print-Version vor.

DOI: 10.17185/duepublico/79246

URN: urn:nbn:de:hbz:465-20231113-083537-3

Alle Rechte vorbehalten.

Diese Arbeit wurde im Zeitraum von September 2018 bis April 2021 an der Fakultät für Chemie der

Universität Duisburg-Essen

in der Arbeitsgruppe von

Prof. Dr. Malte Behrens

angefertigt.

Tag der Abgabe: 04 September 2023

Gutachter: *Prof. Dr. Malte Behrens*

Prof. Dr. Jan-Dierk Grunwaldt

Prüfungs-Vorsitzender: *PD Dr. Holger Somnitz*

Tag der mündlichen Prüfung: 20.10.2023

- Ich weiß, dass ich nicht weiß. -

Sokrates 469-399 v. Chr.

Loosely translated: “I know (as a knowing person) that I don’t know.”

Preface

“I know that I don’t know.” This citation escorted me through all the steps of my doctorate. As scientist I focused on increasing the knowledge. Especially, I was highly interested to increase my knowledge in catalyst preparation. During the research in the laboratories, I recognized, that scientists have a huge knowledge, but it seems to be so small, that it is often impossible to explore the complete field of one research topic. At the same time, learning new skills in the lab also requires a critical view on the results. Since nobody can have the absolute knowledge and we are learning for our complete life, as scientists we have to review the results of our research with a critical thinking, to avoid, that we create false knowledge. But at the same time, we must be careful, because this generated knowledge isn’t the absolute knowledge. The best example for this is methanol synthesis. This reaction has been topic of research for over 60 years. At this time, the knowledge about the catalysts which are the most important gear in methanol synthesis, increased drastically. However, still today researchers working in this field, most often on one specific catalyst, the copper/zinc oxide (Cu/ZnO), to learn more about the active site and to find out, why this catalyst behaves as it does. During the decades of research, the analysis techniques evolution enabled more accurate or deeper analysis. With this, postulates based on “old” knowledge about the catalyst could be confirmed or even more precise developed. Therefore, as scientists, we should be happy about our results, but we never should think, that we generated the absolute knowledge. The world is so fantastic and huge, that we only observe one very tiny, small part of it within our life. We know things, but at the same time we are unknowing.



Neunkhausen, the 04/09/2023

Benjamin Mockenhaupt

Acknowledgement

A lot of person have supported me during my time as PhD. Therefore, I have to be grateful to people, who enabled me to increase my knowledge.

My personal interest was to learn more about catalyst preparation, especially the co-precipitation. This was possible, as I was allowed to do my PhD at the group of Prof. Dr. Malte Behrens in Essen. The greatest thanks contribute to him as my supervisor and mentor. Prof. Behrens educated me a lot from the material preparation over the characterization methods. I was able to learn a lot of new skills and to contribute to several grateful collaborations, where hydrogenation catalysts were investigated. One of my favourites was the priority program SPP2080 of Prof. Dr. Jan-Dierk Grunwaldt in Karlsruhe. I enjoyed the time within this project a lot. Various research groups contributed to this research field, so that one could learn a lot of new things with every visit. But also within our consortium of Prof. Grunwaldt, Prof. Studt and Prof. Behrens we always had fruitful and very interesting discussions. This research collaboration allowed me to visit a synchrotron facility and to do operando experiments at this were Lakshmi Pandit educated and showed me the complete setup and allowed me to work with her. Thank you for this grateful time, Lakshmi. For this possibility, I have additionally to thanks gratefully Prof. Dr. Jan-Dierk Grunwaldt to allow me to contribute in the SPP 2080 program and to come to KIT to visit the synchrotron facility ANKA and beamline CAT-ACT. Additionally, I have to thanks him that he took over the co-reviewer part of my thesis.

I also thanks Prof. Matthias Epple and Prof. Stephan Schulz for the access to their characterization facilities. Especially, I will thank Robin Meya for the analysis of all my prepared materials, which sometimes could become a challenge due to the high production rate. But also, a grateful thanks to Dr. Kateryna Loza, who investigated some samples in SEM and who educated me about the possibilities to improve microscopic investigations by proper sample preparation. This knowledge helped me a lot to get proper results of SEM and TEM analysis of my samples.

But beside the professors, the group members, are often responsible for the personal evolution. With that I will thanks to my group colleagues in Essen, Fatih Özcan, who showed me the first precipitation experiments and who supported me during hydrogenation experiments at University of Utrecht. I have to thanks to Prof. Dr. Petra E. de Jongh and Remco Dalebout who allowed Fatih and me to do some experiments of our catalysts in their 16 fold parallel reactor plant of Avantium, my lovely Flowrence® or "Florence". I liked, yes, I loved this machine a lot, that I successfully convinced Prof. Behrens to invest in such a hydrogenation laboratory plant.

Acknowledgement

On the other side I thank my further colleagues of the Behrens group in Essen Jil Gieser, Maik Dreyer, Anna Rabe, Gereon Behrendt, Denise Rein, Steffie Becker, Sharif Najafi and Klaus Friedel. A special and grateful thanks contribute to Jil Lorean Gieser, who provided me with her hands and eyes, to perform the chemisorption measurements on my copper catalysts with the BelCat B device. At the same time I was in Kiel to support the group of Prof. Behrens at this site. There, in the northern Germany, I get to know some other very nice people. I thank Anna Wolf, Patrik Hauberg and Sebastian Mangelsen for teaching me very well in XRD analysis and showing me, how poor my knowledge in this topic was. They helped me together to get a better understanding what is possible with x-ray diffraction and what I can learn from this technique. Especially Sebastian alias Seba helped me a lot with XRD analysis and Patrik helped me over my time in Kiel by searching my samples, do gas phase treatments on some of them and shipping them to my collaborators to Siegen. With this I have to thank to my other collaborators, Prof. Dr. Jörn Schmedt auf der Günne and Jan-Konrad Wied. The investigation of the doped zinc oxides has shown me how important solid state NMR can become and that this is a wonderful complementary analysis technique to get more insights into very low doped samples. Another special thanks contribute to Prof. Dr. Martin Muhler and Philipp Schwiderowski who started a collaboration with Prof. Behrens group to investigate the copper based catalysts during methanol synthesis. Only the group of Prof. Muhler was able to inject isobaric a probe molecule during methanol synthesis into the gas stream. I know Philipp since he started his master thesis at Prof. Muhler's group and with this thesis our collaboration became very interesting, and a lot of nice discussions followed.

Since my PhD was not finished but I started already at TU Delft University, I will thank my special nice colleagues in the Netherlands. First of all, I thank Prof. Dr. Atsushi Urakawa, he made it possible for me to start in his group on a challenging project without my PhD. But also, I thank Min Li, Nat Phongprueksathat, Pratik Gholkar, Jose Palomo, Donato Pinto and Sorin Bunea and our Japanese friend Tomone Sasayama for very nice discussions about copper based methanol synthesis. Also a special thanks for inspiration to the Team of Building 67: Ahmad Alrefaei and Afreen Akhtar.

But beside the scientific stuff I have to thank my family.

The special thanks contribute to my parents Anne and Andreas Mockenhaupt. They supported me in an unaffordable way. They took care of my chicken, ducks and geese breeds over the week, so that I could delight in them on weekends. If my parents wouldn't have done it, I had to give up my breeding of the special chicken race: Sundanese game fowl (zu deutsch:

Sundanesische Kampfhühner). But also, they supported me with inspiration and ideas if any problem happened and showed me solution pathways. Also, they took care of my personal mind, they impelled me to do other activities like hunting, working on our farm, to get rid of stress and to stop thinking all the time only about work and catalysts. Also my siblings Barbara, Johanna and Jakob supported me with stability and help, if I have had any concern.

A special thanks contribute to my partner Alina. Beside the ups and downs of the daily life it was never easy for me to reconcile the science and relationship. I thank you for your trust in me and in my decisions and the support if anything was too difficult for me.

If I have forgotten anyone, please forgive me. A lot of people I know contributed in an unexpected way to the success of this thesis.

List of contents

Abbreviations	VII
Symbols and formula units.....	XI
Chemistry	XIII
Abstract.....	XV
Kurzzusammenfassung.....	XIX
1 Introduction	1
2 State of the Art	5
2.1 CO ₂ hydrogenation reactions	5
2.1.1 Methanol synthesis.....	5
2.1.2 Higher alcohol synthesis	9
2.1.3 Reverse water-gas shift reaction	11
2.2 Characterization of copper-surface areas by chemisorption methods	13
2.2.1 N ₂ O reactive frontal chromatography	13
2.2.2 Temperature programmed hydrogen desorption.....	14
2.2.3 Transient hydrogen adsorption.....	15
2.2.4 Benefit and limitation of the chemisorption methods	16
2.3 Material synthesis	17
2.3.1 Material preparation via (co-)precipitation	17
3 Experimental	25
3.1 Copper surface determination	25
4 On the secondary promotion effect of Al and Ga on Cu/ZnO methanol synthesis catalysts	29
4.1 Introduction.....	30
4.2 Experimental section.....	32
4.2.1 Precursor synthesis.....	32
4.2.2 Oxide synthesis (Pre-catalysts).....	32

4.2.3	Characterization methods.....	33
4.2.4	Catalytic testing.....	36
4.2.5	Nomenclature	37
4.3	Results and discussion	37
4.3.1	Synthesis and characterization of the pre-catalysts.....	37
4.3.2	The reduced state before catalysis	40
4.3.3	Summary of the Microstructural Characterization and the Secondary Promotion Effect.....	52
4.3.4	Catalysis of the copper zinc oxide-based catalysts	54
4.3.5	Summary of the catalytic results and the effect of the secondary promoter	63
4.4	Conclusion	66
5	Phase evolution, speciation and solubility limit of aluminium doping in zinc oxide catalyst supports synthesized <i>via</i> co-precipitated hydrozincite precursors	69
5.1	Introduction.....	70
5.2	Experimental section.....	73
5.2.1	Sample labelling.....	73
5.2.2	Precursor synthesis.....	73
5.2.3	Zinc oxide synthesis.....	74
5.2.4	Characterization methods.....	74
5.3	Results and Discussion.....	77
5.3.1	Characterization of the Al doped hydrozincite precursors.....	77
5.3.2	Characterization of the doped zinc oxide samples	88
5.4	Conclusion	101
6	Phase evolution and solubility limit of gallium doping in zinc oxide catalyst supports synthesized <i>via</i> co-precipitated hydrozincite precursors	103
6.1	Introduction.....	104

6.2	Experimental section.....	106
6.2.1	Precursor synthesis.....	106
6.2.2	The precursor of the zinc oxide sample was synthesized by co-precipitation. The precipitation was carried out in an automated stirred tank reactor (OptiMax, Mettler Toledo) from 1 M metal salt nitrate solution (see SI, Table SI 11.20 on page 260)	
	Precursor synthesis.....	106
6.2.3	Zinc oxide synthesis.....	107
6.2.4	Sample labelling.....	107
6.3	Characterization methods.....	107
6.4	Results and Discussion.....	108
6.4.1	Characterization of the Hydrozincite precursors	108
6.4.2	Characterization of the zinc oxides	116
6.5	Conclusion	122
7	High-pressure pulsing of Ammonia results in Carbamate as strongly inhibiting Adsorbate of Methanol Synthesis over Cu/ZnO/Al ₂ O ₃	125
7.1	Introduction.....	126
7.2	Experimental section.....	128
7.2.1	Catalyst synthesis and characterization.....	128
7.2.2	Catalytic testing and ammonia pulse chemisorption.....	130
7.2.3	Density Functional Theory (DFT) calculations	130
7.3	Results and discussion	131
7.3.1	Catalyst characterization	131
7.3.2	Catalytic performance in methanol synthesis	134
7.3.3	High pressure pulse experiments	135
7.4	Conclusion	142
8	Cu-Co/ZnAl ₂ O ₄ catalysts for CO conversion to higher alcohols synthesized from co-precipitated hydrotalcite precursors	143
8.1	Introduction.....	144

8.2	Experimental section.....	147
8.2.1	Catalyst synthesis and characterization.....	147
8.2.2	Catalytic testing.....	149
8.3	Results and discussion	150
8.3.1	Catalyst synthesis and characterization.....	150
8.3.2	Activity test in CO hydrogenation	155
8.3.3	Characterization of the spent catalysts after passivation in air	161
8.4	Conclusion	165
9	Conclusion and Outlook.....	167
10	References	171
11	Appendix	187
11.1	Synthesis numbers of prepared precursors.....	187
11.2	List of figures	193
11.3	List of Tables	200
11.4	List of Reaction equations.....	201
11.5	List of maths equations	202
11.6	Supporting Information to "On the secondary promotion effect of Al and Ga on Cu/ZnO methanol synthesis catalysts"	203
11.6.1	Catalyst preparation	204
11.6.2	Characterization methods.....	204
11.6.3	DFT calculations	225
11.6.4	Catalysis	226
11.6.5	Characterization of the spent catalysts.....	228
11.7	Supporting Information to "Phase evolution, speciation and solubility limit of aluminium doping in zinc oxide catalyst supports synthesized <i>via</i> co-precipitated hydrozincite precursors"	231
11.7.1	Description of the crystal structure of hydrozincite.....	232
11.7.2	Materials used for co-precipitation	232

11.7.3	Time resolved ageing of $x_{Al} = 0.02$ Al doped hydrozincite	233
11.7.4	Synthesis of the aluminium-rich side-phase zaccagnaite.....	236
11.7.5	Characterization of the hydrozincite precursors of the aluminium concentration variation	239
11.7.6	Characterization of the zinc oxides	246
11.8	Supporting Information to "Phase evolution and solubility limit of gallium doping in zinc oxide catalyst supports synthesized via co-precipitated hydrozincite precursors"	259
11.8.1	Precursor synthesis.....	260
11.8.2	Synthesis of the gallium rich side phase Zaccagnaite	260
11.8.3	Characterization of the Hydrozincite precursors	261
11.8.4	Characterization of the Zinc oxides	264
11.9	Supporting Information to "High-pressure pulsing of Ammonia results in Carbamate as strongly inhibiting Adsorbate of Methanol Synthesis over Cu/ZnO/Al ₂ O ₃ "	269
11.9.1	Characterization methods.....	270
11.9.2	Catalytic performance in methanol synthesis	274
11.10	Supporting Information to "Cu-Co/ZnAl ₂ O ₄ catalysts for CO conversion to higher alcohols synthesized from co-precipitated hydrotalcite precursors"	279
11.10.1	Catalyst synthesis and characterization.....	280
11.10.2	Activity test in CO hydrogenation	285
11.10.3	Characterization of the spent catalysts after passivation in air	291
12	Publications	295
13	Curriculum vitae.....	299
14	Declaration of Authorship (Eidesstattliche Erklärung)	301

Abbreviations

AAS	Atomic absorption spectroscopy
ASE	Atomic Simulation Environment
BEEF-vdW	Bayesian Error Estimation Functional with van der Waals correlations
BET	Brunauer-Emmett-Teller surface area of the solid
BJH	Barrett-Joyner-Halenda (pore size determination)
Cat	Catalyst
$C_p dT$	Enthalpy changes by temperature difference at constant pressure
CZA	copper/zinc oxide/aluminum oxide
DFT	Density functional theory
DMA	di-methylamin
DRIFTS	Diffuse reflectance Infrared Fourier Transformed Spectroscopy
DTG	Differential thermogravimetry
EA	Elemental analysis
ED	Electron diffraction
E_{tot}	total energy
FFF	Given atoms are fixed
FFT	Fast Fourier transformation
FHI-Std.	Fritz-Haber-Institute (Berlin)-Standard CZA catalyst (68Cu:29Zn:3Al)
FWHM	Full width at the half of the maximum height
GC	Gas chromatograph
Gof	Goodness of fit

Abbreviations

HAADF	High-angle annular dark-field
HAT	Hydrothermal
HRTEM	High resolution transmission electron microscopy
IR	infrared spectroscopy
MAS NMR	Magic angle spinning nuclear magnet resonance spectroscopy
Max.	maximum
MS	Mass spectrometry
N2O-RFC	N2O reactive frontal chromatography
PAW	projector augmented wave method
PL	power law (maths)
PXRD	Powder x-ray diffractometry
rel	relative
RWGS	Reverse water gas shift reaction
S	Entropy
SEM	Scanning electron microscopy
SI	Supporting Information
SMSI	Strong metal support interaction
solv.	solvothermal
STEM	Scanning transmission electron microscopy
surf	Surface
TEM	Transmission electron microscopy

TPD	Temperature programmed desorption
TPR	Temperature programmed reduction
TTT	Given atoms are relaxed
UV-Vis	UV–visible spectrophotometry
VASP	Vienna ab initio simulation package
XRD	x-ray diffractometry
ZPE	zero point energy

Symbols and formula units

A	Area below the graph	
a_{Cu}	Specific surface area of a copper atom	$\text{m}^2 \text{atom}^{-1}$
A_i	Specific area (<i>e.g.</i> , $i = \text{BET}$; $i = \text{Cu}$)	$\text{m}^2 \text{g}^{-1}$
a_{rel}	Relative catalyst activity	
β	Heating ramp	$^{\circ}\text{C min}^{-1}$
β_{FWHM}	FWHM of the diffraction reflection	
d	Plane distance of crystal facet	nm
D_j	Dispersion of component j	%
d_j	Crystallite size of component j	nm
δ_{obs}	Chemical shift observed in NMR-spectroscopy	ppm
E_a	Activation energy	kJ mol^{-1}
E_g	Band gap	eV
f	Shape factor (<i>e.g.</i> , $f = 6$ for spheres)	
k	Form shape factor	
k	Rate constant	$\mu\text{mol g}^{-1} \text{min}^{-1}$
k_0	Pre-exponential factor	$\mu\text{mol g}^{-1} \text{min}^{-1}$
λ	Wavelength	nm
m	Mass	g
m	Order of reaction	
N	Molar amount	mol

Symbols and formula units

N_A	Avogadro constant ($6.02214076 \cdot 10^{23}$)	atoms mol ⁻¹
ν_j	Stoichiometric coefficient of component j	
θ	Diffraction angle	°
R	Ideal gas constant ($8.314 \text{ J mol}^{-1} \text{ K}^{-1}$)	$\text{J mol}^{-1} \text{ K}^{-1}$
R^2	Fit quality	%
r_{MeOH}	Methanol formation rate	$\mu\text{mol g}^{-1} \text{ min}^{-1}$
S_j	Selectivity of product j	%
T	Time	s
V_{Zn}	Point defect because of a substituted zinc atom in the lattice (<i>e.g.</i> , $\text{Al}_{\text{Zn}} = \text{Al substituted Zn site}$)	
$W_{i, \text{solid}}$	weight fraction of component i of the solid	
X	stoichiometric factor	
X_j	Conversion of educt j	%
$\Delta_{\text{RH}}^0_{298}$	Reaction enthalpy at 298 K	kJ mol^{-1}
P	density	kg dm^{-3}

Chemistry

Al	Aluminium
Al ₂ O ₃	Aluminium oxide
A ⁿ⁻	Anion with the negative charge n
Ar	Argon
CH ₃ OH	Methanol
CO	Carbon monoxide
Co	Cobalt
CO ₂	Carbon dioxide
CO ₃ ²⁻	Carbonate ion
Cu	Copper
CuO	Copper oxide
CZ	Copper / zinc oxide (methanol catalyst)
CZA	Copper oxide / zinc oxide / aluminium oxide (methanol catalyst)
CZG	Copper / zinc oxide / gallium oxide (methanol catalyst)
DMA	Di-methylamine
Ga	Gallium
H ₂	Hydrogen
H ₂ O	Water
HZ	Hydrozincite

In	Indium
In ₂ O ₃	Indium oxide
K ₂ CO ₃	Potassium carbonate
LDH	Layered double hydroxide
LDO	Layered double oxide
MeOH	Methanol
MgO	Magnesium oxide
M ^{II}	divalent metal ion (like Cu and Zn)
M ^{III}	trivalent metal ion (like Al or Ga)
MMA	Mono-methylamine
MMO	Mixed metal oxide
N ₂	Nitrogen
Ni	Nickle
OH ⁻	Hydroxide ion
SiO ₂	Silica oxide
TMA	Tri-methylamine
Zn	Zinc
ZnO	Zinc oxide
ZnO _x	Partial reduced zinc oxide (with unknown oxidation state)

Abstract

Methanol synthesis is one of the important processes of the chemical industry. Because of the usage of the product molecule as fuel, platform chemical and hydrogen storage material. By using anthropogenic CO₂ a sustainable carbon neutral chemical industry can be realized.

The hydrogenation of CO and/or CO₂ to methanol is performed on a Cu/ZnO (CZ) catalyst. As state of the art, the Cu/ZnO:Al (CZA) catalyst is highly active in this process. But up to nowadays, the role of aluminium as promotor is not completely understood. Therefore, the structural and electronic effect of Al and Ga as ternary metals in Cu/ZnO catalysts for the methanol synthesis was investigated. For this purpose, three zincian malachite-derived catalysts with the nominal Cu:Zn ratio of 70:30 were synthesized: an unpromoted, binary catalyst (CZ) and two ternary catalysts with either 3 mol% Al (CZA) or Ga (CZG). Both Al and Ga showed to have a strong impact on the catalyst's properties. Alongside the catalyst treatment from the co-precipitated precursors phase to the activated and reduced catalyst, an improved microstructure and an increased BET surface area was found for the secondary promotor (Al or Ga) containing catalysts. Moreover, a sequence of chemisorption experiments allowed to quantify and differentiate between Cu^{surf} and Zn^{red} surface species in the activated catalysts. Considering several analysis techniques like chemisorption method or diffuse reflectance infrared Fourier transform spectroscopy (DRIFT), an additional electronic promotion of Al and Ga could be determined. This promotion effect is related to doped ZnO phases, as it was demonstrated by X-ray absorption near edge spectroscopy (XANES) and enhances the reducibility of the ZnO by forming more Zn^{red} sites. This effect is stronger for Al, leading to a more pronounced Zn overlayer on the Cu surface and strong metal support interactions (SMSI). In the methanol synthesis, this led to a performance in the order CZA>CZG>CZ.

To further address the observed electronic effects of ZnO by doping with a trivalent cation like Al³⁺ or Ga³⁺, ZnO as a model support was synthesized according to the preparation method of the methanol synthesis catalyst.

To determine the aluminium speciation and the solubility limit of the aluminium cation on zinc positions, a series of zinc oxides with varying aluminium contents was synthesized by a subsequent calcination of the co-precipitated precursors. The synthesis was inspired by the industrial synthesis of the methanol synthesis catalyst via crystalline precursors, here hydrozincite Zn₅(OH)₆(CO₃)₂ was employed. Short precipitate ageing time, low ageing temperature and low aluminium contents below 3 mol% metal were advantageous to suppress crystalline side-phases in the precursor, which caused an aluminium segregation and non-

uniform aluminium distribution in the solid. This was observed also after calcination at 320 °C by transmission electron microscopy (TEM), although zinc oxide was the only crystalline phase. At lower aluminium contents, however, the dopant was found preferably on the zinc sites of the zinc oxide lattice based on the $\text{Al}_{\text{Zn}}^{\bullet}$ signal dominating the ^{27}Al nuclear magnetic resonance (NMR) spectra. The solubility limit regarding this species was determined to be approximately $x = 0.013$ or 1.3 % of all metal cations. Annealing experiments showed that aluminium was kinetically trapped on the $\text{Al}_{\text{Zn}}^{\bullet}$ site and segregated into zinc oxide and ZnAl_2O_4 spinel upon further heating. This shows that lower calcination temperatures such as applied in catalyst synthesis favour the aluminium doping on that specific site.

Instead of aluminium gallium can also be used as a zinc oxide dopant. Because of the closer ionic radius of gallium and zinc, a better incorporation into the zincite lattice is assumed. Analogous to the aluminium series, a series with varying amounts of Ga was prepared and investigated regarding phase purity and solubility limit. Up to a doping level of 4 % Ga, the precursor phase was free of impurities indicating a homogeneous cation distribution. A further increase of the dopant result in a defective hydrozincite structure and an additional side phase, which was in analogy to the Al doping series determined to be a zaccagnaite-like phase. Decomposition at low temperature (around 320 °C) resulted in ZnO phase without any side phases. An increased Ga content >6 % increased the defects in the ZnO structure, as it was determined by powder X-ray diffraction (PXRD) and Raman spectroscopy. From ^{71}Ga solid state NMR a solubility limit couldn't be clearly derived due to strong line broadening. However, up to 6 % Ga content, the four-fold coordinated Ga environment was dominant. From band gap determination there was found a limit of 4 % Ga ($x_{\text{Ga}} = 0.04$) in ZnO to which the band gap was unaffected. Combining the results of PXRD analysis of the precursor phase together with the NMR, X-ray photoelectron spectroscopy (XPS) and UV–visible spectrophotometry (UV-Vis) results of the ZnO phase, a solubility limit around 4 % is expected.

Beside the structural and compositional investigation of the copper based catalyst, the investigation of the active site of the methanol synthesis is still of interest but under controversial debate. Ammonia has been used as a probe molecule as it was found to inhibit the methanol synthesis in CO_2 containing synthesis gas during reaction. The poisoning effect was investigated using an industrial type of copper/zinc oxide/alumina catalyst. During steady state methanol synthesis in a $\text{CO}_2/\text{CO}/\text{H}_2$ synthesis gas, isobaric tri-methylamine (TMA) and ammonia injections poisoned the methanol formation, with the poisoning of ammonia being significantly stronger than that of TMA. Together with density functional theory (DFT) calculations, a mechanism of ammonia poisoning could be derived: ammonia activation takes

place on adsorbed oxygen or hydroxyl groups followed by the formation of stable carbamate on the active site. Further hydrogenation of the carbamate to TMA was calculated to exhibit high barriers, thus being rather slow, explaining why ammonia poisoning has a longer term effect.

Copper is known as a typical methanol formation catalyst. The combination of a Fischer-Tropsch active metal like cobalt together with copper as a bi-metallic catalyst for alcohol formation was investigated as a suitable combination in the higher alcohol synthesis. Typically, higher alcohol synthesis (HAS) is performed from CO-containing synthesis gas with an approximately equimolar hydrogen-to-carbon monoxide ($H_2:CO$) ratio. To investigate the effect of the Cu:Co composition in the presence of zinc for higher $H_2:CO$ ratios on HAS, a series of Cu-Co/ $ZnAl_2O_4$ catalysts was synthesized from co-precipitated hydrotalcite-like precursors with different cobalt-rich Cu:Co ratios and compared to their monometallic pure cobalt and copper counterparts. The addition of copper strongly facilitated cobalt oxide reduction upon catalyst activation and resulted in much smaller domain sizes for the crystalline metallic phases. The catalysts were evaluated at $H_2:CO$ ratios of 4 at 20 bar or 60 bar in a temperature range between 200 °C and 380 °C at a relatively low space velocity. Copper addition resulted in an increased formation of higher alcohols and hydrocarbons. The monometallic catalysts produced mainly C_1 products (CH_4 on Co/ $ZnAl_2O_4$ and CH_3OH on Cu/ $ZnAl_2O_4$), while the best catalyst with respect to ethanol yield reached a selectivity of 4.5 % and had a molar composition of Cu:Co ratio of 0.6 ($x = 0.375$). The microstructure of the bi-metallic spent catalysts clearly confirmed a close interaction of both metal species. The pure cobalt catalyst showed strong coking, which was effectively suppressed on the copper-containing samples. Despite these promotional effects of copper, the hydrocarbon selectivity dominated over the formation of (higher) alcohols on all cobalt-containing catalysts.

Kurzzusammenfassung

Die Methanolsynthese stellt einen wichtigen Prozess der chemischen Industrie dar. Denn das Produktmolekül kann als Kraftstoff, Basischemikalie oder Wasserstoffträger genutzt werden. Gerade wenn anthropogenes CO₂ genutzt wird, kann eine Kohlenstoffneutrale Industrie realisiert werden.

Die Hydrierung von CO und/oder CO₂ zu Methanol erfolgt an einem Cu/ZnO-Katalysator. Nach Stand der Technik ist der Cu/ZnO:Al (CZA)-Katalysator in diesem Prozess hoch aktiv. Allerdings ist die Rolle von Aluminium als Promotor bis heute nicht vollständig geklärt. Daher wurde der strukturelle und elektronische Effekt von Al und Ga als ternäre Metalle im Cu/ZnO-Katalysator für die Methanolsynthese untersucht. Zu diesem Zweck wurden drei vom Zink-Malachit abgeleitete Katalysatoren mit einem nominalen Cu:Zn-Verhältnis von 70:30 synthetisiert: ein unpromotierter binärer Katalysator (CZ) und zwei ternäre Katalysatoren mit entweder 3 mol% Al (CZA) oder Ga (CZG). Es zeigte sich, dass sowohl Al als auch Ga einen starken Einfluss auf die Struktur des Katalysators hatten. Entlang der Herstellungsrouten von der co-präzipitierten Präkursorphase bis hin zum aktivierten und reduzierten Katalysator wurde eine optimierte Mikrostruktur und eine vergrößerte BET-Oberfläche für die sekundären Promotoren (Al oder Ga) enthaltenden Katalysatoren gefunden. Darüber hinaus ermöglichte eine Reihe von Chemisorptionsexperimenten die Quantifizierung und Unterscheidung von Cu^{surf}- und Zn^{red}-Oberflächenspezies der aktivierten Katalysatoren. Unter Berücksichtigung verschiedener Analysetechniken wie der Chemisorptionsmethode oder der diffuse Reflexions-Fouriertransformationsinfrarotspektroskopie (DRIFT) konnte eine zusätzliche elektronische Promotierung von Al und Ga festgestellt werden. Dieser Promotierungseffekt hängt mit der dotierten ZnO-Phase zusammen, wie Röntgen-Nahkanten-Absorptions-Spektroskopie (XANES) gezeigt hat und vereinfacht die Reduktion des ZnO und somit die Bildung von mehr Zn^{red} Oberflächenspezies. Dieser Effekt ist bei Al stärker und führt zu einer ausgeprägteren Zn-Schicht auf der Cu-Oberfläche und führt somit zu einem ausgeprägteren SMSI. Dies resultierte in einer Aktivität in der Methanolsynthese in folgender Reihenfolge CZA>CZG>CZ.

Um die elektronischen Effekte von ZnO durch die Dotierung mit einem dreiwertigen Kation wie Al³⁺ oder Ga³⁺ zu untersuchen, wurde ZnO als Modellträger gemäß der Herstellungsmethode des Methanolsynthesekatalysators synthetisiert.

Um die Aluminiumspezies und die Löslichkeitsgrenze des Aluminiumkations auf einer Zinkpositionen zu bestimmen, wurde eine Reihe von Zinkoxiden mit unterschiedlichen Aluminiumgehalten durch die Kalzinierung von vorher präzipitierten Präkursoren hergestellt.

Die Synthese wurde von der industriellen Herstellung des Methanolsynthesekatalysators über eine kristalline Präkursorphase abgeleitet, welche in diesem Falle das Hydrozinkit $\text{Zn}_5(\text{OH})_6(\text{CO}_3)_2$ war. Eine kurze Alterungszeit, eine niedrige Alterungstemperatur und niedrige Aluminiumgehalte unter 3 mol% (Metall basiert) waren vorteilhaft, um kristalline Nebenphasen im Präkursor zu unterdrücken, die eine Aluminiumsegregation und eine ungleichmäßige Aluminiumverteilung im Feststoff verursachen würde. Dies wurde auch nach der Kalzinierung bei 320 °C in der Transmissionselektronenmikroskopie (TEM) beobachtet, obwohl Zinkoxid die einzige kristalline Phase war. Bei niedrigeren Aluminiumgehalten wurde Al als Dotierung jedoch bevorzugt auf den Zinkplätzen des Zinkoxidgitters durch das $\text{Al}_{\text{Zn}}^\bullet$ -Signal, welches die ^{27}Al -NMR-Spektren dominierte, nachgewiesen. Die Löslichkeitsgrenze dieser Spezies wurde auf ungefähr $x = 0,013$ oder 1,3 % aller Metallkationen festgelegt. Kalzinierungsexperimente zeigten, dass Aluminium kinetisch an der $\text{Al}_{\text{Zn}}^\bullet$ -Stelle gebunden wurde und sich bei weiterem Erhitzen in Zinkoxid und ZnAl_2O_4 -Spinell umformte. Dies bedeutet, dass niedrigere Kalzinierungstemperaturen, wie sie bei der Katalysatorsynthese angewendet werden, die Aluminiumdotierung an dieser spezifischen Stelle begünstigen.

Anstelle von Aluminium kann auch Gallium als Dotierung im Zinkoxid verwendet werden. Aufgrund des ähnlicheren Ionenradius von Gallium und Zink wird ein besserer Einbau in das Zinkitgitter angenommen. Analog zur Aluminiumreihe wurde eine Reihe mit variierenden Ga-Anteilen hergestellt und hinsichtlich ihrer Phasenreinheit und Löslichkeitsgrenze untersucht. Bis zu einem Dotierungsgrad von 4 % Ga war die Präkursorphase unter Berücksichtigung einer homogenen Kationenverteilung frei von Verunreinigungen. Eine weitere Erhöhung der Dotierung führte zu einer defektreichen Hydrozinkitstruktur und zu einer zusätzlichen Nebenphase, die in Analogie zur Al-Dotierungsreihe als Zaccagnaite-ähnliche Phase bestimmt wurde. Die Zersetzung bei niedriger Temperatur (ca. 320 °C) resultierte in einer ZnO-Phase ohne Nebenphasen. Ein erhöhter Ga-Gehalt >6 % erhöhte die Defekte in der ZnO-Struktur, wie durch PXRD- und Raman-Spektroskopie festgestellt werden konnten. Aufgrund der starken Linienverbreiterung konnte aus dem ^{71}Ga Festkörper-NMR keine genaue Löslichkeitsgrenze abgeleitet werden. Bis zu einem Gehalt von 6 % Ga dominierte jedoch das vierfach koordinierte Galliumion. Bei der Bestimmung der Bandkante wurde bei 4 % Ga ($x_{\text{Ga}} = 0,04$) im ZnO ein Limit gefunden, bis zu dem die Bandlücke unbeeinflusst blieb. Die Kombination der Ergebnisse aus der PXRD-Analyse der Präkursoren mit denen der NMR-Spektroskopie, XPS-Analyse und UV-Vis Spektroskopie, lässt ein Löslichkeitslimit um die Dotierung von 4 % Ga im ZnO vermuten.

Neben der Struktur und der Zusammensetzung des kupferbasierten Katalysators ist auch das aktive Zentrum nach wie vor von wissenschaftlichem Interesse und wird kontrovers diskutiert. Ammoniak wurde als Sondenmolekül verwendet, da festgestellt wurde, dass es die Methanolsynthese in CO₂-haltigem Synthesegas während der Reaktion inhibiert. Die Inhibierung wurde mit einem industriellen Kupfer/Zinkoxid/Aluminiumoxid-Katalysator untersucht. Während der stationären Methanolsynthese in einem CO₂/CO/H₂-haltigen Synthesegas vergifteten isobar injiziertes TMA und Ammoniak die Methanolbildung, wobei die Vergiftung durch Ammoniak deutlich stärker war als die durch Trimethylamin (TMA). Unter Einsatz der Dichtefunktionaltheorie (DFT) konnte ein Mechanismus der Ammoniakvergiftung abgeleitet werden: Die Ammoniakaktivierung erfolgt an adsorbierten Sauerstoff- oder Hydroxylgruppen, gefolgt von der Bildung von stabilem Carbamat am aktiven Zentrum. Es wurde berechnet, dass die weitere Hydrierung des Carbamats zu TMA hohe Barrieren aufweist und daher eher langsam verläuft, was erklärt, warum eine Ammoniakvergiftung eine längerfristige Wirkung hat.

Kupfer ist als typischer Katalysator für die Methanolsynthese bekannt. Die Kombination eines Fischer-Tropsch-Aktivmetalls wie Kobalt zusammen mit Kupfer zu einem bi-metallischen Katalysator für die Alkoholbildung wurde als geeignete Kombination für die Synthese höherer Alkohole (HAS) untersucht. Typischerweise wird die Synthese höherer Alkohole aus CO-haltigem Synthesegas mit einem äquimolaren Verhältnis von Wasserstoff zu Kohlenstoffmonoxid (H₂:CO) durchgeführt. Um den Einfluss der Cu:Co-Zusammensetzung in Gegenwart von Zink in höheren H₂:CO-Synthesegasverhältnissen auf die Bildung höherer Alkohole zu untersuchen, wurde eine Reihe von Cu-Co/ZnAl₂O₄-Katalysatoren aus co-gefällten Hydrotalcit-artigen Präkursoren mit unterschiedlichen kobaltreichen Cu:Co-Verhältnissen synthetisiert und mit ihren monometallischen Analoga aus reinem Kobalt und Kupfer verglichen. Die Zugabe von Kupfer vereinfachte die Kobaltoxidreduktion bei der Katalysatoraktivierung erheblich und resultierte in kleineren Domänengrößen für die kristallinen Metallphasen. Die Katalysatoren wurden in einem Synthesegas von H₂:CO = 4 bei 20 bar oder 60 bar in einem Temperaturbereich zwischen 200 °C und 380 °C bei relativ niedriger Raumgeschwindigkeit untersucht. Durch die Zugabe von Kupfer kam es zu einer verstärkten Bildung höherer Alkohole und Kohlenwasserstoffe. Die monometallischen Katalysatoren produzierten hauptsächlich C₁-Produkte (CH₄ bei Co/ZnAl₂O₄ und CH₃OH bei Cu/ZnAl₂O₄), während der beste Katalysator in Bezug auf die Ethanolausbeute eine Selektivität von 4,5 % erreichte und ein molares Cu:Co-Verhältnis von 0,6 ($x = 0,375$) aufwies. Nach der Katalyse konnte eine verbesserte Wechselwirkung der beiden Metallspezies durch die

Mikrostruktur der bi-metallischen Katalysatoren bestätigt werden. Der reine Kobaltkatalysator zeigte eine starke Verkokung, die bei den kupferhaltigen Proben effektiv unterdrückt wurde. Trotz dieser promotierenden Wirkung von Kupfer dominierte bei allen kobalthaltigen Katalysatoren die Kohlenwasserstoffselektivität gegenüber der Bildung von (höheren) Alkoholen.

1 Introduction

The methanol synthesis represents one of the important processes of the chemical industry. Methanol is used as platform chemical, fuel additive, solvent or as energy carrier. The process evolution was mainly influenced by a co-evolution of the catalyst which began around hundred years ago.¹⁻³

Nowadays, the methanol production in the low temperature process is performed with a copper/zinc oxide/aluminium oxide (CZA) catalyst, which was found as the most active and stable catalyst at around 200 – 300 °C and 50 – 100 bar.^{1, 3-5} This catalyst is marked up by copper and zinc oxide synergy reflecting a high catalyst performance by a simultaneous increased stability and long lifetime of copper nanoparticles of the catalyst.^{6,7} One function of the zinc oxide is the structural promotion, prohibiting copper sintering and increasing the copper particle dispersion.^{6,7} The optimum dispersion is aimed at an equal amount of both compounds building up the optimum copper/promoter interaction.⁸ This close interaction will be initiated by the synthesis step of a catalyst precursor phase. Common synthesis routes of a copper/zinc oxide catalyst, with increasing abundance, are: impregnation method, citrate route, sol-gel synthesis and co-precipitation.⁹

The most popular synthesis route *via* co-precipitation is limited to a metal composition of 70 % copper and 30 % zinc because of the malachite precursor phase $(\text{Cu, Zn, (Al)})_2\text{CO}_3(\text{OH})_2$. Beside the ideal case of equal amount of copper and zinc, the increased ratio in the malachite structure, the main advantage of this precursor phase is the homogeneous distribution of the components resulting in a highly nanostructured metal oxide and active catalyst.^{10, 11} As a negative example, an equal metal amount of a Cu/ZnO catalyst can be synthesized via a co-precipitated but meso-structured aurichalcite $(\text{Cu, Zn})_5(\text{CO}_3)_2(\text{OH})_6$ precursor phase achieving a lower copper surface area and catalytic performance in methanol synthesis.¹⁰ From that point of view the structure-advantages of the copper enriched malachite precursor system does dominate the ideal striven composition.¹⁰

It is undisputed that copper is the catalytic active metal in methanol synthesis, which was demonstrated by structural promoter variations like MgO, SiO₂ or Al₂O₃.¹²⁻¹⁴ Only the combination of copper and zinc oxide does result in a highly active catalyst not only in CO but also in CO₂ hydrogenation to Methanol, making this composition special and gave evidence, that there is more than only structural promotion, which is called the copper-zinc-synergy.^{12,}

The main characteristic of the copper-zinc synergy are the described dynamic and reversible structural changes by wetting/de-wetting of copper particles on zinc oxide or *vice versa*.^{9, 17-20} There are strong metal support interactions (SMSI) found, which describes the formed overlayers of zinc oxide on copper particles by somehow lifting the clearly separated state between Cu and ZnO under reducing and most often under catalyst activating conditions.^{7, 15, 20-22} In the temperature range of 250 °C to 340 °C at atmospheric pressure, the zinc oxide starts to reduce in the presence of copper and forms a surface-alloy/zinc oxide-interphase. The alloy phase does increase by consuming the ZnO phase with increasing temperature resulting in a bulk Cu-Zn-alloy at temperatures above 340 °C.²³⁻²⁵ There is a controversial debate in the community, discussing the relevance of a copper-zinc oxide-interphase or a copper-zinc-alloy phase as the methanol active site in the catalyst.²⁶⁻²⁸ The main issue of the debate is probably the intermixing of operando- and idealised, at ambient pressure performed, surface state investigations on the CZA catalyst.²⁵ However, there is evidence, that both, the formed alloy and the copper-zinc oxide interphase, does affect the methanol activity of the Cu/ZnO catalyst, not only as an temperature-activity correlation and the knowledge of the present alloy under these conditions^{23, 25} but also by an enhanced activity of a catalyst with 70 % reduced zinc and a residue of 30 % ZnO in contrast to a catalyst with complete alloyed copper particles in CO hydrogenation to methanol²⁴. There is also evidence, that the catalyst has multiple sites and that multiple factors affect the catalyst performance like the copper-zinc oxide interaction, present defects or the copper particle size.^{8, 12, 15, 22, 24, 29} The clearest promotion effect of zinc oxide is observed in the enhanced carbon dioxide conversion to methanol in contrast to the poorly active copper metal, which represents on the downside an efficient carbon monoxide to methanol converting catalyst.^{14, 16} From operando spectroscopy, there is a greater evidence for a defective ZnO phase, containing oxygen vacancies, rather than a formed Cu-Zn-alloy.²⁵ The catalytic performance, of a CZA, in CO₂ hydrogenation is unstable because of the inhibition effect of the couple-product water. The catalyst lose performance because of the repealed SMSI by a decreased Cu/ZnO interphase due to a highly crystalline and in mobility restricted zinc oxide or a formed Zn-Al-spinel phase.^{30, 31} This formed spinel phase could to some extent prevent the copper particle sintering and acts with that as an additional promoter at the expense of SMSI and activity.³¹⁻³³ However, the contribution of the third most often used component, the aluminium, is so far not clearly resolved because of the high complexity of the copper based catalyst.

From the preparative site it is known, that up to 3 % - 4 % aluminium can be incorporated into the zinc containing malachite structure suppressing side phases (*e.g.*, aurichalcite) and increases

the zinc amount in this precursor phase.³⁴ This amount of aluminium was also found to enhance the specific copper surface area by an increased copper dispersion and stabilization resulting in an enhanced activity compared to the Cu/ZnO catalyst.^{4,34} The localization of the aluminium ion is complicated because of the low amount and the low electron density. But a defect enriched ZnO was found as an effect of aluminium indicating the presence nearby the zinc oxide phase.^{4,33} One suggestion is the modified zinc oxide surface by segregated aluminium oxide species acting as a structure promoter prohibiting copper particle sintering.³⁵

The intrinsic methanol formation rate can be increased, if aluminium is used as a ternary promoter and increases with aluminium incorporation up to 3 % of the metal content.^{4,34} The correlation of increase of the methanol formation and the presence of aluminium in the catalyst can be explained by an enhanced copper surface area, which increased by around $2.5 \text{ m}^2 \text{ g}^{-1}$ as a result of copper, zinc oxide and aluminium oxide interactions by a simultaneously increased methanol formation rate of about $100 \mu\text{mol g}^{-1} \text{ h}^{-1}$ in comparison to a binary Cu/ZnO catalyst.³⁶

Beside structural effects, there is also evidence of an electronic promotion effect of Al and Ga acting as a dopant of zinc oxide, as it is known from semiconductor applications, and enhances the SMSI, which was determined by an increased copper surface area and intrinsic catalyst activity.^{34,37,38} Because of the similar ionic radius of Ga^{3+} to Zn^{2+} , an increased incorporation of Ga^{3+} into the zinc oxide lattice is expected resulting in an enhanced SMSI.^{37,39} Catalytic evaluation of aluminium and gallium containing ternary catalysts support the suggested activity enhancement in dependence of the trivalent promoter cation.^{40,41} One proposed mechanism is the enhanced carbon oxide activation and intermediate stabilization at oxygen vacancies induced by trivalent cation incorporation into the zinc oxide promoter.^{13,26,42-44} For gallium incorporated cations an increased number of oxygen vacancies are expected, because of the reducibility of gallium oxide in contrast to aluminium oxide at catalyst activating temperatures.^{13,45-47}

The state of the art investigations on methanol synthesis catalysts does result in two major research questions of this thesis:

One question is the effect of the trivalent cation on catalysis and the promotion effect on methanol catalysis. Because of the difficult spectroscopic analysis of low quantities of aluminium, gallium could be used as analogue, which is more accessible in spectroscopic analysis. This does only work, if gallium does behave quite similar to aluminium. To clarify the promotion effect of the trivalent cation methanol synthesis should be performed with

Cu/ZnO/Al₂O₃, Cu/ZnO/Ga₂O₃ and Cu/ZnO reference catalysts from a co-precipitated malachite precursor. It would be expected that an enhanced electronic promotion will be measured in an increased number of defects of the zinc oxide and a lowered copper surface area, as an increased zinc oxide reducibility and mobility. Therefore, a combination of the N₂O-RFC and H₂-TA methods should be used to answer the question. The electronic effect should then be represented in the catalytic activity, becoming equal if normalized to the main promotion effect of the trivalent cation. On the other hand, it would be suggested, that there are probably stability differences of the catalysts during methanol synthesis, which then must be an effect of the used trivalent cation demonstrating the structural promotion effect.

The second question does address the zinc oxide promoter. If the main promotion effect of aluminium or gallium is rather of electronic than of structural nature, one would suggest, that an optimum doped zinc oxide support enhances the catalytic performance of later deposited copper particles. Therefore, a detailed understanding of the trivalent cation incorporation into the zinc oxide lattice is necessary. To clarify that question a series of Al and Ga doped zinc oxides with varying amounts of trivalent cations will be synthesized in a similar manner to typical co-precipitation conditions of the ternary methanol catalyst. To investigate pure or doped zinc oxide supports, the zinc hydroxycarbonate precursor, hydrozincite, (Zn)₅(OH)₆(CO₃)₂ is chosen. The focus of this thesis is located on the synthesis and proper characterization of the doped zinc oxides in a manner, that following investigations could build up by studying the promotional effect after impregnating the supports with copper particles.

Regarding the mechanism of methanol formation on an industrial type of Cu/ZnO:Al catalyst, high pressure isobaric injection of ammonia will be used to address the active site under industrial methanol synthesis conditions.

Additionally, an estimation of the promotion effect of zinc oxide on other metal catalysts like cobalt-copper in higher alcohol synthesis will be demonstrated.

2 State of the Art

This chapter gives a brief overview of the most relevant topics of the herein addressed research fields. The communicated basics should support a better understanding of the performed investigations. A brief overview about CO₂ hydrogenation reactions and the use of chemisorption methods to characterize copper catalysts, followed by a description of different material classes will be given.

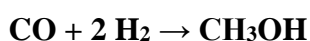
2.1 CO₂ hydrogenation reactions

Because of the climate change, the world community does focus on the reduction of the greenhouse gas, carbon dioxide. There is an increased emission of carbon dioxide over decades, which strongly correlated with the industrialization of countries and has to be lowered to prevent global warming.⁴⁸ The chemical conversion of carbon dioxide does simultaneously offer possible ways to get rid of that greenhouse gas like the synthesis of plastics, mineralization processes (building blocks) but also in hydrogenations like methanol synthesis, higher alcohols or CO synthesis.⁴⁹⁻⁵²

In the following subchapters the methanol synthesis, higher alcohol synthesis and revers water gas shift reactions are briefly introduced.

2.1.1 Methanol synthesis

Methanol synthesis is an old process established 1923 by BASF with an ZnO-Cr₂O₃ catalyst converting carbon oxide synthesis gas to methanol around 200 bar - 300 bar and 300 °C – 400 °C.^{1, 3, 5} With the established desulphurization process a sulphur poison free synthesis gas could be generated and allowed the industrial use of the high active Cu/ZnO/Al₂O₃ catalyst at 200 °C - 300 °C and 50 bar – 100 bar.^{1, 3, 5, 51, 53} Typically the feed gas for methanol synthesis is generated by natural gas reformation, coal- and/or biomass gasification or by partial oxidation of heavy oils.^{1, 5, 53} However, in the context of methanol synthesis a synthesis gas is a combination of carbon oxides like CO or CO₂ and hydrogen. The methanol reaction from carbon monoxide is shown in R 2.1, the reaction from carbon dioxide is visualized in R 2.2 and the water-gas shift side reaction is demonstrated in R 2.3.^{3, 53} The methanol synthesis is an exothermic process which is thermodynamically favoured at low temperatures and high pressures because of the volume contraction by product formation.^{3, 53}



$$\Delta_{\text{R}}H_{298}^0 = -91 \text{ kJ mol}^{-1}$$

R 2.1



Therefore, the early methanol process with the harsh reaction conditions, to reach fast kinetics on relatively low performing catalysts, are far from ideal thermodynamics with low methanol yield.^{51, 54} However, the exothermicity needs a gas phase cooling from process engineering point of view but also thermal stable catalysts which tolerate a temperature increase of the catalyst bed.^{1, 51, 53} A highly active methanol synthesis catalyst, which is stable against sinter effects, is the Cu/ZnO/Al₂O₃ catalyst.^{6, 32} This catalyst has been intensively investigated and will be introduced at this point.

2.1.1.1 Catalysts in methanol synthesis

In Methanol synthesis several catalysts can be used and are investigated. Different reaction conditions and synthesis gas composition can maximize the kinetic performance of each individual catalyst. Major examples are the co-precipitated Cu/ZnO/Al₂O₃-, the intermetallic Ni-Ga- and In₂O₃-based catalysts.^{9, 55, 56}

2.1.1.1.1 Cu/ZnO/Al₂O₃

This state of the art methanol synthesis catalyst is mainly synthesized via co-precipitation.⁸ But there are also alternative synthesis routes like sol-gel synthesis or impregnation method available.⁹ Using the co-precipitation approach, a nanostructured catalyst with a close contact of copper oxide and zinc oxide particles can be synthesized.⁵⁷ The addition of 3 % aluminium (metal based) increase the zinc substitution into the malachite precursor structure and improves the copper surface area resulting in an enhanced intrinsic catalyst activity.^{34, 57} Zinc oxide and aluminium oxide do act as structural promoters avoiding copper particle sintering during methanol synthesis.^{6, 32, 33, 35} Beside this structural mode of operation there is also a special interplay between copper and zinc oxide demonstrating a synergistic effect by reversible redox changes of the Cu/ZnO interphase depending on the gas phase conditions.^{9, 17-19} This was mainly exemplified by the poor activity of copper metal and zinc oxide in separated tests in methanol synthesis.¹⁵ Only the combination of copper and zinc oxide was found to be a highly active catalyst.¹⁵ Under activation and reaction conditions in reducing gas atmosphere, zinc oxide starts to reduce and migrate on the copper surface area establishing strong metal support interactions.^{20, 22} In the range of 240 °C – 340 °C a surface alloy is created, which ends up in a bulk alloy if higher temperatures or pressures are used.²³⁻²⁵ Nevertheless, the catalyst is able to

convert pure CO as well as pure CO₂ synthesis gas with a methanol-selectivity above 90 %.^{14, 50, 58, 59} The disadvantage of carbon dioxide hydrogenation with the ternary metal catalyst is the couple-product water, which poisons the catalyst and enhances copper particle sintering.^{30, 31, 59, 60} This can be suppressed by inserting some amounts of carbon monoxide into the synthesis gas. The carbon monoxide will be in situ consumed by the formed water in the water-gas shift reaction forming carbon dioxide, which then will be consecutively converted to methanol.^{58, 61} The formed water does additionally enhance zinc oxide recrystallization revealing to some extent the SMSI.³⁰⁻³² Additionally the segregation of a zinc-aluminium-spinel in the ternary metal catalyst could happen, which then leads to a re-distribution of the aluminium promotor and affects the reducibility of zinc.³¹⁻³³ Aluminium and gallium as trivalent cations are expected to induce electronic promotion effects on the copper catalyst possibly causing facilitated zinc oxide reduction or an increased number of oxygen vacancies.^{25, 35, 37, 43}

However, this catalyst represents a complex and multi-site system. This is mainly demonstrated by the simultaneous inhibition of the methanol formation sites, while in parallel ethylene hydrogenation reaction remains unaffected.²⁹ Temperature stable carbonate species, defective zinc oxide phases and copper particle size are further features which are found to influence the activity and stability of the catalyst in methanol synthesis.^{8, 12, 15, 22, 62}

Beside the typical Cu/ZnO catalyst, various other metal compositions are also active in methanol synthesis.⁹ One of the promising systems, which has a similar electronic structure to the Cu/ZnO catalyst is the Ni-Ga intermetallic compound⁵⁵ to which a short review will be given.

2.1.1.1.2 *Ni-Ga intermetallic compound*

From a theoretical point of view the beneficial electronic nature of the copper-zinc synergy could be equivalently obtained by a combination of metals. Such a system was found in the combination of nickel and gallium by the Ni₃Ga and Ni₅Ga₃ compositions as promising candidates.⁵⁵

In contrast to copper based catalysts, this intermetallic catalyst is often synthesized by incipient wetness impregnation of a support like silica and the intermetallic compound is created by reducing the metal salt precursor leading to small and active particles in contrast to calcined samples.^{55, 63} Catalytic investigations of this materials in carbon dioxide hydrogenation have an equal activity and selectivity to the binary Cu/ZnO catalyst, if performed at ambient pressure in the temperature range of 160 °C – 260 °C with a CO₂ synthesis gas.^{55, 63} It was found, that the intermetallic compound Ni₅Ga₃ was the most promising catalyst keeping up a performance

like the state of the art Cu/ZnO catalyst.⁶³ However, the material was found to be also active in high pressure carbon dioxide to methanol reaction with an optimum temperature at 250 °C and a methanol yield of around 72 %. The deactivation of the catalyst was described to be a segregation process of a Ni-Ga-spinel and gallium oxide.⁶⁴

Because of the already mentioned importance of oxygen vacancies in catalytic activity of methanol formation, the In₂O₃ based catalyst will be introduced.

2.1.1.1.3 *In₂O₃ in CO₂ hydrogenation to methanol*

Indium oxide is a stable and active oxidic catalyst in carbon dioxide conversion to methanol. In comparison to the state of the art CZA catalyst, the oxide reaches a selectivity to 100 % methanol and suppresses efficiently the reverse water-gas shift reaction at reaction conditions around 200 °C – 300 °C and 50 bar with H₂:CO₂ = 4.^{65,66} The reason for the strong activity are oxygen vacancies which can be introduced by temperature treatment in an inert or reducing atmosphere.⁶⁵ Theoretical DFT calculations have shown, that the 111 indium oxide surface plane can be reduced into a special state, creating up to five monolayer of reduced indium on indium oxide.⁶⁷ The reduction degree of indium oxide does increase with the reduction potential of the atmosphere by simultaneously lowering the energy of adsorbate states.^{65,67} Therefore, a moderate amount of oxygen vacancies of around one monolayer does improve the carbon dioxide hydrogenation reaction and reaches nearby the optimum energetic surface state to catalyse methanol formation.⁶⁷ This theoretical view can explain the catalytic activity by activating indium oxide by a thermal treatment in inert- instead of reducing gas.^{65,67,68} However interestingly, the indium oxide catalyst showed a catalytic activity which is in direct opposite to the copper catalyst in methanol formation. Indium oxide is highly active in converting a pure carbon dioxide synthesis gas to methanol by a resistance against water poisoning and can be promoted by carbon monoxide in the synthesis gas, restoring catalytic active oxygen vacancies but poisoning the catalyst if it is the only carbon source for methanol synthesis.⁶⁵ Copper has a high activity in carbon monoxide conversion reaction and can be boosted by traces of carbon dioxide in the synthesis gas feed but deactivates because of water formation and in case of pure carbon dioxide as source for methanol formation and in absence of zinc oxide.^{14,16,30,31,58,59} Similar to the copper-zinc oxide system, indium oxide has a strong synergistic effect with zirconium oxide, which is expected to be of electronic nature.^{65,66} One explanation from theoretical analysis is, that zirconium oxide does prohibit indium oxide reduction and controls the number of oxygen vacancies receiving maximum activity.⁶⁷

This catalyst does demonstrate clearly that oxygen vacancies plays an important role in carbon dioxide conversion. Therefore, a promotion effect with regard of this defect sites could be a chance to improve the Cu/ZnO:M^{III} catalyst in CO₂ to methanol reaction. A relationship of oxygen vacancies and activity was already described for zinc oxide based catalyst but could receive new attention, with the knowledge from investigations of the indium oxide catalyst.^{35, 42, 43, 69}

Beside methanol other alcohols can be synthesized from carbon dioxide synthesis gas. The higher alcohol synthesis will be described in the following sub-chapter.

2.1.2 Higher alcohol synthesis

Higher alcohol synthesis (HAS) is a process variation of the Fischer-Tropsch synthesis (FTS) with a high potential towards the reduction of the CO₂ footprint if biomass and biogas or CO₂-reformed natural gas are used as sources of carbon monoxide.^{70, 71} Advantages of this process lie in the possibility to tune the octane/cetane number of combustion fuels and to synthesize higher alcohols as platform chemicals.^{72, 73}

The FTS can be distinguished into the high temperature (300 °C – 350 °C @ ~30 bar) and the low temperature processes (200 °C – 250 °C @ ~30 bar).⁷⁴⁻⁷⁶ For the low temperature process cobalt-based catalysts are typically used, synthesizing long chain hydrocarbons, which enables a further product upgrade by a cracking process.^{53, 74}

FTS catalysts does typically contain iron, ruthenium, molybdenum, nickel and cobalt as mono metal catalyst or in various combinations.^{74, 76, 77} Because of the high price for ruthenium and the kinetic inhibition of iron by the coupled product water, cobalt seems to be a promising and cost-effective candidate also for HAS.^{74, 76} The reaction equation of the higher alcohol synthesis is described in R 2.4 from carbon monoxide and in R 2.5 from carbon dioxide feed gas.



From methanol synthesis copper/zinc oxide is known as a catalyst forming a C₁ alcohol.^{12, 15, 51} From that finding, a potassium promoted CZA catalyst was investigated in higher alcohol formation from carbon monoxide synthesis gas.⁷⁸ This catalyst was mainly active in methanol synthesis but formed additionally butanol with a selectivity of 25 % if it was promoted with 0.5 % K₂CO₃.⁷⁸ In contrast to methanol, the higher alcohol synthesis requires higher

temperatures (*e.g.*, 400 °C) and a lower residence time.⁷⁹ It is suggested that the formed methanol is consecutively consumed forming higher alcohols in a homologation reaction.⁷⁹⁻⁸¹ This makes copper to a valuable tandem metal of a typical FTS active catalyst. The copper-cobalt combination is one combination which should balance the dissociative adsorption of CO, which is needed for chain growth and the associative adsorption of CO, which gives access to the higher alcohol formation.^{80, 82} A systematic study have shown, that copper does facilitate the reduction of a cobalt-copper catalyst and increase the cobalt dispersion.⁸³

In a catalytic test of Co-Cu-Al catalysts prepared from an ex-hydrotalcite-like precursor phase, it was found, that a ratio of Cu:Co = 0.5 was more selective to higher alcohols ($S \approx 50\%$) at 240 °C @ 30 bar and with $H_2:CO = 2$.⁸⁴ Investigations of potassium promoted Co-Cu-Mo catalysts demonstrated the high performance of a $Cu/(Cu+Co) = 0.3$ catalyst reaching an alcohol selectivity of around 47 % at 270 °C and 50 bar with $H_2:CO = 1$ synthesis gas.⁸⁵ This are only two representatives of the manifold literature about cobalt-copper catalysts. However, there is evidence, that a cobalt-copper alloy was formed enhancing the catalyst activity in higher alcohol formation.^{80, 82, 84, 85} The alloy formation was determined by XRD analysis as a reflection in between the angles of metallic copper and metallic cobalt.^{84, 85} TEM analysis have supported the XRD results.^{84, 85} With a view on a phase diagram, one would not expect alloy formation below 600 °C.⁸⁶ This indicates, that nanomaterials behave differently or that probably a surface alloy could have arisen.⁸³⁻⁸⁶

Beside the discussion about the active phase of the bimetallic catalyst, promoters are also in this catalytic system of interest. Based on the knowledge of methanol synthesis, the promotion effect of zinc oxide must be also considered. Zinc was found to build a zinc-aluminium-spinel phase, if aluminium is used as support. This spinel phase does act as structural promoter increasing the metal particle dispersion, avoiding sintering of the metals and does to some extend prevent the re-oxidation of cobalt.⁸³ Studies on a Co-Cu/ZnO/Al₂O₃ catalyst could demonstrate, that a catalyst with low sodium content does behave like an unpromoted one. There was evidence, that zinc oxide has developed strong metal support interactions with copper because of the methanol formation rate despite the large copper particles.^{87, 88} Such basic sites, like the methanol active centres, are expected as crucial for intermediate stabilization supporting the higher alcohol formation *via* formate species, as it is known from methanol synthesis catalysts.^{16, 80, 87-90}

The hydrocarbon selectivity was attributed to reduced cobalt, which was not in direct contact with copper and deactivated coke deposition. Additionally, cobalt carbide could act as well as a CO activating site enhancing higher alcohol formation.^{87, 88}

The above description about the higher alcohol synthesis, should demonstrate, that this process builds up on methanol synthesis addressing a similar question to the structural promotion effect of ZnO:M^{III} to avoid sintering of the metal particles as well as the electronic effect by creating a SMSI enhancing alcohol formation and with that in an indirect way the higher alcohol synthesis.

As a last important reaction system, the reverse water-gas shift reaction will be introduced. This reaction can be equally catalysed by copper-zinc oxide catalysts in the methanol synthesis and to some extend in the HAS.

2.1.3 Reverse water-gas shift reaction

The reverse water-gas shift reaction R 2.6 is the back reaction of the water-gas shift reaction shown in R 2.3 in the chapter 2.1.1 Methanol synthesis on page 5. This equimolar reaction is pressure independent and because of the endothermic reaction enthalpy, the reaction is favoured at higher temperatures.⁹¹ In the subchapter above, higher alcohol formation was mainly described from carbon monoxide synthesis gas. To achieve that, the carbon dioxide will be converted to carbon monoxide changing the primary carbon source.⁹² The water-gas shift reaction was introduced in chapter 2.1.1 Methanol synthesis on page 5 as a possible reaction preventing catalyst deactivation by consuming water and providing simultaneously the more favoured carbon dioxide as educts for methanol formation.^{30, 58, 61} Because of the reversibility of chemical reactions, it is not surprising, that the reverse water-gas shift (RWGS) reaction will be catalysed by Cu/ZnO.^{93, 94} Typically temperatures around 170 – 280 °C at ambient pressure are used.⁹³



Zinc oxide does rather act as a structural promoter preventing copper particle sintering during RWGS than enhancing catalyst activity by the copper-zinc-synergy as seen by the absence of a clear correlation of catalytic activity and surface oxygen coverage.^{6, 95} One reason of that could be, that during the conversion of carbon dioxide to carbon monoxide an oxygen is left on the copper surface area which consecutively will be hydrogenated to water which then desorbs.⁹⁶ In that case an oxygen covered copper surface would inhibit the desired reaction. A

composition-activity study has demonstrated, that the RWGS activity of Cu/ZnO is to some extent independent of the Cu/ZnO interphase but more dependent of the composition. An increased activity in RWGS was determined for compositions of Cu:Zn = 40:60 and Cu:Zn = 50:50 demonstrating an activated ZnO by an increased number of oxygen vacancies activating the CO₂, as it was confirmed by trivalent cation doped ZnO impregnated with copper, then a copper-zinc synergistic effect.^{37,94} The effect of oxygen vacancies on the RWGS activity was also demonstrated on Cu-Al spinel in comparison to a Co-Al spinel in the temperature range of 250 °C – 400 °C. The Cu-Al spinel had a higher number of oxygen vacancies which activated carbon dioxide for the RWGS reaction. Contrarily, the Co-Al spinel contained a low amount of oxygen vacancies and was less active in the reaction. A treatment in sodium hydroxide had enriched the oxygen vacancies concentration and with that the activity of the Co-Al spinel catalyst increased.⁹⁷ The Ni/Al₂O₃ catalyst is highly active in RWGS obtaining equilibrium conversion at 700 °C with a contact time of 100 ms and a maintained catalyst stability up to 1000 °C without any sinter effects.⁹¹

Altogether, the short excursion through the different reaction systems should have visualized, that Cu/ZnO can be used in many reaction systems as catalyst. Both, the activation of carbon dioxide and carbon monoxide are possible, but the reaction conditions, the availability of specific surface sites or additional promoters define the preferred reactant and product, demonstrating a close connection of the catalytic processes and the catalyst nature and the motivation on the clarification of this interplay.

The copper based catalysts are often compared regarding their specific copper surface area. For this reason, the chemisorption methods to determine the copper surface area will be elucidated in the next section.

2.2 Characterization of copper-surface areas by chemisorption methods

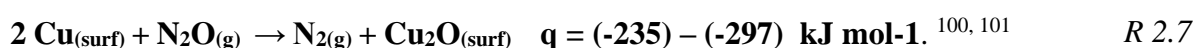
The copper surface area determination is a common tool to determine the possible intrinsic activity of copper catalysts. Because of the undisputed knowledge, that copper is the active metal in methanol synthesis, the copper surface area can be depicted as a measure for a certain reactivity. In principle in heterogeneous catalysis, there is a rule of thumb, that an increased surface area of a solid catalyst result in an increased possible activity because of more exposed catalytic active sites. From that point of view, the specific surface determination of the reactive metal, like copper, does increase the accuracy of the prepeded rule of thumb allowing a more accurate description of the catalyst's intrinsic activity, which is found by a linear correlation of the copper surface area and the catalyst activity.^{98,99}

There are three common technics which can be used to determine the copper surface area: the temperature programmed desorption (H₂-TPD) and the transient adsorption (H₂-TA) of hydrogen as well as the reactive frontal chromatography (N₂O-RFC) of N₂O.

In the following sections each method will be introduced followed by a discussion of the significance regarding the catalytic active surface.

2.2.1 N₂O reactive frontal chromatography

The N₂O reactive frontal chromatography is a method of N₂O decomposition on the copper surface. The reaction is shown in R 2.7. During the reaction a heat around 235 - 297 kcal mol⁻¹ will be released because of the exothermic character.^{100, 101}



To avoid copper particle sintering because of the released heat a low contact time is required to keep the sample isothermal.¹⁰² The reaction does create a half monolayer of oxygen on the reduced copper surface, by forming the cuprous oxide (Cu₂O).¹⁰³ In general the method can be performed by pulse sequence or flow method, without any restrictions or quality loss.¹⁰²⁻¹⁰⁴ The flow method can be performed in any tubular reactor with coupled analytics and does not need a separation of the N₂O residue as in pulse experiments with thermal conductivity detector (TCD).^{103, 104} The immediate consumption of the N₂O and the resulting nitrogen evolution has given the name of reactive frontal chromatography to this method.¹⁰³ R 2.7 is complete, when the breakthrough point of N₂O is reached.¹⁰³ An example of a typical concentration profile is given in Figure 2.1.

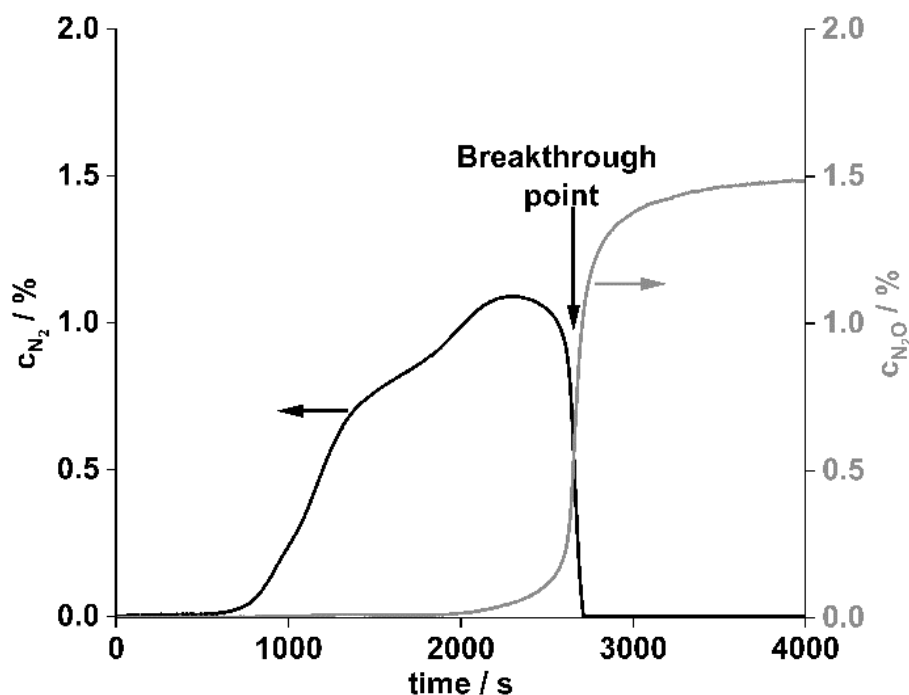


Figure 2.1: Typical concentration profile of a N_2O -RFC measured by mass spectroscopy.

This method is less affected by the used N_2O concentration at room temperature as long as the reaction heat can be removed but is strongly affected by the reaction-temperature.^{102, 103} Too high temperature leads to an enhanced reactivity, which will enable a complete surface oxidation of the different copper facets but does also lead to a sub-surface/bulk oxidation of the copper particles. The formation of bulk copper oxide does start at temperatures around >90 °C and can be enhanced by other metal oxides.¹⁰³⁻¹⁰⁶ Beside the bulk oxidation, a cycle of reduction and oxidation decreases the copper surface area, because of the altering of the copper particles.¹⁰³

2.2.2 Temperature programmed hydrogen desorption

The temperature programmed adsorption is an alternative characterization method to determine the copper surface area. Contrarily to the N_2O -RFC, this method does require a proper cooling of the catalyst bed to reach temperatures of -195 °C.¹⁰⁷ The proposed reaction equation of the adsorption (from left to right) is shown in R 2.8.¹⁰⁸



Before investigating the desorption process, the reduced catalyst is treated with hydrogen to achieve an equilibrium of adsorbed hydrogen and gas phase.¹⁰⁷ A complete surface coverage can be reached after adsorption for one hour at 15 bar and pure hydrogen, whereas a double of time at ambient pressure does only result in a nearby covered copper surface of around 84 %

and 27 % if dilute hydrogen for 6 hours was used.¹⁰⁸ The treatment in hydrogen is performed for roughly one hour at 220 °C followed by cooling to -23 °C and afterwards to -195 °C. Before the desorption is performed, the gas atmosphere is changed to helium as mobile carrier gas.^{107, 108} Dissociative adsorbed hydrogen at polycrystalline copper does associatively desorb at around 27 °C whereas a desorption around 230 °C was assigned to some copper-zinc oxide interactions.¹⁰⁷⁻¹⁰⁹ The H₂-TPD method has the advantage, that it is reproducible without changing the copper surface area in contrast to the N₂O-RFC where an ageing was observed after a certain number of cycles.^{103, 107} Among the measurement variables, the flow rate, cooling- and heating ramp as well as the pre-treatment conditions do affect the measurement and should be kept constant for catalyst comparison.¹⁰⁷

2.2.3 Transient hydrogen adsorption

From the N₂O-RFC copper surface oxidation, one could examine the amount of oxygen and thus the copper surface area, by initializing the back reaction, as it was performed by Chinchen *et al.*¹⁰³ and Naumann d'Alnoncourt *et al.*¹¹⁰ with CO as probe molecule. These experiments have demonstrated that the back titration does work and reproduce the N₂O-RFC results.^{103, 110} The mechanism of that reduction process is of autocatalytic nature for the Cu₂O surface but requires a temperature around or above 240 °C.^{103, 111} On the other hand, the back titration can also performed with hydrogen at room temperature.¹¹²

The back reaction with hydrogen is described in R 2.9. The titration of the Cu₂O surface with hydrogen does only reduce the surface layer of copper and the formed water stay adsorbed on the copper surface.¹¹²



The back titration with hydrogen of a Cu₂O surface is shown in Figure 2.2. The typical drop of the hydrogen signal indicates the reduction. Because of the low amount consumed hydrogen, a low gas concentration and a high catalyst amount is needed. Another disadvantage of that method is, that it has a lower accuracy by underestimating the real copper surface area around 12 %.¹¹²

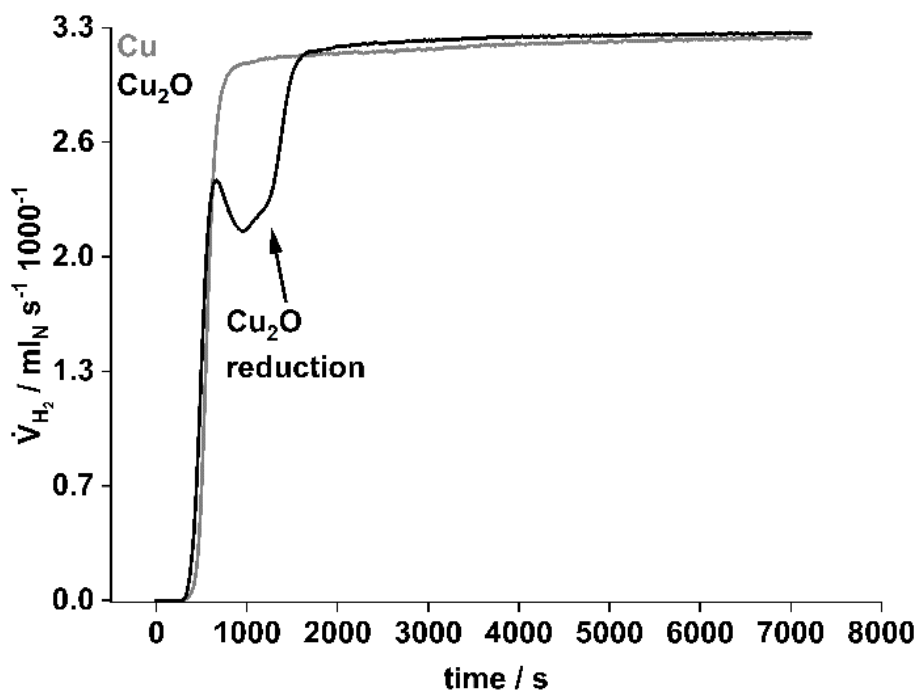


Figure 2.2: Back titration of Cu_2O with H_2 at room temperature, analysed by MS.

2.2.4 Benefit and limitation of the chemisorption methods

The above described chemisorption methods are regularly used to describe copper catalysts. The accordance of the different characterization methods was reviewed and found to agree with each other as long as no zinc oxide is present. The assumed molecular hydrogen adsorption on two copper atoms could be experimentally corrected to a ratio of $\text{Cu}:\text{H}_2 = 3$.^{69, 113} The presence of zinc does complicate the copper surface determination because of reduced Zn sites forming a surface alloy, which does additionally react with N_2O to form ZnO .^{22-25, 69} That is the reason, why for zinc containing catalysts the N_2O -RFC method results in overestimated copper surface areas.^{69, 113} There is no evidence, that the observed hydrogen desorption at 30°C is affected by Cu-Zn surface alloy or by partial reduced ZnO_x sites, contrarily a clear copper surface decrease was determined by increasing zinc content in the copper surface which was in alignment with H_2 -TPD analysis of the same samples.^{107, 112, 114} If the zinc sites are oxidized, temperatures around 250°C are needed, to establish again a copper-zinc surface alloy.²³ Therefore, the back titration with CO is disadvantageous as it could rebuild defective zinc oxide sites (as it was shown by the In_2O_3 methanol catalyst), which would cause a similar error to N_2O -RFC.^{65, 103} From that point of view, the H_2 -TA has the advantage, that it can be performed at room temperature, reducing Cu_2O without affecting ZnO and recovering only the copper surface.¹¹² With that knowledge, the Cu/ZnO catalyst can be characterized in an extended way, resolving the defective zinc oxide sites, the copper surface area and the surface alloy, by combining N_2O -RFC and H_2 -TPD or H_2 -TA analysis.^{69, 112, 114}

However, the only inert supports for copper catalysts are copper itself and carbon.¹¹³ Several metal oxides have been affected the chemisorption methods and illustrate the need of careful validation of the characterization data.¹¹³

2.3 Material synthesis

This chapter is used to introduce the material classes and precursor systems of prepared catalysts or support materials. The main preparation method was co-precipitation with followed calcination of the precursors to obtain defined material states for further investigations. Therefore, the precursor classes and their corresponding oxides are introduced.

2.3.1 Material preparation via (co-)precipitation

Precipitation does describe the preparation of a solid from a solution. In a simpler way and in the context of inorganic chemistry, it means, that an acid and a base must be brought together, from which a salt can be formed. The co-precipitation does describe the same process, but with more than one component, which has to form a solid (*e.g.*, Cu and Zn).^{8, 115} The precipitation method is a commonly used process in catalytic material preparation. Some advantages are the homogeneity of the solid, the control of metal composition but also the possibility to separate the catalyst from a liquid by filtration.¹¹⁵

The next subchapters describe some minerals which can be synthesized by (co-)precipitation and are representatives of typical precursor systems used in heterogeneous catalysis.

2.3.1.1 From malachite precursor phase to the activated form of catalyst

Malachite is the name of a copper hydroxycarbonate with the sum formula $\text{Cu}_2\text{CO}_3(\text{OH})_2$. The monoclinic unit cell of the crystal structure is visualized in Figure 2.3.¹¹⁶

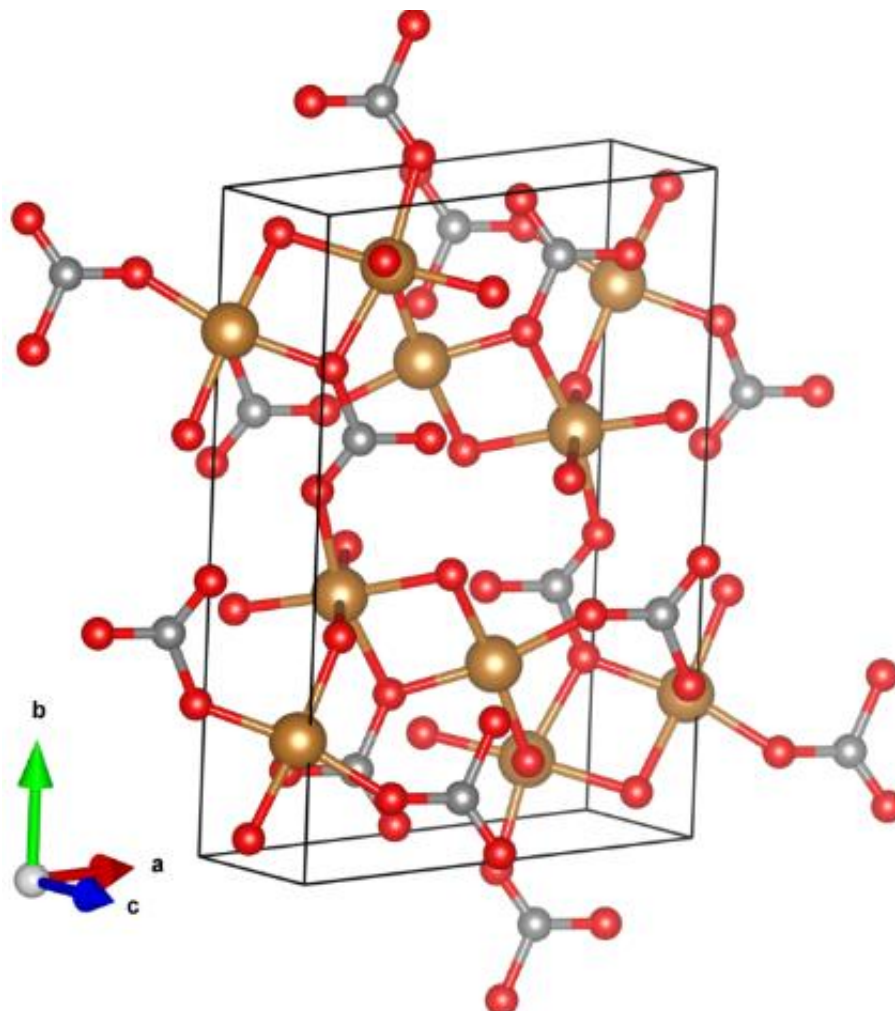


Figure 2.3: Visualisation of the malachite structure of one unit cell. The copper atoms are brownish-red, carbon atoms are grey and the oxygen atoms are red coloured. The picture was created with VESTAS¹¹⁷ from the ICSD reference:#30609¹¹⁶.

In catalyst preparation, the Zn substitution of copper atoms of the malachite structure is used to synthesize a homogeneous copper-zinc precursor phase. The resulted zinc substituted malachite structure $(\text{Cu}_{1-x}, \text{Zn}_x)_2\text{CO}_3(\text{OH})_2$ is often called zincian malachite and is limited to a maximum substitution of around 30 % Zinc.¹⁰ A further increase of zinc does result in the side-phase aurichalcite, which is less beneficial for the synthesis of Cu/ZnO catalysts than malachite.¹⁰ From characterization perspective, the success of zinc substitution into the malachite structure is often determined by the decreased lattice distance of the 20-1 and 21-1 plane, because of the reduced Jahn-Teller distortion of the CuO_6 octahedra by substitution them with the more uniform ZnO_6 octahedra.^{118,119} It was further found, that the structure does allow to incorporate

beside zinc additionally up to 3 % – 4 % aluminium, which is of high interest regarding the state of the art copper methanol catalyst (CZA).^{34, 57}

Typically, the precipitation is performed from metal nitrates with sodium carbonate as precipitation agent at 65 °C with a *pH* of 6 – 7 and an ageing time of around one hour. After precipitation an amorphous little specific solid is formed which crystallizes, because of the supersaturated solution, during the ageing step into the malachite structure indicated by a *pH*-drop and by colour change of the solid from blue to green.^{8, 33, 57, 120}

The obtained precursor is afterwards decomposed into the corresponding metal oxides in a temperature range of 330 °C – 400 °C, which can be activated in a further step reducing CuO to Cu with diluted hydrogen at 160 °C – 250 °C.^{8, 15, 62}

2.3.1.2 **Synthesis of hydrotalcite-like precursors and their mixed metal oxides**

Hydrotalcite is a mineral which was originally assigned to a solid containing magnesium-aluminium hydroxides and carbonates. This mineral has a layer structure formed by a mixture of binary and ternary metal ions and is additionally known as a “layered double hydroxide” material.¹²¹ Layered double hydroxides are in general layered materials with the general stoichiometric formula of: $[M^{II}_{1-x}M^{III}_x(OH)_{2x}]^{x+}(A^{n-})_{x/n} \cdot mH_2O$ with M^{II} as a divalent cation like Mg or Zn which is partially substituted by M^{III} , a trivalent cation like Al or Ga. The interlayer anion (A^{n-}) can be carbonate-, nitrate- or other anions which compensate the additional positive charge, introduced by the trivalent cation, of the metal hydroxide strata.¹²¹⁻¹²³ An example of a layer-interlayer arrangement is given in Figure 2.4. Brucite $Mg(OH)_2$ forms the motive of a layer by developing $Mg(OH)_6$ octahedra. The layers are connected to each other by electrostatic adsorption and hydrogen bonds.¹²¹

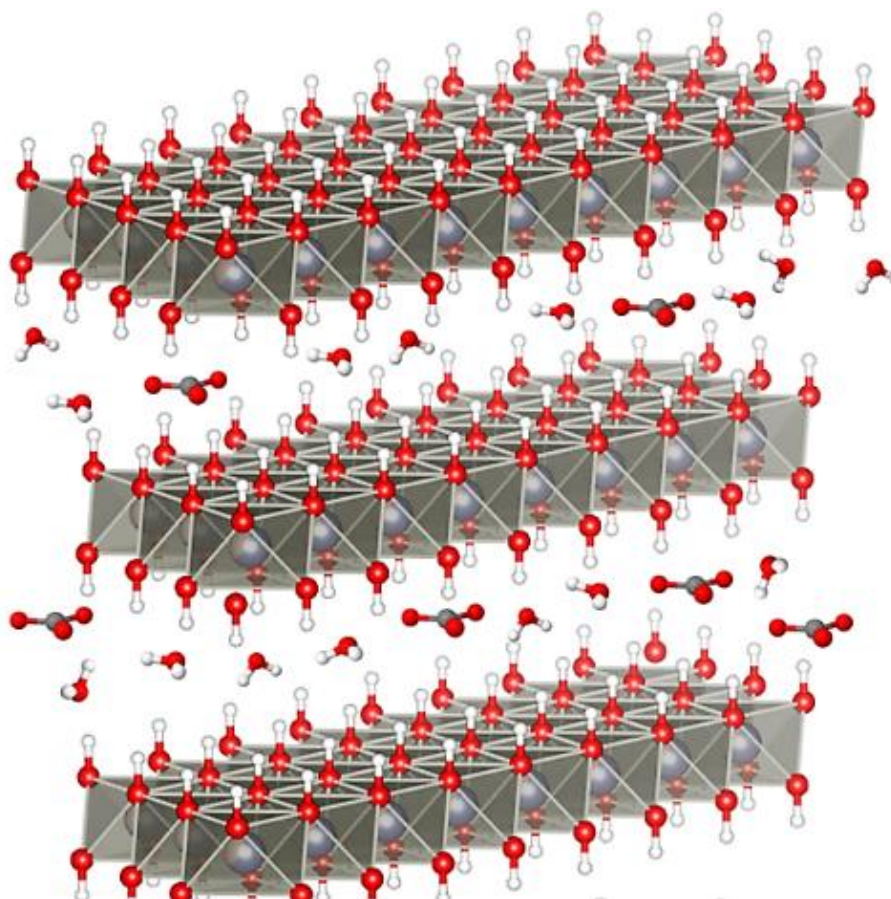


Figure 2.4: Example of a hydrotalcite-like layered motive with carbonate ions and water in the interlayer. Oxygen atoms are red, Carbon is grey, hydrogen is white, with grey brownish octahedra containing zinc (purple-blue) and aluminium (brown-grey) metal ions. The layer was created with VESTAS¹¹⁷ as a variation of the ICSD reference 155052¹²².

The heat treatment up to 500 °C of hydrotalcite-like materials forms, dependent of the cations, mixed metal oxides, also named layered double oxides, which are characterized by a uniform cationic distribution because of the single-phase precursor.^{121, 123} The precursor class enables the possibility of spinel formation, which are temperature stable oxides with metal catalyst stabilizing character expanding the application range of metal catalysis to high temperatures (e.g., Methane dry reformation at 900 °C).^{32, 33, 121, 124}

The material synthesis of hydrotalcite-like precursors is often performed at a constant pH around 8-9 to reach a precipitation of all cations and at 50 °C – 60 °C with ageing time around 30 – 60 minutes. In general, the precipitation can be performed with sodium hydroxide as precipitation agent but most important is the presence of enough interlayer anion to allow the crystallization of the hydrotalcite-like precursor phase.^{121, 123-125}

2.3.1.3 Synthesis of hydrozincite precursors and zinc oxides

Hydrozincite is a hydroxy carbonate mineral of zinc. This mineral of monoclinic structure has the stoichiometric formula of $\text{Zn}_5(\text{CO}_3)_2(\text{OH})_6$ which is similar to the copper containing aurichalcite structure.^{126, 127} Hydrozincite contains octahedral- and tetrahedral coordinated zinc atoms in the ratio 3:2.¹²⁶ The structure of hydrozincite was depicted as a negatively charged sheet with $[\text{Zn}_3(\text{OH})_6\text{O}_2]^{4-}$ as motif, built of uniform octahedra. To compensate the charge, the sheets are connected to each other via a tetrahedrally coordinated zinc atom and a carbonate bonded by one oxygen to the sheet motif.¹²⁶ Earlier investigations found that the sheet structure can be distorted, which was observed as a hydroxide group enrichment and a carbonate depletion by breaking the layer sequence. Interestingly, this distortion was reversible by treating with carbon dioxide reconstituting the layer structure.^{126, 128} The unit cell of this material is shown in Figure 2.5.

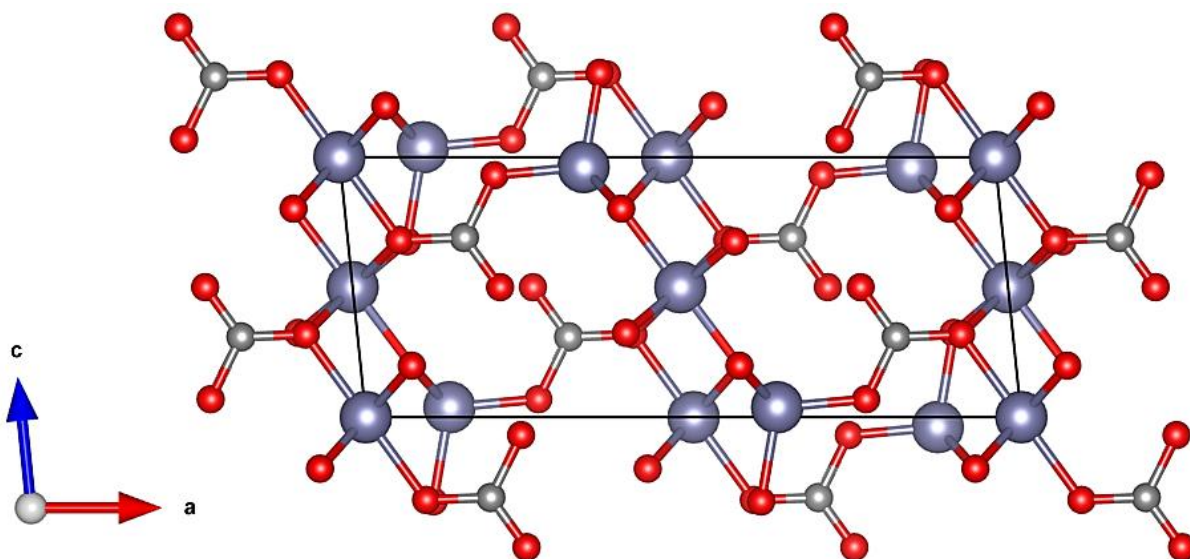


Figure 2.5: Demonstration of the unit cell of hydrozincite. The *b*-axis is parallel to the viewing direction. The zinc atoms are purple blue, the oxygen atoms are red and carbon is grey coloured. The figure is created with VESTAS¹¹⁷ from the ICSD reference #16583¹²⁶.

In terms of catalysis, this material is of interest as a model support, representing the zinc oxide of a typical Cu/ZnO catalyst. Because of the similarity to malachite or aurichalcite, which are also materials for catalysis applications, the hydrozincite can analogously synthesized via precipitation.^{35, 37, 129}

The synthesis of hydrozincite is typically performed by precipitating a zinc nitrate solution with sodium carbonate at $pH = 6.5 - 7$ at $65\text{ }^\circ\text{C}$ followed by ageing of around two hours in the mother liquor. This method does allow to incorporate trivalent cations, which after decomposition in air at $330\text{ }^\circ\text{C}$ does form a doped zinc oxide ($\text{ZnO}:\text{M}^{\text{III}}$).^{37, 129}

The doping of zinc oxide is not only in terms of heterogeneous catalysis but also in terms of semi-conductors of interest by tuning the electronic structure. In both areas oxygen vacancies and band-gap energies are expected to enhance the material properties.^{38, 130}

2.3.1.3.1 Zinc oxide

Zinc oxide can crystallize in the wurtzite, sphalerite or rock salt structures. At ambient conditions, the wurtzite structure is thermodynamically more stable and represents therefore the main common zinc oxide structure. The wurtzite structure is formed by two interpenetrating hexagonal lattices with tetrahedrally coordinated zinc atoms.³⁸ The unit cell and the hexagonal character of the zinc oxide structure are demonstrated in Figure 2.6.

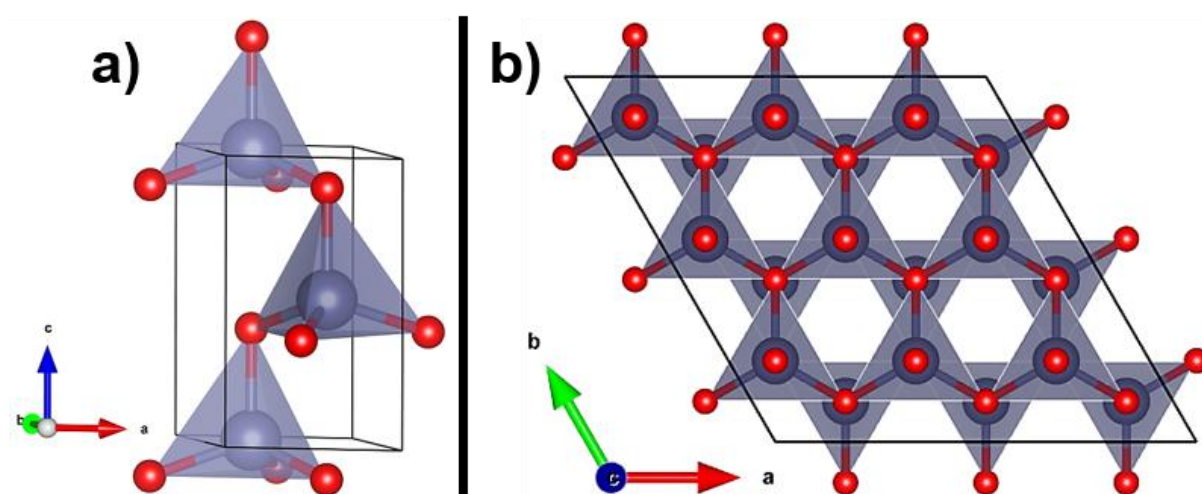


Figure 2.6: Visualisation of the wurtzite ZnO unit cell in a) and the hexagonal structure along the c-axis of three unit cells in b) (the c-axis is parallel to the viewing direction). Zinc atoms are purple-blue and oxygen atoms are red coloured. The pictures are prepared in VESTAS¹¹⁷ from the ICSD reference #26170¹³¹.

There is a variety of preparation methods which sometimes involves a precursor phase, like precipitation or sol-gel process but also direct routes are possible like precipitation, solvothermal synthesis or spray-pyrolysis.^{130, 132} This oxide is characterized by a direct band gap of around 3.37 eV.^{38, 130} Zinc oxide contains intrinsic and extrinsic defects. Intrinsic defects are naturally present in the oxides and are often a result of the oxide preparation history like heat treatment or ageing. Such defects are for example oxygen vacancies, zinc- or oxygen interstitials.^{38, 130, 133} This intrinsic defects do affect the band gap energy as well as extrinsic defects caused by ion substitution like Al or Ga incorporated into the zinc oxide host lattice.^{130, 133, 134} This extrinsic defects are used for band gap engineering. N-type doping (donor doping) is the insertion of an additional negative charge increasing the electron concentration, contrarily to the p-type doping (acceptor doping) which inserts an additional positive charge increasing

the hole concentration.^{130, 135} Hence, if electronic processes are of important relevance for an application, a band gap narrowing and n-doping is envisaged. Group 13 elements are known as n-type semiconductor dopants and used to engineer the band gap of zinc oxide.¹³⁶ But such a doping must not have to result in a narrowed band gap, because of the energy nature of the valence- and conducting band.¹³⁶ In general, an electron will be lifted from the highest valence band state to the lowest free conducting band state. If the lowest free conducting band state is occupied by an electron, introduced by dopant incorporation into the host lattice, the excited electron has to join the next free lower energy level, which is on higher energy state. This phenomenon is named *Burstein-Moss effect*.^{137, 138} On the other hand does a perfect substitution of a zinc ion by a trivalent cation, like Al, narrow the band gap as a renormalization process.¹³⁹ Other defects like strains could induce a band gap shrinkage whereas a side phase of an isolator does widen the band gap and inhibit electron conductivity.¹⁴⁰⁻¹⁴³ Because of the most promising approach to enhance the opto-electronic properties of zinc oxide by an trivalent cation doped zinc site (M^{III}_{Zn}), a variety of research groups have determined the solubility limit for Al_{Zn} .¹³⁹

The determined solubility limits are in range of 0.3 % and 5.4 %.¹⁴³⁻¹⁴⁹ The results of investigation supported by solid state NMR seemed to be plausible because of the sensitivity to the Al_{Zn} defect isolating the solubility limit to a smaller range of 0.3 % – 1 % after temperature treatments around 300 °C – 850 °C of the precursor phase.^{142, 143, 149}

However, the higher determined solubility limit of 1 % after calcination at 300 °C gives evidence, that a similar doping effect could be induced by catalyst preparation because of selected temperatures for a mild calcination and reduction.^{8, 33, 142}

3 Experimental

Each chapter does contain a brief description of the individual experimental part. Nonetheless, because of importance, the maths behind the chemisorption methods will be introduced.

3.1 Copper surface determination

The chemisorption experiments to determine the copper surface area are performed in a BelCat B from Bel Japan Incorporation. The variety of gas connections allows the use of a specific gas for each experiment.

For the chemisorption experiment were 100 mg copper catalyst in the sieve fraction of 125 – 250 μm applied. The catalyst bed was fixed with quartz glass wool to prevent a flushing out. Before each experiment was started, the catalyst was dried for one hour in 120 °C in 35 $\text{ml}_\text{N} \text{min}^{-1}$ of argon. To avoid thermal stress a heating rate equivalent to the calcination (2 °C min^{-1}) was applied. The chemisorption measurements were carried out in the following sequence: H_2 -TA of the Oxide, TPR, H_2 -TA of the reduced state, N_2O -RFC, H_2 -TA of the Cu_2O , N_2O -RFC, TPR. The experimental conditions are listed in Table 3.1. Before each experiment was started, the catalyst bed was flushed with the dilution gas of the following experiment. If the MS was used as analytics, the trap was bypassed. Before starting a new experiment, the MS was calibrated by a calibration gas of 2 % H_2 , 1 % N_2 and Helium to reach highest accuracy.

Table 3.1: Experiment conditions of the individual measurement step of the chemisorption analysis.

<i>Experiment</i>	<i>Temperature / holding time</i>	<i>Volume flow</i>	<i>Gas composition</i>	<i>Analytic</i>
H_2 -TA	40 °C / 60 Min	8 $\text{ml}_\text{N} \text{min}^{-1}$	2 vol.- % H_2/He	MS
N_2O -RFC	60 °C / 60 Min	5 $\text{ml}_\text{N} \text{min}^{-1}$	1 vol.- % $\text{N}_2\text{O}/\text{He}$	MS
TPR	275 °C / 240 Min	35 $\text{ml}_\text{N} \text{min}^{-1}$	5 vol.- % H_2/Ar	TCD

As shown in section 2.2.3 on page 15 the H_2 -TA signal of the back titration of Cu_2O does vary in the shape in contrast to the “blank” measurement of the reduced sample. If one think about adsorption processes during the H_2 -TA experiment, the adsorption would result in a variation of the slope of the H_2 -Signal (assumption: all measurements are performed at strictly equal conditions). Then the measurement of the Cu_2O surface could be corrected by this adsorption

term, if both measurements are subtracted from each another. This treatment yield in the reaction term, as the consumed amount hydrogen caused by back titration. From that thinking the question about the meaningfulness to measure the CuO surface by H₂-TA rises. Therefore, the measurement was expressed by a system of equations.

The expression of only the adsorption term, measured by the slope change between an inert (CuO) surface and an adsorptive surface (Cu) is given by:

$$n_{H_2-adsorbed} = A_{H_2TA,CuO} - A_{H_2TA,Cu} \quad M\ 3.1$$

With that the expression of the reaction measurement of Cu₂O would be given as:

$$n_{H_2-adsorbed} + n_{H_2-consumed} = A_{H_2TA,CuO} - A_{H_2TA,Cu_2O} \quad M\ 3.2$$

The subtraction of both equation does result in the equation of the separated reaction term.

$$n_{H_2-consumed} = A_{H_2TA,Cu} - A_{H_2TA,Cu_2O} \quad M\ 3.3$$

This mathematical examination does demonstrate that the measurement of the inert surface is only necessary for illustration rather than for measurement evaluation.

From the H₂-TA and N₂O-RFC experiment, one can calculate the copper surface area by the equation M 3.4 with the area of one copper atom: $0.068 \cdot 10^{-18} \text{ m}^2 \text{ atom}^{-1}$.¹⁵⁰

$$A_{Cu} = \frac{n_i \cdot N_A \cdot a}{x \cdot m_{Catalyst}} \forall i = H_{2-consumed} \mid i = N_{2-evolved} \quad M\ 3.4$$

The precision of the copper surface area determination could be proven by calculating the copper crystallite size from the H₂-TA results. The interpretation has to be done carefully, because of the covered parts of the surface by ZnO, the copper crystallite size will be overestimated. However, it is expected, that the copper crystallite size (*ex* H₂-TA) will be in a closer range to the crystallite size determined by XRD analysis than the copper crystallite size determined by N₂O-RFC. If this is not true, further investigations on method improvements must be done.

$$d_{Cu} = \frac{f \cdot W_{Cu,solid}}{A_{Cu} \cdot \rho_{Cu}} \quad M\ 3.5$$

With the combination of the methods, according to literature^{69, 112, 114} the defective zinc sites can be calculated as followed:

$$n_{\text{ZnO}_{\text{defects}}} = n_{\text{N}_2\text{-evolved}} - n_{\text{H}_2\text{-consumed}} \quad M\ 3.6$$

The knowledge about the copper and zinc content in the catalyst can be used to calculate a dispersion, which means, that a specific fraction of copper is in touch with the gas phase and another specific fraction of zinc oxide is in touch with gas phase and copper surface.

The dispersion could additionally be calculated by the surface area. This analysis requires the knowledge of the surface area, determined by nitrogen physisorption of the activated catalyst and the strict analogous mathematical treatment of H₂-TA and N₂O-RFC results. Because of some deviations about the space occupied by one copper atom^{69, 103, 150}, one value must be chosen and kept constant for comparison. If calculating specific surface areas, they must be based on the mass of inserted metal oxide, to become comparable. The minor mass deviation of some non-decomposed precursor species is expected to be smaller than the mass deviation of a completely reduced catalyst. The normalizing of the surface area to the mass of a reduced catalyst forbids a comparison of different measurements (*e.g.*, BET and N₂O-RFC) and inhibits an analysis of the surface evolution.

The dispersion is expressed as:

$$D_j = \frac{n_i M_j}{W_{j, \text{solid}} \cdot x} \cdot 100 \% \quad \forall i = \text{H}_2\text{-consumed} \mid i = \text{N}_2\text{-evolved} \quad M\ 3.7$$

4 On the secondary promotion effect of Al and Ga on Cu/ZnO methanol synthesis catalysts

Benjamin Mockenhaupt^{ab}, Jil Gieser^a, Sharif Najafishirtari^{ab}, Lorena Baumgarten^{cd}, Jelena Jelic^d, Thomas Lunkenbein^e, Erik-Jan Ras^f, Jan-Dierk Grunwaldt^{cd}, Felix Studt^{cd}, Malte Behrens^{*ab}

- a. B. Mockenhaupt, J. Gieser, M. Behrens, Institute of Inorganic Chemistry, University of Duisburg-Essen, Universitätsstr. 7, 45141 Essen (Germany).
- b. B. Mockenhaupt, S. Najafishirtari, M. Behrens, Institute of Inorganic Chemistry, Christian-Albrecht University of Kiel, Max-Eyth-Str. 2, 24118 Kiel (Germany), E-Mail: mbehrens@ac.uni-kiel.de.
- c. L. Baumgarten, F. Studt, J.-D. Grunwaldt, Institute for Chemical Technology and Polymer Chemistry (ITCP), Karlsruhe Institute of Technology (KIT), 76131 Karlsruhe (Germany).
- d. L. Baumgarten, J. Jelic, F. Studt, J.-D. Grunwaldt, Institute of Catalysis Research and Technology (IKFT), Karlsruhe Institute of Technology (KIT), 76344 Eggenstein-Leopoldshafen (Germany).
- e. T. Lunkenbein, Department of Inorganic Chemistry, Fritz-Haber-Institut der Max-Planck Gesellschaft, Faradayweg 4–6, 14195 Berlin (Germany).
- f. E.-J. Ras, Avantium Technologies B.V., 1014 BV Amsterdam (The Netherlands).

* Corresponding author

Contribution of the authors

- B.M.: conceptualization, visualization, data curation, and writing—original draft preparation.
J.G.: conceptualization, chemisorption analysis, visualization, data curation, and writing—reviewing and editing.
S.N.: conceptualization, DRIFT analysis, visualization, data curation, and writing—reviewing and editing.
L.B.: conceptualization, XANES analysis, visualization, data curation, and writing—reviewing and editing.
J.J.: conceptualization, DFT calculations, and writing—reviewing and editing.
T.L.: conceptualization, TEM analysis, validation, and writing—reviewing.
E.J.R.: conceptualization, catalysis, data curation, validation and writing—reviewing.
J.D.G: conceptualization, funding acquisition, supervision, and writing—reviewing and editing.
F.S.: conceptualization, funding acquisition, supervision, and writing—reviewing and editing.
M.B.: conceptualization, project administration, funding acquisition, validation, and writing—reviewing and editing.

Abstract

The structural and electronic effect of Al and Ga as ternary metals in Cu/ZnO catalysts for the methanol synthesis was examined. For this purpose, three zincian malachite-derived catalysts with the nominal Cu:Zn ratio of 70:30 were synthesized: an unpromoted, binary catalyst (CZ) and two ternary catalysts with either 3 mol% Al (CZA) or Ga (CZG). Both Al and Ga showed to have a strong impact on the catalyst's structure. Alongside the catalyst treatment from the co-precipitated precursors phase to the activated and reduced catalyst an improved microstructure and an increased BET surface area was found for the secondary promotor (Al or Ga) containing catalysts. Moreover, a sequence of chemisorption experiments allowed to quantify and differentiate between Cu^{surf} and Zn^{red} surface species in the activated catalysts. Considering the specific copper surface areas, DRIFTS data and catalytic results, an additional electronic promotion of Al and Ga could be determined. This promotion effect is related to doped ZnO phases, as it was demonstrated by XANES and enhances the reducibility of the ZnO by forming more Zn^{red} sites. This effect is stronger for Al, leading to a more pronounced Zn overlayer on the Cu surface and SMSI. In the methanol synthesis, this led to a performance in the order $\text{CZA} > \text{CZG} > \text{CZ}$.

4.1 Introduction

Methanol synthesis is among the most important processes of the chemical industry. Methanol is used as platform chemical, fuel additive or solvent. Moreover, it has great potential as an energy carrier as it is an attractive target molecule of power-to-liquid approaches if anthropogenic CO_2 and so-called green hydrogen is used in the synthesis gas.^{51, 151} Historically, the industrial process evolution was mainly influenced by the co-evolution of the catalyst material,¹⁻³ which is a composite catalyst comprised of a large fraction of Cu metal (typically >60 %), zinc oxide and additional promoters (typically <10 %) since the access to sulphur-free synthesis gas in the 1970s.¹⁵²

The composition of the current state-of-the-art catalyst has not changed much since then and currently, methanol is produced in the low temperature process at approximately 250 °C and at least 50 bar over such copper/zinc oxide/aluminium oxide (CZA) catalyst, while other promoters might also be present.^{4,5} This catalyst was subject of intensive research with the aim to understand its functionality and to rationally optimize its synthesis and it is of ongoing great interest today. It is well known that both copper and zinc oxide are needed to receive the highest catalyst performance by a high activity and a simultaneously increased stability and long

lifetime of the copper nanoparticles in the catalyst. The main reason for the increased stability is the structural promotion effect of zinc oxide, which prohibits copper sintering and increase the copper particle dispersion.^{6, 7} This can be seen in the catalyst's typical microstructure, which is comprised of small zinc oxide particles located between the larger copper particles (around 10 nm) preventing them from sintering and forming porous sponge-like aggregates as a result of the co-precipitation synthesis.^{34, 153} For an optimal copper/zinc ratio to reach the highest dispersion a roughly equimolar amount of both components was proposed.⁸ However, because the maximum zinc amount in the preferred co-precipitated precursor phase, zincian malachite, is limited to approximately 30 %, the molar composition of the industrial catalyst is around 70:30 Cu/Zn.^{10, 11} The zinc oxide phase thus is denoted the primary promoter to copper metal in this contribution and it operates as a structural promoter increasing and stabilizing the exposed copper surface area.

Beside this rather static model of structural promotion of zinc oxide, the famous and widely studied copper-zinc synergy furthermore leads to an additional form of promotion. These strong, dynamic and reversible copper-zinc oxide interactions rather operate *via* an electronic effect leading to a high intrinsic activity.^{9, 17-19} At reducing conditions, a few zinc oxide species migrate on top of the copper particles as a result of strong metal support interactions (SMSI) giving rise to an "inverse" surface configuration with reduced zinc oxide species decorating the metal surface.^{15, 20, 21} Upon catalyst reduction in hydrogen, even a surface-alloy was observed.^{24, 112, 114, 154} In the temperature range between 250 °C and 340 °C, it co-exists with (partially oxidized) ZnO_x surface species and transforms into a bulk alloy at higher temperatures.¹⁵⁴ While the promoting role of this SMSI for methanol synthesis is well established, there is a controversial debate, whether a bi-phasic copper-zinc oxide interface with a perimeter ($0 < x < 1$) or a monophasic metallic copper-zinc surface alloy ($x = 0$) is the better description of the active surface of the Cu/ZnO catalyst.²⁵⁻²⁸ Independent of the exact value of x , we will refer to these species as reduced zinc surface species Zn^{red} in this paper to contrast the metallic copper surface sites (Cu) that are not promoted by zinc and the fully oxidized ZnO support ($x = 1$), which likely acts as a reservoir for the Zn^{red} species.

In this work, we acknowledge the dual role, structural and electronic, of the primary zinc oxide promoter, but we will not aim at addressing the exact nature of Zn^{red}, which has been proposed to be responsible for activation of the formate intermediate for further hydrogenation towards methanol.^{16, 22, 155, 156} We rather investigate on the role of the secondary promoter aluminium oxide by comparing three catalysts with a Cu:Zn ratio of 70:30. Two of them contain 3 mol% (metal basis) of a secondary promoter and one is a binary reference catalyst Cu/ZnO (CZ). The

two promoting species are aluminium as in the industrial catalysts (CZA), and its higher homologue gallium (CZG). Gallium has been recently identified to be an interesting promoter for CZ,^{34, 37} and the relatively low amount of 3 mol% secondary promoter has been shown previously to lead to a maximal promotion effect.³⁴ The CZA catalyst with 3 mol% Al is a well-studied catalyst material, previously named FHI-Std.,⁵⁷ which has been deeply characterized and employed as a benchmark in numerous contributions.^{14, 20, 31, 57, 157} Herein, we report advanced chemisorption experiments on the three catalysts CZ, CZA and CZG in addition to numerous other characterization methods to find evidence for another dual role of the secondary promoter, structural and electronic, in methanol synthesis from CO and CO₂ at industrially relevant long time-scales. We use this new information to propose a general and comprehensive picture of the catalyst's microstructure and its dynamic surface state in methanol synthesis including the dual roles of both primary and secondary promoters.

4.2 Experimental section

4.2.1 Precursor synthesis

The precursors of the three catalysts Cu/ZnO:Al (CZA), Cu/ZnO:Ga (CZG) and Cu/ZnO (CZ) were synthesized by the well-reported coprecipitation technique, *e.g.*, by Schumann *et al.*⁵⁷

The precipitation was carried out in an automated stirred tank reactor from 1 M mixed metal salt nitrate (Table SI 11.5) solutions at a temperature of 65 °C. During the precipitation the *pH* was held constant at 6.5 using 1.6 M sodium carbonate solution as precipitating agent. The dosing rate of the metal solution was adjusted to 2.5 g min⁻¹. After the typical *pH* drop was observed⁵⁷, the ageing was proceeded for an additional one hour without further *pH* control. Afterwards the precursor was washed with deionized water 15 times, until the conductivity of the filtrate was lower than 100 μS cm⁻¹. After drying at 80 °C for a minimum of 14 hours in a heating cabinet, the precursors were analysed regarding their composition, phase purity and surface areas.

4.2.2 Oxide synthesis (Pre-catalysts)

The co-precipitated precursors were decomposed into their corresponding oxides in a muffle furnace (Nabertherm LE 6/11/B150) in static air at 350 °C with a heating ramp of 2 °C min⁻¹ and a holding time at the target temperature of 3 h.

4.2.3 Characterization methods

Powder X-ray diffractometry (PXRD) of the precursors, calcined pre-catalysts and spent catalysts after methanol syntheses were recorded with Cu-K α radiation on a STOE Stadi-P equipped with a germanium 111 monochromator and a MYTHEN 1 K detector. The diffractograms were recorded at room temperature in the range of 2° to 80° 2 θ . The samples of the reduced catalysts were prepared in sealed capillaries of 0.5 mm diameter. The reduced sample of CZG (CZG-red.) was recorded with Mo-K α radiation on the same device described above. Therefore, the general scattering vector q in Å $^{-1}$ is used for comparison of the pattern recorded with different X-ray wavelengths.

Atomic absorption spectroscopy (AAS) was performed on a Thermo Fisher Scientific iCE-3500 AAS after dissolving the sample in nitric acid.

Thermogravimetric analysis (TGA) was performed for the precursor materials on a STA 449 F3 Jupiter from Netzsch. The sample was heated at a rate of 5 °C min $^{-1}$ up to 1000 °C in flowing synthetic air.

Nitrogen physisorption was measured at 77 K in a Nova 3200e sorption station from Quantachrome. Before recording the isotherms, the samples were degassed under vacuum at 80 °C (precursors) or 100 °C (oxides) for 5 h. Afterwards the isotherm profiles in a partial pressure range between $p/p_0 = 0.0$ and 1 referred to a reference cell were recorded. The multipoint BET surface area was determined by applying the *Brunauer-Emmett-Teller* (BET) equation in the range of increasing adsorption volume by using the micropore assistant of the software NovaWin.

Diffuse reflectance Infrared Fourier Transformed Spectroscopy (DRIFTS) experiments were performed using a Nicolet™ iS20 FTIR spectrometer from Thermo Fisher Scientific, equipped with a DRIFTS cell (Praying Mantis™, Harrick Scientific Products Inc.) and a Mercury Cadmium Telluride detector (MCT) cooled with liquid nitrogen. The DRIFTS cell outlet gas stream was analysed continuously during the experiment by an on-line mass spectrometer (Pfeiffer Vacuum Omnistar GSD 320 with QMG 220). Using a four-port selector valve, the inlet gas was switched between two different streams, one for purging and/or reduction of the catalysts (He or 5 vol% H $_2$ in He) and the other containing the probe gas (0.2 vol% CO in He). A flow-through configuration was applied in all segments with a total flowrate of 80 cm 3_N min $^{-1}$. At first, the loaded samples (~40 mg fine powder) were reduced by 5 vol% H $_2$ in He at 275 °C for 1 h (at a heating rate of 5 °C min $^{-1}$), after which the cell was cooled down to 10 °C at the maximal rate. Once the temperature stabilized, the gas was changed to He and the cell was

purged for 10 min to remove traces of H₂ followed by collecting the background spectrum in He. The collection of the time-series adsorption spectra was then initiated, and the gas stream was switched to the CO probe mixture after collecting the first spectrum in He (corresponding to time 0). After 40 min of adsorption, the gas stream was switched back to He and the desorption was monitored for another 40 min.

X-ray absorption spectroscopy (XAS) was measured at the CAT-ACT beamline at Karlsruhe Institute of Technology (KIT) Light Source¹⁵⁸. In an *in situ* TPR experiment, the sample CZG was treated in 20 % H₂ in N₂ and heated to 250 °C (5 K min⁻¹). The temperature was held for 1 h. The X-ray absorption near-edge structure (XANES) data was recorded at the Ga K-edge (10367 eV) in transmission mode using a Si 111 double-crystal monochromator and ionization chambers for determining the X-ray intensity. The raw data was then treated with Athena software package¹⁵⁹. The edge energies of the spectra were determined using the first maxima in the first derivative of the spectra. Subsequently, the background was adjusted, and the spectra were normalized. The sample preparation included grinding of the samples and thorough mixing with SiC, before pressing the mixture into pellets and granulating to a sieve fraction of 100-200 μm. The spectra recorded at 250 °C were merged and the pre-edge region was modelled for refinement using the software Larch¹⁶⁰. The reference data for the linear combination analysis was recorded at HASYLAB at DESY³⁴. The samples were measured in the range of 9570 eV - 10580 eV including the Ga K-edge (10367 eV) in transmission mode. For the pure Ga₂O₃ references, 12 mg of sample were diluted with 88 mg of polyethylene, before the mixtures were pressed to 13 mm diameter pellets. Data analysis such as energy calibration, background subtraction and normalization were performed using the Athena software package. To combine both data sets for analysis, the spectra were aligned with respect to the energy. Linear combination analysis was performed using Larch software.

Density Functional Theory (DFT) calculations were performed using the Vienna Ab Initio Simulation Package (VASP)^{161, 162}. The Bayesian Error Estimation Functional with van der Waals correlations (BEEF-vdW)¹⁶³ with the projector augmented wave method (PAW)^{164, 165} and a plane-wave basis set with a cut-off energy of 450 eV were used. The infinite slab models for the ZnO (110) termination consist of four layer-thick 4×2 super-cells, separated by more than 16 Å in the z direction. Ga and Al containing materials were constructed by substitution of one Zn atom in the ZnO (110) surface layer. The bottom two layers were kept fixed and the upper two layers were allowed to relax during geometry optimizations. The Brillouin zone was sampled using a 2×5×1 Monkhorst–Pack k-point grid¹⁶⁶. The convergence criterion for the geometry optimizations was a maximum force of 0.01 eV/Å. For the bulk calculations we have

used $2 \times 2 \times 2$ large ZnO unit cell. Ga and Al substitution in the bulk was modelled by substitution of one Zn atom with Ga or Al. For each system (ZnO, ZnO₋₁, Zn₋₁O, GaZnO, GaZnO₋₁, GaZn₋₁O, AlZnO, AlZnO₋₁ and AlZn₋₁O) lattice optimization was performed. The Brillouin zone was sampled using a $5 \times 5 \times 3$ Monkhorst–Pack k-point grid. All optimized structures are given in the SI.

Temperature programmed reduction (TPR) of 100 mg pre-catalyst of a 125-250 μm sieve fraction was performed in a quartz glass U-shape tube reactor on a BelCat-B from Bel Japan Incorporation. Before the reduction profile was recorded, the sample was dried by heating up with $5\text{ }^\circ\text{C min}^{-1}$ to $100\text{ }^\circ\text{C}$ in 80 ml min^{-1} Argon stream. The temperature was held for 60 minutes to ensure a complete drying of the sample. Afterwards, the temperature programmed reduction was performed. As a reducing atmosphere, 5 vol% H₂ in Ar with a volume flow of $35\text{ ml}_\text{N min}^{-1}$ at ambient pressure was used. Starting from $40\text{ }^\circ\text{C}$ the sample was heated up to $275\text{ }^\circ\text{C}$ with a heating ramp of $2\text{ }^\circ\text{C min}^{-1}$. After reaching the target temperature, it was held for 4 h to ensure a complete recording of the reduction profile and a complete reduction of copper oxide. The formed water during reduction was separated by a mole sieve to enable the analysis of the consumed H₂ via a thermal conductivity detector (TCD). The calibration of the hydrogen signal was performed by using CuO from Alfa Aesar as reference material.

H₂-transient adsorption (H₂-TA) was recorded in the same apparatus, in which the TPR was performed, but a calibrated Omnistar GSD 320 with a quadrupole mass spectrometer (Pfeiffer Vacuum Omnistar GSD 320 with QMG 220) was additionally used with He as an internal standard for the product stream analysis. Before the adsorption experiment was performed, the lines and the reactor were flushed with He at $40\text{ }^\circ\text{C}$ for 30 minutes. The adsorption profile was measured with 2 vol% H₂ in He with a volume flow of $8\text{ ml}_\text{N min}^{-1}$ for 120 minutes.

N₂O-reactive frontal chromatography (N₂O-RFC) was measured subsequent to a reduction experiment (*e.g.*, TPR or H₂-TA). After flushing the reactor with He for 45 minutes at $130\text{ }^\circ\text{C}$ (heating ramp $5\text{ }^\circ\text{C min}^{-1}$), it was cooled to $40\text{ }^\circ\text{C}$. The measurement was performed using a calibrated quadrupole mass spectrometer (Pfeiffer Vacuum Omnistar GSD 320 with QMG 220) with He as internal standard and 1 vol% N₂O in He with $5\text{ ml}_\text{N min}^{-1}$ for 60 minutes. The data evaluation was performed by using the calculations according to DIN 66136-1¹⁵⁰. The stoichiometric coefficient (0.481) and specific copper surface area ($6.80 \cdot 10^{-20}\text{ m}^2$ (copper atoms)⁻¹) were taken from the reported study by Chatterjee *et al.*¹¹³.

The measurements of the nitrogen capacities of the spent samples and of the therein compared fresh catalysts were performed after reduction at $240\text{ }^\circ\text{C}$ with 5 vol% H₂ in Inert and a heating

ramp of $5\text{ }^{\circ}\text{C min}^{-1}$. The temperature was held for 2 hours before switching to the N_2O feed gas and measuring the N_2O -RFC.

4.2.4 Catalytic testing

Catalytic testing of the synthesized copper catalysts was performed in a 2.6 mm inner diameter reactor of a 64-fold parallel Flowrence® plant by Avantium technologies. A varying amount of 75 mg, 150 mg and 225 mg of the pre-catalysts with a sieve fraction of 125-250 μm and diluted with an equal amount of silica (SiO_2) was used to archive different gas hourly space velocities (GHSVs). The catalyst bed was placed between a post- and a pre-bed to ensure isothermal behaviour and a proper prewarming and intermixing of the gas stream.

Before the catalytic tests were performed, the catalysts were activated by heating in $10\text{ ml}_\text{N min}^{-1}$ 5 vol% H_2 in N_2 with a heating ramp of $5\text{ }^{\circ}\text{C min}^{-1}$ up to $275\text{ }^{\circ}\text{C}$. The targeted temperature was held for 4 h to ensure a complete activation. Afterwards the catalysts were aged in a $\text{H}_2:\text{CO} = 2$ feed gas at $235\text{ }^{\circ}\text{C}$ and 30 bar over a formation period of 100 hours. Afterwards, the first activity test was recorded under these reference conditions followed by process condition variations. Between 200 h and 1200 h time on stream, selected process conditions were varied like the $\text{H}_2:\text{CO}$ ratio (1.5, 2, 2.5), the pressure (20 bar, 30 bar, 40 bar) and $\text{CO}_2:\text{CO}$ ratio ($x_{\text{CO}_2} = 0.15$, $x_{\text{CO}_2} = 0.3$, $x_{\text{CO}_2} = 0.5$). During these process variations, a complete set of each catalyst, corresponding to the three different GHSVs was kept at $205\text{ }^{\circ}\text{C}$, $220\text{ }^{\circ}\text{C}$, $235\text{ }^{\circ}\text{C}$ and $245\text{ }^{\circ}\text{C}$ in separated heating blocks. After the $\text{H}_2:\text{CO}$ ratio and pressure variation, the reference conditions of 30 bar, $\text{H}_2:\text{CO} = 2$ and $235\text{ }^{\circ}\text{C}$ were used to investigate the activity change for each reactor in pure CO/H_2 syngas. Afterwards the $\text{CO}_2:\text{CO}$ ratio variation was performed by substituting CO with CO_2 at constant $\text{H}_2:\text{CO}_x$ ratio of 2. As the last step, the reference conditions were applied again to each reactor to determine catalyst activity changes.

The catalysts were passivated after the reaction by cooling down and opening the reactor lid while flowing simultaneously helium through the reactors at $80\text{ }^{\circ}\text{C}$ to ensure a careful oxidation.

The equilibrium product composition for methanol synthesis was calculated with Aspen Plus® by Gibbs free energy minimization using the reaction conditions as input parameter.

4.2.5 Nomenclature

The synthesized materials will be described by the abbreviations of their metal compositions CZA (Cu/ZnO:Al), CZG (Cu/ZnO:Ga) and CZ (Cu/ZnO). The state of the material will be written using suffixes of the metal composition like CZA-prec. of the CZA precursor. The following other suffixes are used: -calc. (calcined), -red. (reduced), -post cat.-red. (after catalysis re-reduced).

4.3 Results and discussion

4.3.1 Synthesis and characterization of the pre-catalysts

The catalysts in this study have been synthesized according to the industrial protocol by co-precipitation of malachite-based precursors. The molar cationic ratio was targeted to Cu:Zn = 70:30 and to Cu:Zn:M = 68:29:3 for an additional trivalent cation M = Al or Ga as secondary promoter to reach the highest zinc incorporation into the malachite structure.^{10, 34} The catalyst CZA is a reproduction of a benchmark catalyst previously named FHI-Std.⁵⁷, which has been employed in numerous contributions.^{14, 20, 31, 57, 157} One major difference to state-of-the-art commercial catalysts is the lower amount of the secondary promoter Al, which is around 10 % in common formulations.^{1, 15, 152} This modification is based on the observed performance improvement at a lower content of 3 % in previous work.³⁴ The metal composition after co-precipitation was determined by AAS and is shown in Table 4.1. The results were close to the nominal composition for all three samples.

Table 4.1: Metal ratios determined by atomic absorption spectroscopy (AAS) of the precursors after dissolving in nitric acid. The trivalent cation is in case of the CZA-prec. and CZG-prec. the aluminium and the gallium ion, respectively. The last column contains the determined spacing of the 20-1 reflection determined by PXRD.

Sample	$X_{(Cu/\Sigma M)}$ mol%	$X_{(Zn/\Sigma M)}$ mol%	$X_{(M^{III}/\Sigma M)}$ mol%	d_{20-1} Å
CZA-prec.	68 ± 1.4	29 ± 1.4	3 ± 0.04	2.762
CZG-prec.	69 ± 1.4	28 ± 1.5	3 ± 0.1	2.758
CZ-prec.	69 ± 1.5	31 ± 1.5	0	2.789

The precipitates mainly crystallized in a malachite structure ($(\text{Cu}, \text{Zn})_2\text{CO}_3(\text{OH})_2$), as it is shown by the PXRD pattern in Figure 4.1 a). Only the binary CZ-prec. contains a side phase, which was assigned to aurichalcite ($(\text{Cu}, \text{Zn})_5(\text{CO}_3)_2(\text{OH})_6$). This zinc-enriched side phase can act as a sink for the primary structural promoter Zn and lead to a loss of the highly active nanostructure.¹⁰ The qualitative analysis of the PXRD pattern visualizes, that the reflections of the binary CZ precursors are sharper and more separated than in the pattern of CZA-prec. and CZG-prec. The broader reflections in case of the presence of a trivalent cation as secondary promoter indicates that the crystallites in these materials are more nanoscopic than in the binary reference catalyst, resulting in an increased surface area, as shown in Figure 4.2. Furthermore, the incorporation of a trivalent cation has also suppressed the side phase formation, resulting in a phase pure malachite structure, as it was expected from literature¹⁰ (Figure 4.1 a)). The determined spacings of the 20-1 planes of the malachite structure are listed in Table 4.1. The d -spacing of CZ-prec. was determined to be 2.79 Å and was found at a higher value in comparison to the other samples. With increasing Zn incorporation into the malachite structure, the d -spacing decreases, as evident by comparing the binary CZ precursor to pure malachite $\text{Cu}_2\text{CO}_3(\text{OH})_2$ ($d_{20-1} = 2.85$ Å). The presence of the secondary promoter thus resulted in a further decreased of the d_{20-1} -spacing to 2.762 Å for CZA-prec. and 2.758 Å for CZG-prec. indicating a higher degree of substitution of Cu by both promoters in the precursors. Hence, a better approach to desired equimolar dilution of Cu is achieved, as it was expected for such ternary precursor systems.³⁴

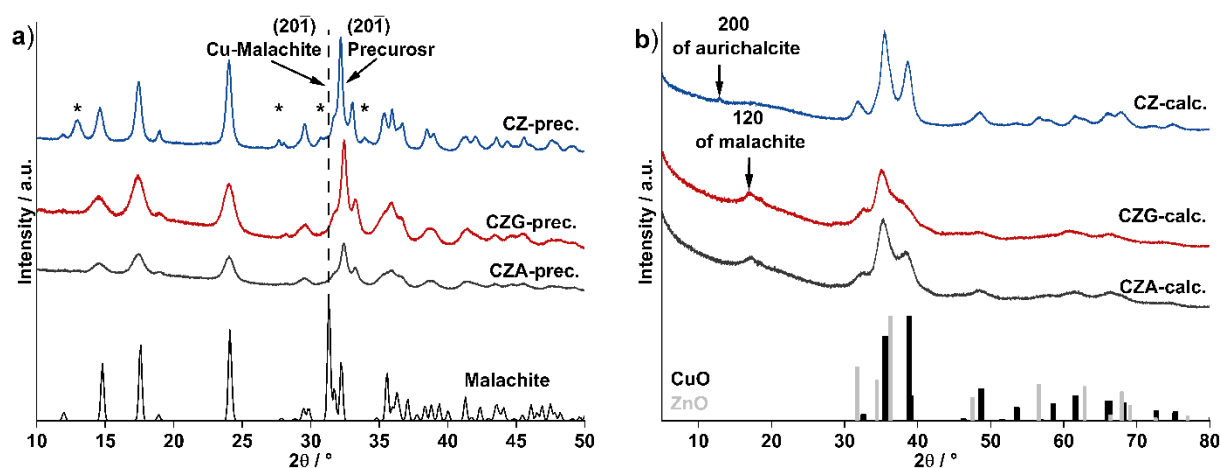


Figure 4.1: Powder X-ray diffraction pattern of the co-precipitated precursors (left side a)) in comparison to the Cu-malachite reference from ICSD database (#15384). The asterisk visualizes peak positions of the aurichalcite side-phase (ICSD #75324). On the right side the corresponding oxides after calcination for 3 h at 350 °C in static air with a heating ramp of 2 °C min⁻¹ are shown (b)). The black reference pattern corresponds to CuO (COD#004105685) and the grey pattern to ZnO (COD#002300450).

To avoid sintering and to receive highly inter-dispersed oxides, the precursor decomposition was performed under the mildest possible calcination conditions at 350 °C in air, which is a typical temperature for methanol synthesis catalyst preparation.⁸ However, these conditions did not result in a complete precursor decomposition, as the 120 reflection of malachite ($2\theta \approx 18^\circ$) in CZA-calc. and CZG-calc. and the 200 aurichalcite reflection ($2\theta \approx 13^\circ$) in CZ-calc. indicate poorly crystalline residues of the precursors (Figure 4.1 b)). The calcination behaviour is consistent with the results of the TG analysis (supporting information Figure SI 11.1), indicating a full precursor decomposition at around 550 °C, which is not compatible with the targeted non-sintered microstructure of the catalysts. Importantly, the major decomposition happens around 320 – 350 °C, rendering this temperature high enough for dehydroxylation but low enough to conserve a good cation intermixing and thus the targeted microstructure.⁶² A side effect of this low calcination temperature is the presence of high temperature stable carbonates which are discussed to stabilize the oxide inter-dispersion after calcination and to increase the copper dispersion in the final catalysts.^{33, 62}

Comparing the three calcined samples, a clear difference in the success of an improved microstructure on the nanoscale becomes evident. The peak widths of the expected ZnO and CuO phases in the PXRD patterns (Figure 4.1 b)) become broader in the order CZ-calc. < CZA-cal. < CZG-calc. indicating a decrease in the crystallite sizes. The same order is observed for an increasing BET surface area (CZ-calc. << CZA-cal. < CZG-calc.), with values around 100 m²g⁻¹ for the two secondary promoted samples, which is in the range of industrial catalysts. This clearly indicates a structural promoting effect of the secondary promoter, which also has been suggested in the literature already on the stage of the calcined catalysts.^{15, 32, 167} This allows tracing its origin back to the precursor state, where the secondary promoter suppressed the crystallization of the aurichalcite side-phase and thus helped to incorporate all species in a single substituted malachite phase. The higher degree of substitution gives rise to a more inter-dispersed calcined material with uniform distribution of the species, smaller oxide crystallites and larger specific surface areas. In this respect, the structural promotion of Ga as a secondary promoter seems slightly more efficient compared to the industrially applied Al. A very clear difference, however, was found in the comparison of CZA-cal. and CZG-calc. to the binary sample CZ-calc. suggesting the structural promotion is mostly determined by the presence or absence of the refractory oxide and to a lesser extent by its nature being Al or Ga.

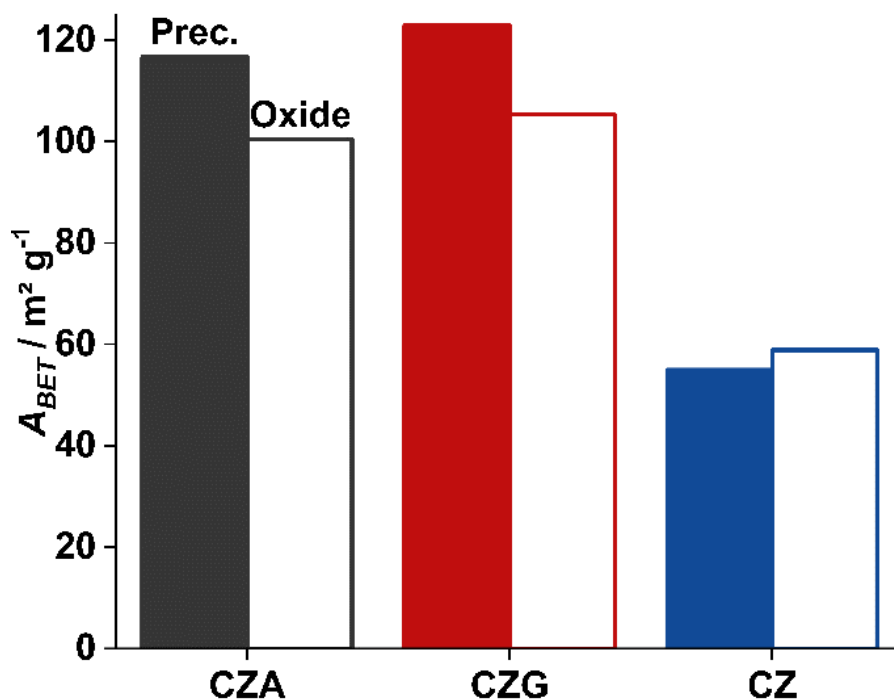


Figure 4.2: Surface areas of the co-precipitated precursors (coloured column) and their corresponding oxides (white column) after calcinating at 350 °C for 3 h in static air.

4.3.2 The reduced state before catalysis

4.3.2.1 Characterization of the activated catalysts

After calcination of the precursors, the pre-catalysts CZ-calc., CZA-calc. and CZG-calc. were reduced by TPR and the resulting samples CZ-red., CZA-red. and CZG-red. were investigated by chemisorption methods and PXRD to characterize them right after activation, representing the fresh state of the catalysts before the catalytic experiments.

The TPR profiles are shown in the supporting information in Figure SI 11.5 on page 214. For each sample, completion of reduction was found already at 200 °C. The targeted temperature was set to 275 °C with a holding time of 4 h assure complete reduction, trigger the evolution of the typical microstructure and to allow for formation of Zn^{red} species due to SMSI, but to minimize sintering. The analytical degree of reduction based on copper was found to be close to 100 % at this temperature for all samples (SI Table SI 11.11), indicating that a possible reduction of ZnO to form Zn^{red} is not coupled to a large hydrogen consumption, which Zn^{red} has been clearly evidenced at more elevated temperatures when bulk brass alloy was formed, but the overall low amount of Zn^{red} forming under these conditions and/or its stoichiometry ZnO_x with x being close to two makes it hard to determine by TPR experiments. The highest hydrogen uptake rate, found to be at 159 °C for CZ-calc. and 176 °C – 189 °C for the ternary catalysts, can be related to the reduction of copper, which is a typical temperature for these

catalysts.⁴¹ The reduction of copper was also confirmed by PXRD analysis of the reduced samples, which is shown in Figure 4.3, by the presence of the 111 and 002 reflections of metallic copper in all catalyst. In analogy to the calcined state, the weaker and broader reflections of CZA-red. and CZG-red. indicate a smaller crystallite size. Also, the zinc oxide phase ($2 \text{ \AA}^{-1} < q < 3 \text{ \AA}^{-1}$) in CZA-red. and CZG-red. are clearly different from CZ-red. and almost XRD-amorphous. In contrast, clear and sharper reflections of ZnO indicate larger crystallites for CZ-red. Comparing the crystallite sizes of the copper determined by application of the Scherrer equation to the 111 reflection (Table 4.2), a value of 6 nm - 7 nm was determined for CZA-red. and CZG-red. compared to a more than doubled value of 17 nm for CZ-red. This difference is also reflected in the BET surface areas of the reduced catalysts, which were 72 and 65 $\text{m}^2 \text{ g}^{-1}$ for CZA-red. and CZG-red., respectively, but only less than half for CZ-red. (26 $\text{m}^2 \text{ g}^{-1}$). These results confirm that the improved microstructure due to a secondary promoter like Al or Ga was successfully carried over from the calcined catalysts to the activated reduced catalysts.^{4, 34} This structural promotion effect is again explained with a geometrical spacing or steric effect leading to smaller crystallites of Cu and ZnO in the presence of the secondary promoter.

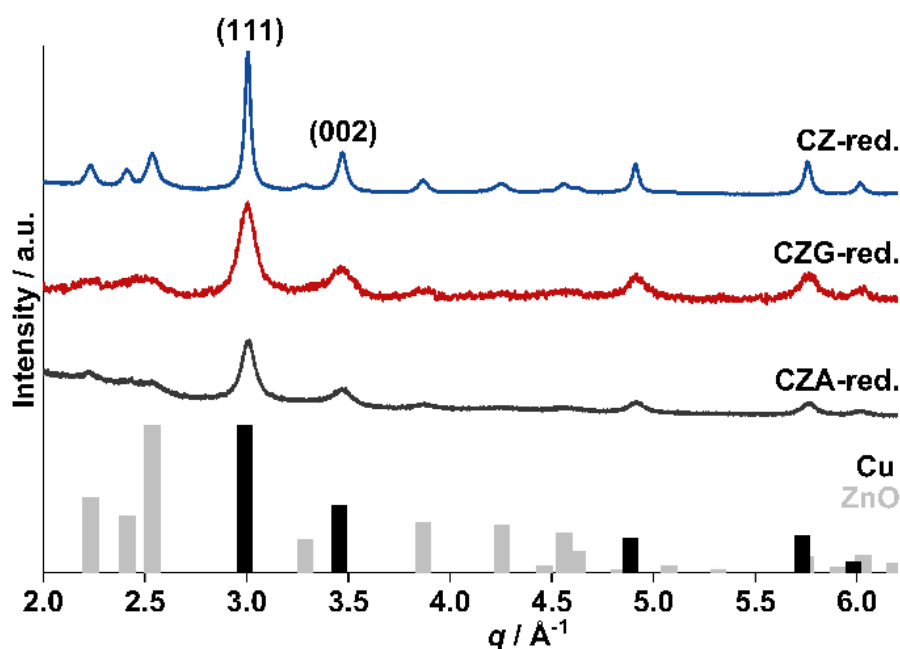


Figure 4.3: Powder XRD pattern of the reduced CZA (black, lower pattern), CZG (red, middle pattern) and CZ (blue, upper pattern) catalysts. The bar charts of the references are related to zinc oxide (grey, #002300450) and metallic copper (black, #001512504) are taken from COD database. The activation was performed with a flowrate of $10 \text{ ml}_N \text{ min}^{-1}$ of 5 vol% Hydrogen in Argon heating up the calcined sample ($125 - 250 \mu\text{m}$ sieve fraction) to $275 \text{ }^\circ\text{C}$ with a heating rate of $2 \text{ }^\circ\text{C min}^{-1}$ and holding the temperature for 4 h to ensure complete reduction.

HR-TEM of CZA, in this case an earlier preparation of the FHI-Std. catalyst (Figure 4.4 a)), shows the above-mentioned microstructure of alternating metallic Cu and ZnO nanoparticles that aggregate into a porous arrangement, which is typical for industrial-type methanol synthesis catalysts.¹⁶⁸ These poorly crystalline ZnO particles adopt to the usual Wurtzite structure and represent the primary structural promotion by Zn (coloured red in Figure 4.4). Close inspection of the images reveals an additional overgrowth of the Cu particles, which was described as a ZnO_x-layer with graphitic structure.²⁰ This represents the Zn^{red} species and thus the primary electronic promotion by Zn (coloured yellow in Figure 4). Note that the state of Zn^{red} detected in the TEM at vacuum and room temperature is likely changed dynamically in the presence of the feed gas at operation conditions.³¹ In this work, we assume that the red coloured ZnO support particles act as a reservoir for the yellow coloured Zn^{red} as depicted by the arrows in Figure 4.4.

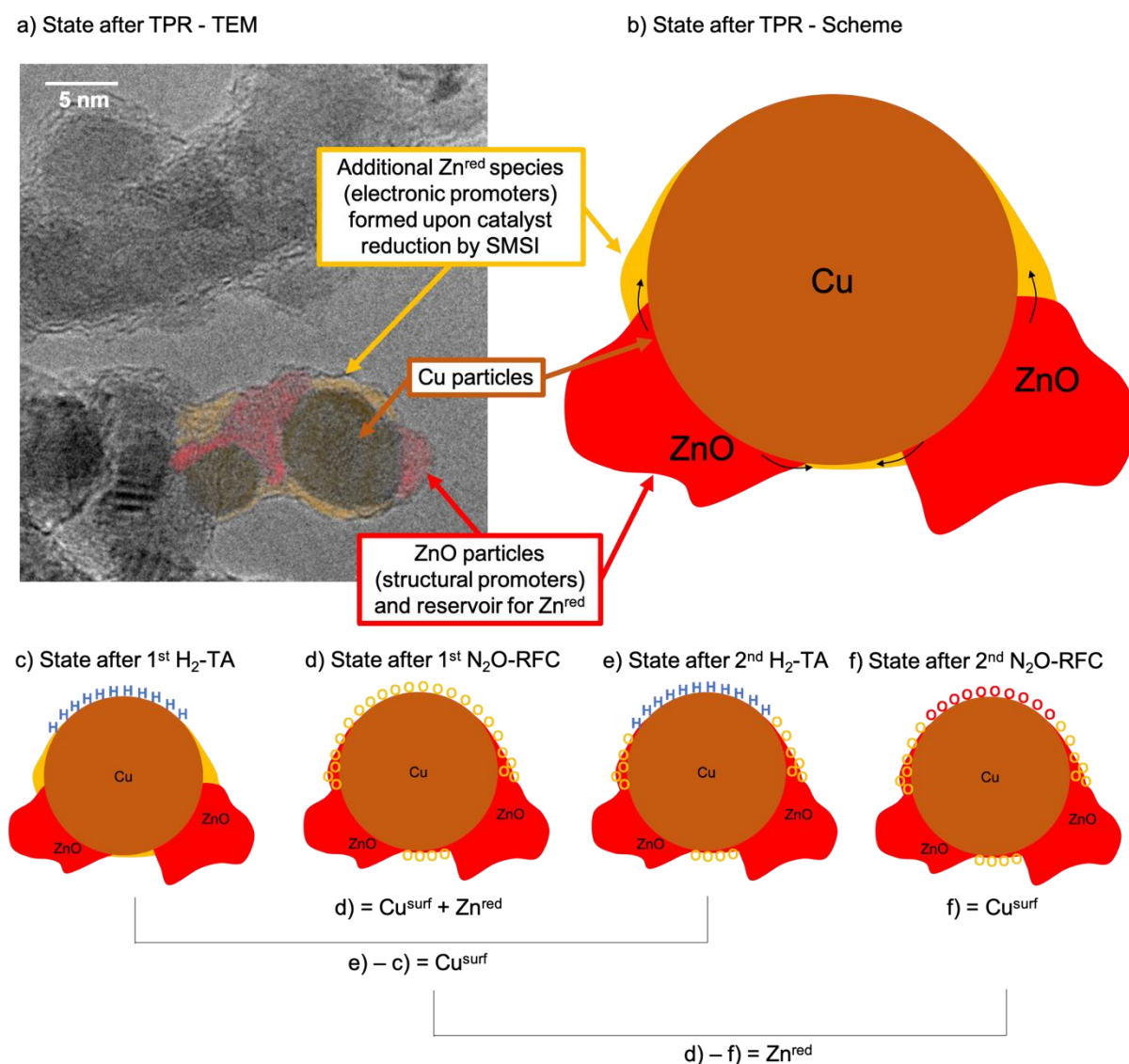


Figure 4.4: a) Representative HRTEM image of the microstructure of CZA-red. with coloration to illustrate the main components Cu particles (brown), ZnO particles (red) and Zn^{red} species (orange); the original TEM images can be found in the SI as Figure SI 11.6 on page 215. b) Schematic representation of this microstructure after TPR. c) - f) Assumed surface states after the steps in the series of chemisorption experiments with c) hydrogen coverage of Cu^{surf}, d) oxidation of Zn^{red} and Cu^{surf}, e) re-reduction of Cu^{surf} only, f) re-oxidation of Cu^{surf} only. Before each step, the reactor was purged to receive a clean, adsorbate-free surface. The assumed meaning of the chemisorption capacities is summarized at the bottom. The Zn^{red} species is represented here as a potentially porous, overgrown ZnO_{1-x} layer on the Cu particle inspired by the TEM work of Lunkenbein et al.²⁰ However, based on the chemisorption data, no claim in such direction is intended. A surface alloy state can be considered accordingly, in which case the orange layer thickness could represent the Zn fraction in its composition. A dynamic switching between overgrowth and alloy and intermediate states depending on the operating conditions of the working catalysts as suggested by Pandit et al.¹⁵⁴ seems likely.

Thus, for a full description of the catalyst's microstructure, also the dynamic SMSI and its electronical promoting effect must be considered beyond purely steric arguments. For this purpose, an advanced chemisorption procedure was applied on the three reduced catalysts CZ-red., CZA-red. and CZG-red. to address the formation of Zn^{red} species. After TPR, four consecutive chemisorption measurements have been conducted using hydrogen, N_2O , hydrogen and again N_2O as probe molecules, but without intermediate reduction at high temperature. The resulting series of H_2 transient adsorption (H_2 -TA) and N_2O reactive frontal chromatography (N_2O -RFC) experiments are shown in SI in chapter 11.6.2.4 "Nitrogen capacities from chemisorption experiments" starting on page 212.

N_2O -RFC is based on the decomposition of N_2O into O^* and N_2 at the surface and is well-established.^{69, 103, 104, 112} The N_2O chemisorption capacity was for a long time thought to happen only on metallic Cu surface species Cu^{surf} and the results were routinely recalculated into specific Cu surface areas based on a stoichiometry of $\text{Cu}^{\text{surf}}:\text{O}$ of 2:1 and the surface atom density of Cu111. However, the results reported by Kuld *et al.*¹¹² and Fichtl *et al.*⁶⁹ clearly showed that also Zn^{red} species can be re-oxidized by N_2O leading to a higher capacity compared with hydrogen as a probe molecule and thus to an overestimation of Cu^{surf} in Zn-promoted catalysts.

Our chemisorption analysis adapts the measurement protocols of Kuld *et al.*¹¹² and Fichtl *et al.*⁶⁹ presented in their chemisorption analyses of Cu-based catalysts and takes their conclusions into account. After activation by TPR at 275 °C, the reduction of Cu has generated metallic Cu surface sites Cu^{surf} and possibly additional Zn^{red} .¹⁵⁴ In the first H_2 -TA, Cu^{surf} is covered by hydrogen, while based on a H_2 -TPD experiment of Fichtl *et al.*,⁶⁹ in which no hydrogen desorption from Zn^{red} up to 127 °C was observed, Zn^{red} is assumed not to interact with hydrogen strongly.^{69, 112} Thus, we can assume that this first H_2 -TA experiment only probes Cu^{surf} with a given adsorption capacity. After purging to clean the surface from any adsorbate, a regular N_2O -RFC was conducted. We assume that the N_2O chemisorption capacity in this chemisorption step is a measure for the sum of Cu^{surf} and Zn^{red} species at the catalyst's surface, which are converted to $\text{Cu}^{\text{surf}}_2\text{O}$ and ZnO by O^* .¹¹² In a second H_2 -TA, Cu^+ in $\text{Cu}^{\text{surf}}_2\text{O}$ is reduced back to Cu^{surf} and subsequently, hydrogen is adsorbed on the newly generated metallic surface. However, due to the lower temperature of this experiment compared to the initial TPR, ZnO can be assumed to remain in its oxidized state without the re-formation of Zn^{red} .^{112, 154} Thus, the second H_2 -TA will probe the re-reduction of the $\text{Cu}^{\text{surf}}_2\text{O}$ layer plus the adsorption capacity due to Cu^{surf} . As the latter was already determined in the first H_2 -TA, the amount of Cu^{surf} can

be calculated by the difference in the adsorption capacities of the H₂-TAs prior and after N₂O-RFC following Kuld *et al.*¹¹².

Furthermore, a fourth chemisorption experiment or second N₂O-RFC will start from a state with Cu^{surf}, but no Zn^{red} at the surface, which already has been converted in the first N₂O-RFC and cannot be re-formed at low temperature. This is why the second N₂O-RFC can be referred to as a “Zn^{red}-corrected N₂O-RFC” for Cu supported on reducible oxides. Like the two H₂-TAs, the difference in N₂O chemisorption capacities of the first (Cu^{surf} + Zn^{red}) and the second measurement (Cu^{surf} only) can be used to determine the amount of Zn^{red}.

For the sake of a better comparison, the surface states of the three catalysts are discussed based on the nitrogen releases (or O* capacities) during N₂O-RFC before and after intermediate H₂-TA. With this method, the sum of Cu^{surf} and Zn^{red} in the first N₂O-RFC can be directly compared to the Cu^{surf} only in the second N₂O-RFC, and the amount of Zn^{red} is the difference of the two values. (Figure 4.5). Comparison of the relative differences among the samples in Cu^{surf} determined by this method and independently by the comparison of the two H₂-TAs shows a slight deviation of the Cu^{surf} determined by N₂O-RFC (SI, Figure SI 11.10). The results derived from H₂-TA underestimates the N₂-capacities of the second N₂O-RFC by around 24 % - 50 %. Such underestimation can be explained with the error of the analysis of low H₂ concentrations and the minimal concentration changes. Kuld *et al.*¹¹² described a underestimation of the Cu^{surf} by 12 % compared to the correct H₂-TPD analysis¹¹². The H₂-capacities are in a similar range for CZA and CZG and significantly higher than for CZ. Overall, the H₂-TA describes the Cu^{surf} sites in a similar way as found for the N₂-capacities, but because of the above-described uncertainties, only the results of the N₂-capacities are considered in the following comparison as a more reliable description of the Cu^{surf} sites.

The nitrogen release of the reduced catalysts assigned to Cu^{surf} show a trend CZA-red. ≈ CZG-red. >> CZ-red. with a similar amount of Cu^{surf} in CZA-red. and CZG-red., which is more than doubled compared to CZ-red., and thus is consistent semi-quantitatively with the BET surface areas, with the differences in crystallize sizes and with the results of the H₂-TA. We thus propose that the structural promotion effect by the secondary promoters directly results in increased amounts of Cu^{surf} sites due the above-discussed described steric arguments. The mechanisms of structural secondary promotion can be traced back to precursor chemistry: Starting from the catalyst synthesis, the secondary promoters influence the phase composition and BET surface area of the precursors and calcined materials. This finally yields an increased Cu dispersion due to smaller Cu particles that is reflected in the amount of Cu^{surf}. This structural

promoting effect of Al or Ga is rather similar for both types of secondary promoters. If a specific Cu surface area is calculated from Cu^{surf} , the results are roughly 20 % of the BET surface area for all three samples suggesting a similar microstructure of the catalysts with a more or less linear size-scaling effect due to structural promotion by the secondary promoter (Table 4.2).

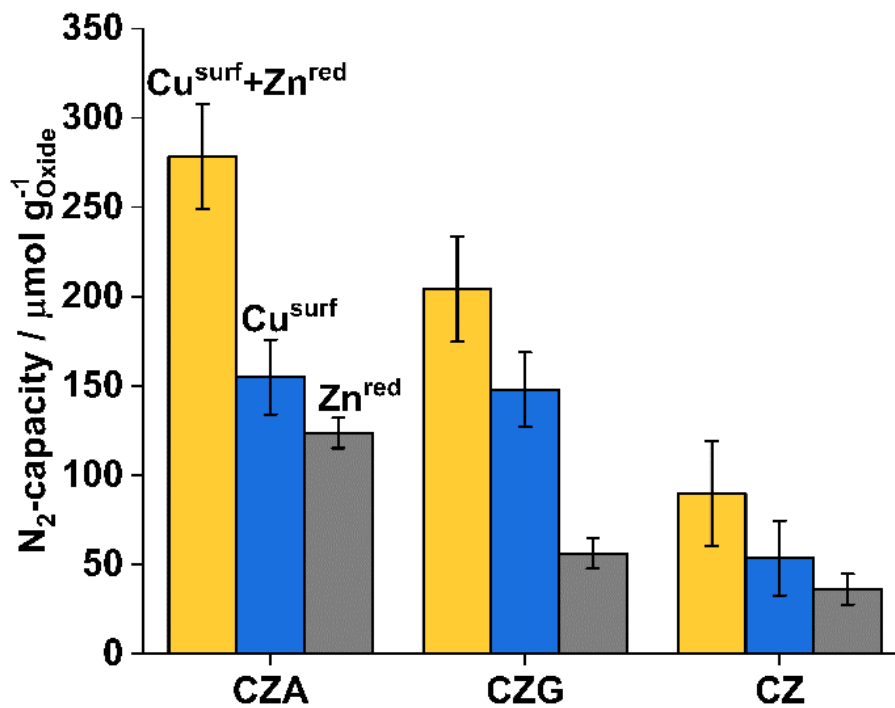


Figure 4.5: Nitrogen capacities of N₂O-RFC of the prepared catalysts. The first column of each catalyst corresponds to the titration after reduction at 275 °C in 5 % H₂/Ar ($\text{Cu}^{\text{surf}}+\text{Zn}^{\text{red}}$). The second column per catalyst corresponds to the Cu^{surf} sites, determined by N₂O-RFC after reduction in H₂-TA. The last column of each catalyst is the calculated amount of the reduced Zn species (Zn^{red}) of the two previous columns.

Table 4.2: Comparison of the surface areas of the catalysts after activating at 275 °C for 4 h. The calculations of the crystallite size ($d_{Cu, reduced, PXRD}$) were performed on the Cu 111 reflection by applying the Scherrer equation. The surface area $A_{BET, reduced}$ was determined by N_2 physisorption, and the surface area $A_{Cu^{surf}}$ was determined by N_2O -RFC after carefully reducing the Cu_2O by H_2 -TA. $D_{A_{Cu^{surf}} vs. A_{BET, reduced}}$ describes the quantity of exposed Cu surface to the total surface of the reduced catalyst.

Sample	$A_{BET, reduced}$ $m^2 g^{-1}_{Oxide}$	$A_{Cu^{surf}}$ $m^2 g^{-1}_{Calc.}$	$D_{A_{Cu^{surf}} vs. A_{BET, reduced}}$ reduced %	$d_{Cu, reduced, PXRD}$ nm
CZA	72	13	18	7
CZG	65	13	20	6
CZ	26	5	19	17

Interestingly, the amount of Zn^{red} determined using the above-described chemisorption method on our catalysts revealed quite different results suggesting an effect of the secondary promoter also on the SMSI in terms of electronic promotion. The trend was CZA-red. >> CZG-red. \approx CZ-red. with the amount of Zn^{red} being clearly highest for CZA-red. Note that these details cannot be deduced from the first N_2O -RFC alone, which shows the sum of Cu^{surf} and Zn^{red} with a trend CZA-red. > CZG-red. > CZ-red. as an information on both structural and electronic promotion. In fact, for the secondarily promoted samples, the increased nitrogen release right of CZA-red. after reduction is strongly affected by the re-oxidation of Zn^{red} sites.

Based on chemisorption alone, no information about the detailed nature of Zn^{red} is possible. However, its re-oxidation by O^* during N_2O -RFC is anyway compatible with both, the partial and full reduction models leading to ZnO_{1-x} overgrowth ($x < 1$)^{20, 60, 114} or surface alloy formation^{21, 112, 154} ($x = 0$). The dynamic formation of intermediate states with the co-existence of ZnO_{1-x} and the surface alloy also seems likely and has been suggested by Pandit *et al.*¹⁵⁴ based on DFT calculations and Zn K-edge XAFS investigations of an inverse $ZnO_{1-x}/Cu/MgO$ catalyst subjected to different reduction temperatures.¹⁵⁴ In this study, all catalysts have been subjected to the same reduction treatment at 275 °C in hydrogen and differences in the extent of reduction, *i.e.* different extents of Zn^{red} formation, should be due to the different promotion of the catalysts. Interestingly, considering that at full reduction Cu^{surf} and Zn^{red} might be present

in a surface alloy Cu_3Zn ^{112, 154} and assuming an oxidation into $\text{Cu}^{\text{surf}}_2\text{O}$ and ZnO by N_2O -RFC,^{69, 112} a $\text{Zn}^{\text{red}}:\text{Cu}^{\text{surf}}$ ratio of 1:1.5 would be expected, which is only slightly exceeded in CZA-red. and clearly not achieved in CZG-red (SI, Table SI 11.12). Due to the low capacities of CZ-red. in the range of the error of the measurement, no safe conclusions on such ratios are possible for this binary catalyst. However, we clearly find different amounts of Zn^{red} with CZA-red. having reached an almost fully reduced state of the surface if surface alloy formation with a Cu_3Zn stoichiometry is assumed, and significant lower extent on Zn^{red} formation in CZG-red. at an otherwise similar microstructure and a similar amount of Cu^{surf} . This result indicates that the different reducibility for the ZnO components depends on the secondary promoter, and that this electronic promoting effect strongly depends on the nature of the secondary promoter being Al or Ga, while the structural promotion was quite similar (see above).

However, despite the higher amount of Zn^{red} in CZA-red. than in CZG-red., DRIFTS investigation of CO sorption experiments of the catalysts demonstrates that the electronic effect on the sorption properties was similarly effective in these two catalysts and substantially less effective in CZ-red. Both on CZA-red. and CZG-red., CO chemisorption was hardly possible and only CZ-red. showed the expected vibration band for adsorbed CO on Cu^{surf} at initially 2112 cm^{-1} , assigned to defective Cu sites, Cu^{red} with or without very thin ZnO coverage¹⁶⁹⁻¹⁷¹ and an additional band at 2140 cm^{-1} which correspond to Cu^+ sites¹⁷¹ as a residue of incomplete copper reduction. After longer exposure, the band at 2140 cm^{-1} disappeared (Figure 4.6, 40 min) as completion of Cu^+ reduction to Cu^0 by CO and a slight red-shift to 2105 cm^{-1} was detected which is assigned to Cu^{red} on an oxidic surface giving evidence for a close Cu-ZnO interaction.¹⁷¹ Simultaneously, the absorption around 2091 cm^{-1} could be assigned to a Cu/ZnO interphase¹⁷⁰ or a linear CO adsorption on Cu 110 facet¹⁷¹. However, wavenumbers below 2100 cm^{-1} can be assigned to metallic Cu^0 ^{169, 171} but still no band developed on the secondarily promoted catalysts. This suggests that the catalyst surface was completely modified and did not allow for the on-top adsorption of CO on Cu^{surf} , likely due to Zn^{red} species (Figure 4.6). Similar results have been reported before¹⁶⁹, and are interpreted here as a successful modification of all Cu^{surf} sites on the smaller Cu particles in CZA-red. and CZG-red. by the clearly detected Zn^{red} in both catalysts due to the enhanced reducibility of zinc as a result of the electronic promotion with the secondary promoter. The larger Cu particles on CZ-red. with a lower amount of Zn^{red} , however, seem to still expose unmodified Cu^{surf} .

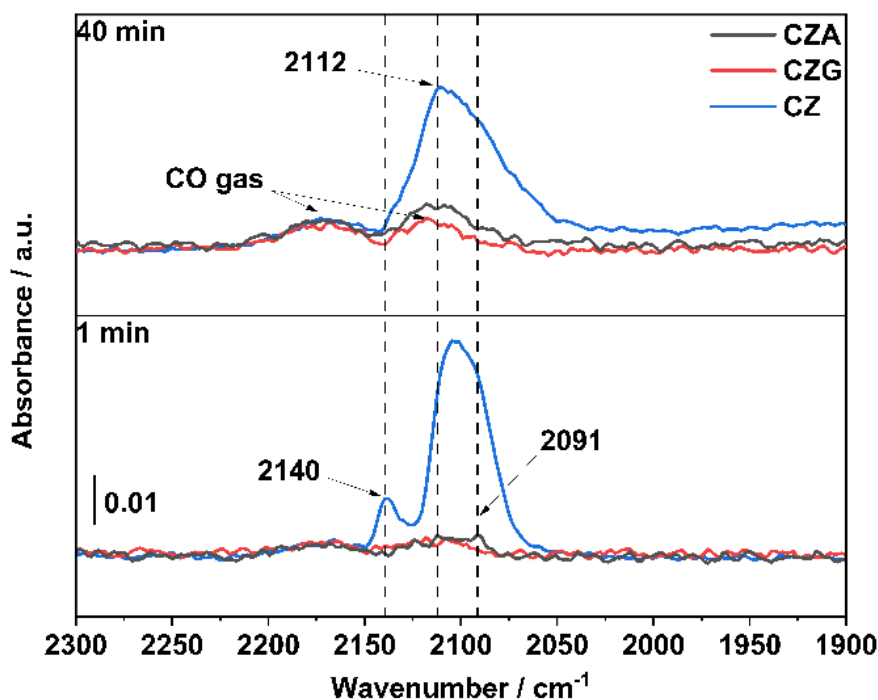


Figure 4.6: CO adsorption DRIFT spectra of the carbonyl region recorded at 1 and 40 min of exposure to 0.2 vol% CO in He at 10 °C after reduction for 4 hours at 275 °C with 5 % H₂ in He.

4.3.2.2 Promoter Speciation and Reducibility of Ga and Al doped ZnO

To find an explanation for the electronic promotion effect of the secondary promoter detected in the chemisorption and DRIFTS results to modify the adsorption properties of the Cu surface, we have investigated the hypothesis that the secondary promoter Al or Ga is at least partially incorporated into the primary promoter ZnO as a dopant.³⁴ The speciation of the secondary promoter is not easy to determine due to the low amount and high dispersion. A fraction, however, was found in the ZnO component for Al by ²⁷Al MAS-NMR in the reduced and for Ga by Ga K-edge XANES in the pre-catalyst.³⁴ We have recently confirmed that the incorporation of Al in ZnO is possible by co-precipitation using a synthesis route that is analogous to the catalysts synthesis but without the copper component, yielding diamagnetic samples that were analysed by ²⁷Al MAS-NMR and determined the solubility limit of Al³⁺ residing in the Zn²⁺-sites of ZnO for this synthesis method to 1.3 mol% Al in ZnO:Al.¹⁷² Optical spectroscopy confirmed the modification of the opto-electronic properties of ZnO due to doping. We hypothesize that these modifications of one SMSI component in the catalyst can be responsible for the observed altered adsorption properties of the Cu surface in the catalysts.

For CZG-red., the speciation of the secondary promoter was further analysed by Ga K-edge XANES after *in situ*-reduction. The catalyst was reduced in 20 % H₂ in N₂ in a cell reactor¹⁷³

and Ga K-edge XANES spectra were recorded at 250 °C in flowing hydrogen representing the activated state of the fresh catalyst. XANES spectra of Ga-oxide reference materials were combined to a model fitting the CZG spectrum (Figure 4.7) using linear combination analysis. According to the data of the eight best fits generated, the ZnO/3 %Ga (a Ga doped ZnO (ZnO:Ga)) data was required as the main component in any of the cases to result in the most reasonable fits. (Supporting Information). It is therefore suggested that just like in the ZnO/3 %Ga reference, Ga³⁺ is incorporated in the ZnO lattice in the CZG sample.

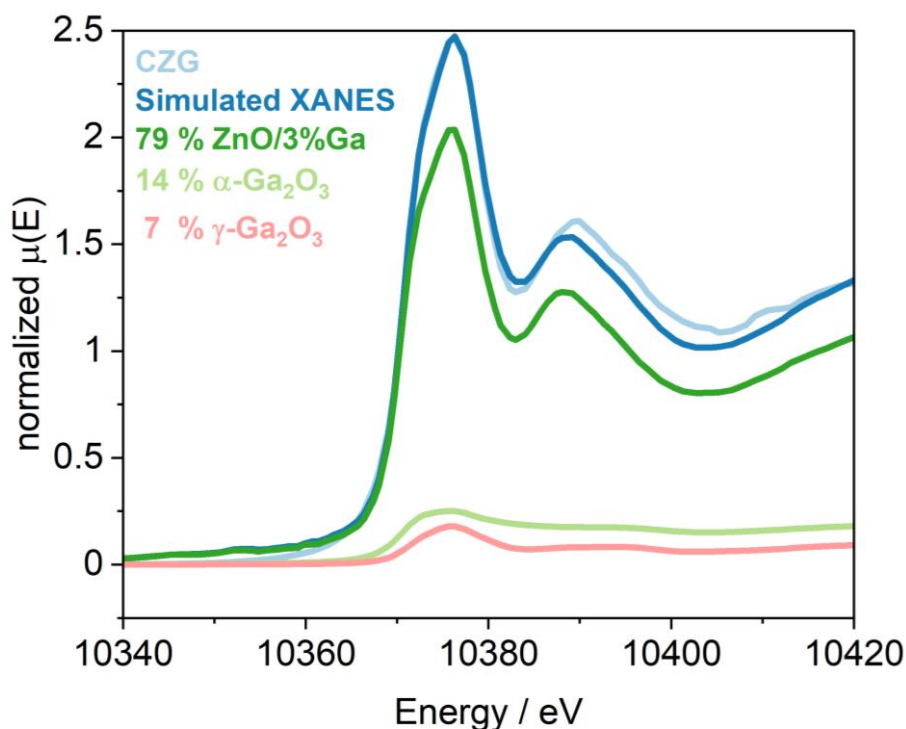


Figure 4.7: Ga K-edge XANES spectra of the activated CZG catalyst at 250 °C in 20 % H₂ in N₂ and results of the linear combination fit using the experimental spectra of gallium oxide reference materials.

This result confirms that after reduction, a fraction of Ga is present as a dopant to the primary promoter ZnO. This fraction is estimated to be larger than proposed in the literature for Ga in the pre-catalyst state or for Al in the reduced state,³⁴ which might be explained with the lower size mismatch between Zn and Ga compared to Zn and Al and a possibly higher solubility limit.

To connect the doped state of ZnO with the observed modification of the Cu surface, the effect of the dopant on the SMSI, *i.e.*, on the reducibility of ZnO was investigated by DFT assuming that an increased reducibility of the primary promoter directly affects the amount of Zn^{red} on the catalyst's surface. Reducibility of the Ga and Al doped ZnO was tested in two ways – by formation of oxygen vacancy and Zn vacancy. First a four layers thick 4×2 large ZnO 110 slab was used and calculated single surface oxygen and Zn vacancy formation energies as the

reference. Then analogous calculations for a system in which single Zn atoms were substituted by Ga or Al were performed. Similarly, bulk ZnO with and without substitution by Ga and Al were investigated.

The results are present in the Table 4.3 and the structures are shown as SI in Figure SI 11.16. The results show that oxygen vacancy formation is easiest for the undoped ZnO and is slightly less favoured for Ga and Al substituted systems. This result reflects the higher valence of the trivalent dopant, which requires more oxygen atoms for charge compensation. On the other hand, formation of Zn vacancies, which can be seen as the system's ability to act as a reservoir for Zn^{red} assuming that the Zn atom migrates from ZnO to the Cu surface due to SMSI, is favoured in Ga and Al doped systems in particular in the bulk. This means that a removal of Zn results in a transfer of positive charge to the Ga and Al dopants and the system is stabilized in this way. With this model, the stronger electronic promotion of the secondarily promoted catalysts observed in the experiments can be explained. Interestingly, looking at the two secondary promoters the results suggest that Zn^{red} formation from Al doping is indeed favoured compared to the Ga dopant, explaining the stronger electronic promotion effect of CZA compared to CZG reflected in a higher Zn^{red} amount determined by chemisorption. Thus, we propose a scenario, in which the secondary electronic promotion by Al and Ga are explained by their presence as dopant to the primary promoter ZnO. As such they promote its primary electronic promotion function as reservoir for Zn^{red} by increasing its reducibility and favouring a Zn^{red} spillover to the copper particle.

Table 4.3: Oxygen and Zn vacancy formations on the Ga(Al):ZnO 110 surface referenced to the values for ZnO(110). Oxygen and Zn vacancy formation in the Ga(Al):ZnO bulk referenced to the values for ZnO.

<i>Composition</i>	<i>Oxygen vacancy formation energy eV</i>	<i>Zn vacancy formation energy eV</i>
<i>ZnO(110)</i>	0	0
<i>GaZnO(110)</i>	+0.21	-0.76
<i>AlZnO(110)</i>	+0.36	-0.80
<i>ZnO – bulk</i>	0	0
<i>GaZnO – bulk</i>	+0.41	-2.15
<i>AlZnO - bulk</i>	+0.34	-2.47

4.3.3 Summary of the Microstructural Characterization and the Secondary Promotion Effect

The characterization of the freshly reduced state of the catalysts CZA, CZG and CZ demonstrate that the secondary promoter affects the catalysts in at least two distinguishable ways: (i) It acts as a structural promoter leading to a higher Cu dispersion and larger specific Cu surface areas, and (ii) it acts as an electronic promoter and by increasing the reducibility of ZnO, enhancing SMSI and leading to a more efficient coverage of the Cu surface with Zn^{red} species.

The former structural promoting effect is mainly explained by the effect of the secondary promoter on the phase evolution during catalyst synthesis favouring a more nano-sized malachite precursor material with a higher degree of substitution. This promotion is carried over from the precursor to the pre-catalyst and finally to the reduced catalyst and was found to be similar for CZA and GZG leading to a larger amount of exposed metallic Cu sites with a clear distinction from the binary CZ. The latter electronic effect is explained by an activation of the Zn^{red}-reservoir in the primary promoter. DFT calculations are in agreement with the chemisorption data, showing that this contribution is stronger for Al compared to Ga as a secondary promoter, leading to a higher amount of exposed Zn^{red} on CZA compared to CZG.

Nonetheless both catalysts show a complete modification of the adsorption properties of Cu in the DRIFTS results, which was not reached for the binary CZ.

From these results, the following picture of the three catalyst's microstructures can be derived, as schematically shown in Figure 4.8. The CZA and CZG contain similarly small nanoparticles of Cu (brown) and ZnO:M (dark grey), which are significantly larger in CZ. This difference is, *e.g.*, reflected in the crystallite size analysis by PXRD, which corresponds to a metal surface area as represented by the green area. Sequential chemisorption was able to further discriminate the surface states and to distinguish between exposed Cu^{surf} (blue area) and Zn^{red} (yellow coverage). The amount of Cu^{surf} was similar for CZA and CZG and higher than in CZ in accordance with a more or less fixed ratio of the “green” and “blue” areas. The amount of Zn^{red} , however, was different in all three samples. Zn^{red} is represented in Figure 4.8 inspired by the ZnO_{1-x} overgrowth model²⁰ in which the thickness of the overgrowth is a measure for the amount of Zn^{red} . However, the same considerations hold true for the Cu-Zn surface alloy model,¹¹² in which the thickness of the yellow parts in Figure 8 would represent the Zn content of the alloy and thus is an analogous measure of Zn^{red} . The amount of Zn^{red} is the highest in CZA. It is moderate in CZG, but still sufficient to modify all Cu-based adsorption sites as shown by DRIFTS. Least Zn^{red} is found in CZ, where also unmodified Cu^{surf} sites are exposed. This model of the microstructure and surface properties of the three catalysts will be used in the following to discuss the catalytic activity and stability.

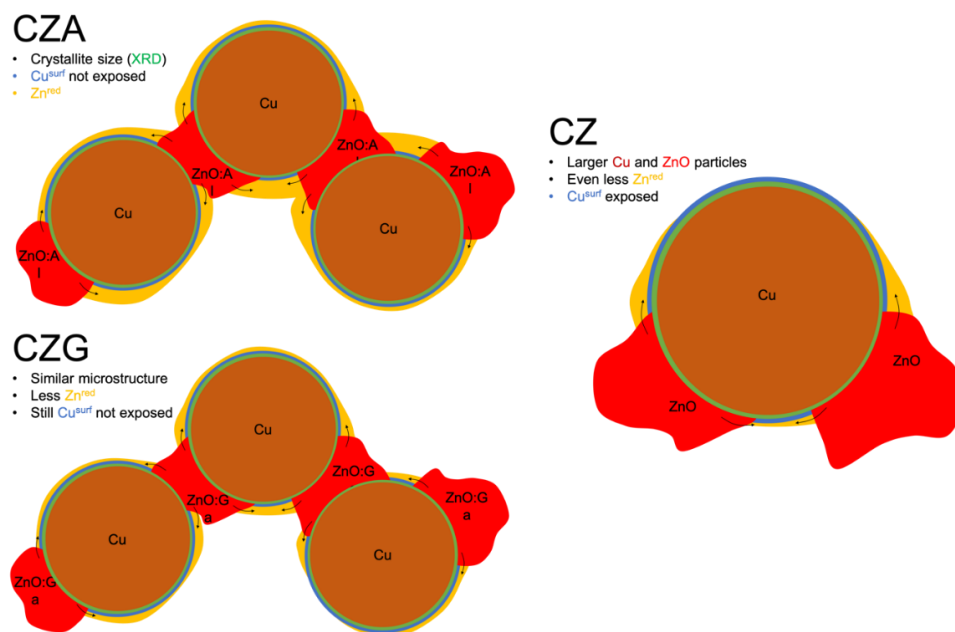


Figure 4.8: Schematic visualization of the Cu microstructure and the Cu-Zn interaction depending on the secondary promoter. The value of the PXRD crystallite size is demonstrated as green ring, the Cu^{surf} sites determined by N_2O -RFC are presented as a blue ring and the $\text{Cu}^{\text{surf}} + \text{Zn}^{\text{red}}$ sites are presented as a yellow surface.

4.3.4 Catalysis of the copper zinc oxide-based catalysts

All three catalysts were tested in methanol synthesis under industrial conditions. An overview on the methanol yields along the time on stream (TOS) after reduction and stabilization for around 200 hours is given in Figure 4.9.

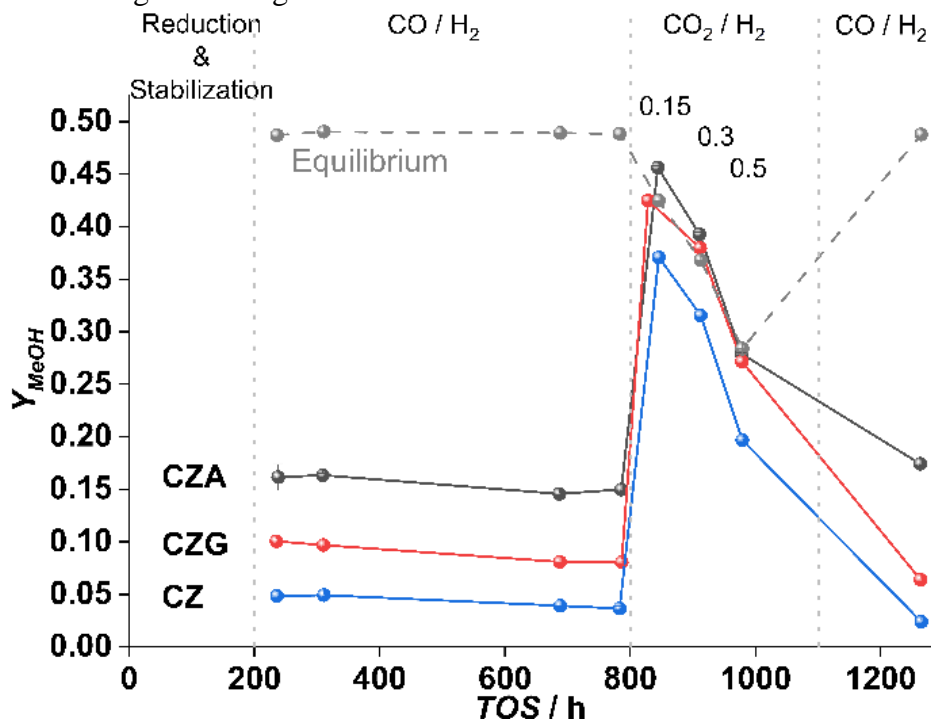


Figure 4.9: Methanol yield of the CZA (black), CZG (red) and CZ (blue) catalysts (125 – 250 μm particle size fraction) at 235 °C and GHSV = 1700 h^{-1} . The feed gas was $\text{H}_2:\text{CO}_x=2$ if not indicated differently. The pressure was 30 bar. The dashed line corresponds to the equilibrium determined by Gibbs minimization. The lines are to guide the eyes.

First the catalysts were tested in CO hydrogenation using stoichiometric feed gas at the experiment's reference conditions. Afterwards, the hydrogen partial pressure and the reactor pressure are changed to determine the influences of these process parameters on the catalytic performance. Each catalyst was investigated at four different temperatures (205 °C, 220 °C, 235 °C and 245 °C) and at three different GHSVs (1200 h^{-1} , 1700 h^{-1} and 3600 h^{-1}).

As shown in Figure 4.9, during CO hydrogenation at 235 °C, the equilibrium methanol formation was not reached. Only after adding 15 % - 50 % CO_2 as carbon source, the methanol yield reached the equilibrium in case of CZA and CZG as catalysts. Therefore, the methanol synthesis using CO as feed gas will be discussed on the results obtained at a GHSV of 1700 h^{-1} , where the catalyst activity was high allowing a good comparison, but still far away from the equilibrium. In case of a mixed synthesis gas ($\text{CO}+\text{CO}_2$), the higher GHSV of 3600 h^{-1} will be used for discussion of the results, since the CZA catalyst reached at 1700 h^{-1} already the equilibrium, as shown in Figure 4.9.

4.3.4.1 Activity in CO hydrogenation to methanol

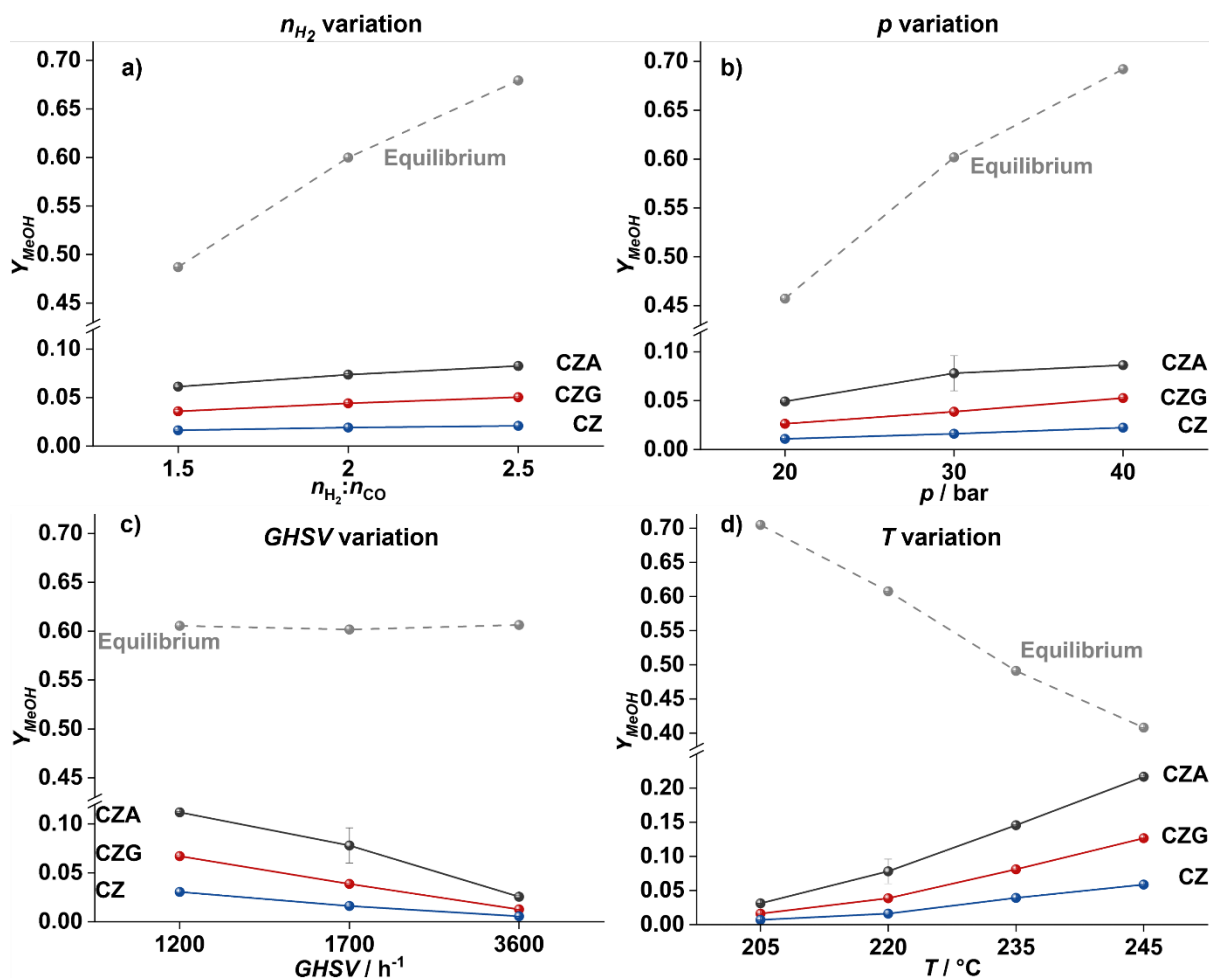


Figure 4.10: Methanol yield during CO hydrogenation of the catalysts CZA (black), CZG (red) and CZ (blue), all with a 125-250 μm size fraction. In a) the hydrogen partial pressure variation at 1700 h^{-1} , 30 bar, 220 $^{\circ}C$, in b) the pressure variation at 1700 h^{-1} , $H_2:CO = 2$ and 220 $^{\circ}C$, in c) the gas hourly space velocity (GHSV) variation at $H_2:CO = 2$, 220 $^{\circ}C$ and 30 bar and in d) the temperature variation at 1700 h^{-1} , $H_2:CO = 2$ and 30 bar are shown. The dashed line corresponds to the equilibrium determined by Gibbs minimization. The lines are to guide the eyes.

During CO hydrogenation the CZA catalysts reached a higher methanol yield at all conditions followed by CZG and CZ as it is shown in Figure 4.10.

By increasing the hydrogen partial pressure (Figure 4.10 a)), the methanol yield of the catalysts slightly increased. This increase of the catalyst kinetics is much less pronounced compared to the equilibrium methanol yield. However, the catalysts performances are far away from equilibrium and therefore, the hydrogen activation does not become a limiting factor. Only, if the catalysts had reached the equilibrium yield of methanol, an increase of hydrogen partial pressure could increase the methanol yield substantially. Besides, the variation was in a very

small range of 0.5 vol% concentration change. The pressure variation (Figure 4.10 b)) demonstrates that the methanol yield strongly follows the reaction pressure. This is not surprising, since methanol synthesis is a mol reducing reaction and therefore it is favoured by thermodynamics at higher pressure and the catalyst performance follows this trend, while their relative kinetic differences remain. Even at these conditions, the catalysts did not reach equilibrium in methanol yield with a GHSV of 1700 h^{-1} at $220 \text{ }^\circ\text{C}$.

Comparing the catalyst's performance dependence on the GHSV (Figure 4.10 c)), the methanol yield increased with increasing contact time or decreasing GHSV as expected. For CO hydrogenation to methanol, no product inhibition effects like in industrial syngas mixtures are expected as in contrast to methanol synthesis from CO_2 , there is no inhibiting coupled product H_2O . In the whole GHSV range investigated here, the kinetics of the catalysts are too slow to reach equilibrium yield, proving that the tests were done in a kinetically controlled regime as required for a proper activity comparison. The activity ranking of the three catalysts is still valid: CZA was the more active catalyst followed by CZG and CZ. To reach higher methanol yield in CO hydrogenation, the contact time could be lowered and optimized as in industrial processes.¹⁵²

Regarding the temperature variation, thermodynamics Favor methanol synthesis at lower temperature, because of the exothermicity. On the other hand, the catalysts kinetics is slow at lower temperature and increases with temperature according to the Arrhenius behaviour as shown in Figure 4.10 d). At $245 \text{ }^\circ\text{C}$ the catalysts approach the equilibrium methanol yield compared to the kinetic regime at 205 or $220 \text{ }^\circ\text{C}$. Comparing the three catalysts, CZA shows again a higher activity than the CZG and CZ. Comparing the line shape of all three catalysts, the secondary promoted catalysts shows a stronger kinetics towards the methanol equilibrium than the reference catalyst. This trend is reflected by the lower apparent activation energy in methanol formation for the secondary promoted catalysts. The apparent activation energies was determined to 99 kJ mol^{-1} for CZA, 104 kJ mol^{-1} for CZG and 109 kJ mol^{-1} for the reference catalyst (SI Figure SI 11.18 and Table SI 11.14). This values are in accordance with the reported apparent activation energy in CO rich synthesis gas around 100 kJ mol^{-1} by Fichtl *et al.*³⁰ Therefore, the secondary promoted catalysts are facilitated in methanol formation, which allows to reach faster the equilibrium yield compared to the CZ catalyst.

In summary, normalized to CZ, the effect of the secondary promoter on the activity of CO hydrogenation was 372 % for CZA and 207 % for CZG at the reference conditions and this

trend remained rather consistent during the process parameter variation, while the absolute values were affected in an expected manner.

4.3.4.2 Stability in CO hydrogenation to methanol

To evaluate the methanol formation rate evolution of the three catalysts, only the CO feed gas experimentations at reference conditions of $T = 235\text{ }^{\circ}\text{C}$, $\text{GHSV} = 1700\text{ h}^{-1}$, $\text{H}_2:\text{CO} = 2$ and 30 bar after different times on stream (TOS) are considered. The experiment covers over 600 h TOS after reduction and stabilization. They show that the catalysts have lost their initial methanol activity continuously (Figure 4.11 a)). The relative formation rates (shown in Figure 4.11 b)) reveal that CZA was the most stable catalyst and lost 15 % of its initial activity, followed by CZG (23 %) and the binary CZ catalyst (30 %). The main reason of deactivation of copper catalysts is the sintering of the reduced metal at temperatures close to the Hüttig temperature of $\sim 180\text{ }^{\circ}\text{C}$, caused by its meta stable facets, Ostwald ripening and coalescence of copper.^{30, 59, 174-176} The different deactivation rates of the three catalysts demonstrate that the secondary promoters execute their structural promotion effect effectively over long TOS and have a conserving influence on the catalyst's microstructure. Since each catalyst had the same history, it can be concluded that Al as secondary promoter has a stronger conserving effect than Ga, while their structural effect on the evolution of the microstructure during catalyst synthesis was rather similar (see above). The absence of a secondary promoter leads to lower activity and stability of the primary promoter zinc oxide alone. The steric effect of structural promotion by the presence of refractory oxides to prevent copper sintering has already been reported previously.^{6, 59, 167} Under finite conditions of pure CO hydrogenation, catalyst deactivation is observed to be relatively low and stabilizing intermediates were suggested as the reason.⁵⁹ While the differences in our three catalysts can be traced back again to the secondary promoter effect, such intermediates may also play a role in our experiment and contribute to the overall acceptable stability performance. Yet it has to be considered that finite conditions were not present, since the catalysts did not reach equilibrium methanol yield (Figure 4.9 and Figure 4.10).

Deactivation of solid catalysts follows in general a potential decay function. Since in the herein reported case, our catalysts were subjected to a formation period of more than two hundred hours TOS before the first data point was measured, the region with steepest slope with the first strongest deactivation part was not recorded and a linear fit was applied.^{30, 155} The fitted linear slopes are shown in Figure 4.11 a). In this comparison, CZG was the least stable catalyst with the highest deactivation rate, followed by CZA and CZ. This suggests a stronger absolute

deactivation of the secondarily promoted catalysts, but the methanol activity as well as the relative stability (b)) was still clearly higher than for the CZ catalysts.

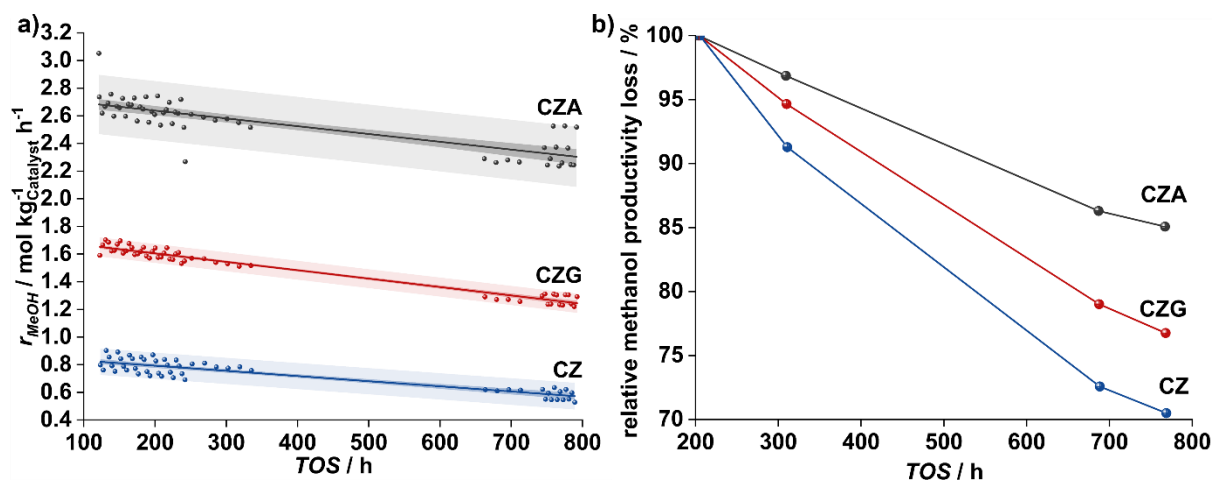


Figure 4.11: a) Methanol formation evolution of the copper based catalysts during CO hydrogenation. The line corresponds to a linear fit of the activity loss whereas the dark coloured area represents the 95 % confidence interval and the lighter coloured area represent the 95 % prediction band. b) Relative methanol production evolution of each catalyst normalized the initial methanol formation rate to 100 %. Reaction conditions: 235 °C, $\text{H}_2:\text{CO} = 2$, 30 bar and GHSV of 1700 h^{-1} .

To better understand the structural changes and to relate them to the deactivation of the catalyst during methanol synthesis, the spent catalysts were investigated by PXRD analysis (Figure SI 11.19). Note that the spent samples were recovered after the stability experiment described above plus the subsequent variation in CO_2 partial pressure, which might have had an additional influence on the catalyst's microstructure. The copper component was detected as a mixture of metallic Cu and CuO the latter being the product of catalyst passivation and handling in air. Compared with the fresh state, the initially faint reflections of zinc oxide in catalysts containing the secondary promoter are more pronounced after reaction. Interestingly, for the lower GHSV of 1200 h^{-1} , more intense reflections of ZnO (and CuO) are present in CZA and CZG than for the highest GHSV of 3600 h^{-1} . Therefore, the almost amorphous primary promoter ZnO in the fresh catalyst was crystallized after reaction to an extent that depends on the contact time. Based on our data, it cannot be decided if this was an effect of CO hydrogenation, CO_2 hydrogenation, which leads to H_2O as coupled product with a potentially crystallization accelerating effect, or both. Comparing the Cu phase ratios in the PXRD pattern qualitatively, CZA contained the lowest fraction of non-oxidized Cu species, which was highest for the binary CZ. This trend is tentatively explained by the smaller Cu particles in the two secondarily promoted samples, which tend to be oxidized earlier and to a higher extent upon

air contact ¹⁷⁷ during passivation and sample transfer than the larger particles in CZ. For a more suitable comparison with the fresh state, the spent samples were re-reduced and re-analysed by PXRD (Figure 4.12). Compared to the fresh state shown in Figure 4.3, the copper reflections became more intense and sharper, which indicates larger crystallites, and that Cu was indeed sintered over time during methanol synthesis. The crystallite sizes based on the Cu 111 reflections, which were 6 nm for CZA and 7 nm for CZG in the fresh state, were now determined to be 12 nm for CZA and 13 nm for CZG after methanol synthesis (Table 4.2 and Figure 4.12). This indicates a strong sintering of the Cu nanoparticles, even if the catalyst was held under isothermal conditions at only 235 °C. Such a drastic increase was not determined for the CZ reference catalyst, but the initial crystallite size of 17 nm was only slightly increased to 19 nm, which could be a hint that this corresponds to a stable Cu particle size for the applied conditions. Interestingly, this relative particle size increase estimated by the PXRD peak width does not correspond to the N₂O capacities of a third N₂O-RFC experiment after re-reduction, which dropped by around 60 % (CZA), 50 % (CZG) and 65 % (CZ) compared to the first N₂O-RFC of the fresh catalysts (Figure 4.13 a)). The excessive loss in N₂O chemisorption capacity detecting Cu^{surf} and Zn^{red} in the light of the smallest Cu particle growth in CZ suggests that this catalyst undergoes an overproportioned loss of Zn^{red} sites during deactivation compared to the secondarily promoted catalysts. Unfortunately, the amount of sample was not sufficient for a renewed sequential chemisorption series of N₂O-RFCs and H₂-TAs. However, the absolute N₂O capacities of CZA and CZG were similar and still larger than for CZ reflecting the trends in Cu particle size.

We can conclude that all three catalysts were subjected to sintering during operation as a major contribution to catalyst deactivation. The initially larger Cu particle size in CZ and the therefore lower absolute size increase explains the apparent higher absolute stability of this catalyst. The sintering of CZA and CZG was rather comparable.

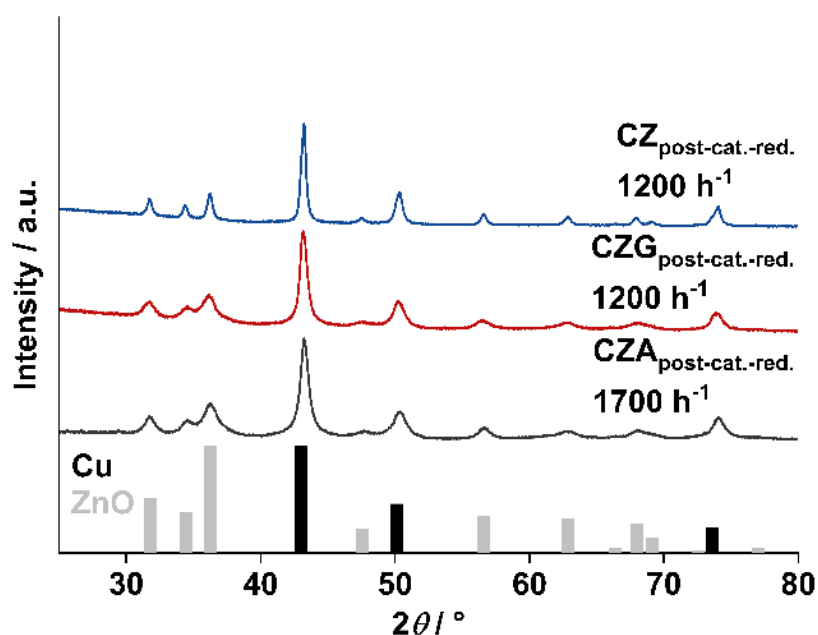


Figure 4.12: Reduced catalysts after methanol synthesis for around 1200 h time on stream at 30 bar, 235 °C, $H_2:CO_x = 2$. The bar charts of the references are from COD (in black for copper (001512504), in grey for zinc oxide (002300450)). The reduction was performed with 5 % H_2 in Ar with a heating ramp of 2 °C min^{-1} to the target temperature 275 °C, which was held for 4 h.

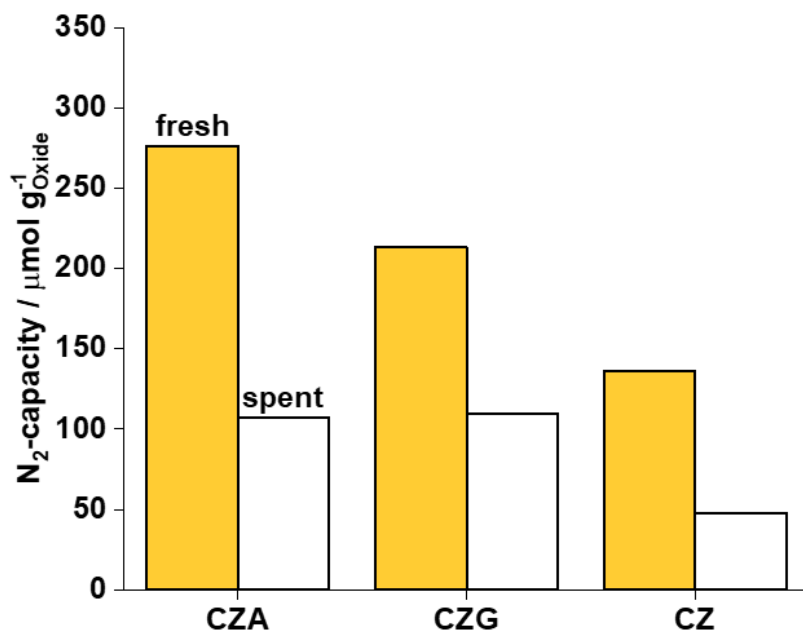


Figure 4.13: Comparison of the specific copper surface area determined by N_2O -RFC for the fresh and spent catalysts after 1200 h time on stream at 235 °C, GHSV of 1700 h^{-1} , $H_2:CO_x = 2$, 30 bar.

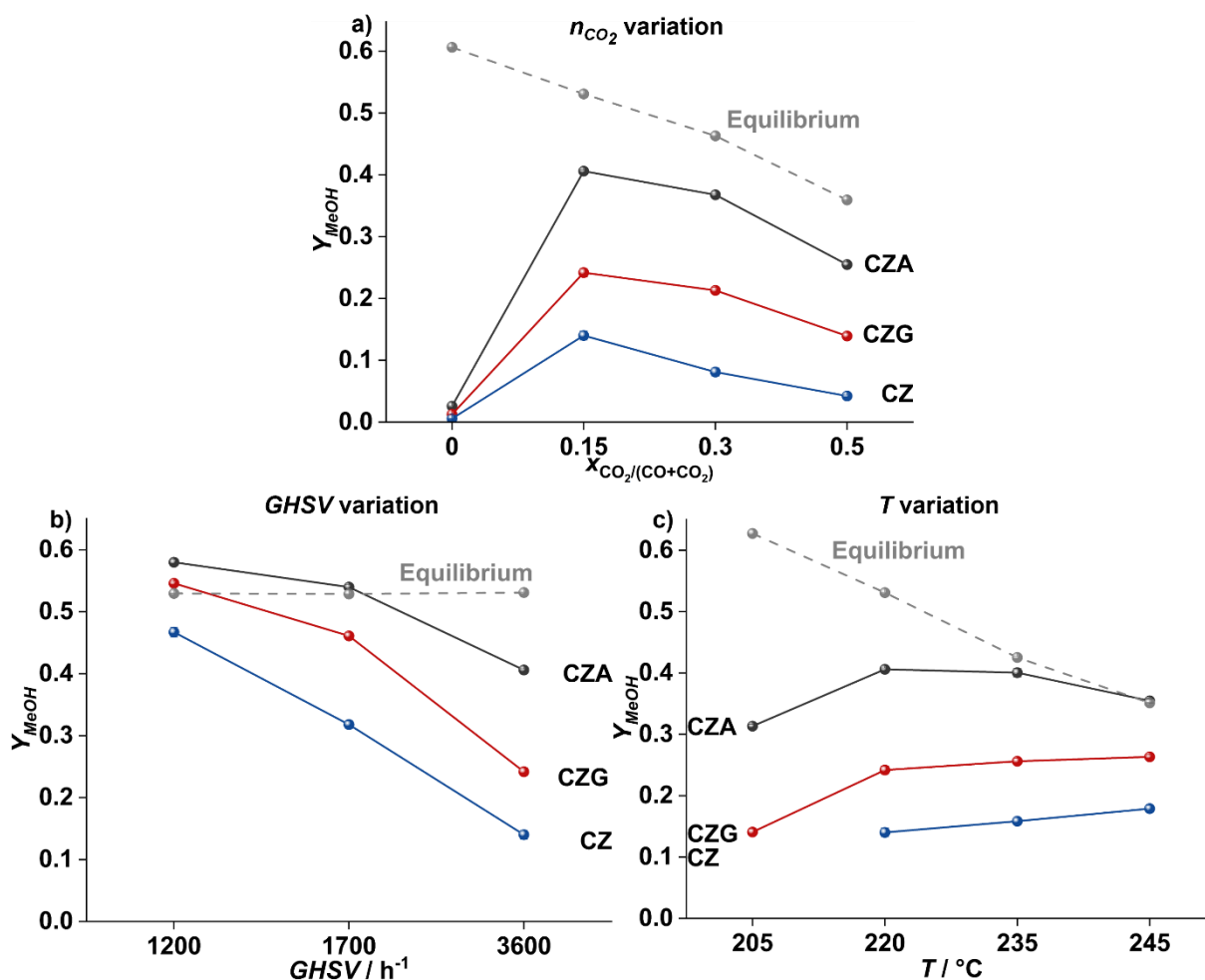
4.3.4.3 Activity in hydrogenation to methanol in presence of CO₂

Figure 4.14: Methanol yield during CO+CO₂ hydrogenation at H₂:CO_x = 2 and 30 bar with 125-250 μm size fraction of the catalysts. In a) the CO₂ amount variation at 220 °C and GHSV = 3600 h⁻¹ in b) the GHSV variation at 220 °C and $x_{CO_2} = 0.15$ and in c) the Temperature variation at GHSV = 3600 h⁻¹ and $x_{CO_2} = 0.15$ are shown. In black the performance of the CZA, in red the performance of the CZG and in blue the performance of the CZ catalyst in methanol synthesis are presented. The dashed line correspond to the equilibrium determined by Gibbs minimization. The lines are to guide the eyes.

To investigate the effect of a mixed carbon source as in industrial feeds for methanol synthesis, CO was gradually substituted by CO₂, while maintaining a H₂:CO_x ratio of two. A low amount of 15 % CO₂ increased the methanol yield significantly for each catalyst (Figure 4.14 a)). Further increasing CO₂ concentration results in a decreasing methanol yield. Nevertheless, the methanol yield stayed on a higher level than for pure CO hydrogenation even for 50 % CO₂. The catalysts follow the shape of the equilibrium line with a rather constant approach for each catalyst. Like in CO hydrogenation, the secondarily promoted catalysts were always more

active than the binary CZ reference catalyst and among them, CZA showed a higher performance than CZG.

The boost of CO hydrogenation to methanol by addition CO₂ was previously described by several researchers with the strongest effect found between 2 % and around 12 % CO₂ concentration into the feed gas.^{58, 178, 179} From a mechanistic point of view, this boost can be explained by a change of the reaction route from a formyl intermediate with CO as precursor to methanol to a formate intermediate from a CO₂ precursor.⁵ The insertion of CO₂ into the feed gas allows formate as an intermediate, leaving after hydrogenation to methanol a surface oxygen or hydroxyl group, which enables the activation in terms of the water gas shift reaction CO towards CO₂ and new formate that can be hydrogenated to methanol.^{5, 16, 155} Simultaneously, the formed methanol can promote the methanol synthesis *via* an autocatalytic pathway involving methyl formate at a later stage of the reaction mechanism.¹⁸⁰ However, further increase in the CO₂ concentration leads to high water concentrations into the product stream, poisoning the catalyst by product inhibition.⁵⁸ Furthermore the ZnO promoter undergoes structural changes at the cost of the SMSI effect, inhibiting the autocatalytic pathway of methanol.^{30, 31, 180} As described by Sahibzada *et al.*,⁵⁸ this decay in methanol yield with increasing CO₂ content can only be observed at finite conversion, whereas at differential conversion the product inhibition is not observed and the methanol formation rate increases linearly with CO₂ content due to the faster reaction of the CO₂ precursor.⁶¹

In our experiment, the decay of methanol yield at 30 % and 50 % CO₂ thus indicates integral conditions and the boosted methanol formation has brought in particular CZA strongly towards the equilibrium yield. Upon decreasing the GHSV, the methanol yields of all three catalysts converge towards the equilibrium yield, which is reached for CZA at 1700 h⁻¹ and also for CZG at 1200 h⁻¹ (Figure 4.14 b)). The slight exceeding of the equilibrium yield in Figure 4.14 b) is likely due to uncertainties of the calculated equilibrium line based on the thermodynamics of ideal gases and due to calibration errors of the GC. For a robust comparison of the three catalysts in the feed containing 15 % of CO₂, proximity to equilibrium has to be avoided at high GHSV and low temperature.

This is the case for the data points at the most left-hand side of Figure 4.14 c) showing the effect of temperature on methanol synthesis from a mixed synthesis gas. At lower temperature, a lower methanol formation was observed for each catalyst. Moreover, the initial productivity increased with increasing temperature caused by their accelerated kinetics, bringing the reactions towards equilibrium. Already at 235 °C, CZA reached equilibrium methanol yield and then follows the

equilibrium line to 245 °C. The measurement at 220 °C of this catalyst might already be affected by too integral conditions to obtain clean kinetic data. CZG and CZ did not reach equilibrium at 245 °C, but all three catalysts show the expected convergence of productivity as equilibrium is approached at higher temperatures. For the comparative evaluation of the catalysts, the most differential data point was chosen for CZA, which is the one at highest GHSV and lowest temperature of 205 °C. Unfortunately, at these conditions, there was zero activity of CZ, which is why only the comparison between CZA and CZG was possible and for the comparison of CZG and CZ, the data at 220 °C was used, where these two catalysts are still far from equilibrium.

In summary, the overall methanol formation rates have been boosted compared to pure CO hydrogenation, but both secondary promoted catalysts are always more active than the binary reference CZ also in the presence of CO₂. The relative effect of secondary promotion was 173 % for CZG and 457 % for CZA referenced to CZ at the above-mentioned conditions.

4.3.5 Summary of the catalytic results and the effect of the secondary promoter

The secondarily promoted Cu/ZnO catalysts outperform the binary reference catalysts clearly in methanol synthesis from CO and CO₂. During the reaction, the catalysts sinter, but all show a relatively stable performance. In particular, the structural promotion effect of the secondary promoters observed during the evolution of a highly dispersed microstructure, was stable and the smaller Cu particle size was conserved for long time on stream compared to CZ. The similar microstructure of the two catalysts with the secondary promoter was not reflected in similar catalytic activities, but CZA was clearly the more active catalyst than CZG for both carbon precursors CO and CO₂. This can be ascribed to the more effective electronic promotion by Al compared to Ga when introduced as dopant to ZnO (see above). While the promoting effect of Ga addition was similar for CO and CO₂ hydrogenation leading to an activity of roughly 173 % of that of CZ, the addition of Al showed a larger impact in CO₂ hydrogenation (457 %) than in CO hydrogenation (371 %). Considering that CZA show the larger electronic promotion effect with a higher amount of Zn^{red}, this results is in line with the proposal that Zn^{red} helps the formate intermediate to be activated in the CO₂ pathway to methanol.²²

Quantitative linking of the characterization results of the fresh catalyst with the catalyst performance in our long-term experiment is challenging, since the catalysts were shown to change, *e.g.* by sintering, during the experiment and such structural changes will affect the performance depending to the pretreatment and to the conditions inside the reactor.^{17, 181} Our

samples were tested for more than 800 hours with feed gas variation and the first activity data are taken after 200 hours. Therefore, we cannot assign if the structural changes happened in the formation period, in the CO hydrogenation or in the CO₂ hydrogenation sections of the experiment or in combinations thereof and cannot link them to the different performance parameters. Nevertheless, with that in mind, an attempt was made to apply the turnover frequencies (TOF) concept using the chemisorption properties of a freshly reduced catalyst and the earliest catalytic data point of the CO hydrogenation reference activity data around 200 hours TOS and the CO₂ hydrogenation data (15 % CO₂) obtained at 220 °C and GHSV = 3600 h⁻¹. The same activation protocol was followed for the chemisorption and the catalytic experiments ($T_{\text{red}} = 275$ °C),

An approximately similar TOF is expected for the methanol formation sites under the following assumptions:

- (i) the active sites involve Cu^{surf}, *e.g.*, for hydrogen or formyl¹⁶ activation.
- (ii) They also contain Zn^{red}, *e.g.*, for the activation of O-bound intermediates^{22, 114} such as formate or methoxy.
- (iii) Both surface species will be the same for each of the three catalysts, but
- (iv) their total (structural promotion) and relative concentrations (electronic promotion) are different.

The different TOFs based on Cu^{surf}+Zn^{red}, Cu^{surf} only and Zn^{red} only (of the fresh catalysts) as well as the corresponding methanol productivities (at the above-mentioned conditions) are shown in Figure 4.15 a) for CO hydrogenation and in Figure 15 b) for CO₂ hydrogenation.

The productivities of the catalysts follow the same trend in both reactions that was already described above: CZA reached the highest methanol productivity followed by CZG and the binary CZ. Because the combined Cu^{surf}+Zn^{red} sites have the largest chemisorption capacities, the TOF based on these sites were lowest. But for CO hydrogenation, only these TOFs of the combined sites show the expected similar values. This demonstrates that indeed both Cu^{surf} and Zn^{red} sites might be involved in the active sites for CO hydrogenation. Based on the potential diagram presented by Studt *et al.*,¹⁶ it may be speculated that the former activate the C-bound formyl intermediates early in the mechanism, which spill over to the latter once the intermediate changes to O-bound methoxy. Contrarily, a scattering of the TOFs was found for the Cu^{surf}- and Zn^{red} sites. The scattering shows that the synergetic interplay of Cu^{surf} and Zn^{red}, *e.g.*, in form of a surface alloy or interface sites, plays a major role for the methanol activity of the catalysts in line with earlier investigations.^{112, 156} This hypothesis is in line with the previously observed scaling of activity with the chemisorption capacity determined by N₂O-RFC,¹² but enhances

the interpretation beyond a pure Cu surface area effect taking also the $\text{Cu}^{\text{surf}}\text{-Zn}^{\text{red}}$ synergy into account.

For CO_2 hydrogenation, the productivities in methanol synthesis are as described above. The CZA and CZG are more productive than the CZ reference catalyst. However, the TOFs based on $\text{Cu}^{\text{surf}}+\text{Zn}^{\text{red}}$ are closer than the pure Cu^{surf} or Zn^{red} sites. Beside the fact, that more than 80 % of the carbon source is CO and a strong reducible synthesis gas mixture was applied to the catalysts, a strong deviation of TOF is not expected. On the other hand, CO_2 is preferably converted to methanol in a mixed synthesis gas⁶¹ leaving surface oxygen and hydroxyl groups, which enables the activation of CO as a formate intermediate and following the formate route to methanol^{99, 155}. In this case of a mixed feed gas composition, Zn^{red} can be considered as a thermodynamic sink taking out the redundant oxygen by oxidizing to ZnO.^{22, 26, 157} In this case, the TOF should follow the Zn^{red} trend more than the combination of Cu^{surf} and Zn^{red} . However, it can be assumed, that the present CO in synthesis gas is activated as formate on such oxidized Zn^{red} species and scavenging the formed water. The experiments does not deliver hints to the extent of re-oxidized Zn^{red} species. Therefore, it can be possible, that only few sites are oxidized and accelerate the methanol formation. That would be the reason that the methanol synthesis appears more on both Cu^{surf} and Zn^{red} sites.

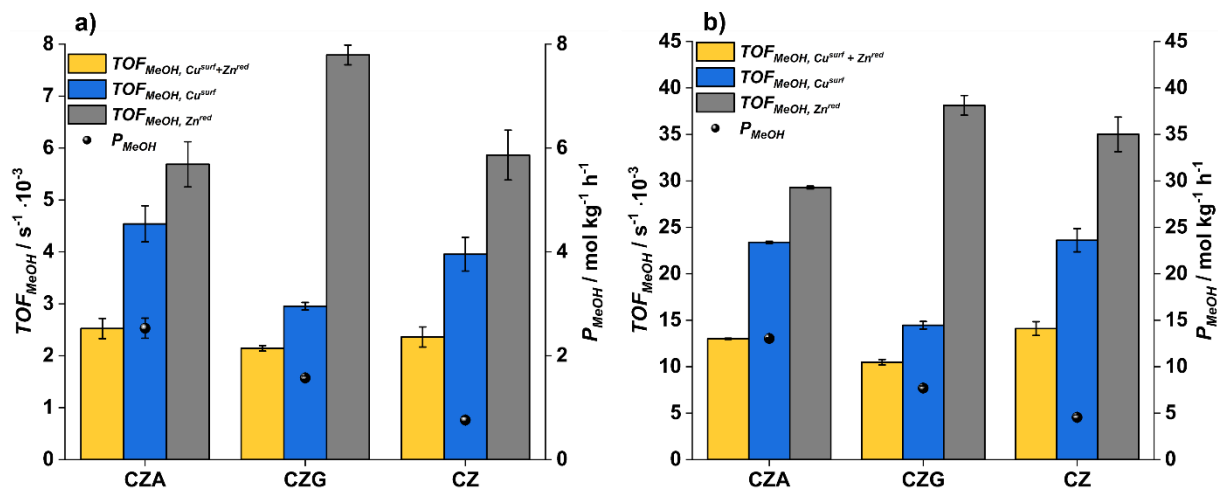


Figure 4.15: Turnover frequency of the CZA, CZG and CZ in methanol synthesis a) at 1700 h^{-1} , $235 \text{ }^\circ\text{C}$, $\text{H}_2:\text{CO} = 2$ and 30 bar after 200 h TOS and b) at 3600 h^{-1} , $220 \text{ }^\circ\text{C}$, $\text{H}_2:\text{CO}_x = 2$, $x_{\text{CO}_2} = 0.15$ and 30 bar after 800 h. The first column (yellow) is based on the $\text{Cu}^{\text{surf}}+\text{Zn}^{\text{red}}$, the second column (blue) is based on the Cu^{surf} and the third column (grey) is based on the Zn^{red} , determined by $\text{N}_2\text{O-RFC}$.

4.4 Conclusion

In this work, we have adapted an advanced sequence of chemisorption experiments for the investigation of the secondary promotion effect on Cu/ZnO catalysts for methanol synthesis. Therein, ZnO acts a primary promoter that has both a structural and an electronic function which is based on ZnO nanoparticles and reduced zinc surface species Zn^{red} , respectively. We were able to quantify the absolute chemisorption capacities as well as the ratio of metallic Cu surface sites Cu^{surf} to Zn^{red} sites for three catalysts without secondary promoter (CZ) and with 3 mol% of Al (CZA) or Ga (CZG) as secondary promoters. The major results of the secondary promotion effect are:

- There is a strong structural promotion effect if the secondary promoters are present that roughly doubles the total chemisorption capacities of CZA and CZG compared to CZ. This result is consistent with physisorption data and smaller crystallite sizes.
- This secondary structural promotion effect is similar for Al and Ga and can be explained by a more efficient nano-structuring and Zn distribution already in the co-precipitated precursors, which is carried over to the activated catalysts.
- In addition, an electronic promotion effect was present, which caused different amounts of Zn^{red} at the catalyst's surfaces. This effect was clearly stronger for Al than for Ga acting as secondary promoter. DRIFTS confirmed that still the effect was strong enough on CZG to fully modify the adsorption properties towards CO, while only on CZ typical features of free Cu^{surf} were detected.
- This secondary electronic promotion effect can be explained by doping of the primary promoter ZnO by Al or Ga. Such doping was confirmed in the activated catalyst CZG by Ga K-edge XANES. DFT calculations show that, with a secondary promoter doped ZnO acts as a more efficient reservoir for Zn^{red} species by stabilizing the resulting Zn vacancies. In line with the experimental observations, a stronger effect was found for Al compared to Ga.
- In methanol synthesis from CO or CO_2 , CZA was the most active catalyst followed by CZG and CZ. After industrially relevant test duration of 800 hours' time on stream, the structural promotion effect was mitigated by Cu sintering, but still partially maintained. This led to similar crystallite sizes and chemisorption capacities of the spent CZA and CZG, while CZ showed larger particles and lower surface area.
- The better performance of CZA compared to CZG despite their similar fresh and spent microstructure is explained by the secondary electronic promoting effect, leading to more Zn^{red} on the former catalyst.

- Based on the almost fourfold activity increase of CZA relative to CZ in CO₂ hydrogenation and only roughly threefold activity increase in CO hydrogenation, we conclude that Zn^{red} species are more relevant in the latter reaction, which is consistent with the idea of activation of formate intermediates on such sites.

Altogether, a comprehensive model including Al or Ga addition to a binary Cu/ZnO catalyst was introduced. A way of the secondary promoter strengthening the effects of the primary promoter ZnO in the methanol synthesis has been proposed and an enhanced picture of the active catalyst's microstructure has been presented.

Supporting Information

Supporting Information for this article can be found in chapter 11.6 (Supporting Information to "On the secondary promotion effect of Al and Ga on Cu/ZnO methanol synthesis catalysts") starting from page 203.

Acknowledgements

We gratefully acknowledge Deutsche Forschungsgemeinschaft (DFG, German Research Foundation) for funding through the priority program SPP 2080 "Catalysts and reactors under dynamic conditions for energy storage and conversion" (project numbers 406903668, 406483183/ZO 369/2-1) and the state of Baden-Württemberg for bwHPC (bwUniCluster and JUSTUS, RV bw17D01).

A great thanks to Gereon Behrendt (University Duisburg-Essen) for the catalyst synthesis and to Tabea Gross (TU München) for N₂O-RFC of the fresh and spent sample. We also thank Daria Otyuskaya (Avantium) for performing the catalytic measurements.

5 Phase evolution, speciation and solubility limit of aluminium doping in zinc oxide catalyst supports synthesized *via* co-precipitated hydrozincite precursors

Benjamin Mockenhaupt ^{**ac}, Jan Konrad Wied ^{**b}, Sebastian Mangelsen ^c, Ulrich Schürmann ^d, Lorenz Kienle ^d, Jörn Schmedt auf der Günne ^{*b}, Malte Behrens ^{*ac}

- a. B. Mockenhaupt, Prof. Dr. M. Behrens, Institute of Inorganic Chemistry, University of Duisburg-Essen, Universitätsstr. 7, 45141 Essen (Germany), E-mail: mbehrens@ac.uni-kiel.de.
- b. J. K. Wied, Prof. Dr. J. Schmedt auf der Günne, Institute of Inorganic Chemistry, University of Siegen, Adolf-Reichwein-Straße 2, 57076 Siegen (Germany), E-mail: gunnej@chemie.uni-siegen.de.
- c. B. Mockenhaupt, Dr. S. Mangelsen, Prof. Dr. M. Behrens, Institute of Inorganic Chemistry, Christian-Albrecht University of Kiel, Max-Eyth-Str. 2, 24118 Kiel (Germany)
- d. Dr. U. Schürmann, Prof. Dr. Lorenz Kienle, Institute for Materials Science, Christian-Albrecht University of Kiel, Kaiserstraße 2, 24143 Kiel (Germany)

** both authors contributed equally.

* Corresponding author.

Manuscript published as: Mockenhaupt, B., Wied, J. K., Mangelsen, S., Schürmann, U., Kienle, L., auf der Günne, J. S., & Behrens, M. (2023). Phase evolution, speciation and solubility limit of aluminium doping in zinc oxide catalyst supports synthesized via co-precipitated hydrozincite precursors. *Dalton Transactions*, 52(16), 5321-5335.

Contribution of the authors

- B.M. synthesized the materials and contributed to the characterization, data analysis and wrote the first draft of the manuscript.
- J.K.W. conducted the NMR experiments, the data analysis and contributed to the preparation of the manuscript.
- S.M. conducted the XRD refinements, contributed to experiments, design of experiments, data analysis and evaluation and preparation of the manuscript.
- U.S. conducted the TEM measurements, contributed to design of experiments, data analysis and preparation of the manuscript.
- L.K., J.S.G and M.B. contributed to conceptualization of the work, acquisition of the financial support, provision of study materials, reagents, materials, instrumentation, computing resources and other analysis tools and preparation and editing of the manuscript.

Abstract

The preparation of Al-doped ZnO via thermal decomposition of crystalline precursors, with a particular emphasis on kinetic effects on the solubility limits, was studied. The promoting effect of Al^{3+} on the catalyst system is discussed for methanol synthesis where ZnO:Al is employed as a support material for copper nanoparticles. The synthesis of the Al-doped zinc oxides in this study was inspired by the industrial synthesis of the methanol synthesis catalyst via a co-precipitated crystalline precursors, here: hydrozincite $\text{Zn}_5(\text{OH})_6(\text{CO}_3)_2$. To determine the aluminium speciation and the solubility limit of the aluminium cation on zinc positions, a series of zinc oxides with varying aluminium contents was synthesized by calcination of the precursors. Short precipitate ageing time, low ageing temperature and aluminium contents below 3 mol% metal were advantageous to suppress crystalline side-phases in the precursor, which caused an aluminium segregation and non-uniform aluminium distribution in the solid. Even if zinc oxide was the only crystalline phase, TEM revealed such segregation in samples calcined at 320 °C. Only at very low aluminium contents, the dopant was found preferably on the zinc sites of the zinc oxide structure based on the $\text{Al}_{\text{Zn}}^{\bullet}$ signal dominating the ^{27}Al NMR spectra. The solubility limit regarding this species was determined to be approximately $x_{\text{Al}} = 0.013$ or 1.3 % of all metal cations. Annealing experiments showed that aluminium was kinetically trapped on the $\text{Al}_{\text{Zn}}^{\bullet}$ site and segregated into ZnAl_2O_4 upon further heating. This shows that lower calcination temperatures such as applied in catalyst synthesis conserve a higher aluminium doping concentration on that specific site than is expected thermodynamically.

5.1 Introduction

Zinc oxide is a typical semiconductor material with a wide direct band gap around 3.3 eV.¹⁸²⁻¹⁸⁵ Several studies addressed the band gap engineering to improve the optical or electronic properties.^{183, 186} Incorporation of a trivalent cation like aluminium in the zinc oxide lattice introduces one extra electron, which results in a promoted n-type semiconductor.¹⁸⁷

Hence, the electronic conductivity of such a doped zinc oxide increases by the increased Fermi level and the facilitated excitation of the additional electron to the conducting band, which should be associated with a lowered band gap energy.¹⁸⁸⁻¹⁹¹ Such improvement of the electronic properties of zinc oxide is not only of interest in the field of semiconductor applications, but also in the field of catalysis.

Typically, a copper/zinc oxide catalyst contains around 10 % aluminium oxide for industrial methanol synthesis from CO_x/H_2 mixtures (synthesis gas). It has been demonstrated that aluminium promotes the catalytic activity by improving and stabilizing the nano-structuring of the catalyst (structural promoter) as well as the strong metal-support interactions between zinc oxide and the copper nanoparticles (electronic promoter). Small amounts of this trivalent cation also increase catalyst lifetime and reduce copper sintering.^{31, 34, 153} The doping effect of bivalent (Mg^{2+}) and trivalent cations (Al^{3+} , Ga^{3+}) in zinc oxide supports on the activity in methanol synthesis was further investigated,³⁷ and it was found that a lower band gap energy of the doped zinc oxide is correlated with a higher catalytic activity after impregnating it with copper. Such a lowered band gap was discussed because of aluminium incorporation similar to semiconductor research. Contrarily, a bivalent cation does not lower the band gap nor improve the catalytic activity significantly.³⁷ This finding is in line with studies, which found a correlation in conductivity increase by trivalent cationic-doped zinc oxides and a decrease for cationic dopants of lower valency.^{192, 193} These results led to the hypothesis, that beside the structural impact also electronic properties affect the catalysis in a positive way, which can be introduced by the incorporation of the Al^{3+} cation and could be related to the reducibility of doped zinc oxide under the hydrogenation conditions in methanol synthesis.³⁷

In both fields, semiconductors and catalysis, the efficiency of the promoting effect depends on the maximum incorporation of aluminium ions in zinc oxide and on their lattice site substituting zinc ions ($\text{Al}_{\text{Zn}}^{\bullet}$) in the zinc oxide lattice.¹³⁹ Contrarily, a segregated aluminium oxide side-phase in a doped zinc oxide sample could suppress the electronic promotion by its insulating properties.^{146, 194} Thus, the determination of the maximum substitution limit of aluminium atoms in the zinc oxide lattice is of high importance. This can be a quite difficult task because of various side phases which can be formed. The solubility limit depends on the synthesis route and was estimated to be between 0.1 at% and 5.2 at% aluminium in zinc oxide.^{144-147, 149, 195} The determination of the substitution was performed with several techniques, like optical measurements¹⁴⁶, the reduction of dichromate¹⁹⁵, scanning electron microscopy with energy dispersive X-ray spectroscopy (SEM-EDX) analysis¹⁴⁵, Raman-spectroscopy¹⁴⁴, resistivity measurements¹⁴⁷ and ^{27}Al solid state nuclear magnetic resonance (NMR) spectroscopy.¹⁴⁹ With the help of ^{27}Al NMR different aluminium environments can be resolved and assigned to the different coordination numbers of aluminium.^{143, 148, 149, 196} In this regard the ^{27}Al NMR signal at $\delta_{\text{iso}} = 82.6$ ppm could unambiguously be assigned to aluminium on a zinc position in the ZnO crystal structure $\text{Al}_{\text{Zn}}^{\bullet}$,¹⁹⁶ and Knight shifted signal gave evidence of the targeted n-doping leading to an electronic conductivity.¹⁴²

With that method, the solubility limit is determined in a closer range of 0.3 at% to < 2 at% aluminium in ZnO depending on the synthesis procedure and the synthesis temperature.^{142, 143, 148, 149, 196} The inconsistencies regarding the solubility limit are subject of this contribution. The hypothesis of a solubility limit is consistent with quantum-chemical investigations that suggested a solubility limitation by the formation of the spinel ZnAl_2O_4 , which acts as “thermodynamic sink” and inhibits formation of highly doped ZnO variants.¹⁹⁷ This is in agreement with earlier experimental work, where for a $\text{ZnO}/\text{Al}_2\text{O}_3$ mixture at temperatures lower than 1250 °C a solubility limit of $\leq 0.2\%$ was suggested by X-ray diffraction.¹⁹⁸ To the best of our knowledge, the solubility limit has not been investigated to that level of details in the context of catalyst synthesis with different occurring side-phases which impose a thermodynamic limit as suggested by theory.¹⁹⁷ Clearly, such an investigation requires an analytical technique which can identify and quantify the different chemical environments of the Al atoms and a low-temperature synthesis approach to stabilize high Al substitution levels.

In the field of catalysis, the calcination temperatures are typically lower than the annealing temperatures of semiconductors. At lower temperatures such as 300 - 400 °C the $\text{Al}_{\text{Zn}}^\bullet$ NMR signal was observed to have a high intensity.^{142, 143} Furthermore it was found that the metallic character of ZnO:Al depends on the atmosphere, *i.e.* a reductive atmosphere may increase the metallicity of ZnO:Al as indicated from the formation of a Knight shifted ^{27}Al NMR signal.^{196, 199} For methanol synthesis, which inspired this work, the zinc oxide catalyst support is calcined in an oxidative atmosphere at a comparable temperature around 350 °C.⁸ It is the goal of this work to investigate the solubility limit of Al-doped zinc oxide for materials that represent the catalyst support formed by this method.

To determine the maximum amount of aluminium substituted zinc sites, a series of zinc oxides with varying aluminium content was synthesized using co-precipitation of crystalline hydroxycarbonate precursors, which is the established method for synthesizing Cu/ZnO:Al catalysts. In this case, the copper component was omitted to focus on the support.¹²⁹ This has the advantage, that the aluminium and zinc components are well distributed. In addition, no organic molecules are involved, which could interfere optical measurements. However, this procedure opens another question, namely that of the substitution chemistry in the hydroxycarbonate precursor. The aluminium doping of a specific precursor phase, like the hydrozincite phase used here, should facilitate the formation of doped oxides upon thermal decomposition of the precursor and increase the inter-dispersion of both elements after calcination. Within our study, the question towards maximum substitution limit of Al^{3+} ions on the zinc sites in the hydrozincite precursor phase as well as in the zinc oxide structure will be addressed. We further

aim at studying the aluminium dopant also under hydrogenation conditions that are relevant for methanol synthesis in forthcoming work. Finally, copper can be deposited on these supports with the aim to relate the catalytic properties to detailed knowledge of the aluminium species and amount. Here, we report on the as-prepared state of the catalyst support.

5.2 Experimental section

5.2.1 Sample labelling

The samples are labelled according to their nominal aluminium content relative to the total amount of metal atoms, *i.e.* the cation-based molar aluminium fraction x_{Al} calculated as shown in equation M 5.1.

$$x_{Al} = \frac{n_{Al}}{n_{Al} + n_{Zn}} \quad M\ 5.1$$

Here, n_i is the molar amount of element i ($i = \text{Zn}, \text{Al}$). Nominal values refer to the amount utilized during synthesis, which was found to match satisfactorily to the experimental values determined by ICP optical emission spectroscopy as discussed below in detail.

5.2.2 Precursor synthesis

The hydrozincite precursor was synthesized by co-precipitation with small amount of aluminium. The precipitation was carried out in a 1L automated stirred tank reactor (OptiMax1001, Mettler Toledo) using 1 M metal salt nitrate solutions at a temperature of 65 °C and at a constant pH of 6.5. Appropriate ratios of zinc and aluminium nitrate, with a purity $\geq 98\%$ (SI, Table SI 11.17), were chosen to reach nominal compositions ranging from 0 % to 10 % Al ($0 \leq x_{Al} \leq 0.1$). As precipitating agent, 1.6 M sodium carbonate solution was co-fed into the reactor. The dosing rate of metal salt solution was adjusted to 4.2 g min⁻¹. After precipitation, approximately 300 mL of precipitate slurry was obtained and aged for 10 minutes without further pH control in the mother liquor. The precursor was washed with deionized water 10 times, to reach a conductivity of the filtrate lower than 100 $\mu\text{S cm}^{-1}$ and was subsequently dried at 80 °C for minimum 14 h. This synthetic procedure corresponds to the industrial preparation of the Cu/ZnO:Al catalyst for methanol synthesis⁵⁷ with omittance of copper salts in the co-precipitation.

For a time-resolved ageing experiment, a synthesis as described above was carried out with aluminium content of 2 % ($x_{Al} = 0.02$). After the finish of co-precipitation, the first sample ($t = 0$ min) was taken out of the reactor before precipitate ageing. At ageing times of 10 min,

30 min, 60 min and 120 min, additional samples were collected. The total amount of the slurry removed was around 30 ml. After 120 min, the remaining suspension was aged for additional 12 hours in a Teflon-lined steel autoclave (275 ml) under solvothermal conditions at 130 °C. The Teflon-lined steel autoclave was maximum filled by 2/3 of its total volume. The samples were centrifuged and three times washed with deionized water to get rid of excess ions, and afterwards dried at 80 °C for minimum 14 h.

A brief description of the hydrozincite crystal structure is provided as supporting information and visualized in Figure SI 11.20.

5.2.3 Zinc oxide synthesis

The zinc oxide samples were synthesized by calcination of ground hydrozincite precursor obtained from the above-described co-precipitation synthesis. The calcination was performed at 320 °C with a heating ramp of 2 °C min⁻¹ for 4 h in a muffle furnace of Narbertherm (LE 6/11/B150) in static air (without any volume flow). Such calcination temperature is known from the synthesis of typical industrial methanol catalysts⁵⁷. Further calcination experiments at higher temperatures were performed under similar conditions except for varying the target temperature.

5.2.4 Characterization methods

Powder x-ray diffraction (PXRD) analysis of the precursor phases was performed on a Panalytical X'Pert Pro MPD diffractometer in Bragg-Brentano geometry with Ni-filtered Cu-K_α radiation and a fixed divergence slit (1/2°) and a PIXcel 1D detector. The patterns were recorded at room temperature between 4° and 90° 2θ. Temperature resolved PXRD data was recorded on the same instrument using an Anton Paar HTK 1200 N heating chamber. The sample was measured in static air, the temperature was varied in the range of 35 – 350 °C with increments of 20 °C up to 110 °C and 5 °C further to 350 °C. The collection time for each pattern was around 30 min.

X-ray analysis of the time resolved ageing samples and of the calcined samples was performed on a Bruker D8 advance with Cu-K_α radiation and a LYNXEYE XE-T detector. The diffractograms were recorded in reflection in a Bragg-Brentano geometry at room temperature between 5° and 90° 2θ. Phase analysis was performed by comparing the recorded pattern with structural data from ICSD and COD databases.

5 Phase evolution, speciation and solubility limit of aluminium doping in zinc oxide catalyst supports synthesized via co-precipitated hydrozincite precursors

Pawley fits were carried out using TOPAS Academic version 6.0.²⁰⁰ Instrumental line broadening was described using the fundamental parameter approach²⁰¹ as implemented in TOPAS and cross-checked against a measurement of LaB₆ (NIST SRM 660c).

Brunauer-Emmett-Teller (BET) surface measurement was performed as nitrogen physisorption at 77 K in a Nova 3200e sorption station from Quantachrome. Before recording the isotherms, the samples were degassed under vacuum at 100 °C (hydrozincite) and 250 °C (zinc oxide) for 5 h. Afterwards the isothermal profiles between $p/p_0 = 0.0$ and 1 referred to a reference cell were recorded. The multipoint BET surface area was determined by applying the Brunauer-Emmett-Teller equation to a specific range of each sample, determined by the micropore assistant of the NovaWin Software only considering the volume increase.

Scanning electron microscopy (SEM) micrographs of the zinc oxides of the high temperature series and of the hydrozincites and their corresponding zinc oxides series of the time resolved ageing experiment were taken on an Apreo S LoVac electron microscope of Thermo Fisher Scientific. A suspension of around 1 mg sample in 2 ml Ethanol was used for drop-casting of 200 μ L on single crystal silicon plates. Afterwards the sample holder was dried at 80 °C on a hot plate. The images of the hydrozincite precursors of the aluminium concentration series and their corresponding zinc oxides were taken on a Zeiss Gemini Ultra Plus with an Oxford EDX detector. A spatula tip of the sample was dispersed on a carbon covered stainless steel pin mount sample holder.

Transmission electron microscopy (TEM) analyses were performed on a FEI Tecnai F30 G² STwin (300 kV, FEG) equipped with an EDX detector (Si/Li, EDAX). The TEM samples were ground and dispersed in n-Butanol (spatula tip sample in few drops of n-Butanol) and prepared on Cu lacey TEM grids. The pure zaccagnaite reference sample was prepared in a dry state without n-Butanol.

Infrared resonance spectroscopy (IR) was performed on a Bruker Alpha FT-IR spectrometer with attenuate total reflection (ATR) unit. The spectra were recorded between 400 cm^{-1} and 4000 cm^{-1} . To suppress water and CO₂ signals from the atmosphere, the device was placed in a glovebox of MBraun with argon atmosphere.

UV/Vis-spectroscopy at ≤ 88 K was performed on a Varian Cary 5000 Spectrometer. The sample was diluted with KBr and the pellet was adjusted in a solid sample holder. After flushing with nitrogen, the room temperature (25 °C) spectrum was recorded under vacuum. The 88 K (-185 °C) spectrum was recorded after cooling down with liquid nitrogen. When the sample was heated up to room temperature (27 °C) the spectrum was recorded to determine sample changes.

The band gap determination was performed by differentiation of the raw data, to determine the changing point. At this point, where the first deviation became a minimum, the wavelength was calculated to the electrical energy in eV. This method was used only to determine qualitatively the band gap energy change by UV/Vis spectroscopy in dependency of the aluminium incorporation.

Raman-spectroscopy of the powders was performed in a powder sample holder positioned in 45° to the laser beam in a MacroRam spectrometer of Horiba Scientific. A 785 nm laser with an intensity of 90 mW was used. The Raman shifts were recorded in the range of 100 cm⁻¹ to 3500 cm⁻¹.

Solid state NMR-spectroscopy of all ²⁷Al solid-state NMR experiments were performed on the Bruker Avance Neo NMR spectrometer with a magnetic field of 14.1 T using a commercial Bruker MAS probe head with a non-Al-stabilized zirconia ceramic rotor with 3.2 mm outer diameter at a frequency of 156.375 MHz. The chemical shift of ²⁷Al is reported relative to a 1.1 mol kg⁻¹ solution of Al(NO₃)₃ in D₂O on a deshielding scale.^{202, 203} The referencing was done by using 1 % TMS in CDCl₃ as external secondary reference for the ¹H resonance frequency using the Ξ scale as suggested by the IUPAC. All ²⁷Al MAS NMR measurements were performed using 20 kHz spinning frequency and continuous wave ¹H decoupling. For quantitative ²⁷Al MAS NMR measurements the resonance frequency was selected according to the ²⁷Al MAS NMR signal at $\delta_{iso} = 82.6$ ppm and the nutation frequency was adjusted for the excitation of solely the central transition. The NMR data were processed with the topspin 4.1.4 software. Typical recycle delays were of the order of 30 s ($>3T_1$) and a few thousands scans were accumulated. The peak areas were determined by deconvolution into mixed Gaussian/Lorentzian profile functions with the program deconv2Dxy.²⁰⁴

5.3 Results and Discussion

5.3.1 Characterization of the Al doped hydrozincite precursors

5.3.1.1 Time-resolved ageing of the precipitate in the mother liquor at 65 °C

Before the composition variation series of aluminium doped hydrozincites was synthesized, the influence of the ageing time on the precursor phase was investigated. Therefore, an aluminium content of 2 % metal based ($x_{Al} = 0.02$) was used. The PXRD pattern of the different ageing times are shown in Figure 5.1. Immediately after finishing the co-precipitation, the hydrozincite phase was formed. This phase was present up to 120 minutes of ageing time and there were no significant changes of the PXRD pattern observed. After an additional solvothermal treatment of the 120 minutes aged precursor suspension, additional reflections are observed in the PXRD pattern. These reflections are visible at $2\theta = 11.8^\circ$ and $2\theta = 23.6^\circ$ and were assigned to an aluminium-containing hydrotalcite-like phase. This side phase is known as zaccagnaite, with the chemical formula $Zn_4Al_2(OH)_{12}(CO_3) \cdot 3H_2O$.^{205, 206} This result shows that the aluminium requires elevated temperatures to segregate in this specific crystalline phase and should be either amorphous or incorporated into the hydrozincite phase in the samples obtained at ambient co-precipitation and ageing. A small shoulder (compare Figure 5.1 b)) at the lower-angle side of the first reflection in the PXRD pattern of the sample aged for 120 minutes may indicate that a few very small crystallites of zaccagnaite have already formed after prolonged ageing at ambient conditions.

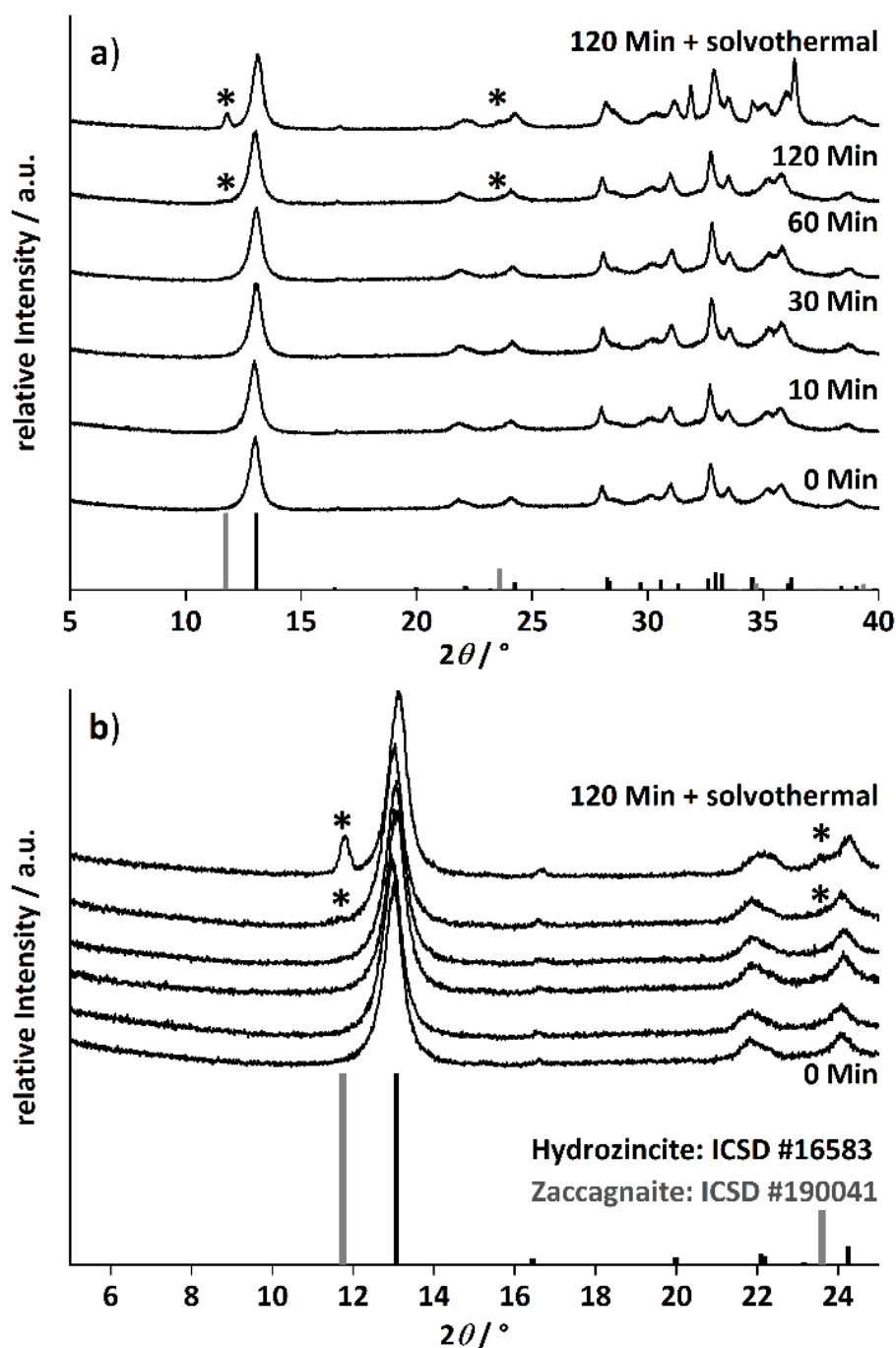


Figure 5.1: PXRD data of a co-precipitated zinc-aluminium precursor with an aluminium content of $x_{Al} = 0.02$ at different ageing times. The ageing was performed between 0 min (immediately after co-precipitation) and 120 min. The remaining suspension was aged for additional 12 hours at 130 °C in a solvothermal reactor (120 Min + solvothermal). The grey bars correspond to the zaccagnaite (ICSD#190041) and the black bars to hydrozincite (ICSD#16583) references. a) is an overview, while b) shows a more detailed zoom for better identification of the side-phase zaccagnaite, whose reflections are marked with asterisks. In b) the patterns are sorted likewise as in a).

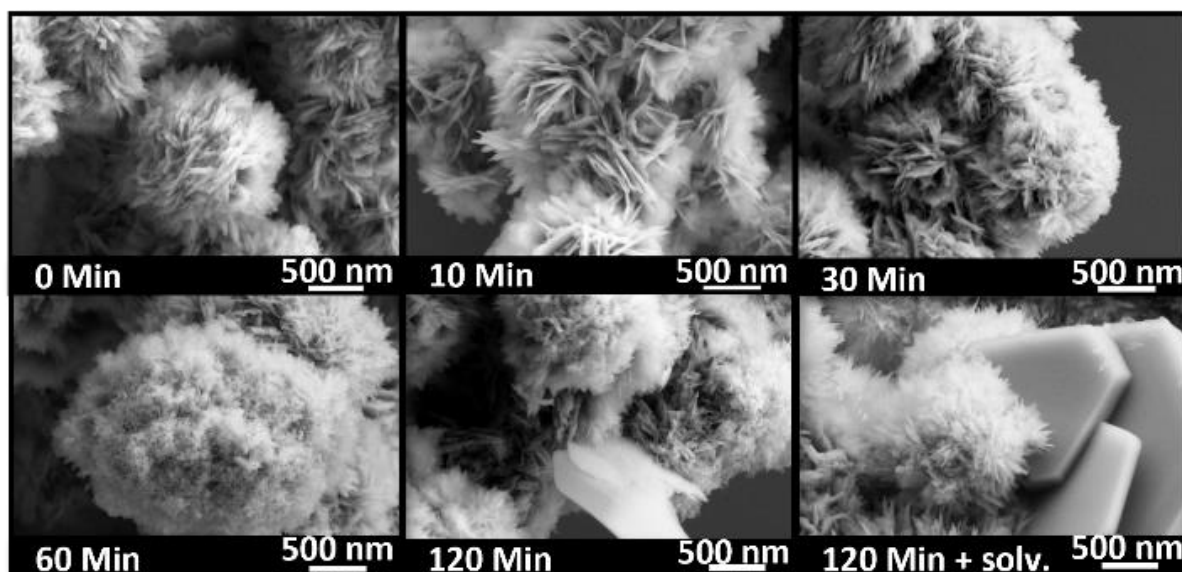


Figure 5.2: SEM images depicting the morphology of the precursor materials recovered at different ageing times after co-precipitation at 65 °C and a pH of 6.4 of a zinc-aluminium solution with an aluminium content of $x_{Al} = 0.02$.

The morphology of the samples was investigated by SEM and the micrographs of the samples obtained at different ageing times are shown in Figure 5.2. The morphology was similar up to an ageing time of 30 minutes. Aggregated platelets were intergrown to spheres and other larger aggregates, as they are shown in the supporting information (Figure SI 11.23 and Figure SI 11.30). After 60 minutes of ageing, the platelet size seemed to decrease and additional larger thin platelets are observed after 120 min of ageing. These larger platelets have grown even thicker and show well defined facets after the solvothermal treatment as shown in Figure 5.2. In combination with the temporal evolution of the crystalline phases known from the PXRD results, the immediately formed aggregated spheres are assigned to the hydrozincite phase and the larger platelets formed between 60 and 120 min of ageing, which grow under solvothermal conditions to a crystal habitus well-known for hydrotalcite-like materials, 121 are assigned to zaccagnaite.

The investigation of the ageing time series at 2 % aluminium demonstrated, that aluminium will thermodynamically favour an incorporation into the zaccagnaite phase, which evolved after 120 minutes ageing time and further grows by solvothermal treatment. This results in an aluminium segregation and in an inhomogeneous aluminium distribution in the solid. To suppress this untargeted phase and to receive a more homogeneously doped hydrozincite, the ageing time was set to 10 min for the aluminium concentration variation series. With that shortened ageing time, a kinetically controlled aluminium incorporation into the hydrozincite phase should be favoured.

An increase in the BET surface area of the precursor after 120 minutes ageing time gives an additional indirect hint for a homogeneous aluminium distribution at short ageing times (Figure SI 11.24). The surface area of the precursor samples aged up to 60 minutes varied around $12 \text{ m}^2 \text{ g}^{-1}$ and found to grow to $28 \text{ m}^2 \text{ g}^{-1}$ after solvothermal treatment despite the newly grown phase clearly exhibiting larger particles. This might be explained by the effect of the aluminium ex-solution on the hydrozincite material leaving a more porous morphology. More evidence for an incorporation of aluminium into this phase is presented below for the aluminium concentration series.

5.3.1.2 Aluminium concentration variation

To avoid side-phase formation, the ageing time was reduced to 10 minutes, to kinetically trap the aluminium ions in the hydrozincite structure. The aluminium content was varied between 0 % ($x_{\text{Al}} = 0$) and 10 % ($x_{\text{Al}} = 0.1$) in different intervals and the recovered precursors were analysed regarding crystalline phase composition by PXRD (Figure 5.3, selected range and Figure SI 11.28 complete range). For all synthesized precursors, hydrozincite is determined as the main crystalline phase. An aluminium content higher than $x_{\text{Al}} = 0.02$ resulted in small quantities of the above-described aluminium-rich side phase zaccagnaite despite the low ageing time (Figure 5.3 b)).

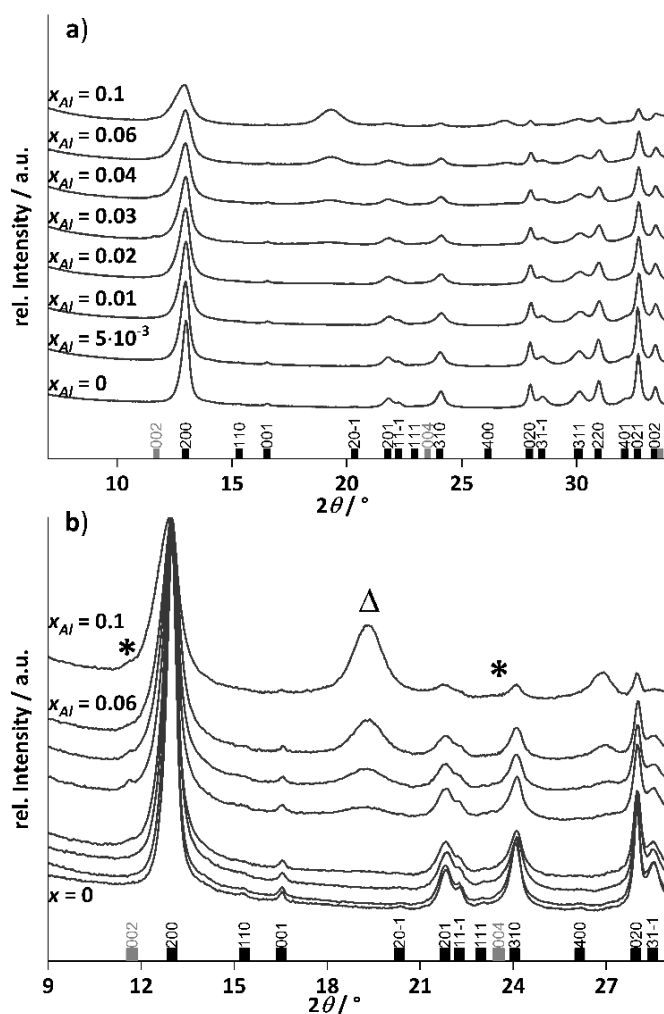


Figure 5.3: PXRD pattern of the co-precipitated aluminium-doped hydrozincite precursors with different cation-based molar aluminium fractions x_{Al} . The reference pattern of the hydrozincite was taken from the ICSD (#16583, black bars) as well as the reference pattern of zaccagnaite (#190041, grey bars). a) is an overview with indexation of the reflections, while b) is a zoom at lower diffraction angles to better distinguish the zaccagnaite side-phase (marked with asterisks). The triangle marks an additional reflection discussed in the main text below.

The weak reflections present as shoulders to the first hydrozincite peak indicate that the zaccagnaite structure is present in low concentration (marked with asterisks). Given that this reflection is hardly discernible and broadened, *i.e.* on the level of detection, it may account to ~ 1 wt% - 2 wt%. However, the relative intensity of the zaccagnaite reflections does not increase linearly with the aluminium content after their first appearance, which excludes a simple aluminium saturation of the hydrozincite phase with all excess aluminium being segregated into zaccagnaite.

The diffraction pattern of the hydrozincite shows noticeable changes with increasing incorporation of Al: There are slight shifts in the position of the reflections, which become

noticeable in particular at higher diffraction angles. The cell volume of the samples was extracted via a Pawley fit and the results are summarized in Figure 5.4.

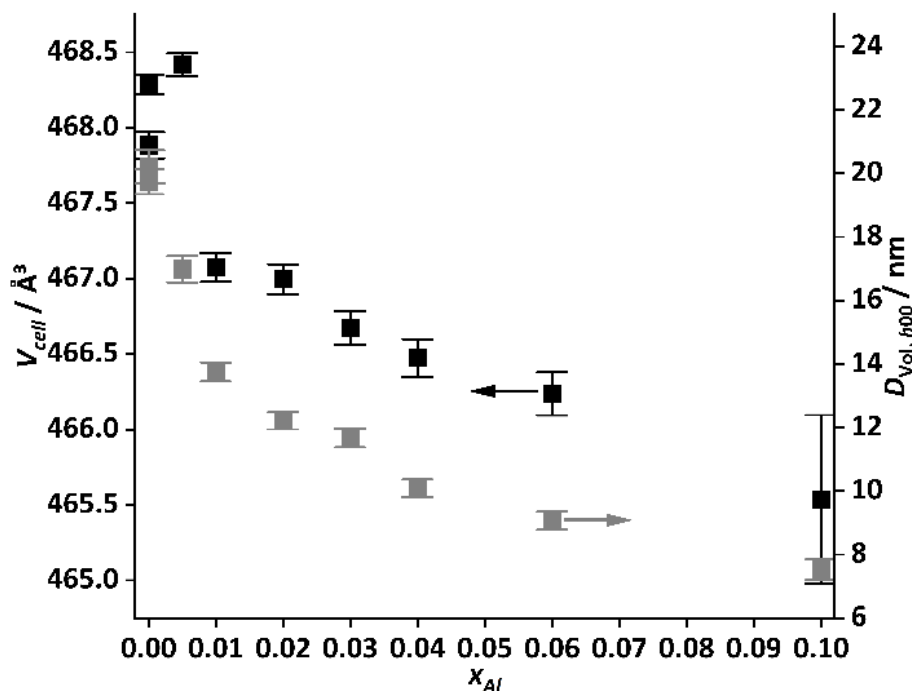


Figure 5.4: Cell volume and volume weighted average domain size estimated from the $h00$ reflections of the hydrozincite samples versus cation-based molar aluminium fraction x_{Al} .

The cell shrinks by $\sim 2 \text{ Å}^3$ for the hydrozincite containing 10 at% Al compared to the unsubstituted compound, which can be expected from the lower ionic radius of Al^{3+} (54 pm) compared to Zn^{2+} (74 pm).²⁰⁷ For $x_{Al} = 0.1$ the error becomes fairly large, which is expected due to the overall broadening of the reflections. This in turn hampers a precise determination of the lattice parameters. The line broadening was modelled assuming the effect to be caused by finite crystallite size, which can be justified by the information from electron microscopy. The crystallite size was found to be anisotropic, not unexpected for a layered material.

Furthermore, reflections of type $h00$, $0k0$ and $00l$ are fairly sharp, where the first one describes the stacking of the layers while the latter two are related to the layer constitution. The cross plane reflections (*e.g.*, 201, 301, 311) show stronger broadening, *i.e.* there is a loss of coherence among the layers, which is commonly observed for stacking faults in layered materials^{208, 209} and was described earlier for synthetic hydrozincites¹²⁶. For an estimation of the crystallite size the value for the $h00$ reflections is reported, which varies with a similar non-monotonous dependence on x_{Al} as the cell volume does.

Aside of the zaccagnaite side phase there are two prominent reflections located at 19.5° and $26.8^\circ 2\theta$ appearing with increasing amount of Al^{3+} in the sample. They could not be assigned

to any phase after extensive search in the COD and ICSD databases. Interestingly, the one located at $19.5^\circ 2\theta$ has a d -spacing in excellent agreement with the a parameter and may be indexed as 300 reflection, which is forbidden in the space group $C2/m$ that hydrozincite crystallizes in. For the second reflection no such coincidence could be identified.

To further investigate the origin of these additional reflections, temperature resolved PXRD analysis of the sample with the highest aluminium content ($x_{Al} = 0.1$) was performed (Figure 5.5).

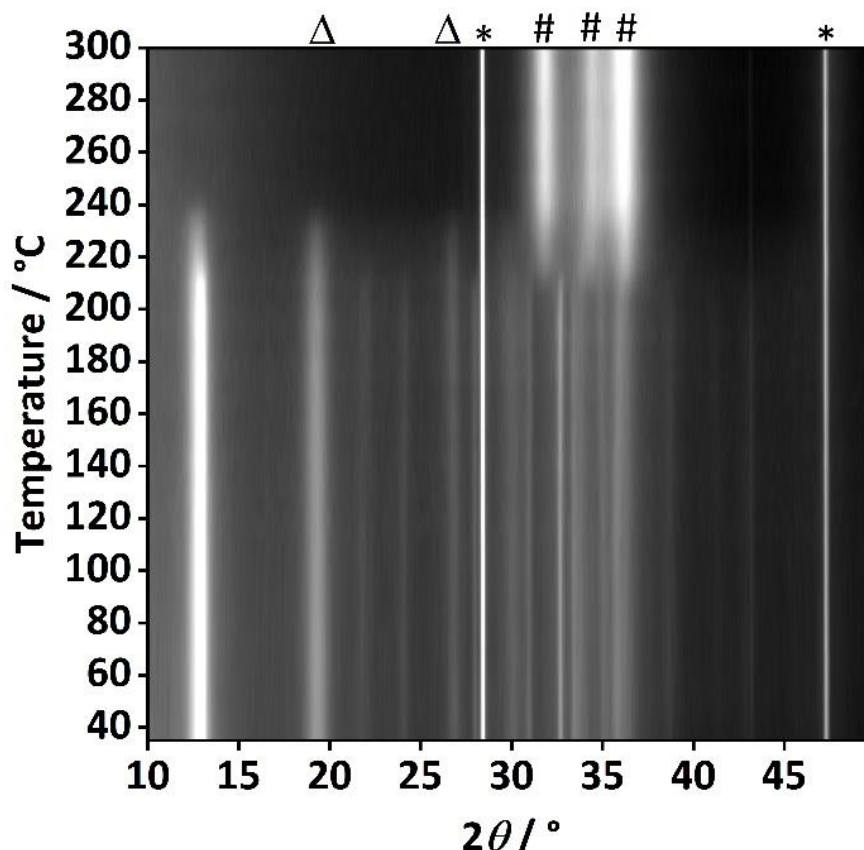


Figure 5.5: Temperature-resolved PXRD analysis of the thermal decomposition of the hydrozincite precursor containing 10 % aluminium ($x_{Al} = 0.1$). The PXRD analysis was performed with silicon as standard and in static air. The reflection positions are labelled as follows: silicon (*), ZnO (#) and additional unassigned reflections (Δ).

At 215 °C the decomposition starts, which is evidenced by the most intense reflections of the hydrozincite phase (e.g., at $2\theta = 12.9^\circ$) losing intensity. Complete decomposition is achieved at 250 °C. Simultaneously, the zinc oxide reflections evolved and further increase in intensity as the temperature was elevated, at 300 °C already well-defined reflections of ZnO are visible. This prompt crystallization is markedly different from the case of zaccagnaite (Figure SI 11.27), where even at 600 °C only very broad reflections of ZnO can be observed. This may be related to the presence of amorphous alumina, hampering the diffusion and

crystallite growth of ZnO. Interestingly, the additional reflection at $2\theta = 19.5^\circ$ behaved like those assigned to the hydrozincite regarding the thermal decomposition, which further indicates that they do belong to a disordered hydrozincite phase and not to any side-phase.

The potentially high degree of substitution of Zn^{2+} by Al^{3+} is likely to cause significant changes in the structure of hydrozincite. This raises the question how the additional positive charge is compensated. Three possible scenarios, illustrated in Figure 5.6, affecting the cation- or anion lattice shall be outlined: The surplus positive charge may be compensated by additional anions (OH^- or CO_3^{2-}) that may be introduced in the interlayer space and lead to a chemical formula $(\text{Zn}_{5-5x}\text{Al}_{5x}(\text{OH})_{6+5x}(\text{CO}_3)_2)$ or $(\text{Zn}_{5-5x}\text{Al}_{5x}(\text{OH})_6(\text{CO}_3)_{2+2.5x})$. Also, deprotonation of hydroxyl groups could compensate the extra charge according to a chemical formula $(\text{Zn}_{5-5x}\text{Al}_{5x}(\text{OH})_{6-5x}(\text{O})_{5x}(\text{CO}_3)_2)$. Alternatively, for any two Al^{3+} cations one Zn^{2+} cation might become a vacancy, which could affect in particular the Zn^{2+} in tetrahedral coordination since the layer made up of Zn-O octahedra already contains vacancies in the neighbourhood of the tetrahedrally coordinated Zn^{2+} , which could be filled with Al^{3+} : $(\text{Zn}_{5-7.5x}\text{Al}_{5x}(\text{OH})_6(\text{CO}_3)_2)$. A loss of those tetrahedral sites would also disrupt the link between the layers facilitated by the carbonate anions, which would allow for an increased number of stacking faults. This in turn would be a viable explanation for the increasing line width and change of relative intensities in the diffraction patterns with increasing Al content. However, the full structure determination of the potentially modified hydrozincite phase is beyond the scope of the present work.

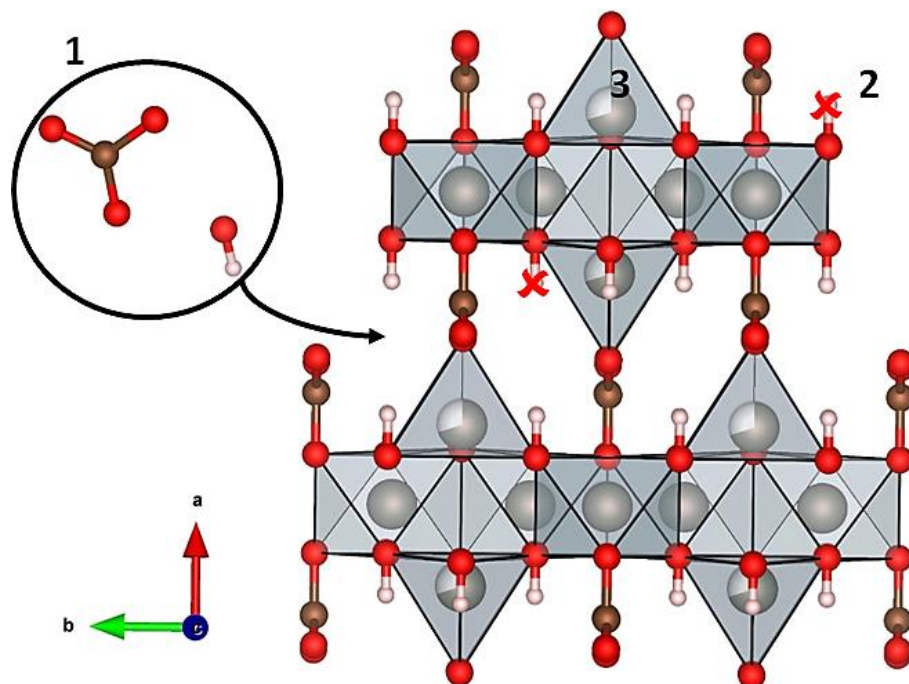


Figure 5.6: Schematic depiction of potential defects in hydrozincite for balancing the surplus positive charge resulting from substitution of Zn^{2+} by Al^{3+} : 1. Additional anions occupy the interlayer space. 2. Deprotonation of OH to form O^{2-} anions. 3. Vacancies on Zn^{2+} sites. The hydrogen atoms were placed at 0.9 \AA distance and are not part of the crystal structure. ^{117, 126}

SEM analysis of the concentration series shown in Figure 5.7 revealed that the sample with an aluminium amount $x_{\text{Al}} = 0.01$ contained aggregates of platelets, which formed spherical structures, as already observed in the ageing time series. Based on the assignment introduced above for the ageing time series, first additional larger platelets (highlighted by the arrows), which are encountered in the precursor with $x_{\text{Al}} = 0.03$ aluminium content, are assigned to the zaccagnaite side-phase. Selected SEM-EDX spectra of these larger platelets are shown in the supporting information in Figure SI 11.31 and the results are listed in Table SI 11.18. The median cationic ratio of $\text{Zn}^{2+}:\text{Al}^{3+} = 3$ agreed well with the expected composition of zaccagnaite. ¹²¹ TEM analysis of the precursors was complicated due to high beam sensitivity and is described as supporting information (Figure SI 11.26).

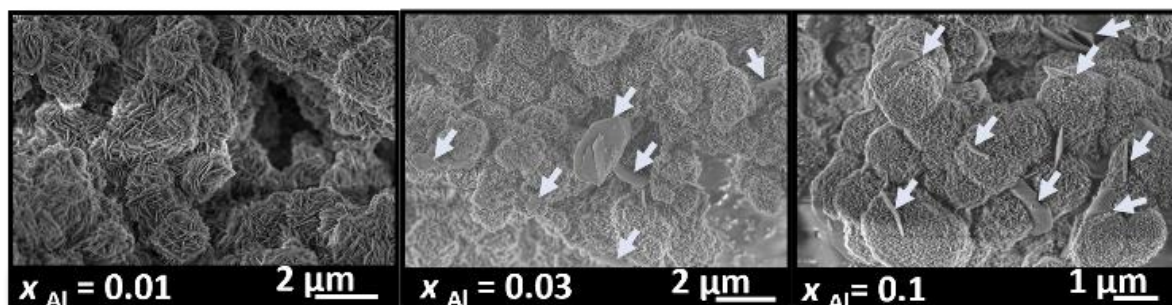


Figure 5.7: Morphology evolution in dependency of the aluminium content of the hydrozincite precursors. The arrows show the regions containing larger platelets and x_{Al} indicated the cation-based molar aluminium fraction.

In order to characterize the aluminium environment in the hydrozincite precursors, a ^{27}Al MAS NMR spectrum of the hydrozincite sample containing 3 % aluminium ($x_{Al} = 0.03$) was recorded (Figure 5.8). The single peak at $\delta_{obs} = 14$ ppm is indicative of aluminium occupying an octahedrally coordinated site, *i.e.* substituting a Zn atom in the hydrozincite structure.²⁰⁴ ^{27}Al NMR peaks corresponding to a different coordination number are not observed. In comparison the ^{27}Al NMR spectrum of zaccagnaite $Zn_4Al_2(OH)_{12}(CO_3) \cdot 3H_2O$ exhibits two different signals at $\delta_{obs} = 15$ ppm and $\delta_{obs} = 13$ ppm. A ^{27}Al 5QMAS NMR spectrum (Figure SI 11.47) does not resolve any further peaks and shows fairly broad signals, which is fully consistent with the published disordered crystal structure²⁰⁶.

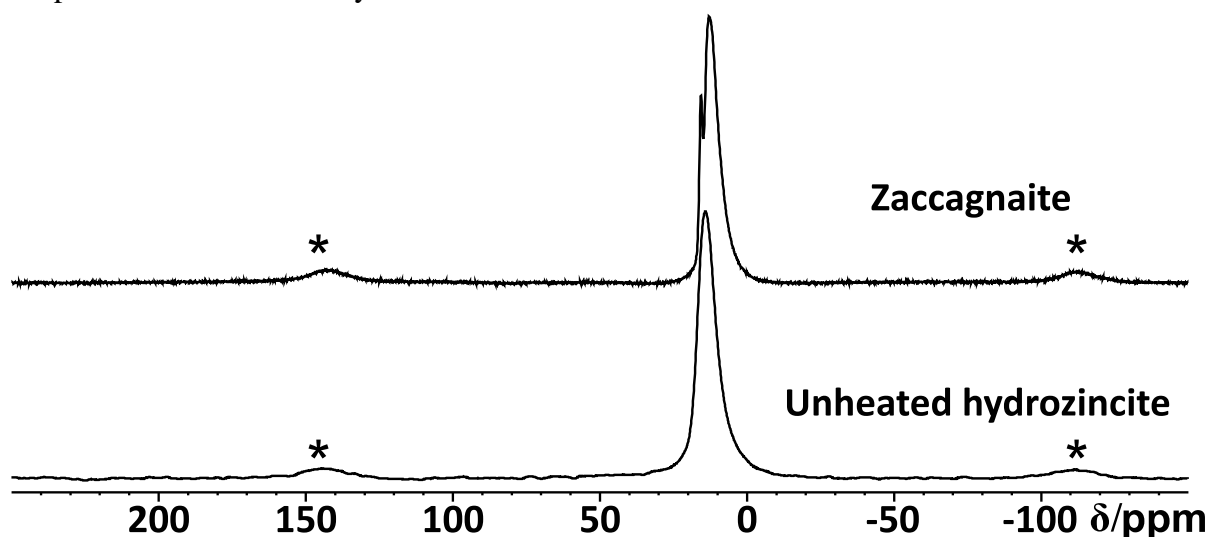


Figure 5.8: Stack plot of ^{27}Al MAS NMR spectra of a coprecipitated hydrozincite precursor with $x_{Al} = 0.03$ aluminium incorporation and zaccagnaite. Spinning side bands are labelled with an asterisk (*).

To further investigate the precursor samples, infrared and Raman spectroscopy have been applied. In the infrared spectra shown in Figure 5.9, bands typical for hydrozincite were found.²¹⁰ For a better comparison between hydrozincite and side-phases, a phase-pure

zaccagnaite sample was synthesized as described in the supporting information (chapter 11.7.4 “Synthesis of the aluminium-rich side-phase zaccagnaite” on page 236, *i.e.* Figure SI 11.25) and used as reference for the analysis of vibrational spectroscopy data. The infrared spectra (Figure 5.9) show a rather gradual evolution with increasing aluminium content and a clear difference to the zaccagnaite reference pattern demonstrating that the observed bands can be assigned to the hydrozincite phase. The strongest changes are observed for the two antisymmetric carbonate stretching modes (ν_3 , 1502 cm^{-1} - 1396 cm^{-1})²¹¹ when the aluminium content exceeds $x_{\text{Al}} = 0.03$, *i.e.* in the same compositional range where the unassigned reflections in PXRD at $2\theta = 19.5^\circ$ and $2\theta = 26.8^\circ$ arise. At the same time, the band at 948 cm^{-1} disappears, which - in analogy to the hydrotalcite-like materials - is related to hydrogen bonds between hydroxyls and carbonate.^{212, 213} Such hydrogen bonds are also present in hydrozincite¹²⁶ and thus the vanishing of this band indicates breaking of these bonds. These gradual changes support the defective hydrozincite structure by aluminium incorporation in agreement with the observed additional reflections in PXRD (Figure 5.3). An infrared band at 621 cm^{-1} appeared for $x_{\text{Al}} > 0.01$ and increased with the aluminium content. For hydrotalcites, this band was assigned to hydroxyl groups between the sheets.²¹⁴ These observations suggest that the anions of hydrozincite are affected by the charge compensating mechanism when zinc is substituted by aluminium through coordination changes of carbonate and hydroxyl. A similar gradual evolution with increasing aluminium content was also found by Raman spectroscopy (Figure SI 11.36). The Raman modes at 564 cm^{-1} (Zn-OH) and 494 cm^{-1} (Me-OH) were present in the samples with $x_{\text{Al}} = 0.06$ and $x_{\text{Al}} = 0.1$ and represent the side-phase²¹⁵⁻²¹⁷ zaccagnaite in agreement with the PXRD results.

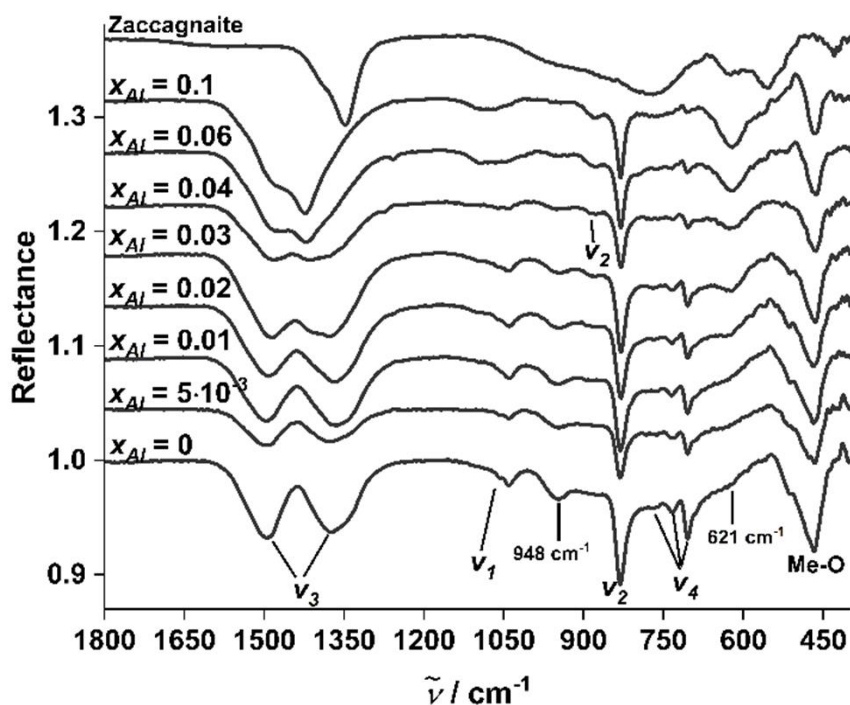


Figure 5.9: Vibrational infrared spectroscopy of aluminium doped hydrozincites with different cation-based molar aluminium fractions x_{Al} in comparison with the aluminium rich zaccagnaite side phase $Zn_4Al_2(OH)_{12}(CO_3) \cdot 3H_2O$.

5.3.1.3 Summarizing the precursor part

It was established that short ageing time and low aluminium content can suppress the segregation of crystalline zaccagnaite. The samples without this aluminium side phase are interesting candidates for the synthesis of aluminium-doped zinc oxide due to their more uniform dopant distribution. The creation of structural defects is suggested for charge compensation upon substitution of zinc in crystalline hydrozincite.

5.3.2 Characterization of the doped zinc oxide samples

5.3.2.1 Aluminium concentration variation

The thermogravimetric (TG) analysis of the precursors confirmed a complete decomposition already at 300 °C (Figure SI 11.32 and Figure SI 11.33). Thus, calcination of the doped hydrozincite precursors was carried out for 4 h at 320 °C and the formation of phase pure zinc oxide was confirmed by PXRD analysis (Figure 5.10 a)). A decrease in the size of the coherently scattering domains with increasing aluminium amount suggests successful incorporation of aluminium (Figure 5.10 b)). The data further shows that the pronounced anisotropy of the domain size (larger along c-axis) diminishes with x_{Al} , such that rather spherical crystallites are deduced. The apparent domain size for $h0l$ and hkl type reflections is

even lower than for the two principal axes, indicating defects like stacking faults in the ZnO samples.^{218, 219} Contrarily to the powder patterns of the precursor series, no crystalline side phases were observed after calcination. This is in line with the expected decomposition product of hydrozincite and the fact that the decomposition of zaccagnaite gives rise to an amorphous material (as shown in SI in Figure SI 11.25 and Figure SI 11.27), which should form a physical mixture with the crystalline ex-hydrozincite zinc oxide fraction. A further hint for defects was found by Raman spectroscopy from the overtone mode $A_1^{\text{TO+LO}}$ in the samples with $x_{\text{Al}} = 0.06$ and $x_{\text{Al}} = 0.1$ (see Figure SI 11.40 on page 249 and accompanying discussion). These samples originate from the precursors with the most pronounced changes in the PXRD patterns.

Nitrogen physisorption measurements revealed a surface area enlargement after calcination as a result of the decomposition of the hydroxycarbonate by simultaneous pore formation due to water and carbon dioxide emission. There is a clear trend towards larger surface areas for increasing aluminium content with a local maximum at $x_{\text{Al}} = 0.005$ ranging from $31 \text{ m}^2\text{g}^{-1}$ ($x_{\text{Al}} = 0$, Figure SI 11.38) to $106 \text{ m}^2\text{g}^{-1}$ ($x_{\text{Al}} = 0.1$, Figure SI 11.38). The main pore fraction are 10 nm mesopores for the samples up to $x_{\text{Al}} = 0.02$. With an increase in the aluminium content this fraction increased. For a higher amount than $x_{\text{Al}} = 0.03$ the pore fraction of the 20-30 nm pores starts to increase with further increase in the total pore volume (Figure SI 11.39).

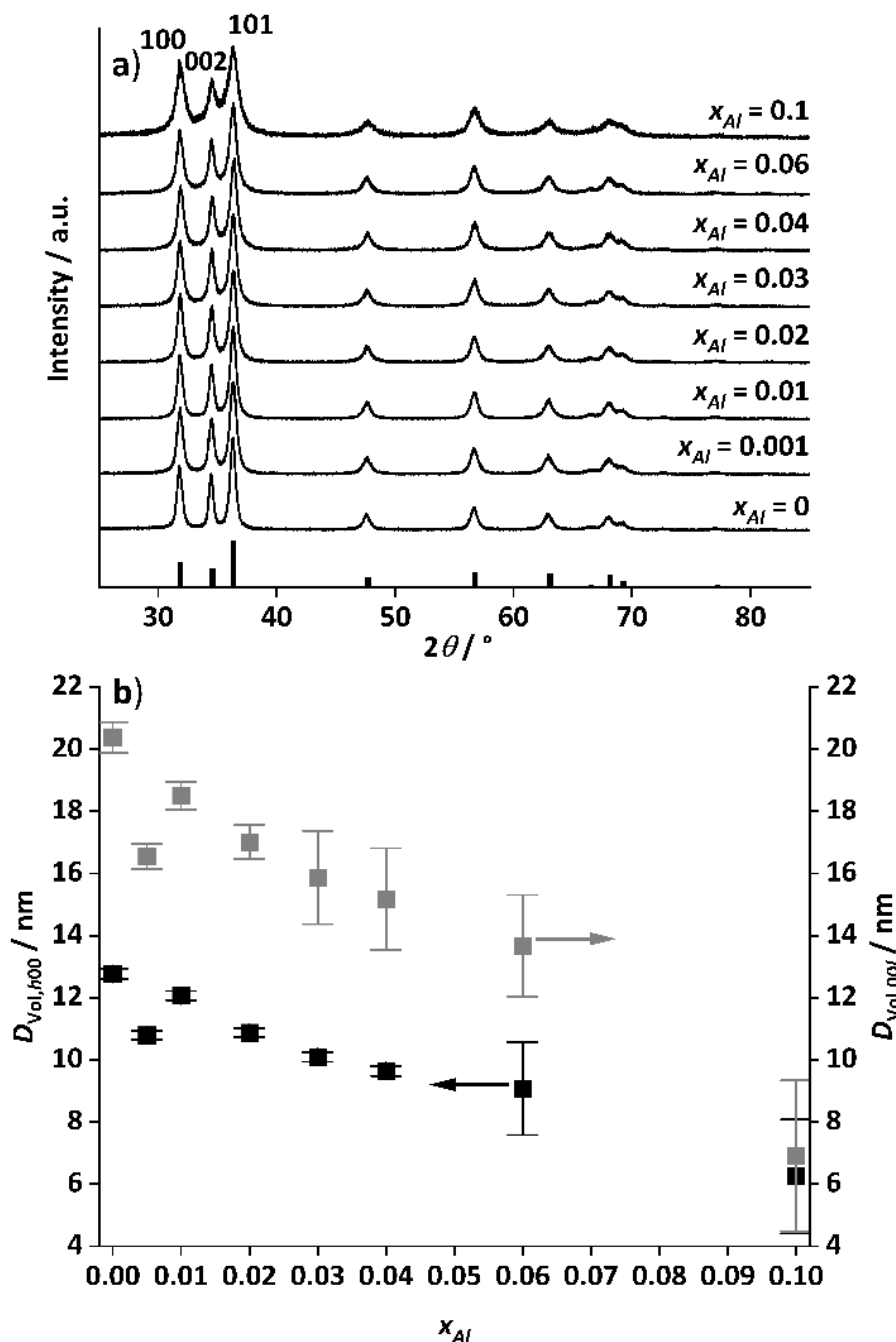


Figure 5.10: Powder XRD pattern of the aluminium doped zinc oxides a) after calcination of the hydrozincite precursors at 320 °C with 2 °C min⁻¹ heating ramp and 4 h holding time in static air. The reference pattern (black bars) was taken from COD, zinc oxide (#2107059). b) Sizes of the coherently scattering domains for the h00 and 00l reflections extracted via Pawley fit from the patterns shown in a) as function of the cation-based molar aluminium fraction x_{Al} .

5.3.2.2 Aluminium distribution in doped zinc oxide

Electron diffraction (ED) of a region showing projections of the aggregated spheres (Figure 5.11 b)) confirms that this part of the sample consists of ZnO in the wurtzite-type structure in agreement with the PXRD results, although the reflections are diffuse and not sharp

as expected for a defect-free crystal. However, as already suggested by the SEM investigation of this sample's precursor, a different kind of particle morphologies was also detected by TEM, an example of which is shown in Figure 5.11 c). Relatively large platelets with diameters up to 1 μm and ill-defined edges were found decorated with the above-mentioned nano-scaled material that comprises the spheres. Interestingly, high-resolution TEM and Fast Fourier Transforms (FFT) of the resulting micrographs show that these thin platelets are porous and yet oriented like a single crystal with a $\{101\}$ zone axis of ZnO (Figure 5.11 d)). The pores and grains of this material are sub-10 nm.

The larger dimension of this platelet particle suggests that it originates from the zaccagnaite precursor side-phase. Indeed, EDX measurements were performed at several sample positions in the Scanning TEM (STEM) mode and, hereby, a wide range of Al contents can be found that are all larger than the nominal 3 % and span from 4.5 % up to 38.6 % (Figure SI 11.41). The highest aluminium concentrations were found where this thin ex-zaccagnaite platelet is not decorated by the nano-scaled ex-hydrozincite material indicated by the dark contrast in the high-angle annular dark field (HAADF)-STEM image. It is intriguing that it is at these aluminium-rich positions where the FFT has shown zinc oxide as only crystalline component. This suggests that the zinc and aluminium fractions of zaccagnaite have segregated upon decomposition into nano-crystalline zinc oxide and amorphous alumina at a very small scale.

In summary, the electron microscopy investigation revealed the co-existence of two material systems in the sample with 3 % aluminium. The major fraction of the material is ex-hydrozincite, *i.e.* crystalline zinc oxide with an aluminium content close to the nominal value. A minor, but increasing fraction, starting at $x_{Al} = 0.03$ according to (precursor) PXRD, is ex-zaccagnaite and thus aluminium-richer and nano-structured in a complex manner containing crystalline zinc oxide and amorphous alumina segregated probably at the platelet surface.

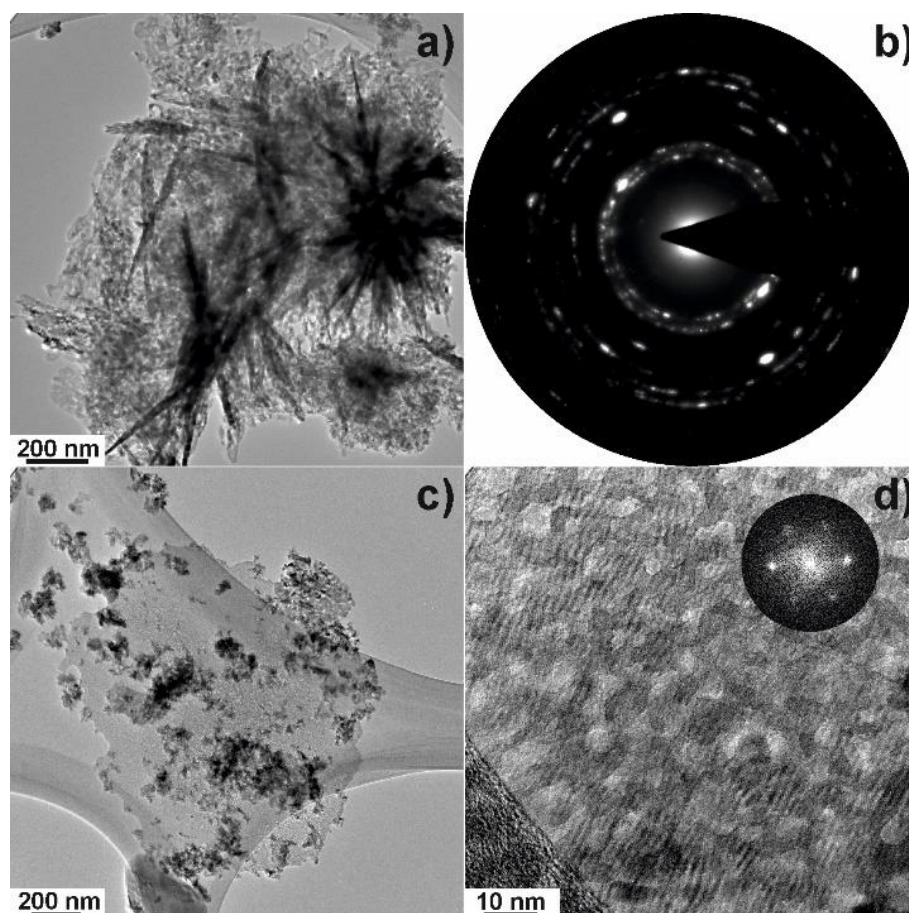


Figure 5.11: TEM-analysis of an aluminium doped zinc oxide sample (with $x_{Al} = 0.03$). Image a) visualizes a typical aggregate as it was also found by SEM. The corresponding electron diffraction pattern is shown in figure b). The image in c) shows a large single crystal with some fractions of the typical aggregate structure on top. A HRTEM micrograph of a part of that single crystal is shown in d) with the corresponding FFT pattern.

5.3.2.3 Aluminium speciation in the doped zinc oxides

For a characterization of the aluminium environment during the decomposition process a series of ZnO samples with $x_{Al} = 0.005$ incorporated and different annealing temperatures was investigated by ^{27}Al MAS NMR (Figure 5.12).

After the decomposition of the hydrozincite there are two different signals observable: $\delta_{obs} = 82$ ppm and $\delta_{obs} = 12$ ppm. The sharp signal at $\delta_{obs} = 82$ ppm, has unambiguously been assigned to Al^{3+} on a zinc position inside the ZnO crystal structure, Al_{Zn}^{\bullet} .¹⁴³ This small linewidth reflects the low quadrupolar coupling constant and an ordered environment of the Al_{Zn}^{\bullet} defect. In contrast zaccagnaite has a disordered crystal structure²⁰⁶ and even without Al substitution hydrozincite has been reported to have a strong tendency for stacking disorder.¹²⁶

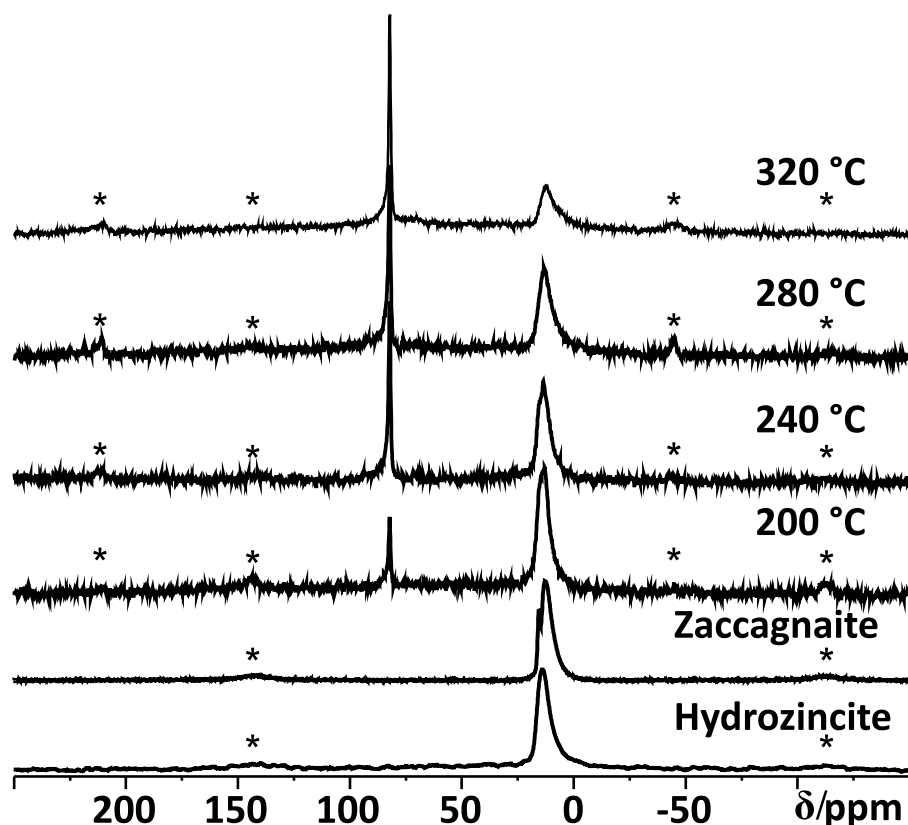


Figure 5.12: Stack plot of ^{27}Al MAS NMR spectra of the unheated hydrozincite, zaccagnaite and after being annealed at 200 °C, 240 °C, 280 °C and 320 °C for 4h in static air with a heating ramp of 2 °C min $^{-1}$ with $x_{\text{Al}} = 0.005$ aluminium incorporation. All spectra were recorded with a spinning frequency of 20 kHz. Spinning side bands are signed with an asterisk (*).

The second signal at $\delta_{\text{obs}} = 12$ ppm can result from unreacted hydrozincite, but also from a disordered sixfold coordinated aluminium environment at the surface of ZnO particles.¹⁹⁶ With increasing temperatures up to 320 °C, a growth of the $\text{Al}_{\text{Zn}}^{\bullet}$ signal is observed at the expense of the signal assigned to Al in unreacted hydrozincite (or in sixfold coordination). Here the greatest build-up occurs between 200 and 240 °C, which is consistent with the formation of ZnO described by variable temperature PXRD (Figure 5.5) and the decomposition of hydrozincite. The presence of a zaccagnaite side phase could not be observed by ^{27}Al MAS NMR during the decomposition of the hydrozincite.

In order to find out whether the in-literature-postulated solubility limit of Al^{3+} in ZnO^{142, 143, 148, 196, 197} is an explanation for the occurrence of extra peaks a series of samples with different aluminium concentrations was investigated (Figure 5.13).

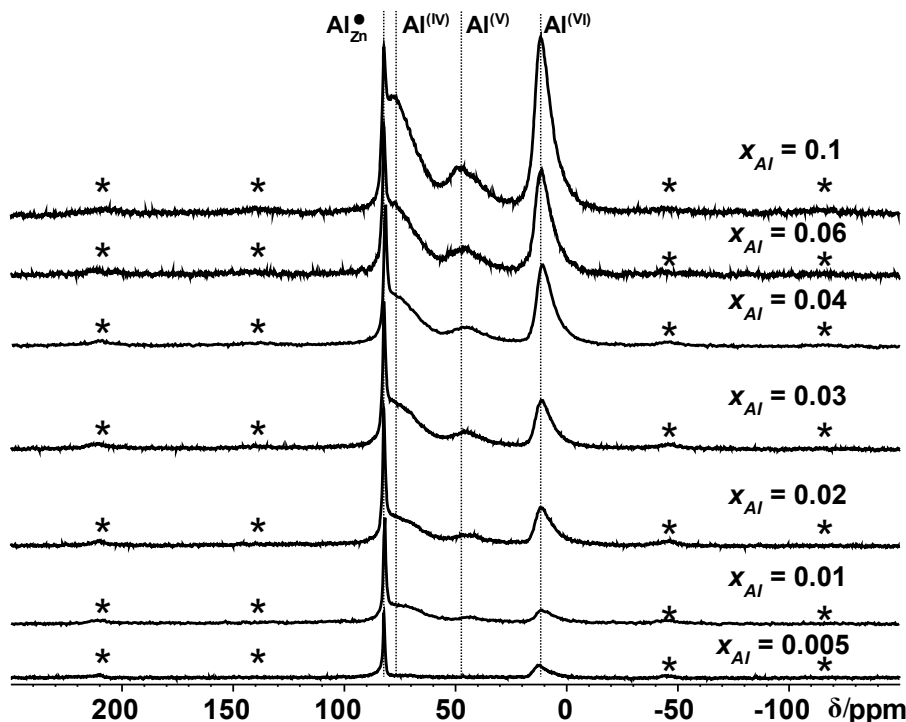


Figure 5.13: Stack plot of ^{27}Al MAS NMR spectra of zinc oxide, annealed with $320\text{ }^\circ\text{C}$ for 4 h, with different cation-based molar aluminium fractions x_{Al} . All spectra were recorded with a spinning frequency of 20 kHz. Spinning side bands are signed with an asterisk (*).

With increasing aluminium concentration two further signals are observed: $\delta_{\text{obs}} = 75\text{ ppm}$ and $\delta_{\text{obs}} = 47\text{ ppm}$. Their chemical shift indicates that $\delta_{\text{obs}} = 75\text{ ppm}$ corresponds to a fourfold coordinated aluminium environment, while $\delta_{\text{obs}} = 47\text{ ppm}$ corresponds to a fivefold coordinated aluminium environment. Due to their broad line shape and their continuous growth with increasing aluminium concentrations $\delta_{\text{obs}} = 75\text{ ppm}$, $\delta_{\text{obs}} = 47\text{ ppm}$ and $\delta_{\text{obs}} = 12\text{ ppm}$ can be assigned to disordered aluminium environments not situated within the crystal structure of ZnO. This is consistent with the observation that with increasing aluminium concentration a steady particle growth is observed for $x_{\text{Al}} \geq 0.02$ (see previous section Figure 5.2). This interpretation is consistent with the areas of high Al concentration in the TEM experiments (Figure SI 11.55), which is expected when the Al concentration is low within ZnO and the surplus of Al is found segregated from ZnO in form of side phases. TEM experiments provide information from local projections along the electron beam and are thus not expected to return the (lower) average bulk value.

To obtain a better estimate for the maximum degree of Al substitution which can be achieved under these conditions the amount of $\text{Al}_{\text{Zn}}^{\text{I}}$ signal at $\delta_{\text{obs}} = 82\text{ ppm}$ is determined as a function of the degree of substitution x_{Al} (Figure 5.14). What can clearly be seen is that the signal/mass ratio increases only up to values of 2 %. By interpolation with two linear functions the

“saturation limit” can be determined to $x_{Al} = 0.013$. This agrees with the reported rough estimates of < 2 mol% aluminium content in zinc oxide from other NMR studies.^{148, 196}

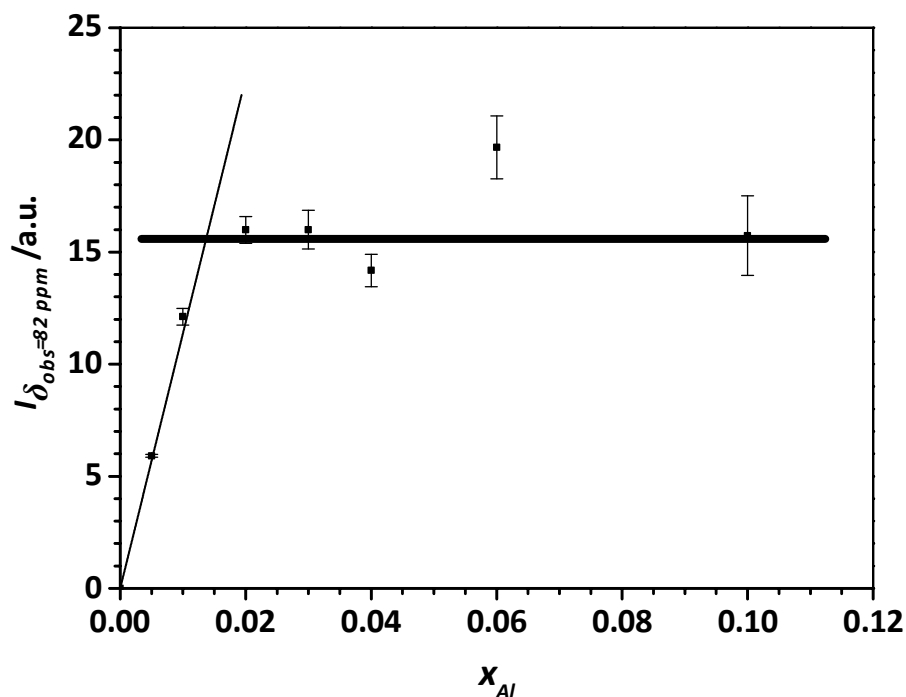


Figure 5.14: ^{27}Al -signal/mass ratio of the ^{27}Al MAS NMR signal at $\delta_{obs} = 82$ ppm of zinc oxide, annealed with 320 °C for 4 h, with different cation-based molar aluminium fractions x_{Al} . The NMR spectra were excited with selective $\pi/2$ pulse and the peak area determined by deconvolution with Gaussian/Lorentzian profiles. The error bars are estimated, by taking an error of 1 % of the four-fold coordinated aluminium ^{27}Al MAS NMR signals. The lines to interpolate the substitution limit were obtained by fitting linear functions into the corresponding data points.

5.3.2.4 Optical band gap of doped zinc oxides

Because of the expected influence of the aluminium doping on Al_{Zn}^{\bullet} sites, UV/Vis spectroscopy was performed on the zinc oxide samples. The results of the band gap energies are shown in Figure 5.15.

The band gap determination was performed at room temperature and at -185 °C to exclude heat effects. Afterwards, the measurement was repeated upon temperature increase back to 27 °C to check for thermally induced changes. The similar band gap energies before (25 °C) and after (27 °C) cooling demonstrate good reversibility within an error of around 6 meV. A band gap near 3.30 eV was found for pure zinc oxide at room temperature, which is in alignment with reported values around 3.3 eV¹⁸²⁻¹⁸⁵. No clear trend was observed at low doping level, while a slight increase in band gap energy was determined for aluminium contents above 1 %. This might be caused to the segregation of aluminium in ex-zaccagnaite regions as it was suggested

by the TEM results. Because of the wide band gap of aluminium oxide (ca. 5.6 eV), the presence of disordered alumina could shift the band gap energy of the material to higher values.²²⁰ Generally, the band gap can be affected by defects, free excitons, impurities and by the lattice site occupied by the dopant.^{139, 140, 221-225} To exclude free excitons, the band gap energies were recorded at -185 °C. Compared to the room temperature spectra, the absolute energies shifted to higher values. The band gap energy of the undoped ZnO was increased to 3.37 eV at -185 °C. However, the relative trend between the samples was mostly maintained with the exception that the lowest band gap was determined for the sample with $x_{\text{Al}} = 0.01$ in the cryogenic measurements (3.36 eV), which is in the range of the highest occupancy of the $\text{Al}_{\text{Zn}}^{\bullet}$ site. This finding is in agreement with the model of the band gap renormalisation, which predicts an optimal band gap for zinc oxide, if aluminium substitutes a zinc site.¹³⁹

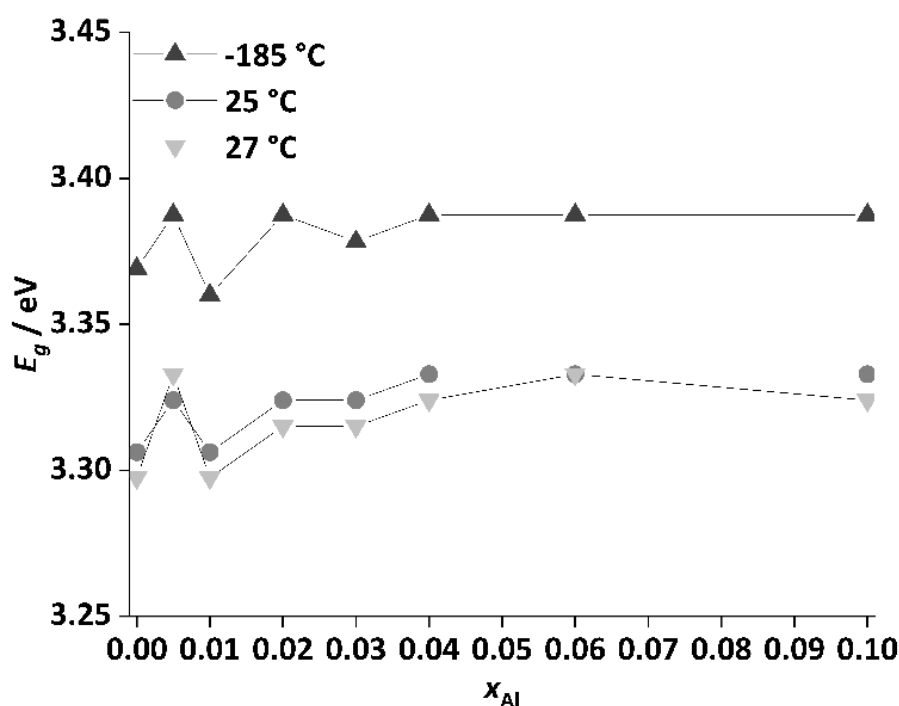


Figure 5.15: Band gap energies of the aluminium doped zinc oxides with different cation-based molar aluminium fraction x_{Al} . The measurements were performed at room temperature (25 °C, circles) at -185 °C (triangles) and at 27 °C after cryogenic temperature measurement (upside down triangle). The measurements were performed under vacuum in transmission mode on a pellet containing dried KBr as diluent. The lines are to guide the eye.

The behaviour of the zinc oxide sample with $x_{\text{Al}} = 0.005$ aluminium with its wider band gap than $x_{\text{Al}} = 0$ and $x_{\text{Al}} = 0.01$, however, cannot be explained easily so far. This observation might be related to the Burstein-Moss effect, which predicts a band gap widening if the lowest conduction band states are occupied by electrons introduced by the dopant and the next free

lower level is at higher energies compared to the undoped sample.^{137, 138} Altogether, the band gap trend is complex and likely caused by several effects such as the *Burstein-Moss effect*, proper $\text{Al}_{\text{Zn}}^{\bullet}$ doping and the segregation of alumina when the solubility limited is exceeded.

5.3.2.5 Doped zinc oxides at higher calcination temperature

Often, calcination temperatures higher than 320 °C are used to synthesize aluminium doped zinc oxides and to investigate their opto-electrochemical properties.^{144, 147, 149, 196} A temperature series of aluminium doped hydrozincite with $x_{\text{Al}} = 0.03$ was prepared to investigate the effect of higher calcination temperature and to learn about the thermodynamics of the doped system. Undoped zinc oxide was treated in the same way as a reference material. The $x_{\text{Al}} = 0.03$ sample was chosen because this was the maximum amount aluminium which could be incorporated into the hydrozincite with only very little side-phase formation observable in PXRD. The calcination of the hydrozincite precursor was always performed by heating up in air from room temperature to the target dwell temperatures, which were held for four hours. Powder XRD shows that the reflections become sharper after calcination at higher temperatures (Figure 5.16) indicating that the crystallinity of the sample increased with temperature as expected. At a temperature of 920 °C, reflections of the ZnAl_2O_4 spinel phase were observed, which increased in intensity with further temperature increase. Simultaneously, a change in morphology was observed by SEM. The images of the undoped sample (Figure 5.17) demonstrate that the morphology at 420 °C is still similar to that described above for 320 °C calcination temperature. At 520 °C the platelets were thicker, and a few larger holes demonstrate a beginning sinter effect. Further increase in temperature resulted in an enhanced sinter effect and an enlargement of the particles, losing their original nanostructure. At 1100 °C the zinc oxide has crystallized into bulky, roundish particles with a clearly decreased porosity.

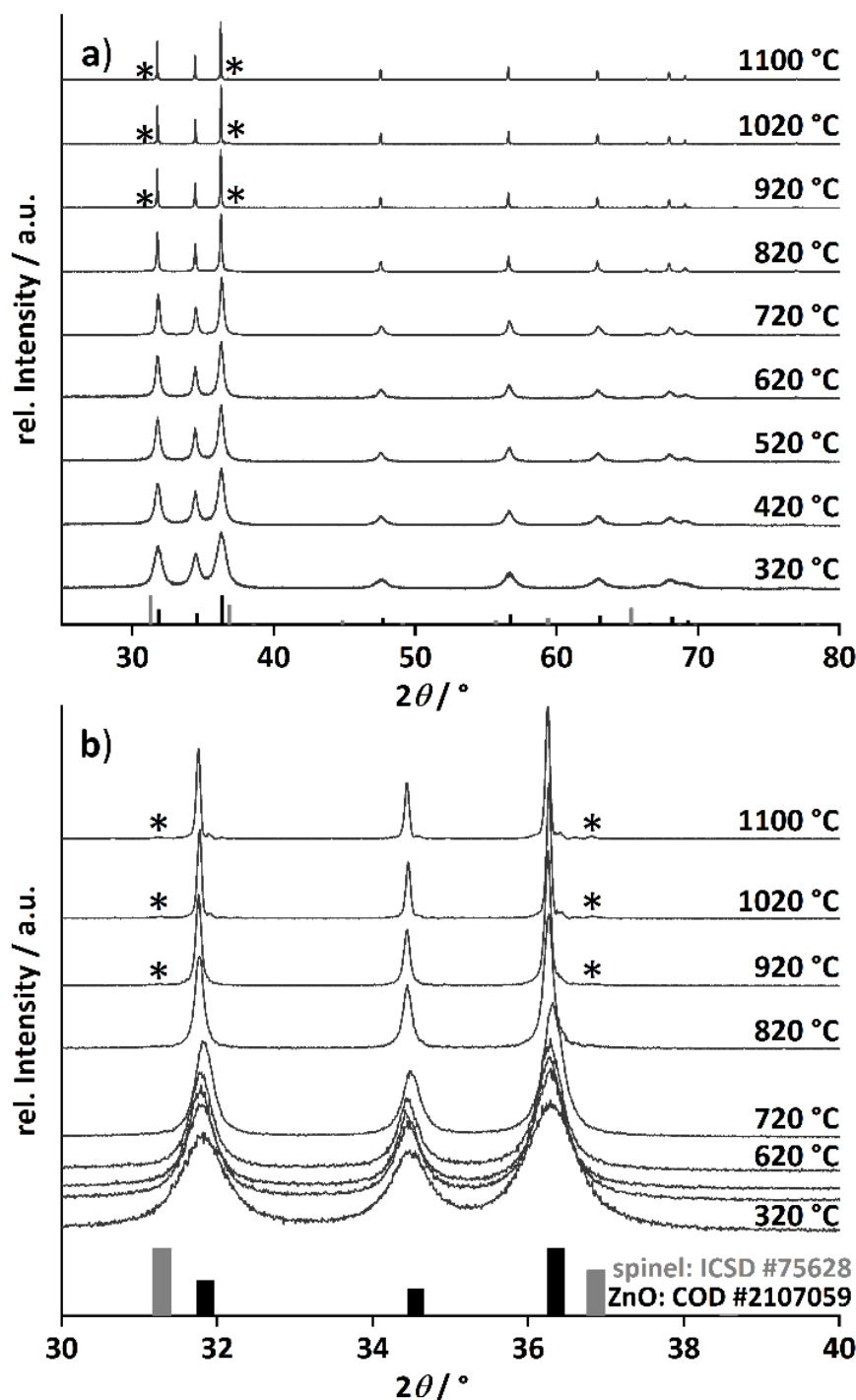


Figure 5.16: Powder XRD pattern of the aluminium doped zinc oxide with a cation-based molar aluminium fraction $x_{Al} = 0.03$ after calcination of the hydrozincite precursors at different temperatures with $2\text{ }^\circ\text{C min}^{-1}$ heating ramp and 4 h holding time in static air. Reflections assigned to ZnAl_2O_4 spinel are marked with an asterisk (*). The reference pattern of zinc oxide (black bars) was taken from COD (#2107059) and the reference pattern of zinc-aluminium spinel (grey bars and asterisks in pattern) was taken from ICSD database (#75628). In a) the complete range is shown. In b) a zoom of the pattern with spinel reflections is presented.

5 Phase evolution, speciation and solubility limit of aluminium doping in zinc oxide catalyst supports synthesized via co-precipitated hydrozincite precursors

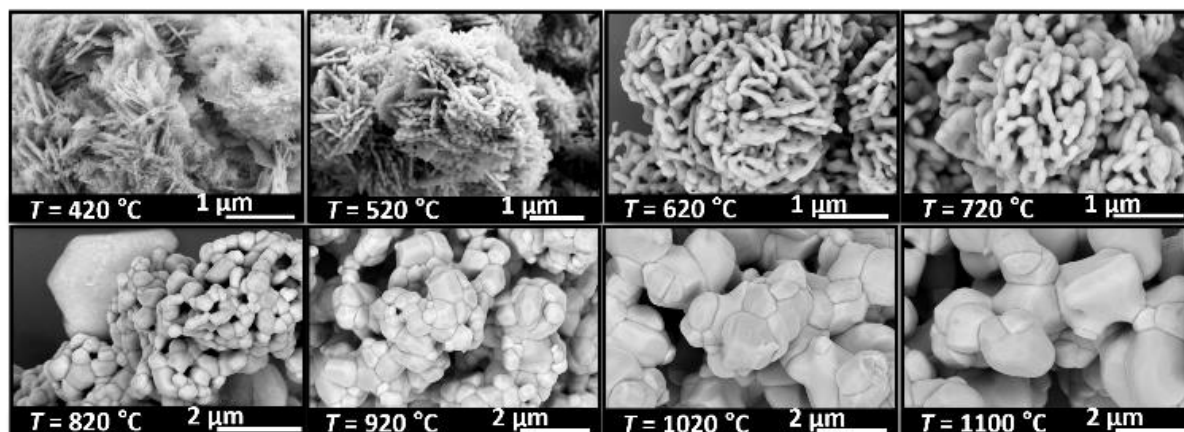


Figure 5.17: Morphology evolution depending on the calcination temperature of the undoped zinc oxide. Calcination was performed with $2\text{ }^{\circ}\text{C min}^{-1}$ heating ramp and 4 h holding time in static air.

In order to obtain insight into the effect of thermal annealing on the presence of the different aluminium species ^{27}Al MAS NMR was performed (Figure 5.18). Up to $620\text{ }^{\circ}\text{C}$ the presence of the four different aluminium species is observed, as aforementioned. During this process a decrease in the $\text{Al}_{\text{Zn}}^{\bullet}$ signal is observed (Figure SI 11.46). In thermodynamic equilibrium the Al substitution limit is expected to be determined by the formation of spinel ZnAl_2O_4 side phase,²²⁶ which under low-temperature conditions amounts to a concentration limit far below the observed values.¹⁹⁸ The expected higher substitution levels of the low-temperature route can be explained by the higher chemical potential of Al in the amorphous surface layers formed, which are less favourable to Al than that of the spinel phase. The formation of the spinel phase as seen by ^{27}Al NMR (Figure 5.18) begins at annealing temperature of $720\text{ }^{\circ}\text{C}$ upwards and drastically reduces the amount of Al in all phases but not in the spinel phase ZnAl_2O_4 . This is shown by the presence of an additional signal at $\delta_{\text{obs}} = 15\text{ ppm}$ corresponding to ZnAl_2O_4 .¹⁹⁶

At temperatures of $820\text{ }^{\circ}\text{C}$ the $\text{Al}_{\text{Zn}}^{\bullet}$ signal in ZnO has dropped below the detection limit of $x_{\text{Al}} = 0.0005$, which is consistent with the low equilibrium values determined in a previous study.¹⁴⁹ We note that all (NMR visible) Al is consumed by the formed spinel ZnAl_2O_4 phase. At these high annealing temperatures only two ^{27}Al MAS NMR signals are observed: $\delta_{\text{obs}} = 15\text{ ppm}$, which corresponds to the octahedral coordinated aluminium environment in the ZnAl_2O_4 crystal structure and $\delta_{\text{obs}} = 75\text{ ppm}$, which likely results from a cation inversion defect of the zinc and aluminium.^{226, 227}

What can be concluded is that the low-temperature approach achieves a much higher Al^{3+} substitution of the Zn^{2+} ions in ZnO than the equilibrium concentration would permit. Furthermore, this high substitution level can be maintained up to a temperature of about $720\text{ }^{\circ}\text{C}$

5 Phase evolution, speciation and solubility limit of aluminium doping in zinc oxide catalyst supports synthesized via co-precipitated hydrozincite precursors

when the activation energy for the formation of spinel crystallite is overcome and low thermodynamic substitution levels in ZnO are observed. It can be concluded that n-doping of ZnO by Al is thus stable under the conditions relevant for the catalytic process.

Together with the results from the composition series, where the Al_{Zn}^{\bullet} increased up to $x_{Al} = 0.01$ after the calcination of an aluminium-doped hydrozincite, the observation made for the temperature series indicates that the substitution on a zinc site is rather a kinetic effect and can be facilitated by a properly formed precursor acting as a kinetic trap. A further increase in the aluminium content does not result in an increased number of substituted sites but increases the side-phase amount in the precursors phase which has a negative effect on the opto-electrochemical properties. A calcination temperature above 320 °C minimizes the number of substituted sites and is therefore disadvantageous. The results clearly demonstrate that the presence of aluminium-doped zinc oxide containing the Al_{Zn}^{\bullet} species must be considered as a component of a typical methanol catalyst support.³⁴

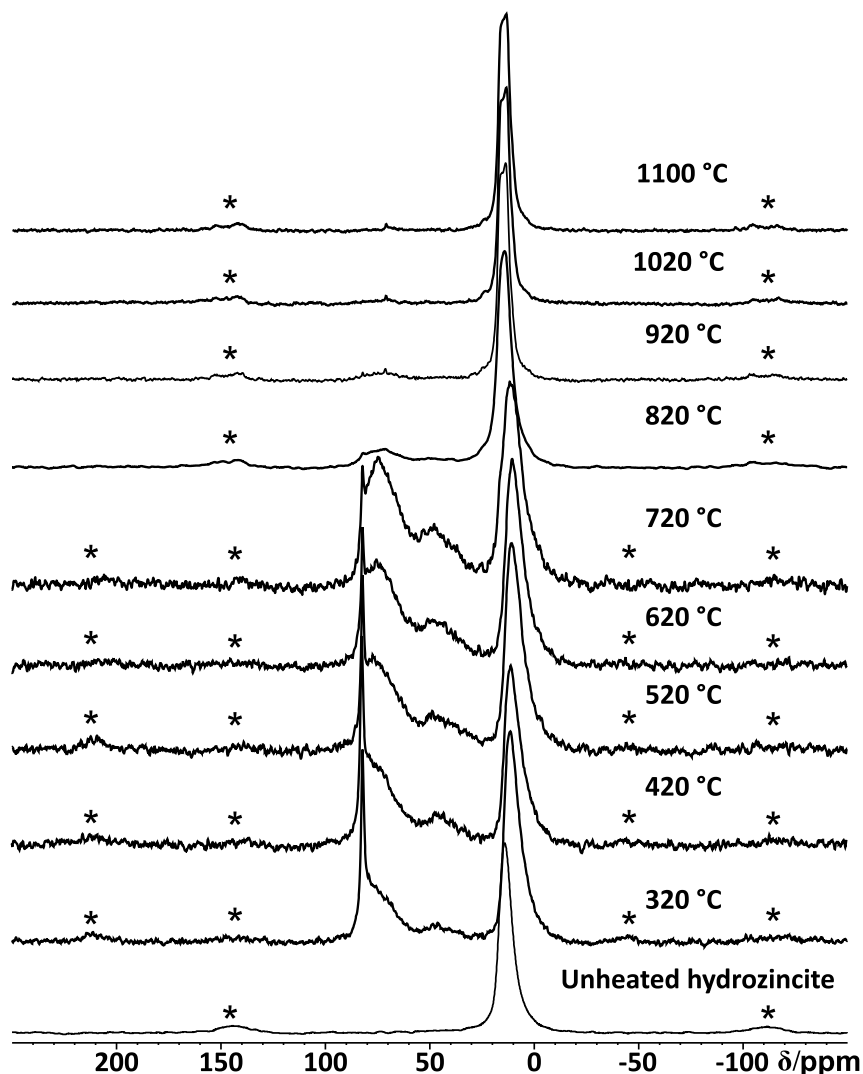


Figure 5.18: Stack plot of the ^{27}Al MAS NMR spectra of aluminium doped zinc oxide with a cation-based molar aluminium fraction $x_{\text{Al}} = 0.03$ after calcination at different temperatures. All spectra were recorded at a spinning frequency of 20 kHz. Spinning side bands are labelled with an asterisk (*).

5.4 Conclusion

The aluminium speciation was found to be complex when co-precipitation of hydrozincite precursors, $\text{Zn}_5(\text{OH})_6(\text{CO}_3)_2$, is used as a method inspired by catalyst synthesis to prepare aluminium-doped zinc oxide support materials. Thermodynamically favoured aluminium segregation into an aluminium-rich crystalline zaccagnaite side-phase, $\text{Zn}_4\text{Al}_2(\text{OH})_{12}(\text{CO}_3) \cdot 3\text{H}_2\text{O}$, was observed at aluminium contents higher than $x_{\text{Al}} = 0.013$, for long ageing times and after solvothermal treatment. This side-phase was found to be responsible for a non-uniform aluminium distribution in the precursors and later in the calcined samples. Still, the results suggest that hydrozincite can take up aluminium in an octahedral coordination even for $x_{\text{Al}} > 0.02$ leading to the formation of defects due to charge compensation in the

hydroxycarbonate. Calcination at 320 °C leads to formation of zinc oxide as the only crystalline phase, but electron microscopy and ^{27}Al NMR revealed non-uniform aluminium distribution and presence of diverse aluminium species for a doping level of $x_{\text{Al}} = 0.03$ and larger. Such complexity is based on the ex-zaccagnaite regions, which were found to segregate into nano-crystalline zinc oxide with an aligned crystallographic orientation and into amorphous alumina. At lower aluminium contents, however, the dopant was found preferably on the zinc sites of the zinc oxide lattice based on the $\text{Al}_{\text{Zn}}^{\bullet}$ signal dominating the NMR spectra. The solubility limit regarding this species was determined to be approximately $x_{\text{Al}} = 0.013$ or 1.3 % of all metal cations. Annealing experiments showed that the substitution of zinc by aluminium is a kinetic driven process. The aluminium was kinetically trapped on the $\text{Al}_{\text{Zn}}^{\bullet}$ site up to a substitution limit which is much higher than the thermodynamic limit set by a segregation into zinc oxide and ZnAl_2O_4 spinel. This shows that lower calcination temperatures such as applied in catalyst synthesis favour the aluminium doping on that specific site. The investigation of these support materials under hydrogenation conditions and their application in catalytic reaction will be addressed in forthcoming work.

Supporting Information

Supporting Information are provided in chapter 11.7 (Supporting Information to "Phase evolution, speciation and solubility limit of aluminium doping in zinc oxide catalyst supports synthesized *via* co-precipitated hydrozincite precursors") on page 231.

Acknowledgements

We gratefully thanks Dr. K. Loza (University Duisburg-Essen) and Dr. C. Szillus (University of Kiel) for REM analysis of the prepared materials.

6 Phase evolution and solubility limit of gallium doping in zinc oxide catalyst supports synthesized *via* co-precipitated hydrozincite precursors

Benjamin Mockenhaupt ^{**ac}, Jan Konrad Wied ^{**b}, Sebastian Mangelsen ^c, Ulrich Schürmann ^d, Lorenz Kienle ^d, Jörn Schmedt auf der Günne ^{*b}, Malte Behrens ^{*ac}

- a. B. Mockenhaupt, Prof. Dr. M. Behrens, Institute of Inorganic Chemistry, University of Duisburg-Essen, Universitätsstr. 7, 45141 Essen (Germany), E-mail: mbehrens@ac.uni-kiel.de.
- b. J. K. Wied, Prof. Dr. J. Schmedt auf der Günne, Institute of Inorganic Chemistry, University of Siegen, Adolf-Reichwein-Straße 2, 57076 Siegen (Germany), E-mail: gunnej@chemie.uni-siegen.de.
- c. B. Mockenhaupt, Dr. S. Mangelsen, Prof. Dr. M. Behrens, Institute of Inorganic Chemistry, Christian-Albrecht University of Kiel, Max-Eyth-Str. 2, 24118 Kiel (Germany)
- d. Dr. U. Schürmann, Prof. Dr. Lorenz Kienle, Institute for Materials Science, Christian-Albrecht University of Kiel, Kaiserstraße 2, 24143 Kiel (Germany)

** both authors contributed equally.

* Corresponding author.

Contribution of the authors

- B.M. synthesized the materials and contributed to the characterization, data analysis and wrote the first draft of the manuscript.
- J.K.W. conducted the NMR experiments, the data analysis.
- S.M. evaluation and reviewing of the manuscript.
- U.S. conducted the TEM measurements, contributed to design of experiments and data analysis.
- L.K., J.S.G and M.B. contributed to conceptualization of the work, acquisition of the financial support, provision of study materials, reagents, materials, instrumentation, computing resources and other analysis tools.

Abstract

Beside aluminium gallium can also be used as a dopant of zinc oxide. Because of the similar ionic radius of gallium to the zinc, a better incorporation into the zincite lattice is assumed. To synthesize defined zinc oxides, the co-precipitation approach was used. In this investigation hydrozincite was employed as precursor, which allows a decomposition to zinc oxide at low temperatures around 320 °C. The materials were characterized by powder x-ray diffraction (PXRD), infrared, Raman and UV/Vis spectroscopy, N₂ physisorption and by NMR spectroscopy. This combination supports the determination of possible side phases and allowed estimation of solubility limit of Ga in zincite. Up to $x_{\text{Ga}} = 0.04$ gallium content the zinc oxides were equal in their characteristics and no side phase was present in the precursor phase, suggesting a solubility limit around this concentration. A further increase of Ga content resulted in phase impure and defect rich precursor phase as well as in highly defect enriched ZnO structure.

6.1 Introduction

The opto-electronic promotion of zinc oxide is often done by aluminium incorporation.^{141, 194} It is found by theory, that this cation has the best promotion effect regarding the band gap optimization.¹³⁹ In case of a band gap renormalization gallium was predicted as the worst doping cation as the hybridization of the Ga_{4s} orbital with the zinc oxide conducting band does not decrease the s orbital energy.¹³⁹ Because of the low substitution limit of aluminium in the zinc oxide, the worse doping effect of gallium could be probably compensated by a higher number of substituted zinc sites.²²⁸ The better incorporation should be a result of a closer ionic radius of the gallium cation to the zinc ion (coordination number = 4: $r_{\text{Al}^{3+}} = 0.53 \text{ \AA} < r_{\text{Ga}^{3+}} = 0.61 \text{ \AA} < r_{\text{Zn}^{2+}} = 0.74 \text{ \AA}$).²²⁹ Therefore, gallium incorporated zinc oxide raised increasing attention due to the possible utilization in LCD displays or other display applications²³⁰, solar- or photovoltaic cells^{137, 231} and as organic LED²³². But the promotion effect is not only of interest in the field of electrical application but also in the field of heterogeneous catalysis.

Studies on the co-precipitated copper zinc oxide methanol catalyst demonstrate, that the incorporation of trivalent cations increase the copper surface area by improving the microstructure of the catalyst from a precursor stage.²³³ Thus, a gallium promoted catalyst demonstrate enhanced methanol activity compared to the unpromoted catalyst.²³³ To prove beside the structural promotion effect also the opto-electronic promotion effect in the context of catalysis, gallium doped zinc oxide was synthesized by co-precipitation and impregnated

with copper.³⁷ This catalyst was found to be more active in reverse water gas shift reaction and showed a comparable activity in methanol synthesis compared to the aluminium promoted catalyst.³⁷ The influence of gallium as an additional promotor beside zinc oxide was also shown for methanol steam reforming catalyst. Gallium containing catalysts suppressed the carbon monoxide formation and enhance the activity in methanol conversion.²³⁴ The incorporation of a trivalent cation into the zinc oxide introduces an additional electron and enhances the n-type semiconducting properties.²³⁵ For an optimum doping effect it is crucial, that the incorporated cation substitute a zinc site.¹³⁹ In this context the solubility limit of gallium in zinc oxide will be of interest.

Early research on gallium doped zinc oxides have determined a solubility limit, which means the substitution on a zinc position (Ga_{Zn}^{\bullet}) to be in the range of 0.5 mol% to 2.8 mol% (metal-based). These solubility limits were determined after annealing the samples at temperature in the range of 550 – 1000 °C, based on the analysis methods by: dichromate reduction, electron microscopy, dissolving experiments with HCl, resistivity measurements and Raman spectroscopy.^{144, 195, 228, 236, 237}

Our work was inspired by the typically Cu/ZnO preparation route, where lower temperatures around 350 °C were used to decompose the precursor phase to the metal oxides.^{8, 57} Based on previous studies on aluminium doped zinc oxides, the low temperature treatment is expected to be beneficial for trivalent cation doping of the ZnO.^{142, 143, 172}

However, from the spectroscopic point of view, investigations on aluminium promoted zinc oxides have demonstrated that ²⁷Al NMR spectroscopy was a suitable method to determine the substitution quality.^{142, 143} Hence, it is interesting, that for gallium doped zinc oxides such analysis methods are rarely reported. This can probably be owed by the line broadening due to the smaller nuclear spin quantum number compared to ²⁷Al.²³⁸ Nevertheless, the ⁷¹Ga NMR should be more favourable than the ⁶⁹Ga NMR because it has a smaller quadrupole moment and a larger gyromagnetic ratio.²³⁸ In one investigation, gallium and zinc solid state NMR was used to resolve the defects in the gallium doped zinc oxides. The similar quadrupole interactions of ⁶⁷Zn and ⁶⁹Ga was found result from gallium occupying a zinc site.¹⁹⁹ The corresponding signal was aligned to around 40-50 kHz.¹⁹⁹ From varying oxygen content in the samples (oxygen rich or oxygen poor) it was claimed, that the signal of ⁶⁹Ga at around 100 ppm correspond to gallium on a zinc position.¹⁹⁹ The doped zinc oxides were synthesized by heating zinc oxide and gallium metal to 1200 °C. At this conditions the gallium should exchange a zinc atom, which leave the oxide matrix.¹⁹⁹

Given the fact, that the substitution limit of gallium in zinc oxide is quite difficult to determine and that there are few reports about gallium NMR spectroscopy, the investigations of a systematic series of zinc oxides with varying gallium amount will be presented to resolve the solubility question in a similar manner like it was performed for the aluminium doping.¹⁷² To ensure a homogeneous distribution of gallium in the sample the synthesis *via* a co-precipitated crystalline precursor phase was used, similar to that described in previous works.¹⁷² This method has the advantage, that gallium and zinc are homogeneous distributed in a precursor phase which predefines the origin state for the decomposition to a zinc oxide because of the close contact. The decomposition of that specific precursor phase can be performed at low temperature around 300 °C and enable the synthesis of a defined and promoted zinc oxide. The synthesized doped zinc oxides were investigated by their phase purity using x-ray diffractometry, IR- and Raman- and NMR spectroscopy. That methods will be used in combination with UV/Vis spectroscopy to estimate a relationship between doping quality and band gap energy.

6.2 Experimental section

6.2.1 Precursor synthesis

The precursor of the zinc oxide sample was synthesized by co-precipitation. The precipitation was carried out in an automated stirred tank reactor (OptiMax, Mettler Toledo) from 1 M metal salt nitrate solution (see SI, Table SI 11.20 on page 260) at a temperature of 65 °C and at a constant *pH* of 6.5. As precipitating agent, 1.6 M sodium carbonate solution was used. The dosing rate of metal solution was adjusted to 4.2 g min⁻¹. After precipitation, the precipitate was aged for 10 minutes without further pH control in the mother liquor. The precursor was washed with deionized water 10 times, to reach a conductivity of the filtrate lower than 100 μS cm⁻¹ and dried at 80 °C over night in a heating cabinet.

6.2.2 Zinc oxide synthesis

The zinc oxide was synthesized by calcination of the grinded hydrozincite from co-precipitation. The calcination was performed at 320 °C with a heating ramp of 2 °C min⁻¹ for 4 h in a Nabertherm (LE 6/11/B150) muffle furnace in static air (without any volume flow).

6.2.3 Sample labelling

The samples are labelled according to their gallium content relative to the total amount of metal atoms either as percentage or as a value x_{Ga} representing the nominal metal-based ratio of gallium calculated as shown in equation M 6.1.

$$x_{Ga} = \frac{n_{Ga}}{n_{Ga} + n_{Zn}} \quad M\ 6.1$$

Here, n_i is the molar amount of element i ($i = Zn, Ga$).

6.3 Characterization methods

Powder x-ray diffraction (PXRD) analysis was performed on a Bruker D8 advance with copper K-alpha radiation and a LYNXEYE XE-T detector. The diffractograms were recorded in reflection in a Bragg-Brentano geometry at room temperature between 5° and 90° of the angle 2θ . Phase analysis was performed by comparing the recorded with structural data from ICSD and COD databases.

Brunauer-Emmett-Teller (BET) analysis

The specific surface areas were measured by nitrogen physisorption at 77 K in a Nova 3200e sorption station from Quantachrome. Before recording the isotherms, the samples were degassed under vacuum at 100 °C (hydrozincite) and 250 °C (zinc oxide) for 5 h. Afterwards the isothermal profiles between $p/p_0 = 0.0$ and 1 referred to a reference cell were recorded. The multipoint BET surface area was determined by applying the Brunauer-Emmett-Teller equation in a sample specific range determined by the Micropore-Assistant of the NovaWin software by only considering the increasing volume.

Infrared resonance spectroscopy (IR) characterization was performed on a Bruker Alpha FT-IR spectrometer with attenuate total reflection (ATR) unit. The spectra were recorded between 400 cm⁻¹ and 4000 cm⁻¹ at room temperature. To suppress water and CO₂ signals from the atmosphere, the device was placed in a glovebox of MBraun with argon atmosphere.

UV/Vis-Spectroscopy was performed at room temperature in a 2600i spectrometer of Shimadzu in the range of 200 to 900 nm. The sample was pressed into the solid sample holder to create a flat surface. The spectra were recorded in reflection with BaSO₄ as reference material. The

band gap determination was performed by differentiation of the raw data, to determine the changing point. At this point, where the first derivative was zero, the wavelength was calculated to the electrical energy in eV. This method was used only to determine qualitatively the band gap energy change by UV/Vis spectroscopy in dependency of the gallium incorporation.

RAMAN-Spectroscopy of the powders was performed in a powder sample holder positioned in 45° to the laser beam in a MacroRam spectrometer of Horiba Scientific. A 785 nm laser with an intensity of 90 mW was used. The Raman shifts were recorded in the range of 100 cm⁻¹ to 3500 cm⁻¹.

Scanning electron microscopy (SEM) of the doped ZnO samples were taken on a Zeiss Gemini Ultra Plus with an Oxford EDX detector. A spatula tip of the sample was dispersed on a carbon covered stainless steel pin mount sample holder.

Transmission electron microscopy (TEM) were performed on a FEI Tecnai F30 G2 STwin (300 kV, FEG) equipped with an EDX detector (Si/Li, EDAX). The TEM samples were ground and dispersed in n-Butanol (spatula tip sample in few drops of n-Butanol) and prepared on Cu lacey TEM grids.

Solid state NMR-Spectroscopy

All Ga solid-state NMR experiments were performed on the Bruker Avance Neo NMR spectrometer with a magnetic field of 14.1 T using a Bruker 3.2 mm probe head at a frequency of 156.375 MHz.

6.4 Results and Discussion

6.4.1 Characterization of the Hydrozincite precursors

The co-precipitated precursors are characterized by PXRD. The patterns are shown in Figure 6.1. The samples up to $x_{Ga} = 0.04$ gallium content are crystalline and phase pure hydrozincite materials. The reflections become broader as more gallium was incorporated, indicating, that gallium is introduced into the crystal phase as shown in Figure 6.2 exemplified on the 200 reflection. For a gallium content $x_{Ga} > 0.04$ an additional reflection of a side phase at around $2\theta = 12^\circ$ evolved, which is assigned to a hydrotalcite type crystalline phase. The mineral of the aluminium rich hydrotalcite type side phase is called zaccagnaite with the stoichiometric formula: $Zn_4Al_2(OH)_{12}(CO_3) \cdot 3H_2O$.²⁰⁵ This side phase was also found in a study about Al incorporation into hydrozincites and zinc oxides.¹⁷² In this case now, instead of aluminium gallium was incorporated, resulting in a similar to zaccagnaite Ga,Zn layered double

6 Phase evolution and solubility limit of gallium doping in zinc oxide catalyst supports synthesized via co-precipitated hydrozincite precursors

hydroxide (Ga,Zn LDH) side phase. For the samples with a higher gallium content $x_{Ga} > 0.06$, the main hydrozincite reflections are present, but the reflections are so broadened, that only the main intense reflections are visible. Additionally, a new reflection at the angle of $2\theta = 6.45^\circ$ and $2\theta = 19.49^\circ$ evolved for $x_{Ga} > 0.06$. Since this new evolved position is reproduced by $x_{Ga} = 0.1$ and $x_{Ga} = 0.15$ gallium containing samples, it is related to the gallium incorporation. From ICSD and COD Database the allocation to a specific crystal system was not possible. The additional reflection at $2\theta = 19.49^\circ$ was also observed in a previous investigation with aluminium as trivalent cation and was found to correspond to a defect enriched hydrozincite with broken symmetry.¹⁷² Therefore, in situ PXRD during calcination was performed. Analogous to the Al incorporated hydrozincite¹⁷², the gallium doped precursor decomposed at around 220°C to ZnO, which was additionally confirmed by TG analysis (compare SI Figure SI 11.49). Contrarily to hydrozincite, the zaccagnaite-like side phase reflection disappeared at around 120°C (see Figure 6.3). The additional reflections of the precursor phase at $2\theta = 6.45^\circ$ and $2\theta = 19.49^\circ$ behaved like the hydrozincite phase and can be affiliated to that precursor material.

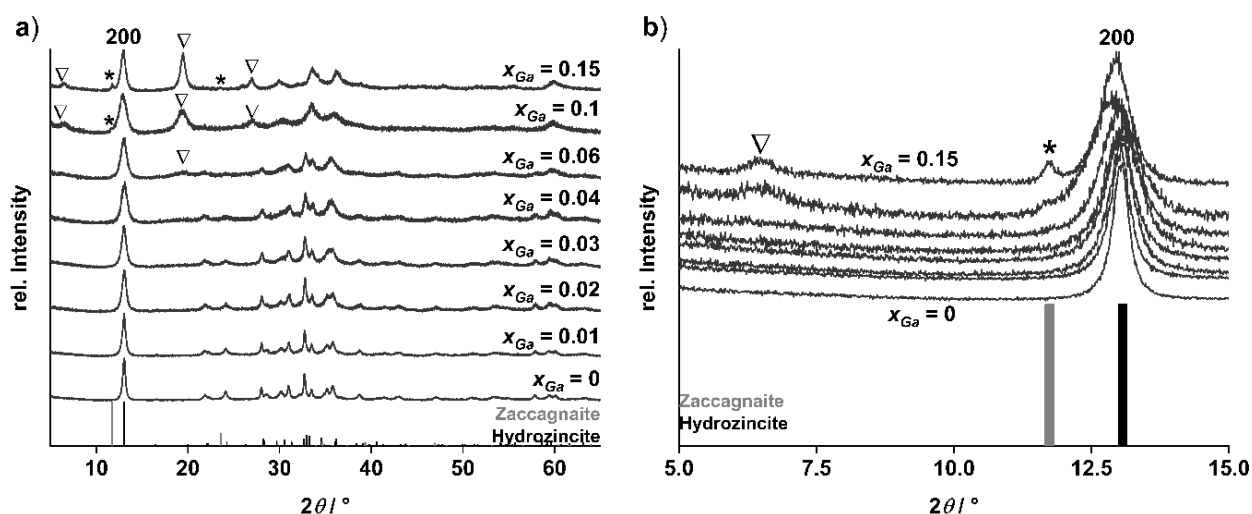


Figure 6.1: Powder PXRD pattern of the co-precipitated gallium doped hydrozincite precursors (a). In b) is a higher resolution of the range up to $2\theta = 15^\circ$ shown, to demonstrate the zaccagnaite-like phase evolution. The reference pattern was taken from ICSD, hydrozincite in black (#16583) and the zaccagnaite-like in dark grey (#190041, *). The new and unknown reflections at $2\theta = 6.45^\circ$ and $2\theta = 19.45^\circ$ are marked with a triangle. x_{Ga} is the metal-based fraction of gallium.

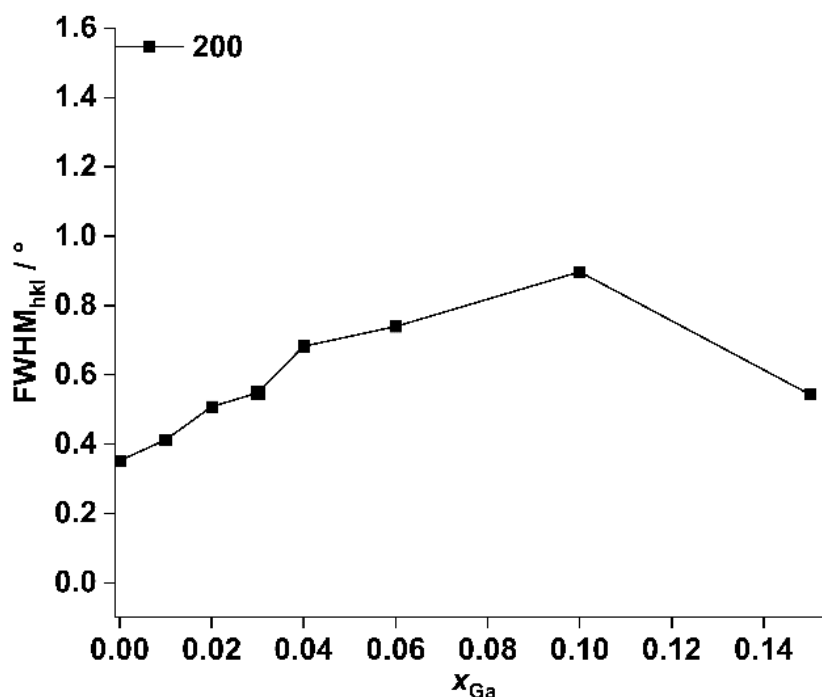


Figure 6.2: Demonstration of the 200 reflection broadening of the hydrozincite precursor phase in dependency of the gallium incorporation. x_{Ga} is the metal-based fraction of gallium.

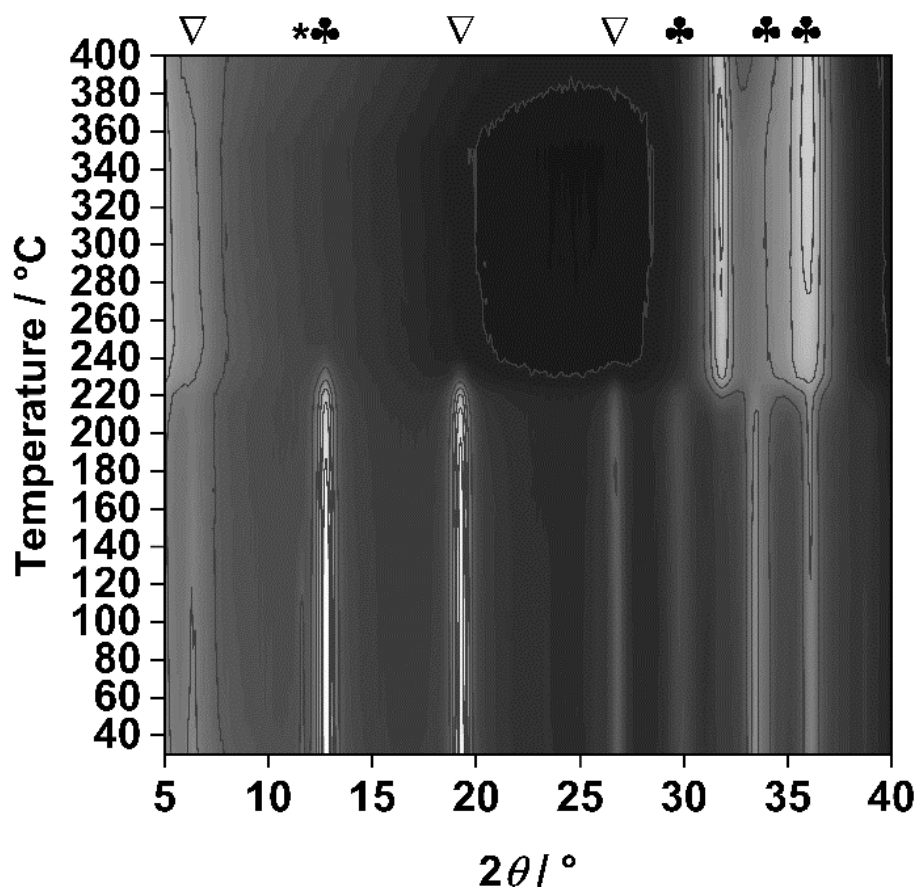


Figure 6.3: Temperature-resolved PXRD analysis of the thermal decomposition of the hydrozincite precursor containing 15 % gallium ($x_{Ga} = 0.15$). The PXRD analysis was performed in static air. The reflection positions are labelled as followed: zaccagnaite-like (), hydrozincite (♣) and additional reflections (▽).*

To determine structural changes, infrared spectroscopy was performed. The spectra are shown in Figure 6.4. Typically infrared modes for hydrozincite ($x_{\text{Ga}} = 0$) are the ν_3 mode (1370 cm^{-1} & 1500 cm^{-1}) which corresponds to the antisymmetric carbonate stretching and the ν_1 mode (1045 cm^{-1}) which corresponds to the symmetric carbonate stretching mode.²¹⁰ Whereas the ν_4 mode (704 cm^{-1}) corresponds to the antisymmetric OCO bending mode and the ν_2 mode (836 cm^{-1}) to the out-of-plane OCO bending mode.^{210, 211}

Contrarily, the zaccagnaite-like side phase contains three strong signals at 1343 cm^{-1} , 767 cm^{-1} and 521 cm^{-1} .

To evaluate first, for which doping level the side phase can be expected by IR active modes, the modes of the zaccagnaite-like phase are compared to the Ga doped hydrozincite series.

The mode at 521 cm^{-1} is related to a M-OH translation mode²¹⁴ and is clearly present in the zaccagnaite-like sample. Only the hydrozincite doped with 10 % and 15 % Ga showed a weak signal at this position, which indicate, that this samples contained small fractions of the side phase.

The mode at 767 cm^{-1} of the zaccagnaite-like phase can be assigned to a M-OH translation mode²¹⁵ which can be related to the significant amount of hydroxyl groups present in this material. However, this very pronounced signal must be linked to the gallium ion, since it was not so intense as Al was used as trivalent cation.¹⁷²

The mode at 1343 cm^{-1} can be aligned to an antisymmetric carbonate stretching mode (ν_3). This mode is also typical for the hydrozincite phase in the region of 1370 cm^{-1} and 1500 cm^{-1} . But this mode is tailored into two separated signals in case for hydrozincite and collapse to one signal for the zaccagnaite-like material.

The split into two ν_3 modes in the hydrozincite structure is explained by the change of the carbonate site symmetry to either D_3 , C_s or to C_s and C_{2v} .²³⁹ If the site symmetry is C_s the ν_3 and ν_4 mode will split into two signals, like it can be observed in Figure 6.4.²¹¹ This split in the modes is a hint of defects and distortions in the carbonate sublattice of the hydrozincite.^{210, 240, 241} However, the C_s site symmetry seems to be stable up to 4 % gallium incorporation. A higher incorporation result in the shift of the ν_3 modes towards higher wavenumbers and the collapse of both signals to one signal started. Simultaneously, the mode ν_4 vanish. This break in symmetry by Ga incorporation demonstrate, that the hydrozincite structure is enriched in defects and starts to change, as it was observed in PXRD by additional and broaden reflections. The increased defects in the hydrozincite structure as well as the additional modes at 521 cm^{-1} ,

which can be related to the zaccagnaite-like side phase, indicates a change in the more thermodynamically favoured structure. A doping with larger fractions of 10 % gallium may represent a two-phase system of hydrozincite and zaccagnaite-like material, which will change towards a one phase system if the stoichiometry for a hydrotalcite structure is reached.

Interestingly, when the ν_4 mode in the hydrozincite structure start to decline ($x_{Ga} > 0.04$), the symmetric OCO bending mode ν_2 (836 cm^{-1}) appears. Simultaneously, the mode at 623 cm^{-1} increases with the dopant amount. From hydrotalcite studies, the mode at 623 cm^{-1} can be related to translation of hydroxyl groups.²¹⁴ The hydroxyl group increase with increasing dopant concentration must be due to charge compensation of the Ga^{3+} ion. Since this mode is correspond to hydroxyl sites between sheets, it can be assumed, that the increase of this mode increased the number of sheets. Simultaneously, the carbonate sites decrease, as the signals of the ν_3 mode broadened and the ν_4 mode vanished. However, the carbonates, which are present in the structure change the position from an antisymmetric (ν_4) to a symmetric OCO bending site, which is indicated by the appearance of the ν_2 mode. The change in the carbonate sublattice is also observed by the mode at 950 cm^{-1} . This mode disappears when the first structural changes in the hydrozincite started at $x_{Ga} = 0.02$ and represents the hydrogen bond between a carbonate and a hydroxyl anion. In this early stage ($x_{Ga} = 0.02$) it can be assumed, that the dopant changed the carbonate orientation, which break up the hydrogen bond. Further increase of the dopant concentration led to a break in the C_s symmetry of the hydrozincite structure and carbonate becomes substituted by hydroxide ions for charge compensation introduced by Ga^{3+} incorporation into the hydrozincite lattice.

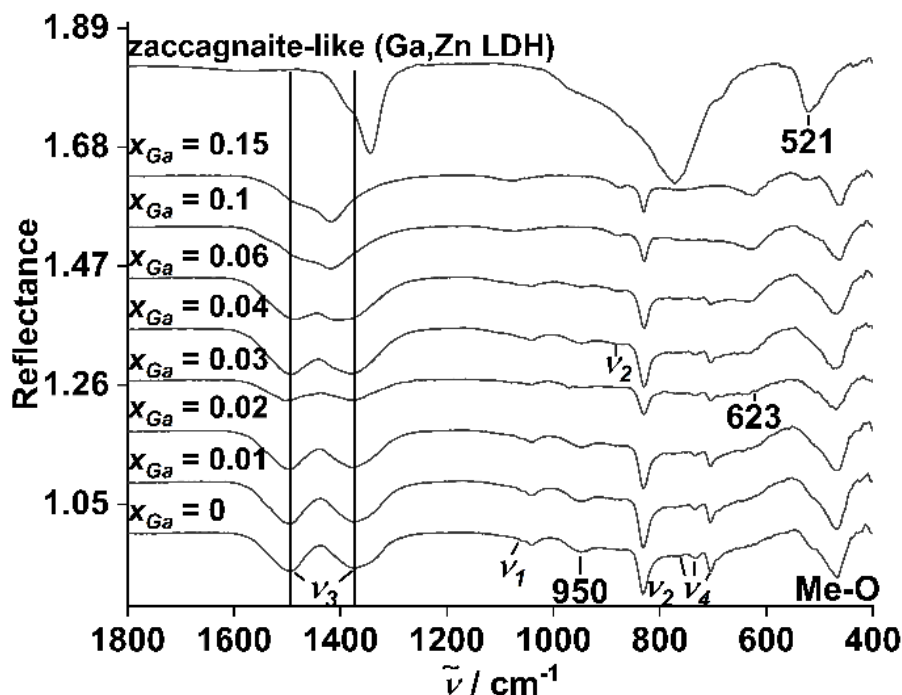


Figure 6.4: Infrared spectroscopy of the gallium doped hydrozincites with the expected zaccagnaite-like side phase. With x_{Ga} as the metal-based fraction of gallium.

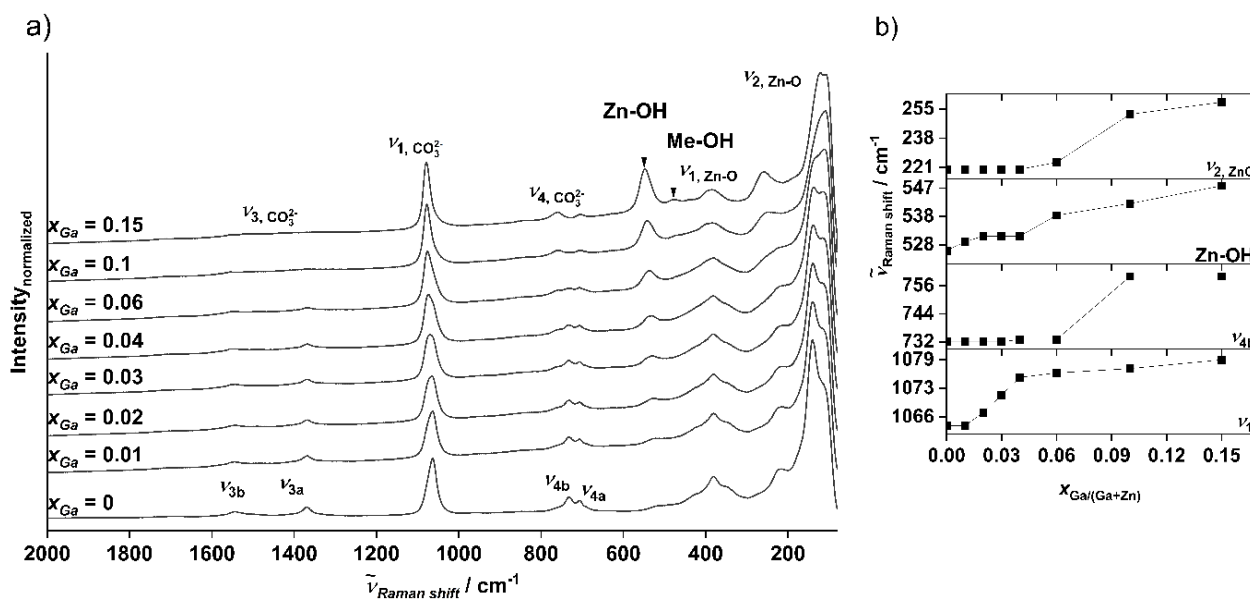


Figure 6.5: Raman spectra of the gallium doped hydrozincite series. x_{Ga} is the metal-based fraction of gallium. In a) the spectra are shown, b) shows the Raman shift of selected signals depending on x_{Ga} .

For a better insight into side phase formation, Raman spectroscopy on the gallium doped hydrozincites was performed. The spectra of the samples are presented in Figure 6.5. The typical carbonate modes are: the antisymmetric carbonate stretching mode ν_3 ($\nu_{3b} = 1545 \text{ cm}^{-1}$ & $\nu_{3a} = 1368 \text{ cm}^{-1}$), the symmetric carbonate stretching mode ν_1 (1064 cm^{-1}) and the in phase

6 Phase evolution and solubility limit of gallium doping in zinc oxide catalyst supports synthesized via co-precipitated hydrozincite precursors

carbonate bending mode ν_4 ($\nu_{4b} = 1545 \text{ cm}^{-1}$ & $\nu_{4a} = 1368 \text{ cm}^{-1}$).²⁴¹ The bands below 600 cm^{-1} correspond to M-O or M-OH modes,^{211, 215, 241} here assigned as $\nu_{1, \text{ZnO}}$ (384 cm^{-1}) and the $\nu_{2, \text{ZnO}}$ (220 cm^{-1}).

Since zaccagnaite is a material which is related to the hydrozincite (layered double hydroxide, LDH) minerals, reported investigation of this material class are used to determine from this material expected modes.^{172, 215-217}

In this work, we focus on the structural changes of the hydrozincite structure induced by the Ga^{3+} incorporation.

In analogy to the IR spectroscopy, the main carbonates modes as described above are present in the undoped sample ($x_{\text{Ga}} = 0$). Similar as in the IR spectroscopy, the ν_3 mode start to decline with Ga incorporation. Especially the ν_{3b} mode is almost vanished for $x_{\text{Ga}} = 0.06$ whereas the ν_{3a} mode was still present. Since this modes indicates the carbonate lattice distortion, as described in the IR spectroscopy, the mode becomes Raman inactive and disappeared completely for $x_{\text{Ga}} = 0.1$ and $x_{\text{Ga}} = 0.15$ but was still present in the IR spectra (see Figure 6.4). Due to the broken symmetry in the hydrozincite structure, described in the IR section, the ν_4 mode broadened and vanished for $x_{\text{Ga}} > 0.04$. In Raman spectroscopy this mode broadened as well but was still present for higher doping levels than 4 %. The mode separated into signals in which ν_{4b} was still more pronounced compared to the ν_{4a} mode. Since for example the ν_3 mode vanished in Raman spectroscopy, but was still in IR spectroscopy active, this means, that the symmetry of the carbonate ion responsible for this mode was completely changed. Similar for the ν_4 mode, which stayed Raman active but became IR inactive. Possibly, both modes are linked and describe the similar carbonate ion in the structure, which cause simultaneously changes in the IR and Raman spectroscopy by deviating from the original carbonate symmetry.

However, the symmetric carbonate stretching mode (ν_1) was still Raman active but with increasing doping levels of $x_{\text{Ga}} > 0.01$ a blue shift of this mode was observed. This blue shift seemed to be stable after reaching a level of 4 % Ga in the hydrozincite and was also observed for the cationic lattice modes like $\nu_{1, \text{ZnO}}$ and for the Zn-OH mode (compare Figure 6.5 b)). This blue shift indicates a strengthening of the bonds. Since Ga is slightly heavier than Zn,²²⁹ a change of the coordination from Zn to Ga could explain such a shift and the increase of the modes. Therefore, this shift gives clear evidence of the Ga incorporation into the hydrozincite structure.

So far, Raman spectroscopy has elucidated structural changes in the carbonate lattice of the hydrozincite structure.

Regarding the phase purity, the signal at 477 cm^{-1} (Me-OH) was described for hydrotalcite materials.²¹⁵ This mode was only observed for 10 % and 15 % Ga doped hydrozincites, where indications for a zaccagnaite-like side phase were found in IR spectroscopy but also where this side phase could be determined by PXRD analysis, described in the previous section. Regarding, the M-OH active modes, the Zn-OH mode correlates with the increasing Ga amount in the hydrozincite. This mode was also present in the undoped hydrozincite, so that it is not a clear indication, that a side phase was formed. But the increase in intensity and the blue shift indicates, that this mode was also mainly affected by Ga incorporation. As explained in the IR spectroscopy section, above, the additional cationic charge may be compensated by additional hydroxyl groups, which explains the increase of hydroxyl group corresponding modes in the spectroscopic methods.

The BET surface areas, shown in Figure 6.6 (white bars), are quite similar and varies between $11 - 19\text{ m}^2\text{g}^{-1}$ over the complete doping range for the (substituted) hydrozincite samples. The surface areas of the doped zinc oxides will be discussed later.

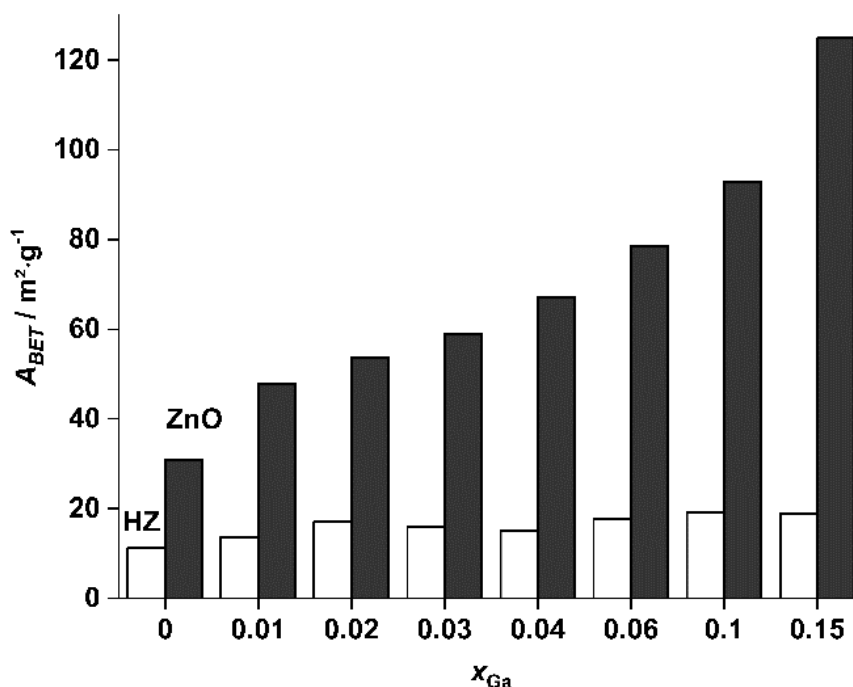


Figure 6.6: Evolution of the BET-surface for the gallium doped hydrozincites (white columns; HZ) and their zinc oxides (black filled columns; ZnO) after calcination at $320\text{ }^\circ\text{C}$ for 4 h in static air.

6.4.2 Characterization of the zinc oxides

By calcination of the gallium doped hydrozincite precursors at 320 °C in static air they were transformed to their corresponding zinc oxides. The PXRD pattern of these samples are shown in Figure 6.7 a).

The reflection positions correspond to zinc oxide without any side phase. Regarding the detected zaccagnaite-like side phase in the precursor characterization, the absence of additional reflections in the PXRD pattern led to the expectation, that it was decomposed to a defective ZnO phase, similar to the zaccagnaite side phase in the ZnO:Al study¹⁷². This expectation is supported by electron diffractometry during TEM analysis (shown in SI Figure SI 11.55), where a highly distorted ZnO was found for a decomposed, large single crystal, which is aligned to the zaccagnaite-like side phase, analogous to the findings in the ZnO:Al investigation¹⁷² and in analogy to the findings in PXRD of the precursors (Figure 6.1) and SEM microscopy (Figure SI 11.56). With increasing gallium content, the reflections broaden, which indicates the successful incorporation of Ga³⁺ in the ZnO lattice.

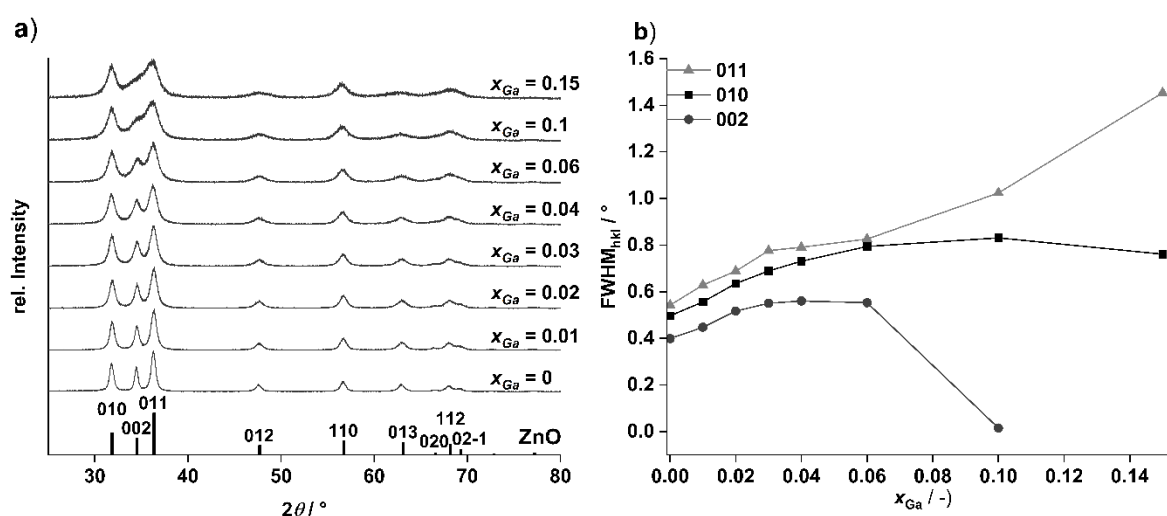


Figure 6.7: a) PXRD patterns of the gallium doped zinc oxides after calcination of the hydrozincite precursors. The reference positions were taken from COD, zinc oxide in black (#2107059). x_{Ga} is the metal-based fraction of gallium. In b) is the reflection broadening as the fullwidth of the half maximum (FWHM) in dependency of the gallium incorporation is shown. The lines are to guide the eyes.

The zinc oxide reflections, especially the 002 plane at $2\theta = 34.5^\circ$ are affected by increasing gallium incorporation (see Figure 6.7 b)). The FWHM of the 002-reflection dropped down for a gallium content of $x_{Ga} > 0.06$ because of the hardly to identify 002 reflection. This indicates that the lattice is strongly affected by the gallium incorporation and may induces defects like in the hydrozincite lattice, discussed in the precursor characterization. However, the main changes

6 Phase evolution and solubility limit of gallium doping in zinc oxide catalyst supports synthesized via co-precipitated hydrozincite precursors

in the reflections happened for a larger gallium content than $x_{Ga} \geq 0.06$. It is expected that a defect rich zinc oxide increases the surface area of this material. In Figure 6.6 (black bars) the expected BET surface areas are shown. Since the precursors have similar and in comparison, lower surface areas, the steady increase of the surface areas of the ZnO series calls for an explanation. First, the decreasing crystallite size leads to an increase in surface area per mass. Both, the increased defectiveness of the Ga:HZ and the crystallization of ZnO being hampered by the incorporation of Ga which can explain this decrease in crystallite size, which is supported by SEM analysis of the Ga doped ZnO (Figure 6.8). The aggregates of the ZnO decreased in size with increasing Ga content. Especially, for the ZnO doped with 15 % Ga, additional platelets on top of the typical ZnO structure were observed. Due to the typical shape for LDH crystallites and because of the observed side phase reflections of a zaccagnaite-like phase in PXRD, IR and Raman in the precursor characterization, this platelets are expected to be the zaccagnaite-like side phase. This is in alignment with the earlier reported study of Al doped ZnO.¹⁷²

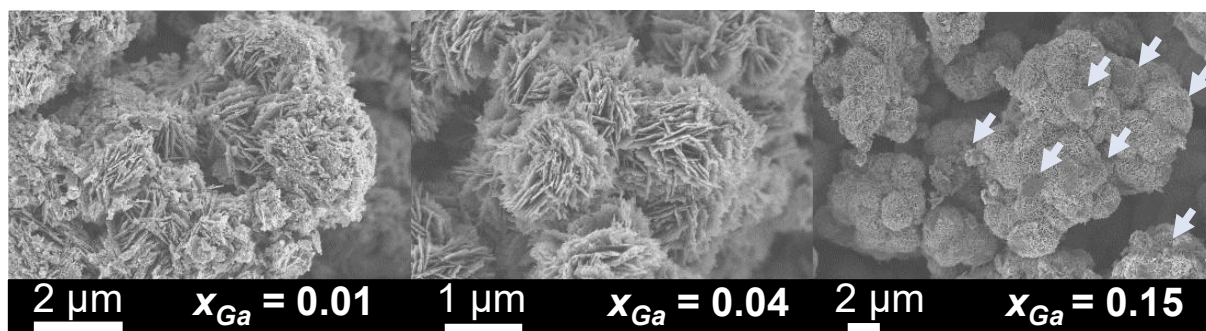


Figure 6.8: SEM micrographs of selected samples of the Ga doped ZnO. The arrows mark position of the additional platelets.

However, the natural BET surface increase of the undoped material, *e.g.*, from $11 \text{ m}^2\text{g}^{-1}$ to $31 \text{ m}^2\text{g}^{-1}$ for $x_{Ga} = 0$, is related to pore formation, which clearly can be seen in higher resolved SEM micrographs (SI, Figure SI 11.56). The further increase with increasing Ga content is then related to the smaller crystallite sizes and hence, smaller aggregates and due to the additional side phase. From the BJH analysis of the desorption isotherm an increase in small mesopores with increasing gallium content up to 4 % was found (compare SI Figure SI 11.53). Upon further increase of the gallium content, nanopores as well as larger mesopores were additionally determined.

The Raman spectra for the samples calcined at 320 °C are shown in Figure 6.9.

The Raman modes, which correspond to the ZnO lattice can be depicted from the undoped ZnO (Figure 6.9 for $x_{Ga} = 0$). The cationic lattice of the Zn ions are Raman active as E_2^{low} mode

(109 cm^{-1}), whereas the anionic oxygen lattice as E_2^{high} mode (434 cm^{-1}) Raman active is.^{38, 242, 243} At 329 cm^{-1} the mode is assigned to the difference of E_2^{high} and E_2^{low} ($E_2^{\text{high}} - E_2^{\text{low}}$) whereas the $2E_2^{\text{low}}$ mode, as an overtone of the E_2^{low} mode, at 205 cm^{-1} evolved.^{242, 243} The polar A_1^{TO} was assigned for a Raman shift of 381 cm^{-1} . The A_1 mode typically split into transversal optical (TO) and longitudinal optical (LO) modes.^{242, 243} For the undoped ZnO only the transversal optical mode was present. In comparison to the ZnO, the calcined zaccagnaite-like reference material didn't show clear Raman signals (SI, Figure SI 11.57).

A low Ga amount incorporated into the ZnO ($x_{\text{Ga}} = 0.01$) resulted in an increase of the E_2 modes, compared to the undoped ZnO. Contrarily to the E_2 mode, the clear signal of the A_1^{TO} mode vanished with Ga incorporation. Possibly, the signal of this mode is broadened and collapsed with the signal of the broadened E_2^{high} mode. The additional signal of the A_1^{LO} (568 cm^{-1}) and the $A_1^{\text{TA+LO}}$ (628 cm^{-1}) modes gives evidence for a broadening of the A_1^{TO} mode instead of their absence.

The broadening of the E_2^{high} mode shows, that the oxygen lattice is affected by the Ga incorporation. Especially for the Ga amount of $x_{\text{Ga}} > 0.06$ the E_2^{high} and $E_2^{\text{high}} - E_2^{\text{low}}$ modes broaden strongly and creates a broad halo for a gallium content of $x_{\text{Ga}} = 0.15$. This effect on the oxygen lattice gives evidence, that defects are present in the ZnO structure affected by the Ga incorporation.

The A_1 mode corresponds to lattice vibrations parallel to the c -axis,³⁸ and includes also polarization, which is in parallel to the c -axis for the longitudinal and perpendicular to the c -axis for the transversal mode²⁴⁴. In nanocrystalline material, the acoustic phonons beside the optical phonons can evolve.²⁴⁵ Therefore, additional overtones as the $A_1^{\text{TA+LO}}$ and $A_1^{\text{LA+TO}}$ mode are present.

The $A_1^{\text{LA+TO}}$ mode didn't show a clear peak but a broad signal for each ZnO, which increased with increasing Ga incorporation and collapsed almost with the $A_1^{\text{TA+LO}}$ overtone at $x_{\text{Ga}} = 0.15$. Contrarily, the $A_1^{\text{TA+LO}}$ overtone showed a clear signal and started to evolve from the lowest Ga doping ($x_{\text{Ga}} = 0.01$, 627 cm^{-1}). This overtone showed a clear blue shift with increasing Ga content ($x_{\text{Ga}} = 0.1$, 635 cm^{-1}). Because of the slightly higher weight of Ga compared to Zn,²²⁹ this blue shift gives evidence of the Ga incorporation into the ZnO structure. However, the effect of the Ga incorporation onto the mode perpendicular to the c -axis (A_1^{TO}) is hardly to evaluate due to the broadening of the E_2^{high} mode. Nonetheless, the mode parallel to the c -axis (A_1^{LO} , 573 cm^{-1}) evolved by Ga incorporation ($x_{\text{Ga}} = 0.01$) but broadened with increasing Ga content. An increased Ga content of 10 % - 15 % showed the strongest broadening of the A_1^{LO}

mode indicating, that the gallium incorporation caused defects, which affects the c -axis, as it was also shown in the PXRD analysis by the broadened 002 reflection. Interestingly, even for this high Ga content, the overtone $A_1^{\text{TO+LO}}$ became prominent, whereas for the lower Ga containing samples only an increased baseline was observed. The mode $A_1^{\text{TO+LO}}$ results of a propagation of an extraordinary phonon in an arbitrary directions, indicating isotropic properties.²⁴⁴ Compared to the lower Ga amounts, the isotropic effect became suddenly pronounced for $x_{\text{Ga}} = 0.1$ and $x_{\text{Ga}} = 0.15$ which may can be linked with the smaller aggregates, found for $x_{\text{Ga}} = 0.15$ in SEM analysis.

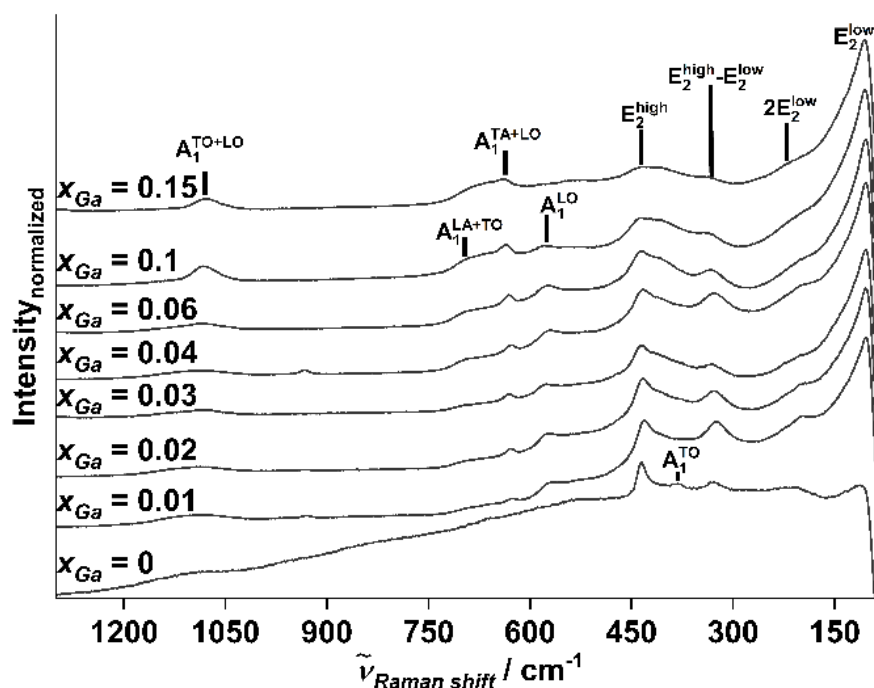


Figure 6.9: Raman spectra of the gallium doped zinc oxides. The modes are labelled with abbreviations for: Longitudinal optical mode (LO), transversal optical mode (TO), transversal acoustic mode (TA).

6.4.2.1 Gallium speciation in the doped zinc oxides

^{71}Ga MAS solid state NMR was performed for the gallium doped zinc oxides, to determine the coordination sites of the Ga ion incorporated into the ZnO (Figure 6.10). This method allows to determine and quantify the Ga incorporated onto a Zn position ($\text{Ga}_{\text{Zn}}^{\bullet}$) like it was already reported for aluminum doped zinc oxides.^{143, 172} From the ZnO:Al case, a sharp signal on a higher chemical shift for a four-fold coordinated (Ga^{IV}) would be expected, as a result of the highly symmetric environment of a gallium ion on a zinc position.^{143, 172} Due to the strong line broadening of the gallium NMR signal²³⁸, that sharp and intense signal cannot be observed. Nevertheless, all doped zinc oxides showed a signal in the region of Ga^{IV} (labelled as GaO_4). Comparing the case of the ZnO:Al, the signal around 200 ppm would be expected, to be a four-

fold coordinated Ga ion in ZnO but not on a Zn position of the lattice.^{143, 172} In case of Ga as dopant, both four-fold coordinated Ga-environments cannot be distinguished and therefore, no conclusion on the amount of Ga incorporated onto a Zn position can be drawn. However, the signal for the four-fold coordinated Ga increased in intensity with increasing gallium content but broadens at the same time. It is highly likely, that after saturation of the zinc position, more gallium was in a four-fold coordinated environment incorporated into the zinc lattice, which resulted in the signal broadening.

Nonetheless, for the samples with 10 % and 15 % gallium content additionally the five-fold ($\text{Ga}^{\text{V}}/\text{GaO}_5$) and six-fold coordinated gallium signal appears ($\text{Ga}^{\text{VI}}/\text{GaO}_6$). For this samples, a zaccagnaite-like side phase was determined in the precursor characterization. The characterization of the corresponding zinc oxides has shown, that the ZnO was phase pure but enriched by defects. Therefore, it can be assumed, that this additional chemical shifts are from the decomposed zaccagnaite-like side phase.

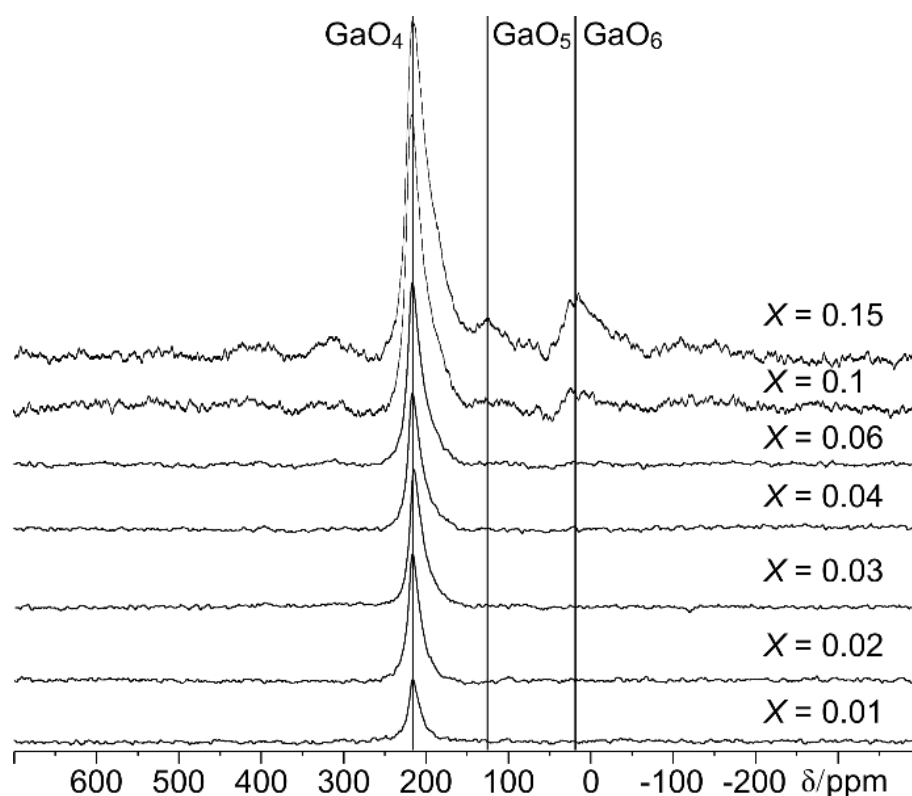


Figure 6.10: Stack plot of ^{71}Ga MAS NMR spectra of the gallium doped zinc oxides.

Additionally, XPS analysis showed an increased Ga:Zn ratio, for a higher doping than $x_{\text{Ga}} > 0.04$ (compare SI, Figure SI 11.59). For $x_{\text{Ga}} < 0.06$, the Ga:Zn ratio matched to the ratio determined by AAS, demonstrating, that a homogeneous Ga incorporation into the host structure was reached. Only the surface seems to be Ga enriched, which would be in alignment with the hypothesis of a surface near segregation of amorphous Ga_2O_3 or Al_2O_3 species¹⁷² after

calcination. However, the finding from XPS combined with the NMR spectroscopic results gives evidence, that an incorporation of more than 4 % Ga result in an increase of Ga coordination sites, different to the targeted Ga_{Zn}^{\bullet} doping site, so that a solubility limit around $x_{Ga} = 0.04$ is expected. Such undesired side phases, present in ZnO are expected to affect the opto-electronic properties of the material in a negative way.^{143, 172}

6.4.2.2 Opto-electronic properties

The optical band gap energies of the series are shown in Figure 6.11. Regarding a perfect substitution of a zinc site, the band gap of zinc oxide should not change drastically.¹³⁹ The band gaps determined at room temperature are in the range of 3.31 eV, which is in line with reported band gap energies.^{182, 184} From the values of the doping series, the band gap can be considered as equal up to 4 % gallium doped zinc oxide. For higher gallium contents, the band gap starts to increase. This increase can be explained by the *Burstein-Moss effect*, where the dopant occupies the lowest energy level of the conducting band, so that the excited electron has to reach a higher energy level, which results in an increased band gap.^{137, 138} The band gap of the oxide derived from the zaccagnaite-like material was determined to be 4 eV. Therefore, if this side phase increases during co-precipitation, the average band gap energy of the corresponding ZnO will increase. Regarding the doping quality it can be concluded, that up to 4 % (metal-based) gallium content the band gap was not affected and that possible band gap narrowing and widening effects are compensating. For a larger dopant concentration, the effects for band gap widening increase. This results support the findings from the NMR and XPS analysis, from which the solubility limit close to 4 % was expected (see above).

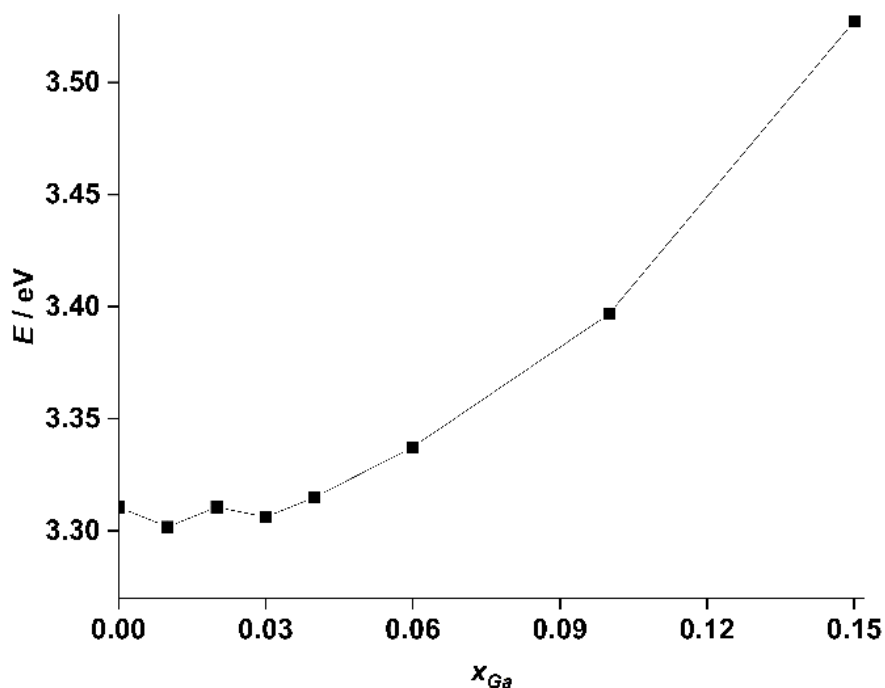


Figure 6.11: Band gap energies of the gallium doped zinc oxides. The line is to guide the eyes.

6.5 Conclusion

The co-precipitation allows to synthesize well defined precursors, which afterwards can be decomposed to zinc oxides. This approach has the advantage, that possible inhomogeneities are avoided by using a suitable precursor system in which the cations are dispersed by incorporation leading to a doped ZnO after controlled decomposition. In this investigation, from co-precipitated gallium doped hydrozincites, a zaccagnaite-like side phase was found by PXRD analysis for a gallium content above 6 % (metal-based). A careful analysis with infrared and Raman spectroscopy confirmed structural changes by induced defects and a distorted hydrozincite lattice, which can be induced for charge compensation. The calcination led to the decomposition of the precursor to a zinc oxide without any additional side phase determined by PXRD. The structural change because of the incorporated gallium ion was confirmed by the reflection broadening of the PXRD pattern and additionally by Raman spectroscopy. The chemical environment of the Ga ion was determined by ^{71}Ga NMR spectroscopy and has shown, that up to $x_{Ga} = 0.06$ no five-fold or six-fold coordinated Ga was present. Unfortunately, no clear conclusion on the Ga incorporated onto a Zn position in the ZnO lattice could be drawn, due to line broadening of the signals and the missing differentiation of the two expected signals for the four-fold coordinated Ga ion. Considering the line broadening and the XPS results a solubility limit for Ga incorporation into the ZnO structure around 4 % is expected. From UV-Vis spectroscopy, a band gap of around 3.3 eV was determined for the Ga:ZnO series up to $x_{Ga} = 0.04$, supporting a solubility limit around this concentration. A further increase in Ga

content resulted in an increased band gap, which can be explained either by a *Burstein-Moss effect* or by isolating effects of the decomposed Ga enriched zaccagnaite-like side phase present in samples for $x_{\text{Ga}} > 0.06$.

Supporting Information

Supporting Information are provided in chapter 11.8 (Supporting Information to "Phase evolution and solubility limit of gallium doping in zinc oxide catalyst supports synthesized via co-precipitated hydrozincite precursors") starting from page 259.

Acknowledgements

M.B. gratefully acknowledges the financial support from the Mercator Research Centre Ruhr (MERCUR, MERCUR, Pe-2018-0034). We also thank Dr. C. Szillus (Kiel University) for SEM analysis of the prepared materials and Prof. M. Epple and Robin Meya (University Duisburg-Essen) for elemental analysis as well as Dr. U. Schürmann for XPS analysis.

7 High-pressure pulsing of Ammonia results in Carbamate as strongly inhibiting Adsorbate of Methanol Synthesis over Cu/ZnO/Al₂O₃

Benjamin Mockenhaupt ^{**ab}, Philipp Schwiderowski ^{**c}, Jelena Jelic ^d, Felix Studt ^d, Martin Muhler ^{ce}, Malte Behrens ^{*ab}

- a. B. Mockenhaupt, M. Behrens, Institute of Inorganic Chemistry, University of Duisburg-Essen, Universitätsstr. 7, 45141 Essen (Germany), E-Mail: mbehrens@ac.uni-kiel.de.
- b. B. Mockenhaupt, M. Behrens, Institute of Inorganic Chemistry, Christian-Albrecht University of Kiel, Max-Eyth-Str. 2, 24118 Kiel (Germany).
- c. P. Schwiderowski, M. Muhler Laboratory of Industrial Chemistry, Ruhr-University Bochum, Universitätsstraße 150, 44780 Bochum (Germany), E-Mail: muhler@techem.rub.de.
- d. J. Jelic, F. Studt Institute of Catalysis Research and Technology, Karlsruhe Institute of Technology, 76344 Eggenstein-Leopoldshafen (Germany), E-Mail: felix.studt@kit.edu.
- e. M. Muhler Max Planck Institute for Chemical Energy Conversion (MPI CEC), 45470 Mülheim an der Ruhr (Germany).

******These authors contributed equally.

*****Corresponding author.

The article was published at the Journal of Physical Chemistry in February 2023. Benjamin Mockenhaupt, Philipp Schwiderowski, Jelena Jelic, Felix Studt, Martin Muhler, and Malte Behrens, High-pressure pulsing of Ammonia results in Carbamate as strongly inhibiting Adsorbate of Methanol Synthesis over Cu/ZnO/Al₂O₃, *The Journal of Physical Chemistry C* **2023** 127 (7), 3497-3505, DOI: 10.1021/acs.jpcc.2c08823.

Contribution of the authors

- B.M.: conceptualization, visualization, data curation, and writing—original draft preparation.
P.S.: conceptualization, visualization, data curation, and writing—original draft preparation.
J.J.: conceptualization, DFT calculations, and writing—reviewing and editing.
F.S.: conceptualization, funding acquisition, supervision, and writing—reviewing and editing.
M.M.: conceptualization, project administration, funding acquisition, validation, and writing—reviewing and editing.
M.B.: conceptualization, project administration, funding acquisition, validation, and writing—reviewing and editing.

ABSTRACT

The active site of the industrially used Cu/ZnO catalyst for the formation of methanol is controversially debated to date. Ammonia has been used as a probe molecule as it was found to inhibit methanol synthesis in CO₂-containing synthesis gas. Herein, we investigate the poisoning effect using an industrial-type Cu/ZnO/Al₂O₃ catalyst synthesized by co-precipitation. During steady-state methanol synthesis in a CO₂/CO/H₂ synthesis gas, isobaric trimethylamine (TMA) and ammonia injections poisoned methanol formation reversibly, with the poisoning of ammonia being significantly stronger than that of TMA. Based on DFT calculations, a mechanism of ammonia poisoning was derived: ammonia activation takes place on adsorbed oxygen or hydroxyl groups followed by the reaction with CO₂ forming a stable carbamate on the active site. Further hydrogenation of the carbamate to methylamine was calculated to exhibit high barriers, thus being rather slow, explaining why ammonia poisoning has a longer-term effect, as TMA cannot form a strongly bound carbamate species exclusively acting as weakly bound site-blocking species.

7.1 Introduction

The industrial methanol synthesis process currently received great attention again because of the promising potential in power-to-liquid concepts for the mitigation of greenhouse gas emissions and as an alternative to fossil energy carriers. Methanol is in particular interesting, because it can be used both in the fuel and the chemistry sectors.^{2, 51, 246-248}

Industrially, methanol is synthesized from syngas mixture containing CO, CO₂ and H₂ at pressures of 50 – 100 bar and temperatures of 200 – 300 °C over Cu/ZnO-based catalysts.¹ As in many industrial catalytic processes, the technological application of methanol synthesis has preceded the full understanding of the underlying chemistry, which has led to a vast amount of empirical knowledge that has been complemented by a growing fundamental and mechanistic insight in the last decades.^{1, 51} However, the exact detailed reaction mechanism, the nature of the active sites of high-performance catalysts, and the interplay of the catalyst's surface with the feed gas components are debated to this day.²⁶⁻²⁸ Among the most important open question is the dynamic effect of the so-called “Cu-Zn synergy” on the nature of the active site responsible for methanol formation.¹⁶ New experiments and calculations allow a more and more detailed understanding, which could be key to a knowledge-based adaption of the current industrial process for future power-to-methanol applications.

For example, the zinc coverage on the copper nanoparticle was interpreted as a surface alloy, which strongly affects the methanol synthesis activity of the catalyst and can be determined by chemisorption methods.^{112, 114} This behaviour may be due to an enhanced methanol formation route via zinc formate determined by spectroscopy with isotopic labelled carbon dioxide sources.²⁴⁹ Nevertheless, the change of the catalyst surface, and in particular the oxidation state of Zn, depends strongly on the redox potential of the gas phase. At rather oxidizing conditions (CO₂-rich) Cu/ZnO can be assumed, which changes via Cu-Zn^{δ+} to a Cu-Zn surface alloy for which ZnO acts as a Zn reservoir at reducing conditions (CO-rich).^{249 250} Hence, the catalyst is typically activated under strongly reducing conditions (H₂ in inert gas and 250 °C), and the Cu-Zn surface alloy and the activated Cu-Zn^{δ+} interface site are likely candidates for the active site in methanol formation from carbon dioxide.²⁵⁰ This surface alloy is found to co-exist with ZnO_x islands, and thus with Cu-Zn^{δ+} interface sites, after catalyst activation at temperatures in the range of 200 – 340 °C. At temperatures above 340 °C a bulk brass alloy is formed by continuous consumption of the zinc oxide species, which are in close contact with the copper particles.¹⁵⁴

Recently, a new experimental approach for surface characterization of working Cu/ZnO/Al₂O₃ catalysts has been presented. Laudenschleger *et al.*²⁹ introduced high-pressure pulses of ammonia (NH₃) as a new tool to probe the active site of an industrial Cu/ZnO/Al₂O₃ catalyst during methanol synthesis. This method complements the traditional *ex situ* chemisorption methods based on N₂O decomposition and hydrogen temperature-programmed desorption (H₂-TPD). These have already shown that depending on the catalyst composition and the used feed gas, a linear relationship between the copper surface area and the activity in methanol synthesis is observed. The contribution of partially reduced zinc oxide to the N₂O decomposition capacity, however, increases the complexity to accurately characterize the catalyst's surface,^{69, 99, 112} as the amount of reduced zinc oxide will depend on the pre-treatment conditions^{112 154} at low temperature and might not represent the working state of the catalyst.²⁵

Contrarily to these chemisorption methods, the new *operando* ammonia pulse experiments are conducted on the working catalyst and the first results confirmed the important role of Cu-Zn^{δ+} interface sites.²⁹ The upstream isobaric injection of ammonia leads to a sudden temporary poisoning of methanol formation. The linear increase of poisoning strength as a function of the CO₂ content in the synthesis gas and the absent poisoning of the parallel ethylene hydrogenation probe reaction as well as of the pure CO hydrogenation, which are both considered to take place on the unpromoted Cu⁰ sites, makes this method sensitive to the Zn^{δ+}-promoted CO₂ conversion sites on the Cu/ZnO catalyst.²⁹

Ammonia introduced as pulses was observed to be converted to trimethylamine (TMA). Here, we report experiments using a well-characterized highly active Cu/ZnO/Al₂O₃ methanol synthesis catalysts of academic origin. This is a reproduction of a benchmark catalyst whose synthesis history and structural properties are fully disclosed and thus allow for the establishment of structure-activity correlations. Furthermore, we combine the experimental data with density functional theory (DFT) to identify the reaction mechanism of the TMA formation and especially to uncover its active site, which leads to poisoning of methanol formation, thus being identical to the active site for CO₂ hydrogenation to methanol.

7.2 Experimental section

7.2.1 Catalyst synthesis and characterization

The investigated catalyst is an alumina-promoted copper/zinc oxide catalyst that was self-prepared from a coprecipitated precursor using a preparation recipe that was inspired by the established industrial synthesis. It is comprised of precursor co-precipitation, ageing in the mother liquor, recovery, calcination in air and finally reduction in a diluted hydrogen stream directly prior to the catalytic experiments. Its synthesis was a reproduction of the catalyst described earlier as Cu/ZnO:Al, which has been itself subject of several studies or has been used as benchmark catalyst for activity comparison and is here abbreviated CZA. In more details, the precursor of the investigated catalyst was synthesized via co-precipitation according to Schumann *et al.*⁵⁷. The precipitation was carried out in an automated stirred tank reactor (OptiMax, Mettler Toledo) from 1 M metal salt nitrate solution at a temperature of 65 °C. During the precipitation with 1.6 M sodium carbonate solution and using a dosing rate of 2.5 g min⁻¹ the pH was held constant at 6.5. Afterwards, the co-precipitate was aged in its mother liquid without further pH control. After the typical pH drop⁵⁷ had been observed, ageing was continued for 1 h. In a following procedure, the precursor was washed with deionized water 15 times to remove the sodium and nitrate ions followed by drying the precipitate in a heating chamber at 80 °C over night. The recovered powder was grinded and afterwards calcined at 350 °C for 3 h using a heating ramp of 2 °C min⁻¹ in a muffle furnace with static air. The calcination temperature deviates from the procedure described by Schumann *et al.*⁵⁷ and their catalyst denoted FHI-Std., for which 330 °C have been used. The increase of the calcination temperature by 20 °C was necessary for a more complete decomposition of the hydroxycarbonate precursor but may come at the cost of a slightly lower specific surface area due to stronger sintering (Table 7.1).

The metal composition was chosen as 68:29:3 in CZA. The co-precipitated precursor, the corresponding oxide and the reduced catalyst were characterized by the following methods.

Atomic absorption spectroscopy (AAS) was performed on a Thermo Fisher iCE-3500 AAS after dissolving the sample in nitric acid overnight. The nominal metal ratio was 68:29:3, and this close to the experimentally found values of 69(+/-1.5):29(+/-1.4):2(+/-0.003).

Powder X-ray diffractometry (XRD) patterns of the co-precipitated precursor, the calcined and pre-catalyst were recorded on a Bruker D8 ADVANCE in Bragg-Brentano geometry with a LYNXEYE XE-T detector using Cu K-alpha radiation. Phase analysis was performed using structural data from ICSD and COD databases.

Surface area analysis by nitrogen physisorption of precursors and calcined samples were determined by applying the Brunauer-Emmett-Teller (BET) equation to the N₂ adsorption data in the range of 0.07 to 0.3 of the pressure ratio measured at -196 °C. The sample was first degassed under vacuum at 80 °C for 2 h to remove any adsorbates. The determination of the pore sizes was done by applying the Barrett-Joyner-Halenda (BJH) method to the desorption isotherm. The measurement was carried out in a BET analysis set-up NOVA 3200e of Quantachrome and analysed with the NovaWin software.

Temperature programmed reduction (TPR) of 100 mg of a 250 - 355 µm sieve fraction was performed in a quartz glass U-shape tube reactor with an inner diameter of about 4 mm. As reducing atmosphere 4.6 % H₂ in Ar with a volume flow of 84.1 ml min⁻¹ at ambient pressure was used. Starting from room temperature the sample was heated up to 240 °C with a heating ramp of 1 °C min⁻¹. After reaching the target temperature, it was held for 30 minutes to ensure recording the complete reduction profile. The formed water during reduction was separated by a cooling trap to enable the analysis of the consumed H₂ via a thermal conductivity detector (Hydros 100).

N₂O reactive frontal chromatography (N₂O-RFC) was analysed in a similar reactor with the same mass loading and sieve fraction as used for TPR. Before recording the N₂O consumption the sample was reduced in a gas containing 2.1 % H₂ in He. To ensure a completely adsorbate-free surface the reduced sample was treated for 1 h at 220 °C in a He stream followed by cooling to room temperature. The N₂O decomposition experiment was performed with 1 % N₂O in He at room temperature and atmospheric pressure. The consumption of N₂O was determined by a calibrated quadrupole mass spectrometer (Balzer GAM 400). Calculating the metal surface areas and other quantities related to N₂O-RFC were performed according to DIN 66136-1.¹⁵⁰

7.2.2 Catalytic testing and ammonia pulse chemisorption

Activation: For the activation, the 200 mg of catalyst in the sieve fraction 255 - 350 μm were heated to 175 $^{\circ}\text{C}$ with a heating rate of 1 $^{\circ}\text{C min}^{-1}$ using a gas flow rate of 500 $\text{ml}_\text{N min}^{-1} \text{g}_{\text{cat}}^{-1}$ of 2 vol% H_2 in N_2 for 15 h. Then, the temperature was increased to 240 $^{\circ}\text{C}$ with 1 $^{\circ}\text{C min}^{-1}$ and held for 30 min.

Aging of the catalyst: To reach steady-state conditions in a relative short period of time, the corresponding catalyst sample was aged before performing the kinetic experiments. For an investigation of the initial activity the catalyst was run under kinetically controlled conditions in 13.5 vol% CO , 3.5 vol% CO_2 , 73.5 vol% H_2 and 9.5 vol% N_2 syngas with a volume flow of 666 $\text{ml}_\text{N min}^{-1} \text{g}_{\text{cat}}^{-1}$ at 210 $^{\circ}\text{C}$ and 60 bar for one week.

For the further aging process, the reaction temperature was set at 250 $^{\circ}\text{C}$ and the volume flow to the minimal possible value to reach equilibrium-controlled conditions to ensure a reproducible deactivation. By exposing the whole catalyst bed to high conversion conditions according to the study of *Fichtl et al.*²⁵¹, steady state was reached after another week.

High-pressure pulse experiments with NH_3 and TMA: Similar to the aging process as standard syngas mixture, the following composition was used: 13.5 vol% CO , 3.5 vol% CO_2 , 73.5 vol% H_2 and 9.5 vol% N_2 . The kinetically controlled measurements were performed in the differential region at 210 $^{\circ}\text{C}$ and 60 bar with a syngas flow of 666 $\text{ml}_\text{N min}^{-1} \text{g}_{\text{Catalyst}}^{-1}$. A constant volume of 1 ml N_2 containing various mole fractions from 0 to 2000 ppm of NH_3 and TMA were injected into the upstream synthesis gas as isobaric pulses.

7.2.3 Density Functional Theory (DFT) calculations

Density Functional Theory (DFT) calculations were performed using the Vienna Ab Initio Simulation Package (VASP)^{161, 162, 252, 253} in connection with the Atomic Simulation Environment (ASE).^{254, 255} The Bayesian Error Estimation Functional with van der Waals correlations (BEEF-vdW)¹⁶³ with the projector augmented wave method (PAW)^{164, 165} and a plane-wave basis set with a cutoff energy of 450 eV were used. The choice of the BEEF-vdW functional is motivated by its performance with respect to adsorption energies^{256, 257} and transition states²⁵⁸ on transition metal surfaces, and in particular by its successful description of surface processes related to CO_2 hydrogenation to methanol.^{16, 259}

Infinite slab models for the Cu 211 termination consist of four layer-thick 3×3 super-cells, separated by more than 16 \AA in the z direction. Zinc containing alloys were constructed by substitution of Cu with Zn atoms along the Cu 211 edge (denoted ZnCu 211). The bottom two

layers were kept fixed and the upper 2 layers were allowed to relax during geometry optimizations. The Brillouin zone was sampled using a 5×4×1 Monkhorst–Pack k-point grid³⁸ for both, Cu 211 and ZnCu 211. The convergence criterion for the geometry optimizations was a maximum force of 0.01 eV/Å. Transition states are obtained using constrained optimizations. All transition states were verified to contain a single imaginary harmonic frequency corresponding to the transition vector of the reaction. All adsorption energies were corrected by zero-point energy (ZPE) contributions. Entropic contributions to the free energy were calculated within the harmonic approximation for adsorbates, entropic contributions for gas-phase species were obtained from tabulated values (see SI for all data). All optimized structures of adsorbates and transition states are given in the SI of the published work.

7.3 Results and discussion

7.3.1 Catalyst characterization

The composition (Figure SI 11.60, Table SI 11.21), the XRD pattern of the precursor (Figure SI 11.61) and of the calcined form (Figure SI 11.62), the N₂ adsorption isotherms (Figure SI 11.63, Table SI 11.22), the TPR curve (Figure SI 11.64 a)) and the N₂O-RFC profile (Figure SI 11.64 b)) of the CZA catalyst are presented as supporting information. In agreement with previous results, XRD confirmed that the precursor of the catalyst mainly crystallized in a malachite structure (Figure SI 11.61) and that the typical by-phase³⁴ of Al-rich hydrotalcite is hardly observed but cannot be completely ruled out based on the powder patterns. The shift of the 20 $\bar{1}$ peak correspond to a d-spacing of 2.754 Å and is in line to the results obtained by Schumann *et al.*⁵⁷. This value indicates a proper substitution of Cu²⁺ by Zn²⁺ and Al³⁺ cations. The calcination at 350 °C for 3 h resulted in the transformation to a poorly crystalline metal oxide mixture and only a small crystalline residue of the malachite precursor phase was still present (Figure SI 11.62). The broad peak at $2\theta \approx 35^\circ$ indicates a nanostructured CuO – ZnO composite as expected for industrial-type catalyst synthesis.⁵⁷ The TPR experiment in 5 % H₂ showed that the reduction of CuO to Cu⁰ reached a maximum rate at 170 °C and was complete at 200 °C (Figure SI 11.64 a)). Relating the amount of Cu determined by AAS with the amount of consumed H₂, the degree of reduction was determined to be 100 % after the TPR experiment. After reduction, metallic Cu⁰ and nanostructured ZnO were identified by XRD analysis (Figure SI 11.64 c)). According to a simple Scherrer analysis of the Cu 111 reflection, the crystallite size of metallic copper was determined to amount to 7 nm, which is around 3 nm larger compared with Schumann *et al.*⁵⁷ which may be due to the slightly harsher calcination

conditions resulting in larger CuO crystallites. The reduced catalyst was also characterized by N₂O-RFC (Figure SI 11.64 b)) resulting in a specific Cu metal surface area of 27 m² g⁻¹ (Table 7.1). In relation to the BET surface of the oxide (93 m² g⁻¹), this value is almost one third of the previous oxide surface area. The N₂O-RFC results of a Cu/ZnO catalysts, however, must be interpreted carefully. Fichtl *et al.*⁶⁹ demonstrated that partially reduced ZnO_{1-x} (*e.g.*, oxygen vacancies) in a Zn-containing catalyst does react with N₂O.⁶⁹ Partial reduction of ZnO that contributes to the N₂O chemisorption capacity was also reported by Kuld *et al.*¹¹². Therefore, Cu surface area and the Cu dispersion may be over-estimated and the crystallite size underestimated by N₂O data. This discussion is of high relevance when comparing different catalysts, but in this study on a single catalyst material, we refrain from a further interpretation of the N₂O RFC data showing values that are in the range previously reported for industrial catalysts.^{69,99}

Table 7.1 summarizes key properties of the synthesized catalyst and compares them with data reported for the original commercial catalyst used by Laudenschleger *et al.*²⁹ and to the original report of the reproduced benchmark catalyst synthesis by Schumann *et al.*⁵⁷ The comparison shows that the synthesized catalyst represents very well the expected properties of the commercial CZA. The here reported reproduction of the benchmark synthesis thus resulted in a similar catalyst with only slightly lower values in specific surface area of the calcined pre-catalyst and N₂O-chemisorption capacity of the reduced catalyst. This could be caused by enhanced CuO sintering during calcination.

7 High-pressure pulsing of Ammonia results in Carbamate as strongly inhibiting Adsorbate of Methanol Synthesis over Cu/ZnO/Al₂O₃

Table 7.1: Characterization of the self-prepared CZA (Cu/ZnO:Al) catalyst in comparison to the published commercial CZA and FHI-Std. benchmark catalyst. The BET surface area (A_{BET}) was measured by N₂ physisorption. a) The Cu surface area (A_{Cu}) and the -dispersion (D_{Cu}) are calculated from the N₂O-RFC method. b) The Cu crystallite size (d_{Cu}) was determined by applying the Scherrer equation to the Cu 111 reflection and by Rietveld refinement for the FHI-Std. catalyst.⁵⁷ The temperature with the maximum hydrogen consumption rate ($T_{max, Reduction}$) was determined from the TPR profile with a heating rate of 1 °C min⁻¹(CZA) and 6 °C min⁻¹ (FHI-Std.⁵⁷).

Catalyst property	CZA (Cu/ZnO:Al) of this study	Commercial CZA reported by Laudenschleger et al. ²⁹	FHI-Std. reported by Schumann et al. ⁵⁷
A_{BET} $m^2 g^{-1}$	93	NA	118
$A_{Cu}^{a)}$ $m^2 g^{-1}$	27	28	38
$D_{Cu}^{a)}$ %	18	NA	8
$d_{Cu}^{b)}$ nm	7	NA	4.47
$T_{max, Reduction}$ °C	170	170	211

7.3.2 Catalytic performance in methanol synthesis

Methanol synthesis was conducted over the above-described catalysts at 210 °C and 60 bar in a feed composed of 13.5 % CO / 3.5 % CO₂ / 73.5 % H₂ / 9.5 % N₂. To ensure that the catalyst is stable in conversion on the time scale of the pulse experimentations, it was operated for more than 100 h under these conditions right after activation. The investigated catalyst lost about 20 % activity after reaching the first maximum methanol formation rate (Figure 7.1). After that drastic loss the deactivation of CZA decelerated and stabilized at around 70 % of its original activity. Such an initial activity drop is typical for Cu-based methanol synthesis catalysts in the first 50 h time on stream.^{30, 260} Within this time frame the catalyst may lose up to 60 % of its origin activity.²⁶¹ The main reason is thermally induced Cu particle sintering which can be enhanced if the ZnO spacer additionally is consumed by *in situ* formation of ZnAl₂O₄ or Zn-OH species due to water formation in CO₂-containing synthesis gas.^{59, 251, 260} The observed deactivation of the CZA catalyst was stronger in the first 20 h than expected from a similar catalyst and similar ageing reported by Fichtl *et al.*³⁰ resulting in a higher rate constant (k) and order (m) of the deactivation rate (Figure 1). In contrast to the compared deactivation kinetics (Figure 1, power-law fit according to Fichtl *et al.*³⁰) the CZA catalyst stabilized its productivity faster at a methanol formation rate of about 336 $\mu\text{mol g}^{-1} \text{min}^{-1}$, which is in line with previously reported activity data of about 350 $\mu\text{mol g}^{-1} \text{min}^{-1}$ of a similar catalyst at similar reaction conditions.¹⁶

After about 130 h time-on-stream the catalyst was further aged for one more week at 250 °C with a lower flow rate of 26 ml_N min⁻¹ under equilibrium-controlled conditions analogous to Fichtl *et al.*³⁰. This treatment resulted in a sufficiently stable performance over the time period of the pulsing experiments.

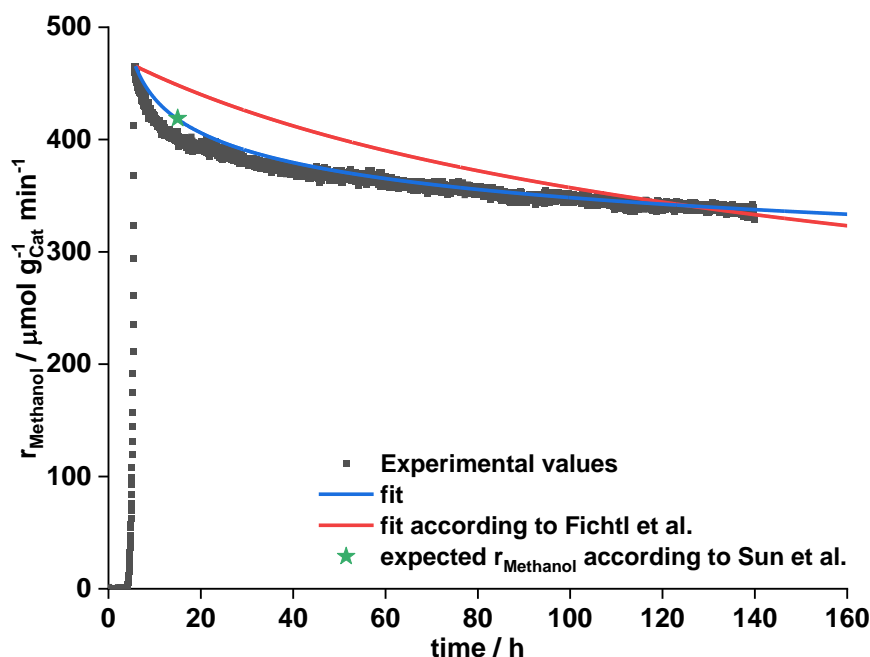


Figure 7.1: Ageing of CZA in a mixed synthesis gas containing CO/CO₂/H₂ under differential reaction conditions. The volume flow was set to 666 ml min⁻¹ g_{Catalyst}⁻¹ at 60 bar and 210 °C. This procedure was chosen to age the catalyst in the first week while investigating in parallel the initial thermal deactivation under kinetically controlled reaction conditions. The deactivation values were estimated by fitting a power law to the methanol formation rate according to Fichtl et al.³⁰. The parameters obtained by Fichtl et al.³⁰ were determined with a similar CZA catalyst at similar reaction conditions (220 °C, 60 bar, 1.39 vol% CO, 3.60 vol% CO₂, 62.68 vol% H₂, WHSV = 0.51 h⁻¹).³⁰ The point marked with an asterisk was calculated by the deactivation data reported by Sun et al.⁵⁹ for a similar catalyst and synthesis gas (60 % Cu/28 % Zn/11 % Al; CO₂/(CO+CO₂) = 0.8). The kinetic parameter are listed in the SI in Table SI 11.23.

7.3.3 High pressure pulse experiments

After reaching steady-state conversion, the experiments of Laudenschleger *et al.*²⁹ were reproduced using the CZA catalyst. In Figure 7.2 the results of the temporary poisoning by NH₃ are shown using a CO/CO₂/H₂ synthesis gas at 60 bar and 210 °C. The isobaric injection of 1 ml pure N₂ results only in a sharp negative dilution peak in the methanol content of the off-gas (see Figure 7.2, 0 ppm NH₃). The original methanol amount is recovered immediately. Also, the NH₃-containing pulses cause the methanol content first to decrease to the same lowest level as in the dilution peak due to the same volume which was injected into the upstream gas (Figure 7.2, *e.g.*, 500 ppm NH₃). However, compared with the dilution effect, reacting probe molecules like NH₃ have an additional effect on the regeneration time, which strongly increases with increasing amount of pulsed NH₃ (Figure 7.2, 500 ppm NH₃ vs. 2000 ppm NH₃).

This behaviour demonstrates a temporary reversible poisoning of the active sites. Since it is known^{29, 261} that ammonia is converted in a stepwise manner under these conditions to monomethylamine (MMA), dimethylamine (DMA) and finally to trimethylamine (TMA), the decelerated formation of methanol can have two contributions: competitive adsorption on the active surface and/or competition of the C₁ intermediates ending up in methylamine and not in methanol. To estimate these contributions, the same experiment can be performed pulsing TMA instead of NH₃.²⁹ The decrease in methanol during the injections of different amounts of TMA confirms that this molecule also acts as a reversible poison (Figure 7.3). As no further methylation is possible in case of TMA, this effect is clearly caused by the reversible adsorption of TMA on the methanol-forming active sites, as it was also previously described by Laudenschleger *et al.*²⁹. This is supported by the TMA profile that was recorded during the pulsing, which inversely resembles the methanol profile when the dilution peak is subtracted. Adsorption, however, is weak enough for TMA to desorb again relatively fast. Thus, the methanol mole fraction is recovered quite fast compared with the same amount of pulsed NH₃. In case of pulsing 2000 ppm TMA (Figure 7.3, 2000 ppm TMA) the original methanol formation rate is reached again after about 25 minutes. For the same amount of NH₃ (Figure 7.2, 2000 ppm NH₃), the completely recovered methanol content was reached after about 50 minutes.

We thus conclude in agreement with previous reports that NH₃ has an additional poisoning effect, namely the scavenging of C₁ surface species that are precursors to methanol. It is assumed that NH₃ reacts with an intermediate of methanol synthesis to form TMA.²⁹ However, this would lead to a stoichiometric consumption of methanol and does not explain the retarded recovery of the origin methanol formation rate. The most likely reason is that the adsorption of NH₃ or any intermediate in the reaction pathway to TMA is much stronger than the adsorption of TMA itself.

Interestingly, in the same experiment, but using a CO₂-free syngas feed consisting of CO and H₂, neither a poisoning effect of NH₃ nor a conversion of this probe molecule to TMA was observed suggesting that rather reactant-like early intermediates in the CO₂ hydrogenation reaction are selectively reacting with NH₃. Regarding the proposed reaction mechanism of CO₂ to methanol,^{16, 51, 262, 263} formate species are possible candidates for this reaction. Therefore, density functional theory (DFT) calculations were conducted to study the hypothesis of a reaction between adsorbed NH₃ and surface formate species and their impact on methanol synthesis.

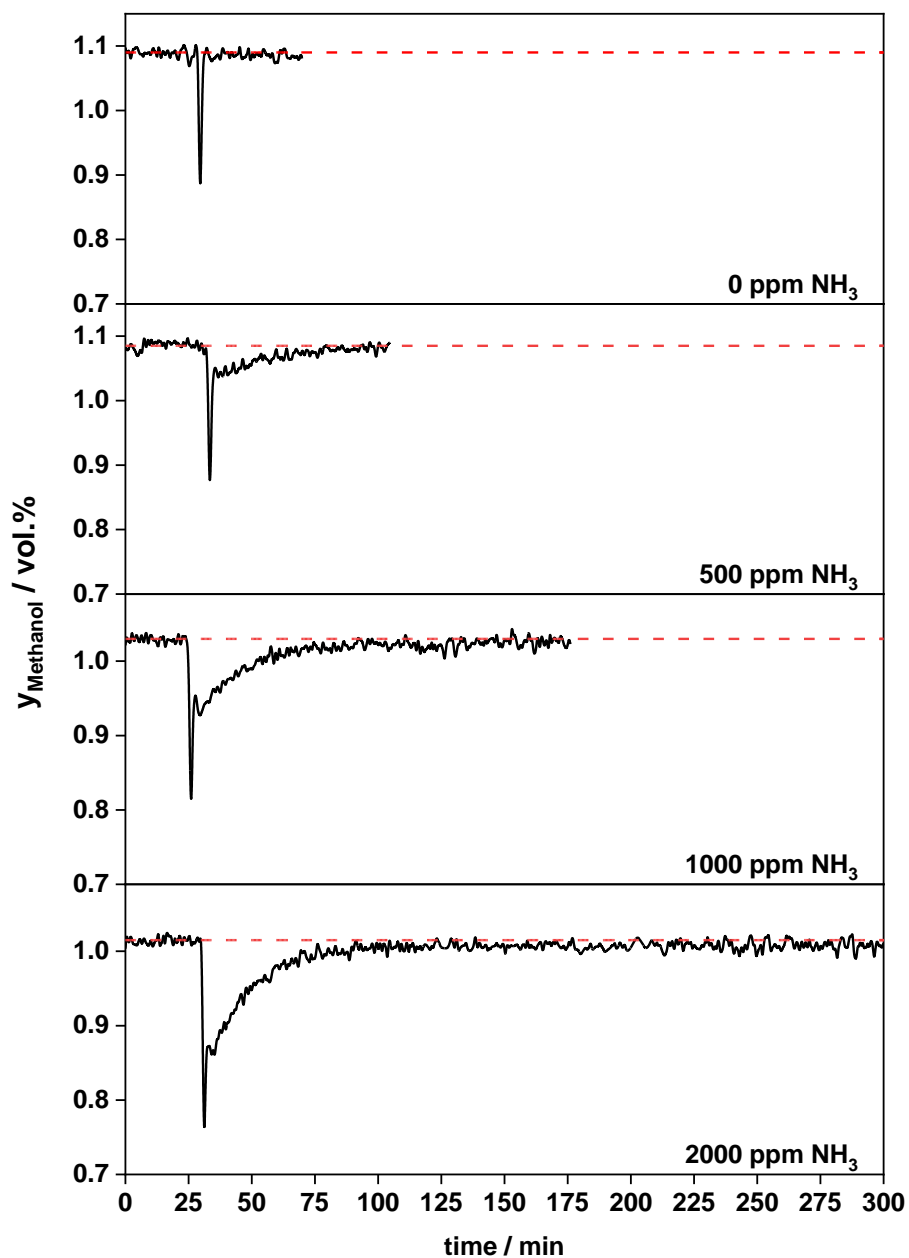


Figure 7.2: Methanol formation poisoned by injecting 1 ml N₂ containing different amounts of NH₃ into the inlet gas during methanol synthesis in 13.5 vol% CO / 3.5 vol% CO₂ / 73.5 vol% H₂ / 9.5 vol% N₂ using 200 mg (sieve fraction 255 – 300 μm) of the CZA catalyst at 60 bar and 210 °C. To demonstrate the dilution effect only 1 ml pure nitrogen was injected into the inlet gas stream (0 ppm NH₃).

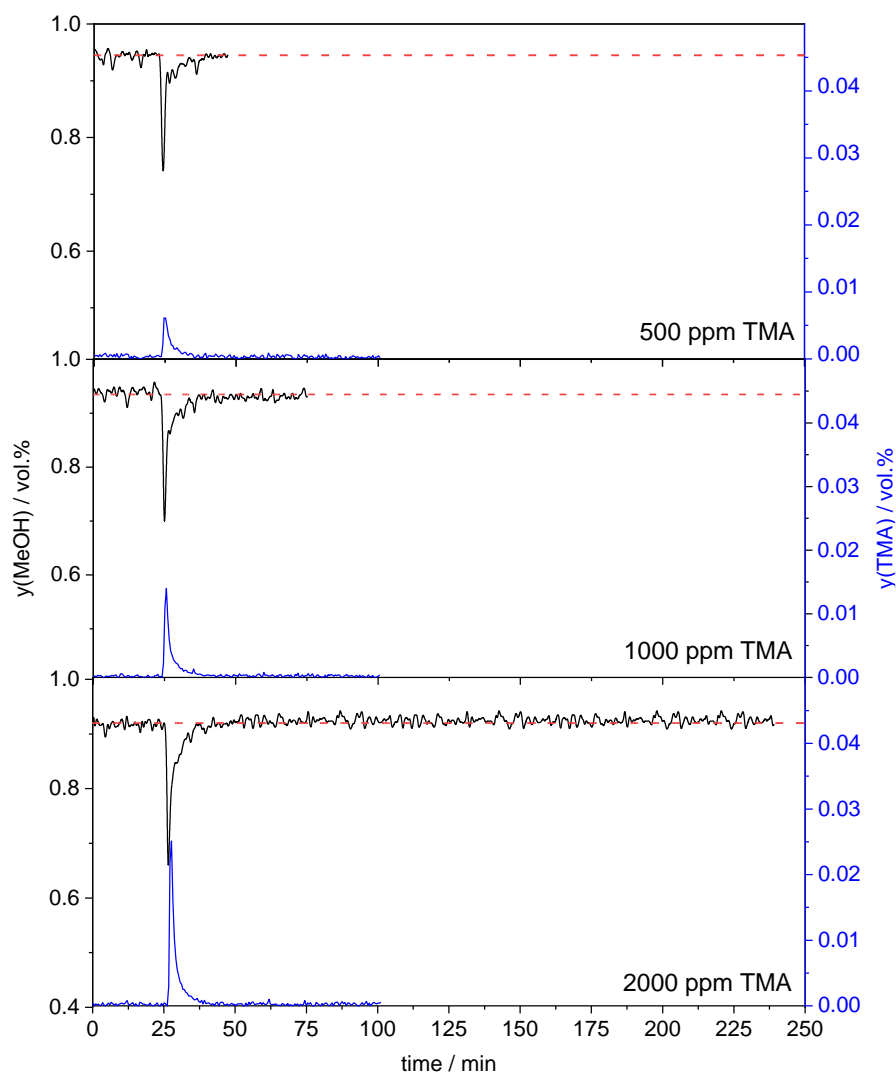


Figure 7.3: Methanol formation poisoned by injecting 1 ml N₂ containing different amounts of TMA into the inlet gas during methanol synthesis in 13.5 vol% CO / 3.5 vol% CO₂ / 73.5 vol% H₂ / 9.5 vol% N₂ using 200 mg (sieve fraction 255 – 300 μm) of the CZA catalyst at 60 bar and 210 °C. The methanol content determined by the downstream analytics is illustrated as the upper curve (black, in each graph) and the measured TMA concentration in blue (lower curve in each graph).

7.3.3.1 DFT calculations

In order to shed light on the influence of NH₃ and possible reaction intermediates formed during CO₂ hydrogenation, we turned to DFT calculations using two structural models of the active site that have been introduced in earlier work.¹⁶ Since undercoordinated sites have been shown to play an important role in methanol synthesis,²² stepped Cu surfaces are used to represent the active sites. Zn alloying into the Cu step has also been suggested as a plausible model representing the Cu-ZnO_x synergy.¹⁶ Our two models (see Figure 7.4) are thus a stepped Cu

211 surface and a fully Zn-decorated Cu 211 step, denoted Cu 211 and ZnCu 211, respectively. We start by investigating the adsorption and activation of NH₃ on these surfaces. Figure 7.4 shows the free energy diagram of NH₃ adsorption and activation at 500 K. As shown in Figure 7.4 a), adsorption of NH₃ is endothermic at these conditions on both surfaces ($\Delta G^{500K} = 0.24$ eV on Cu 211 and 0.30 eV on ZnCu 211). Activation of NH₃ on these surfaces to produce chemisorbed NH₂* and H* is also slightly endothermic and accompanied by a rather high reaction barrier (1.91 eV for Cu 211 and 1.84 eV for ZnCu 211). These results indicate that copper as well as Zn-modified Cu surfaces are incapable of activating NH₃ at low temperatures of 500K, in line with the known fact that Cu is not a good NH₃ decomposition catalyst.²⁶⁴ During methanol synthesis, conversion of CO₂ to methanol produces surface oxygen, that is subsequently hydrogenated forming H₂O.^{13, 99} We investigated the effect of surface oxygen species (O* and OH*) on the activation of NH₃. As can be seen in Figure 7.4, the presence of O* (see Figure 7.4 b)) and to a similar degree OH* (see Figure 7.4 c)) lower the activation barrier of NH₃ dissociation substantially and also make the reaction step downhill in energy. The reaction barrier for surface oxygen activated step is 0.71 eV and 0.91 eV for Cu 211 and ZnCu 211, respectively. We thus speculate that activation of NH₃ is only possible if oxygen or hydroxyl groups are present on the Cu or Zn-Cu surfaces. This also explains why we do not observe the poisoning effect of NH₃ in dry CO/H₂-containing syngas, as this does not produce any surface oxygen species. The experimentally observed effect of poisoning of TMA is initially like that of NH₃, but only in the short term (see experimental observations, Figure 7.3). Our calculated values for the adsorption free energy of TMA is $\Delta G^{500K} = 0.21$ eV and 0.3 eV on Cu 211 and ZnCu 211, respectively. The adsorption energy of MMA and DMA are also in the same range. All adsorption energies are summarized in Table 2. As is obvious from the calculated interactions, adsorption of these molecules proceeds mostly through physisorption. There should not be large influences when going from NH₃ to TMA judged from the adsorption energies of the various ammonia derivatives. Experimentally, however, TMA has a less strong poisoning effect than ammonia. In addition, the adsorption free energies are positive, hinting at a very weak poisoning effect, in contrast to the experimental observation.

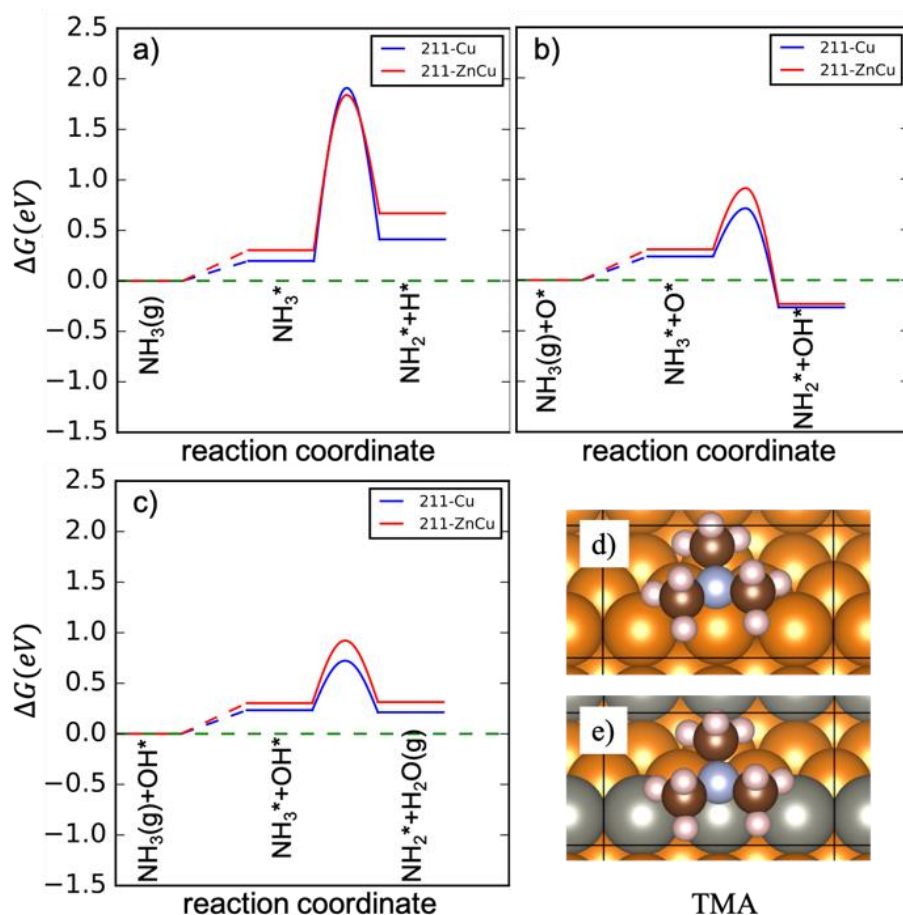


Figure 7.4: Gibbs free energy diagrams: a) NH_3 activation b) oxygen-assisted NH_3 activation, c) OH-assisted NH_3 activation, over Cu 211 and ZnCu 211 at $T = 500$ K, $p_{\text{NH}_3} = 0.05$ bar, $p_{\text{CO}_2} = 2.1$ bar, $p_{\text{H}_2} = 44$ bar, d) TMA adsorption geometry on Cu 211 with 0.21 eV binding energy and e) TMA adsorption geometry on ZnCu 211 with 0.3 eV binding energy.

Table 7.2: Calculated adsorption energies of NH_3 , MMA, DMA and TMA on Cu 211 and ZnCu 211 surfaces. All energies are ZPE corrected and in eV. Entropic contributions to the free energy are given in the SI.

ΔH adsorption eV	NH_3	MMA	DMA	TMA
Cu 211	-0.63	-0.78	-0.79	-0.75
ZnCu 211	-0.57	-0.69	-0.74	-0.70

We therefore investigated the pathway after ammonia activation with oxygen forming MMA on the surface. Figure 7.5 depicts the free energy diagram of the reaction of NH_3 and CO_2 starting with an oxygen-covered surface for both Cu 211 and ZnCu 211. Interestingly, we identified the reaction of CO_2 and NH_2^* to $\text{NH}_2\text{-COO}^*$ (carbamate) of being both

7 High-pressure pulsing of Ammonia results in Carbamate as strongly inhibiting Adsorbate of Methanol Synthesis over Cu/ZnO/Al₂O₃

mechanistically feasible (reaction barriers of 0.82 and 1.03 eV, for Cu 211 and ZnCu 211, respectively) and downhill in energy. In fact, the chemisorption of carbamate is the lowest energy point in the reaction mechanism, being -0.50 eV (Cu 211) and -0.46 eV (ZnCu 211). Further reaction of carbamate through hydrogenation proceeds via NH₂-COOH* and NH₂-CHO* with relatively high barriers. Carbamate is thus formed fast, but hydrogenated slowly, eventually resulting in a high coverage of carbamate on the surfaces that is only reduced slowly once NH₃ is taken out of the feed. This interpretation is supported by the experimentally observed slow recovery of the origin methanol activity after NH₃ pulses in comparison to the fast activity recovery after TMA pulses (compare Figure 7.2 and Figure 7.3). The reported simultaneous hydrogenation of ethylene and CO₂ in synthesis gas was not limited by activated hydrogen.²⁹ Contrarily, during NH₃ poisoning, ethylene hydrogenation was unaffected whereas methanol formation was poisoned but not completely stopped.²⁹ This observation indicates that hydrogen was activated rapidly and that dissociative hydrogen chemisorption can be excluded as a rate-determining step.

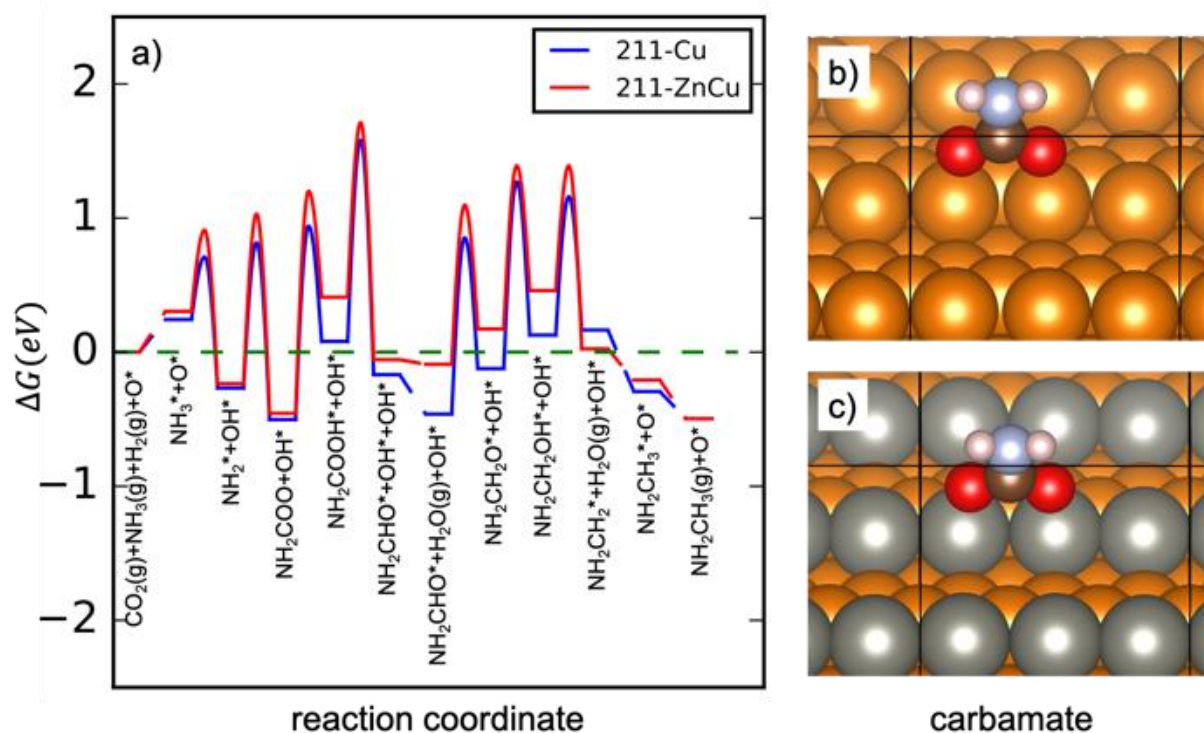


Figure 7.5: a) Calculated Gibbs free energy diagram for the NH₃ methylation over Cu 211 and ZnCu 211 in the presence of surface oxygen at $T = 500$ K, $p_{\text{NH}_3} = 0.05$ bar, $p_{\text{CO}_2} = 2.1$ bar, $p_{\text{H}_2} = 44$ bar, b) carbamate at Cu 211 edge, c) carbamate at ZnCu 211 edge.

This mechanism can explain the strong poisoning effect of ammonia, as carbamate blocks the active site on which formate would be hydrogenated to methanol. Since TMA cannot form a carbamate-like intermediate, the above-described poisoning mechanism cannot be present in

agreement with our experimental observation that TMA poisoning is much shorter lived, which we ascribe to simple physisorption without the formation of intermediates.

7.4 Conclusion

A combined experimental and theoretical study of the poisoning effect of NH₃ during the conversion of syngas (CO₂/CO/H₂) to methanol over an industrial-type Cu/ZnO:Al catalyst is presented. This catalyst was prepared via co-precipitation and represented in its characteristics an industrial methanol synthesis catalyst. The poisoning effect during methanol synthesis from a CO₂-containing feed gas reported earlier was reproduced and the interpretation of the experimental results was supported by DFT calculations to identify the stronger poison effect of NH₃ compared with trimethylamine. Extensive DFT calculations on two active site models representative of Cu and Cu/ZnO catalysts were performed proposing adsorbed carbamate (H₂N-CO_{2,ads}) as a possible intermediate blocking the active sites. This investigation shows that carbamate can form readily from the reaction of NH₂* and CO₂ but is a stable species that undergoes further hydrogenation rather slowly, explaining its strongly poisoning effect. Importantly, NH₂* can only be formed in the presence of surface oxygen species, such that this effect is not observed for pure CO feeds. TMA as well as NH₃ and the other methylamines do not bind strongly to the surface according to the calculated adsorption energies. Hence, TMA is not as poisonous as ammonia, because it cannot form a strongly bound carbamate species.

Supporting Information

Supporting Information for this article can be found under DOI: 10.1021/acs.jpcc.2c08823 or in chapter 11.9 (Supporting Information to "High-pressure pulsing of Ammonia results in Carbamate as strongly inhibiting Adsorbate of Methanol Synthesis over Cu/ZnO/Al₂O₃") starting from page 269.

Acknowledgements

We gratefully acknowledge Deutsche Forschungsgemeinschaft (DFG, German Research Foundation) for funding through the priority program SPP 2080 "Catalysts and reactors under dynamic conditions for energy storage and conversion" (project numbers 406903668, 406483183/ZO 369/2-1), the German Federal Ministry of Education and Research (Bundesministerium für Bildung und Forschung, BMBF, Verbundvorhaben Carbon2Chem, L-2: MeOH Synthese, FKZ:03EW0006E) and the state of Baden-Württemberg for bwHPC (bwUniCluster and JUSTUS, RV bw17D01). A great thanks to Gereon Behrendt for the catalyst synthesis.

8 Cu-Co/ZnAl₂O₄ catalysts for CO conversion to higher alcohols synthesized from co-precipitated hydrotalcite precursors

Benjamin Mockenhaupt^{ad}, Fatih Özcan^b, Remco Dalebout^c, Sebastian Mangelsen^d, Thomas Machowski^a, Petra E. de Jongh^c, Malte Behrens^{ad}

- a. B. Mockenhaupt, Prof. Dr. M. Behrens, Institute of Inorganic Chemistry, University of Duisburg-Essen Universitätsstr. 7, 45141 Essen (Germany), E-mail: mbehrens@ac.uni-kiel.de.
- b. F. Özcan, Institute for Combustion and Gas Dynamics, NanoEnergieTechnikZentrum (NETZ), Carl-Benz-Straße 199, D-47057 Duisburg (Germany).
- c. R. Dalebout, Prof. Dr. Petrah de Jongh, Institute of inorganic chemistry and catalysis, Utrecht University, Universiteitsweg 99, NL-3584 CG Utrecht (Netherlands), E-mail: P.E.deJongh@uu.nl.
- d. B. Mockenhaupt, Dr. S. Mangelsen, Prof. Dr. M. Behrens, Institute of Inorganic Chemistry, Christian-Albrecht University of Kiel, Max-Eyth-Str. 2, 24118 Kiel (Germany).

The article was published at *Chemie Ingenieur Technik* in October 2022.

Mockenhaupt, B., Özcan, F., Dalebout, R., Mangelsen, S., Machowski, T., de Jongh, P.E. and Behrens, M., Cu-Co/ZnAl₂O₄ Catalysts for CO Conversion to Higher Alcohols Synthesized from Co-Precipitated Hydrotalcite Precursors, *Chemie Ingenieur Technik*, **2022** 94, 1784-1797, DOI: 10.1002/cite.202200171.

Contribution of the authors

B.M.: planning catalytic tests, visualization, data curation, original draft preparation.

F.Ö.: Catalyst preparation, planning of the catalytic tests.

R.D.: Planning and Performance of the catalytic tests.

S.M.: XRD analysis, Rietveld refinement, manuscript editing.

T.M.: Catalyst preparation and characterization.

P.E.d.J.: Advising support, manuscript editing.

M.B.: Advising support, manuscript editing.

All co-authors have contributed to data analysis and discussion.

Abstract

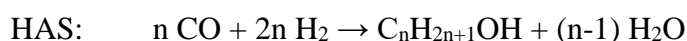
The role of Cu:Co composition in co-precipitated bi-metallic Cu-Co/ZnAl₂O₄ catalysts on higher alcohol synthesis (HAS) was investigated at H₂:CO=4. The addition of Cu strongly facilitated Co reduction upon catalyst activation and suppressed coke deposition during HAS. Formation of predominantly hydrocarbons and higher alcohols was observed on the bi-metallic catalysts. Co/ZnAl₂O₄ produced mainly CH₄ and Cu/ZnAl₂O₄ mainly CH₃OH, while at Cu:Co = 0.6 the best ethanol selectivity of 4.5 % was reached. The microstructure of the spent catalysts confirmed a close interaction of Cu and Co.

8.1 Introduction

Fischer-Tropsch synthesis (FTS) is an established process technology, based on reformed natural gas, with a high potential towards the reduction of the CO₂ footprint if biogas or CO₂-reforming of natural gas are used as sources of synthesis gas^{71,265}. Advantages of this process lie in the possibility to tune the octane/cetane number of combustion fuels and to synthesize higher alcohols⁷².

The FTS can be distinguished into the high temperature (300 °C – 350 °C @ ~30 bar) and the low-temperature processes (200 °C – 250 °C @ ~30 bar)⁷⁴⁻⁷⁶. For the low-temperature process Co-based catalysts are typically used, yielding long-chain hydrocarbons, which enables a further product upgrade by a cracking process.^{53,74} In Methane and carbon dioxide, formed by the consecutive water-gas shift reaction, are low-value products and therefore undesired in the FTS process^{74,76}. In addition to synthetic fuel production, the higher alcohol synthesis (HAS) has received increasing attention, because such alcohols can be used as feedstock chemicals for several applications in the chemical industry²⁶⁶.

Iron, cobalt and ruthenium are typical FTS-active metals. Because of the high price for ruthenium and the kinetic inhibition of iron by the coupled product water, cobalt seems to be a promising and cost-effective candidate also for HAS (R 8.1)^{74,76}. Further advantages of Co are the high activity in the low-temperature process as well as the stability, but it usually exhibits a high selectivity to hydrocarbons, which is desired in conventional FTS, but not in HAS^{74,76}. To shift the product selectivity from hydrocarbons to higher alcohols, especially for carbon monoxide-rich synthesis gas, the combination of Co and Cu have been identified as a promising combination²⁶⁶.



R 8.1

According to a simplified picture of the current knowledge^{72, 88, 265, 267}, the dissociative adsorption of CO on a cobalt surface enables a chain growth mechanism, which is important for long-chain products, but simultaneously increases possible catalyst inhibition by coke formation. Introducing Cu into a Co catalyst can increase the activity to alcohols, primarily to methanol, which is the major product on pure Cu catalysts, and iso-butanol because of the associative adsorption of CO and hydrogen spill over. Methane is a typical by-product as the optimum binding energies of the adsorbed intermediates in the methane and ethanol formation reactions are similar. Thus, methane formation will be hard to exclude in the HAS. Because of the higher exothermicity of the ethanol formation (R 8.2) and the higher molar reduction compared to methanation (R 8.3), low temperature and moderate pressure should thermodynamically favour the ethanol selectivity. Additionally, formed methanol can also act as an in-situ synthesized carbon source, facilitating the formation of higher alcohols⁸⁰⁻⁸².



Theoretically, a Cu-Co -alloy could balance the dissociative CO adsorption on the Cu-Co surface to enable chain growth and the associative adsorption of CO to enable conservation of the C–O bond^{80, 82}. However, according to the phase diagram, Cu and Co do not form an alloy at temperatures below 600 °C⁸⁶, leading to segregation of the two metals. The controlled formation of alcohols instead of hydrocarbons with a cobalt-based catalyst thus poses a complex challenge and requires fine-tuning of the catalyst, its composition and microstructure⁸⁰. It has been shown that nanosized alloy formation may occur during reduction, when Cu and Co are in close contact in a pre-catalyst phase, like in a CuCoMo-catalyst⁸⁵ or in a CuCoAl-catalyst derived from an ex-hydrotalcite precursor phase⁸⁴.

An early study on alkali metal-promoted CuO/CoO/Cr₂O₃ catalysts in HAS reported that pure copper catalysts produced methanol, whereas a Cu-rich Cu-Co/Cr₂O₃ catalyst changed the selectivity to hydrocarbons or to higher alcohols, depending on the chromium concentrations. On Co-rich CuO/CoO/Cr₂O₃ catalysts, rather the formation of hydrocarbons was favoured²⁶⁸. These results already established the composition dependency of selectivity on a ternary catalyst component such as chromium. Addition of zinc is known to have an enormous effect on methanol synthesis on copper-based catalysts being able to tune the reactant selectivity between carbon monoxide and dioxide,¹⁴ but the presence of zinc in Cu-Co tri-metallic catalysts for HAS is not studied to an extent comparable to methanol synthesis. So far it is well

understood, that ZnO acts as a steric promoter preventing sintering and suppresses methane formation due to intermediate stabilization in CuCoZnAl containing catalysts. Additionally, ZnO has a positive effect on the selectivity towards alcohols and limits/mitigates the cobalt carbide formation^{83, 236, 269, 270}.

To enable the close contact between copper and cobalt, the incorporation of zinc, and at the same time the stabilization of the metallic phases in high dispersion thus avoiding deactivation by sintering effects, catalyst synthesis from a co-precipitated hydrotalcite precursor phase is a suitable method as has been previously demonstrated for CuCoAl⁸⁴. In such single-source precursors, the joint cationic lattice of divalent copper, cobalt and zinc in one crystalline hydrotalcite phase enables the homogeneous distribution of the catalytically active species. In addition, a trivalent metal cation is needed to allow crystallization of the hydrotalcite structure¹²¹. Using Al³⁺ in a Zn:Al atomic ratio of 1:2 will formally give rise to a Cu-Co/ZnAl₂O₄ composition of the resulting catalyst after calcination and reduction of the hydrotalcite precursor. Aluminium as trivalent cation was previously discussed to enhance the catalyst performance due to the presence of stabilized Cu⁺ species, which could be beneficial for the associative adsorption of CO⁸⁹. The presence of basic sites, like surface OH-Groups or low coordinated O²⁻-sites, in a CuCoAl catalyst is expected to lead to the formation of formate species, which could be an important intermediate for higher alcohols, as it is known from copper in methanol synthesis^{16, 80, 89, 90}. Zinc promotes the formation of methanol from formate, which leads to the question whether the addition of zinc oxide to the Al₂O₃-catalyst support (forming a ZnAl₂O₄ spinel), can also promote the formation of higher alcohols.

To address these questions, the group of Muhler investigated a hydrotalcite-derived catalyst series with systematically varied molar Cu:Co ratios from 1.4 to 3.6 and its catalytic performance in an equimolar H₂:CO synthesis gas at 60 bar and 280 °C⁸⁸. Copper enrichment resulted in a decreased conversion, but an increased selectivity towards methanol and ethanol and a moderate selectivity to hydrocarbons (below 50 % in total).⁸⁸ In comparison, a zinc oxide-free catalyst has reached a higher CO conversion (36.2 % without Zn vs. 2.2 % with Zn) but accompanied by a simultaneously increased methane and methanol selectivity^{88, 89}.

In this study, we present a series of cobalt-rich Cu-Co /ZnAl₂O₄ catalysts that have been synthesized by a co-precipitation of hydrotalcite-based precursors and are compared to pure cobalt or copper reference catalysts. The performance of the catalysts has been investigated in the CO hydrogenation at lower pressure, decreased gas hourly space velocity and an increased hydrogen-to-carbon monoxide ratio compared to the study of Muhler and co-workers

hypothesizing that these conditions could be beneficial for the higher alcohol yield on a zinc-promoted copper-cobalt catalyst^{88, 89}. It was suggested that the enhanced catalyst–reactant contact time supports the chain growth resulting in heavier HAS products. The increased water partial pressure could promote HAS by suppressing hydrocarbon formation and enable simultaneously the HAS via a formate mechanism by an in situ established water-gas shift cycle^{271, 272}. In addition, our catalysts contained zinc and aluminium in a stoichiometric composition to form a stable spinel structure and thereby suppressing the incorporation of the catalytically active copper and cobalt species into a spinel structure. With such a ZnAl₂O₄ support the zinc promotion compared to “free” zinc oxide will be moderated to mitigate the above-described dramatic breakdown of conversion, which may be related by active surface coverage with zinc species due to strong metal support interaction⁸⁷. Finally, the hydrogen-enriched carbon monoxide synthesis gas was expected to avoid hydrogen becoming limiting and to suppress coke formation. This work addresses the effect of the Cu:Co ratio in such ZnAl₂O₄-supported catalysts on the selectivity and coking behaviour in HAS.

8.2 Experimental section

8.2.1 Catalyst synthesis and characterization

8.2.1.1 Co-precipitation of hydrotalcite precursors and synthesis of mixed metal oxides (MMO)

The investigated precursor samples [(Co_{1-x}Cu_x)₇ZnAl₂(OH)₆]CO₃ · *m* H₂O with $x = n_{\text{Cu}}/(n_{\text{Cu}}+n_{\text{Co}})$ were synthesized via co-precipitation according to Chakrapani *et al.*¹²⁵ in an automated stirred tank reactor (OptiMax 1001) from Mettler Toledo. Before co-precipitation was carried out, the reactor was filled with 200 mL deionized water and heated to 50 °C. The precipitation was carried out at a *pH* of 8.5 from a 0.4 M metal nitrate solution, prepared from metal nitrate salts with a purity ≥ 98 % (see also in SI Table SI 11.25), under stirring (300 rpm) and with a dosing rate of 2.08 g min⁻¹. As precipitation agent a 0.6 M sodium hydroxide and 0.09 M sodium carbonate containing solution was used. After precipitation was performed, the ageing process started without any *pH* control at the same temperature (50 °C) for another 1 h in the mother liquor. Afterwards, the precipitate was collected and washed several times with deionized water to remove excess ions until the conductivity of the washing water was less than 100 μS cm⁻¹ as measured with an immersion probe. The recovered powder was dried in a desiccator for 3 days under vacuum. Next, the dried precursor materials were calcined at 350 °C

with a heating ramp of 2 °C min⁻¹ in static air in a muffle furnace. The temperature was held for three hours.

8.2.1.2 Characterization of precursors, MMOs and spent catalysts

Powder X-ray diffractometry (PXRD) patterns of the calcined pre-catalysts and spent catalysts after CO hydrogenation were recorded with Mo-K_{α1} radiation on a Stadi-P from STOE, equipped with a Johansson-type germanium 111 monochromator and a MYTHEN 1 K detector. Line positions were calibrated against Silicon (NIST SRM 640d). The diffraction patterns were recorded at room temperature in the range of 3° to 36° 2θ. The patterns of the precursors samples after co-precipitation were recorded on a Bruker D8 advance with Cu-K_α radiation and a LYNXEYE XE-T detector. The patterns were recorded in Bragg-Brentano geometry at room temperature between 5° and 90° 2θ. Phase analysis was performed using structural data from ICSD and COD databases. Rietveld refinements²⁷³ were carried out in TOPAS Academic²⁰⁰ Version 6.0. The instrumental contributions to line broadening were determined via a Pawley fit²⁷⁴ from a measurement of LaB₆ (NIST SRM 660c) using a Thompson-Cox-Hastings profile. Microstructural effects leading to line broadening were modelled as an isotropic size effect and the volume average column height D_{Vol}. For the samples with larger amounts of hcp Co (in Cu-Co -catalysts compositions with $x = 0$ and $x = 0.125$) a simplified anisotropic model was used, which improved the fit significantly. Strain was omitted since this led to high correlations among the microstructure parameters. Due to this simplification the D_{Vol} should be regarded as apparent domain sizes that represents all microstructural effects. For the ccp metal the intensities especially for the 111 and 200 reflections differ significantly from those calculated for the bulk material due to stacking faults. Thus stacking faults were modelled as implemented in TOPAS Academic V.6.0²⁷⁵, parameters were adjusted manually to achieve a reasonable fit.

Infrared spectroscopic characterization (IR) of the precursors and calcined samples was performed on a Bruker Alpha-Platinum Fourier-transform infrared (FT-IR) spectrophotometer with attenuate total reflection (ATR) unit. The spectra were recorded between 400 cm⁻¹ and 4000 cm⁻¹. The spent samples after catalysis were analysed on a Bruker Alpha-P ATR spectrophotometer. The recorded range was from 100 cm⁻¹ to 4000 cm⁻¹.

Chemical composition of the spent catalysts was determined by C, H, N, S analysis in a Euro EA 3000 elemental analyser from EuroVector. The combustion was performed in excess O₂ at 1000 °C with He as carrier gas. The detection occurred in a thermal conduction cell.

Thermogravimetric analysis (TGA) was performed for the precursor materials on a STA 449 F3 Jupiter from Netzsch. The sample was heated by a heating rate of 5 °C min⁻¹ up to 1000 °C in synthetic air. The spent samples were analysed in a STA 1600 from Linseis. The sample was heated up to 1000 °C in synthetic air by a heating ramp of 4 °C min⁻¹.

Nitrogen physisorption was measured at 77 K in a Nova 3200e sorption station from Quantachrome and the data was analysed by the method of Brunauer-Emmett-Teller (BET). Before recording the isotherms, the samples were degassed under vacuum at 80 °C (hydrotalcites) or 100 °C (oxides) for 5 h. Afterwards the isothermal profiles between $p/p_0 = 0.0$ and 1 were recorded. The multipoint BET surface area was determined by applying the BET equation in an individual range for each sample of p/p_0 only considering the increasing volume by using the micropore BET assistant of the NovaWin software.

Temperature programmed reduction (TPR) of 30 mg of a 250 - 355 µm sieve fraction of the calcined oxides was performed in a quartz glass U-shape tube reactor on a BelCat-B from Bel Japan Incorporation. First, the sample was dried by heating up with 7 °C min⁻¹ to 100 °C in 50 ml min⁻¹ of pure Ar. The temperature was held for 60 minutes to ensure a complete drying of the sample. Afterwards, the temperature programmed reduction was performed. As reducing atmosphere, 6.4 vol% H₂ in Ar with a volume flow of 80 mL_N min⁻¹ at ambient pressure was used. Starting from room temperature the sample was heated up to 800 °C with a heating ramp of 6 °C min⁻¹. After reaching the target temperature, it was held for 15 minutes to ensure a complete recording of the reduction profile. The formed water during reduction was separated by a mole sieve to enable the analysis of the consumed H₂ via a thermal conductivity detector. The TPR profile of the pure copper sample was recorded using a BelCat II from Bel Japan Inc using 60 mg of a 250 - 355 µm sieve fraction. The pre-treatment and TPR recording were performed as described above. The hydrogen consumption was determined by thermal conductivity, which changes proportional to the consumed hydrogen.

8.2.2 Catalytic testing

Catalytic testing of the synthesized mixed metal oxides was performed in a 16-fold parallel Flowrence® plant of Avantium. Around 179 mg of a sieve fraction of 38 µm – 125 µm was diluted with an equal amount of silicon carbide (SiC). The catalyst bed was placed in between a pre- and post-catalytic bed of SiC to ensure isothermal properties and to improve the warming up and mixing of the inlet gas stream. Before CO hydrogenation was performed, the catalytic materials were activated in pure hydrogen by heating up to with 6 °C min⁻¹ to 120 °C under atmospheric pressure. The total volume flow was set to 200 mL_N min⁻¹ and divided for the

individual reactors, meaning that each reactor of the 16-fold plant contained a partial volume flow of 12.5 mL_N min⁻¹. After 30 minutes holding time, the temperature was increased up to 250 °C with the same heating ramp. At this temperature, the reduction was performed for an additional 4 h to ensure a complete reduction of the catalyst. CO hydrogenation was performed using a hydrogen-to-carbon monoxide ratio of 4 and a total volume flow of 75 mL_N min⁻¹ resulting in a GHSV of around 2800 h⁻¹ per catalyst bed. The temperature was varied from 200 °C to 300 °C in 25 °C steps at a pressure of 20 bar. Afterwards, the initial temperature of 200 °C was re-adjusted to evaluate the catalyst activity change in dependence of the temperature program. This step was followed by a second cycle of the same temperature program at a pressure of 60 bar without exposing the catalyst to ambient conditions. Each temperature step was held for 12 h to have enough time to take two gas chromatograph (GC) samples of each reactor. To study the thermal stability of the catalysts, the maximum temperature was raised to 380 °C and held for six hours. After this high-temperature treatment in synthesis gas, the catalysts were cooled back to 200 °C to determine their activity change. This last process condition was held for six hours. Afterwards, the catalyst beds were cooled down to room temperature in pure He. The catalysts were passivated by opening the reactor lid in a helium gas stream, to enable a smooth ventilation and slow air contact to re-oxidize the catalysts carefully. The data were evaluated by calculating the average of the two data points, representing the mean activity data over six hours. The selectivity are based on the carbon balance and the whole data evaluation is described in detail in the supporting information.

8.3 Results and discussion

8.3.1 Catalyst synthesis and characterization

A catalyst series with varying copper-cobalt ratios as well as the pure cobalt and copper reference catalysts were synthesized by co-precipitation. The conditions of the co-precipitation were set to favour the formation of crystalline hydrotalcite materials. The typical chemical formula of a hydrotalcite mineral with carbonate ions in the interlayer can be as follows: [M^{II}₈M^{III}₂[(OH)₂₀CO₃]_m·m H₂O with M^{II} as divalent cations (Co, Cu and Zn) and M^{III} as a trivalent cation (Al). In order to vary the metal ratios of the catalyst precursors, the composition was predefined by the metal salt solution and the nominal stoichiometric formula of the prepared precursors are listed in Table 8.1. The nominal copper fraction of the catalytic active metals ($x = n_{\text{Cu}} / (n_{\text{Cu}} + n_{\text{Co}})^{-1}$) will be used as sample label for the precursors, calcined, reduced and spent catalysts.

8 Cu-Co/ZnAl₂O₄ catalysts for CO conversion to higher alcohols synthesized from co-precipitated hydrotalcite precursors

Table 8.1: Nominal metal composition of the co-precipitated cobalt–copper catalysts. The ratio of zinc to aluminium was chosen to be in the stoichiometric ratio of a spinel structure. x is the nominal fraction of copper based on the catalytic active metal (Co + Cu).

nominal Co, Cu fractions	$x_{Cu/(Cu+Co)}$, nominal	nominal precursor composition
0 % Co, 100 % Cu	1	[Cu ₇ ZnAl ₂ (OH) ₂₀]CO ₃ · m H ₂ O
50 % Co, 50 % Cu	0.5	[Co _{3.5} Cu _{3.5} ZnAl ₂ (OH) ₂₀]CO ₃ · m H ₂ O
62.5 % Co, 37.5 % Cu	0.375	[Co _{4.375} Cu _{2.625} ZnAl ₂ (OH) ₂₀]CO ₃ · m H ₂ O
75 % Co, 25 % Cu	0.25	[Co _{5.25} Cu _{1.75} ZnAl ₂ (OH) ₂₀]CO ₃ · m H ₂ O
87.5 % Co, 12.5 % Cu	0.125	[Co _{6.125} Cu _{0.875} ZnAl ₂ (OH) ₂₀]CO ₃ · m H ₂ O
100 % Co, 0 % Cu	0	[Co ₇ ZnAl ₂ (OH) ₂₀]CO ₃ · m H ₂ O

The powders prepared via co-precipitation were analysed by PXRD, the patterns are shown in Figure 8.1 a). The reflections can be assigned to the hydrotalcite structure without any additional reflections. This indicates crystalline phase purity and implies that a metal cation distribution close to the nominal composition is present in the hydrotalcite precursor, which enables a close contact in the resulting catalyst. Furthermore, with increasing copper content the 00 l reflections (like $2\theta = 11.6^\circ$ and $2\theta = 23.4^\circ$) become much sharper, indicating an increased domain size (from 7 nm to 30 nm, see Figure 8.1 b)), *i.e.* a larger number of stacked layers. From the severely broadened cross plane reflections 0 kl (*e.g.*, 012, 015, 018) substantial stacking disorder can be deduced, which is common in nanoscale layered materials. Since the only observed reflection with $l = 0$, which is 110, is of low intensity, no reasonable information on the in-plane domain size is available. The lattice parameters evolve according to the change in chemical composition. While a shows a near constant value of 3.09 Å for $x = 0 - 0.5$ it drops to 3.05 Å for $x = 1$. Even more sensitive is c , which drops from 23.28 Å to 22.53 Å when substituting Co²⁺ for Cu²⁺ in a near linear way. The significant contraction of the unit cell along this axis cannot be explained by the rather similar ionic radii (75 pm and 73 pm, respectively) and may indicate a decrease in water content in the interlayer space, which would be a viable explanation.

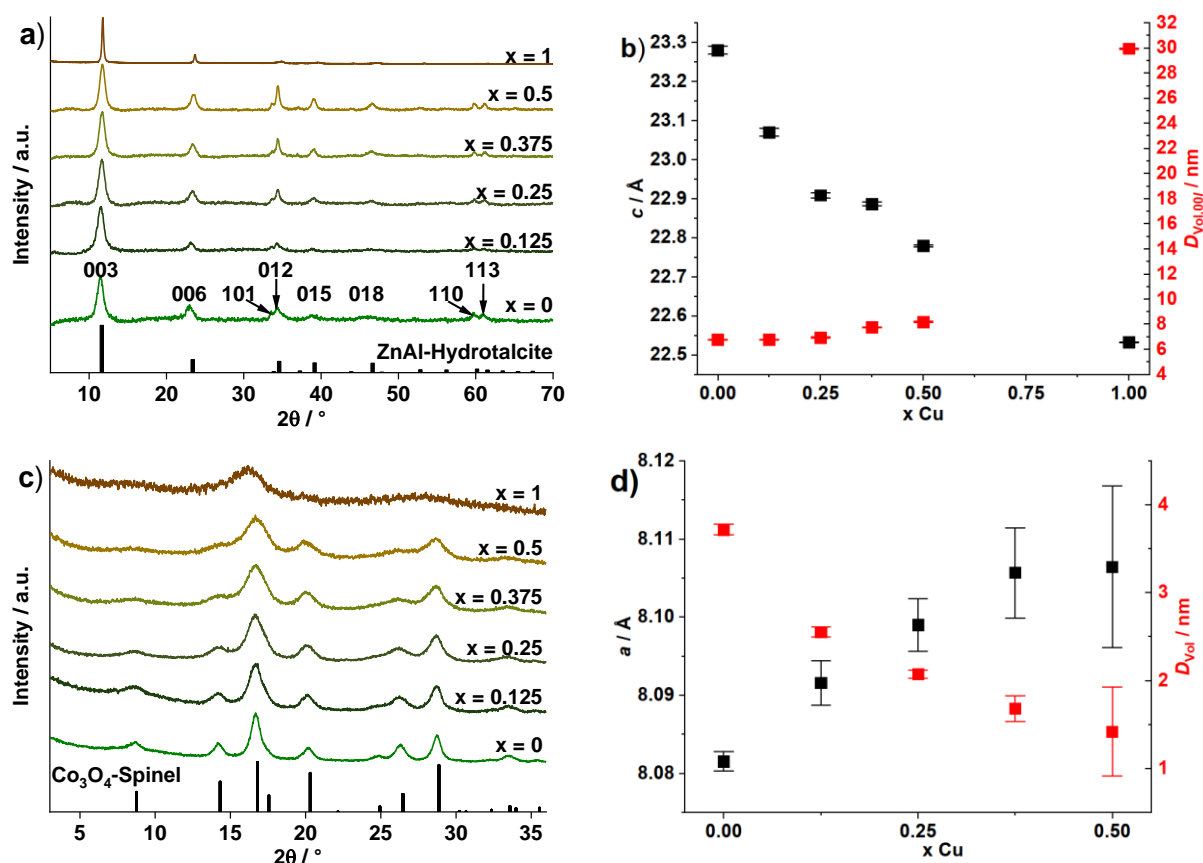


Figure 8.1: Powder XRD pattern of the co-precipitated $[(\text{Co}_{1-x}\text{Cu}_x)_7\text{ZnAl}_2(\text{OH})_{20}]\text{CO}_3 \cdot m \text{H}_2\text{O}$ hydrotalcite precursors (a) with $x = n_{\text{Cu}} / (n_{\text{Cu}} + n_{\text{Co}})^{-1}$. The reference was taken from the ICSD database for a Zn-Al-Hydrotalcite (#155052). The reflections are labelled with the corresponding Miller indices taken from the reference. In b) the variation of the lattice parameter c and domain size along the c -axis is plotted as function of chemical composition. The PXRD patterns (c) of the mixed metal oxides after calcination at 350 °C in static air of the corresponding hydrotalcite precursor. The reference of Co_3O_4 -spinel was taken from ICSD database (#26091). The extracted lattice parameter a and isotropic domain size are plotted in panel d).

IR spectroscopy (shown and discussed as supporting information in Figure SI 11.65 a)) shows spectra expected for hydrotalcite materials and support the above-described hypothesis by the decreasing water deformation mode and the additional weaker hydroxyl stretching mode by increasing copper content. The calcinations to the corresponding mixed metal oxides (MMO) were performed at 350 °C in an analogous way as it is known for copper-based methanol synthesis catalysts.⁸ This temperature leads to decomposition of the hydrotalcite structure but does not cause a complete decomposition of the carbonate species. It rather leads to a remainder of so-called high-temperature carbonate, which is discussed to mitigate metal oxide sintering and results in a more nanostructured catalyst.⁶² This was also confirmed for our copper-rich

samples by thermogravimetric analysis of all prepared precursors (shown and discussed as supporting information in Figure SI 11.66). The PXRD patterns of the MMOs shown in Figure 8.1 c) confirm the complete decomposition of the precursor phase. On the Co-rich side, the formation of a spinel phase is evident with a lattice parameter of $a = 8.08 \text{ \AA}$ (Figure 8.1 d)). The broad reflections were refined as isotropic domain size with $D_{Vol} = 3.7(5) \text{ nm}$. However, it should be noted that a discrimination among different spinel phases (*e.g.*, ZnAl₂O₄ and Co₃O₄ or a mixed phase) is not possible given the similar lattice parameters and the broad reflections. Thus, the values can only be understood as the sample average. Still a trend can be deduced, with increasing Cu content up to $x = 0.5$ the domain size decreases down to $1.5(5) \text{ nm}$ and a increases slightly to $8.1(1) \text{ \AA}$. For $x = 1$ the sample can be regarded as amorphous since only one broad halo is visible.

Interestingly, the pure cobalt sample ($x = 0$) has the highest specific surface area after calcination, shown in as supporting information in Figure SI 11.69. The accessible surface areas of the precursors were in the same range around $80 \text{ m}^2 \text{ g}^{-1}$, except for the pure copper containing ($x = 1$) hydrotalcite reaching only roughly half of that value. The increase in surface area due to the calcination is attributed to the released water and carbonates leading to pore formation in the materials. Additionally, the temperature was low enough to avoid metal oxide sintering yielding a porous material.⁶² The oxide surface areas of the copper-rich MMOs ($x = 0.25-0.50$) were similar and reached values around $100 \text{ m}^2 \text{ g}^{-1}$. Contrarily, the cobalt-rich samples ($x = 0-0.125$) reached even higher surface areas above $160 \text{ m}^2 \text{ g}^{-1}$ showing that large specific surface areas of the MMO pre-catalysts can be achieved for the more crystalline samples (Figure 8.1 c)) that do not contain high-temperature carbonate.

The TPR results of the catalyst series are shown in Figure 8.2. The temperature labels refer to the temperature of highest rate of hydrogen consumption. The cobalt-free sample ($x = 1$) shows a slight increase in the hydrogen consumption signal starting at $\approx 200 \text{ }^\circ\text{C}$ and reaching the maximum rate at about $334 \text{ }^\circ\text{C}$. Afterwards, an additional broad signal was observed around $537 \text{ }^\circ\text{C}$. These two temperature ranges indicate that there are two different reducible species present in that sample. The one at lower temperature is assigned to copper oxide being reduced to copper metal, while the one at higher temperature can be attributed to zinc oxide reduction and brass formation.¹⁵⁴ A similar behaviour was observed for the pure cobalt sample ($x = 0$), where the low-temperature reaction is assigned to Co₃O₄ reduction to CoO and the high-temperature peak to formation of cobalt metal as discussed in detail in the supporting information.

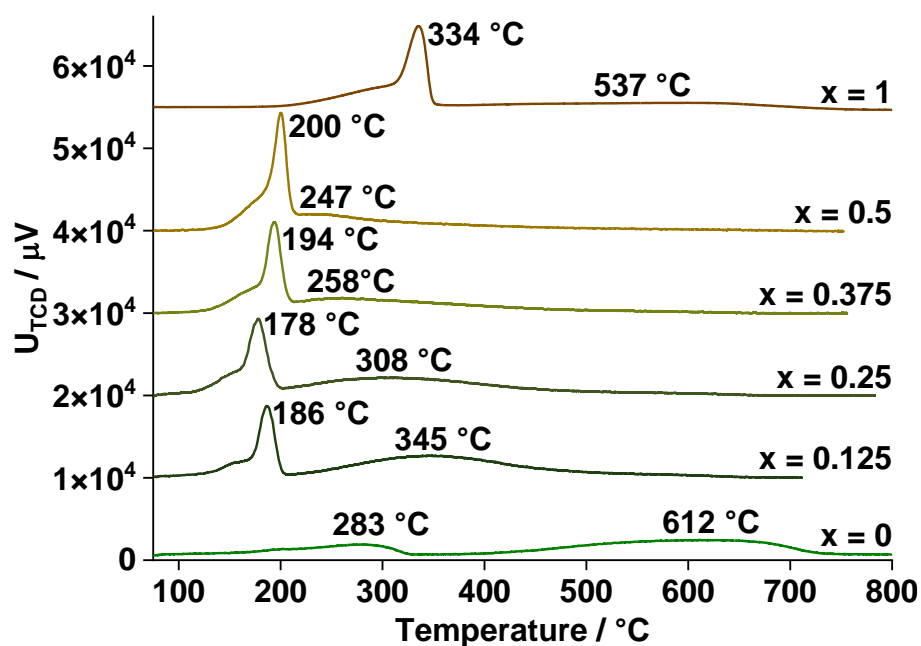


Figure 8.2: TPR profiles of a sieve fraction of 250 – 355 μm of the prepared pre-catalysts. The reduction was measured in 6 vol% H_2 in Ar with a heating rate of $6\text{ }^\circ\text{C min}^{-1}$. The labelled temperatures indicate the maximum hydrogen consumption.

The TPR analysis of the binary Cu-Co samples demonstrates that the copper reduction is lowered gradually to 180 $^\circ\text{C}$ with increasing amounts of cobalt. The typical shape of the CuO reduction with a shoulder assigned to intermediate Cu(I) formation^{276, 277} remained unaltered. Additionally, a second broad peak was observed at temperatures higher than the CuO reduction peak and was found to increase with the cobalt content in the Cu-Co samples. This additional peak was similar in shape to the second reduction process observed in the pure cobalt or copper sample at higher temperature and was not followed by any other reduction peak upon further heating. As the formation of brass was not observed in hydrotalcite-derived copper catalysts at these low temperatures^{276, 277}, this broad peak is tentatively assigned to the cobalt metal formation shifted by the presence of metallic copper to lower temperatures compared to the pure cobalt reference. This effect is likely caused by spillover of activated hydrogen from the freshly formed copper metal particles⁸⁵. With lowering cobalt content, this second feature can be shifted down in temperature to 247 $^\circ\text{C}$ for the equimolar sample ($x = 0.5$), in comparison to 612 $^\circ\text{C}$ in the pure cobalt sample ($x = 0$, Figure 8.2). A small amount of copper ($x = 0.125$) does already facilitate the reduction of cobalt oxide, but the maximum hydrogen uptake at high temperature is shifted only to 345 $^\circ\text{C}$. These findings suggest that after the activation of the catalysts at 250 $^\circ\text{C}$ with pure hydrogen, only the copper-rich binary catalyst $x = 0.5$ can be safely expected to contain fully reduced copper and cobalt species before CO hydrogenation

started. Thus, this catalyst will be discussed in more detail below as a representative of the bi-metallic samples.

8.3.2 Activity test in CO hydrogenation

The reference temperature of the CO hydrogenation was chosen to be 200 °C to remain in the kinetic regime preventing thermodynamic limitations. The binary Cu-Co catalysts performed in a similar manner in the catalytic activity tests. C₅₊ products were sometimes present but only as a very minor fraction. Therefore, the discussion of the catalyst's composition-dependent activity and selectivity will be conducted in the following for three selected ZnAl₂O₄-supported catalysts, the pure Co- ($x = 0$), the pure Cu- ($x = 1$) and the binary catalyst with an equal molar ratio Cu:Co = 1 ($x = 0.5$) based on the selectivity for linear C₁ to C₄ products. The conversions and selectivity of all investigated Cu-Co catalysts are shown and discussed as supporting information in the Figure SI 11.71 to Figure SI 11.75. The process parameters over the time on stream of the catalytic test are also provided as supporting information in Figure SI 11.70.

8.3.2.1 CO hydrogenation at 20 bar

After activation in pure hydrogen at 250 °C for 4 h, the pure Co and Cu catalysts reached low CO conversions at 200 °C and 20 bar as shown in Figure 8.3 a). Generally, low conversion was expected for Cu catalysts compared to Co. Based on the TPR profiles (Figure 8.2), the reduction temperature of 250 °C likely resulted in an incomplete reduction of these MMOs giving rise to the low activities for both catalysts. The high CO₂ content in the product gas stream (shown as supporting information in Figure SI 11.73 a)) indicated on-going reduction and supports this assumption. The pure cobalt and copper catalysts formed only low amounts of hydrocarbons or long chain alcohols (Figure 8.3 b) - c)) from which the water molecule could be re-consumed by water-gas-shift reaction to form CO₂. Therefore, the CO₂ selectivity rather indicates on-going reduction of the MMOs.

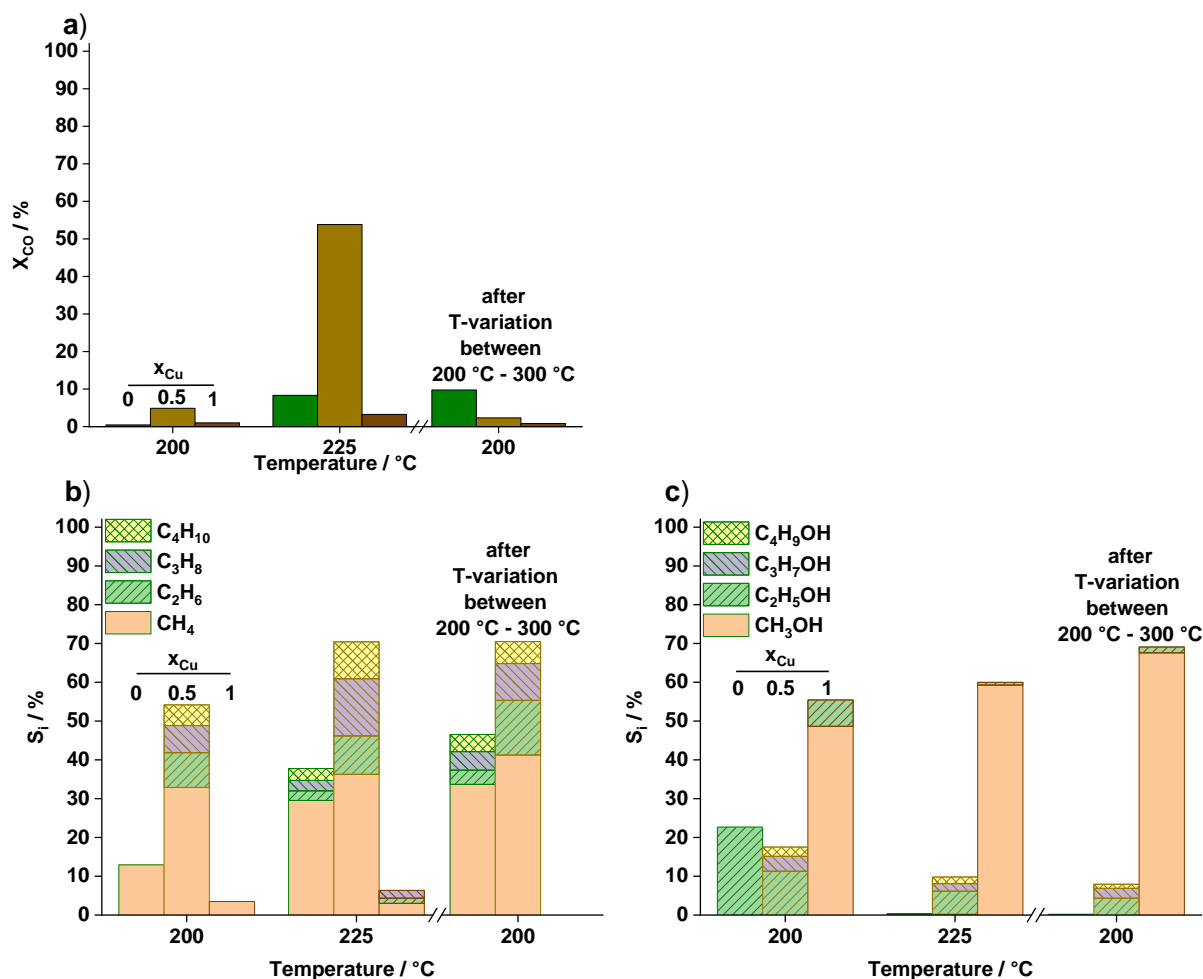


Figure 8.3: In a) the CO conversion of selected catalysts and temperatures ($x = 0$ (left bar), $x = 0.5$ and $x = 1$ (right bar)) at 20 bar are shown. Below are the corresponding selectivity and product distribution (n -C₁ to n -C₄) in the alkane- (b) and alcohol- (c) formation presented. The second run at 200 °C was performed after the temperature variation (T-variation) to reference activity changes due to catalyst ageing. The total volume flow was set to 75 mL_N min⁻¹ with H₂:CO = 4 and GHSV = 2800 h⁻¹.

The binary Cu-Co ($x = 0.5$) catalyst showed higher conversion and selectivity to hydrocarbons and the increase in reaction temperature by 25 °C further enhanced the activity of Cu, Co and CuCo catalysts but also the hydrocarbon selectivity. Traces of ethanol was formed for the pure Co catalyst ($x = 0$) at 225 °C (Figure 8.3 c)). The binary Cu-Co ($x = 0.5$) catalyst formed alcohols, but less with lower selectivity level than at 200 °C. On the pure Cu catalyst ($x = 1$), the product distribution shifted towards methanol with increasing temperature with a simultaneous selectivity of around 10 % for C₁ to C₄ hydrocarbons. Because of this hydrocarbon formation with water as a by-product, the selectivity of CO₂ was for this catalyst almost constant over the temperature range and is assigned to the water gas shift reaction.

Temperatures of 250 °C – 300 °C at 20 bar resulted in complete CO conversion for all cobalt-containing catalysts (compare SI Figure SI 11.71). Thus, the catalytic performance will be discussed only in the kinetic region at 200 °C – 225 °C. The datapoint at 200 °C before the catalyst has been exposed to harsher catalytic conditions (250 °C – 300 °C) will be compared to the datapoint after returning to 200 °C in temperature program (compare process scheme in SI Figure SI 11.70)) as a rough measure of catalyst stability. Back at 200 °C (after T-variation in Figure 8.3), the activity was enhanced, compared to the initial catalytic performance at 200 °C, for the pure Co catalyst and slightly lowered for the mixed Cu-Co catalyst ($x = 0.5$) but almost equal for the copper catalyst, which formed, as expected, mainly methanol with only a small amount of ethanol (compare SI Figure SI 11.71 b)-c)). The increase in the activity of the Co catalyst ($x = 0$) can be attributed to a more complete reduction under high pressure in a strongly reducing H₂/CO atmosphere which might compensate the need for higher temperature as it was expected from TPR results (Figure 8.2). Simultaneously, the hydrocarbon selectivity increased, with predominantly methane being formed, and the selectivity towards ethanol completely vanished, as expected for a pure cobalt catalyst.⁸³ The initial ethanol formation (at low conversion) thus was not stable and cannot be assigned to the effect of zinc on the cobalt catalyst but rather to the still oxidized nature of the catalyst after incomplete activation.

Stable C₂ to C₄ alcohol formation at 200 °C was observed only over the Cu-Co mixed catalysts. This selectivity is ascribed to the interplay between both metals and confirms the promotional effect of bi-metallic catalysts explained by theory⁸⁰ and reported in the literature^{84, 88}. Interestingly, as shown in the SI Figure SI 11.71, already a relatively low amount of copper (12.5 at% Cu in the catalyst with $x = 0.125$) in the cobalt catalyst resulted in an increase of the ethanol selectivity from 0.3 % to 4 % at 200 °C and 20 bar after the temperature treatment. The best catalyst at these conditions, was a cobalt-rich binary sample with $x = 0.375$ with an ethanol selectivity of 4.5 % (shown in the SI Figure SI 11.71 c) and Figure SI 11.74).

8.3.2.2 CO hydrogenation at 60 bar

The increase of the pressure from 20 to 60 bar favours the CO conversion as is expected for a reaction with volume contraction such as HAS (R 8.1). The CO conversion of the pure Co catalyst ($x = 0$) increased with increasing pressure roughly by factor of three (compare Figure 8.3, second run (after T-variation) at 200 °C with Figure 8.4, first run at 200 °C). However, the conversion increased only slightly for the copper-containing catalysts. The observed formation of the C₁- to C₄-alcohols at low temperatures (<250 °C) and the formation of hydrocarbons with increasing temperature (>225 °C) agrees with theory⁸⁴. In our study, the

product distribution remained similar for all catalysts, only the overall selectivity was increased. Also, the reference run at 200 °C at 60 bar (Figure 8.4, 200 °C, after T-variation) did not show any strong change of the CO conversion or the selectivity of the copper containing samples in comparison to the previous catalytic test at 200 °C, indicating a stable performance and product distribution.

In comparison with reported results on similar catalysts, our ethanol selectivity are modestly (Figure 8.4 c)). The herein reported copper-cobalt catalyst with equimolar ratio ($x = 0.5$) reached a selectivity to ethanol of 2.5 % at a full conversion at 60 bar and 250 °C whereas a similar catalyst prepared in the group of Muhler reached a selectivity of 7.5 % at a conversion of 9.3 % at 60 bar, a higher GHSV around 9600 h⁻¹ and 280 °C⁸⁸. In the herein presented study, no ethanol formation was observed at a temperature around 250 °C for our self-prepared Cu-Co catalyst ($x = 0.5$, GHSV \approx 2800 h⁻¹, full conversion). The main differences between literature catalytic performance and this study are the lower reaction temperature and the higher hydrogen excess in the herein described experiments (H₂:CO = 4 vs H₂:CO = 1),⁸⁸ which is a composition closer to methanation stoichiometry than to ethanol formation. An additional difference is the copper content, which was $x = 0.6$ of the above-mentioned literature reference⁸⁸ and $x = 0.5$ for the herein reported catalyst.

The CO conversion on the pure cobalt catalyst ($x = 0$) kept changing at the different reference measurements over the complete catalysis run of 165 hours at varying conditions, also in the experiments conducted at 60 bar. The CO conversion changed from 26 % to 84 % during the temperature variation in between of the two measurements at 200 °C of the first and second run (Figure 8.4). The main products were hydrocarbons. This activity increase must be related to some structural changes of the pure cobalt catalyst ($x = 0$). The absence of CO₂ formation during the temperature treatment (SI, Figure SI 11.73 b)) does in this case exclude a reduction of cobalt oxide residues as it was suggested in the catalytic tests at 20 bar. It further indicates that a steady extent of reduction has been reached without WGS activity. A promotion of zinc oxide in a similar manner as it is known from copper-methanol catalysts was not observed for cobalt catalysts but a stabilizing effect was reported covering the catalyst activity⁸³. Therefore, the increase in conversion of the pure cobalt catalyst must be caused by a structural rearrangement of the activated cobalt species.

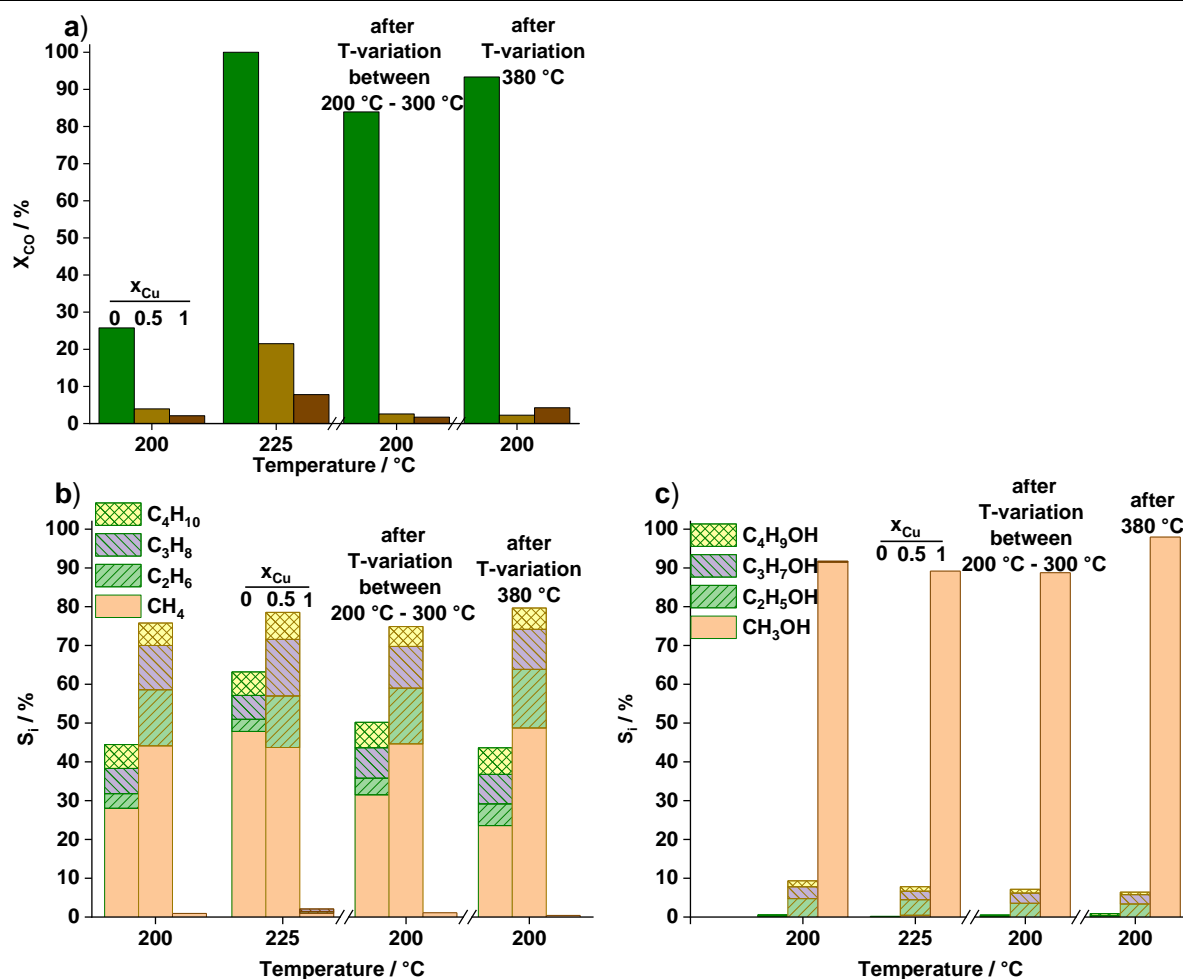


Figure 8.4: In a) are the CO conversion of selected catalysts ($x = 0$ (left bar), $x = 0.5$ and $x = 1$ (right bar)) at 60 bar shown. Below are the corresponding selectivity and product distribution (n -C₁ to n -C₄) in the alkane- (b) and alcohol- (c) formation presented. The second run at 200 °C was performed after the temperature variation (T-variation) to reference activity changes due to catalyst ageing. The third run at 200 °C was performed after 380 °C (after 380 °C) to reference activity changes due to possible sintering effects. The total volume flow was set to 75 mL_N min⁻¹ with H₂:CO = 4.

During the following thermal stability test at 380 °C still further improvement of the CO conversion to 93 % was observed after returning to kinetic control at 200 °C (see Figure 8.4 and SI Figure SI 11.72). Again, at the 380 °C test no CO₂ formation was observed. The high selectivity of hydrocarbons and the absence of alcohols (compare SI Figure SI 11.72 b) - c)) lead more to the conclusion, that probably the products have changed the active site of the cobalt catalyst. Since it is known that cobalt forms cobalt carbide at higher temperatures, the carburization would be noticed by a lowered CO conversion, which was not the case in our catalytic tests.²⁷⁸ On the other hand, a change of the cobalt phase induced by hydrocarbon deposition and hydrogenation could have activated the cobalt catalyst by forming a more active

hcp cobalt site, which was to some extent found in the spent sample (compare Figure 8.5 b)).^{279, 280}

A slightly increased CO conversion over the pure Cu catalyst ($x = 1$) from 2 % at 200 °C before 380 °C and 60 bar (Figure 8.4 a)) to 4 % at 200 °C after 380 °C and 60 bar and an increased CO₂ selectivity during CO hydrogenation at 380 °C (Figure SI 11.73 b)) were observed and may indicate an on-going activation process of this catalyst beside the WGS activity as it was observed over the complete temperature range. Simultaneously, the selectivity of methanol increased by 10 % from 89 % to 99 %. This behaviour might be explained by enhanced strong metal–support interaction as the ZnAl₂O₄ support starts to reduce at higher temperatures in accordance with the hypothesis that a Cu–Zn surface alloy can favour methanol synthesis^{24, 154}. Also, on-going sintering can lead to a gradual activity increase of supported Cu catalysts .

In summary, it was shown, that the cobalt catalyst ($x = 0$) changed the active site during reaction after reaching full activation and that for the hydrotalcite-derived copper catalyst ($x = 1$), the CO conversion and methanol selectivity increased after developing a highly active site at high temperature treatment. However, subsequent activation played a much smaller role for the bi-metallic catalysts due to strongly lowered reduction temperatures of these samples.

Instead, the CO conversion of the mixed Cu-Co catalysts decreased only slightly over 63 hours of time (SI Figure SI 11.72 and Figure SI 11.70) during the temperature variation test up to 300 °C at 60 bar, likely due to particle growth caused by the strongly reducing atmosphere and the relatively high temperature that, according to the TPR profiles (Figure 8.2), should lead to a full reduction. Their performance in the run at 200 °C and 60 bar resulted in an unaffected selectivity towards alcohols from C₂ to C₄ (SI Figure SI 11.72 c)) demonstrating again that the catalysts are quite stable in product formation at these strongly reducing conditions upon temperature and pressure variations. Up to the last reference experiment at 200 °C at 60 bar, the catalysts reached 150 hours on stream before the thermal stability test at 380 °C was performed.

During the high temperature catalysis at 380 °C, the binary catalysts reached full conversion and formed only hydrocarbons (compare SI Figure SI 11.72). Their catalytic performance in CO conversion was reduced by half comparing the kinetic experiments at 200 °C of the initial run and after 380 °C. The maximum activity loss of 55 % was observed for a cobalt rich $x = 0.25$ catalyst. This activity loss could be caused by metal sintering or coking. However, the selectivity were unaffected by the temperature treatment.

8.3.3 Characterization of the spent catalysts after passivation in air

To better understand the state of the catalysts and especially the above-described dynamic changes of the copper-free Co catalyst ($x = 0$), the spent samples were analysed after careful air contact as described in the experimental section. The PXRD patterns of the spent catalysts are presented in Figure 8.5 a). They were all analysed with Rietveld refinement to extract the lattice parameters and the quantitative composition of the assigned phases (shown in SI Figure SI 11.79). Due to a partial overlap of reflections and correlation with the background, the estimated error in the quantification was 1 % - 2 % and the microstructure was treated only in a simplified manner without distinguishing size and strain effects to not over parametrize the fits. Because both copper and cobalt can crystallize in the ccp structure with similar lattice parameters only one ccp phase was modelled. For the ccp metal, a model for stacking faults was included to account for the resulting altered intensities, which are well known to occur in this material ²².

All samples contain a spinel phase after catalytic treatment up to 380 °C, which is assigned to the ZnAl₂O₄ support. It accounts in all samples for ~ 40 wt% (see Figure 8.5 b)) of the sample and a significant inversion between Zn²⁺ and Al³⁺ across their sites of ~30 % was found. The expected weight fraction of the ZnAl₂O₄ in a fully reduced catalyst with composition Cu₇ZnAl₂O₄ (*c.f.* composition of the precursor) would be ~30 %. This overestimation of the weight fraction by ~ 10 % may in part due to errors in the quantification but may as well indicate amorphous content in the sample.

There is a significant change in lattice parameter of the spinel phase with chemical composition of the catalysts, in particular a shrinkage of the cell parameter a with increasing Cu content (Figure 8.5 c)). The domain size shows a minimum at around $x = 0.25 - 0.375$, which indicates either a smaller crystallite size or could also be caused by substitution. A substitution of Zn²⁺ by Co²⁺ seems to be a likely case ²⁸¹, which would render the spinel support at least chemically active in an interaction with the catalyst.

In addition to the spinel phase, metallic phases are present in all samples. For the copper-rich samples with $x = 1$ and 0.5 only ccp metal was found, while for lower values of x a coexistence of ccp and hcp metal was observed (Figure 8.5 b)). The sample with $x = 0$, *i.e.* only cobalt as catalyst, needs special attention here: Firstly, the coexistence of a hcp and ccp metal phase suggests that cobalt adopts both polymorphs here. The thermodynamically stable form is hcp, both at room temperature and even at the highest catalyst test temperature (380 °C). The coexistence of both polymorphs in various specimen and the complex dependency on heat

treatment and particle size is long known.²⁸² However, alloying with other metals (*e.g.*, Zn) could contribute to further stabilizing (partially) the ccp phase, since a Co rich alloy with Zn adopts the ccp structure²⁸³. The lattice parameters of both phases are well in agreement with those reported in literature for hcp and ccp Co²⁸⁴. Secondly, the metal phases show a much higher crystallinity in the pure cobalt catalyst ($x = 0$, Figure 8.5 a)) as compared to all other compositions. As soon as copper is introduced the domain size of the metal phases decreases substantially from 35 nm for $x = 0$ to 6.5 nm for $x = 1$ (see Figure 8.5 d)), where the most significant drop down to 10 nm already occurs with a small addition of copper, *i.e.* for $x = 0.125$. It should be noted that these domain sizes rather underestimate the actual domain size, since no strain was modelled for the sake of stabilizing the fit. But strain is expected due to the well-known defective nature of ccp metal nanoparticles. The actual metal particle size will be underestimated even by a higher extent as these may consist of several domains. Furthermore, the formation of Cu₂O due to passivation will also reduce the average domain size of the ccp phase since the oxide will grow at the expense of the metal.

When tracing the evolution of the cell parameter of the ccp phase (see Figure 8.5 d)) with chemical composition of the catalyst a virtually linear trend is evident suggesting alloying of Cu and Co. This is surprising since no miscibility between Cu and Co is known in the bulk. The difference plots do not indicate the need for additional phases to fit the patterns and favour such single metal phase scenario. Still, one should bear in mind that two coexisting ccp phases may cause such linear change in apparent cell parameter by a constant shift of their phase fractions as an alternative scenario. Given the similar lattice parameters, severe line broadening and limited angular range it is virtually impossible to discriminate among the two scenarios.

However, the situation is even more complex if we consider the presence of reduced zinc in the catalysts, according to the Cu/ZnO methanol catalyst^{24, 154, 280}, there is a reasonable possibility that cobalt and zinc form mixed particles or a surface alloy with a cobalt-rich core under reaction conditions in a ccp phase²⁸⁵, which can be undetected by XPRD as in the case of Cu/ZnO. Additionally, it can be discussed, that the Cu-Co mixed phase creates a CuCo surface alloy representing multiple weak CO adsorption sites lowering the C–O dissociation and increasing the selectivity towards oxygenated FTS products²⁸⁶. The nanostructure of the catalyst could enhance the number of such CuCo surface alloy enhancing the alcohol formation. In this scenario, depending on the reaction conditions, the yield of alcohols can be seen as an indicator of such a Cu-Co mixed phase whereas the hydrocarbon formation refers to the fraction of active pure Co surface. Alternatively, methanol formation on (pure) Cu was discussed, which could promote HAS by in situ formed methanol⁸⁰.

Additionally, all copper containing samples contain a detectable amount of Cu₂O that increases with x (Figure 8.5 b)), which results likely from the treatment of the catalysts in air after the experiments. It should be noted that CoO may have formed as well, as the two compounds Cu₂O and CoO show very similar diffraction patterns. Given the broad reflections a distinction is not possible. For the sample containing only cobalt, the formation of significant amounts of crystalline CoO is not evident, which implies a quantitative reduction of the oxidic (spinel) pre-catalyst under reaction conditions. Furthermore, this sample contains minor amounts of SiC, which was used as diluent for the catalyst during activity tests. This sample is also unique in showing two additional reflections at 9.8° and 10.9° 2θ, which remain unassigned after searching the databases. Based on IR and TGA results (see SI Figure SI 11.76 - Figure SI 11.78) they are tentatively assigned to crystalline fractions of hydrocarbon waxes or other carbonaceous deposits²⁸⁷.

The formation of cobalt carbide and graphitic hydrocarbons was observed previously on Cu-Co catalysts with different cobalt-to-copper ratios²⁸⁸. Formation of cobalt carbide was not observed in the PXRD patterns of the spent samples (Figure 8.5 a)) since no corresponding additional reflections could be observed. This leads to the conclusion that bulk cobalt carbide could only be present as a minor phase or in an amorphous state if present at all. Surface carbide is expected to lower hydrocarbon selectivity and enhance the formation of alcohols because of the enhanced associative adsorption of CO. Simultaneously, the carbide formation results in a deactivation of the catalytic performance, which was observed before to stabilize only after 40 h time on stream^{288,289}. Such a behaviour was not found in this study supporting the absence of cobalt carbides in these Cu-Co/ZnAl₂O₄ catalysts at the applied reaction conditions.

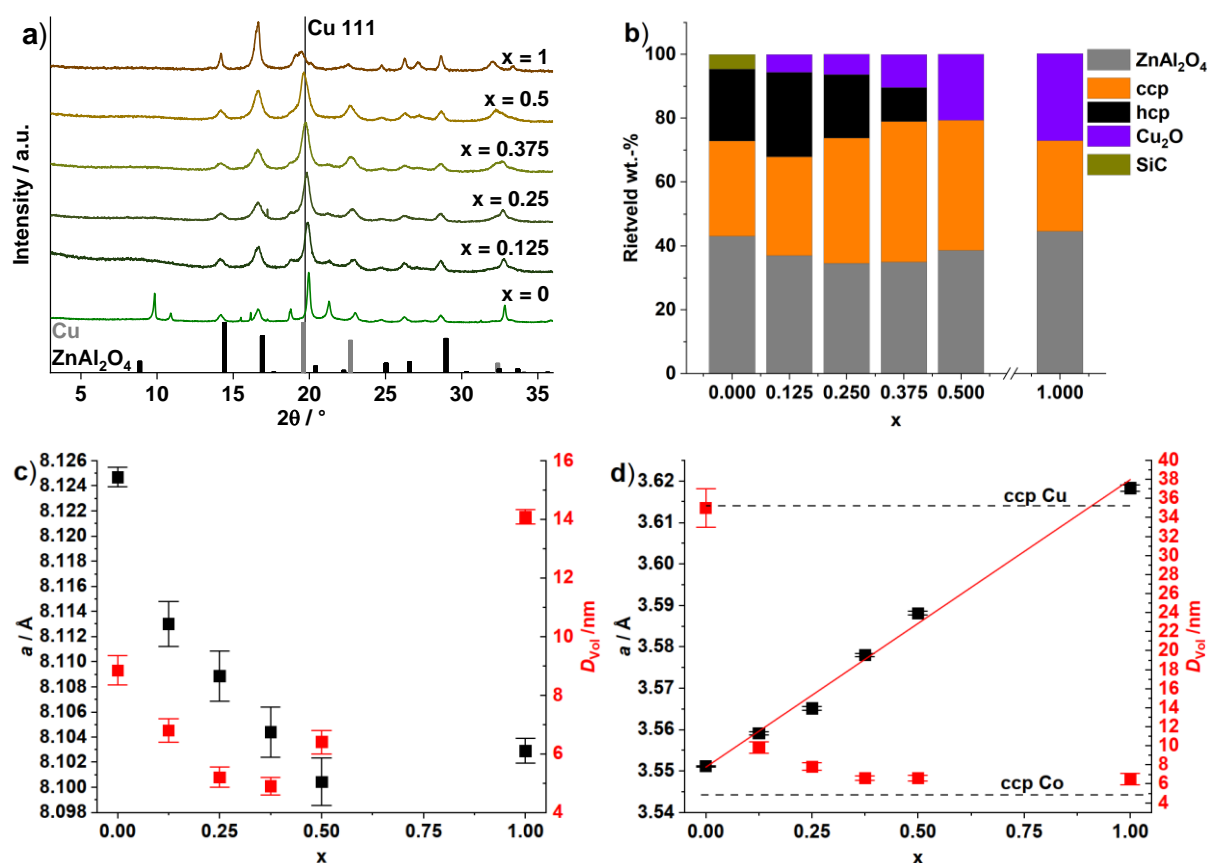


Figure 8.5: Powder XRD analysis of the spent catalysts after CO hydrogenation at 20 bar / 60 bar and 200 °C - 380 °C after passivation at room temperature with air. The complete pattern is visualized in a) with the dark grey bars corresponding to the Cu (ccp) reference (ICSD#7954) and the black bars corresponding to the ZnAl₂O₄ reference (ICSD#609005). The resulting quantification of the assigned phases by a Rietveld refinement is shown in b). c) Compositional dependence of the cell parameter and domain size of the spinel phase. d) The ccp phase shows a significant expansion of the cell parameter with the copper content x . The red line is a linear fit to all data points, the dashed lines indicate the lattice parameters for bulk ccp Cu and Co taken from several entries of the ICSD (#627115, 627114, 622435, 44989). The apparent domain size shows a drastic initial decrease upon addition of copper in the catalyst system.

IR spectroscopy of the spent samples (shown as SI in Figure SI 11.76) shows for the copper-containing catalysts, absorption bands between 1541 cm⁻¹ and 1393 cm⁻¹, which probably correspond to carbonate stretching modes, similar as in the calcined catalysts. However, unlike there, this carbonate is not necessarily a residue of the synthesis but rather additional surface carbonate formed from CO₂. Only for the pure cobalt catalyst with $x = 0$, strong absorption bands around 3000 cm⁻¹ and 1500 cm⁻¹ were observed. These strong bands at 1474 cm⁻¹ and 1460 cm⁻¹ can be assigned to methyl groups of formed coke or aliphatic hydrocarbons.

Asymmetric C–H bending can give rise to the band at wavenumber 1460 cm⁻¹.^{290, 291} In the range of 3000 cm⁻¹ and 2800 cm⁻¹, C–H stretching modes are excited.²⁹¹ The band at 2953 cm⁻¹ could be assigned to asymmetric CH₃ stretching, whereas the bands at 2912 cm⁻¹ and 2844 cm⁻¹ could be C–H stretching modes of CH₃ or CH₂ groups.²⁹¹ IR spectroscopy thus gives evidence of carbon enrichment in the pure cobalt catalyst, which was also confirmed by C, H analysis (Figure SI 11.77), where carbon was found to be 30 wt% of the recovered catalyst. Additionally, a thermogravimetric analysis of the spent sample shows a drastic mass loss around 300 °C of about 28 % of the cobalt catalyst (Figure SI 11.78), which corresponds to the burning off of the deposited coke. However, the stability of the catalytic performance of the cobalt catalyst was good over the 165 hours of run time, despite the coke formation.

All copper-containing catalysts contained only small amounts of carbon and hydrogen, which can be assigned to carbonate groups or re-adsorbed water, as neither the IR spectra nor the TG analysis delivered clear further evidence for coke formation or burn-off. The TGA curves showed a mass gain due to metal oxidation rather than a mass loss due to burn-off of deposited hydrocarbons. This also confirms that the catalyst passivation was successful and substantial fraction of the catalyst have remained in the metallic state. These results show that the presence of copper strongly suppresses the formation of coke during HAS on the catalysts studied here. Such a promotion by copper was also observed by Cu-Ni or Cu-Co catalysts in other reaction systems²⁹²⁻²⁹⁴. To the best of our knowledge the promotion effect of copper on the coke suppression was not yet discussed in the context of higher alcohol synthesis.

8.4 Conclusion

The addition of copper prevents coke formation on cobalt catalysts and enhances the selectivity towards alcohols at temperatures below 250 °C in Cu-Co/ZnAl₂O₄ catalysts. Bi-metallic catalysts showed a clearly different behaviour, which was beneficial for HAS, compared to the pure copper or cobalt catalysts. The PXRD data suggests a possible alloy formation of Cu and Co in the ccp phase, which would imply a close interaction of both metals. Relatively low pressure (20 bar) and temperatures above 225 °C result in complete conversion at an GHSV of around 2800 h⁻¹ in a synthesis gas stream of a H₂:CO ratio of 4. Unfortunately, these process conditions were found not to result in an increase in the HAS activity of the catalysts. Compared to literature reports, the selectivity to higher alcohols of the studied catalysts was low at otherwise high activity. However, a copper content of already 12.5 at%, which is accompanied by a significant drop of the domain size of the ccp phase compared to the pure cobalt catalyst, has a positive effect on the alcohol selectivity from CO hydrogenation and on the mitigation of

coking. Nevertheless, the hydrocarbon selectivity was found to be always predominant in this hydrogen-rich synthesis gas. Another important effect of copper was the facilitated reduction of the cobalt oxide. The activity of the pure copper catalyst was enhanced and methanol formation was improved after a treatment in reducing gas at 380 °C. These results demonstrated the necessity of higher temperatures to reach a completely activated state of this Cu/ZnAl₂O₄ catalyst from a hydrotalcite precursor. The activation of the pure cobalt catalyst was also not complete prior to the catalytic experiment and proceeded after each temperature or pressure variation. Even though significant coke formation was found for this catalyst, it showed –just like the other hydrotalcite-derived catalysts studied here– a stable catalytic performance after it was fully activated up to 165 hours on stream.

Supporting Information

Supporting Information for this article can be found under DOI: 10.1002/cite.202200171 or in chapter 11.10 (Supporting Information to "Cu-Co/ZnAl₂O₄ catalysts for CO conversion to higher alcohols synthesized from co-precipitated hydrotalcite precursors") starting from page 279.

Acknowledgment

This work was supported by the Mercator Research Center Ruhr (MERCUR Pe-2018-0034). F.Ö. thanks the International Max Planck Research School RECHARGE for support. Prof. S. Schulz and Prof. M. Epple of the University of Duisburg-Essen are gratefully acknowledged for allocating access to their characterization facilities.

9 Conclusion and Outlook

The role of Al and Ga as secondary promoter was investigated in a copper-based catalyst and evaluated regarding the structural promotion and the catalytic performance. It was found that the secondary promoter (*e.g.*, Al or Ga) increased the microstructure during co-precipitation and this microstructure was covered along the treatment processes and even in catalysis resulting in highly active catalysts which are stable for more than 800 h time on stream. Beside this structural promotion, an enhanced reduction of the ZnO was found by chemisorption methods. This enhanced ZnO reduction resulted in an increased amount of Zn^{red} species which was found to be higher for Al than for Ga and demonstrate an electronic promotion of the ZnO phase. Therefore, the secondary promoter can be related to the ZnO phase, which was confirmed by XANES and DFT calculations. DFT calculations confirmed that the secondary promoter stabilizes the Zn vacancies and improves the ZnO reduction to form Zn^{red} surface species which was determined to be stronger for Al than for Ga. This effect improved the Cu-Zn interaction, as it was confirmed by a complete coverage of the copper surface by DRIFT, and by an enhanced catalytic activity which ranked as: CZA>CZG>CZ.

To resolve the electronic promotion effect of Al and Ga on the ZnO phase, a series of varying Al doped ZnO was prepared according to the catalyst preparation *via* co-precipitation. Thermodynamically favoured segregation into an aluminium-rich crystalline zaccagnaite side-phase, $\text{Zn}_4\text{Al}_2(\text{OH})_{12}(\text{CO}_3) \cdot 3\text{H}_2\text{O}$, was observed at aluminium contents higher than $x_{\text{Al}} = 0.02$, for long ageing times and after hydrothermal treatment. This side-phase was found to be responsible for a non-uniform aluminium distribution in the precursors and later in the calcined samples. Still, the results suggest that hydrozincite can take up aluminium in an octahedral coordination even for $x_{\text{Al}} > 0.02$ leading to the formation of defects due to charge compensation in the hydroxycarbonate. Calcination at 320 °C leads to formation of zinc oxide as the only crystalline phase, but electron microscopy and ^{27}Al NMR revealed non-uniform aluminium distribution and presence of diverse aluminium species for a doping level of $x_{\text{Al}} = 0.03$ and larger. Such complexity is based on the ex-zaccagnaite regions, which were found to segregate into nano-crystalline zinc oxide with an aligned crystallographic orientation and into amorphous alumina. At lower aluminium contents, however, the dopant was found preferably on the zinc sites of the zinc oxide lattice based on the $\text{Al}_{\text{Zn}}^{\bullet}$ signal dominating the NMR spectra. The solubility limit regarding this species was determined to be approximately $x_{\text{Al}} = 0.013$ or 1.3% of all metal cations. Annealing experiments showed that aluminium was kinetically trapped on the $\text{Al}_{\text{Zn}}^{\bullet}$ site and segregated into zinc oxide and ZnAl_2O_4 spinel upon further heating.

This shows that lower calcination temperatures such as applied in catalyst synthesis favour the aluminium doping on that specific site.

The doping of ZnO with Ga was performed like the ZnO:Al investigation. Co-precipitation was performed at lower Temperatures and with short ageing time. The zaccagnaite-like side phase was determined for Ga contents $>6\%$, which was almost double of the aluminium content. A careful analysis with infrared and Raman spectroscopy confirmed structural changes by induced defects and a distorted hydrozincite lattice, as a result of charge compensation. The calcination at relative low Temperature, as applied for methanol synthesis catalyst preparation, led to the decomposition of the precursor to a zinc oxide without any additional side phase determined by PXRD. The structural change because of the incorporated gallium ion was beside the reflection broadening of the PXRD pattern additionally by Raman spectroscopy confirmed. In both analytics an effect on the c-axis of the ZnO structure was determined due to Ga incorporation. The chemical environment of the Ga ion was determined by ^{71}Ga NMR spectroscopy and has shown, that up to $x_{\text{Ga}} = 0.06$ no five-fold or six-fold coordinated Ga was present. No conclusion on the Ga incorporated onto a Zn position in the ZnO lattice could be drawn, due to line broadening of the signals and the missing differentiation of the two expected signals for the four-fold coordinated Ga ion. From UV-Vis spectroscopy, a band gap of around 3.3 eV was determined for the ZnO:Ga. Up to $x_{\text{Ga}} = 0.04$, the band gap could be considered as equal for the lower doped ZnO and supports a solubility limit around this concentration ($x_{\text{Ga}} = 0.04$). A further increase in Ga content resulted in an increased band gap, which can be explained either by a Burstein-Moss effect or by isolating effects of the decomposed Ga enriched zaccagnaite-like side phase present in samples for $x_{\text{Ga}} > 0.06$.

Beside the secondary promotion effect, the active site in methanol synthesis was investigated on an industrial type of Cu/ZnO:Al catalyst by a combination of experimental and theoretical studies of the poisoning effect of ammonia for the conversion of syngas ($\text{CO}_2/\text{CO}/\text{H}_2$). The catalyst was prepared via co-precipitation and represented in its characteristics an industrial methanol formation catalyst. The poisoning effect during methanol synthesis from a CO_2 containing feed gas, reported earlier was reproduced and the interpretation of the experimental results were supported by DFT calculations. Extensive DFT calculations on two active site models representative of copper and Cu/ZnO catalysts were performed. The study confirms but also extends the hypothesis of Laudenschleger *et al.*,²⁹ such that now a possible intermediate blocking the active sites could be proposed. This investigation shows that carbamate can form readily from the reaction of NH_2^* and CO_2 but is a stable species that undergoes further hydrogenation rather slowly, explaining its strongly poisoning effect. Importantly, NH_2^* can

only be formed in the presence of surface oxygen species, such that this effect is not observed for pure CO feeds. TMA as well as ammonia itself do not bind strongly to the surface, hence TMA is not as poisonous as ammonia. The parallel reaction of ethylene hydrogenation further demonstrated that hydrogen can be activated readily under these conditions, both for the hydrogenation of ethylene and CO₂, and is thus not the rate determining step.

Beside the investigation of copper in methanol synthesis, it was also used as a promotor in Fischer-Tropsch to improve the higher alcohol synthesis with cobalt as the FTS active metal. The investigation of a varying copper contents in cobalt rich ratios of Co:Cu/ZnAl₂O₄ catalysts have demonstrated, that the addition of copper prevents coke formation on cobalt catalysts and enhances the selectivity towards alcohols at temperatures below 250 °C in Cu-Co/ZnAl₂O₄ catalysts. Bi-metallic catalysts showed a clearly different behaviour, which was beneficial for HAS, compared to the pure copper or cobalt catalysts. The PXRD data suggests a possible alloy formation of Cu and Co in the ccp phase, which would imply a close interaction of both metals. Relatively low pressure (20 bar) and temperatures above 225 °C result in complete conversion at an GHSV of around 2800 h⁻¹ in a synthesis gas stream of a H₂:CO ratio of 4. These process conditions were found not to result in an increase in the HAS activity of the catalysts. Compared to literature reports, the selectivity to higher alcohols of the studied catalysts was low at otherwise high activity. However, a copper content of already 12.5 at%, which is accompanied by a significant drop of the domain size of the ccp phase compared to the pure cobalt catalyst, has a positive effect on the alcohol selectivity from CO hydrogenation and on the mitigation of coking. Nevertheless, the hydrocarbon selectivity was found to be always predominant in this hydrogen-rich synthesis gas. Another important effect of copper was the facilitated reduction of the cobalt oxide. The activity of the pure copper catalyst was enhanced, and methanol formation was improved after a treatment in reducing gas at 380 °C. These results demonstrated the necessity of higher temperatures to reach a completely activated state of this Cu/ZnAl₂O₄ catalyst from a hydrotalcite precursor. The activation of the pure cobalt catalyst was also not complete prior to the catalytic experiment and proceeded after each temperature or pressure variation. Even though significant coke formation was found for this catalyst, it showed – just like the other hydrotalcite-derived catalysts studied – a stable catalytic performance after it was fully activated up to 165 h on stream.

Regarding the trivalent cation doping of the state-of-the-art Cu/ZnO catalyst, a combination of Al and Ga are recommended in investigation. The study of the solubility limit of Al and Ga in ZnO give evidence, that a higher fraction of Ga maybe incorporated into the ZnO structure without additional side phases. Therefore, an increased amount of Ga is expected to improve

the catalyst activity in a manner as it was found for CZA. However, if Al improves catalyst stability but Ga can be the better dopant regarding solubility in ZnO, a combination of the trivalent cations are expected to improve the catalyst performance by similar improvement of the catalyst stability. To investigate the doping effect and to strengthen the electronic promotion effect of the trivalent cation, the doped ZnO should be used as model supports for a methanol synthesis catalyst. Ideally, the impregnation of the doped ZnO with colloidal Cu, targeting similar concentrations regarding the surface area, can allow to discriminate the role of Al and Ga in the methanol catalyst in a more advanced way. From the results of this thesis, it is expected, that with increasing doping level up to the solubility limit ($x_{\text{Al}} = 0.013$ and $x_{\text{Ga}} \approx 0.04$) the intrinsic methanol activity of the catalyst increases. However, regarding the concentration of around 10% Al and Ga (based on zinc and Al or Ga) in the state-of-the-art catalyst, beside the doping effects also sterically effects are expected to increase the copper particle stability. Therefore, considering the ideal support investigation it would be expected, that a concentration of the secondary promotor (Al or Ga) above the solubility limit has the highest methanol formation rate because of the optimum doping effect and the simultaneously optimum sterically effect, provided as a thermodynamic stable spinel phase, avoiding Cu particle sintering. This research can also be conducted by using Co and Cu as active metals and to investigate the promotor species in other reactions like the higher alcohol synthesis. Beside the effects in catalysis the effects in ZnO dopant can be further investigated. If Al and Ga are used together as ZnO dopants, maybe a higher fraction of trivalent cation can be incorporated into the ZnO structure or one of this metal ions will be more favourable incorporated into the targeted ZnO phase whereas the other species segregates as structural catalyst promotor a top of the surface. This investigation could improve the knowledge about the effect of the secondary promotors Al and Ga on the primary promotor ZnO in methanol synthesis or in other hydrogenation reactions.

10 References

1. G. Bozzano and F. Manenti, *Progress in Energy and Combustion Science*, 2016, **56**, 71-105.
2. K. Räuchle, L. Plass, H. J. Wernicke and M. Bertau, *Energy Technology*, 2016, **4**, 193-200.
3. D. Sheldon, *Johnson Matthey Technology Review*, 2017, **61**, 172-182.
4. J. Bart and R. Sneed, *Catalysis Today*, 1987, **2**, 1-124.
5. F. Dalena, A. Senatore, A. Marino, A. Gordano, M. Basile and A. Basile, in *Methanol*, eds. A. Basile and F. Dalena, Elsevier, 2018, DOI: 10.1016/b978-0-444-63903-5.00001-7, pp. 3-28.
6. M. S. Spencer, *Topics in Catalysis*, 1999, **8**, 259-266.
7. T. Ressler, B. L. Kniep, I. Kasatkin and R. Schlögl, *Angew Chem Int Ed Engl*, 2005, **44**, 4704-4707.
8. M. Behrens and R. Schlögl, *Zeitschrift Fur Anorganische Und Allgemeine Chemie*, 2013, **639**, 2683-2695.
9. A. Alvarez, A. Bansode, A. Urakawa, A. V. Bavykina, T. A. Wezendonk, M. Makkee, J. Gascon and F. Kapteijn, *Chem Rev*, 2017, **117**, 9804-9838.
10. M. Behrens, *Journal of Catalysis*, 2009, **267**, 24-29.
11. G. J. Millar, I. H. Holm, P. J. R. Uwins and J. Drennan, *J Chem Soc Faraday T*, 1998, **94**, 593-600.
12. K. C. Waugh, *Catalysis Today*, 1992, **15**, 51-75.
13. T. Fujitani, M. Saito, Y. Kanai, T. Kakumoto, T. Watanabe, J. Nakamura and T. Uchijima, *Catalysis Letters*, 1994, **25**, 271-276.
14. G. Behrendt, B. Mockenhaupt, N. Prinz, M. Zobel, E. J. Ras and M. Behrens, *Chemcatchem*, 2022, **14**, e202200299.
15. K. Klier, in *Advances in Catalysis*, eds. D. D. Eley, H. Pines and P. B. Weisz, Academic Press, 1982, vol. 31, pp. 243-313.
16. F. Studt, M. Behrens, E. L. Kunkes, N. Thomas, S. Zander, A. Tarasov, J. Schumann, E. Frei, J. B. Varley, F. Abild-Pedersen, J. K. Nørskov and R. Schlögl, *Chemcatchem*, 2015, **7**, 1105-1111.
17. H. Wilmer and O. Hinrichsen, *Catalysis Letters*, 2002, **82**, 117-122.
18. P. L. Hansen, J. B. Wagner, S. Helveg, J. R. Rostrup-Nielsen, B. S. Clausen and H. Topsøe, *Science*, 2002, **295**, 2053-2055.
19. C. V. Ovesen, B. S. Clausen, J. Schiotz, P. Stoltze, H. Topsøe and J. K. Nørskov, *Journal of Catalysis*, 1997, **168**, 133-142.
20. T. Lunkenbein, J. Schumann, M. Behrens, R. Schlögl and M. G. Willinger, *Angew Chem Int Ed Engl*, 2015, **54**, 4544-4548.
21. N. Y. Topsøe and H. Topsøe, *Topics in Catalysis*, 1999, **8**, 267-270.
22. M. Behrens, F. Studt, I. Kasatkin, S. Kühl, M. Havecker, F. Abild-Pedersen, S. Zander, F. Girgsdies, P. Kurr, B. L. Kniep, M. Tovar,

- R. W. Fischer, J. K. Norskov and R. Schlögl, *Science*, 2012, **336**, 893-897.
23. L. Pandit, A. Boubnov, G. Behrendt, B. Mockenhaupt, C. Chowdhury, J. Jelic, A.-L. Hansen, E. Saraci, E.-J. Ras, M. Behrens, F. Studt and J.-D. Grunwaldt, *ChemCatChem*, 2021, DOI: 10.1002/cctc.202100692.
24. R. Dalebout, L. Barberis, G. Totarella, S. J. Turner, C. La Fontaine, F. M. de Groot, X. Carrier, A. M. van der Eerden, F. Meirer and P. E. de Jongh, *ACS Catalysis*, 2022, **12**, 6628-6639.
25. A. Beck, M. Zabilskiy, M. A. Newton, O. Safonova, M. G. Willinger and J. A. van Bokhoven, *Nature Catalysis*, 2021, **4**, 488-497.
26. S. Kattel, P. J. Ramirez, J. G. Chen, J. A. Rodriguez and P. Liu, *Science*, 2017, **355**, 1296-1299.
27. J. Nakamura, T. Fujitani, S. Kuld, S. Helveg, I. Chorkendorff and J. Sehested, *Science*, 2017, **357**, eaan8074.
28. S. Kattel, P. J. Ramirez, J. G. Chen, J. A. Rodriguez and P. Liu, *Science*, 2017, **357**, eaan8210.
29. D. Laudenschleger, H. Ruland and M. Muhler, *Nat Commun*, 2020, **11**, 3898.
30. M. B. Fichtl, D. Schlereth, N. Jacobsen, I. Kasatkin, J. Schumann, M. Behrens, R. Schlögl and O. Hinrichsen, *Applied Catalysis a-General*, 2015, **502**, 262-270.
31. T. Lunkenbein, F. Girgsdies, T. Kandemir, N. Thomas, M. Behrens, R. Schlögl and E. Frei, *Angew Chem Int Ed Engl*, 2016, **55**, 12708-12712.
32. M. V. Twigg and M. S. Spencer, *Topics in Catalysis*, 2003, **22**, 191-203.
33. C. Baltès, S. Vukojevic and F. Schuth, *Journal of Catalysis*, 2008, **258**, 334-344.
34. M. Behrens, S. Zander, P. Kurr, N. Jacobsen, J. Senker, G. Koch, T. Ressler, R. W. Fischer and R. Schlögl, *J Am Chem Soc*, 2013, **135**, 6061-6068.
35. M. Behrens, G. Lolli, N. Muratova, I. Kasatkin, M. Havecker, R. N. d'Alnoncourt, O. Storcheva, K. Kohler, M. Muhler and R. Schlögl, *Phys Chem Chem Phys*, 2013, **15**, 1374-1381.
36. M. Kurtz, N. Bauer, C. Buscher, H. Wilmer, O. Hinrichsen, R. Becker, S. Rabe, K. Merz, M. Driess, R. A. Fischer and M. Muhler, *Catalysis Letters*, 2004, **92**, 49-52.
37. J. Schumann, M. Eichelbaum, T. Lunkenbein, N. Thomas, M. C. Álvarez Galván, R. Schlögl and M. Behrens, *ACS Catalysis*, 2015, **5**, 3260-3270.
38. H. Morkoç and Ü. Özgür, *Zinc Oxide: Fundamentals, Materials and Device Technology*, Wiley, 2008.

39. K. Ellmer, A. Klein and B. Rech, *Transparent Conductive Zinc Oxide: Basics and Applications in Thin Film Solar Cells*, Springer Berlin Heidelberg, 2007.
40. T. Fujitani, M. Saito, Y. Kanai, T. Watanabe, J. Nakamura and T. Uchijima, *Chemistry Letters*, 1994, **23**, 1877-1880.
41. R. Guil-Lopez, N. Mota, J. Llorente, E. Millan, B. Pawelec, R. Garcia, J. L. G. Fierro and R. M. Navarro, *Catalysis Today*, 2020, **355**, 870-881.
42. J. Strunk, K. Kaehler, X. Y. Xia, M. Comotti, F. Schuth, T. Reinecke and M. Muhler, *Applied Catalysis a-General*, 2009, **359**, 121-128.
43. S. Polarz, J. Strunk, V. Ischenko, M. W. van den Berg, O. Hinrichsen, M. Muhler and M. Driess, *Angew Chem Int Ed Engl*, 2006, **45**, 2965-2969.
44. M. Heenemann, M. M. Millet, F. Girgsdies, M. Eichelbaum, T. Risse, R. Schlögl, T. Jones and E. Frei, *Acs Catalysis*, 2020, **10**, 5672-5680.
45. D. W. Readey and G. C. Kuczynski, *Journal of the American Ceramic Society*, 1966, **49**, 26-+.
46. D. P. Butt, Y. Park and T. N. Taylor, *Journal of Nuclear Materials*, 1999, **264**, 71-77.
47. S. Penner, H. Lorenz, W. Jochum, M. Stoger-Pollach, D. Wang, C. Rameshan and B. Klotzer, *Applied Catalysis a-General*, 2009, **358**, 193-202.
48. J. Friedrich and T. Damassa, 2014.
49. D. Damiani, J. T. Litynski, H. G. McIlvried, D. M. Vikara and R. D. Srivastava, *Greenhouse Gases-Science and Technology*, 2012, **2**, 9-19.
50. G. Centi, E. A. Quadrelli and S. Perathoner, *Energy & Environmental Science*, 2013, **6**, 1711-1731.
51. M. Bowker, *ChemCatChem*, 2019, **11**, 4238-4246.
52. X. Y. Xi, F. Zeng, H. Zhang, X. F. Wu, J. Ren, T. Bisswanger, C. Stampfer, J. P. Hofmann, R. Palkovits and H. J. Heeres, *Acs Sustainable Chemistry & Engineering*, 2021, **9**, 6235-6249.
53. A. Jess and P. Wasserscheid, *Chemical Technology: An Integral Textbook*, Wiley, 2013.
54. K. Stangeland, H. L. Li and Z. X. Yu, *Industrial & Engineering Chemistry Research*, 2018, **57**, 4081-4094.
55. F. Studt, I. Sharafutdinov, F. Abild-Pedersen, C. F. Elkjaer, J. S. Hummelshøj, S. Dahl, I. Chorkendorff and J. K. Nørskov, *Nat Chem*, 2014, **6**, 320-324.
56. T. P. Araújo, A. Shah, C. Mondelli, J. A. Stewart, D. Curulla Ferré and J. Pérez-Ramírez, *Applied Catalysis B: Environmental*, 2021, **285**, 119878.

57. J. Schumann, T. Lunkenbein, A. Tarasov, N. Thomas, R. Schlögl and M. Behrens, *Chemcatchem*, 2014, **6**, 2889-2897.
58. M. Sahibzada, I. S. Metcalfe and D. Chadwick, *Journal of Catalysis*, 1998, **174**, 111-118.
59. J. T. Sun, I. S. Metcalfe and M. Sahibzada, *Industrial & Engineering Chemistry Research*, 1999, **38**, 3868-3872.
60. J. D. Grunwaldt, A. M. Molenbroek, N. Y. Topsoe, H. Topsoe and B. S. Clausen, *Journal of Catalysis*, 2000, **194**, 452-460.
61. G. C. Chinchin, P. J. Denny, D. G. Parker, M. S. Spencer and D. A. Whan, *Applied Catalysis*, 1987, **30**, 333-338.
62. J. Schumann, A. Tarasov, N. Thomas, R. Schlögl and M. Behrens, *Applied Catalysis a-General*, 2016, **516**, 117-126.
63. I. Sharafutdinov, C. F. Elkjaer, H. W. P. de Carvalho, D. Gardini, G. L. Chiarello, C. D. Damsgaard, J. B. Wagner, J. D. Grunwaldt, S. Dahl and I. Chorkendorff, *Journal of Catalysis*, 2014, **320**, 77-88.
64. C. L. Chiang, K. S. Lin and Y. G. Lin, *Topics in Catalysis*, 2017, **60**, 685-696.
65. O. Martin, A. J. Martin, C. Mondelli, S. Mitchell, T. F. Segawa, R. Hauert, C. Drouilly, D. Curulla-Ferre and J. Perez-Ramirez, *Angew Chem Int Ed Engl*, 2016, **55**, 6261-6265.
66. T. P. Araújo, A. Shah, C. Mondelli, J. A. Stewart, D. C. Ferré and J. Pérez-Ramírez, *Applied Catalysis B: Environmental*, 2021, **285**, 119878.
67. A. Cao, Z. B. Wang, H. Li and J. K. Norskov, *Acs Catalysis*, 2021, **11**, 1780-1786.
68. S. Ghosh, J. Sebastian, L. Olsson and D. Creaser, *Chemical Engineering Journal*, 2021, **416**, 129120.
69. M. B. Fichtl, J. Schumann, I. Kasatkin, N. Jacobsen, M. Behrens, R. Schlögl, M. Muhler and O. Hinrichsen, *Angew Chem Int Ed Engl*, 2014, **53**, 7043-7047.
70. V. Garcilaso, J. Barrientos, L. F. Bobadilla, O. H. Laguna, M. Boutonnet, M. A. Centeno and J. A. Odriozola, *Renewable Energy*, 2019, **132**, 1141-1150.
71. V. R. Calderone, N. R. Shiju, D. C. Ferre and G. Rothenberg, *Green Chemistry*, 2011, **13**, 1950-1959.
72. K. G. Fang, D. B. Li, M. G. Lin, M. L. Xiang, W. Wei and Y. H. Sun, *Catalysis Today*, 2009, **147**, 133-138.
73. S. Gehrman and N. Tenhumberg, *Chemie Ingenieur Technik*, 2020, **92**, 1444-1458.
74. H. Schulz, *Applied Catalysis a-General*, 1999, **186**, 3-12.
75. M. Martinelli, M. K. Gnanamani, S. LeViness, G. Jacobs and W. D. Shafer, *Applied Catalysis a-General*, 2020, **608**, 117740.
76. H. Jahangiri, J. Bennett, P. Mahjoubi, K. Wilson and S. Gu, *Catalysis Science & Technology*, 2014, **4**, 2210-2229.

77. M. Ao, G. H. Pham, J. Sunarso, M. O. Tade and S. M. Liu, *Acs Catalysis*, 2018, **8**, 7025-7050.
78. K. J. Smith and R. B. Anderson, *Canadian Journal of Chemical Engineering*, 1983, **61**, 40-45.
79. R. B. Anderson, J. Feldman and H. H. Storch, *Industrial and Engineering Chemistry*, 1952, **44**, 2418-2424.
80. A. J. Medford, A. C. Lausche, F. Abild-Pedersen, B. Temel, N. C. Schjodt, J. K. Nørskov and F. Studt, *Topics in Catalysis*, 2014, **57**, 135-142.
81. V. Subramani and S. K. Gangwal, *Energy & Fuels*, 2008, **22**, 814-839.
82. A. Cao, J. Schumann, T. Wang, L. Zhang, J. Xiao, P. Bothra, Y. Liu, F. Abild-Pedersen and J. K. Nørskov, *ACS Catalysis*, 2018, **8**, 10148-10155.
83. J. A. Dalmon, P. Chaumette and C. Mirodatos, *Catalysis Today*, 1992, **15**, 101-127.
84. A. Cao, G. L. Liu, Y. Z. Yue, L. H. Zhang and Y. Liu, *Rsc Advances*, 2015, **5**, 58804-58812.
85. G. Prieto, S. Beijer, M. L. Smith, M. He, Y. Au, Z. Wang, D. A. Bruce, K. P. de Jong, J. J. Spivey and P. E. de Jongh, *Angew Chem Int Ed Engl*, 2014, **53**, 6397-6401.
86. T. Nishizawa and K. Ishida, *Bulletin of Alloy Phase Diagrams*, 1984, **5**, 161-165.
87. J. Anton, J. Nebel, H. Q. Song, C. Froese, P. Weide, H. Ruland, M. Muhler and S. Kaluza, *Journal of Catalysis*, 2016, **335**, 175-186.
88. J. Anton, J. Nebel, C. Gobel, T. Gabrysch, H. Q. Song, C. Froese, H. Ruland, M. Muhler and S. Kaluza, *Topics in Catalysis*, 2016, **59**, 1361-1370.
89. K. Sun, Y. Wu, M. Tan, L. Wang, G. Yang, M. Zhang, W. Zhang and Y. Tan, *ChemCatChem*, 2019, **11**, 2695-2706.
90. I. C. T. Have, J. J. G. Kromwijk, M. Monai, D. Ferri, E. B. Sterk, F. Meirer and B. M. Weckhuysen, *Nat Commun*, 2022, **13**, 324.
91. A. Wolf, A. Jess and C. Kern, *Chemical Engineering & Technology*, 2016, **39**, 1040-1048.
92. L. Pastor-Pérez, F. Baibars, E. Le Sache, H. Arellano-García, S. Gu and T. R. Reina, *Journal of CO2 Utilization*, 2017, **21**, 423-428.
93. M. S. Spencer, *Catalysis Letters*, 1995, **32**, 9-13.
94. C. Á. Galván, J. Schumann, M. Behrens, J. L. G. Fierro, R. Schlögl and E. Frei, *Applied Catalysis B: Environmental*, 2016, **195**, 104-111.
95. J. Nakamura, T. Uchijima, Y. Kanai and T. Fujitani, *Catalysis Today*, 1996, **28**, 223-230.
96. S. Fujita, M. Usui and N. Takezawa, *Journal of Catalysis*, 1992, **134**, 220-225.

97. A. M. Bahmanpour, F. Heroguel, M. Kilic, C. J. Baranowski, P. Schouwink, U. Rothlisberger, J. S. Luterbacher and O. Krocher, *Applied Catalysis B-Environmental*, 2020, **266**, 118669.
98. R. A. Hadden, P. J. Lambert and C. Ranson, *Applied Catalysis a-General*, 1995, **122**, L1-L4.
99. G. C. Chinchin, K. C. Waugh and D. A. Whan, *Applied Catalysis*, 1986, **25**, 101-107.
100. R. M. Dell, F. S. Stone and P. F. Tiley, *Transactions of the Faraday Society*, 1953, **49**, 195-201.
101. J. J. F. Scholten and J. A. Konvalinka, *Transactions of the Faraday Society*, 1969, **65**, 2465-2473.
102. O. Hinrichsen, T. Genger and M. Muhler, *Chemical Engineering & Technology*, 2000, **23**, 956-959.
103. G. C. Chinchin, C. M. Hay, H. D. Vandervell and K. C. Waugh, *Journal of Catalysis*, 1987, **103**, 79-86.
104. J. W. Evans, M. S. Wainwright, A. J. Bridgewater and D. J. Young, *Applied Catalysis*, 1983, **7**, 75-83.
105. B. Dvořák and J. Pašek, *Journal of Catalysis*, 1970, **18**, 108-114.
106. T. J. Osinga, B. Linsen and W. Van Beek, *Journal of Catalysis*, 1967, **7**, 277-279.
107. M. Muhler, L. P. Nielsen, E. Törnqvist, B. S. Clausen and H. Topsøe, *Catalysis letters*, 1992, **14**, 241-249.
108. T. Genger, O. Hinrichsen and M. Muhler, *Catalysis Letters*, 1999, **59**, 137-141.
109. J. Tabatabaei, B. H. Sakakini, M. J. Watson and K. C. Waugh, *Catalysis Letters*, 1999, **59**, 143-149.
110. R. Naumann d'Alnoncourt, B. Graf, X. Xia and M. Muhler, *Journal of Thermal Analysis and Calorimetry*, 2008, **91**, 173-179.
111. F. Yang, Y. Choi, P. Liu, J. Hrbek and J. A. Rodriguez, *The Journal of Physical Chemistry C*, 2010, **114**, 17042-17050.
112. S. Kuld, C. Conradsen, P. G. Moses, I. Chorkendorff and J. Sehested, *Angew Chem Int Ed Engl*, 2014, **53**, 5941-5945.
113. R. Chatterjee, S. Kuld, R. van den Berg, A. L. Chen, W. J. Shen, J. M. Christensen, A. D. Jensen and J. Sehested, *Topics in Catalysis*, 2019, **62**, 649-659.
114. S. Kuld, M. Thorhauge, H. Falsig, C. F. Elkjaer, S. Helveg, I. Chorkendorff and J. Sehested, *Science*, 2016, **352**, 969-974.
115. G. Ertl, H. Knözinger and J. Weitkamp, *Preparation of solid catalysts*, John Wiley & Sons, 2008.
116. A. F. Wells, *Acta Crystallographica*, 1951, **4**, 200-204.
117. K. Momma and F. Izumi, *Journal of Applied Crystallography*, 2011, **44**, 1272-1276.
118. M. Behrens and F. Girgsdies, *Zeitschrift Fur Anorganische Und Allgemeine Chemie*, 2010, **636**, 919-927.

119. M. Behrens, F. Girgsdies, A. Trunschke and R. Schlögl, *European Journal of Inorganic Chemistry*, 2009, **2009**, 1347-1357.
120. K. P. de Jong, *Synthesis of Solid Catalysts*, Wiley, 2009.
121. S. M. Auerbach, K. A. Carrado and P. K. Dutta, *Handbook of Layered Materials*, Taylor & Francis, 2004.
122. G. M. Lombardo, G. C. Pappalardo, F. Punzo, F. Costantino, U. Costantino and M. Sisani, *European Journal of Inorganic Chemistry*, 2005, **2005**, 5026-5034.
123. M. Bellotto, B. Rebours, O. Clause, J. Lynch, D. Bazin and E. Elkaim, *Journal of Physical Chemistry*, 1996, **100**, 8527-8534.
124. K. Mette, S. Kühn, H. Dudder, K. Kahler, A. Tarasov, M. Muhler and M. Behrens, *Chemcatchem*, 2014, **6**, 100-104.
125. K. Chakrapani, F. Ozcan, K. F. Ortega, T. Machowski and M. Behrens, *Chemelectrochem*, 2018, **5**, 93-100.
126. S. Ghose, *Acta Crystallographica*, 1964, **17**, 1051-1057.
127. J. L. Jambor and G. Pouliot, *The Canadian Mineralogist*, 1965, **8**, 385-389.
128. M. Sahli, Doktorwürde Dissertation, Universität zu Bern, 1953.
129. S. J. Miao, R. N. d'Alnoncourt, T. Reinecke, I. Kasatkin, M. Behrens, R. Schlögl and M. Muhler, *European Journal of Inorganic Chemistry*, 2009, **2009**, 910-921.
130. A. Janotti and C. G. Van de Walle, *Reports on Progress in Physics*, 2009, **72**, 126501.
131. S. C. Abrahams and J. L. Bernstein, *Acta Crystallographica Section B Structural Crystallography and Crystal Chemistry*, 1969, **25**, 1233-1236.
132. A. Kolodziejczak-Radzimska and T. Jesionowski, *Materials*, 2014, **7**, 2833-2881.
133. H. von Wenckstern, H. Schmidt, M. Brandt, A. Lajn, R. Pickenhain, M. Lorenz, M. Grundmann, D. M. Hofmann, A. Polity, B. K. Meyer, H. Saal, M. Binnewies, A. Börger, K. D. Becker, V. A. Tikhomirov and K. Jug, *Progress in Solid State Chemistry*, 2009, **37**, 153-172.
134. V. Ischenko, S. Polarz, D. Grote, V. Stavarache, K. Fink and M. Driess, *Adv Funct Mater*, 2005, **15**, 1945-1954.
135. T. Kita, Y. Harada and S. Asahi, *Energy Conversion Efficiency of Solar Cells*, Springer Singapore, 2019.
136. M. D. McCluskey and S. J. Jokela, *J Appl Phys*, 2009, **106**, 071101.
137. D. G. Avery, D. W. Goodwin, W. D. Lawson and T. S. Moss, *P Phys Soc Lond B*, 1954, **67**, 761-767.
138. E. Burstein, *Physical Review*, 1954, **93**, 632-633.
139. A. Walsh, J. L. F. Da Silva and S. H. Wei, *Physical Review B*, 2008, **78**, 075211.
140. Y. Ishikawa, K. Wada, D. D. Cannon, J. F. Liu, H. C. Luan and L. C. Kimerling, *Applied Physics Letters*, 2003, **82**, 2044-2046.

141. Y. L. Zhang, Y. Yang, J. H. Zhao, R. Q. Tan, W. Y. Wang, P. Cui and W. J. Song, *J Mater Sci*, 2011, **46**, 774-780.
142. R. Noriega, J. Rivnay, L. Goris, D. Kalblein, H. Klauk, K. Kern, L. M. Thompson, A. C. Palke, J. F. Stebbins, J. R. Jokisaari, G. Kusinski and A. Salleo, *J Appl Phys*, 2010, **107**.
143. Y. S. Avadhut, J. Weber, E. Hammarberg, C. Feldmann and J. Schmedt auf der Günne, *Phys Chem Chem Phys*, 2012, **14**, 11610-11625.
144. M. H. Yoon, S. H. Lee, H. L. Park, H. K. Kim and M. S. Jang, *J Mater Sci Lett*, 2002, **21**, 1703-1704.
145. K. Shirouzu, T. Ohkusa, M. Hotta, N. Enomoto and J. Hojo, *J Ceram Soc Jpn*, 2007, **115**, 254-258.
146. Y. Okuhara, T. Kato, H. Matsubara, N. Isu and M. Takata, *Thin Solid Films*, 2011, **519**, 2280-2286.
147. S. B. Majumder, M. Jain, P. S. Dobal and R. S. Katiyar, *Mat Sci Eng B-Solid*, 2003, **103**, 16-25.
148. C. Schilling, M. Zahres, C. Mayer and M. Winterer, *J Nanopart Res*, 2014, **16**, 2506.
149. H. Serier, M. Gaudon and M. Menetrier, *Solid State Sciences*, 2009, **11**, 1192-1197.
150. D. I. f. N. e. V. (DIN), *DIN 66136-1: Bestimmung des Dispersionsgrades von Metallen durch Chemisorption-Teil 1: Grundlagen*, Beuth Verlag GmbH, Berlin, 2017.
151. G. A. Olah, G. K. Prakash and A. Goeppert, *J Am Chem Soc*, 2011, **133**, 12881-12898.
152. V. Palma, E. Meloni, C. Ruocco, M. Martino and A. Ricca, in *Methanol*, eds. A. Basile and F. Dalena, Elsevier, 2018, DOI: 10.1016/b978-0-444-63903-5.00002-9, pp. 29-51.
153. M. Behrens, *Catalysis Today*, 2015, **246**, 46-54.
154. L. Pandit, A. Boubnov, G. Behrendt, B. Mockenhaupt, C. Chowdhury, J. Jelic, A. L. Hansen, E. Saraci, E. J. Ras, M. Behrens, F. Studt and J. D. Grunwaldt, *Chemcatchem*, 2021, **13**, 4120-4132.
155. B. Mockenhaupt, P. Schwiderowski, J. Jelic, F. Studt, M. Muhler and M. Behrens, *Journal of Physical Chemistry C*, 2023, **127**, 3497-3505.
156. J. Nakamura, I. Nakamura, T. Uchijima, T. Watanabe and T. Fujitani, in *Studies in Surface Science and Catalysis*, eds. J. W. Hightower, W. Nicholas Delgass, E. Iglesia and A. T. Bell, Elsevier, 1996, vol. 101, pp. 1389-1399.
157. E. Frei, A. Gaur, H. Lichtenberg, L. Zwiener, M. Scherzer, F. Girgsdies, T. Lunkenbein and R. Schlögl, *Chemcatchem*, 2020, **12**, 4029-4033.
158. A. Zimina, K. Dardenne, M. A. Denecke, D. E. Doronkin, E. Huttel, H. Lichtenberg, S. Mangold, T. Pruessmann, J. Rothe, T.

- Spangenberg, R. Steininger, T. Vitova, H. Geckeis and J. D. Grunwaldt, *Review of Scientific Instruments*, 2017, **88**.
159. B. Ravel and M. Newville, *J Synchrotron Radiat*, 2005, **12**, 537-541.
160. M. Newville, 2013.
161. G. Kresse and J. Furthmuller, *Computational Materials Science*, 1996, **6**, 15-50.
162. G. Kresse and J. Furthmuller, *Phys Rev B Condens Matter*, 1996, **54**, 11169-11186.
163. J. Wellendorff, K. T. Lundgaard, A. Mogelhoj, V. Petzold, D. D. Landis, J. K. Nørskov, T. Bligaard and K. W. Jacobsen, *Physical Review B*, 2012, **85**, 235149.
164. G. Kresse and D. Joubert, *Physical Review B*, 1999, **59**, 1758-1775.
165. P. E. Blöchl, *Phys Rev B Condens Matter*, 1994, **50**, 17953-17979.
166. H. J. Monkhorst and J. D. Pack, *Physical Review B*, 1976, **13**, 5188-5192.
167. M. Kurtz, H. Wilmer, T. Genger, O. Hinrichsen and M. Muhler, *Catalysis Letters*, 2003, **86**, 77-80.
168. I. Kasatkin, P. Kurr, B. Kniep, A. Trunschke and R. Schlögl, *Angew Chem Int Ed Engl*, 2007, **46**, 7324-7327.
169. J. Schumann, J. Krohnert, E. Frei, R. Schlögl and A. Trunschke, *Topics in Catalysis*, 2017, **60**, 1735-1743.
170. V. Schott, H. Oberhofer, A. Birkner, M. Xu, Y. Wang, M. Muhler, K. Reuter and C. Woll, *Angew Chem Int Ed Engl*, 2013, **52**, 11925-11929.
171. N. Topsøe, *Journal of Molecular Catalysis A: Chemical*, 1999, **141**, 95-105.
172. B. Mockenhaupt, J. K. Wied, S. Mangelsen, U. Schurmann, L. Kienle, J. Schmedt Auf der Günne and M. Behrens, *Dalton Trans*, 2023, **52**, 5321-5335.
173. L. Pandit, M. A. Serrer, E. Saraçı, A. Boubnov and J. D. Grunwaldt, *Chemistry-Methods*, 2022, **2**, e202100078.
174. M. V. Twigg and M. S. Spencer, *Applied Catalysis a-General*, 2001, **212**, 161-174.
175. C. E. Quincoces, N. E. Amadeo and M. G. González, in *Studies in Surface Science and Catalysis*, eds. C. H. Bartholomew and G. A. Fuentes, Elsevier, 1997, vol. 111, pp. 535-541.
176. M. S. Spencer, *Nature*, 1986, **323**, 685-687.
177. S. Magdassi, M. Grouchko and A. Kamyshny, *Materials*, 2010, **3**, 4626-4638.
178. K. Klier, *Journal of Catalysis*, 1982, **74**, 343-360.
179. O. Martin and J. Perez-Ramirez, *Catalysis Science & Technology*, 2013, **3**, 3343-3352.
180. J. Thrane, S. Kuld, N. D. Nielsen, A. D. Jensen, J. Sehested and J. M. Christensen, *Angew Chem Int Ed Engl*, 2020, **59**, 18189-18193.

181. A. Urakawa, *Nature Catalysis*, 2021, **4**, 447-448.
182. V. Srikant and D. R. Clarke, *J Appl Phys*, 1998, **83**, 5447-5451.
183. K. Davis, R. Yarbrough, M. Froeschle, J. White and H. Rathnayake, *RSC Adv*, 2019, **9**, 14638-14648.
184. M. Izaki and T. Omi, *Applied Physics Letters*, 1996, **68**, 2439-2440.
185. A. Arif, O. Belahssen, S. Gareh and S. Benramache, *Journal of Semiconductors*, 2015, **36**.
186. A. B. Djuricic and Y. H. Leung, *Small*, 2006, **2**, 944-961.
187. K. Hagedorn, W. Li, Q. Liang, S. Dilger, M. Noebels, M. R. Wagner, J. S. Reparaz, A. Dollinger, J. Schmedt auf der Günne, T. Dekorsy, L. Schmidt-Mende and S. Polarz, *Adv Funct Mater*, 2016, **26**, 3424-3437.
188. P. K. Samanta, *Optik*, 2020, **221**.
189. E. R. Martins, *Essentials of Semiconductor Device Physics*, Wiley, 2022.
190. R. P. Huebener, *Conductors, Semiconductors, Superconductors: An Introduction to Solid-State Physics*, Springer International Publishing, 2019.
191. S. Rajendran, M. Naushad, L. C. Ponce and E. Lichtfouse, *Green Photocatalysts for Energy and Environmental Process*, Springer International Publishing, 2019.
192. H. K. Park and J. Heo, *Applied Surface Science*, 2014, **309**, 133-137.
193. I. Y. Kim, S. W. Shin, M. G. Gang, S. H. Lee, K. V. Gurav, P. S. Patil, J. H. Yun, J. Y. Lee and J. H. Kim, *Thin Solid Films*, 2014, **570**, 321-325.
194. K. E. Lee, M. Wang, E. J. Kim and S. H. Hahn, *Curr Appl Phys*, 2009, **9**, 683-687.
195. V. J. Norman, *Australian Journal of Chemistry*, 1969, **22**, 325-329.
196. T. Tsubota, M. Ohtaki, K. Eguchi and H. Arai, *Journal of Materials Chemistry*, 1997, **7**, 85-90.
197. A. Walsh and A. Zunger, *Nat Mater*, 2017, **16**, 964-967.
198. R. Hansson, P. C. Hayes and E. Jak, *Metallurgical and Materials Transactions B-Process Metallurgy and Materials Processing Science*, 2004, **35**, 633-642.
199. N. Roberts, R. P. Wang, A. W. Sleight and W. W. Warren, *Physical Review B*, 1998, **57**, 5734-5741.
200. A. A. Coelho, *Journal of Applied Crystallography*, 2018, **51**, 210-218.
201. R. W. Cheary, A. A. Coelho and J. P. Cline, *J Res Natl Inst Stand Technol*, 2004, **109**, 1-25.
202. R. K. Harris, E. D. Becker, S. M. Cabral de Menezes, R. Goodfellow and P. Granger, *Solid State Nucl Magn Reson*, 2002, **22**, 458-483.

-
203. R. K. Harris, E. D. Becker, S. M. Cabral de Menezes, P. Granger, R. E. Hoffman and K. W. Zilm, *Pure and Applied Chemistry*, 2008, **80**, 59-84.
 204. D. Jardon-Alvarez and J. Schmedt Auf der Günne, *Solid State Nucl Magn Reson*, 2018, **94**, 26-30.
 205. S. Merlino and P. Orlandi, *Am Mineral*, 2001, **86**, 1293-1301.
 206. R. P. Lozano, C. Rossi, A. La Iglesia and E. Matesanz, *Am Mineral*, 2012, **97**, 513-523.
 207. E. J. Riedel, C., *Anorganische Chemie*, Walter de Gruyter, Berlin, New York, 2007.
 208. S. Bette, B. Hinrichsen, D. Pfister and R. E. Dinnebier, *J Appl Crystallogr*, 2020, **53**, 76-87.
 209. S. Mangelsen, B. R. Srinivasan, U. Schurmann, L. Kienle, C. Nather and W. Bensch, *Dalton Transactions*, 2019, **48**, 1184-1201.
 210. R. Sanna, G. De Giudici, A. M. Scorciapino, C. Floris and M. Casu, *Am Mineral*, 2013, **98**, 1219-1226.
 211. D. Stoilova, V. Koleva and V. Vassileva, *Spectrochim Acta A Mol Biomol Spectrosc*, 2002, **58**, 2051-2059.
 212. J. T. Kloprogge, D. Wharton, L. Hickey and R. L. Frost, *Am Mineral*, 2002, **87**, 623-629.
 213. W. Kagunya, R. Baddour-Hadjean, F. Kooli and W. Jones, *Chemical Physics*, 1998, **236**, 225-234.
 214. J. T. Kloprogge and R. L. Frost, *J Solid State Chem*, 1999, **146**, 506-515.
 215. J. T. Kloprogge, L. Hickey and R. L. Frost, *Journal of Raman Spectroscopy*, 2004, **35**, 967-974.
 216. N. Buzgar and A. Apopei, *Journal*, 2014.
 217. S. J. Palmer, R. L. Frost and L. M. Grand, *Journal of Raman Spectroscopy*, 2011, **42**, 1168-1173.
 218. J. P. Cline, M. Leoni, D. Black, A. Henins, J. E. Bonevich, P. S. Whitfield and P. Scardi, *Powder Diffraction*, 2013, **28**, S22-S32.
 219. J. I. Langford, A. Boultif, J. P. Auffredic and D. Louer, *Journal of Applied Crystallography*, 1993, **26**, 22-33.
 220. M. Aguilar-Frutis, M. Garcia and C. Falcony, *Applied Physics Letters*, 1998, **72**, 1700-1702.
 221. A. P. Roth, J. B. Webb and D. F. Williams, *Physical Review B*, 1982, **25**, 7836-7839.
 222. W. Shan, W. Walukiewicz, J. W. Ager, K. M. Yu, H. B. Yuan, H. P. Xin, G. Cantwell and J. J. Song, *Applied Physics Letters*, 2005, **86**.
 223. S. E. Aw, H. S. Tan and C. K. Ong, *J Phys-Condens Mat*, 1991, **3**, 8213-8223.
 224. Y. Gu, I. L. Kuskovsky, M. Yin, S. O'Brien and G. F. Neumark, *Applied Physics Letters*, 2004, **85**, 3833-3835.

225. B. K. Meyer, H. Alves, D. M. Hofmann, W. Kriegseis, D. Forster, F. Bertram, J. Christen, A. Hoffmann, M. Strassburg, M. Dworzak, U. Haboeck and A. V. Rodina, *Phys Status Solidi B*, 2004, **241**, 231-260.
226. C. G. Yang, W. D. Zhu, S. Sen and R. H. R. Castro, *Journal of Physical Chemistry C*, 2019, **123**, 8818-8826.
227. S. Sommer, E. D. Bojesen, N. Lock, H. Kasai, J. Skibsted, E. Nishibori and B. B. Iversen, *Dalton Trans*, 2020, **49**, 13449-13461.
228. H. Serier, A. Demourgues and M. Gaudon, *Inorg Chem*, 2010, **49**, 6853-6858.
229. A. F. Holleman, E. Wiberg and N. Wiberg, *Lehrbuch der anorganischen Chemie*, Walter de Gruyter, 2007.
230. E. W. Forsythe, Y. L. Gao, L. G. Provost and G. S. Tompa, *Journal of Vacuum Science & Technology a-Vacuum Surfaces and Films*, 1999, **17**, 1761-1764.
231. A. de Souza Goncalves, M. R. Davolos, N. Masaki, S. Yanagida, A. Morandeira, J. R. Durrant, J. N. Freitas and A. F. Nogueira, *Dalton Trans*, 2008, DOI: 10.1039/b716724e, 1487-1491.
232. H. S. Das, R. Das, P. K. Nandi, S. Biring and S. K. Maity, *Applied Physics a-Materials Science & Processing*, 2021, **127**, 225.
233. M. Behrens and R. Schlögl, *Zeitschrift für anorganische und allgemeine Chemie*, 2013, **639**, 2683-2695.
234. W. Tong, A. West, K. Cheung, K.-M. Yu and S. C. E. Tsang, *ACS Catalysis*, 2013, **3**, 1231-1244.
235. B. E. Sernelius, K. Berggren, Z. Jin, I. I. Hamberg and C. G. Granqvist, *Phys Rev B Condens Matter*, 1988, **37**, 10244-10248.
236. R. P. Wang, A. W. Sleight and D. Cleary, *Chemistry of Materials*, 1996, **8**, 433-439.
237. G. K. Paul and S. K. Sen, *Materials Letters*, 2002, **57**, 742-746.
238. H. K. C. Timken and E. Oldfield, *Journal of the American Chemical Society*, 1987, **109**, 7669-7673.
239. M. Sato and S. Matsuda, *Z Kristallogr Krist*, 1969, **129**, 405-&.
240. M. C. Hales and R. L. Frost, *Journal of Thermal Analysis and Calorimetry*, 2008, **91**, 855-860.
241. M. C. Hales and R. L. Frost, *Polyhedron*, 2007, **26**, 4955-4962.
242. M. Šćepanović, M. Grujić-Brojčin, K. Vojisavljević, S. Bernik and T. Srećković, *Journal of Raman Spectroscopy*, 2010, **41**, 914-921.
243. R. Cuscó, E. Alarcón-Lladó, J. Ibáñez, L. Artús, J. Jiménez, B. Wang and M. J. Callahan, *Physical Review B*, 2007, **75**, 165202.
244. T. C. Damen, S. P. S. Porto and B. Tell, *Physical Review*, 1966, **142**, 570-&.
245. G. Irmer, *Journal of Raman Spectroscopy*, 2007, **38**, 634-646.
246. H. K. Menrad, *Axel Alkoholkraftstoffe*, 1982.

-
247. S. Verhelst, J. W. G. Turner, L. Sileghem and J. Vancoillie, *Progress in Energy and Combustion Science*, 2019, **70**, 43-88.
 248. G. A. Olah, A. Goepfert and G. K. S. Prakash, *Beyond Oil and Gas: The Methanol Economy*, 2009.
 249. M. Zabilskiy, V. L. Sushkevich, D. Palagin, M. A. Newton, F. Krumeich and J. A. van Bokhoven, *Nature Communications*, 2020, **11**, 2409.
 250. P. Amann, B. Klotzer, D. Degerman, N. Kopfle, T. Gotsch, P. Lomker, C. Rameshan, K. Ploner, D. Bikaljevic, H. Y. Wang, M. Soldemo, M. Shipilin, C. M. Goodwin, J. Gladh, J. Halldin Stenlid, M. Borner, C. Schlueter and A. Nilsson, *Science*, 2022, **376**, 603-608.
 251. M. Fichtl, K. O. Hinrichsen, T. Nilges and K. Köhler, *Efficient Methanol Synthesis Catalysts: Long-Term Stability and Deactivation Phenomena*, Universitätsbibliothek der TU München, 2014.
 252. G. Kresse and J. Hafner, *Phys Rev B Condens Matter*, 1993, **47**, 558-561.
 253. G. Kresse and J. Hafner, *Phys Rev B Condens Matter*, 1994, **49**, 14251-14269.
 254. S. R. Bahn and K. W. Jacobsen, *Computing in Science & Engineering*, 2002, **4**, 56-66.
 255. A. Hjorth Larsen, J. Jorgen Mortensen, J. Blomqvist, I. E. Castelli, R. Christensen, M. Dulak, J. Friis, M. N. Groves, B. Hammer, C. Hargus, E. D. Hermes, P. C. Jennings, P. Bjerre Jensen, J. Kermode, J. R. Kitchin, E. Leonhard Kolsbjerg, J. Kubal, K. Kaasbjerg, S. Lysgaard, J. Bergmann Maronsson, T. Maxson, T. Olsen, L. Pastewka, A. Peterson, C. Rostgaard, J. Schiotz, O. Schutt, M. Strange, K. S. Thygesen, T. Vegge, L. Vilhelmsen, M. Walter, Z. Zeng and K. W. Jacobsen, *J Phys Condens Matter*, 2017, **29**, 273002.
 256. K. Duanmu and D. G. Truhlar, *J Chem Theory Comput*, 2017, **13**, 835-842.
 257. J. Wellendorff, T. L. Silbaugh, D. Garcia-Pintos, J. K. Nørskov, T. Bligaard, F. Studt and C. T. Campbell, *Surface Science*, 2015, **640**, 36-44.
 258. S. Mallikarjun Sharada, T. Bligaard, A. C. Luntz, G.-J. Kroes and J. K. Nørskov, *The Journal of Physical Chemistry C*, 2017, **121**, 19807-19815.
 259. F. Studt, F. Abild-Pedersen, J. B. Varley and J. K. Nørskov, *Catalysis Letters*, 2013, **143**, 71-73.
 260. H. H. Kung, *Catalysis Today*, 1992, **11**, 443-453.
 261. N. F. P. Ribeiro, C. A. Henriques and M. Schmal, *Catalysis Letters*, 2005, **104**, 111-119.
 262. Y.-F. Zhao, Y. Yang, C. Mims, C. H. F. Peden, J. Li and D. Mei, *Journal of Catalysis*, 2011, **281**, 199-211.

263. M. D. Porosoff, B. Yan and J. G. Chen, *Energy & Environmental Science*, 2016, **9**, 62-73.
264. I. Lucentini, X. Garcia, X. Vendrell and J. Llorca, *Industrial & Engineering Chemistry Research*, 2021, **60**, 18560-18611.
265. V. Garcilaso, J. Barrientos, L. Bobadilla, O. Laguna, M. Boutonnet, M. Centeno and J. Odriozola, *Renewable Energy*, 2019, **132**, 1141-1150.
266. P. Forzatti, E. Tronconi and I. Pasquon, *Catalysis Reviews*, 1991, **33**, 109-168.
267. K. Xiao, X. Z. Qi, Z. H. Bao, X. X. Wang, L. S. Zhong, K. G. Fang, M. G. Lin and Y. H. Sun, *Catalysis Science & Technology*, 2013, **3**, 1591-1602.
268. P. Courty, D. Durand, E. Freund and A. Sugier, *Journal of Molecular Catalysis*, 1982, **17**, 241-254.
269. B. C. Enger, V. Froseth, J. Yang, E. Rytter and A. Holmen, *Journal of Catalysis*, 2013, **297**, 187-192.
270. J. A. Singh, A. S. Hoffman, J. Schumann, A. Boubnov, A. S. Asundi, S. S. Nathan, J. Norskov, S. R. Bare and S. F. Bent, *Chemcatchem*, 2019, **11**, 799-809.
271. A. A. Mirzaei, E. Rezazadeh, M. Arsalanfar, M. Abdouss, M. Fatemi and M. Sahebi, *Rsc Advances*, 2015, **5**, 95287-95299.
272. E. van Steen and H. Schulz, *Applied Catalysis A: General*, 1999, **186**, 309-320.
273. H. M. Rietveld, *Acta Crystallographica*, 1967, **22**, 151-&.
274. G. S. Pawley, *Journal of Applied Crystallography*, 1981, **14**, 357-361.
275. A. A. Coelho, J. S. O. Evans and J. W. Lewis, *Journal of Applied Crystallography*, 2016, **49**, 1740-1749.
276. S. Kühn, A. Tarasov, S. Zander, I. Kasatkin and M. Behrens, *Chemistry*, 2014, **20**, 3782-3792.
277. A. Tarasov, S. Kühn, J. Schumann and M. Behrens, *High Temp-High Press*, 2013, **42**, 377-386.
278. P. Hazemann, D. Decottignies, S. Maury, S. Humbert, F. C. Meunier and Y. Schuurman, *Journal of Catalysis*, 2021, **397**, 1-12.
279. G. Kwak, D. E. Kim, Y. T. Kim, H. G. Park, S. C. Kang, K. S. Ha, K. W. Jun and Y. J. Lee, *Catalysis Science & Technology*, 2016, **6**, 4594-4600.
280. R. van den Berg, G. Prieto, G. Korpershoek, L. I. van der Wal, A. J. van Bunningen, S. Laegsgaard-Jorgensen, P. E. de Jongh and K. P. de Jong, *Nat Commun*, 2016, **7**, 13057.
281. J. Popović, E. Tkalčec, B. Gržeta, S. Kurajica and B. Rakvin, *Am Mineral*, 2009, **94**, 771-776.
282. E. A. Owen and D. M. Jones, *P Phys Soc Lond B*, 1954, **67**, 456-466.

-
283. T. B. Massalski, H. Okamoto, P. Subramanian, L. Kacprzak and W. W. Scott, *Binary alloy phase diagrams*, American society for metals Metals Park, OH, 1986.
284. F. Vincent and M. Figlarz, *COMPT REND ACAD SCI*, 1967, **264**, 1270-1273.
285. G. P. Vassiley and M. Jiang, *Journal of phase equilibria and diffusion*, 2004, **25**, 259-268.
286. B. Eren, D. Torres, O. Karslioglu, Z. Liu, C. H. Wu, D. Stacchiola, H. Bluhm, G. A. Somorjai and M. Salmeron, *J Am Chem Soc*, 2018, **140**, 6575-6581.
287. N. E. Tsakoumis, R. Dehghan-Niri, M. Ronning, J. C. Walmsley, O. Borg, E. Rytter and A. Holmen, *Applied Catalysis a-General*, 2014, **479**, 59-69.
288. C. Göbel, S. Schmidt, C. Froese, Q. Fu, Y.-T. Chen, Q. Pan and M. Muhler, *Journal of Catalysis*, 2020, **383**, 33-41.
289. J. Anton, H. Ruland, S. Kaluza and M. Muhler, *Catalysis Letters*, 2015, **145**, 1374-1381.
290. L. P. A. F. Elst, S. Eijsbouts, A. D. van Langeveld and J. A. Moulijn, *Journal of Catalysis*, 2000, **196**, 95-103.
291. C. Leyva, J. Ancheyta, L. Mariey, A. Travert and F. Mauge, *Catalysis Today*, 2014, **220**, 89-96.
292. A. Vizcaíno, A. Carrero and J. Calles, *International Journal of Hydrogen Energy*, 2007, **32**, 1450-1461.
293. D. Homsí, J. A. Rached, S. Aouad, C. Gennequin, E. Dahdah, J. Estephane, H. L. Tidahy, A. Aboukais and E. Abi-Aad, *Environ Sci Pollut Res Int*, 2017, **24**, 9907-9913.
294. F. S. Toniolo, R. N. S. H. Magalhaes, C. A. C. Perez and M. Schmal, *Applied Catalysis B-Environmental*, 2012, **117**, 156-166.
295. C. Hobbs, C. Downing, S. Jaskaniec and V. Nicolosi, *Npj 2d Materials and Applications*, 2021, **5**, 29.
296. R. F. Egerton, P. Li and M. Malac, *Micron*, 2004, **35**, 399-409.
297. W. Zabinski, *The Canadian Mineralogist*, 1966, **8**, 649-652.
298. C. A. Arguello, D. L. Rousseau and S. P. S. Porto, *Physical Review*, 1969, **181**, 1351-&.
299. V. Russo, M. Ghidelli, P. Gondoni, C. S. Casari and A. L. Bassi, *J Appl Phys*, 2014, **115**.
300. T. M. Devine and F. Adar, in *Characterization of Materials*, 2012, DOI: 10.1002/0471266965.com060.pub2, pp. 1-38.
301. F. Adar, *Spectroscopy-U.S.*, 2014, **29**, 14-+.
302. J. P. Amoureux and C. Fernandez, *Solid State Nuclear Magnetic Resonance*, 1998, **10**, 211-223.
303. G. Leofanti, M. Padovan, G. Tozzola and B. Venturelli, *Catalysis Today*, 1998, **41**, 207-219.

304. F. Rey, V. Fornes and J. M. Rojo, *J Chem Soc Faraday T*, 1992, **88**, 2233-2238.
305. R. N. Pease and H. S. Taylor, *Journal of the American Chemical Society*, 1921, **43**, 2179-2188.
306. J. S. Lewis, *Journal of the Chemical Society (Resumed)*, 1932, DOI: 10.1039/jr9320000820, 820-826.
307. O. P. Tkachenko, K. V. Klementiev, M. W. van den Berg, N. Koc, M. Bandyopadhyay, A. Birkner, C. Woll, H. Gies and W. Grunert, *J Phys Chem B*, 2005, **109**, 20979-20988.
308. A. Alejandre, F. Medina, P. Salagre, X. Correig and J. E. Sueiras, *Chemistry of Materials*, 1999, **11**, 939-948.
309. S. Velu, K. Suzuki, S. Hashimoto, N. Satoh, F. Ohashi and S. Tomura, *Journal of Materials Chemistry*, 2001, **11**, 2049-2060.
310. C. W. Tang, C. B. Wang and S. H. Chien, *Thermochimica Acta*, 2008, **473**, 68-73.

11 Appendix

11.1 Synthesis numbers of prepared precursors

Table SI 11.1: Synthesis of Al containing hydrozincites and hydrotalcites. The suffix indicates the ageing time. Hydrotalcites were in general aged for 60 minutes.

<i>Sample</i>	x_{Al}	x_{Ga}	<i>Comment</i>
<i>BM-CP-073</i>	0.0001		HZ
<i>BM-CP-074</i>	0.0001		HZ
<i>BM-CP-084</i>	0.0005	0.03	HZ
<i>BM-CP-085</i>	0.0005	0.03	HZ
<i>BM-CP-044</i>	0.0005		HZ
<i>BM-CP-070</i>	0.0005		HZ
<i>BM-CP-071</i>	0.0005		HZ
<i>BM-CP-043</i>	0.005		HZ
<i>BM-CP-082</i>	0.005		HZ
<i>BM-CP-083</i>	0.005		HZ
<i>BM-CP-007</i>	0.01		HZ
<i>BM-CP-076</i>	0.01		HZ
<i>BM-CP-002</i>	0.02		HZ/ageing series
<i>BM-CP-077</i>	0.02		HZ
<i>BM-CP-003</i>	0.03		HZ
<i>BM-CP-008</i>	0.03		HZ
<i>BM-CP-028</i>	0.03		ageing time $pH = 9$

<i>Sample</i>	x_{Al}	x_{Ga}	<i>Comment</i>
<i>BM-CP-029</i>	0.03		ageing time $pH = 8$
<i>BM-CP-030</i>	0.03		ageing time $pH = 7$
<i>BM-CP-031</i>	0.03		ageing time $pH = 6.4$
<i>BM-CP-045</i>	0.03		HZ
<i>BM-CP-046</i>	0.03		HZ
<i>BM-CP-048</i>	0.03		HZ
<i>BM-CP-053</i>	0.03		HZ
<i>BM-CP-054</i>	0.03		HZ
<i>BM-CP-055</i>	0.03		HZ
<i>BM-CP-078</i>	0.03		HZ
<i>BM-CP-103</i>	0.03		HZ
<i>BM-CP-104</i>	0.03		HZ
<i>BM-CP-105</i>	0.03		HZ
<i>BM-CP-004</i>	0.04		HZ
<i>BM-CP-079</i>	0.04		HZ
<i>BM-CP-005</i>	0.06		HZ
<i>BM-CP-080</i>	0.06		HZ
<i>BM-CP-006</i>	0.1		HZ
<i>BM-CP-081</i>	0.1		HZ
<i>BM-CP-075</i>	0.4		Zaccagnaite

<i>Sample</i>	x_{Al}	x_{Ga}	<i>Comment</i>
<i>BM-CP-085</i>	0.4		Zaccagnaite
<i>BM-CP-086-60</i>	0.4		Zaccagnaite
<i>BM-CP-109</i>	0.67		Zn-Al-Spinel
<i>BM-CP-110</i>	0.67		Zn-Al-Spinel

Table SI 11.2: Synthesis of Ga containing hydrozincites and hydrotalcites. The suffix indicates the ageing time. Hydrotalcites were in general aged for 60 minutes.

<i>Sample</i>	x_{Ga}	<i>Comment</i>
<i>BM-CP-010</i>	0.01	HZ
<i>BM-CP-086-10</i>	0.01	HZ
<i>BM-CP-012</i>	0.02	HZ
<i>BM-CP-042</i>	0.02	HZ
<i>BM-CP-087</i>	0.02	HZ
<i>BM-CP-041</i>	0.02	HZ
<i>BM-CP-009</i>	0.03	HZ
<i>BM-CP-088</i>	0.03	HZ
<i>BM-CP-106</i>	0.03	HZ
<i>BM-CP-107</i>	0.03	HZ
<i>BM-CP-108</i>	0.03	HZ
<i>BM-CP-013</i>	0.04	HZ
<i>BM-CP-089</i>	0.04	HZ

<i>Sample</i>	x_{Ga}	<i>Comment</i>
<i>BM-CP-014</i>	0.06	HZ
<i>BM-CP-090</i>	0.06	HZ
<i>BM-CP-015</i>	0.1	HZ
<i>BM-CP-091</i>	0.1	HZ
<i>BM-CP-092</i>	0.15	HZ
<i>BM-CP-112</i>	0.2	HZ
<i>BM-CP-114</i>	0.4	Ga-Zaccagnaite
<i>BM-CP-111</i>	0.67	Zn-Ga-Spinel

Table SI 11.3: Synthesis of undoped hydrozincites.

<i>Sample</i>	<i>Comment</i>
<i>BM-CP-011</i>	
<i>BM-CP-016</i>	<i>pH</i> variation
<i>BM-CP-017</i>	<i>pH</i> variation
<i>BM-CP-018</i>	<i>pH</i> variation
<i>BM-CP-019</i>	<i>pH</i> variation
<i>BM-CP-020</i>	<i>pH</i> variation
<i>BM-CP-032</i>	<i>pH</i> variation
<i>BM-CP-033</i>	<i>pH</i> variation
<i>BM-CP-034</i>	Reproduction old synthesis, <i>pH</i> = 9
<i>BM-CP-035</i>	Reproduction old synthesis, <i>pH</i> = 8

<i>Sample</i>	<i>Comment</i>
<i>BM-CP-047</i>	
<i>BM-CP-049</i>	
<i>BM-CP-050</i>	
<i>BM-CP-066-HT</i>	hydrothermal ageing
<i>BM-CP-067</i>	
<i>BM-CP-068-UT</i>	Ultraturrax dispersed
<i>BM-CP-069</i>	reference to 68-UT
<i>BM-CP-072-HT</i>	hydrothermal ageing (long time)
<i>BM-CP-100</i>	
<i>BM-CP-101</i>	
<i>BM-CP-102</i>	

Table SI 11.4: Synthesis of Copper catalysts.

<i>Sample</i>	<i>Comment</i>
<i>BM-CP-021</i>	CZG
<i>BM-CP-026</i>	CZG
<i>BM-CP-022</i>	CM(70:30)
<i>BM-CP-023</i>	CM(70:30)
<i>BM-CP-024</i>	CM(70:30)
<i>BM-CP-025</i>	CM(70:30)
<i>BM-CP-027</i>	CM(70:30)
<i>BM-ZnI-002</i>	CM(70:30)+ 5 wt% Zn

11.2 List of figures

- Figure 2.1:** Typical concentration profile of a N₂O-RFC measured by mass spectroscopy.. 14
- Figure 2.2:** Back titration of Cu₂O with H₂ at room temperature, analysed by MS..... 16
- Figure 2.3:** Visualisation of the malachite structure of one unit cell. The copper atoms are brownish-red, carbon atoms are grey and the oxygen atoms are red coloured. The picture was created with VESTAS¹¹⁷ from the ICSD reference:#30609¹¹⁶..... 18
- Figure 2.4:** Example of a hydrotalcite-like layered motive with carbonate ions and water in the interlayer. Oxygen atoms are red, Carbon is grey, hydrogen is white, with grey brownish octahedra containing zinc (purple-blue) and aluminium (brown-grey) metal ions. The layer was created with VESTAS¹¹⁷ as a variation of the ICSD reference 155052¹²²..... 20
- Figure 2.5:** Demonstration of the unit cell of hydrozincite. The b-axis is parallel to the viewing direction. The zinc atoms are purple blue, the oxygen atoms are red and carbon is grey coloured. The figure is created with VESTAS¹¹⁷ from the ICSD reference #16583¹²⁶..... 21
- Figure 2.6:** Visualisation of the wurtzite ZnO unit cell in a) and the hexagonal structure along the c-axis of three unit cells in b) (the c-axis is parallel to the viewing direction). Zinc atoms are purple-blue and oxygen atoms are red coloured. The pictures are prepared in VESTAS¹¹⁷ from the ICSD reference #26170¹³¹..... 22
- Figure 4.1:** Powder X-ray diffraction pattern of the co-precipitated precursors (left side a)) in comparison to the Cu-malachite reference from ICSD database (#15384). The asterisk visualize peak positions of the aurichalcite side-phase (ICSD #75324). On the right side the corresponding oxides after calcination for 3 h at 350 °C in static air with a heating ramp of 2 °C min⁻¹ are shown (b)). The black reference pattern corresponds to CuO (COD#004105685) and the grey pattern to ZnO (COD#002300450). 38
- Figure 4.2:** Surface areas of the co-precipitated precursors (coloured column) and their corresponding oxides (white column) after calcinating at 350 °C for 3 h in static air. 40
- Figure 4.3:** Powder XRD pattern of the reduced CZA (black, lower pattern), CZG (red, middle pattern) and CZ (blue, upper pattern) catalysts. The bar charts of the references are related to zinc oxide (grey, #002300450) and metallic copper (black, #001512504) are taken from COD database. The activation was performed with a flowrate of 10 ml_N min⁻¹ of 5 vol% Hydrogen in Argon heating up the calcined sample (125 – 250 µm sieve fraction) to 275 °C with a heating rate of 2 °C min⁻¹ and holding the temperature for 4 h to ensure complete reduction..... 41
- Figure 4.4:** a) Representative HRTEM image of the microstructure of CZA-red. with coloration to illustrate the main components Cu particles (brown), ZnO particles (red) and Zn^{red} species (orange); the original TEM images can be found in the SI as Figure SI 11.6 on page 216. b) Schematic representation of this microstructure after TPR. c) - f) Assumed surface states after the steps in the series of chemisorption experiments with c) hydrogen coverage of Cu^{surf}, d) oxidation of Zn^{red} and Cu^{surf}, e) re-reduction of Cu^{surf} only, f) re-oxidation of Cu^{surf} only. Before each step, the reactor was purged to receive a clean, adsorbate-free surface. The

assumed meaning of the chemisorption capacities is summarized at the bottom. The Zn^{red} species is represented here as a potentially porous, overgrown ZnO_{1-x} layer on the Cu particle inspired by the TEM work of Lunkenbein et al.²⁰ However, based on the chemisorption data, no claim in such direction is intended. A surface alloy state can be considered accordingly, in which case the orange layer thickness could represent the Zn fraction in its composition. A dynamic switching between overgrowth and alloy and intermediate states depending on the operating conditions of the working catalysts as suggested by Pandit et al.¹⁵⁴ seems likely.

- 43
- Figure 4.5:** Nitrogen capacities of N_2O -RFC of the prepared catalysts. The first column of each catalyst corresponds to the titration after reduction at 275 °C in 5 % H_2/Ar ($Cu^{surf}+Zn^{red}$). The second column per catalyst corresponds to the Cu^{surf} sites, determined by N_2O -RFC after reduction in H_2 -TA. The last column of each catalyst is the calculated amount of the reduced Zn species (Zn^{red}) of the two previous columns. 46
- Figure 4.6:** CO adsorption DRIFT spectra of the carbonyl region recorded at 1 and 40 min of exposure to 0.2 vol% CO in He at 10 °C after reduction for 4 hours at 275 °C with 5 % H_2 in He. 49
- Figure 4.7:** Ga K-edge XANES spectra of the activated CZG catalyst at 250 °C in 20 % H_2 in N_2 and results of the linear combination fit using the experimental spectra of gallium oxide reference materials. 50
- Figure 4.8:** Schematic visualization of the Cu microstructure and the Cu-Zn interaction depending on the secondary promoter. The value of the PXRD crystallite size is demonstrated as green ring, the Cu^{surf} sites determined by N_2O -RFC are presented as a blue ring and the $Cu^{surf}+Zn^{red}$ sites are presented as a yellow surface. 53
- Figure 4.9:** Methanol yield of the CZA (black), CZG (red) and CZ (blue) catalysts (125 – 250 μm particle size fraction) at 235 °C and GHSV = 1700 h^{-1} . The feed gas was $H_2:CO_x=2$ if not indicated differently. The pressure was 30 bar. The dashed line corresponds to the equilibrium determined by Gibbs minimization. The lines are to guide the eyes. 54
- Figure 4.10:** Methanol yield during CO hydrogenation of the catalysts CZA (black), CZG (red) and CZ (blue), all with a 125-250 μm size fraction. In a) the hydrogen partial pressure variation at 1700 h^{-1} , 30 bar, 220 °C, in b) the pressure variation at 1700 h^{-1} , $H_2:CO = 2$ and 220 °C, in c) the gas hourly space velocity (GHSV) variation at $H_2:CO = 2$, 220 °C and 30 bar and in d) the temperature variation at 1700 h^{-1} , $H_2:CO = 2$ and 30 bar are shown. The dashed line corresponds to the equilibrium determined by Gibbs minimization. The lines are to guide the eyes. 55
- Figure 4.11:** a) Methanol formation evolution of the copper based catalysts during CO hydrogenation. The line corresponds to a linear fit of the activity loss whereas the dark coloured area represents the 95 % confidence interval and the lighter coloured area represent the 95 % prediction band. b) Relative methanol production evolution of each catalyst normalized the initial methanol formation rate to 100 %. Reaction conditions: 235 °C, $H_2:CO = 2$, 30 bar and GHSV of 1700 h^{-1} 58
- Figure 4.12:** Reduced catalysts after methanol synthesis for around 1200 h time on stream at 30 bar, 235 °C, $H_2:CO_x = 2$. The bar charts of the references are from COD (in

- black for copper (001512504), in grey for zinc oxide (002300450)). The reduction was performed with 5 % H₂ in Ar with a heating ramp of 2 °C min⁻¹ to the target temperature 275 °C, which was held for 4 h..... 60
- Figure 4.13:** Comparison of the specific copper surface area determined by N₂O-RFC for the fresh and spent catalysts after 1200 h time on stream at 235 °C, GHSV of 1700 h⁻¹, H₂:CO_x = 2, 30 bar..... 60
- Figure 4.14:** Methanol yield during CO+CO₂ hydrogenation at H₂:CO_x = 2 and 30 bar with 125-250 μm size fraction of the catalysts. In a) the CO₂ amount variation at 220 °C and GHSV = 3600 h⁻¹ in b) the GHSV variation at 220 °C and x_{CO₂} = 0.15 and in c) the Temperature variation at GHSV = 3600 h⁻¹ and x_{CO₂} = 0.15 are shown. In black the performance of the CZA, in red the performance of the CZG and in blue the performance of the CZ catalyst in methanol synthesis are presented. The dashed line correspond to the equilibrium determined by Gibbs minimization. The lines are to guide the eyes. 61
- Figure 4.15:** Turnover frequency of the CZA, CZG and CZ in methanol synthesis a) at 1700 h⁻¹, 235 °C, H₂:CO = 2 and 30 bar after 200 h TOS and b) at 3600 h⁻¹, 220 °C, H₂:CO_x = 2, x_{CO₂} = 0.15 and 30 bar after 800 h. The first column (yellow) is based on the Cu^{surf}+Zn^{red}, the second column (blue) is based on the Cu^{surf} and the third column (grey) is based on the Zn^{red}, determined by N₂O-RFC..... 65
- Figure 5.1:** PXRD data of a co-precipitated zinc-aluminium precursor with an aluminium content of x_{Al} = 0.02 at different ageing times. The ageing was performed between 0 min (immediately after co-precipitation) and 120 min. The remaining suspension was aged for additional 12 hours at 130 °C in a solvothermal reactor (120 Min + solvothermal). The grey bars correspond to the zaccagnaite (ICSD#190041) and the black bars to hydrozincite (ICSD#16583) references. a) is an overview, while b) shows a more detailed zoom for better identification of the side-phase zaccagnaite, whose reflections are marked with asterisks. In b) the patterns are sorted likewise as in a). 78
- Figure 5.2:** SEM images depicting the morphology of the precursor materials recovered at different ageing times after co-precipitation at 65 °C and a pH of 6.4 of a zinc-aluminium solution with an aluminium content of x_{Al} = 0.02. 79
- Figure 5.3:** PXRD pattern of the co-precipitated aluminium-doped hydrozincite precursors with different cation-based molar aluminium fractions x_{Al}. The reference pattern of the hydrozincite was taken from the ICSD (#16583, black bars) as well as the reference pattern of zaccagnaite (#190041, grey bars). a) is an overview with indexation of the reflections, while b) is a zoom at lower diffraction angles to better distinguish the zaccagnaite side-phase (marked with asterisks). The triangle marks an additional reflection discussed in the main text below..... 81
- Figure 5.4:** Cell volume and volume weighted average domain size estimated from the h00 reflections of the hydrozincite samples versus cation-based molar aluminium fraction x_{Al}. 82
- Figure 5.5:** Temperature-resolved PXRD analysis of the thermal decomposition of the hydrozincite precursor containing 10 % aluminium (x_{Al} = 0.1). The PXRD analysis was performed with silicon as standard and in static air. The reflection

- positions are labelled as follows: silicon (*), ZnO (#) and additional unassigned reflections (Δ)..... 83
- Figure 5.6:** Schematic depiction of potential defects in hydrozincite for balancing the surplus positive charge resulting from substitution of Zn^{2+} by Al^{3+} : 1. Additional anions occupy the interlayer space. 2. Deprotonation of OH^- to form O^{2-} anions. 3. Vacancies on Zn^+ sites. The hydrogen atoms were placed at 0.9 Å distance and are not part of the crystal structure. ^{117, 126} 85
- Figure 5.7:** Morphology evolution in dependency of the aluminium content of the hydrozincite precursors. The arrows show the regions containing larger platelets and x_{Al} indicated the cation-based molar aluminium fraction. 86
- Figure 5.8:** Stack plot of ^{27}Al MAS NMR spectra of a coprecipitated hydrozincite precursor with $x_{\text{Al}} = 0.03$ aluminium incorporation and zaccagnaite. Spinning side bands are labelled with an asterisk (*). 86
- Figure 5.9:** Vibrational infrared spectroscopy of aluminium doped hydrozincites with different cation-based molar aluminium fractions x_{Al} in comparison with the aluminium rich zaccagnaite side phase $\text{Zn}_4\text{Al}_2(\text{OH})_{12}(\text{CO}_3) \cdot 3\text{H}_2\text{O}$ 88
- Figure 5.10:** Powder XRD pattern of the aluminium doped zinc oxides a) after calcination of the hydrozincite precursors at 320 °C with 2 °C min⁻¹ heating ramp and 4 h holding time in static air. The reference pattern (black bars) was taken from COD, zinc oxide (#2107059). b) Sizes of the coherently scattering domains for the h00 and 00l reflections extracted via Pawley fit from the patterns shown in a) as function of the cation-based molar aluminium fraction x_{Al} 90
- Figure 5.11:** TEM-analysis of an aluminium doped zinc oxide sample (with $x_{\text{Al}} = 0.03$). Image a) visualizes a typical aggregate as it was also found by SEM. The corresponding electron diffraction pattern is shown in figure b). The image in c) shows a large single crystal with some fractions of the typical aggregate structure on top. A HRTEM micrograph of a part of that single crystal is shown in d) with the corresponding FFT pattern..... 92
- Figure 5.12:** Stack plot of ^{27}Al MAS NMR spectra of the unheated hydrozincite, zaccagnaite and after being annealed at 200 °C, 240 °C, 280 °C and 320 °C for 4h in static air with a heating ramp of 2 °C min⁻¹ with $x_{\text{Al}} = 0.005$ aluminium incorporation. All spectra were recorded with a spinning frequency of 20 kHz. Spinning side bands are signed with an asterisk (*). 93
- Figure 5.13:** Stack plot of ^{27}Al MAS NMR spectra of zinc oxide, annealed with 320 °C for 4 h, with different cation-based molar aluminium fractions x_{Al} . All spectra were recorded with a spinning frequency of 20 kHz. Spinning side bands are signed with an asterisk (*). 94
- Figure 5.14:** ^{27}Al -signal/mass ratio of the ^{27}Al MAS NMR signal at $\delta_{\text{obs}} = 82$ ppm of zinc oxide, annealed with 320 °C for 4 h, with different cation-based molar aluminium fractions x_{Al} . The NMR spectra were excited with selective $\pi/2$ pulse and the peak area determined by deconvolution with Gaussian/Lorentzian profiles. The error bars are estimated, by taking an error of 1 % of the four-fold coordinated aluminium ^{27}Al MAS NMR signals. The lines to interpolate the substitution limit were obtained by fitting linear functions into the corresponding data points. 95

- Figure 5.15:** Band gap energies of the aluminium doped zinc oxides with different cation-based molar aluminium fraction x_{Al} . The measurements were performed at room temperature (25 °C, circles) at -185 °C (triangles) and at 27 °C after cryogenic temperature measurement (upside down triangle). The measurements were performed under vacuum in transmission mode on a pellet containing dried KBr as diluent. The lines are to guide the eye. 96
- Figure 5.16:** Powder XRD pattern of the aluminium doped zinc oxide with a cation-based molar aluminium fraction $x_{Al} = 0.03$ after calcination of the hydrozincite precursors at different temperatures with 2 °C min⁻¹ heating ramp and 4 h holding time in static air. Reflections assigned to ZnAl₂O₄ spinel are marked with an asterisk (*). The reference pattern of zinc oxide (black bars) was taken from COD (#2107059) and the reference pattern of zinc-aluminium spinel (grey bars and asterisks in pattern) was taken from ICSD database (#75628). In a) the complete range is shown. In b) a zoom of the pattern with spinel reflections is presented. 98
- Figure 5.17:** Morphology evolution depending on the calcination temperature of the undoped zinc oxide. Calcination was performed with 2 °C min⁻¹ heating ramp and 4 h holding time in static air. 99
- Figure 5.18:** Stack plot of the ²⁷Al MAS NMR spectra of aluminium doped zinc oxide with a cation-based molar aluminium fraction $x_{Al} = 0.03$ after calcination at different temperatures. All spectra were recorded at a spinning frequency of 20 kHz. Spinning side bands are labelled with an asterisk (*). 101
- Figure 6.1:** Powder PXRD pattern of the co-precipitated gallium doped hydrozincite precursors (a)). In b) is a higher resolution of the range up to $2\theta = 15^\circ$ shown, to demonstrate the zaccagnaite-like phase evolution. The reference pattern was taken from ICSD, hydrozincite in black (#16583) and the zaccagnaite-like in dark grey (#190041, *). The new and unknown reflections at $2\theta = 6.45^\circ$ and $2\theta = 19.45^\circ$ are marked with a triangle. x_{Ga} is the metal-based fraction of gallium..... 109
- Figure 6.2:** Demonstration of the 200 reflection broadening of the hydrozincite precursor phase in dependency of the gallium incorporation. x_{Ga} is the metal-based fraction of gallium. 110
- Figure 6.3:** Temperature-resolved PXRD analysis of the thermal decomposition of the hydrozincite precursor containing 15 % gallium ($x_{Ga} = 0.15$). The PXRD analysis was performed in static air. The reflection positions are labelled as followed: zaccagnaite-like (*), hydrozincite (♣) and additional reflections (▼)..... 110
- Figure 6.4:** Infrared spectroscopy of the gallium doped hydrozincites with the expected zaccagnaite-like side phase. With x_{Ga} as the metal-based fraction of gallium. 113
- Figure 6.5:** Raman spectra of the gallium doped hydrozincite series. x_{Ga} is the metal-based fraction of gallium. In a) the spectra are shown, b) shows the Raman shift of selected signals depending on x_{Ga} 113
- Figure 6.6:** Evolution of the BET-surface for the gallium doped hydrozincites (white columns; HZ) and their zinc oxides (black filled columns; ZnO) after calcination at 320 °C for 4 h in static air. 115
- Figure 6.7:** a) PXRD patterns of the gallium doped zinc oxides after calcination of the hydrozincite precursors. The reference positions were taken from COD, zinc oxide

- in black (#2107059). X_{Ga} is the metal-based fraction of gallium. In b) is the reflection broadening as the fullwidth of the half maximum (FWHM) in dependency of the gallium incorporation is shown. The lines are to guide the eyes. 116
- Figure 6.8:** SEM micrographs of selected samples of the Ga doped ZnO. The arrows mark position of the additional platelets. 117
- Figure 6.9:** Raman spectra of the gallium doped zinc oxides. The modes are labelled with abbreviations for: Longitudinal optical mode (LO), transversal optical mode (TO), transversal acoustic mode (TA). 119
- Figure 6.10:** Stack plot of ^{71}Ga MAS NMR spectra of the gallium doped zinc oxides. 120
- Figure 6.11:** Band gap energies of the gallium doped zinc oxides. The line is to guide the eyes. 122
- Figure 7.1:** Ageing of CZA in a mixed synthesis gas containing CO/CO₂/H₂ under differential reaction conditions. The volume flow was set to $666 \text{ ml min}^{-1} \text{ g}_{\text{Catalyst}}^{-1}$ at 60 bar and 210 °C. This procedure was chosen to age the catalyst in the first week while investigating in parallel the initial thermal deactivation under kinetically controlled reaction conditions. The deactivation values were estimated by fitting a power law to the methanol formation rate according to Fichtl et al.³⁰. The parameters obtained by Fichtl et al.³⁰ were determined with a similar CZA catalyst at similar reaction conditions (220 °C, 60 bar, 1.39 vol% CO, 3.60 vol% CO₂, 62.68 vol% H₂, WHSV = 0.51 h⁻¹).³⁰ The point marked with an asterisk was calculated by the deactivation data reported by Sun et al.⁵⁹ for a similar catalyst and synthesis gas (60 % Cu/28 % Zn/11 % Al; CO₂/(CO+CO₂) = 0.8). The kinetic parameter are listed in the SI in Table SI 11.23. 135
- Figure 7.2:** Methanol formation poisoned by injecting 1 ml N₂ containing different amounts of NH₃ into the inlet gas during methanol synthesis in 13.5 vol% CO / 3.5 vol% CO₂ / 73.5 vol% H₂ / 9.5 vol% N₂ using 200 mg (sieve fraction 255 – 300 μm) of the CZA catalyst at 60 bar and 210 °C. To demonstrate the dilution effect only 1 ml pure nitrogen was injected into the inlet gas stream (0 ppm NH₃). 137
- Figure 7.3:** Methanol formation poisoned by injecting 1 ml N₂ containing different amounts of TMA into the inlet gas during methanol synthesis in 13.5 vol% CO / 3.5 vol% CO₂ / 73.5 vol% H₂ / 9.5 vol% N₂ using 200 mg (sieve fraction 255 – 300 μm) of the CZA catalyst at 60 bar and 210 °C. The methanol content determined by the downstream analytics is illustrated as the upper curve (black, in each graph) and the measured TMA concentration in blue (lower curve in each graph). 138
- Figure 7.4:** Gibbs free energy diagrams: a) NH₃ activation b) oxygen-assisted NH₃ activation, c) OH-assisted NH₃ activation, over Cu 211 and ZnCu 211 at T = 500 K, $p_{\text{NH}_3} = 0.05 \text{ bar}$, $p_{\text{CO}_2} = 2.1 \text{ bar}$, $p_{\text{H}_2} = 44 \text{ bar}$, d) TMA adsorption geometry on Cu 211 with 0.21 eV binding energy and e) TMA adsorption geometry on ZnCu 211 with 0.3 eV binding energy. 140
- Figure 7.5:** a) Calculated Gibbs free energy diagram for the NH₃ methylation over Cu 211 and ZnCu 211 in the presence of surface oxygen at T = 500 K, $p_{\text{NH}_3} = 0.05 \text{ bar}$,

- $p_{\text{CO}_2} = 2.1$ bar, $p_{\text{H}_2} = 44$ bar, b) carbamate at Cu 211 edge, c) carbamate at ZnCu 211 edge. 141
- Figure 8.1:** Powder XRD pattern of the co-precipitated $[(\text{Co}_{1-x}\text{Cu}_x)_7\text{ZnAl}_2(\text{OH})_{20}]\text{CO}_3 \cdot m \text{H}_2\text{O}$ hydrotalcite precursors (a) with $x = n_{\text{Cu}} / (n_{\text{Cu}} + n_{\text{Co}})^{-1}$. The reference was taken from the ICSD database for a Zn-Al-Hydrotalcite (#155052). The reflections are labelled with the corresponding Miller indices taken from the reference. In b) the variation of the lattice parameter c and domain size along the c -axis is plotted as function of chemical composition. The PXRD patterns (c) of the mixed metal oxides after calcination at 350 °C in static air of the corresponding hydrotalcite precursor. The reference of Co_3O_4 -spinel was taken from ICSD database (#26091). The extracted lattice parameter a and isotropic domain size are plotted in panel d). 152
- Figure 8.2:** TPR profiles of a sieve fraction of 250 – 355 μm of the prepared pre-catalysts. The reduction was measured in 6 vol% H_2 in Ar with a heating rate of 6 °C min^{-1} . The labelled temperatures indicate the maximum hydrogen consumption..... 154
- Figure 8.3:** In a) the CO conversion of selected catalysts and temperatures ($x = 0$ (left bar), $x = 0.5$ and $x = 1$ (right bar)) at 20 bar are shown. Below are the corresponding selectivity and product distribution ($n\text{-C}_1$ to $n\text{-C}_4$) in the alkane- (b) and alcohol- (c) formation presented. The second run at 200 °C was performed after the temperature variation (T-variation) to reference activity changes due to catalyst ageing. The total volume flow was set to 75 $\text{mL}_N \text{min}^{-1}$ with $\text{H}_2:\text{CO} = 4$ and $\text{GHSV} = 2800 \text{h}^{-1}$ 156
- Figure 8.4:** In a) are the CO conversion of selected catalysts ($x = 0$ (left bar), $x = 0.5$ and $x = 1$ (right bar)) at 60 bar shown. Below are the corresponding selectivity and product distribution ($n\text{-C}_1$ to $n\text{-C}_4$) in the alkane- (b) and alcohol- (c) formation presented. The second run at 200 °C was performed after the temperature variation (T-variation) to reference activity changes due to catalyst ageing. The third run at 200 °C was performed after 380 °C (after 380 °C) to reference activity changes due to possible sintering effects. The total volume flow was set to 75 $\text{mL}_N \text{min}^{-1}$ with $\text{H}_2:\text{CO} = 4$ 159
- Figure 8.5:** Powder XRD analysis of the spent catalysts after CO hydrogenation at 20 bar / 60 bar and 200 °C - 380 °C after passivation at room temperature with air. The complete pattern a visualized in a) with the dark grey bars correspond to the Cu (ccp) reference (ICSD#7954) and the black bars correspond to the ZnAl_2O_4 reference (ICSD#609005). The resulting quantification of the assigned phases by a Rietveld refinement is shown in b). c) Compositional dependence of the cell parameter and domain size of the spinel phase. d) The ccp phase shows a significant expansion of the cell parameter with the copper content x . The red line is a linear fit to all data points, the dashed lines indicate the lattice parameters for bulk ccp Cu and Co taken from several entries of the ICSD (#627115, 627114, 622435, 44989). The apparent domain size shows a drastic initial decrease upon addition of copper in the catalyst system. 164

11.3 List of Tables

Table 3.1: Experiment conditions of the individual measurement step of the chemisorption analysis.	25
Table 4.1: Metal ratios determined by atomic absorption spectroscopy (AAS) of the precursors after dissolving in nitric acid. The trivalent cation is in case of the CZA-prec. and CZG-prec. the aluminium and the gallium ion, respectively. The last column contains the determined spacing of the 20-1 reflection determined by PXRD.	37
Table 4.2: Comparison of the surface areas of the catalysts after activating at 275 °C for 4 h. The calculations of the crystallite size ($d_{\text{Cu, reduced, PXRD}}$) were performed on the Cu 111 reflection by applying the Scherrer equation. The surface area $A_{\text{BET, reduced}}$ was determined by N ₂ physisorption, and the surface area $A_{\text{Cu surf}}$ was determined by N ₂ O-RFC after carefully reducing the Cu ₂ O by H ₂ -TA. $D_{A_{\text{Cu surf}} \text{ vs. } A_{\text{BET, reduced}}}$ describes the quantity of exposed Cu surface to the total surface of the reduced catalyst.	47
Table 4.3: Oxygen and Zn vacancy formations on the Ga(Al):ZnO 110 surface referenced to the values for ZnO(110). Oxygen and Zn vacancy formation in the Ga(Al):ZnO bulk referenced to the values for ZnO.	52
Table 7.1: Characterization of the self-prepared CZA (Cu/ZnO:Al) catalyst in comparison to the published commercial CZA and FHI-Std. benchmark catalyst. The BET surface area (A_{BET}) was measured by N ₂ physisorption. a) The Cu surface area (A_{Cu}) and the -dispersion (D_{Cu}) are calculated from the N ₂ O-RFC method. b) The Cu crystallite size (d_{Cu}) was determined by applying the Scherrer equation to the Cu 111 reflection and by Rietveld refinement for the FHI-Std. catalyst. ⁵⁷ The temperature with the maximum hydrogen consumption rate ($T_{\text{max, Reduction}}$) was determined from the TPR profile with a heating rate of 1 °C min ⁻¹ (CZA) and 6 °C min ⁻¹ (FHI-Std. ⁵⁷).	133
Table 7.2: Calculated adsorption energies of NH ₃ , MMA, DMA and TMA on Cu 211 and ZnCu 211 surfaces. All energies are ZPE corrected and in eV. Entropic contributions to the free energy are given in the SI.	140
Table 8.1: Nominal metal composition of the co-precipitated cobalt–copper catalysts. The ratio of zinc to aluminium was chosen to be in the stoichiometric ratio of a spinel structure. x is the nominal fraction of copper based on the catalytic active metal (Co + Cu).	151

11.4 List of Reaction equations

R 2.1	5
R 2.2	6
R 2.3	6
R 2.4	9
R 2.5	9
R 2.6	11
R 2.7	13
R 2.8	14
R 2.9	15
R 8.1	144
R 8.2	145
R 8.3	145

11.5 List of maths equations

M 3.1	26
M 3.2	26
M 3.3	26
M 3.4	26
M 3.5	26
M 3.6	27
M 3.7	27
M 5.1	73
M 6.1	107
M 12.1	208
M 12.2	208
M 12.3	209
M 12.4	226
M 13.1	271
M 13.2	273
M 13.3	273
M 13.4	273
M 13.5	275
M 13.6	275
M 13.7	285
M 13.8	285

11.6 Supporting Information to "On the secondary promotion effect of Al and Ga on Cu/ZnO methanol synthesis catalysts"

Benjamin Mockenhaupt^{ab}, Jil Gieser^a, Sharif Najafishirtari^{ab}, Lorena Baumgarten^{cd}, Jelena Jelic^d, Thomas Lunkenbein^e, Erik-Jan Ras^f, Jan-Dierk Grunwaldt^{cd}, Felix Studt^{cd}, Malte Behrens^{*ab}

- a. B. Mockenhaupt, J. Gieser, M. Behrens, Institute of Inorganic Chemistry, University of Duisburg-Essen, Universitätsstr. 7, 45141 Essen (Germany).
- b. B. Mockenhaupt, S. Najafishirtari, M. Behrens, Institute of Inorganic Chemistry, Christian-Albrecht University of Kiel, Max-Eyth-Str. 2, 24118 Kiel (Germany), E-Mail: mbehrens@ac.uni-kiel.de.
- c. L. Baumgarten, F. Studt, J.-D. Grunwaldt, Institute for Chemical Technology and Polymer Chemistry (ITCP), Karlsruhe Institute of Technology (KIT), 76131 Karlsruhe (Germany).
- d. L. Baumgarten, J. Jelic, F. Studt, J.-D. Grunwaldt, Institute of Catalysis Research and Technology (IKFT), Karlsruhe Institute of Technology (KIT), 76344 Eggenstein-Leopoldshafen (Germany).
- e. T. Lunkenbein, Department of Inorganic Chemistry, Fritz-Haber-Institut der Max-Planck Gesellschaft, Faradayweg 4–6, 14195 Berlin (Germany).
- f. E.-J. Ras, Avantium Technologies B.V., 1014 BV Amsterdam (The Netherlands).

* Corresponding author

Contribution of the authors

B.M.: conceptualization, visualization, data curation, and writing—original draft preparation.
 J.G.: conceptualization, chemisorption analysis, visualization, data curation, and writing—reviewing and editing.
 S.N.: conceptualization, DRIFT analysis, visualization, data curation, and writing—reviewing and editing.
 L.B.: conceptualization, XANES analysis, visualization, data curation, and writing—reviewing and editing.
 J.J.: conceptualization, DFT calculations, and writing—reviewing and editing.
 T.L.: conceptualization, TEM analysis, validation, and writing—reviewing.
 E.J.R.: conceptualization, catalysis, data curation, validation and writing—reviewing.
 J.D.G: conceptualization, funding acquisition, supervision, and writing—reviewing and editing.
 F.S.: conceptualization, funding acquisition, supervision, and writing—reviewing and editing.
 M.B.: conceptualization, project administration, funding acquisition, validation, and writing—reviewing and editing.

11.6.1 Catalyst preparation

Table SI 11.5: List of the used metal salts for the co-precipitation of the catalyst precursors.

<i>Chemical</i>	<i>Supplier</i>	<i>purity</i>
$Cu(NO_3)_2 \cdot 3 H_2O$	Carl Roth GmbH + Co. KG	$\geq 98 \%$
$Zn(NO_3)_2 \cdot 6 H_2O$	Carl Roth GmbH + Co. KG	$\geq 99 \%$
$Al(NO_3)_3 \cdot 9 H_2O$	Carl Roth GmbH + Co. KG	$\geq 98 \%$

11.6.2 Characterization methods

11.6.2.1 Atomic absorption spectroscopy

Atomic absorption spectroscopy was performed on a Thermo Fisher iCE-3500 AAS after dissolving the sample in nitric acid overnight. Elemental analysis (EA) of C, H, N, S was carried out by combustion of the sample together with V_2O_5 in a EuroVector EA3000.

Table SI 11.6: Detailed atomic absorption analysis of the investigated precursors. The trivalent cation in the case of CZA is aluminium and in the case of CZG gallium. The values are related to the mass of the precursor.

<i>Sample</i>	$X_{(Cu/mPrecursor)}$ wt%	$X_{(Zn/mPrecursor)}$ wt%	$X_{(M^{III}/mPrecursor)}$ wt%	$X_{(C/mPrecursor)}$ wt%	$X_{(H/mPrecursor)}$ wt%
<i>CZA-Prec.</i>	46 ± 1.9	19 ± 2.2	0.8 ± 0.07	4.69 ± 0.06	1 ± 0.05
<i>CZG-Prec.</i>	38 ± 1.6	16 ± 1.9	1.7 ± 0.05	4.99 ± 0.06	1.13 ± 0.05
<i>CZ-Prec.</i>	39 ± 1.6	17 ± 2	0	5.12 ± 0.07	0.88 ± 0.04

Table SI 11.7: Detailed atomic absorption spectroscopic analysis of the calcined samples. The trivalent cation in the case of CZA is aluminium and in the case of CZG gallium. The values are related to the mass of the calcined pre-catalyst.

Sample	$X_{(Cu/mOxide)}$ wt%	$X_{(Zn/mOxide)}$ wt%	$X_{(M^{III}/mOxide)}$ wt%	$X_{(C/mOxide)}$ wt%	$X_{(H/mOxide)}$ wt%
CZA-Calc.	50 ± 2.1	20 ± 2.4	0.68 ± 0.05	1.43 ± 0.02	0.24 ± 0.01
CZG-Calc.	49 ± 2	21 ± 2.4	1.76 ± 0.05	2.92 ± 0.04	0.43 ± 0.02
CZ-Calc.	53 ± 2.2	22 ± 2.6	0	0.33 ± 0.004	0.09 ± 0.004

11.6.2.2 Thermogravimetric analysis (TGA)

Around 24 mg of precursors are used to determine the mass loss because of thermal and oxidative decomposition of the synthesized precursors to their corresponding metal oxides. From the TG analysis (Figure SI 11.1), a strong decomposition step around 350 °C was measured for the binary CZ precursor. The trace of high-temperature stable carbonates was determined to be 4 % which starts to decompose at 380 °C. Besides that, the ternary oxides contained around 10 % high-temperature carbonates after calcination, which is roughly determined from the TG data because of their initialized decomposition at temperatures around 440 °C.

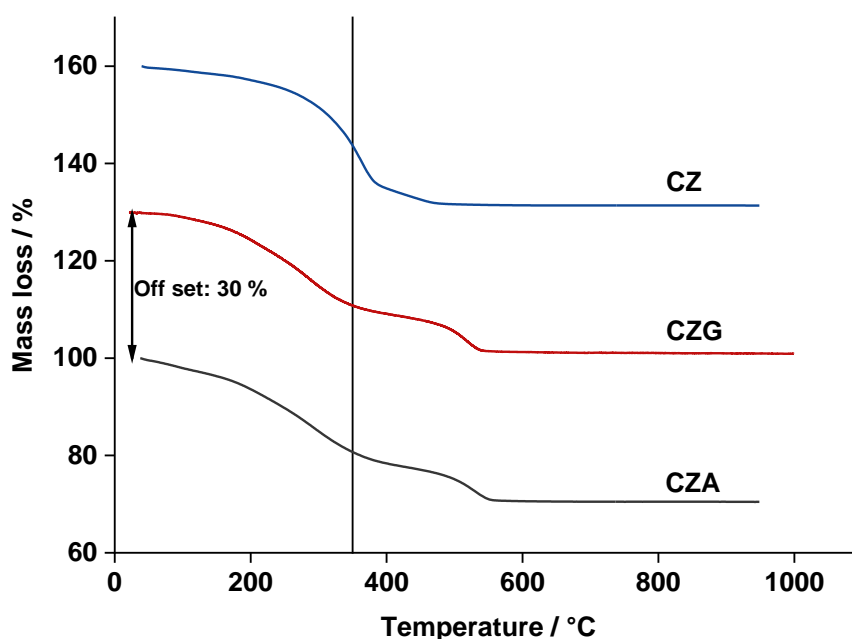


Figure SI 11.1: Thermogravimetric analysis (TGA) of the mass loss as a result of the oxidation of the precursors to their corresponding metal oxides ($Cu/ZnO/Al_2O_3$ (CZA, lower curve),

Cu/ZnO/Ga₂O₃ (CZG, middle curve) and Cu/ZnO (CZ, upper curve) as a function of temperature in synthetic air (20 % Oxygen content). The black line at 350 °C shows the calcination temperature, which was used to create the pre-catalysts in a muffle furnace containing static air.

11.6.2.3 Surface area analysis by nitrogen physisorption

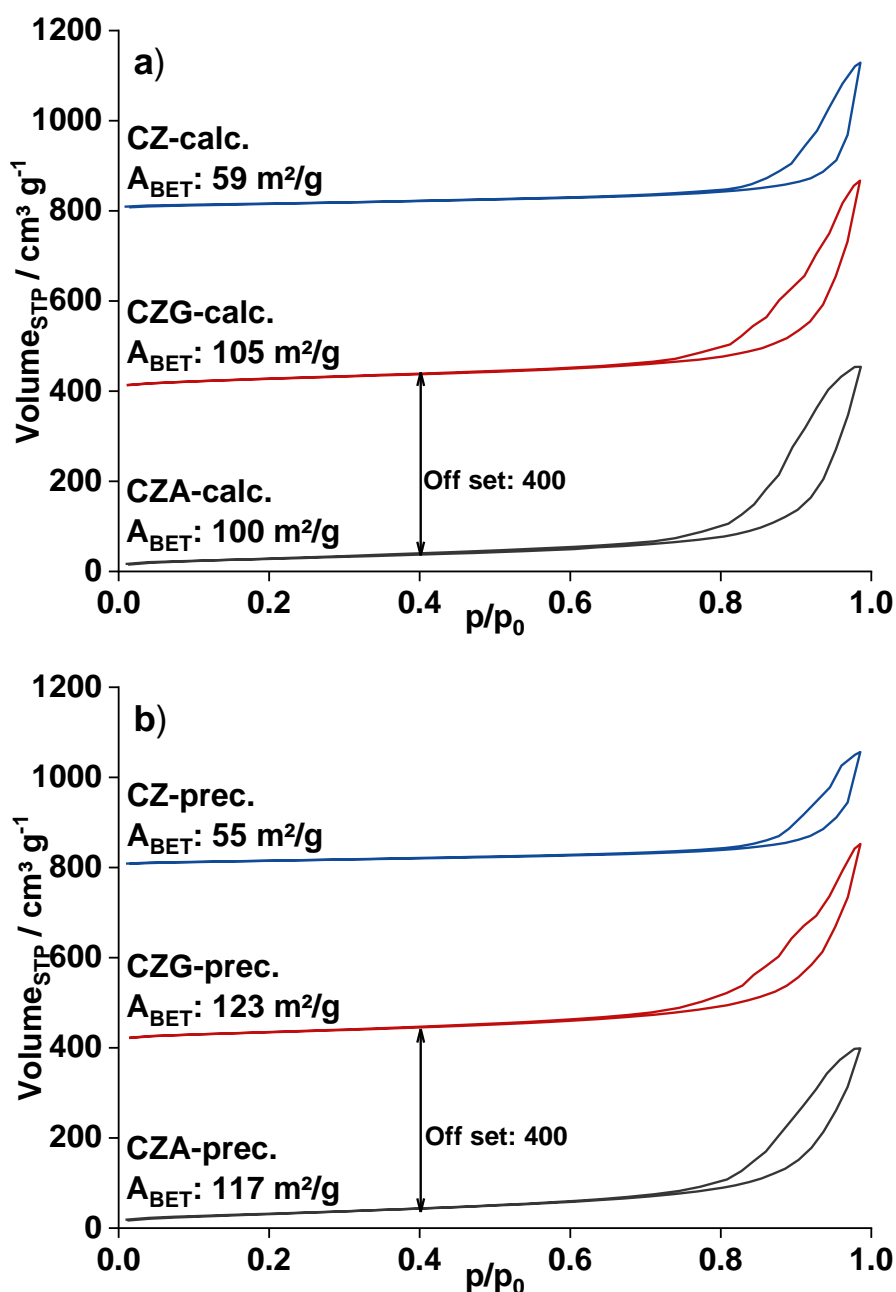


Figure SI 11.2: Nitrogen physisorption isotherms for the determination of BET surface area and pore volume of the synthesized precursors (b) and of the corresponding oxides (a) of the investigated catalysts (*Cu/ZnO/Al₂O₃ (CZA, lower graph), Cu/ZnO/Ga₂O₃ (CZG, middle graph) and Cu/ZnO (CZ, upper graph).*

The surface areas of precursors and calcined samples were determined by applying the Brunauer-Emmett-Teller (BET) equation to the N₂ adsorption data in the range of 0.07 to 0.4 of the pressure ratios measured at -196 °C. The sample was first degassed under a vacuum at 80 °C for 2 h to remove any adsorbates. The corresponding isotherms are shown in Figure SI 11.2. The corresponding pore diameter and pore volumes are listed in Table SI 11.8.

Table SI 11.8: Comparison of the surface areas (as prepared precursors and calcined precursors) determined by nitrogen adsorption of a pressure ratio in the range of 0.07 to 0.4 at -196 °C. The average pore size was determined by desorption isotherm using the BJH method. The BET surface areas were determined with an accuracy of 0.2 m² g⁻¹, the mean pore size has an accuracy of 1 nm, and the total pore volume was determined with an accuracy of 0.82 μl g⁻¹.

Sample	$A_{BET, Prec.}$	$A_{BET, Calc.}$	$d_{Pore, mean}$	$d_{Pore, mean}$	$V_{Pore, total}$	$V_{Pore, total}$
	m ² g ⁻¹ (Prec.)	m ² g ⁻¹ (Calc.)	(Prec.)	(Calc.)	(Prec.)	(Calc.)
			nm	nm	μl g ⁻¹ (Prec.)	μl g ⁻¹ (Calc.)
CZA	117	100	21	28	617	702
CZG	123	105	23	27	699	722
CZ	55	59	29	35	396	509

To avoid large pressure drops in the catalyst bed, the powder samples of the calcined catalysts were pressed and sieved to reach fractions of 125-250 μm of particle size. Therefore, a pressure of 2 tons was supplied for 2 minutes onto the powders. As a result of this pressure impact, the surface area as well as the pore size decreased (compare Figure SI 11.3 and Table SI 11.9). The shape of the isotherms after creating the sieve fraction indicates slit pores, which may be understood as the interparticle pores. However, the catalysts are used with this sieve fraction in TPR-, chemisorption analysis and catalysis. Therefore, the characterization of these particles more accurately describes the state of the material before catalysis. Regarding the surface areas, the absolute values are lowered after forming the sieve fractions (e.g., 100 m² g⁻¹ before and 47 m² g⁻¹ after pressing and sieving for the CZA) but the trend of the differences of the surface areas was still covered. So, the trend was not affected by forming the particles for catalytic tests. On the other hand, surface areas are used as a role of thumb estimation for catalytic activity since the exposed surface is important for gas phase catalysis. Simultaneously, the copper

surface areas, determined by N₂O-RFC, could be discussed in a more accurate context if the total surface area of the catalyst after reduction is known. These surface areas were also determined in the same physisorption device as the “normal” surface areas. The main difference was that the samples were first reduced, as described for the TPR analysis (275 °C for 4 h in 5 % H₂/Ar, β = 2 °C min⁻¹). Afterwards, the sample was transferred to a glove box of MBraun with Argon atmosphere to the quartz glass sample tube for nitrogen physisorption measurements. After weighing the amount of the reduced material, the sample tube was covered with Paraffin, taken out of the glove box, and inserted into the analysing device followed by immediately applying vacuum to the sample and starting the nitrogen physisorption measurement. To compare the surface areas in the right way and to compare it with other thermal characterization methods, the surface area based on the mass of oxide is needed. Therefore, calibrated TPR experiments of the same batch of sample analysed with the same measuring protocol was used together with the copper fraction determined by AAS to calculate the weight fraction of copper in the reduced sample, assuming complete oxidation and shown in equation M 11.1. The corresponding masses and the calculated weight fraction are listed in Table SI 11.10.

$$x_{Cu,red.} = \frac{m_{Oxide} \cdot \frac{x_{Cu,Oxide,AAS}}{100}}{m_{Oxide} - n_{H_2} \cdot M_O} \cdot 100 \% \quad M 11.1$$

Afterward, the oxidic mass of the analysed sample can be recalculated from the weight of the reduced state as followed:

$$m_{Oxide} = m_{red.} + \frac{m_{red.} \cdot \frac{x_{Cu,red.}}{100}}{M_{Cu}} \cdot M_O \quad M 11.2$$

After reduction, the trend of the surface areas as well as the absolute values shifted. The CZA contained after reduction a higher surface area (72 m² g⁻¹ reduced and 47 m² g⁻¹ oxidic, compare in Table SI 11.9) compared to the oxidic state but also compared to the other catalysts. Even for CZG the total surface area increased by 15 m² g⁻¹ after reduction. In both cases, the incomplete hydroxycarbonate precursor decomposition during calcination could lead to pore formation during the reduction step but also the loss of oxygen of the copper nanoparticles could induce a shrinking of these and hence would increase the overall surface area. Additionally, the consumption of ZnO to form the surface alloy under these conditions¹⁵⁴, or even the migration of ZnO around the Cu nanoparticles^{15, 20, 21} could result in a surface area increase if a significant change/rearrangement took place. Interestingly, in the case of the CZ,

the surface area decreased after reduction which in agreement with PXRD analysis of the reduced state and could be related to a more pronounced copper sintering compared to the secondary promotor containing catalysts. However, a comparison of the total surface area of the investigated catalyst and the surface area evolution because of material treatment is summarized in Figure SI 11.4.

Using the N_2O surface area of the copper sites, a dispersion term can be calculated, describing the amount of exposed copper surface on the total surface area. The calculation was performed according to equation M 11.3.

$$D_{A_{Cu} vs. A_{BET}} = \frac{A_{Cu, N_2O-RFC} * 100 \%}{A_{BET, red.}} \quad M 11.3$$

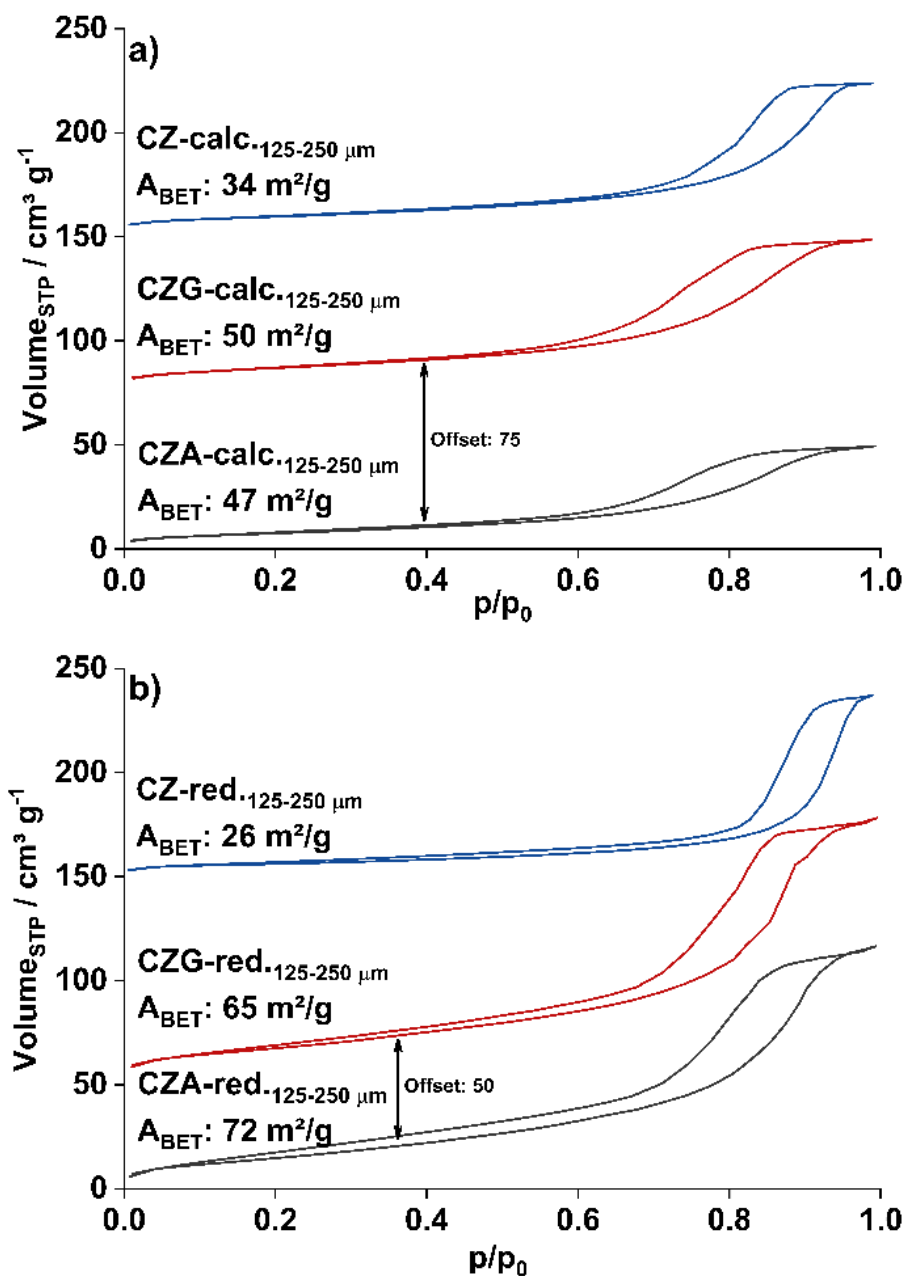


Figure SI 11.3: Nitrogen physisorption isotherms for the determination of BET surface area and pore volume of the 125-250 μm sieve fraction of the calcined pre-catalysts (a) and of the corresponding reduced catalysts (b). The catalysts are sorted from bottom to top in each graph like: (Cu/ZnO:Al (CZA, lower graph), Cu/ZnO:Ga (CZG, middle graph) and Cu/ZnO (CZ, upper graph)).

Table SI 11.9: Comparison of the surface areas of the 125-250 μm sieve fraction (as calcined pre-catalysts (calc.) and reduced catalysts (red.)) determined by nitrogen adsorption of a pressure ratio in the range of 0.07 to 0.4 at $-196\text{ }^\circ\text{C}$. The average pore size was determined by desorption isotherm using the BJH method. The BET surface areas were determined with an accuracy of $0.2\text{ m}^2\text{ g}^{-1}$, the mean pore size has an accuracy of 1 nm , and the total pore volume was determined with an accuracy of $0.82\text{ }\mu\text{l g}^{-1}$.

Sample	$A_{\text{BET, Calc.}}$ $\text{m}^2\text{ g}^{-1}(\text{Oxide})$	$A_{\text{BET, red.}}$ $\text{m}^2\text{ g}^{-1}(\text{Oxide})$	$d_{\text{Pore, mean}}$ (Calc.) nm	$d_{\text{Pore, mean}}$ (red.) nm	$V_{\text{Pore, total}}$ (Calc.) $\mu\text{l g}^{-1}(\text{Oxide})$	$d_{\text{Pore, total}}$ (red.) $\mu\text{l g}^{-1}(\text{Oxide})$
CZA	47	72	8	9	133	213
CZG	50	65	8	9	141	193
CZ	34	26	12	14	118	167

Table SI 11.10: Masses and weight fraction of copper determined for the surface area based on the oxidic mass for each catalyst. The mass of the reduced catalyst was measured in glovebox, the weight fraction of Cu and the mass of oxide were calculated.

Sample	$m_{\text{red. measured}}$ $\text{g}_{\text{red.}}$	$X_{\text{Cu, red. calculated}}$ wt%	$m_{\text{Oxide calculated}}$ g_{Oxide}
CZA	0.033	57.44	0.038
CZG	0.064	55.95	0.073
CZ	0.094	60.56	0.108

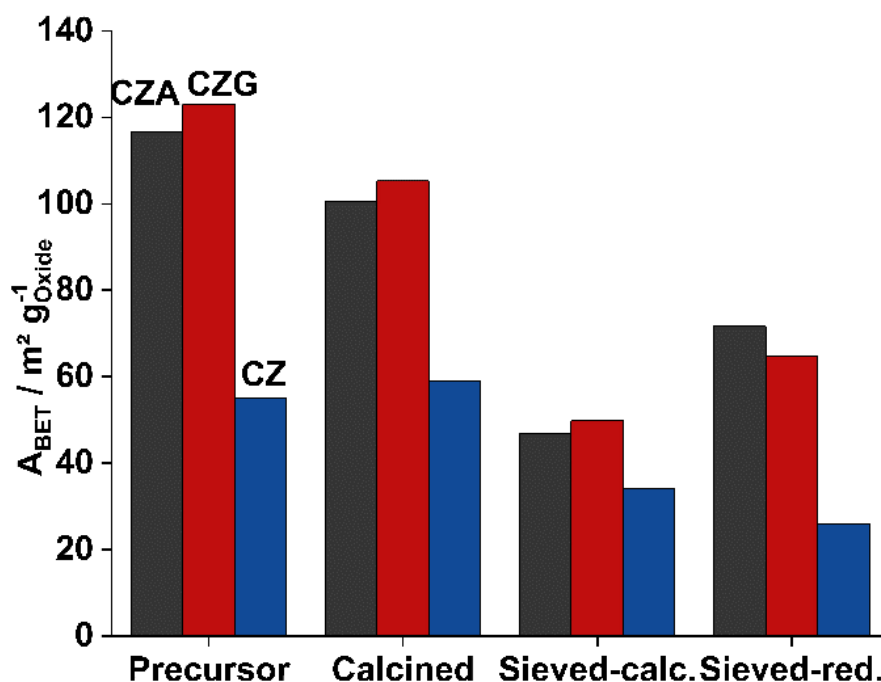
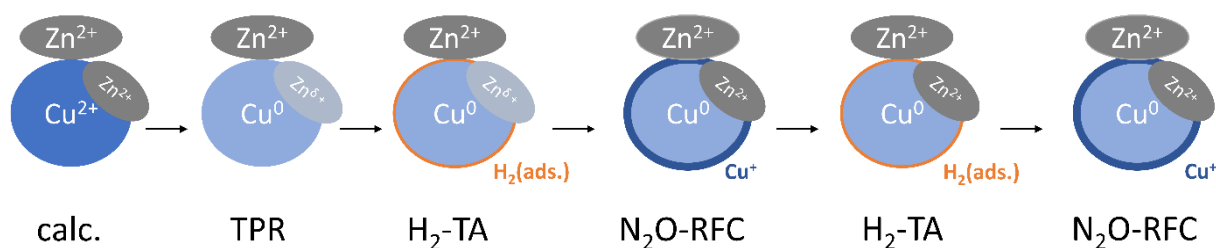


Figure SI 11.4: Comparison of the BET surface areas for the prepared catalysts in different states before the catalytic reaction was performed. The left column is CZA, the middle column is CZG, and the right column is CZ. The label “sieved” correspond to the sieve fraction of 125-250 μm .

11.6.2.4 Nitrogen capacities from chemisorption experiments



Scheme SI 11.1: Series of chemisorption experiments performed to determine the copper surface area. The orange circle depicted for H₂-TAs represents adsorbed hydrogen. The blue circle depicted for N₂O-RFCs represents an oxidic layer of Cu⁺ on the copper nanoparticles. Before each step, the reactor is purged to receive a clean, adsorbate-free surface.

The copper surface area of CZ-red., CZA-red. and CZG-red. was determined by H₂ transient adsorption (H₂-TA) and N₂O reactive frontal chromatography (N₂O-RFC) experiments performed in a certain series (see Scheme SI 11.1). The series adapts the measurement protocols of Kuld *et al.*¹¹² and Fichtl *et al.*⁶⁹ on their chemisorption analyses of Cu-based catalysts and takes into consideration their findings and conclusions. Starting from the calcined material, the catalyst is activated by a temperature-programmed reduction to 275 °C. This results in a material consisting of metallic copper nanoparticles, zinc oxide and a partially reduced zinc

species (Zn^{red}) which correspond to the Cu-Zn surface alloy, that is formed at this reduction temperature¹⁵⁴. In a subsequent H_2 -TA, the Cu^0 surface is covered with hydrogen. In an H_2 -TPD experiment up to 400 K Fichtl *et al.*⁶⁹ showed that for a reduced CZA catalyst, no hydrogen desorbs from the Zn^{red} .⁶⁹ Thus, for our H_2 -TA experiment, we can conclude that Zn^{red} does not interact with hydrogen and does not affect the hydrogen uptake, respectively. After purging at elevated temperatures to clean the surface, N_2O flows into the reactor. By that, the surface of the reduced copper is oxidized to Cu^+ and the Zn^{red} is oxidized to Zn^{2+} . The reoxidation and segregation into the corresponding oxides appeared as the break-up of the Cu-Zn surface alloy in oxidative atmospheres.¹⁵⁴ In a second H_2 -TA, Cu^+ is reduced back to Cu^0 and subsequently, hydrogen is adsorbed on its surface. However, due to the less reducible nature of ZnO compared to Cu^+ , it remains in its oxidized state. Finally, a second N_2O -RFC is performed. The surface of the copper nanoparticles is again oxidized to Cu^+ . But different from the first N_2O -RFC, no reaction with Zn^{red} takes place as it already is in an oxidized state.

According to Kuld *et al.*¹¹², the copper surface area can be calculated by comparing the results of the H_2 -TAs subsequent to reduction and to N_2O exposure, respectively. The H_2 uptake after reduction originates from adsorption of hydrogen on the Cu^0 surface, whereas the uptake after N_2O exposure stems from a reduction of Cu^+ to Cu^0 plus subsequent hydrogen adsorption on Cu^0 . Thus, the difference between those experiments gives the H_2 uptake caused by the reduction of the Cu^+ oxidic layer only. This value can then be converted into the exposed copper surface area. Furthermore, both Kuld *et al.*¹¹² and Fichtl *et al.*⁶⁹ pointed out that for zinc-containing catalysts, the copper surface area determined by N_2O -RFC is too high as the N_2O not only oxidizes the Cu^0 , but also the Zn^{red} . We want to show that this can be avoided by applying our chemisorption series. In the second N_2O -RFC, the initial state of the material is composed of Cu^0 and ZnO only, without Zn^{red} being present. That is why the second N_2O -RFC can be referred to as a "Zn^{red} corrected N_2O -RFC" for reducible oxides. Because of the overestimation of the exposed copper surface by the presence of Zn^{red} , both N_2O -RFC measurements can only be compared to the consumed N_2O /evolved N_2 molecules. Therefore, the N_2 -capacity, which describes the molar amount of released N_2 molecules per mass investigated oxide, is used to compare the catalysts to the gas phase exposed sites.

11.6.2.5 Temperature programmed reduction (TPR) and N_2O reactive frontal chromatography (N_2O -RFC)

The evolution of N_2 molecules in N_2O -RFC was determined by Mass Spectroscopy using a Pfeiffer Vacuum GSD320 with QMG 220. To calculate the metal surface area, the specific

copper density area of $1.47 \cdot 10^{19}$ atoms m^{-2} was used¹¹³. All other quantities were calculated according to DIN 66136-1¹⁵⁰. The integration borders were set to the beginning of nitrogen evolution and the intersection of the decreasing nitrogen evolution and increasing N_2O signal (compare Figure SI 11.7).

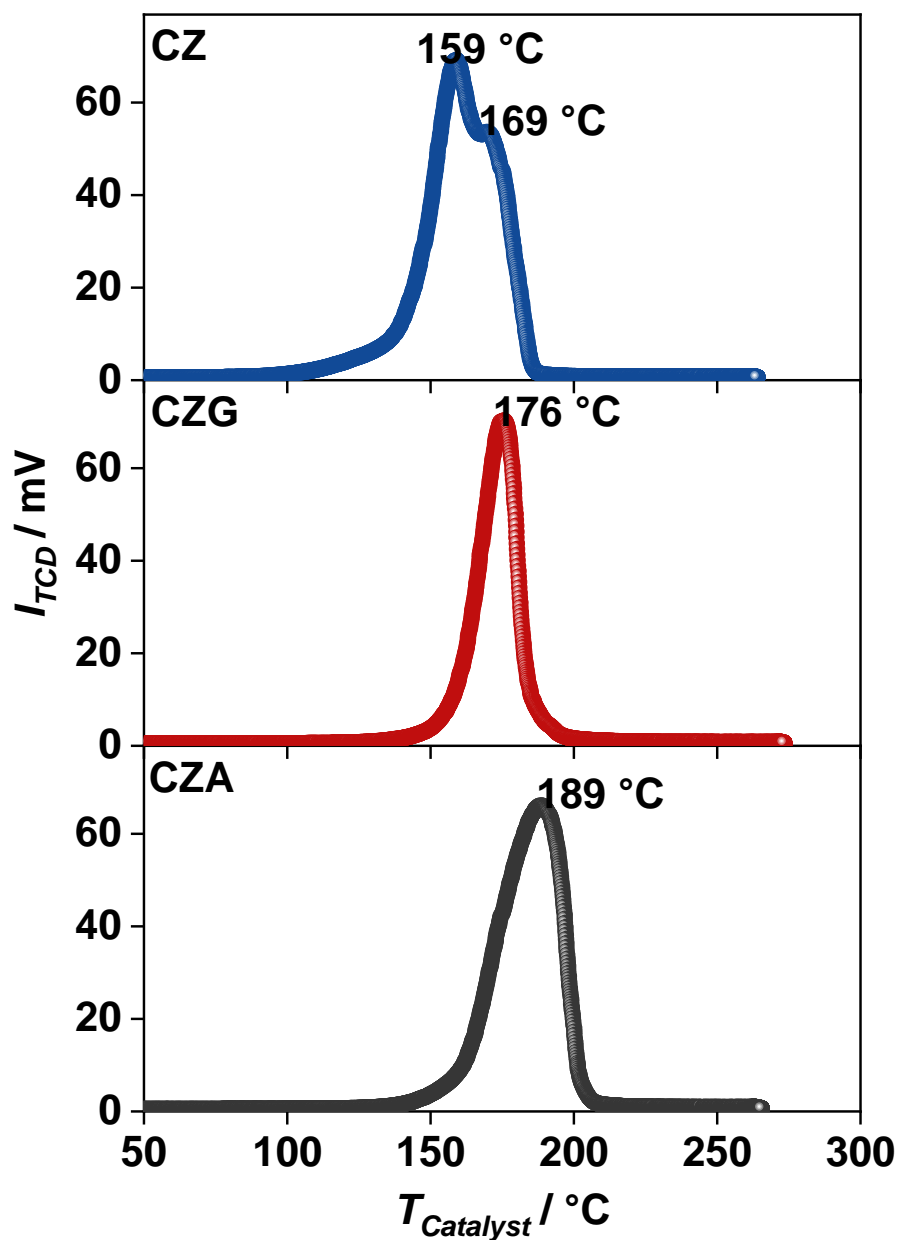


Figure SI 11.5: Temperature programmed reduction of the investigated pre-catalysts to their corresponding activated catalysts (99.3 mg Oxide of Cu/ZnO:Al (CZA, lower profile), 111.5 mg Oxide of Cu/ZnO:Ga (CZG, middle profile) and 106.8 mg Oxide of Cu/ZnO (CZ, upper profile)).

Table SI 11.11: Comparison of the temperature-programmed reduction of the investigated Catalysts and their degree of reduction.

Sample	T_{max} °C	$x_{Cu, reduced}$ -
CZA	164	1.01288
CZG	168	1.03201
CZ	156	1.07963

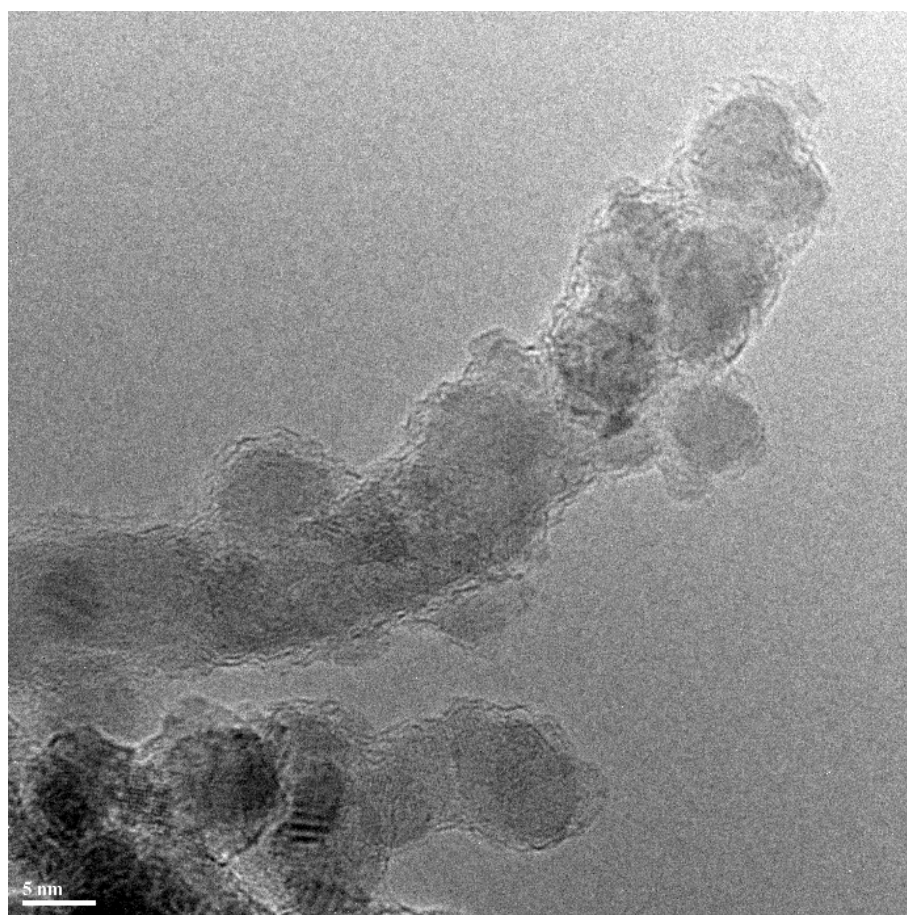


Figure SI 11.6: The original re-presentative HR-TEM image of the microstructure of CZA-red.

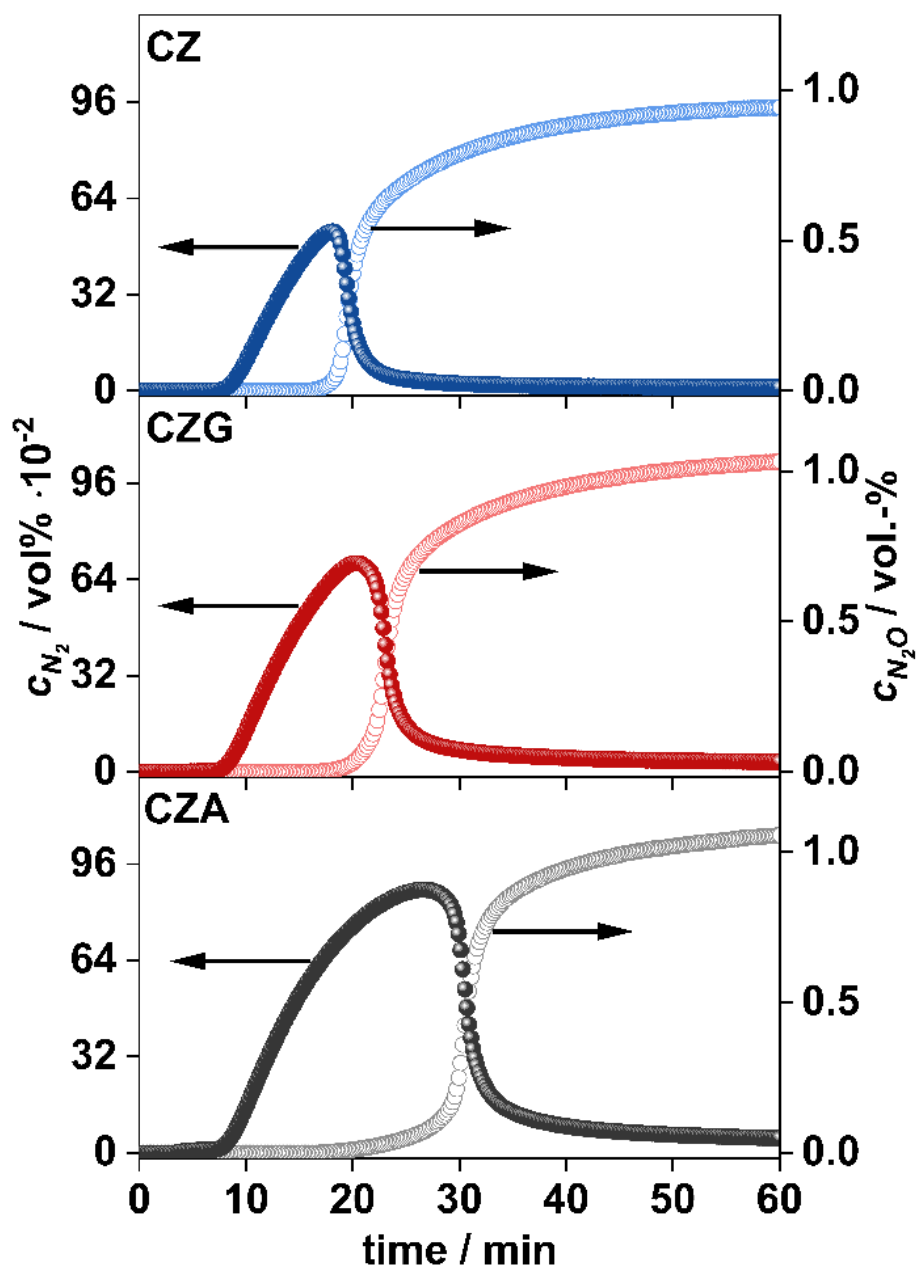


Figure SI 11.7: N_2O -RFC for the determination of the N_2 -capacities of the activated catalysts (100 mg Oxide of 125-250 μm sieve fraction). The reduction was performed at 275 $^\circ\text{C}$, 2 $^\circ\text{C min}^{-1}$ for 4 h in 5 vol% H_2 in Argon. The N_2O concentration is shown as light coloured and the N_2 concentration is shown as dark coloured spheres.

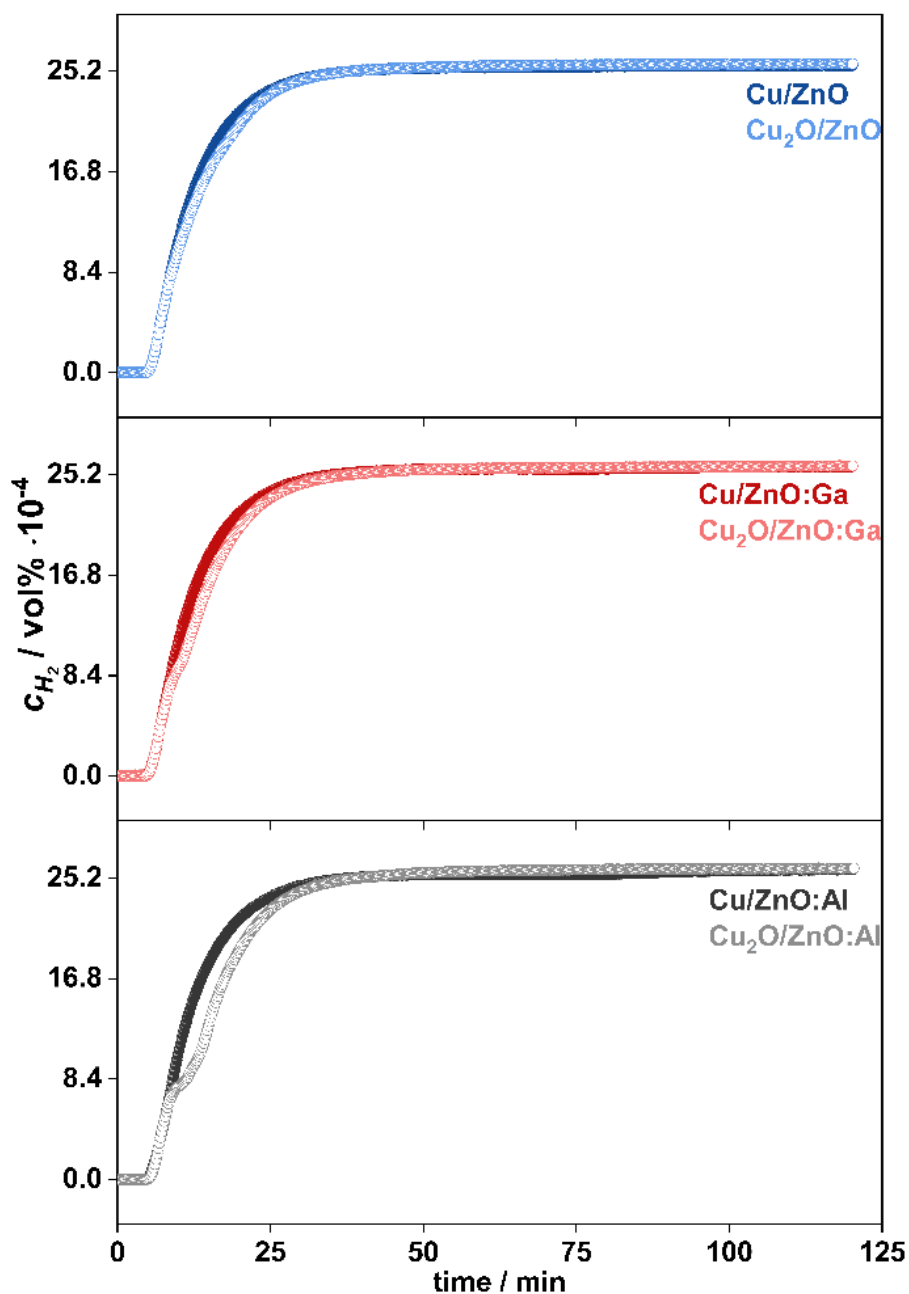


Figure SI 11.8: Transient hydrogen adsorption (H_2 -TA) of the prepared catalysts after reduction ($\text{Cu/ZnO:M}^{\text{III}}$, dark-coloured curves) and after re-oxidation by N_2O -RFC ($\text{Cu}_2\text{O/ZnO:M}^{\text{III}}$, light coloured curves). The H_2 -TA was performed at 60 °C for 60 Min in 2 vol% H_2 in Helium.

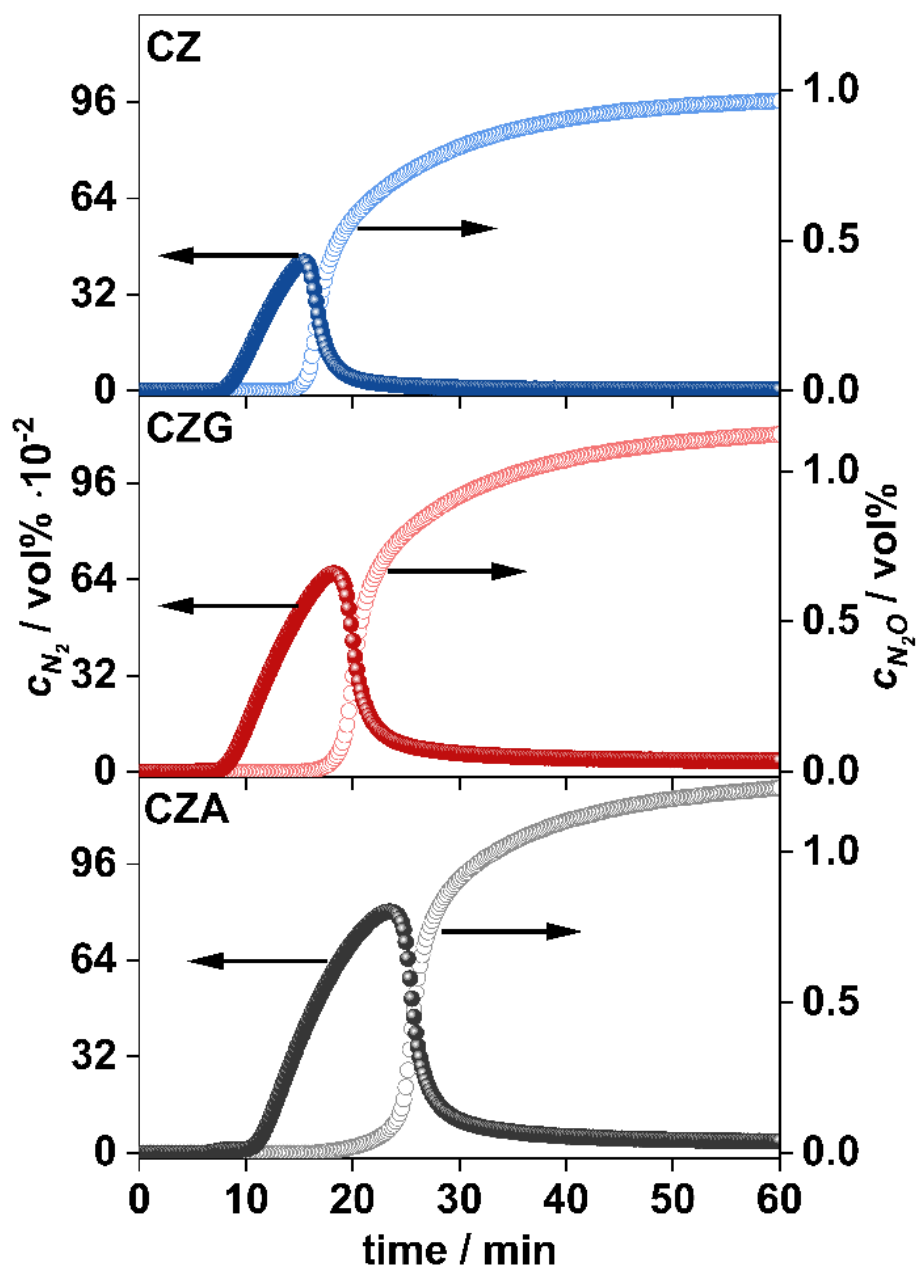


Figure SI 11.9: N_2O -RFC for the determination of the N_2 -capacities of the re-reduced copper sites in a former H_2 -TA experiment of the catalysts (100 mg Oxide of 125-250 μm sieve fraction). The H_2 -TA was performed at 60 °C for 60 Min in 2 vol% H_2 in Helium. The N_2O concentration is shown as light coloured and the N_2 concentration is shown as dark coloured spheres.

Table SI 11.12: Ratio of $Zn^{red}:Cu^{surf}$ sites (expected $Zn^{red}:Cu^{surf}$ ratio of $1:1.5 = 0.67$) determined by N_2 -capacities.

Sample	$R_{N_2\text{-capacities}}$
CZA	0.80
CZG	0.38
CZ	0.67

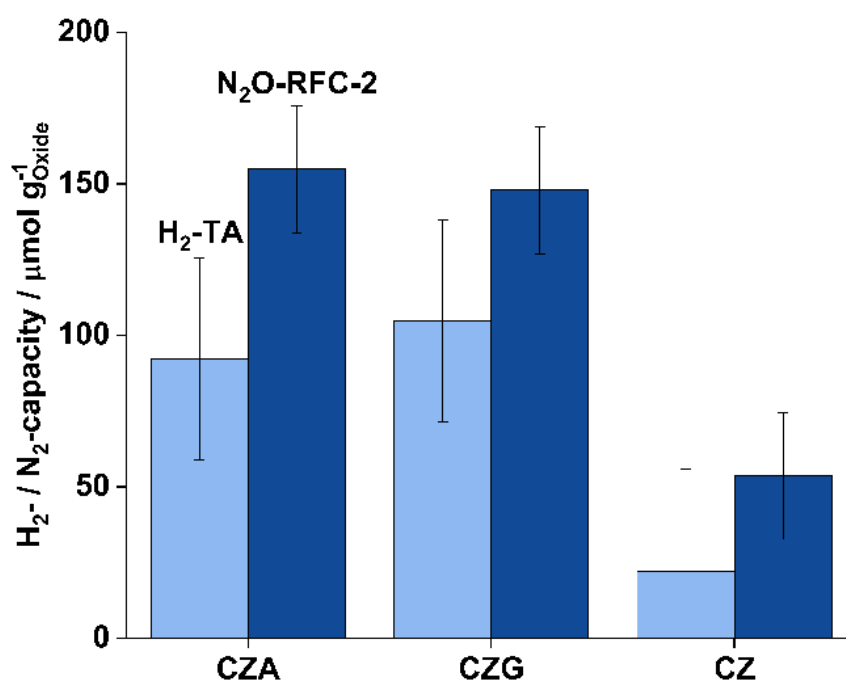


Figure SI 11.10: Comparison of the H_2 - and N_2 -capacities of the Cu^{surf} determined by H_2 -TA and the reoxidation of the Cu^{surf} sites by N_2O -RFC after prior reduction with H_2 -TA method.

11.6.2.6 DRIFTS

The catalysts were reduced by H_2 as specified in the experimental section before the exposure to the CO probe gas. The MS signals of the product gases were continuously monitored to observe the extent of the reduction. The profiles of the mass/charge of 18 corresponding to H_2O , the product of the reduction, are plotted in Figure SI 11.11 which shows quite comparable TPR profiles and seemingly the full reduction of the catalysts, despite the different compositions. Next, the samples were exposed to the probe CO mixture and the evolution of the carbonyl band/s was monitored during 40 min of adsorption. The spectra at 1 min, representing the early

stage of adsorption, as well as 40 min, representing the surface saturation, are compared in Figure SI 11.12.

11.6.2.6.1 *CO adsorption*

For the CZ catalyst, the formation of two distinct bands at 2140 cm^{-1} and 2105 cm^{-1} in addition to a shoulder feature at 2093 cm^{-1} was clearly visible in the first minute of exposure (Figure SI 11.13 and Figure SI 11.12). After 2 minutes of exposure to CO, the carbonyl band absorbance does not further increase, resulting in a saturation of the adsorption sites. Interestingly, the band at 2140 cm^{-1} disappears in the end while the other two were broadened over the course of the experiments. The CZG catalyst showed no carbonyl band at an early time and only a double band of gas-phase CO in the end. On the other hand, the CZA, showed a very small band at 2091 cm^{-1} at early time which grew to a small extent until 40 min. While the bands at smaller wavenumber can be reasonably assigned to Cu^0 species, possibly at different coordination environments, the one at 2140 cm^{-1} indicates the presence of Cu^+ . This band could be then reduced by CO and the corresponding site can be blocked due to the formation of carbonates which can be inferred from the spectra for the carbonates region as shown in Figure SI 11.12. The stacked spectra over time (see Figure SI 11.13) also show that this band on CZ disappears after 1 min. Not observing carbonyl band as significant as the ones on CZ, suggests that there could be a strong metal-support interaction and possibly the coverage and blocking of the Cu sites by a layer of the reducible oxide support, which is in agreement with previously reported DRIFT analysis of a CZA catalyst¹⁶⁹ and the dynamic synergetic effect between Cu and ZnO^{15, 20, 21}. However, the carbonyl band for the CZ catalyst gives evidence for a less pronounced SMSI, which could be related to a more difficult ZnO reduction, as it was described in the DFT section.

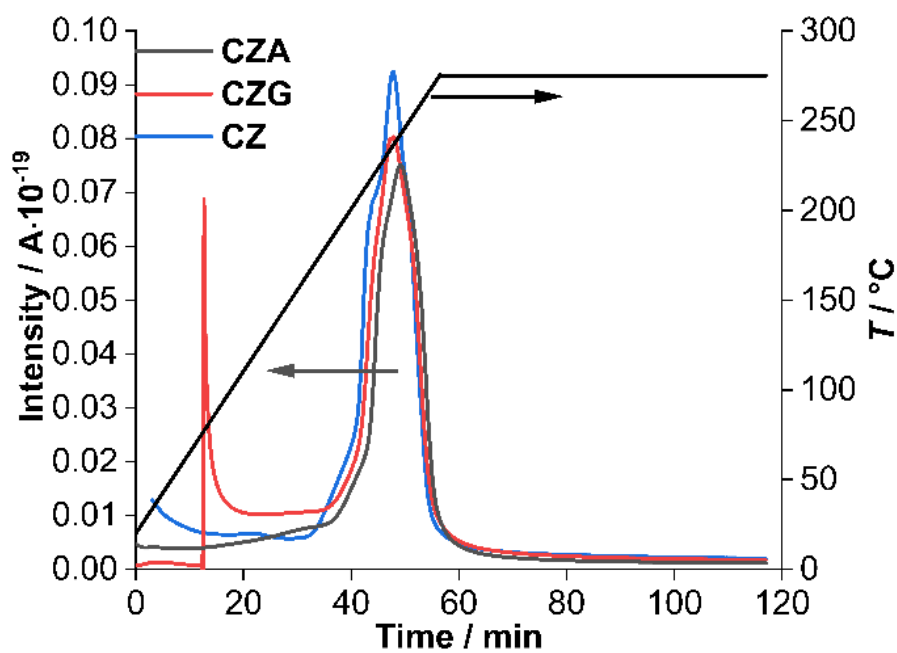


Figure SI 11.11: MS signal of the catalysts for mass/charge of 18 corresponding to H_2O during the reduction.

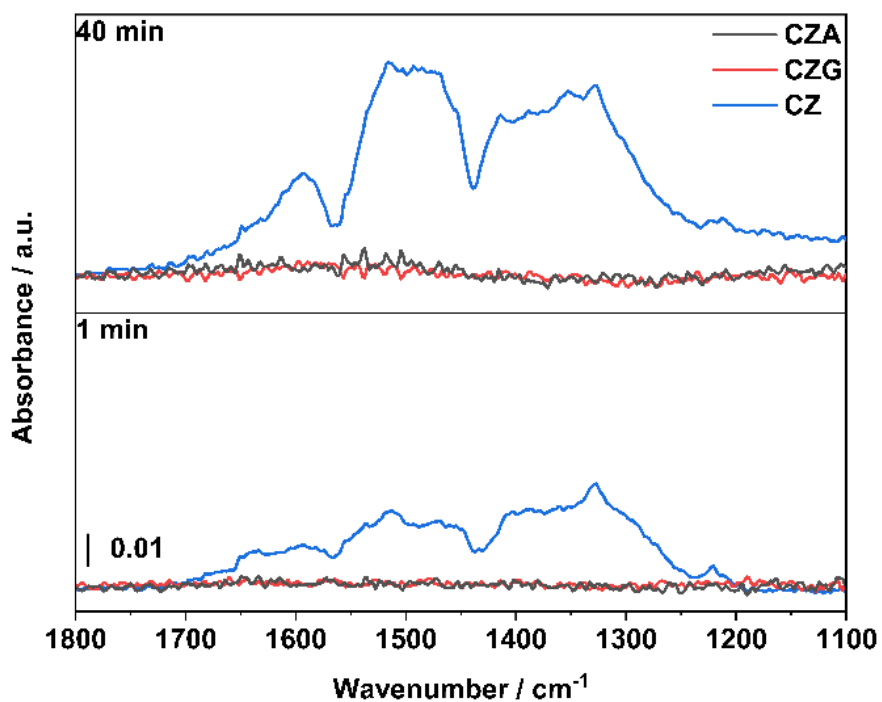


Figure SI 11.12: Adsorption DRIFT spectra of the carbonyl region recorded at 1 and 40 min of exposure to 0.2 vol% CO in He.

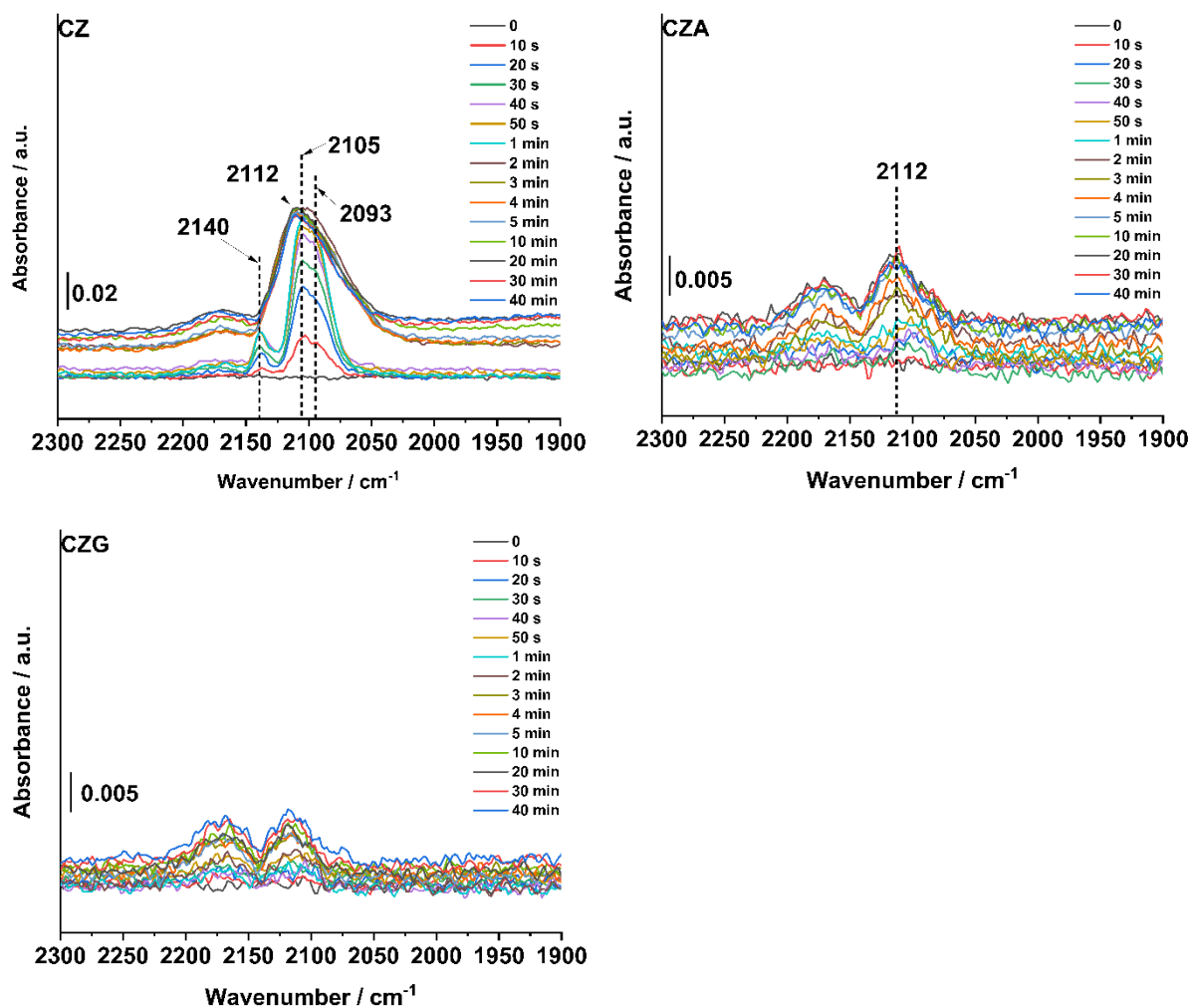


Figure SI 11.13: Time resolved signal evolution of the CO adsorption in the DRIFT spectra. The catalysts were exposed to 0.2 vol% CO in He for 40 minutes after reduction at 275 °C for 1 hour in hydrogen.

11.6.2.7 X-ray absorption spectroscopy and linear combination analysis

Table SI 11.13: Results of linear combination fit of the Ga-K-edge XANES of CZG and the experimental Ga-oxide-reference spectra, which were α -Ga₂O₃, β -Ga₂O₃, γ -Ga₂O₃, ZnGa₂O₄-spinel and ZnO/3 %Ga₂O₃ (ZnO3Ga). Prior to the fitting procedure, all references were energy aligned, the background was subtracted and normalized. For the CZG data, 9 XANES spectra recorded at 250 °C for 1 h were merged. The pre-edge region of the merged spectrum was modelled with the aim to refine the data and facilitate the fitting procedure for this part of the absorption spectrum. The fitting procedure was applied in the region of -30 eV to 100 eV relative to the Ga-K-edge. The energy shift due to the fitting were always close to 0.3 eV. It is apparent that Ga in the reduced CZG is in a similar state as in the ZnO/3 %Ga₂O₃ reference, as it was found in the results of the fit.

Fit no.	Energy shift	R-Factor $\times 10^{-3}$	α -Gallia	ZnO3 Ga	ZnGa2 O3	γ -Gallia	CuZn3 Ga	β -Gallia	total
1	0.3085	2.737	0.1458	0.7860	0.0682	0	-	-	1
2	0.3334	2.761	0.1462	0.7871	-	-	0.0667	0	1
3	0.3259	2.814	0.1746	0.7820	-	0.0434	0	-	1
4	0.3372	2.841	0.2171	0.7829	0	-	-	-	1
5	0.3252	3.090	-	0.7981	-	-	0.2019	0	1
6	0.3221	3.088	-	0.7967	-	0.0159	0.1874	0	1
7	0.3248	3.090	-	0.7980	0.0012	-	0.2008	0	1
8	0.2548	3.155	-	0.7951	0.2049	0	-	-	1

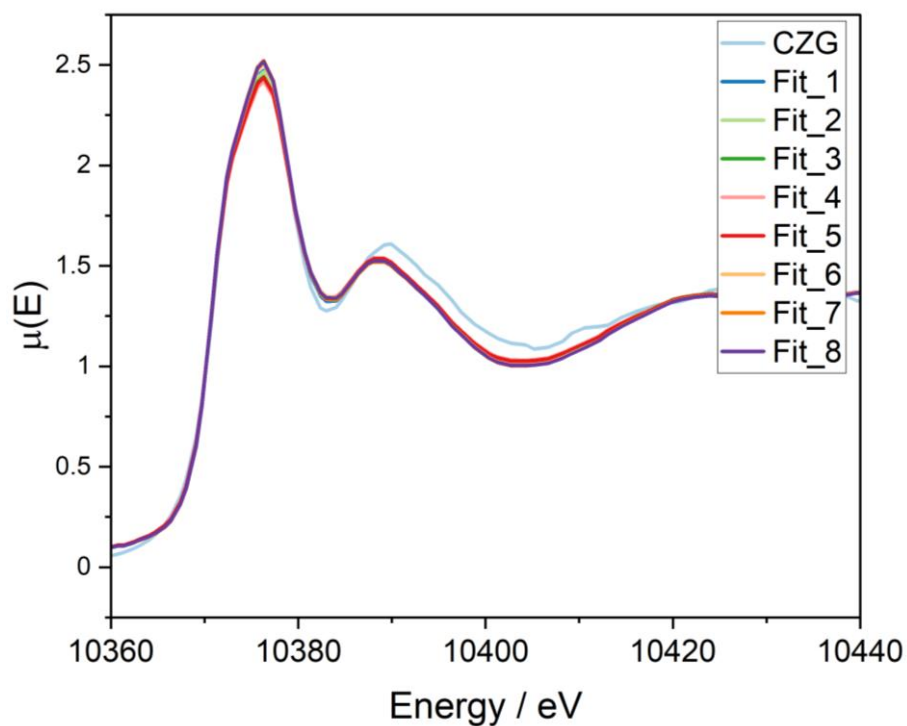


Figure SI 11.14: XANES region of the CZG spectra and 8 best fits.

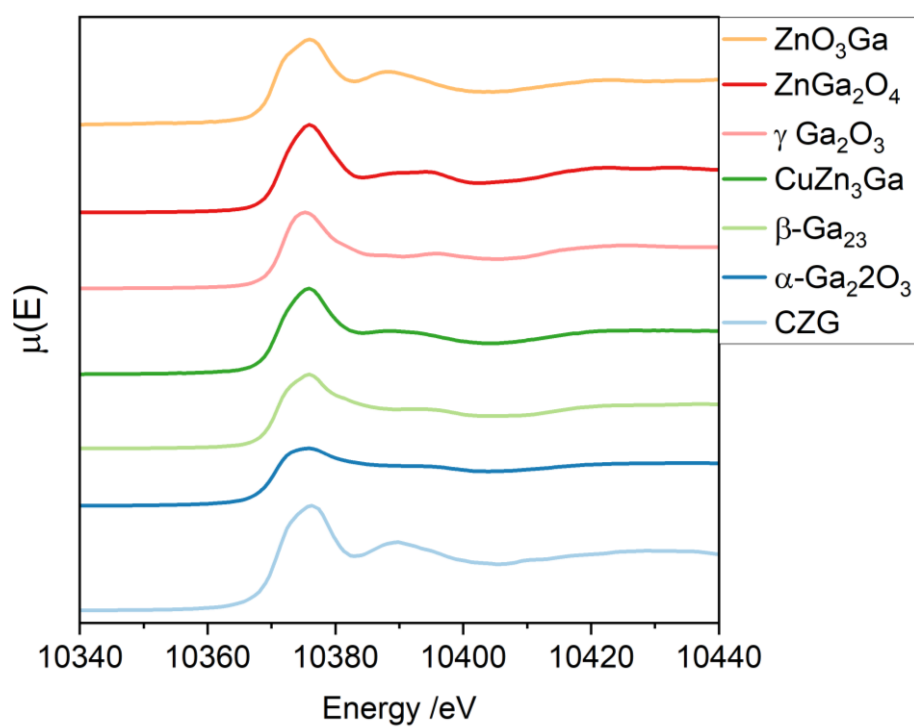


Figure SI 11.15: XANES region of the CZG spectra and the references used for LCA.

11.6.3 DFT calculations

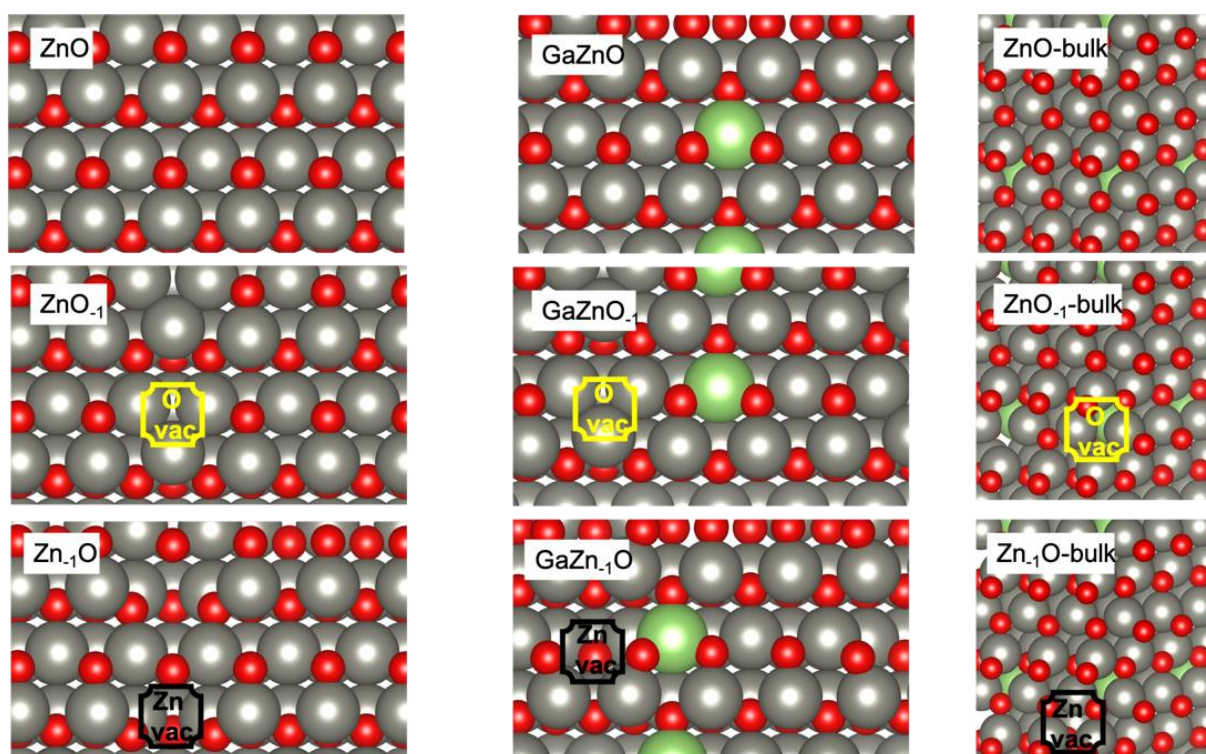


Figure SI 11.16: Structures of ZnO(110), ZnO₋₁(110), Zn₋₁O(110), GaZnO(110), GaZnO₋₁(110), GaZn₋₁O(110), ZnO-bulk, ZnO₋₁-bulk, Zn₋₁O-bulk.

The structure data used for the calculations are shown in the last section of the supporting information in the online version of the published manuscript.

11.6.4 Catalysis

11.6.4.1 Overview

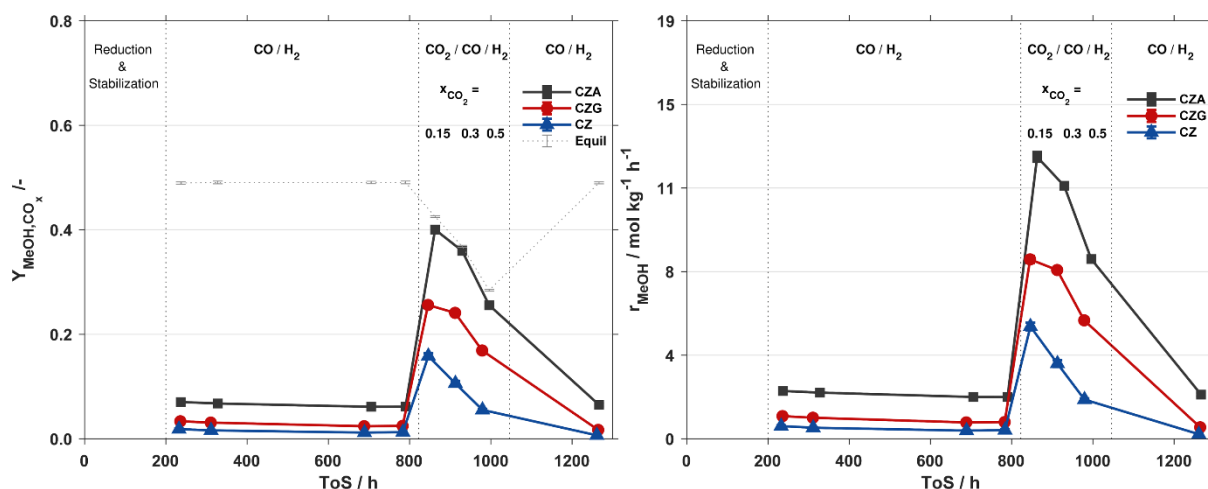


Figure SI 11.17: Methanol yield (left) and methanol formation rate (right) of the CZ-based catalysts (black CZA, red CZG and blue CZ, the dashed line is calculated equilibrium yield) at 235 °C, GHSV = 3600 h⁻¹, H₂:CO_x=2 and 125 – 250 μm particle size.

11.6.4.2 Activity in CO hydrogenation

The apparent activation energy for the methanol formation in CO synthesis gas was determined to Arrhenius' law with k as rate constant, k_0 as pre-exponential factor, E_a as the activation energy and R as the ideal gas constant and T as temperature.

$$k = k_0 \cdot e^{-\frac{E_a}{RT}}$$

M 11.4

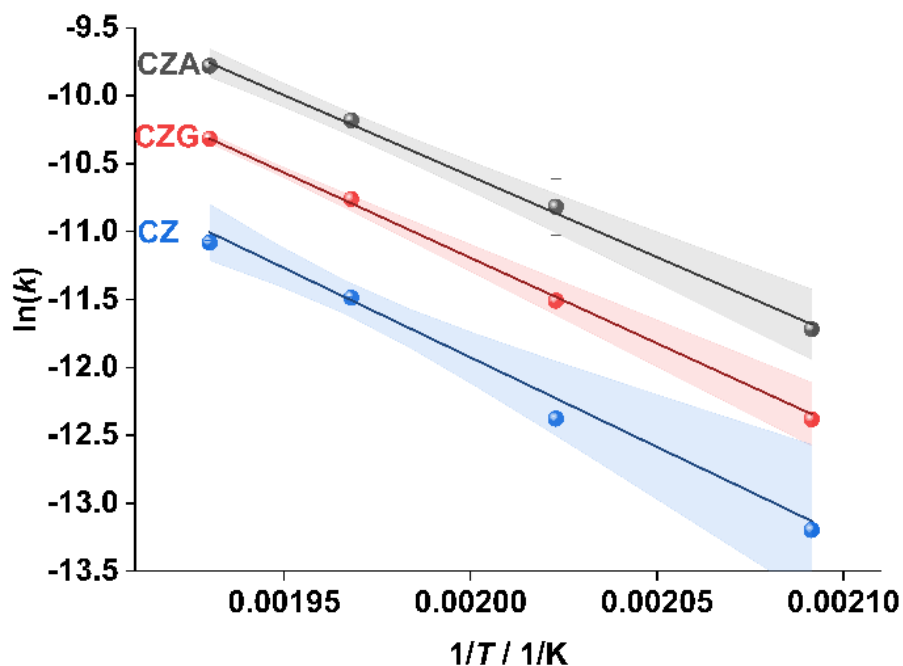


Figure SI 11.18: Arrhenius plot for determining the apparent activation energy in CO hydrogenation at 30 bar, $H_2:CO = 2$, $GHSV = 1700 h^{-1}$ and $T = 205-245 ^\circ C$ for CZA (grey), CZG (red) and CZ (blue). The solid lines are the fit and the coloured area are the confidence interval of 95 %.

Table SI 11.14: Determined kinetic parameters of the Arrhenius plot and determined activation energy for each catalyst in methanol formation at 30 bar, $H_2:CO = 2$, $GHSV = 1700 h^{-1}$ and $T = 205 ^\circ C - 245 ^\circ C$.

Sample	k_0 $\mu mol g^{-1} min^{-1}$	E_a $kJ mol^{-1}$	R^2 %
CZA	13.2 ± 0.9	99.1	99.7
CZG	13.9 ± 0.7	104.4	99.8
CZ	14.4 ± 2	109.4	98.8

11.6.4.2.1 Deactivation

Table SI 11.15: Kinetic data of the fitted deactivation of the investigated catalysts during CO hydrogenation at 235 °C, GHSV = 1700 h⁻¹, H₂:CO=2 and 30 bar.

Sample	m h^{-1}	y $mol\ kg^{-1}\ h^{-1}$	R^2 %
CZA	$-5.64 \cdot 10^{-4} \pm 5.6 \cdot 10^{-5}$	2.75 ± 0.02	65.703
CZG	$-6.07 \cdot 10^{-4} \pm 1.8 \cdot 10^{-5}$	1.73 ± 0.01	95.773
CZ	$-3.73 \cdot 10^{-4} \pm 2.5 \cdot 10^{-5}$	0.87 ± 0.01	81.173

11.6.5 Characterization of the spent catalysts

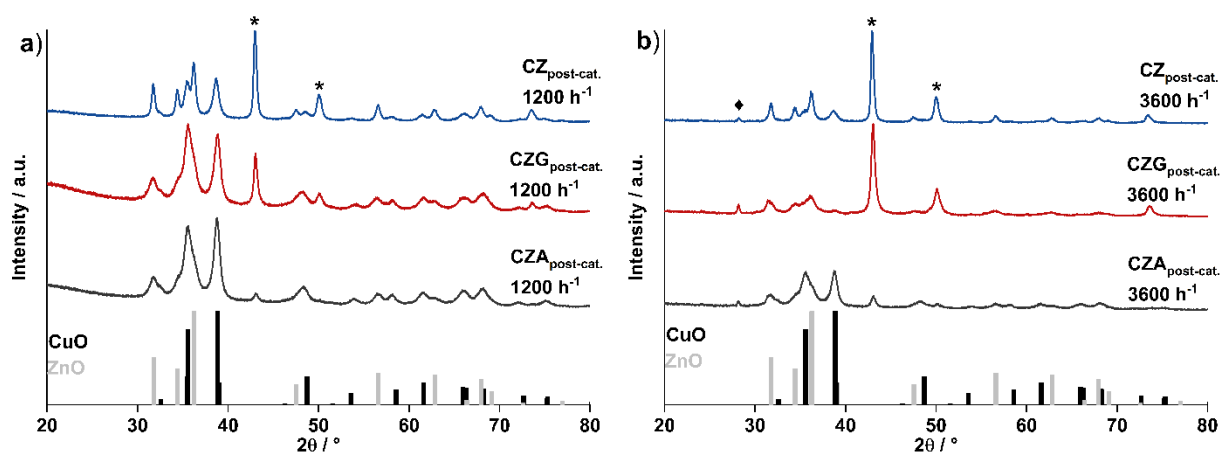


Figure SI 11.19: PXRD analysis of the spent catalysts after 1200 h TOS at 235 °C with a GHSV of a) 1200 h⁻¹ and b) 3600 h⁻¹. The asterisk corresponds to metallic copper reflections whereas the diamond marks reflections corresponding to silicon. The reference patterns were taken from COD database in black for CuO (004105685) and in grey for ZnO (002300450).

Table SI 11.16: Copper crystallite size before and after (spent) methanol synthesis of the reduced catalysts. Reduction was performed at 275 °C, 2 °C min⁻¹, 4 h in 5 % H₂ in Ar. Methanol synthesis was performed mainly in CO feed gas at 235 °C. The crystallite sizes correspond to the GHSV of 1700 h⁻¹ for CZA and GHSV of 1200 h⁻¹ for CZG and CZ.

Sample	$d_{\text{Cu 111, PXRD fresh}}$ nm	$d_{\text{Cu 111, PXRD spent}}$ nm
CZA	7	12
CZG	6	13
CZ	17	19

11.7 Supporting Information to "Phase evolution, speciation and solubility limit of aluminium doping in zinc oxide catalyst supports synthesized via co-precipitated hydrozincite precursors"

Benjamin Mockenhaupt ^{**ac}, Jan Konrad Wied ^{**b}, Sebastian Mangelsen ^c, Ulrich Schürmann ^d, Lorenz Kienle ^d, Jörn Schmedt auf der Günne ^{*b}, Malte Behrens ^{*ac}

- a. B. Mockenhaupt, Prof. Dr. M. Behrens, Institute of Inorganic Chemistry, University of Duisburg-Essen, Universitätsstr. 7, 45141 Essen (Germany), E-mail: mbehrens@ac.uni-kiel.de.
- b. J. K. Wied, Prof. Dr. J. Schmedt auf der Günne, Institute of Inorganic Chemistry, University of Siegen, Adolf-Reichwein-Straße 2, 57076 Siegen (Germany), E-mail: gunnej@chemie.uni-siegen.de.
- c. B. Mockenhaupt, Dr. S. Mangelsen, Prof. Dr. M. Behrens, Institute of Inorganic Chemistry, Christian-Albrecht University of Kiel, Max-Eyth-Str. 2, 24118 Kiel (Germany)
- d. Dr. U. Schürmann, Prof. Dr. Lorenz Kienle, Institute for Materials Science, Christian-Albrecht University of Kiel, Kaiserstraße 2, 24143 Kiel (Germany)

** both authors contributed equally.

* Corresponding author.

Contribution of the authors

- B.M. synthesized the materials and contributed to the characterization, data analysis and wrote the first draft of the manuscript.
- J.K.W. conducted the NMR experiments, the data analysis and contributed to the preparation of the manuscript.
- S.M. conducted the XRD refinements, contributed to experiments, design of experiments, data analysis and evaluation and preparation of the manuscript.
- U.S. conducted the TEM measurements, contributed to design of experiments, data analysis and preparation of the manuscript.
- L.K., J.S.G and M.B. contributed to conceptualization of the work, acquisition of the financial support, provision of study materials, reagents, materials, instrumentation, computing resources and other analysis tools and preparation and editing of the manuscript.

11.7.1 Description of the crystal structure of hydrozincite

The layered structure of hydrozincite (see Figure SI 11.20) consists of layers made up of edge-sharing Zn-O octahedra with ordered voids. Above and below these voids, additional Zn²⁺ resides in tetrahedral coordination, where the CO₃²⁻ anion connects the tips of the tetrahedra with octahedra of the adjacent layer. A detailed description of the hydrozincite structure was reported by Ghose *et al.*¹²⁶

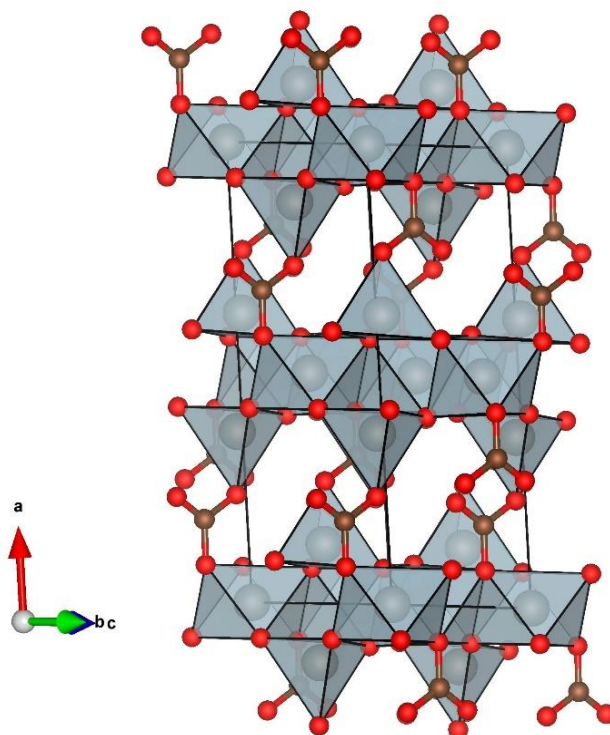


Figure SI 11.20: Crystal structure of hydrozincite with viewing direction parallel to the layers.

¹²⁶ Colour code: red: oxygen, brown: carbon, grey: zinc. ¹¹⁷

11.7.2 Materials used for co-precipitation

Table SI 11.17: List of the used metal salts and their purities for co-precipitation.

Chemicals	Supplier	Purity
$Zn(NO_3)_2 \cdot 6 H_2O$	Carl Roth GmbH + Co. KG	$\geq 99 \%$
$Al(NO_3)_3 \cdot 9 H_2O$	Carl Roth GmbH + Co. KG	$\geq 98 \%$

11.7.3 Time resolved ageing of $x_{Al} = 0.02$ Al doped hydrozincite

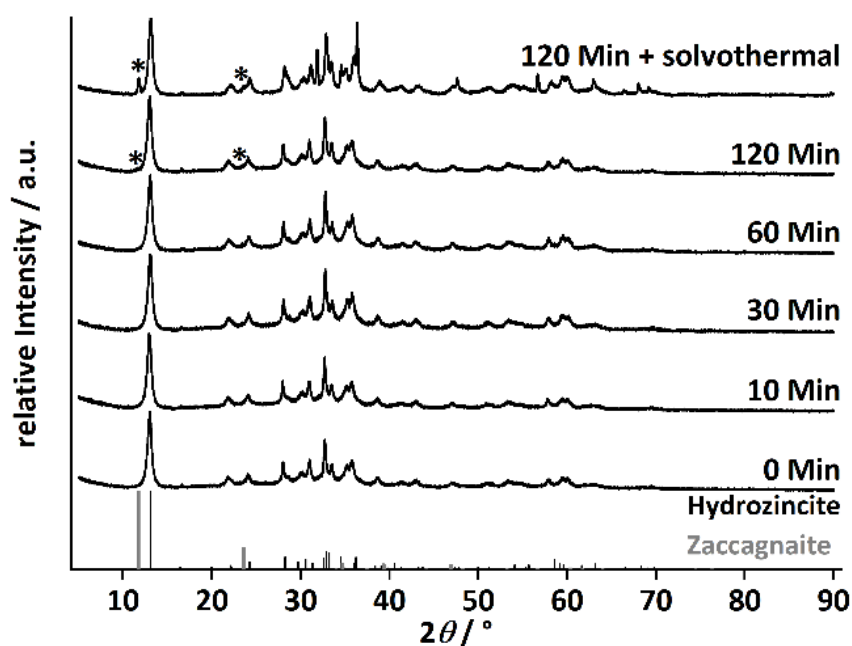


Figure SI 11.21: PXRD data of the time resolved ageing of aluminium doped hydrozincite for $x_{Al} = 0.02$. The ageing was performed from 0 min (immediately after precipitation) to 120 min in the precipitation reactor. The residue after 120 minutes ageing time was treated solvothermal at 130 °C. References are from ICSD: the black bars correspond hydrozincite (#16583) and the grey bars correspond to zaccagnaite (#190041), whose main reflections are marked with an asterisk.

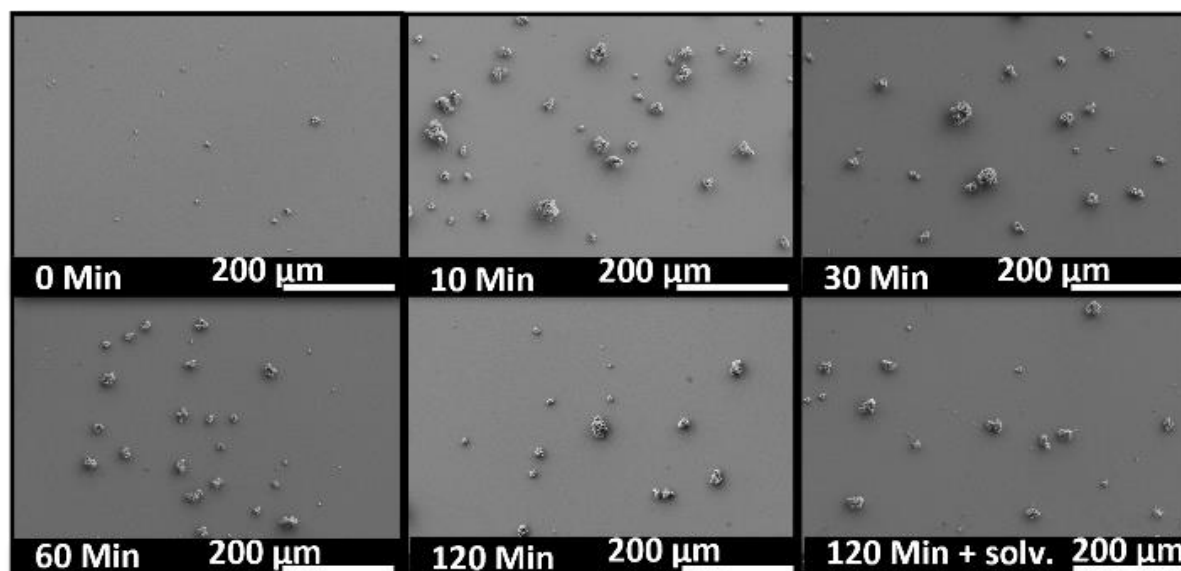


Figure SI 11.22: Overview SEM images of the time resolved ageing experiment with an aluminium incorporation of $x_{Al} = 0.02$ into the precursor phase. The times indicate after which ageing time the sample was taken out of the synthesis reactor. After 120 minutes ageing, the suspension was treated at 130 °C for additional 12 hours in a solvothermal reactor with Teflon liner (picture on the bottom, right, 120 Min + solv.).

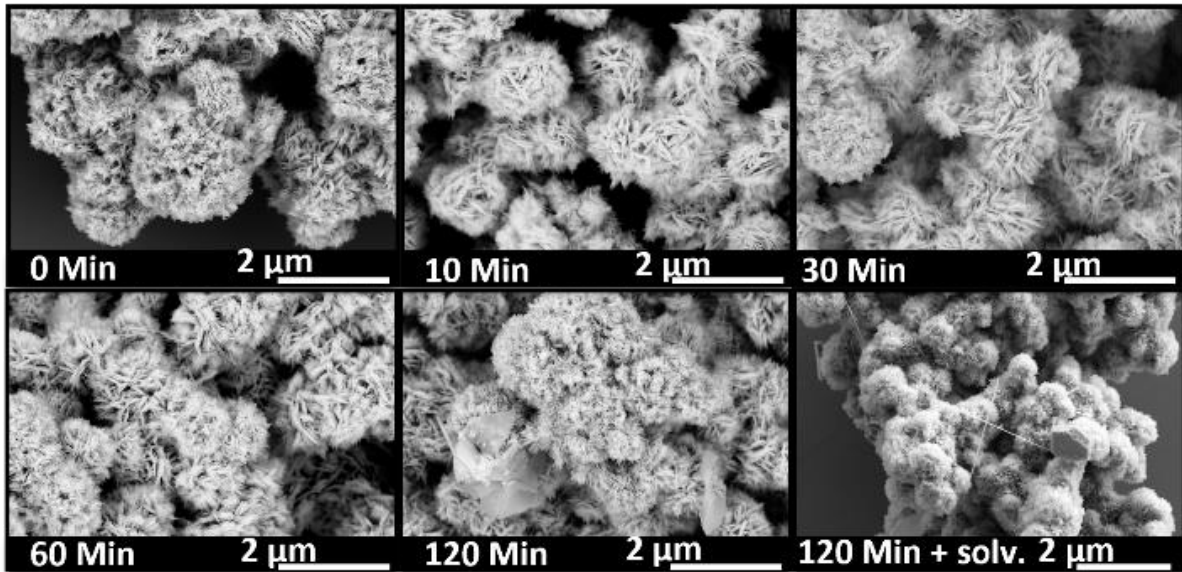


Figure SI 11.23: micrographs of the ZnO:Al synthesized from the precipitates after co-precipitation of a zinc-aluminium solution with an aluminium content of $x_{Al} = 0.02$ and different ageing times. After 120 minutes ageing, the solution was treated at 130 °C for additional 12 hours in a solvothermal reactor with Teflon liner (picture on the bottom, right, 120 Min + solv.). Calcination was performed at 320 °C with a heating ramp of 2 °C min⁻¹ for 4 h in static air.

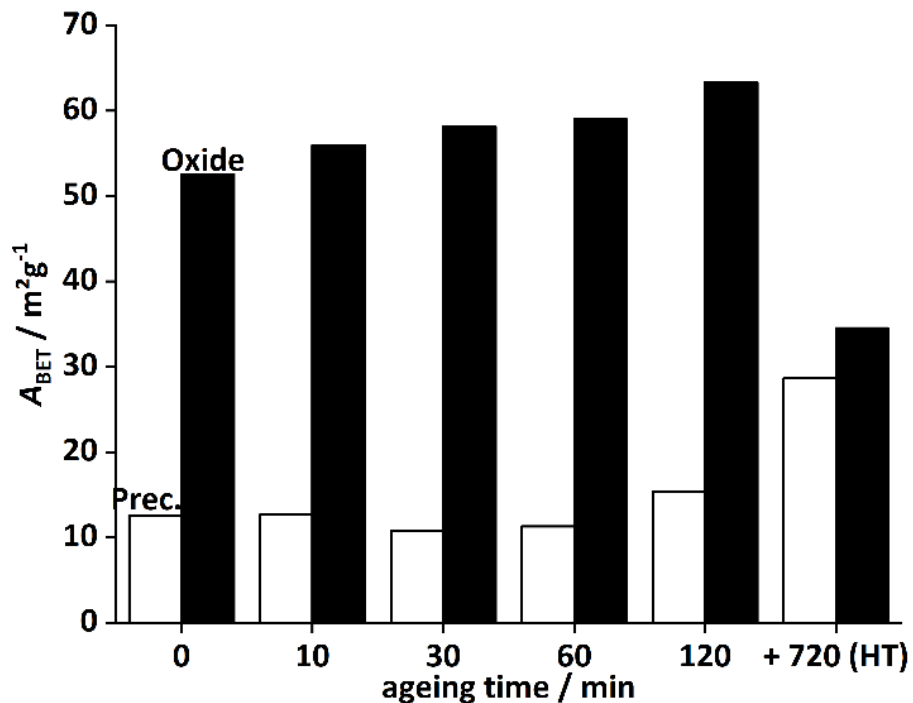


Figure SI 11.24: Evolution of the specific surface area as function of ageing time of the co-precipitated aluminium doped hydrozincites (Prec.) and their corresponding zinc oxides (Oxide). The precipitation was carried out with a zinc-aluminium solution, containing an

aluminium amount of $x_{Al} = 0.02$. After 120 minutes ageing time the suspension was aged for additional 12 hours in a hydrothermal reactor with Teflon liner at 130 °C (+720 (HT)).

The morphology of the hydrozincite powders with $x_{Al} = 0.02$ aluminium incorporation aged for different temperatures is shown in Figure SI 11.22 and Figure SI 11.23. The SEM images show that in the first 10 minutes ageing time the aggregates grew and almost reached their final size (Figure SI 11.22). A closer look into the particle morphology, shown in Figure SI 11.23, demonstrates the change in morphology in dependency of the ageing time. After co-precipitation, the aggregates are formed by small platelets. After 10 minutes, the platelet structure is more clearly present. At 120 minutes, larger additional platelets are observed and aligned to the hydrotalcite side phase (zaccagnaite), as discussed in the main text. From this observation it can be concluded that the aluminium favours an incorporation into a hydrotalcite side phase. The Al enrichment in a hydrotalcite side phase could be thermodynamically favoured, that is why the side phase evolved after 120 minutes ageing time and increased in the solvothermal ageing step. These additional platelets grew out of the aggregates. At the same time, the morphology of the bulk structure was changed to smaller platelets. The further treatment at 130 °C in a solvothermal reactor resulted in an enhanced grow of the larger platelets, which were afterwards substantially thicker. Simultaneously, rods are also formed and present besides the typical aggregates as observed after 10 minutes ageing time.

Simultaneously to the larger platelets, the specific surface area of the precipitate as determined by nitrogen physisorption increased (Figure SI 11.24).

11.7.4 Synthesis of the aluminium-rich side-phase zaccagnaite

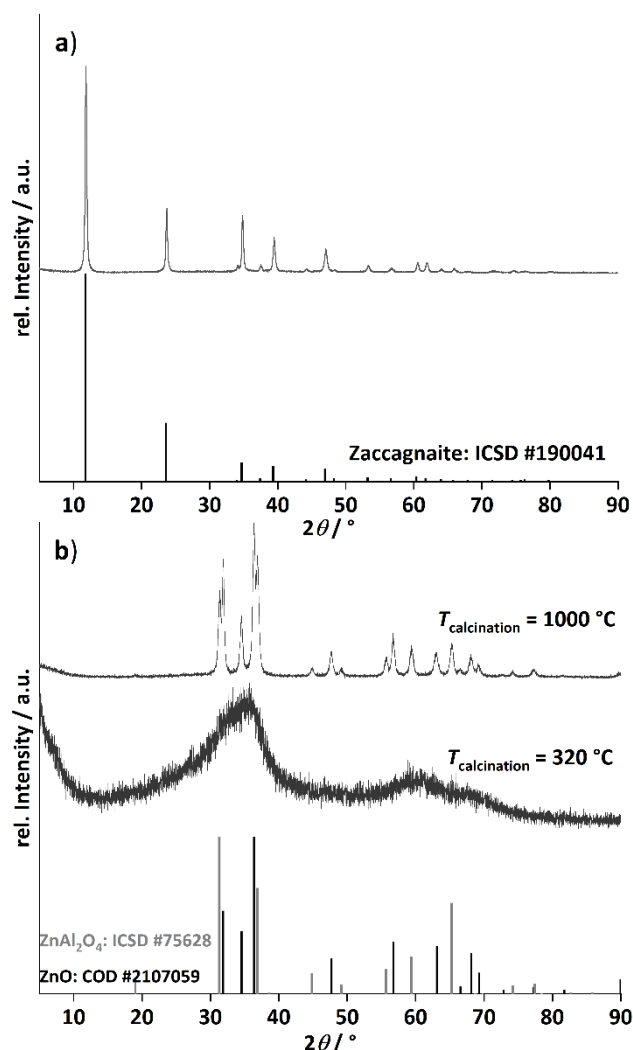


Figure SI 11.25: Powder XRD data of the co-precipitated zaccagnaite precursor a) with reference from ICSD (#190041) and the calcined samples at different temperatures b) with reference for ZnO from COD (#2107059, black, broad bars) and zinc-aluminium spinel from ICSD (#75628, grey bars).

The aluminium-rich side-phase zaccagnaite synthesized as a reference material should nominally contain 33 % of aluminium (metal based). The precipitation was carried out in an automated stirred tank reactor (OptiMax, Mettler Toledo) from 0.4 M metal salt nitrate solution at a temperature of 50 °C and at a constant *pH* of 8.5. As precipitating agent, 0.09 M sodium carbonate together with 0.6 M sodium hydroxide solution were used. The dosing rate of metal solution was adjusted to 2.08 g min⁻¹. After precipitation the precipitate was aged for 60 minutes without further *pH* control in the mother liquor. The precursor was washed with deionized water 10 times, to reach a conductivity of the wastewater lower than 100 μS cm⁻¹ and dried at 80 °C for minimum 14 hours.

The PXRD characterization of the phase pure precursor and the calcined sample is shown in Figure SI 11.25. Calcination at 320 °C resulted in an amorphous solid. The position of the evolved broad halo between $2\theta = 30^\circ - 40^\circ$ is in a range where ZnO as well as the spinel exhibit strong reflections. After calcination at 1000 °C, ZnO as well as the spinel crystallized and segregated. The reflections are quite sharp and small, indicating macroscopic crystallites.

11.7.4.1 Beam damage of the prepared zaccagnaite reference material in TEM investigation

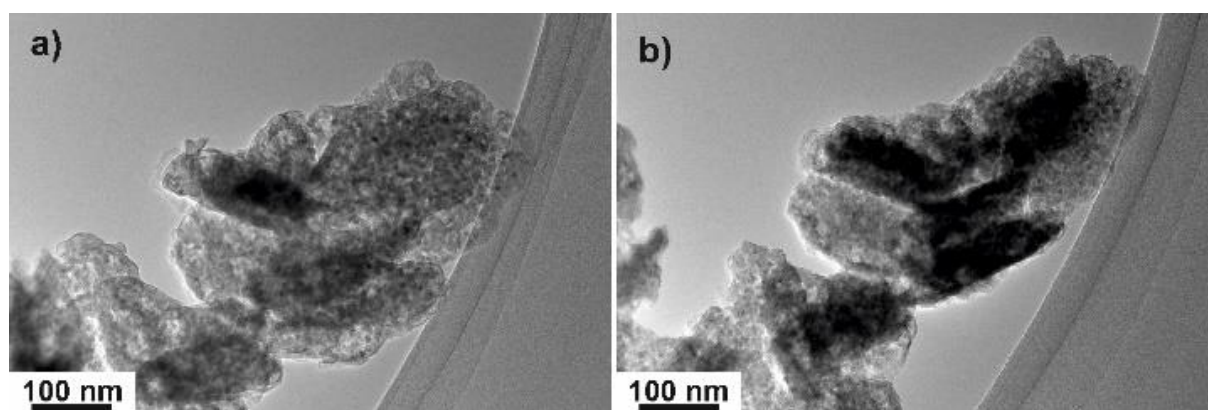


Figure SI 11.26: Demonstration of the morphology changes during electron beam exposure of the prepared zaccagnaite in the TEM: a) shows the pristine material while figure b) was recorded after a beam exposition of some minutes including electron diffraction and EDX analysis. The measurement was performed at room temperature.

In Figure SI 11.26 the morphology change of the zaccagnaite material during TEM-analysis is shown. The measurement was performed at room temperature. From TG-analysis of that material, shown in Figure SI 11.32, the material decomposes at around 150 °C, which is a quite low temperature. Because of the high vacuum and the radiation energy input at TEM-investigations, an earlier decomposition may happen. Therefore, a degradation of the material cannot easily prevent and takes place, as it was observed in a loss of oxygen determined by EDX, which is associated with the emission of the decomposition products H₂O and CO₂. Such change in chemical composition because of beam exposure is known and also found in investigations of nickel-iron layered double hydroxides.^{295, 296} From the finding it was assumed that the zaccagnaite sample decomposed into defect enriched zinc oxide, as the d-values determined by electron diffraction are in the range of ZnO but with a deviation up to 5 %. This result correlates to the reported investigation on nickel-iron layered double hydroxides.²⁹⁵

To demonstrate the origin of the defect enriched ZnO that originates from thermal decomposition of zaccagnaite, *in situ* PXRD analysis of the calcination was performed. The

decomposition starts with a pronounced shift of the $00l$ reflections at around 150 °C as shown in Figure SI 11.27, which is assigned to the loss of inter-layer water and the resulting contraction of the inter-layer distances. A slow crystallization of ZnO was observed by a monotonic change of the PXRD patterns with further increasing temperature. Only above 550 °C, the main reflections of the ZnO became clearly visible. These results support the suggestion that the beam-damaged state and the state after mild thermal decomposition are similar. Furthermore, they provide support for the assumption that the defect enriched ZnO with oriented domains found in the calcined samples, shown in the main text in Figure 5.11, have their origin in the decomposed hydrotalcite-structure of zaccagnaite.

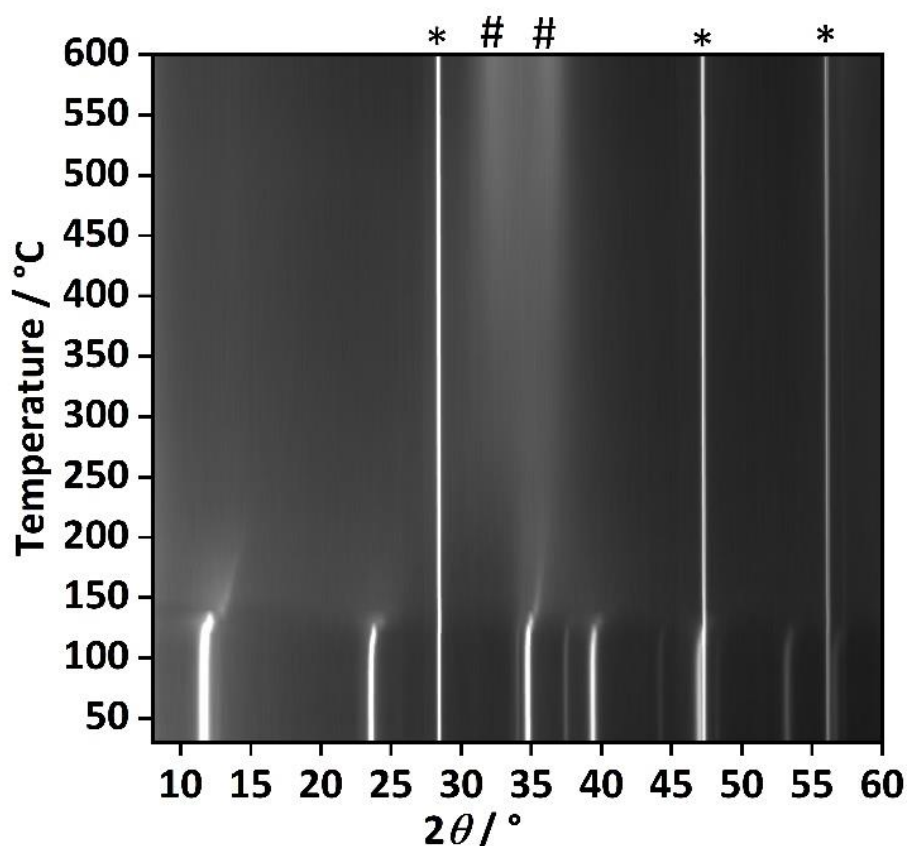


Figure SI 11.27: Temperature resolved PXRD analysis of the decomposition of the Zaccagnaite precursor. The PXRD analysis was performed with silicon as standard and in static air. Reflections of Si (*) and ZnO (#) are indicated by labels.

11.7.5 Characterization of the hydrozincite precursors of the aluminium concentration variation

11.7.5.1 Powder XRD and SEM analysis

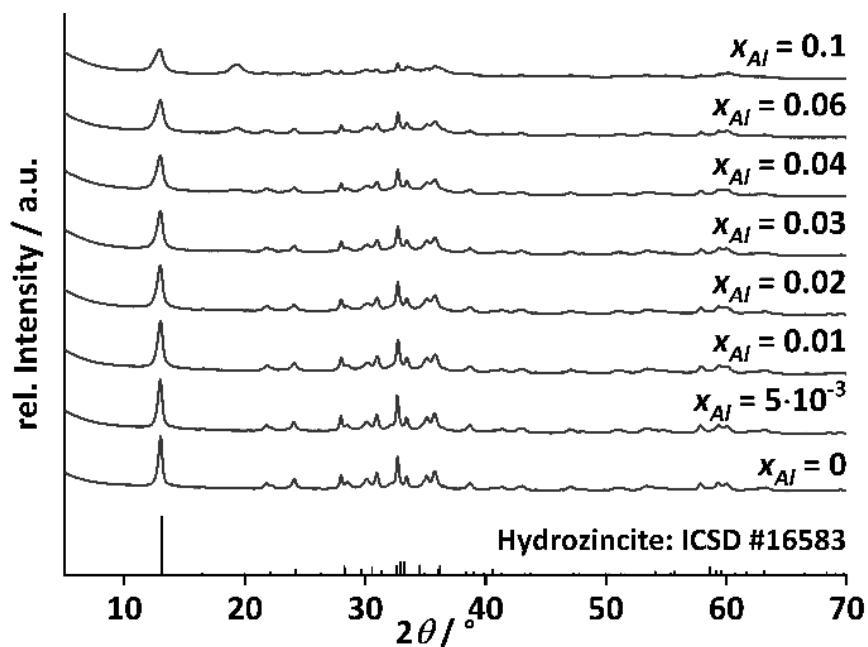


Figure SI 11.28: PXRD data of the co-precipitated aluminium doped hydrozincite precursors $\text{Al}:\text{Zn}_5(\text{OH})_6(\text{CO}_3)_2$. x_{Al} is the metal based aluminium ratio. The black bars correspond to the reference of hydrozincite (ICSD#16583).

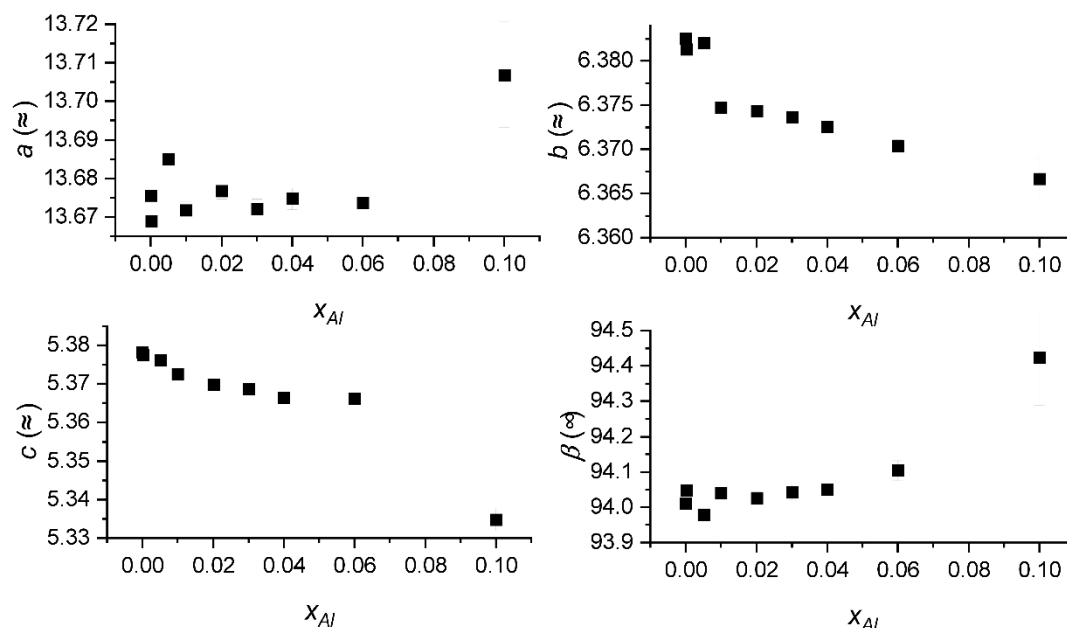


Figure SI 11.29: Lattice parameter of the refined PXRD pattern of the aluminium doped hydrozincites in dependency of the aluminium content.

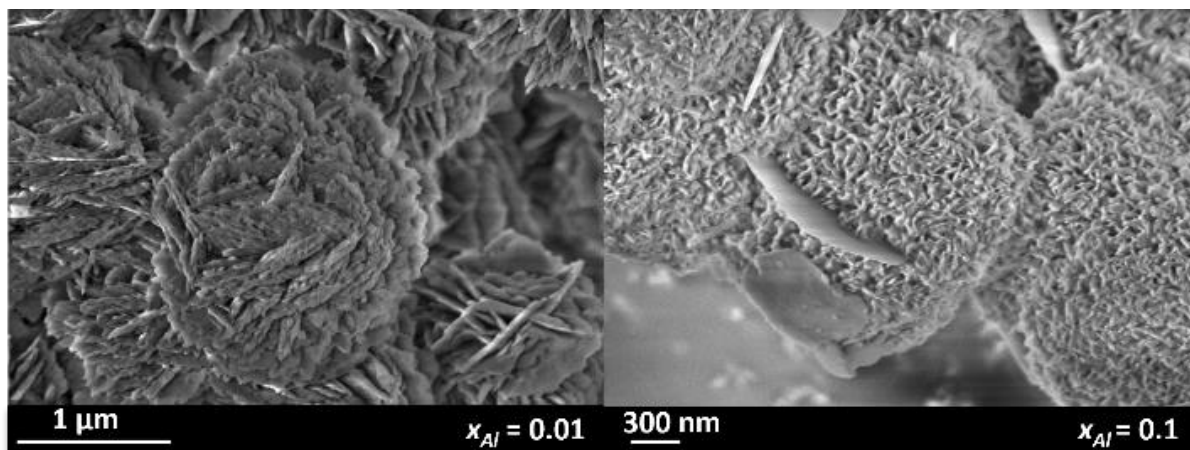


Figure SI 11.30: Morphology comparison in dependency of the aluminium content in aluminium-doped hydrozincites $Al:Zn_5(OH)_6(CO_3)_2$ after co-precipitation and drying. The larger hexagonal platelets are assigned to the aluminium-rich side-phase zaccagnaite (see main text for details).

The influence of the aluminium doping on the particle morphology was determined by SEM analysis of the hydrozincite with $x_{Al} = 0.01$ (Figure SI 11.30 left side) and $x_{Al} = 0.1$ (Figure SI 11.30 right side) aluminium content. For low doping amounts, inter-grown platelets that form spherical aggregates were observed. The doping with $x_{Al} = 0.1$ aluminium content resulted also in spherical aggregates, but they were built up of much smaller primary particles of a platelet shape. Simultaneously the morphology is no longer uniform. Large hexagonal platelets (compare Figure SI 11.30 right image) are present in addition. These platelets are aluminium enriched, which was confirmed by EDX analysis (compare Figure SI 11.31) as listed in Table SI 11.18. The higher doping level resulted into inhomogeneous distributed aluminium in the precursor material due to the segregation of this aluminium-rich side-phase, which was identified as zaccagnaite (see main text for details). This result was also found in the hydrozincite sample with $x_{Al} = 0.03$, where also a hydrotalcite signal was present in the corresponding PXRD pattern (Figure 5.3 b)).

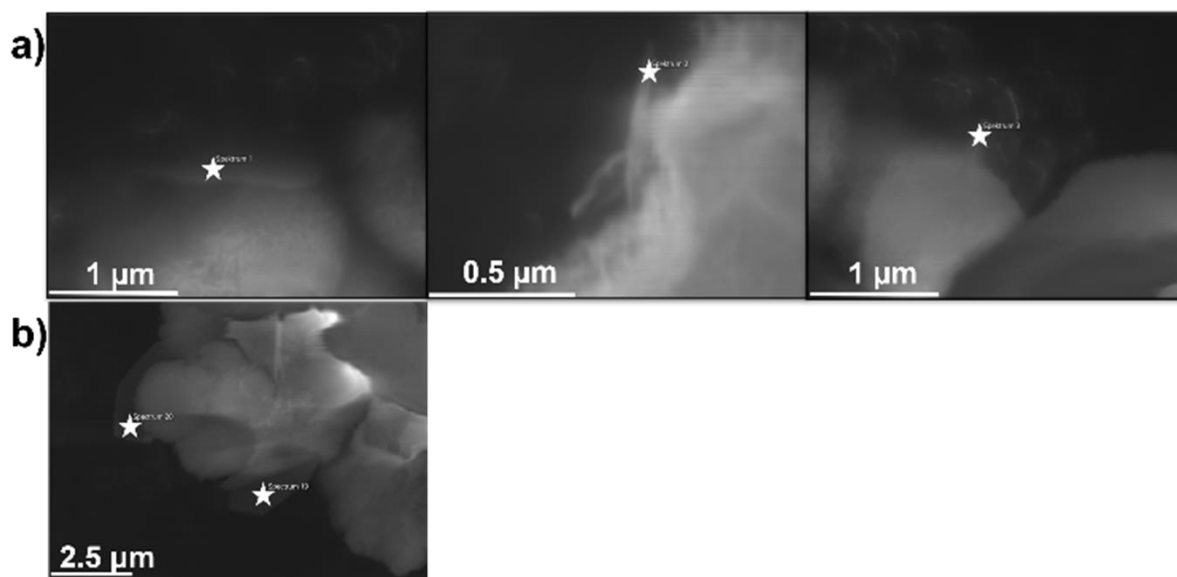


Figure SI 11.31: SEM images of the recorded EDX point spectra of the large hexagonal platelets, from left Spectrum 1, Spectrum 2 and Spectrum 3 the analysed spot is marked with an asterisk. The pictures of a) contained to hydrozincite doped with $x_{Al} = 0.1$ aluminium. The pictures of b) contained to hydrozincite with $x_{Al} = 0.03$ aluminium amount (Spectrum 19 (left) and Spectrum 20 (right)).

Table SI 11.18: Aluminium and zinc ratio of the analysed platelets by SEM-EDX, shown in Figure SI 11.31.

# Spectrum	Zn at%	Al at%	$x_{Al/(Zn+Al)}$	$M^{II}:M^{III}$
1	70	30	0.3	2
2	74	26	0.3	3
3	72	28	0.3	3
19	92	8	0.1	12
20	81	19	0.2	4

11.7.5.2 Thermogravimetric analysis of the precursor samples

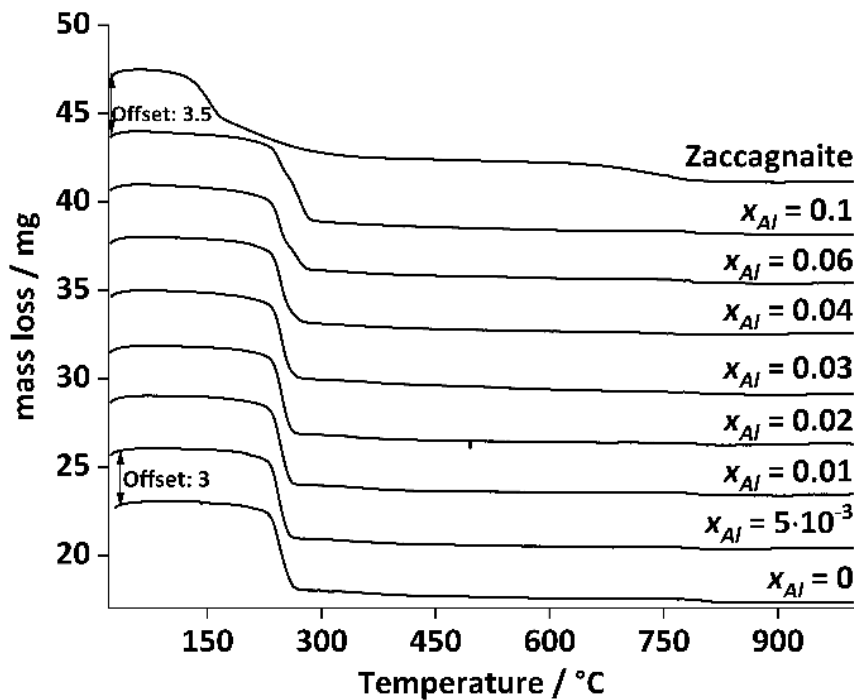


Figure SI 11.32: Thermogravimetric analysis of the decomposition of the hydrozincite precursors in synthetic air with heating ramp of 6 °C min^{-1} up to 1000 °C . x_{Al} is the metal-based fraction.

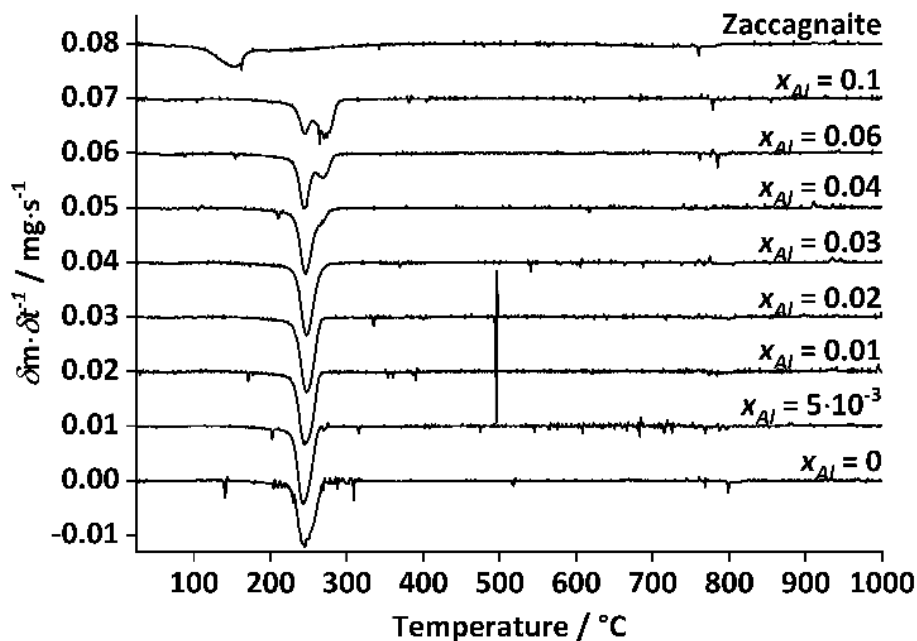


Figure SI 11.33: Differential thermogravimetric analysis of the decomposition of the hydrozincite precursors in synthetic air with heating ramp of 6 °C min^{-1} up to 1000 °C . x_{Al} is the metal-based fraction.

The decomposition of the co-precipitated hydrozincites and of the zaccagnaite reference compound were analysed by thermogravimetric measurements on a STA 1600 from Linseis

(shown in Figure SI 11.32 and Figure SI 11.33) in synthetic air heating the sample from room temperature to 1000 °C with a heating ramp of 6 °C min⁻¹. The hydrozincites start to decompose at around 220 °C and the decomposition process is completed at 300 °C. Therefore, the calcination temperature of 320 °C is high enough to ensure complete transformation but is low enough to create high-surface area materials and to prevent sinter effects. At $x_{Al} = 0.04$ and higher aluminium contents, the DTG signal shows a shoulder or second event at higher temperatures indicating an additional phase beside the hydrozincite. Because of the presence of the zaccagnaite side phase in this samples, found by PXRD analysis, the two decomposition steps could be assigned to the separated decomposition of hydrozincite and hydrotalcite. However, the zaccagnaite reference was found to decompose at lower temperature.

11.7.5.3 Infrared analysis

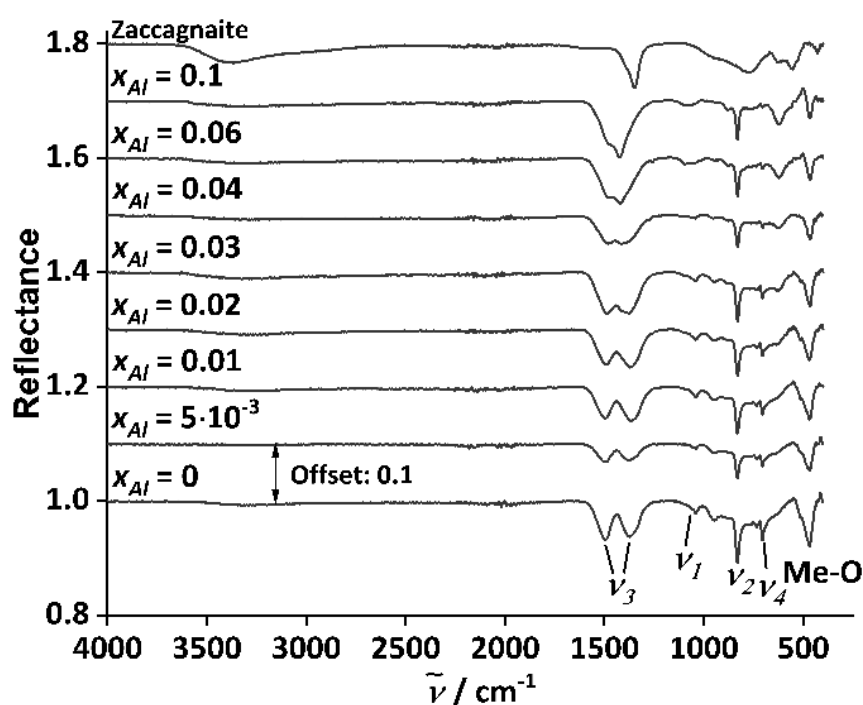


Figure SI 11.34: Complete range infrared spectroscopy of the aluminium doped hydrozincites $Al:Zn_5(OH)_6(CO_3)_2$ in comparison with the aluminium rich hydrotalcite side phase zaccagnaite. x_{Al} is the metal-based fraction of aluminium.

In Figure SI 11.34 the stack plot of the measured infrared spectra of the aluminium doped hydrozincite samples are shown. The main text provides a brief discussion on the changes in the spectra observed with varying aluminium content. Here, the general assignment of the bands and further details are discussed.

In the range of 3600 cm⁻¹ to 3200 cm⁻¹ the stretching band of OH⁻ ions should be detectable, which hints to stacking disorders.²⁴¹ In our synthesis series only one broad weak absorption

band around 3300 cm^{-1} was detected (Figure SI 11.35). This band is originated by the hydrogen bond between a hydroxyl-group and an oxygen of a carbonate ion as well as by the stretching mode of the hydroxide groups.²⁹⁷ In contrast, this mode is more pronounced in the hydrotalcite reference material, caused by the higher amount of hydroxide groups.²¹⁴

The ν_3 modes of the hydrozincite broaden as more aluminium was incorporated. Simultaneous a shift of the ν_3 absorption peak from $\approx 1370\text{ cm}^{-1}$ ($x_{Al} = 0$) to a higher wavenumber 1422 cm^{-1} ($x_{Al} = 0.1$) was induced. The mode at around 1490 cm^{-1} did not shift. The ν_7 mode showed a similar behaviour. This absorption became weaker and simultaneous a shift towards higher wavenumbers can be observed (1041 cm^{-1} to 1081 cm^{-1}). In contrast to this observation, the ν_4 modes became only weaker and did not shift. The signal of the out-of-plane OCO bending mode (ν_2) was in all hydrozincite samples present without shifting, but a second ν_2 mode appeared for higher aluminium content samples. Typically, an LDH phase contains only one ν_3 absorption mode^{211, 212, 214}. The hydrozincites with $x_{Al} = 0.06$ and $x_{Al} = 0.1$ aluminium content seem to change in the ν_3 absorption modes towards a hydrotalcite like signal.

The infrared mode at 621 cm^{-1} appeared for $x_{Al} > 0.01$ and increased with the aluminium content. From hydrotalcite-like materials with different divalent cations, the mode in this region was found to be induced by translation of the hydroxyl groups between the sheets.²¹⁴ The increase in the absorption band in the hydrozincite samples is larger than the mode in the aluminium rich Zaccagnaite sample. Therefore, this mode corresponds more probably to the Zn-OH and to the Al-OH in the hydrozincite, which simultaneously explains the broadening with increasing aluminium content. An increase in the translation mode of hydroxyl-groups does indicate that the amount increased. Therefore, the possibility of an increased number of sheets is given and demonstrates the sublattice change as an incorporated additional charge. An increased number of sheets will result in more but smaller primary particles and in increased defect sites of the host lattice.

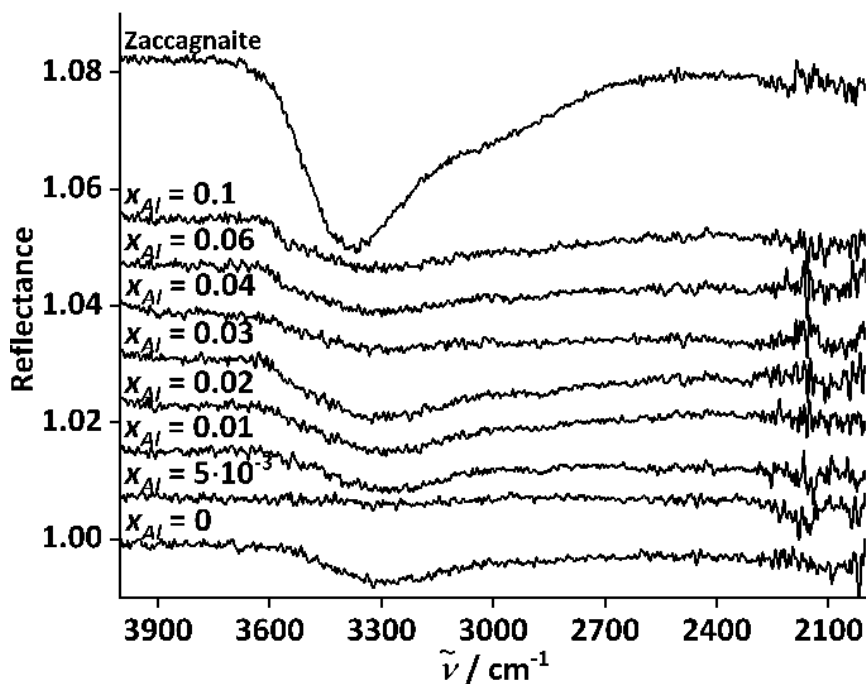


Figure SI 11.35: Focused infrared spectra of the aluminium doped hydrozincites $\text{Al}:\text{Zn}_5(\text{OH})_6(\text{CO}_3)_2$ in comparison with the aluminium rich hydrotalcite side phase to demonstrate the OH stretching mode (around 3300 cm^{-1}).

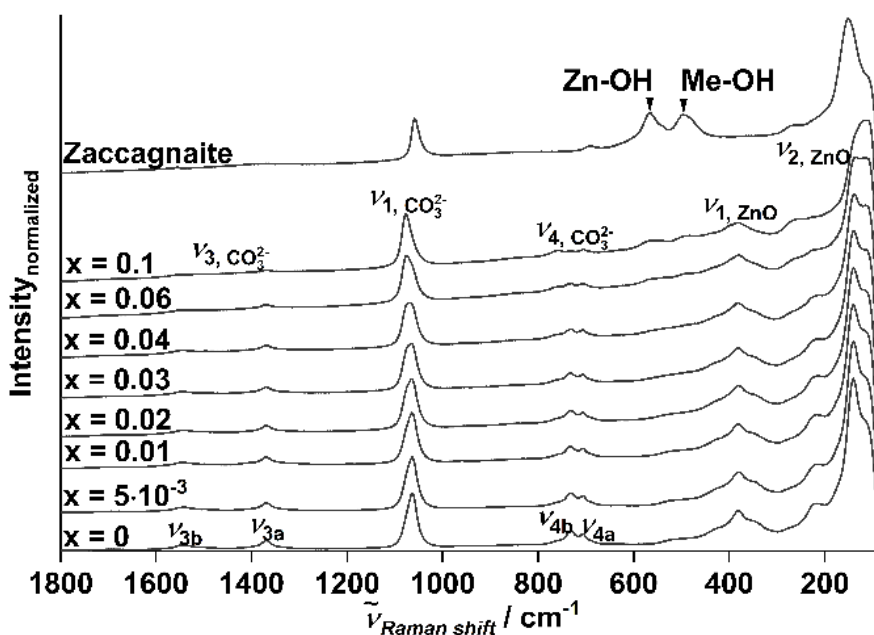


Figure SI 11.36: Raman spectra of the aluminium doped hydrozincites $\text{Al}:\text{Zn}_5(\text{OH})_6(\text{CO}_3)_2$ in comparison with the aluminium rich hydrotalcite side phase.

11.7.6 Characterization of the zinc oxides

11.7.6.1 Elemental composition and nitrogen physisorption

The metal amount was determined with an Avio 200 ICP Optical Emission Spectrometer with a PerkinElmer S23 Autosampler. Before analysis, 5 mg of the metal oxide was dissolved in nitric acid. In Figure SI 11.37 the measured aluminium ratios in comparison with the nominal ratios are plotted. The targeted ratio was reached for samples with lower aluminium content than 6 %. For higher aluminium contents ($x_{Al} > 4\%$) the deviation of the measured composition from the nominal targeted composition was larger.

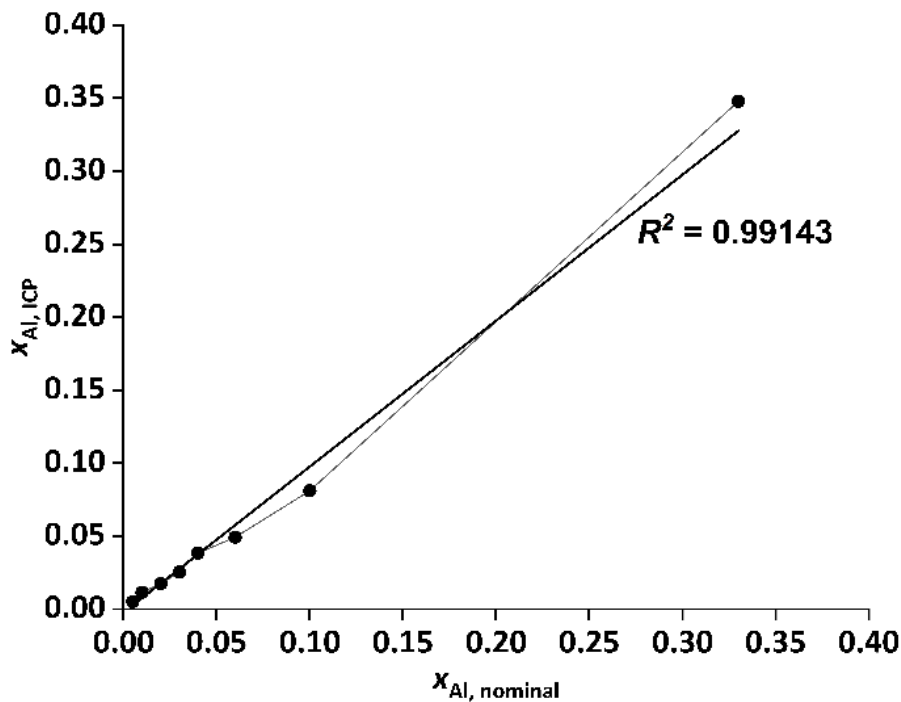


Figure SI 11.37: Metal based aluminium content determined by ICP analysis of the oxides. The line between the datapoints is to guide the eye.

11.7.6.2 Nitrogen physisorption, pore size distribution and pore volume

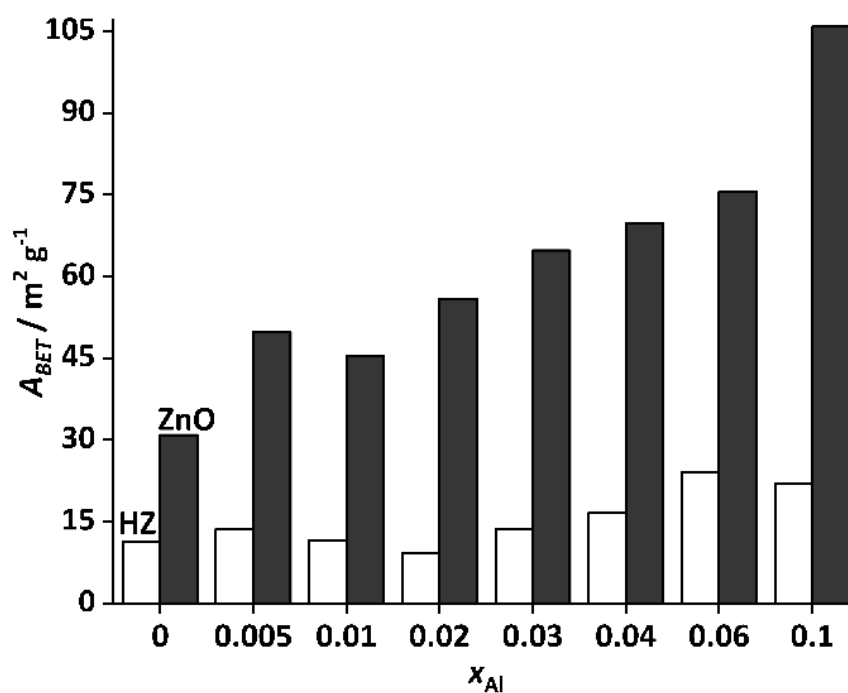


Figure SI 11.38: BET-surface area evolution of aluminium doped hydrozincites (HZ: hydrozincite precursors) and the resulting zinc oxides (ZnO) after calcination at 320 °C for 4 h in static air. x_{Al} indicated the cation-based molar aluminium fraction.

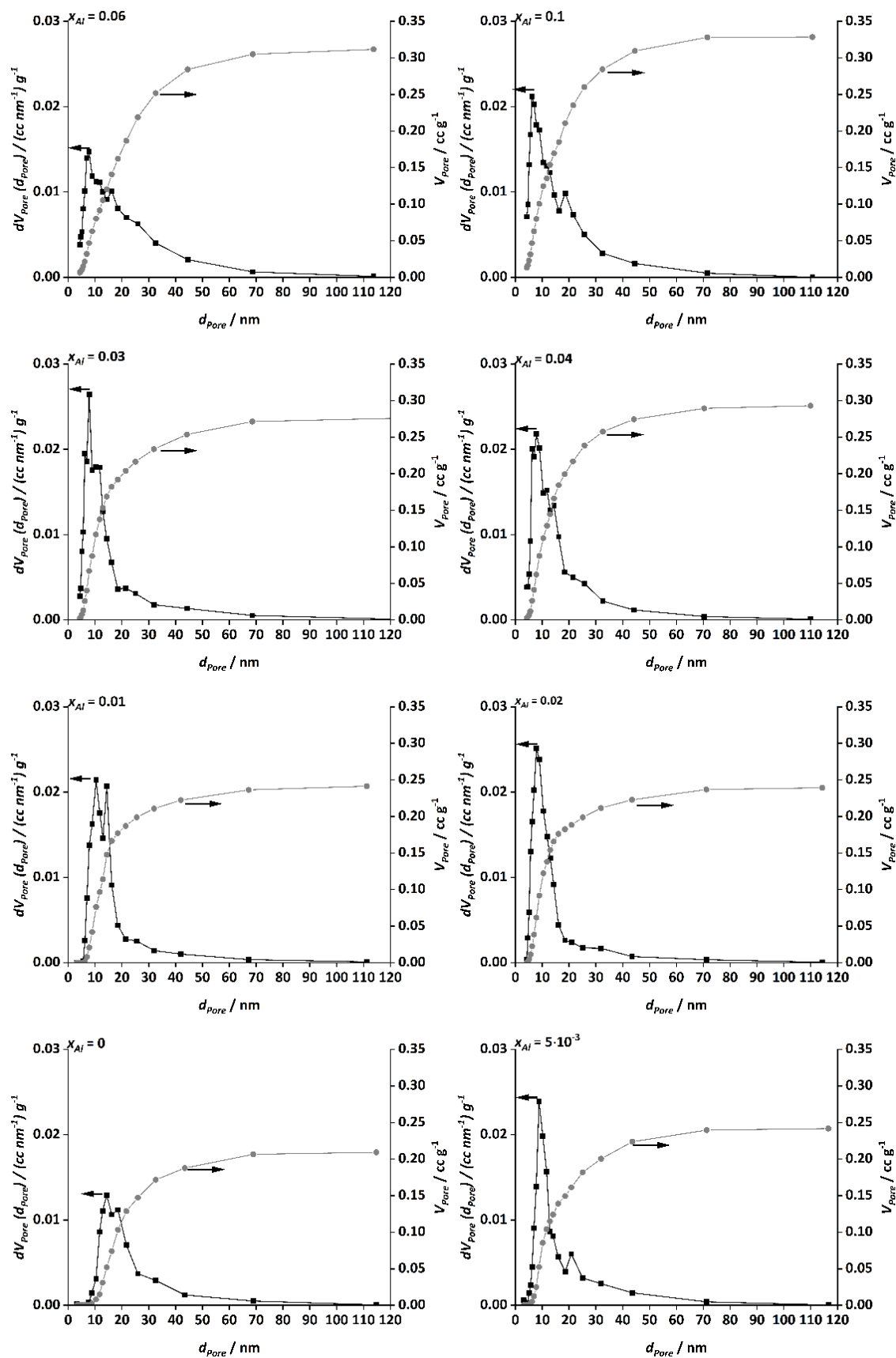


Figure SI 11.39: Pore size and -volume distribution of the aluminium doped zinc oxide series. X_{Al} is the metal-based fraction of Al. The lines are to guide the eye.

11.7.6.3 Raman spectroscopy

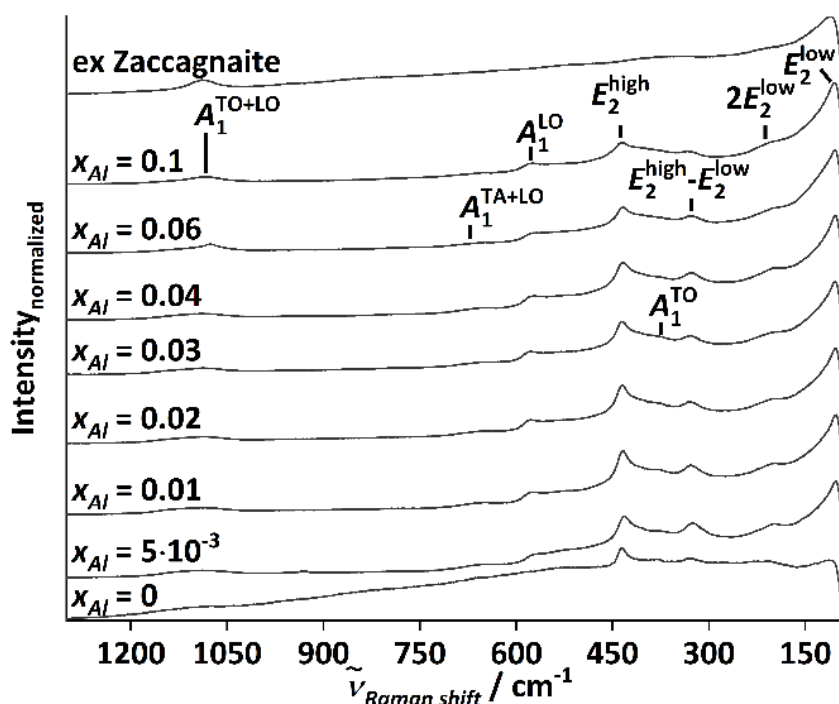


Figure SI 11.40: Raman spectra of the aluminium doped zinc oxides in comparison with the aluminium rich hydrozincite side phase (ex-zaccagnaite). The calcination was performed at 320 °C for 4 h in static air. The modes are labelled with abbreviations for: Longitudinal optical mode (LO), transversal optical mode (TO) and transversal acoustical mode (TA). The Raman spectra were recorded with a wavelength of 785 nm and 90 mW at 45° rotated sample at room temperature.

To determine the influence of the aluminium incorporation onto the zinc oxide, Raman spectra of the doped zinc oxide samples were recorded (compare Figure SI 11.40). The classification of the modes was performed by the description from Arguello *et al.*²⁹⁸ and Cuscó *et al.*²⁴³ The spectra show the non-polar E_2 and the polar A_1 modes as well as some side modes like the acoustic overtone of the E_2^{low} signed as $2E_2^{\text{low}}$.²⁹⁹ The labelled spectrum “ex Zaccagnaite” is the synthesized reference sample of the side-phase, described above, which was calcined under the same conditions as the hydrozincites. The E_2^{low} mode is a result of the vibration of the zinc ions whereas the E_2^{high} mode is more assigned to the oxygens moving perpendicular to the c-axis. The oxygen dominated A_1 mode shows the movement of the oxygen ions in parallel to the c-axis whereby an oscillating polarization by the zinc ions is induced.²⁹⁹ This causes splitting into a longitudinal optical (LO) and a transversal optical (TO) mode.^{299, 300}

Raman spectroscopy should also be sensitive to side phases in a sample.³⁰⁰ Compared to the aluminium doped zinc oxide samples the undoped sample had a higher intensity at the E_2^{high} (O sublattice) mode than at the E_2^{low} (Zn sublattice) mode, but the positions of the bands are

independent of the dopant amount. The ex-zaccagnaite sample was used to verify, at which position a Raman shift can be expected, if this side phase was calcined under the same conditions. Interestingly, only two sharp peaks are visible. One at around 112 cm^{-1} and the second one at around 1085 cm^{-1} . Both peaks are shifted by ca. 5 cm^{-1} towards higher wavenumbers compared to the zinc oxide samples. In case of side-phase formation in the aluminium doped samples, the $A_1^{\text{TO+LO}}$ overtone mode appears more pronounced with increasing aluminium content, especially for the sample containing $x_{Al} = 0.06$ and $x_{Al} = 0.1$ aluminium. Since this mode was also present in the undoped zinc oxide sample and since this mode is a second order mode, it cannot be related to aluminium substituted zinc sites.²⁴³ However, this overtone can be assigned to the naturally occurring defects in zinc oxide.²⁴⁴ By increasing the aluminium content, the PXRD pattern have shown that the 002 reflection (*c*-axis) was affected by the incorporation. This finding can be supported by the increase in the $A_1^{\text{TO+LO}}$ mode, which involves the *c*-plane.

The Raman spectrum of the ex-zaccagnaite sample shows only few Raman modes, which correspond to ZnO, but the shift of about 5 cm^{-1} could support a defect-enriched state of this phase, which is present in high inter-dispersion with additional amorphous aluminium-rich material.³⁰¹ This finding is in accordance with the results observed by TEM analysis.

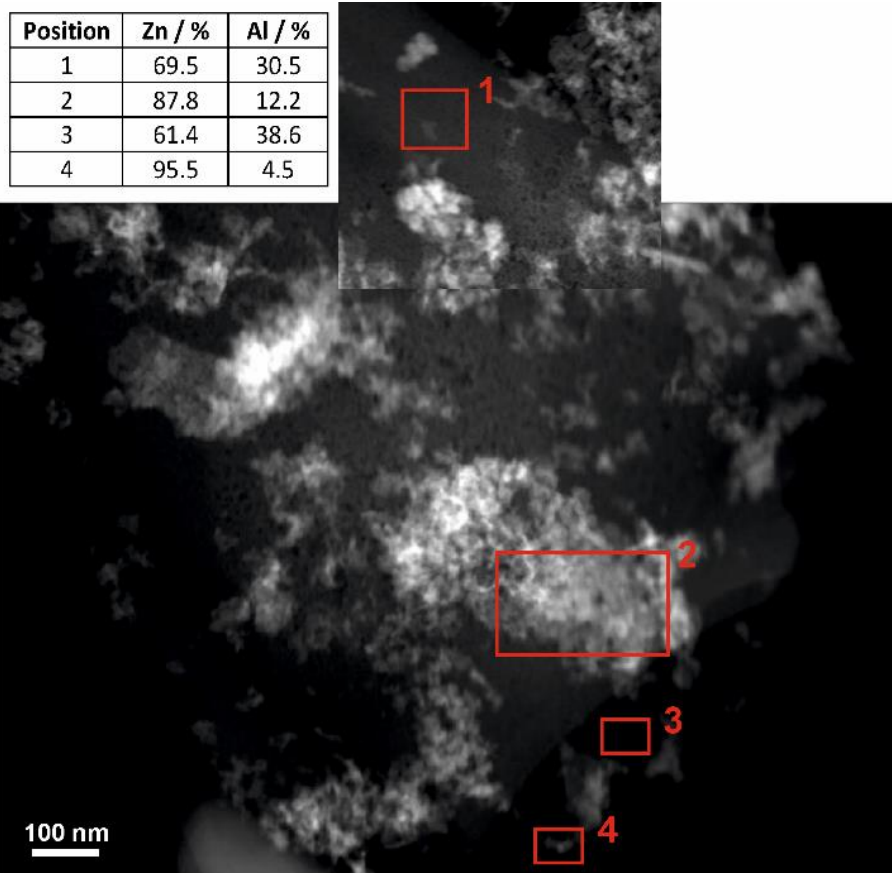
11.7.6.4 TEM-EDX analysis

Figure SI 11.41: STEM-EDX-analysis of an aluminium doped zinc oxide sample with $x_{Al} = 0.03$. The windows visualize the analysed regions from which the mean metal-composition was determined, which are shown in the table.

11.7.6.5

UV/Vis analysis

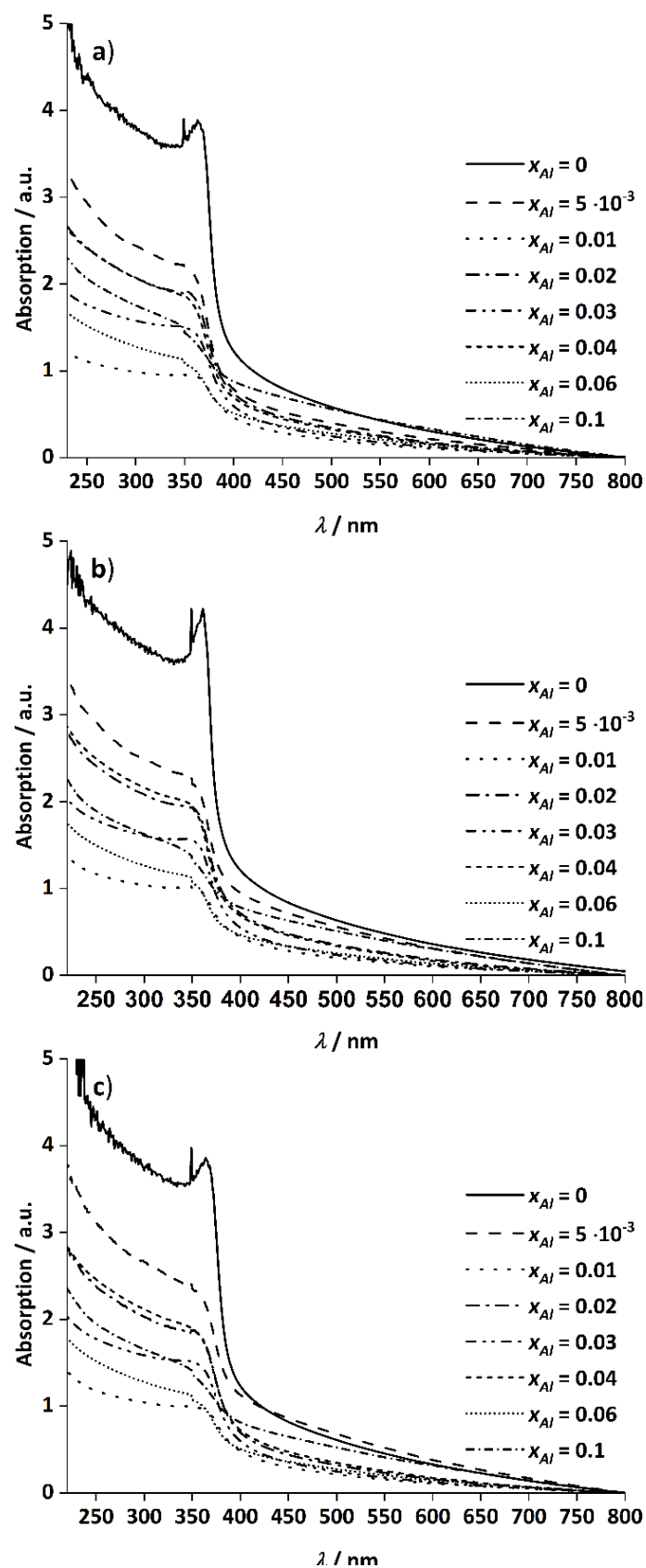


Figure SI 11.42: UV-Vis spectra of the aluminium doped zinc oxides. The spectra were recorded at room temperature (a), at $-185 \text{ }^\circ\text{C}$ (b) and at $27 \text{ }^\circ\text{C}$ (c). The spectra are recorded in transmission geometry and are automatically normalized to 0 for $\lambda = 800 \text{ nm}$.

In Figure SI 11.42 the recorded UV/Vis spectra of the zinc oxide samples are shown. The calcination was performed at 320 °C for each sample. The band gap determination was performed by differentiation of the raw data (Figure SI 11.42), to determine the changing point. This mathematical treatment results in an optimum function, where the minimum corresponds to the changing point. Therefore, the wavelength of this minimum (changing point in Figure SI 11.42) was used to calculate the Band gap energy. Because of the doping effect it is assumed that the absorbance shift towards higher or lower wavelength, as it can be seen by the data in Figure SI 11.42. However, this shift in absorbance can be followed by the shift of the changing point, which can be mathematically evaluated and reduces evaluation errors. The change of these values with variation of the aluminium doping level is discussed in the main text.

To determine the reliability of the measured data, additional measurements were performed with a UV/Vis spectrometer 2600i of Shimadzu in the range of 200 nm to 900 nm. The sample was pressed into the solid sample holder to create a flat surface. The spectra were recorded in reflection with BaSO₄ as reference material. The band gap evaluation was performed as described above. These results are similar to the measurements in transmission mode as it is shown in Figure SI 11.43. To determine the error caused by the preparation method, three additional batches of zinc oxide containing 3 % aluminium ($x_{Al} = 0.03$) are additionally analysed. These batches correspond to different batches of co-precipitated hydrozincite samples. The results are shown in Table SI 11.19. The similar results in band gap energies demonstrate, that the reported data visualize the material properties of the herein reported doping series in a reproducible way.

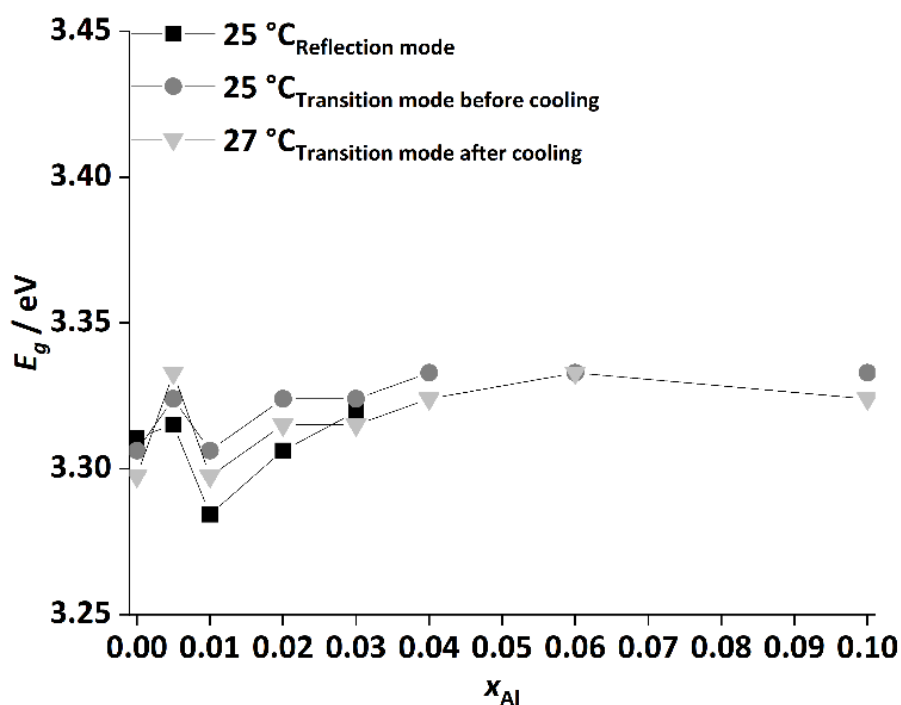


Figure SI 11.43: Comparison of the Band gap energies determined in reflection and transmission mode at room temperature.

Table SI 11.19: List of the reproduced Band gap measurements of different synthesis batches of ZnO:Al with 3 % Al content ($x_{Al} = 0.03$).

x_{Al}	E_g	E_g
	eV	eV
Synthesis number	measured in reflection mode at 25 °C	measured in transmission mode at 25 °C
0.03-S1	3.32	3.32
0.03-S2	3.32	-
0.03-S3	3.32	-
0.03-S4	3.32	-

11.7.6.6 High temperature calcination series

11.7.6.6.1 Precursor characterization and reference calcination temperature

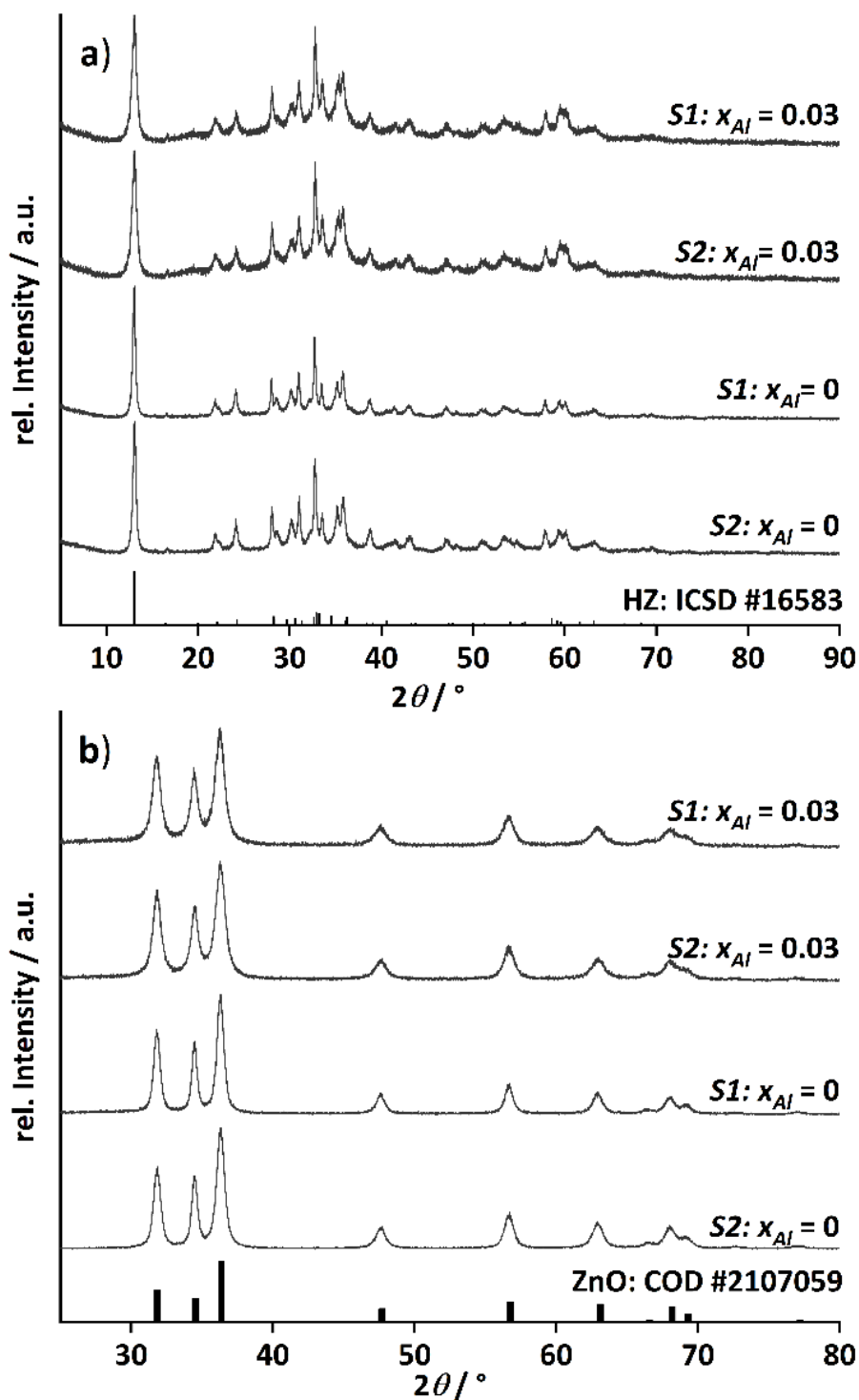


Figure SI 11.44: PXRD pattern of the a) precursor (reference from ICSD: 16583, bars) and b) zinc oxide (Reference from COD: 2107059, bars) after calcination at 320 °C of undoped and with 3 % aluminium doped samples ($x_{Al} = 0.03$). The label S1 and S2 are assigned to two different synthesis batches of the same materials. These batches were investigated in the high temperature annealing experiment.

For the comparative high-temperature calcination experiments, the sample with $x_{Al} = 0.0$ and $x_{Al} = 0.03$ needed to be reproduced to provide enough material for these investigations. The PXRD pattern of the precursors and of the samples calcined at 320 °C of the new batch S2 and the original batch S1 are compared in Fig. S25 showing that the major sample characteristics could be reproduced and that similar materials have been obtained. The following data has been obtained with the batch S2.

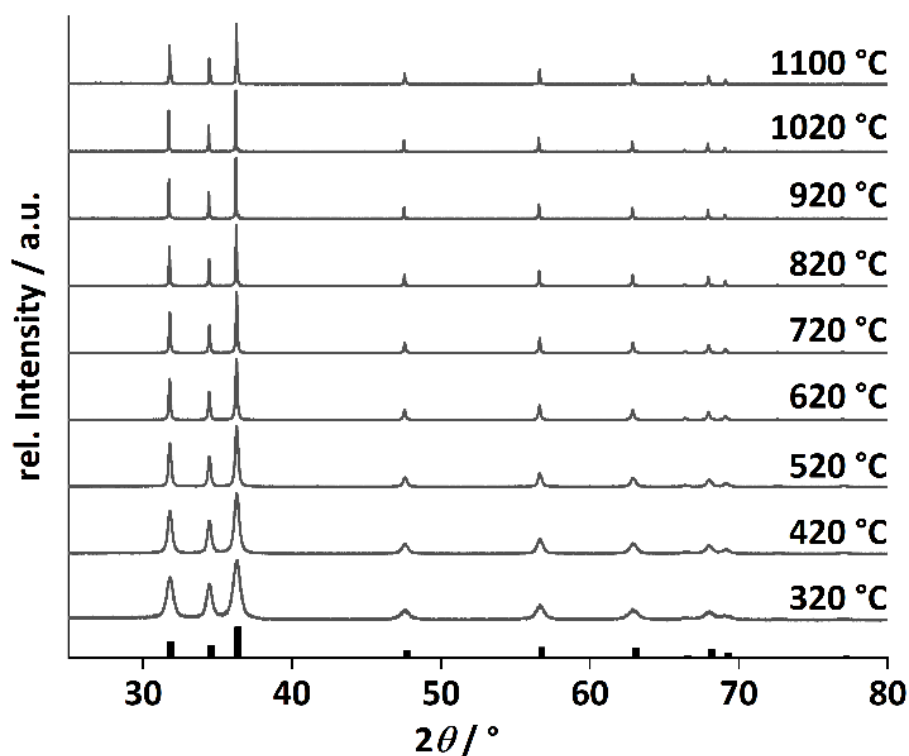


Figure SI 11.45: Powder XRD pattern of the undoped zinc oxides after calcination of the hydrozincite precursors at different temperatures with 2 °C min^{-1} heating ramp and 4 h holding time in static air. The reference pattern of zinc oxide (bars) was taken from COD database (#2107059).

For comparison, an undoped zinc oxide was treated in the same way as the 3 % aluminium doped zinc oxide (see main text). In Fig. S26 the powder XRD pattern are shown. The reflection width decrease was similar as described for the doped zinc oxide material in the main text, indicating an increased crystallite size, as it was also confirmed by SEM analysis.

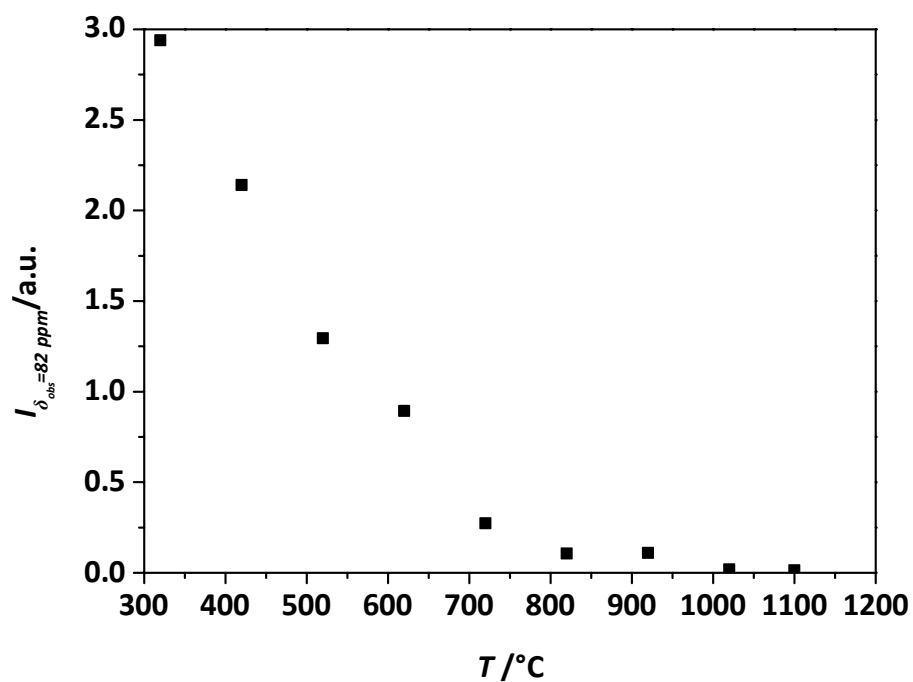


Figure SI 11.46: Qualitative change of the ^{27}Al MAS NMR signal at $\delta_{\text{obs}} = 82$ ppm of the aluminium enriched zinc oxides, $x_{\text{Al}} = 0.03$, with different annealing temperatures applied. Similar measurement conditions were applied for the individual measurements, i.e. it was assumed that the quadruple parameters do not change while recycle delays were bigger than $3 \cdot T_1$.

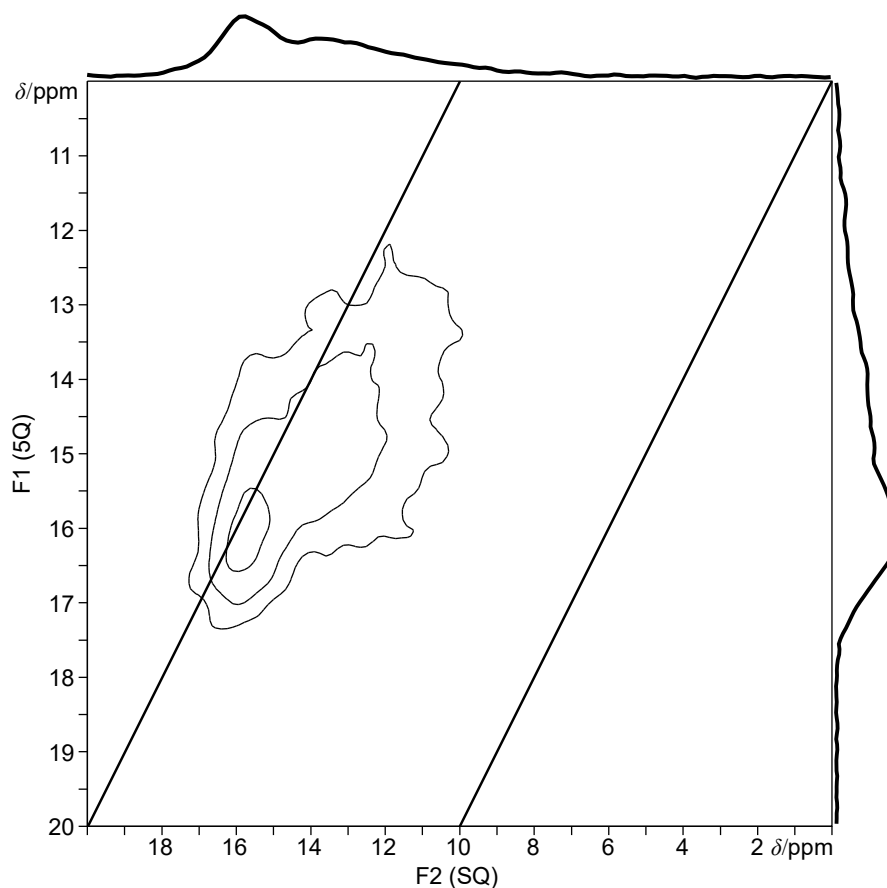


Figure SI 11.47: Sheared ^{27}Al 2D quintuple-quantum MQMAS NMR spectrum of zaccagnaitite acquired at a spinning frequency of 20 kHz. The acquisition was performed at 20.0 kHz sample spinning frequency using a three-pulse sequence with a zero-quantum filter³⁰², with rotor-synchronized sampling of the indirect dimension and a recycle delay of 4 s. The hard pulses were optimized separately, and a selective soft pulse (90°) was determined from ^{27}Al nutation experiments.

11.8 Supporting Information to "Phase evolution and solubility limit of gallium doping in zinc oxide catalyst supports synthesized via co-precipitated hydrozincite precursors"

Benjamin Mockenhaupt ^{**ac}, Jan Konrad Wied ^{**b}, Sebastian Mangelsen ^c, Ulrich Schürmann ^d, Lorenz Kienle ^d, Jörn Schmedt auf der Günne ^{*b}, Malte Behrens ^{*ac}

- a. B. Mockenhaupt, Prof. Dr. M. Behrens, Institute of Inorganic Chemistry, University of Duisburg-Essen, Universitätsstr. 7, 45141 Essen (Germany), E-mail: mbehrens@ac.uni-kiel.de.
- b. J. K. Wied, Prof. Dr. J. Schmedt auf der Günne, Institute of Inorganic Chemistry, University of Siegen, Adolf-Reichwein-Straße 2, 57076 Siegen (Germany), E-mail: gunnej@chemie.uni-siegen.de.
- c. B. Mockenhaupt, Dr. S. Mangelsen, Prof. Dr. M. Behrens, Institute of Inorganic Chemistry, Christian-Albrecht University of Kiel, Max-Eyth-Str. 2, 24118 Kiel (Germany)
- d. Dr. U. Schürmann, Prof. Dr. Lorenz Kienle, Institute for Materials Science, Christian-Albrecht University of Kiel, Kaiserstraße 2, 24143 Kiel (Germany)

** both authors contributed equally.

* Corresponding author.

Contribution of the authors

- B.M. synthesized the materials and contributed to the characterization, data analysis and wrote the first draft of the manuscript.
- J.K.W. conducted the NMR experiments, the data analysis.
- S.M. evaluation and reviewing of the manuscript.
- U.S. conducted the TEM measurements, contributed to design of experiments and data analysis.
- L.K., J.S.G and M.B. contributed to conceptualization of the work, acquisition of the financial support, provision of study materials, reagents, materials, instrumentation, computing resources and other analysis tools.

11.8.1 Precursor synthesis

Table SI 11.20: List of the used chemicals and their purity used for co-precipitation.

Chemicals	Supplier	Purity
$Zn(NO_3)_2 \cdot 6 H_2O$	Carl Roth GmbH + Co. KG	$\geq 99 \%$
$Ga(NO_3)_3 \cdot x H_2O$	Alfa Aesar	$\geq 99 \%$

11.8.2 Synthesis of the gallium rich side phase Zaccagnaite

The gallium rich side phase, the zaccagnaite-like Ga,Zn LDH, was synthesized by co-precipitation. The precipitation was carried out in an automated stirred tank reactor (OptiMax, Mettler Toledo, 1L) from 0.4 M metal salt nitrate solution at a temperature of 50 °C and at a constant *pH* of 8.5. As precipitating agent, 0.09 M sodium carbonate together with 0.6 M sodium hydroxide solution was used. The dosing rate of metal solution was adjusted to 2.08 g min⁻¹. After precipitation the precipitate was aged for 60 minutes without further *pH* control in the mother liquor. The precursor was washed with deionized water 10 times, to reach a conductivity of the filtrate lower than 100 $\mu S\ cm^{-1}$ and dried at 80 °C over night in a drying cabinet.

The PXRD characterization of the phase pure precursor is shown in Figure SI 11.48 a) and the PXRD characterization of the calcined sample is shown in the same figure b).

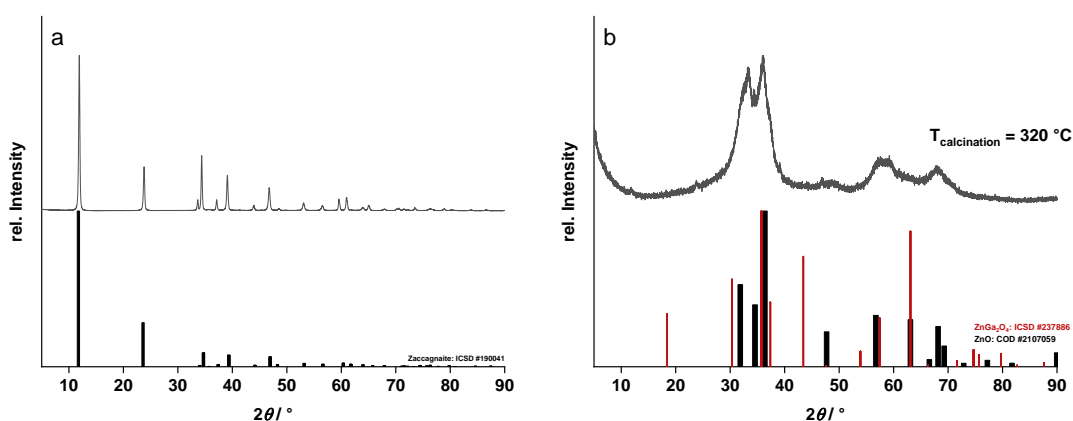


Figure SI 11.48: PXRD characterization of the co-precipitated Ga,Zn LDH (Zaccagnaite-like) precursor (a) with reference from ICSD (#190041) and the calcined samples at 320 °C (b) with reference for ZnO from COD (#2107059, black, broad bars) and zinc-gallium spinel from ICSD (#237886, red, small bars).

11.8.3 Characterization of the Hydrozincite precursors

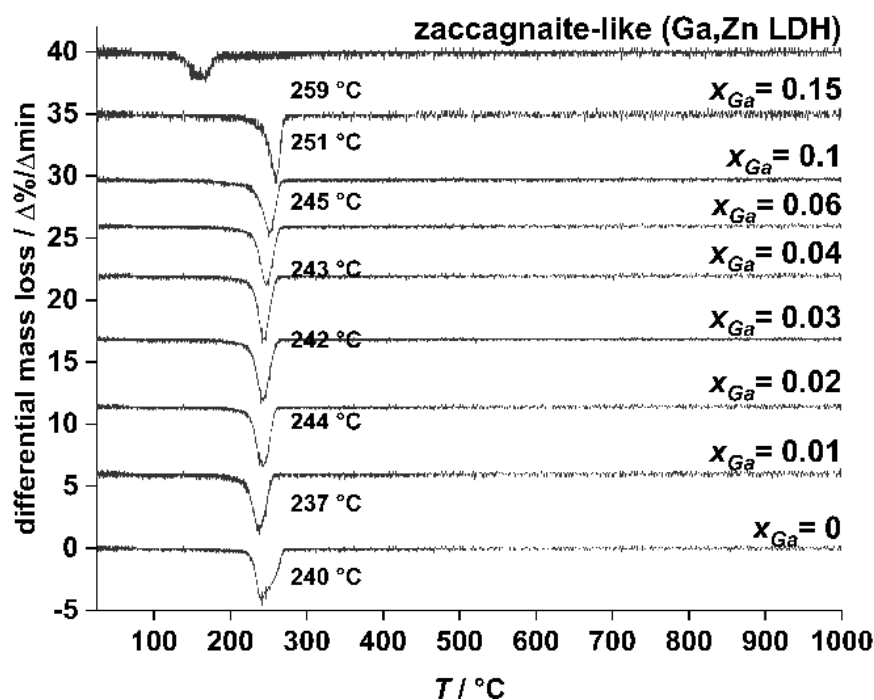


Figure SI 11.49: Differential plot of the thermogravimetric analysis of the decomposition of the hydrozincite precursors in synthetic air into zinc oxide in comparison to the synthesized zaccagnaite-like Ga,Zn LDH. The labelled temperatures correspond to the minimum. X_{Ga} is the metal-based fraction.

The decomposition of the co-precipitated hydrozincites were analysed by thermogravimetric measurements on a STA 409 PC from Netzsch (shown in Figure SI 11.49). The hydrozincites start to decompose at around 220 °C. The transformation into a zinc oxide is completed at 300 °C. Therefore, the calcination temperature of 320 °C is high enough to ensure complete transformation but is low enough to create maximum surface area and to prevent sinter effects.

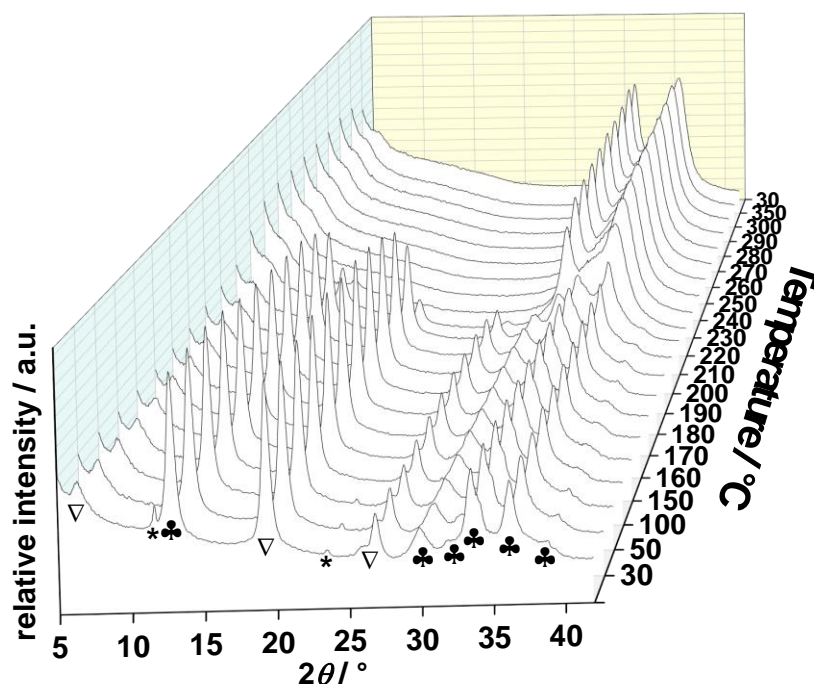


Figure SI 11.50: Temperature resolved PXRD analysis of the decomposition of the hydrozincite precursor containing $x_{\text{Ga}} = 0.15$. The PXRD analysis was performed in static air. The reflection positions are labelled as followed: zaccagnaite = *, hydrozincite = ♣ and additional reflections caused by defects = ∇.

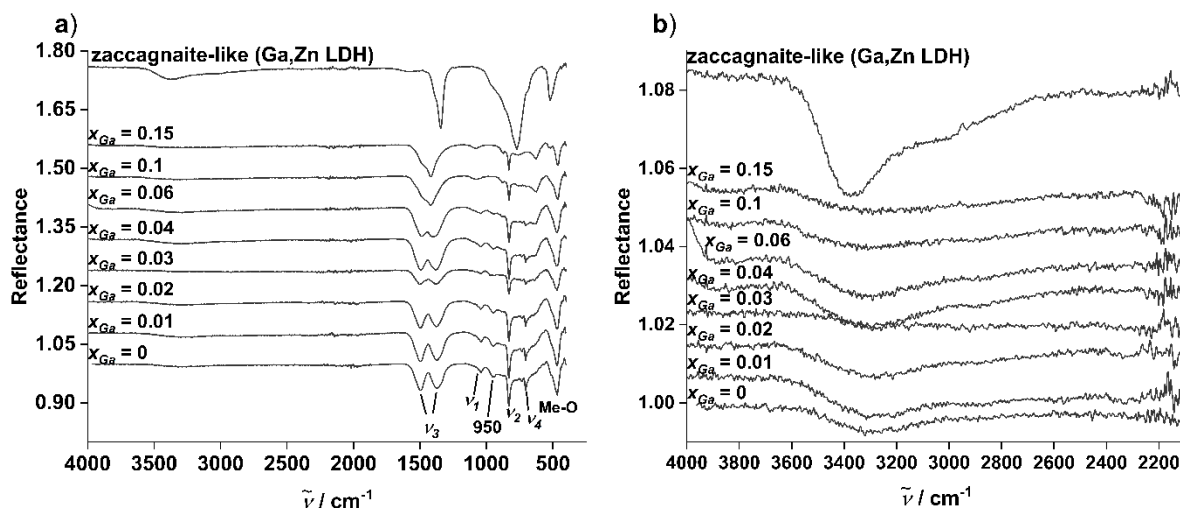


Figure SI 11.51: Complete range infrared spectroscopy of the gallium doped hydrozincites in comparison with the gallium rich zaccagnaite-like side phase (a). x_{Ga} is the metal-based gallium fraction. In b) a higher resolution in the range of $4000 - 2200 \text{ cm}^{-1}$ is demonstrated, to show the OH stretching mode (around 3300 cm^{-1}).

The most details about infrared and Raman spectroscopy was discussed in the main text. For a better understanding, details of the aligned of the 950 cm^{-1} mode in IR spectroscopy (Figure SI 11.51) towards hydrogen bond is discussed.

The Infrared signal at about 950 cm^{-1} cannot be assigned to an infrared mode by reference spectra. From hydrozincite infrared and Raman investigations the range around 950 cm^{-1} is assigned to hydroxyl groups and hydrogen bond interactions with the anionic lattice.^{212,213} From the crystallographic investigation it was found, that for one carbonate two sites are covalent bond to one tetrahedral coordinated and one octahedral coordinated zinc atom.¹²⁶ The third oxygen of the carbonate is hydrogen bonded to three hydroxyl groups.¹²⁶ In the range of $\approx 1500\text{ cm}^{-1}$ to $\approx 600\text{ cm}^{-1}$ mainly carbonate vibrations are present, which can overlap in the range of $\approx 1100\text{ cm}^{-1}$ to $\approx 890\text{ cm}^{-1}$ with hydroxyl liberations.²¹¹ Therefore, the peak in the infrared spectra at 950 cm^{-1} can be assigned to a hydrogen bond between a carbonate- and a hydroxyl group. The carbonates link the zinc sheets to form a three dimensional network of the hydrozincite.¹²⁶

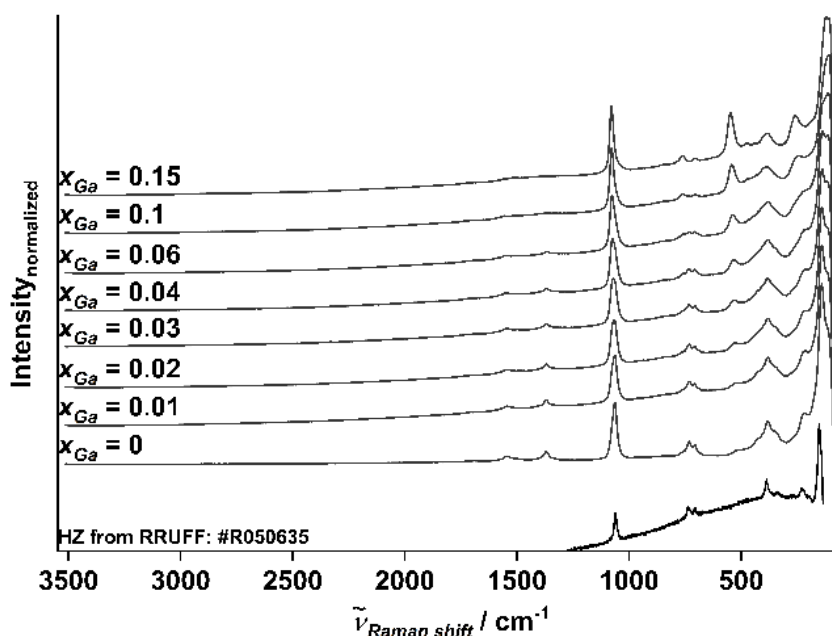


Figure SI 11.52: Complete range Raman spectra of the gallium doped hydrozincites in comparison with a Raman spectrum of a hydrozincite from the RRUFF database. X_{Ga} is the metal-based fraction of gallium.

11.8.4 Characterization of the Zinc oxides

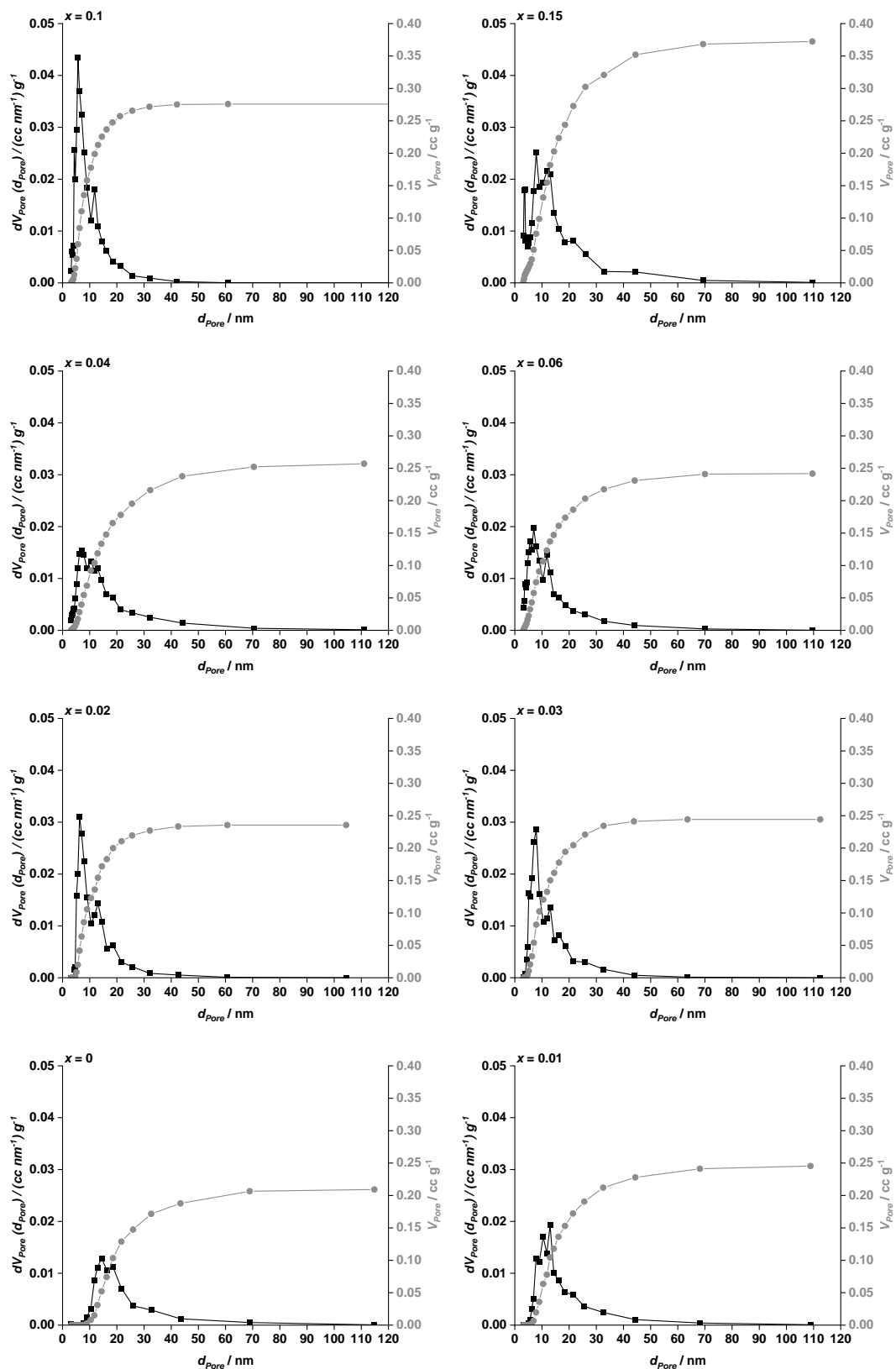


Figure SI 11.53: Pore size and pore volume distribution for the gallium doped zinc oxides. The calculation was performed on the desorption isotherm by BJH method. X is the metal-based fraction of gallium.

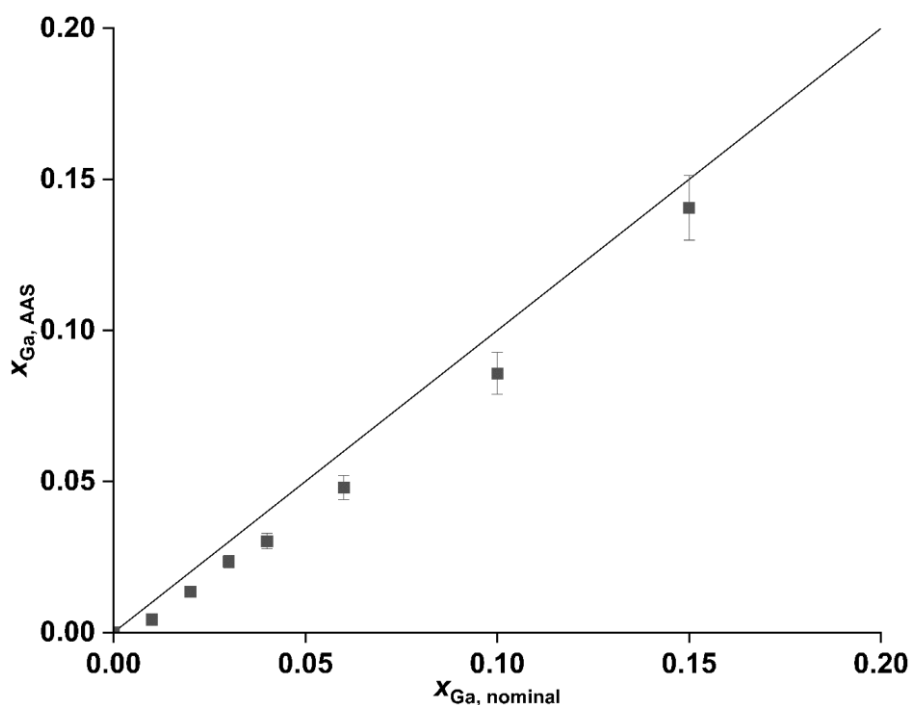


Figure SI 11.54: Metal based gallium content determined by AAS analysis of the ZnO doped with Ga.

The metal composition of the synthesized zinc oxides was determined by atomic absorption spectroscopy (AAS). The results are shown in Figure SI 11.54 in comparison to the ideal composition, shown as straight line. The doping of the zinc oxides was successful, and the nominal composition was reached due to the preparation route.

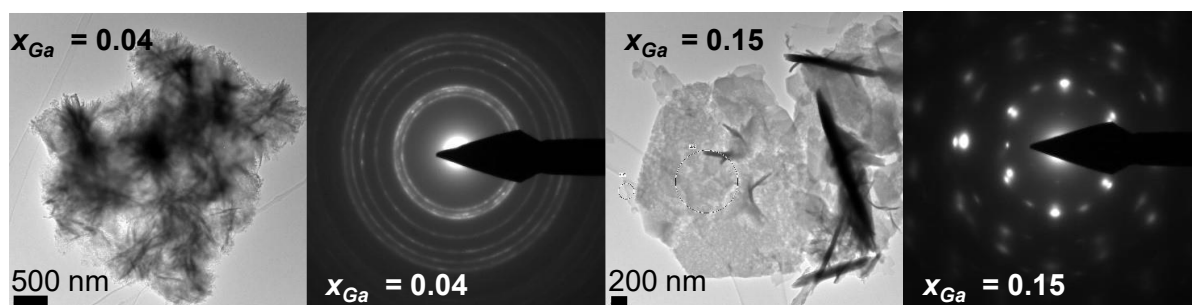


Figure SI 11.55: TEM analysis and corresponding electron diffraction micrographs of a medium Ga doped ZnO ($x_{Ga} = 0.04$) and a heavy Ga doped ZnO ($x_{Ga} = 0.15$).

TEM analysis of selected Ga doped ZnO are shown in Figure SI 11.55. The electron diffraction of the low doped ($x_{Ga} = 0.04$) ZnO shows for ZnO typical diffraction pattern. The analysis of a larger platelet in the heavy doped ZnO ($x_{Ga} = 0.15$) showed a distorted electron pattern different for typical ZnO. This larger platelet is to be assumed a zaccagnaite-like side phase, as it was observed for the Al doped series as well.¹⁷² Even, in case of Al as dopant, the decomposition of the side phase resulted in a highly defective ZnO.¹⁷² The main difference is that in case of

Ga as dopant, the side phase at higher doping levels in the hydrozincite precursor phase ($x_{\text{Ga}} > 0.04$) evolved.

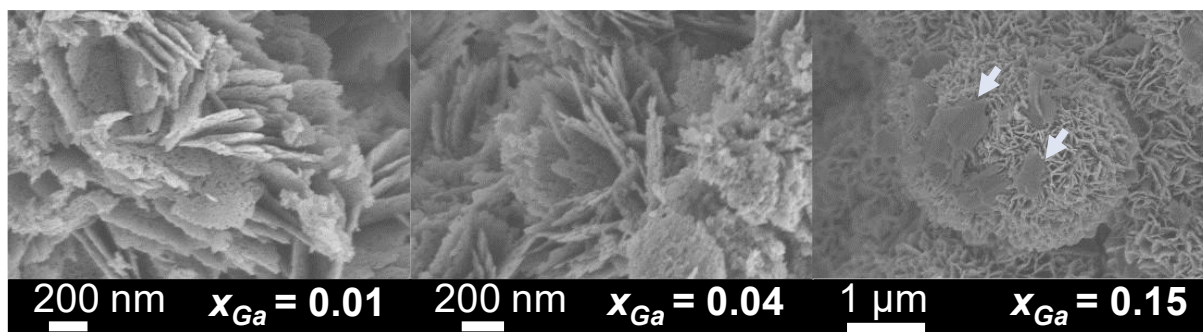


Figure SI 11.56: SEM micrographs with a higher resolution of selected Ga doped ZnO.

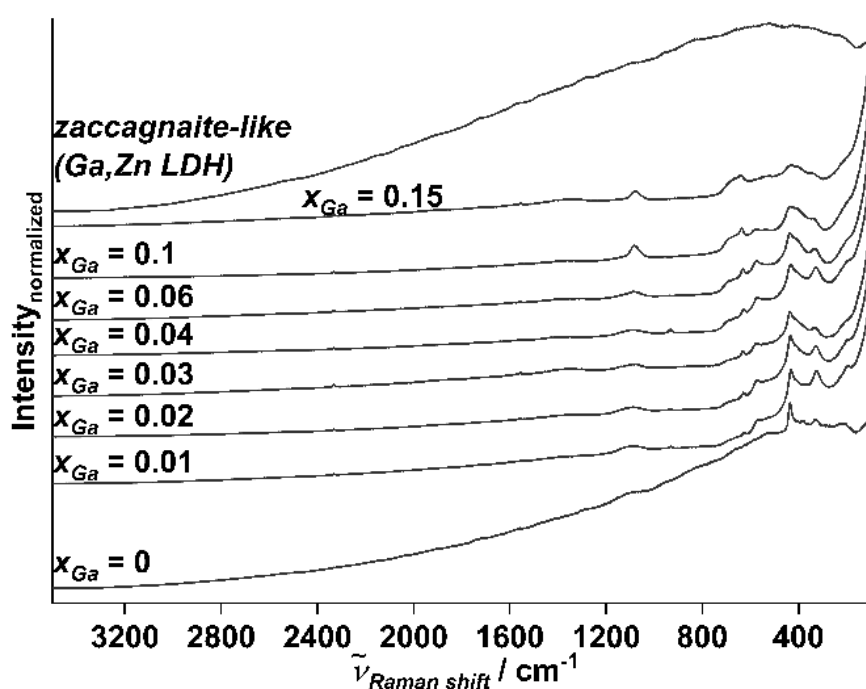


Figure SI 11.57: Complete range Raman spectra of the gallium doped zinc oxides in comparison with the gallium rich side phase (zaccagnaite-like Ga,Zn LDH).

In Figure SI 11.57 the stack plot of the measured Raman spectra of the gallium doped zinc oxide samples are shown.

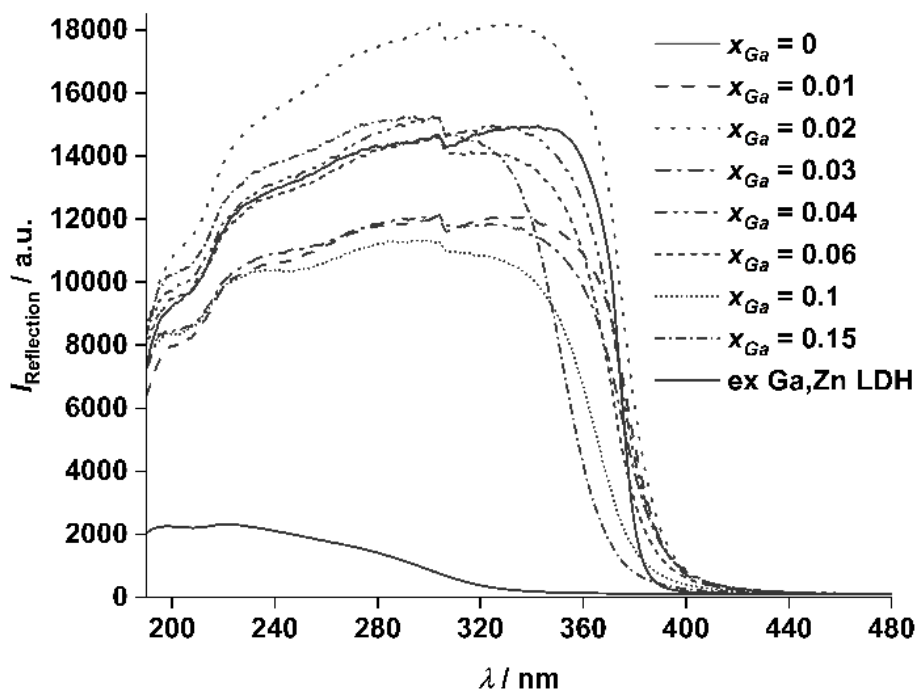


Figure SI 11.58: UV-Vis spectra of the gallium doped zinc oxides. The spectra are normalized to 100 for $\lambda > 480$ nm.

In Figure SI 11.58 the recorded UV/Vis spectra of the zinc oxide samples in comparison with the calcined LDH (*ex*-Ga,Zn LDH) sample are shown. The calcination was performed at 320 °C for each sample. The data were recorded at room temperature with BaSO₄ as reference material. The band gap determination was performed by differentiation of the raw data, to determine the changing point. At this point the wavelength was calculated to the electrical energy in eV.

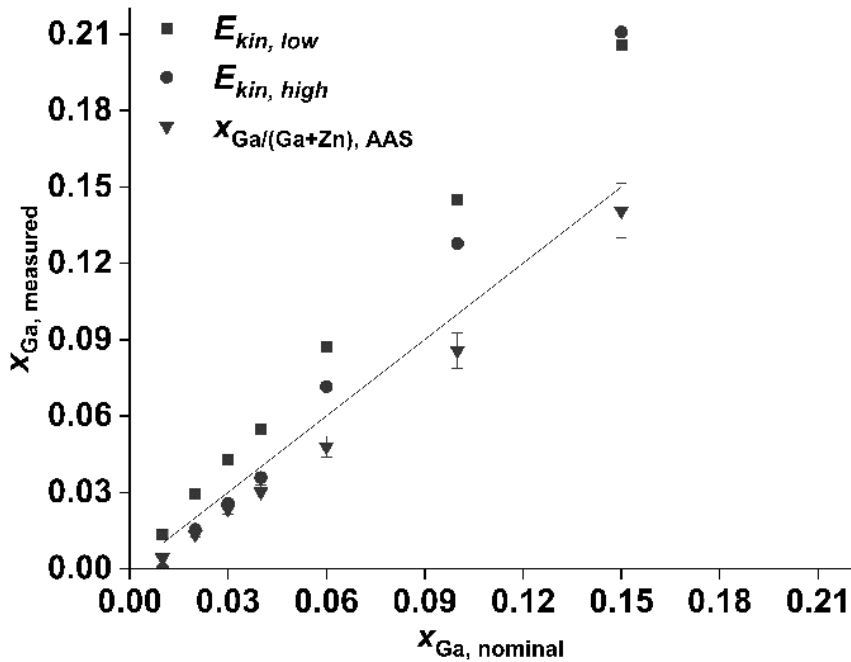


Figure SI 11.59: Metal composition determined by XPS compared to the composition determined by AAS of the gallium doped zinc oxides. $E_{\text{kin, low}}$ correspond to the surface-near layer, whereas $E_{\text{kin, high}}$ to the bulk correspond.

By XPS analysis the near surface layer should be investigated. It was expected that the gallium content would be reach the targeted, *e.g.*, the AAS determined ratios, because of the homogeneous distribution. For Ga and Zn one can distinguish between high energy electrons, which are expected to come from the bulk and low energy electrons, which are expected to come from the near surface layer of the solid. The XPS results in Figure SI 11.59 demonstrate, that the bulk composition determined by XPS has reached the AAS determined composition for gallium contents lower than $x_{\text{Ga}} = 0.06$. The near surface layer was gallium enriched. This picture shifted for a gallium content higher or equal to $x_{\text{Ga}} = 0.06$. The gallium composition was determined to increase for both the bulk and the near surface layer and reached values above the composition determined by AAS. That indicates that the gallium segregated into more enriched islands, whereas the nominal composition of the sample was reached. This result implies that because of the well-defined precursors the gallium must be enriched on local sides in the ZnO during the calcination process.

X-Ray Photoelectron Spectroscopy (XPS) was recorded on an ULVAC-Phi Versaprobe II TM spectrometer using a monochromatized Al-K α beam with a beam size of 100 μm and a spectral resolution of 0.5 eV. A dual beam charge compensation of electrons and slow-moving Argon ions was used to reduce charging effects. All spectra were referenced to the position of the carbon peak at 284.8 eV binding energy. The detected peaks were fitted using the software CasaXPS.

11.9 Supporting Information to "High-pressure pulsing of Ammonia results in Carbamate as strongly inhibiting Adsorbate of Methanol Synthesis over Cu/ZnO/Al₂O₃"

Benjamin Mockenhaupt^{ab**}, Philipp Schwiderowski^{c**}, Jelena Jelic^d, Martin Muhler^c, Felix Studt^d, Malte Behrens^{ab*}

- B. Mockenhaupt, Prof. Dr. M. Behrens. Institute of Inorganic Chemistry, University of Duisburg-Essen, Universitätsstr. 7, 45141 Essen (Germany).
- B. Mockenhaupt, Prof. Dr. M. Behrens, Institute of Inorganic Chemistry, Christian-Albrecht University of Kiel, Max-Eyth-Str. 2, 24118 Kiel (Germany), E-mail: mbehrens@ac.uni-kiel.de.
- P. Schwiderowski, Prof. Dr. M. Muhler, Institute of technical chemistry, Ruhr-University Bochum, Universitätsstraße 150, 44801 Bochum (Germany).
- J. Jelic, Prof. Dr. F. Studt, Institute of Catalysis Research and Technology (IKFT), University of Karlsruhe, Hermann-von-Helmholtz-Platz 1, 76344 Eggenstein-Leopoldshafen (Germany).

**These authors contributed equally.

*Corresponding author.

The article was published at the Journal of Physical Chemistry in February 2023. Benjamin Mockenhaupt, Philipp Schwiderowski, Jelena Jelic, Felix Studt, Martin Muhler, and Malte Behrens, High-pressure pulsing of Ammonia results in Carbamate as strongly inhibiting Adsorbate of Methanol Synthesis over Cu/ZnO/Al₂O₃, *The Journal of Physical Chemistry C* **2023** 127 (7), 3497-3505, DOI: 10.1021/acs.jpcc.2c08823.

Contribution of the authors

- B.M.: conceptualization, visualization, data curation, and writing—original draft preparation.
P.S.: conceptualization, visualization, data curation, and writing—original draft preparation.
J.J.: conceptualization, DFT calculations, and writing—reviewing and editing.
F.S.: conceptualization, funding acquisition, supervision, and writing—reviewing and editing.
M.M.: conceptualization, project administration, funding acquisition, validation, and writing—reviewing and editing.
M.B.: conceptualization, project administration, funding acquisition, validation, and writing—reviewing and editing.

11.9.1 Characterization methods

The catalyst was characterized regarding its metal composition to confirm the success of co-precipitation. In Table S1 the results for the precursor and the calcined oxide are listed. The targeted molar ratio of Cu:Zn:Al 68:29:3 was not exactly reached but close approximated with 69:29:2 (Figure SI 11.60).

Table SI 11.21: Atomic absorption spectroscopy (AAS) of the precursor and calcined sample of the Cu/ZnO:Al (CZA) catalyst. The value of weight percent is based on the mass of investigated precursor or oxide.

Sample	$X_{(Cu)}$	$X_{(Zn)}$	$X_{(Al)}$
	wt%	wt%	wt%
CZA-precursor	38 ± 1.6	17 ± 2	0.44 ± 0.03
CZA-calcined	48 ± 2	20 ± 2.4	0.61 ± 0.05

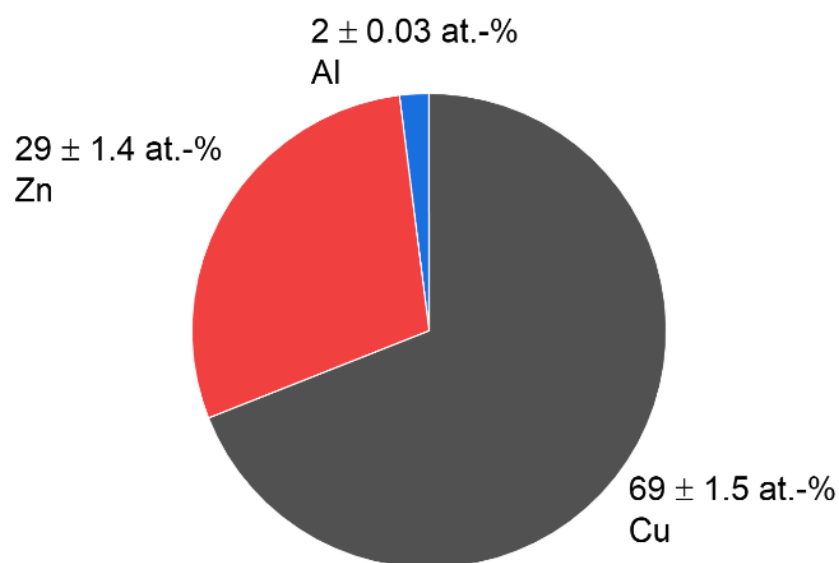


Figure SI 11.60: Molar metal ratio of the pre-catalyst (after calcination), determined by atomic absorption spectroscopy.

11.9.1.1 Powder XRD characterization of the investigated catalyst

The co-precipitate was washed and dried after synthesis. Afterwards, the powder pattern was recorded (Figure SI 11.61) to determine phase purity and the shift of the $20\bar{1}$ lattice planes compared to a pure malachite reference. With the latter value, the success of zinc and aluminium incorporation into the malachite structure can be determined. This $20\bar{1}$ d-spacing was determined using the Bragg equation (M 11.5) and the Cu $K\alpha$ wavelength to 2.754 \AA .

$$2d\sin(\theta) = n\lambda$$

M 11.5

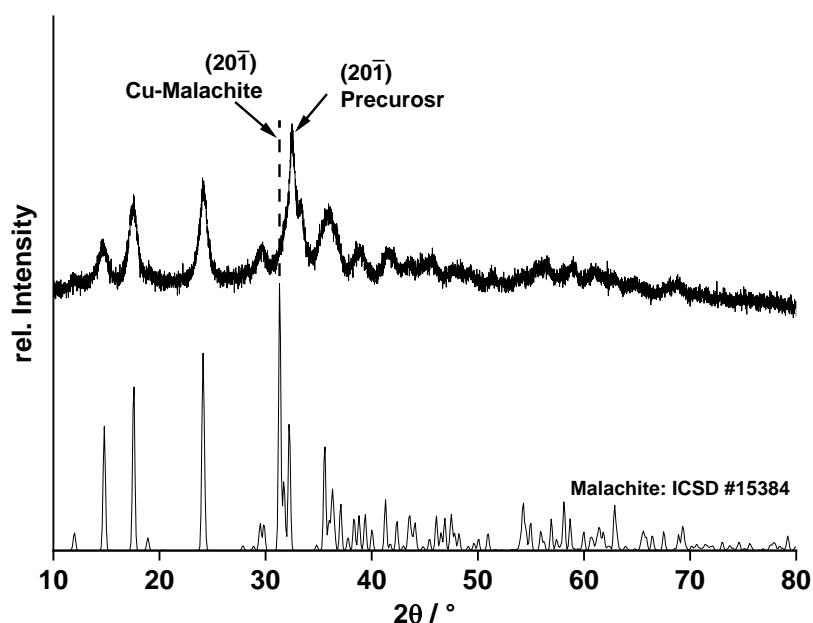


Figure SI 11.61: XRD-Pattern of the co-precipitated precursor with a copper-zinc-malachite (260813) as references from the ICSD database.

The calcination of the precursor at $350 \text{ }^\circ\text{C}$ for 3 h in static air resulted in an oxidized $\text{CuO}/\text{ZnO}:\text{Al}$ pre-catalyst (Figure SI 11.62). A crystalline residue of the zincian malachite precursor is indicated by the presence of the 120 malachite-reflection and demonstrates an incomplete conversion. Nevertheless, the main phase was nanostructured copper oxide and zinc oxide.

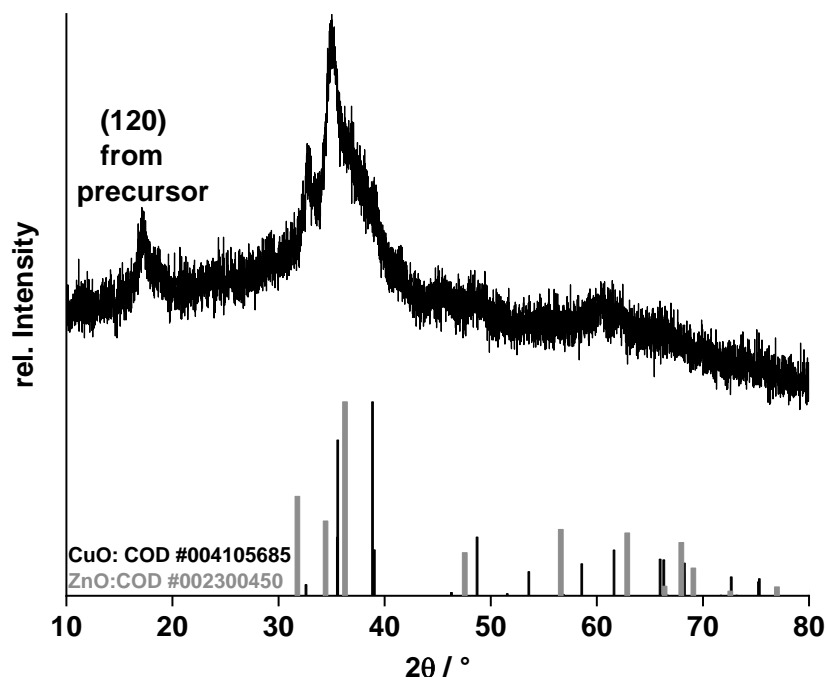


Figure SI 11.62: XRD-pattern of the CuO/ZnO:Al pre-catalyst after calcination at 350 °C for 3 h in static air. The 120 reflection shows crystalline residues of the malachite precursor, demonstrating an incomplete conversion.

11.9.1.2 Surface characterization by N₂ physisorption method

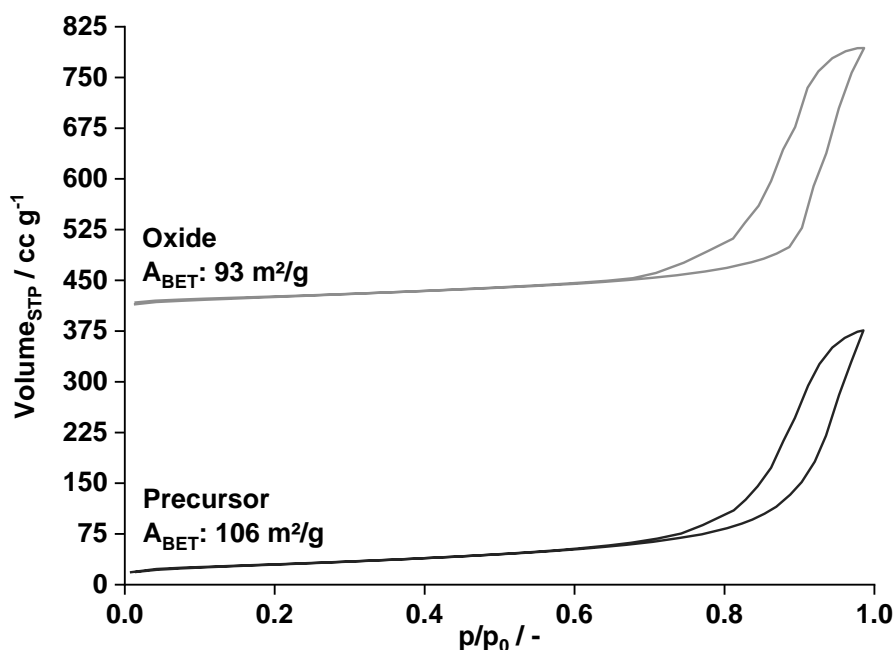


Figure SI 11.63: Nitrogen physisorption measurement to determine the BET surface area at -196 °C for the calcined oxide (upper graph) and the malachite precursor (lower graph). The samples were exposed to vacuum for 2 h at 80 °C to clean the surface from any adsorbate.

The characterization by N₂-physisorption demonstrates the evolution of the surface area of the synthesized catalyst. After co-precipitation the material had a specific surface area of about

106 m² g⁻¹, as shown in Table SI 11.22. The physisorption isotherm (Figure SI 11.63) shows a profile with a H3 hysteresis loop representative of a material with slit-shaped pores.³⁰³ Calcination has not drastically changed the isotherm profile and the pore size, but it has slightly lowered the overall specific surface area, which was reduced by 13 m² g⁻¹ to 93 m² g⁻¹ by metal oxide sintering during calcination at 350 °C.

Table SI 11.22: Nitrogen physisorption analysis using the BET method of the precursor and calcined samples of CZA. The specific surface areas were determined in a partial pressure range of 0.07 to 0.4. The pore size was calculated using the BJH model using the desorption branch of the isotherm.

<i>Sample</i>	<i>A_{BET}</i> <i>m²/g</i>	<i>Pore size</i> <i>nm</i>
<i>CZA-precursor</i>	106	16.2
<i>CZA-calcined</i>	93	16.2

11.9.1.3 Reduction behaviour of the synthesized catalyst and N₂O-RFC profile

The calcined pre-catalyst was activated at 250 °C in diluted hydrogen, as shown in the TPR profile in Figure SI 11.64 a). The XRD analysis confirms the reduced state of the copper particles (Figure SI 11.64 c)). The copper crystallite size of 7 nm was determined by applying the Scherrer equation (M 11.6) on the 111 reflection of Cu. After activation, the specific copper surface area was determined by N₂O-RFC. The evaluation of the N₂O consumption by equation (M 11.7) results in the specific copper surface area. The surface area of a single copper atom (*a_{Cu}*) was assumed to be 68·10⁻²¹ m².¹⁵⁰ The dispersion of the copper atoms was calculated according to equation (M 11.8). This dispersion is overestimated caused by the ZnO present in the catalyst.⁶⁹

$$d_{Cu} = \frac{k\lambda}{\beta_{FWHM} * \cos(\theta_0)} \quad M 11.6$$

$$A_{Cu} = \frac{n_{N_2O} N_A a_{Cu}}{x} \quad M 11.7$$

$$D = \frac{n_{N_2O} M}{Wx} \quad M 11.8$$

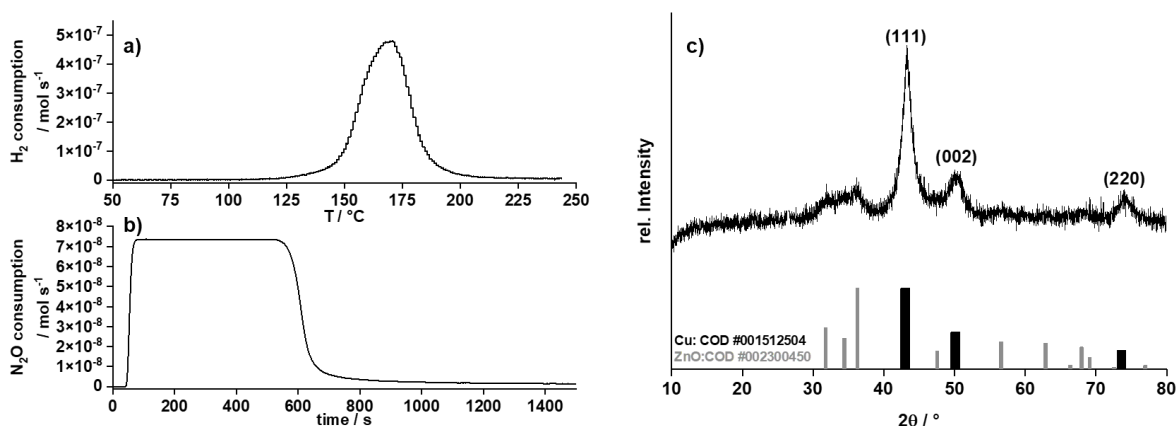


Figure SI 11.64: a) TPR- and N₂O consumption profiles of the CZA catalyst (250-355 μm sieve fraction). TPR was measured in 4.6 % Hydrogen in Argon. b) N₂O-RFC was measured at room temperature with 1 % N₂O in He to determine the copper surface area. c) XRD-pattern of the reduced Cu/ZnO:Al catalyst. Reduction before XRD was performed at 240 °C in 2 % H₂/N₂. The catalyst was afterwards removed from the reactor in an inert manner and transferred into the XRD without air contact. The reference patterns were taken from the COD data base (grey ZnO: 002300450, in black Cu: 001512504).

11.9.2 Catalytic performance in methanol synthesis

The accuracy of the fit in Figure 7.1 of the main text with the determined parameter k and m was 97 % of the experimental data. The fit was performed according to Fichtl *et al.*³⁰ by simple power law (PL) expression (M 11.9). The determined parameter allows a better comparison of the deactivation behaviour of the catalysts. The higher value in m (determined: $m = 12$; reported: $m = 4$) shows that the deactivation of the catalyst of this study was much faster than in case of the catalyst reported in the literature³⁰. Comparing the two curves (Figure 7.1, PL-fit and PL-fit according to Fichtl *et al.*) this becomes obvious, since the CZA catalyst synthesized here showed a strong activity drop in the first 20 h, contrarily to the estimated deactivation calculated from Fichtl *et al.*³⁰ which would be expected caused by a similar catalyst and reaction conditions. The deactivation of the herein reported catalyst fits to the observed deactivation by Sun *et al.*⁵⁹ for a similar catalyst and feed gas composition.⁵⁹ The difference between both models can be easily seen in Figure 7.1 in the main text: the deactivation kinetics reported by Sun *et al.*⁵⁹ represents well the short-term (<10 h) behaviour of the catalyst. Contrarily to this observation, the reported deactivation kinetics by Fichtl *et al.*³⁰ describes well the long-term (>10 h) behaviour of that catalyst.^{59 30} So, both models complement each other and can describe the complete deactivation behaviour of the typical industrial CZA catalyst.

$$\frac{\partial a_{rel}}{\partial t} = -ka_{rel}(t)^m \quad M 11.9$$

$$\forall a_{rel}(t) = \frac{r_{MeOH}(t)}{r_{MeOH,max}(t_0)} \quad M 11.10$$

Table SI 11.23: Kinetic parameter of the deactivation rate of methanol formation. A power law expression (M 11.9) fitted to the methanol formation rate. The data from Fichtl et al.³⁰ were taken from the publication and plotted to the methanol rate shown in Figure 7.1 in the main text.

	k h^{-1}	m
<i>PL-fit</i>	0.0224	12
<i>PL-fit from Fichtl et al.³⁰</i>	0.0043	4

Table SI 11.24: List of the DFT calculated energies (E_{tot}), ZPE, S and $C_p dT$ for the gas phase species, intermediates, and transition states on Cu 211 and ZnCu 211 surfaces.as phase

<i>Gas phase</i>	E^{tot} eV	ZPE eV	S eV	$C_p dT$ eV
CO ₂ (g)	-18.004	0.312	0.0025029	0.186
H ₂ (g)	-7.072	0.284	0.0015044	0.151
H ₂ O(g)	-12.810	0.580	0.0022150	0.183
NH ₃ (g)	-18.429	0.930	0.0022894	0.183
MMA(g)	-33.487	1.715	0.0028110	0.245
DMA(g)	-48.702	2.474	0.0032613	0.324
TMA(g)	-64.023	3.215	0.0036665	0.409

<i>Gas phase</i>	E^{tot}	ZPE	S	$C_p dT$
	eV	eV	eV	eV
Cu 211				
intermediates				
plain	-14.064			
O*	-19.103	0.072	0.0002471	0.071
OH*	-23.648	0.357	0.0004797	0.12
NH ₃ *	-33.196	1.007	0.0010287	0.20
NH ₂ *	-29.215	0.694	0.0002753	0.042
NH ₂ COO*	-48.188	1.09	0.0014996	0.321
NH ₂ COOH*	-51.360	1.38	0.0018423	0.377
NH ₂ CHO*	-45.984	1.253	0.0015019	0.299
NH ₂ CH ₂ O*	-49.570	1.451	0.0011701	0.287
NH ₂ CH ₂ OH*	-53.195	1.878	0.0018027	0.336
NH ₂ CH ₂ *	-43.430	1.174	0.0008114	0.201
MMA*	-48.368	1.784	0.0013246	0.275
DMA*	-63.604	2.522	0.0017274	0.368
TMA*	-78.877	3.26	0.0021302	0.462
Cu 211				
Transition States				
NH ₂ ---H	-31.517	0.934	0.0008066	0.181
NH ₂ H---O	-37.606	1.085	0.001169	0.265

<i>Gas phase</i>	E^{tot}	<i>ZPE</i>	<i>S</i>	$C_p dT$
	eV	eV	eV	eV
NH ₂ H---OH	-42.220	1.229	0.0014312	0.284
NH ₂ ---COO	-46.972	1.002	0.0009384	0.199
NH ₂ COO---H	-50.403	1.175	0.0016174	0.365
NH ₂ CHO-OH	-53.778	1.574	0.0013976	0.265
NH ₂ HOC---H	-48.724	1.5	0.0013870	0.309
NH ₂ CH ₂ O---H	-52.145	1.795	0.0013328	0.328
NH ₂ CH ₂ ---OH	-52.278	1.7	0.0013469	0.328
ZnCu 211				
intermediates				
plain	-7.299			
O*	-12.661	0.072	0.0002471	0.071
OH*	-17.029	0.357	0.0004797	0.12
NH ₃ *	-26.356	1	0.0010287	0.2
NH ₂ *	-22.486	0.701	0.0004941	0.131
NH ₂ COO*	-41.567	1.096	0.0013688	0.317
NH ₂ COOH*	-44.403	1.38	0.0018423	0.377
NH ₂ CHO*	-39.084	1.258	0.0015019	0.303
NH ₂ CH ₂ O*	-42.781	1.451	0.0008701	0.287
NH ₂ CH ₂ OH*	-46.379	1.878	0.0014027	0.336
NH ₂ CH ₂ *	-36.648	1.174	0.0008114	0.201

<i>Gas phase</i>	E^{tot}	<i>ZPE</i>	<i>S</i>	$C_p dT$
	eV	eV	eV	eV
MMA*	-41.5483	1.784	0.0013246	0.275
DMA*	-56.739	2.522	0.0017274	0.368
TMA*	-72.096	3.26	0.0021302	0.462
ZnCu 211				
Transition States				
NH ₂ ---H	-24.747	0.934	0.0008066	0.181
NH ₂ H---O	-30.838	1.065	0.0010154	0.216
NH ₂ H---OH	-35.426	1.259	0.0014312	0.284
NH ₂ ---COO	-40.185	1.004	0.0009384	0.199
NH ₂ COO---H	-43.512	1.161	0.001652	0.363
NH ₂ CHO-OH	-47.021	1.574	0.0014707	0.267
NH ₂ HOC---H	-41.857	1.49	0.0014065	0.311
NH ₂ CH ₂ O---H	-45.168	1.687	0.0014333	0.328
NH ₂ CH ₂ ---OH	-45.590	1.83	0.0012911	0.328

The DFT structures are only shown in the publication file (DOI: 10.1021/acs.jpcc.2c08823).

11.10 Supporting Information to "Cu-Co/ZnAl₂O₄ catalysts for CO conversion to higher alcohols synthesized from co-precipitated hydrotalcite precursors"

Benjamin Mockenhaupt^{ad}, Fatih Özcan^b, Remco Dalebout^c, Sebastian Mangelsen^d, Thomas Machowski^a, Petra E. de Jongh^c, Malte Behrens^{ad}

- a. B. Mockenhaupt, Prof. Dr. M. Behrens, Institute of Inorganic Chemistry, University of Duisburg-Essen Universitätsstr. 7, 45141 Essen (Germany), E-mail: mbehrens@ac.uni-kiel.de.
- b. F. Özcan, Institute for Combustion and Gas Dynamics, NanoEnergieTechnikZentrum (NETZ), Carl-Benz-Straße 199, D-47057 Duisburg (Germany).
- c. R. Dalebout, Prof. Dr. Petra de Jongh, Institute of inorganic chemistry and catalysis, Utrecht University, Universiteitsweg 99, NL-3584 CG Utrecht (Netherlands), E-mail: P.E.deJongh@uu.nl.
- d. B. Mockenhaupt, Dr. S. Mangelsen, Prof. Dr. M. Behrens, Institute of Inorganic Chemistry, Christian-Albrecht University of Kiel, Max-Eyth-Str. 2, 24118 Kiel (Germany).

The article was published at *Chemie Ingenieur Technik* in October 2022.

Mockenhaupt, B., Özcan, F., Dalebout, R., Mangelsen, S., Machowski, T., de Jongh, P.E. and Behrens, M., Cu-Co/ZnAl₂O₄ Catalysts for CO Conversion to Higher Alcohols Synthesized from Co-Precipitated Hydrotalcite Precursors, *Chemie Ingenieur Technik*, **2022** 94, 1784-1797, DOI: 10.1002/cite.202200171.

Contribution of the authors

B.M.: planning catalytic tests, visualization, data curation, original draft preparation.

F.Ö.: Catalyst preparation, planning of the catalytic tests.

R.D.: Planning and Performance of the catalytic tests.

S.M.: XRD analysis, Rietveld refinement, manuscript editing.

T.M.: Catalyst preparation and characterization.

P.E.d.J.: Advising support, manuscript editing.

M.B.: Advising support, manuscript editing.

All co-authors have contributed to data analysis and discussion.

11.10.1 Catalyst synthesis and characterization

Table SI 11.25: Chemicals and their purities which were used for the co-precipitation of the CuCoZnAl hydrotalcite series.

Chemicals	Supplier	Purity
$Co(NO_3)_2 \cdot 6 H_2O$	Carl Roth GmbH + Co. KG	$\geq 99 \%$
$Cu(NO_3)_2 \cdot 3 H_2O$	Carl Roth GmbH + Co. KG	$\geq 99 \%$
$Zn(NO_3)_2 \cdot 6 H_2O$	Carl Roth GmbH + Co. KG	$\geq 99 \%$
$Al(NO_3)_3 \cdot 9 H_2O$	Aldrich Chemistry	98 %
NaOH	Bernd Kraft GmbH	98 %
Na_2CO_3	AppliChem GmbH	99,5 %

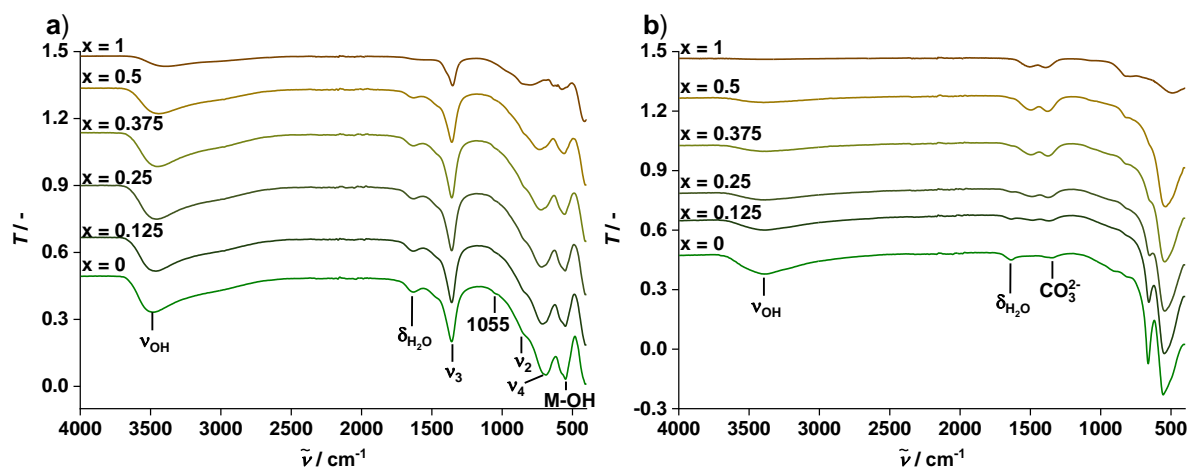


Figure SI 11.65: a) Infrared spectra of the synthesized $[(Co_{1-x}Cu_x)_7ZnAl_2(OH)_{20}]CO_3 \cdot m H_2O$ hydrotalcite precursors and b) their corresponding mixed metal oxides after calcination with $x = n_{Cu} / (n_{Cu} + n_{Co})^{-1}$. The calcination was performed at 350 °C for 3 h in static air with a heating ramp of 2 °C min⁻¹.

The IR spectroscopic results of the precursors, prepared from the salts listed in Table SI 11.25, are shown in Figure SI 11.65 a). The typical hydroxyl-stretching mode (ν_{OH} at 3480 cm⁻¹) as well as the water deformation mode (δ_{H_2O} at 1641 cm⁻¹) are clearly visible together with the different carbonate stretching modes ($\nu_{\#}$)^{121, 214}. The bands are more pronounced for the cobalt-containing samples than for the pure Cu-Zn-Al hydrotalcite sample ($x = 1$). The band at a

wavenumber of 1055 cm^{-1} could be attributed to the ν_1 vibration of the carbonate, becoming IR active by a lowered symmetry caused by a high charge density, as it is known for Ni-Al-hydrocalcite type materials^{121, 212, 214}. Nevertheless, the fingerprint of the IR spectra demonstrates that the synthesized precursors are layered materials, and no side phases could be identified. In comparison to the calcined samples, shown in Figure SI 11.65 b), the loss of carbonate by thermal decomposition in air can be demonstrated. The samples with a copper content between $x = 1$ and $x = 0.25$ had some carbonate species covered at 1500 cm^{-1} and 1400 cm^{-1} , which probably corresponds to the high-temperature stable carbonates. These stable carbonates should act as structural promoter species in catalysis⁶². The OH^- stretching mode, of the calcined samples, around 3500 cm^{-1} and the water bending mode ($\delta_{\text{H}_2\text{O}}$ at 1646 cm^{-1}) was probably caused by a rehydration of the samples after calcination³⁰⁴.

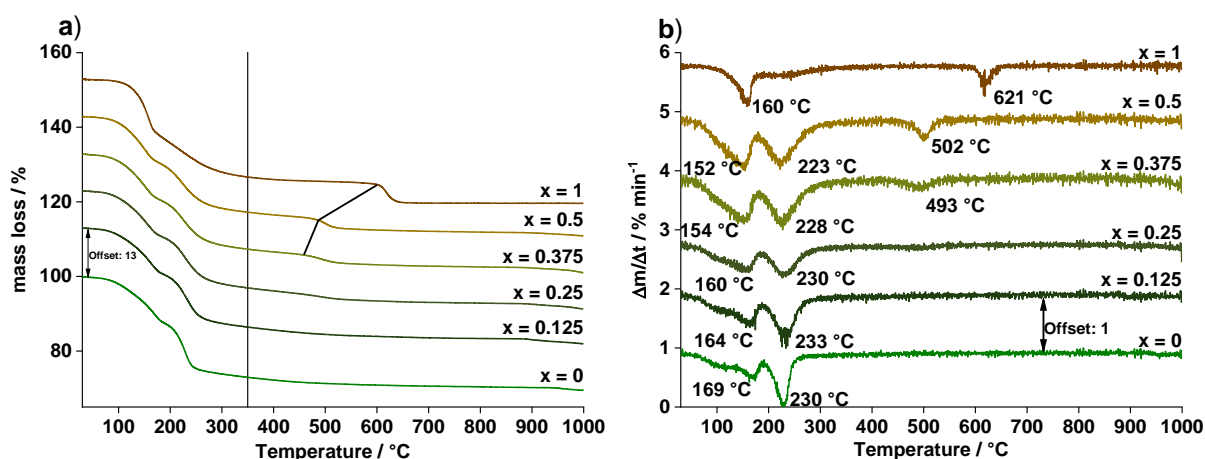


Figure SI 11.66: Thermogravimetric analysis of the precursor decomposition $[(\text{Co}_{1-x}\text{Cu}_x)_7\text{ZnAl}_2(\text{OH})_{20}]\text{CO}_3 \cdot m\text{H}_2\text{O}$ with $x = n\text{Cu} (n\text{Cu}+n\text{Co})^{-1}$ after co-precipitation. a) mass loss of the samples as a function of the temperature. The vertical black line visualizes the calcination temperature at $350\text{ }^\circ\text{C}$. The additional lines between the curves demonstrates the change of high temperature carbonates as a function of the composition. b) differential mass loss per time as a function of the temperature. The thermogravimetric analysis was performed in synthetic air up to $1000\text{ }^\circ\text{C}$ with a heating ramp of $5\text{ }^\circ\text{C min}^{-1}$.

The TG analysis in Figure SI 11.66 was performed to determine the precursors decomposition in comparison with the calcination temperature. There are three regions of weight loss identified. The first is in the range up to $200\text{ }^\circ\text{C}$, where the interlayer water will be removed and first dehydroxylation appears³⁰⁴. Between $200\text{ }^\circ\text{C}$ and $250\text{ }^\circ\text{C}$ the dehydroxylation becomes more pronounced, followed by a slight mass decrease due to the decarboxylation and the formation of the high-temperature, carbonate-stabilized MMOs³⁰⁴. For the copper-rich samples, up to $x = 0.375$ (Cu:Co = 3:8 (at/at)) a fourth decomposition region was identified in

TG analysis, which is above 400 °C and above the chosen calcination temperature. At this third decomposition step, the high-temperature carbonates were removed, followed by sintering of the metal oxides, forming large crystals, as it is demonstrated by the XRD pattern of the samples after TG analysis in Figure SI 11.67^{62, 304}. This decomposition step of the high-temperature carbonates showed a shift towards lower temperatures, as more cobalt was in the precursor incorporated (compare Figure SI 11.66 a)) and vanished, if the copper content has reached one quarter ($x = 0.25$). The absence of high-temperature carbonates for cobalt-rich MMOs ($x < 0.25$) was confirmed by IR spectroscopy (Figure SI 11.65 b). The ν_3 mode of the carbonate was after calcination split into two contributions of the carbonate ion (CO_3^{2-}) which should be a ν_1 and a ν_2 carbonate mode, as it was observed for the copper-containing catalysts with $x > 0.125$ ²¹³. Samples which showed no third decomposition step of the stable carbonate form, showed simultaneously weak ν_1 and ν_2 carbonate modes in the range of 1500 – 1380 cm^{-1} . The stabilization effect of the high-temperature carbonates, *i.e.*, the prevention of metal oxide sintering and the nano-structuring of the catalysts, was the motivation to calcine the precursors at 350 °C.

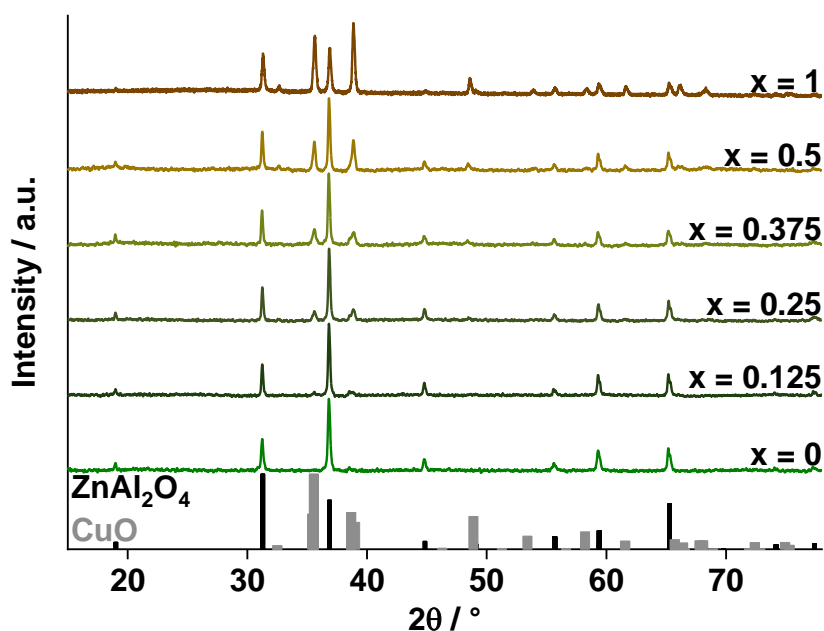


Figure SI 11.67: Powder PXRD pattern of the calcined $[(\text{Co}_{1-x}\text{Cu}_x)_7\text{ZnAl}_2(\text{OH})_{20}]\text{CO}_3 \cdot m \text{H}_2\text{O}$ hydrotalcite precursors with $x = n_{\text{Cu}} / (n_{\text{Cu}} + n_{\text{Co}})^{-1}$. The powder patterns were recorded after thermogravimetric analysis at 1000 °C in synthetic air with a heating ramp of 5 °C min^{-1} . The black bars correspond to the ZnAl_2O_4 reference (ICSD#185709), the broad, dark grey bars are aligned to a CuO reference (ICSD#67850).

The PXRD pattern of the spent samples after TG analysis are shown in Figure SI 11.67. The spinel segregation was observed for all samples as well as the formation of CuO. In comparison to the calcination conditions, the sharp reflections indicate a large crystallite size.

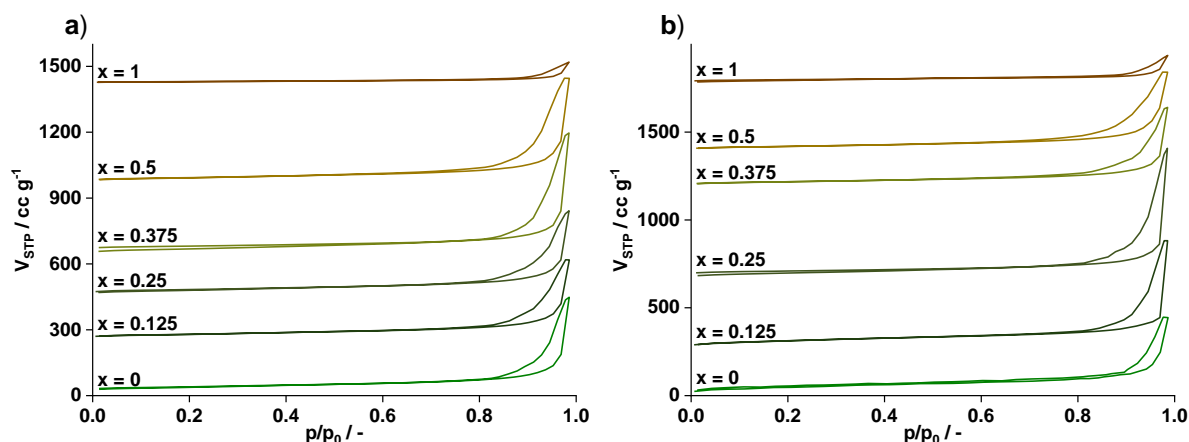


Figure SI 11.68: Nitrogen physisorption isotherms of a) the co-precipitated $[(\text{Co}_{1-x}\text{Cu}_x)_7\text{ZnAl}_2(\text{OH})_{20}]\text{CO}_3 \cdot m \text{H}_2\text{O}$ hydroxaltes and b) their corresponding oxides with $x = n_{\text{Cu}} / (n_{\text{Cu}} + n_{\text{Co}})$. Before recording the isotherms, the samples were degassed in a vacuum at a temperature of a) 80 °C and b) 100 °C for 5 h. The calcination was performed at 350 °C for 3 h in static air with a heating ramp of 2 °C min⁻¹.

The N₂ physisorption isotherms are visualized in Figure SI 11.68. The isotherms are similar for the precursors and calcined samples. The cobalt-containing samples were predominantly mesoporous, whereas the pure copper sample had a poor porosity. The evaluation of the adsorption isotherm resulted in the BET surface areas, shown in Figure SI 11.69, and discussed in the main text.

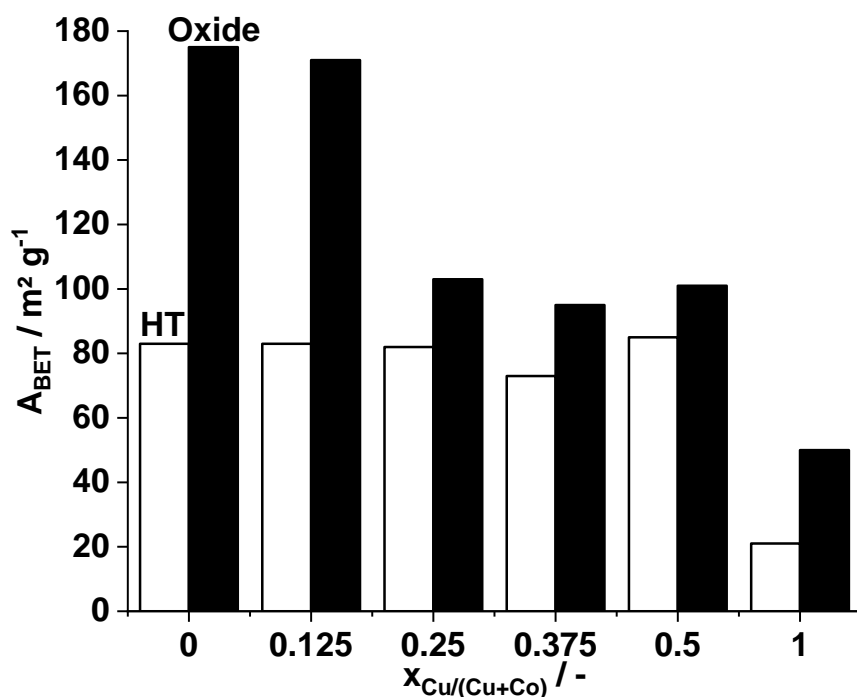


Figure SI 11.69: BET-surface evolution for the synthesized precursors and their corresponding oxides in dependence of the copper-cobalt ratio. With the hydroxalcite (HT) precursor phase in white- and the corresponding MMO (Oxide) in black bars.

11.10.1.1 TPR Results

First, the slight increase in the TCD signal (compare main text Figure 8.2) between 200 °C and 300 °C of the pure copper sample ($x = 1$) will be discussed. In this temperature range, copper oxide starts to reduce and built up the metastable Cu_2O species²⁷⁶. In general, CuO will be reduced fast and in an autocatalytic manner to metallic Cu ^{305, 306}. However, the amorphous XRD pattern of the oxide (Figure 8.1 b)) does exclude completely segregated large crystallites of CuO . Therefore, the reduction is also overlaid with possible CuO segregation from the $\text{ZnO}/\text{Al}_2\text{O}_3$ oxidic matrix²⁷⁶. Once segregated, CuO will be reduced to Cu ^{276, 307} to induce the autocatalytic pathway of the reduction, nuclei of Cu^0 next to CuO are needed³⁰⁷. Such nuclei are formed in the range of 200 °C to 300 °C followed by the autocatalytic accelerated reduction of the bulk CuO at 334 °C, showing a typical reduction profile of CuO . The peak at 537 °C could be attributed to strong interactions of CuO with Al^{3+} of the host oxidic matrix, to form CuAl_2O_4 or to brass formation by the reduction of zinc oxide^{88, 154, 308, 309}.

The reduction of the pure cobalt sample ($x = 0$) appeared also in two steps. One reduction proceeded around 283 °C followed by a clearly separated reduction at 612 °C. The lower reduction temperature seems to be the reduction of easily accessible Co^{3+} to CoO , analogous to the reduction of copper oxide^{88, 310}. The higher reduction temperature is attributed to the

reduction of bivalent bound Co^{2+} (like CoO) and to probably strong interactions of the cobalt-aluminium ions^{88, 309, 310}.

11.10.2 Activity test in CO hydrogenation

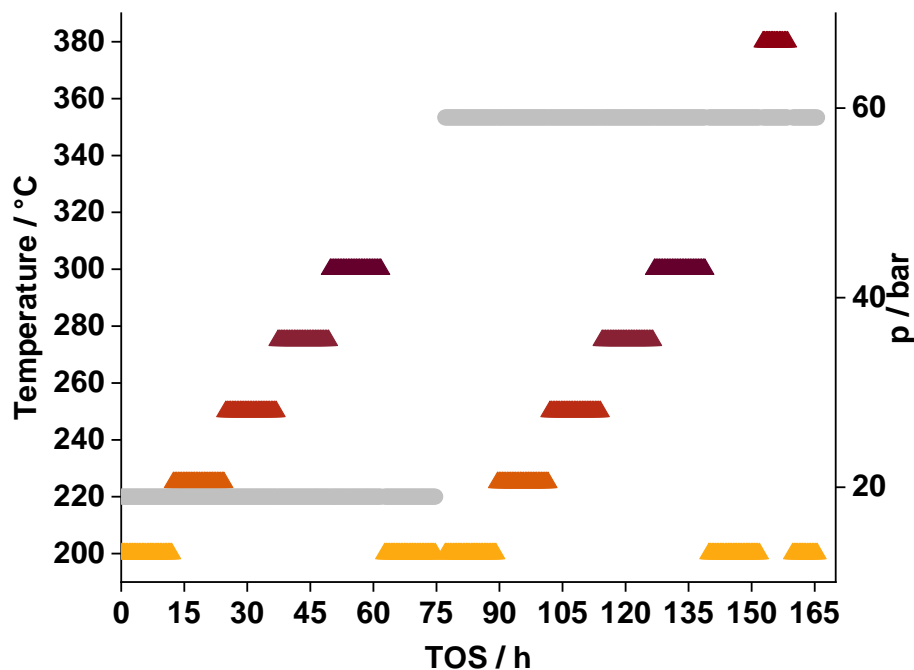


Figure SI 11.70: Process scheme of the performed catalysis of the prepared Co-, CuCo- and Cu-based catalysts. The total volume flow was set to $75 \text{ mL}_N \text{ min}^{-1}$ ($\text{GHSV} \approx 2800$) with $\text{H}_2:\text{CO} = 4$, $\text{GHSV} = 2800 \text{ h}^{-1}$.

The catalytic evaluation of the prepared catalysts was performed by the process conditions shown in Figure SI 11.70. The corresponding activity and selectivity graphs are shown in Figure SI 11.71 and Figure SI 11.73 a) for 20 bar and in Figure SI 11.72 and Figure SI 11.73 b) for 60 bar. Each set of bars corresponds several catalysts at the same conditions and are sorted from left to the right as followed: $x = 0$, $x = 0.125$, $x = 0.25$, $x = 0.375$, $x = 0.5$ and $x = 1$. For an easier demonstration of the results, the selectivity up to C_4 for linear products (hydrocarbons and alcohols) are shown in the main text and in the above-mentioned figures.

The conversion and selectivity were calculated by the following equations:

$$X_{\text{CO}} = \left(1 - \frac{\sum v_i \cdot n_i}{n_{\text{CO}} + \sum v_i \cdot n_i} \right) \cdot 100 \% \quad M 11.11$$

$$S_j = \frac{v_j \cdot n_j}{\sum v_i \cdot n_i} \cdot 100 \% \quad M 11.12$$

The sum of products was determined to 100 % for the carbon balance. The product distributions including CO₂, alkanes, alkenes and oxygenated hydrocarbons are shown in Figure SI 11.75 for each catalyst and process point. The highest carbon number resolved by GC was found to be C₁₇ for the alkanes, C₁₄ for the alkenes and C₇ (heptanol) for the oxygenated products.

If the selectivity does not sum up to 100 % of the herein shown graphs, this means, that the catalyst also produced products of C₅₊ or isomers. The selectivity of such products were found to minor fractions. That was the reason, to focus only on the products up to C₄. Due to the full CO conversion of cobalt-containing catalysts at temperatures above 225 °C, the results of the lower temperature are only discussed in the main text. For completeness, the overall catalytic data of the investigation are shown in the following graphs.

11.10.2.1 Activities and Selectivity at 20 bar

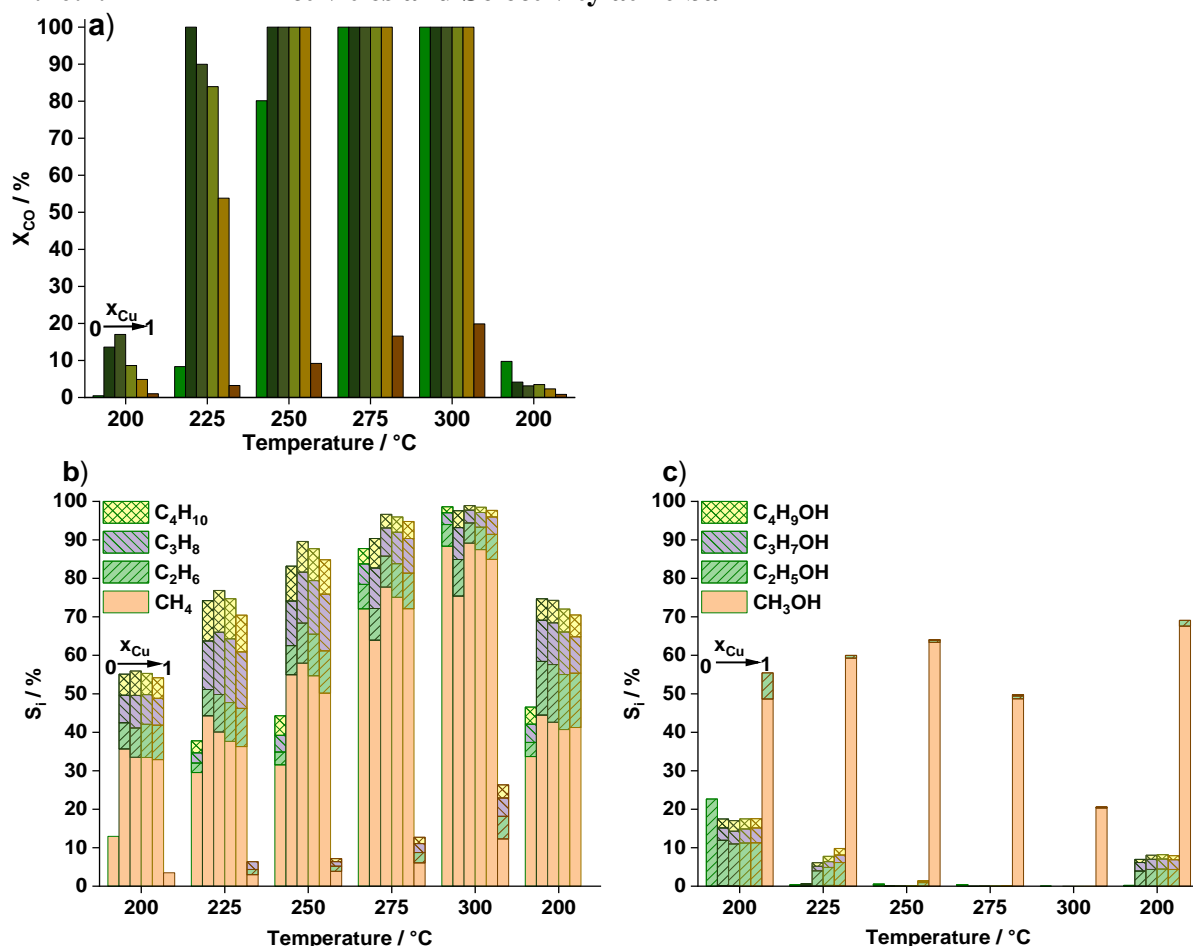


Figure SI 11.71: Temperature-dependent conversions of 100 mg of the prepared catalysts diluted with an equal mass of silicon carbide at 20 bar, H₂:CO = 4 and with a GHSV around 2800 h⁻¹ are shown in a). The corresponding selectivity of n-C₁ to n-C₄ b) -alkanes and c) -alcohols are represented below. The copper amount ($x = n_{Cu} / (n_{Cu} + n_{Co})^{-1}$) increases from left to the right of each bar set ($x = 0$ (left), $x = 0.125$, $x = 0.25$, $x = 0.375$, $x = 0.5$, $x = 1$ (right)).

The activity data (Figure SI 11.71) at 20 bar demonstrate that with increasing temperature, the CO conversion increased to 100 %. Simultaneously, the selectivity towards hydrocarbons increased and reached 100 % for C₁ to C₄ at 300 °C for all cobalt containing catalysts. Only the pure copper catalyst showed a kinetic behaviour over the complete temperature range, which was not limited by mass transport effects or thermodynamics. The increasing temperature led to an increase in hydrocarbon formation of this catalyst but cooling down to 200 °C resulted in a reproducible activity with selectivity towards methanol. Probably the hydrocarbon formation was a result of reached thermodynamic limitation of the methanol synthesis. Therefore, the higher activity will be led to an increased hydrocarbon formation, which than becomes more favoured by thermodynamics.

11.10.2.2 Activities and Selectivity at 60 bar

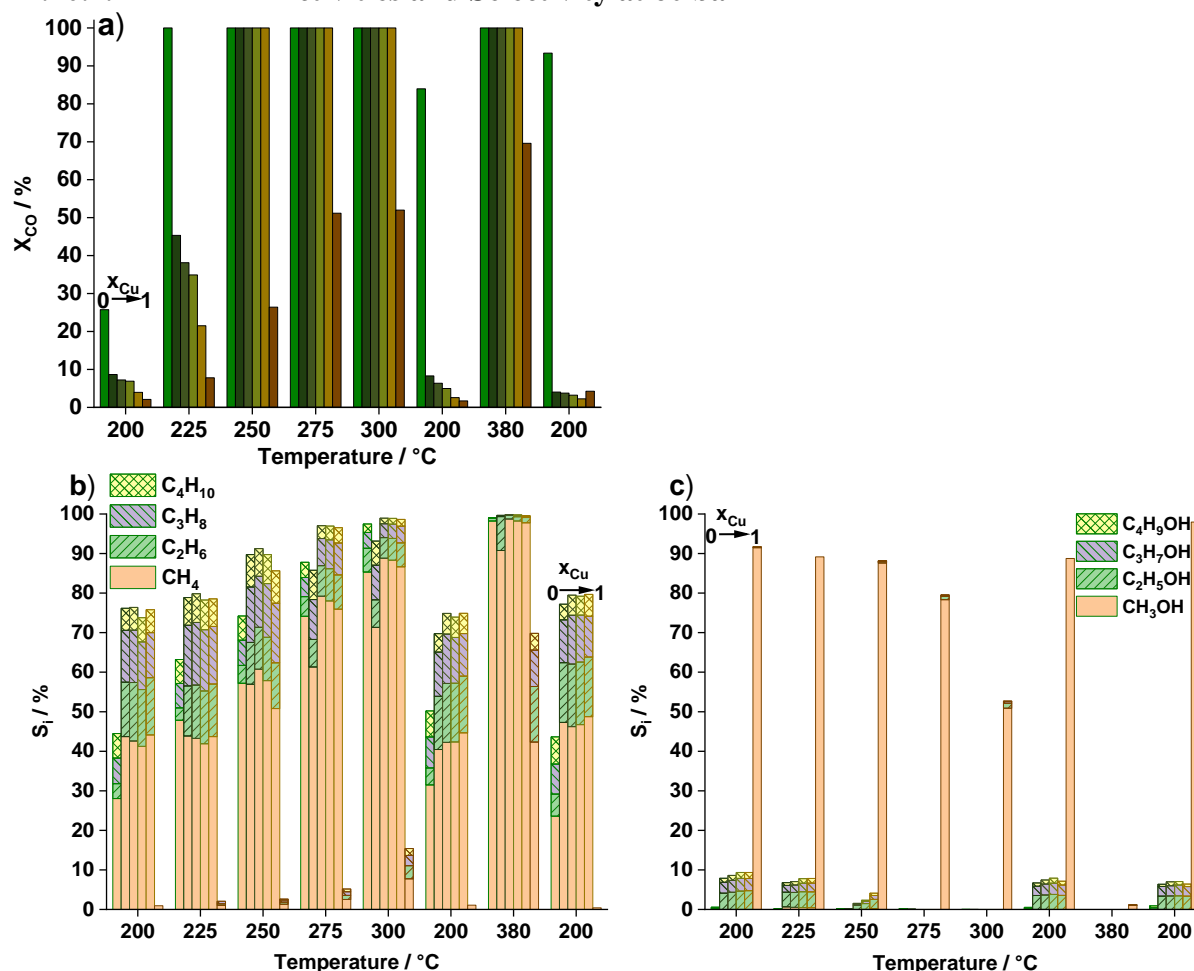


Figure SI 11.72: Temperature-dependent conversions of 100 mg of the prepared catalysts diluted with an equal mass of silicon carbide at 60 bar, H₂:CO = 4 and with a GHSV around 2800 h⁻¹ are shown in a). The corresponding selectivity of n-C₁ to n-C₄ b) -alkanes and c) -alcohols are represented below. The copper amount ($x = n_{Cu} / (n_{Cu} + n_{Co})^{-1}$) increases from left to the right of each bar set ($x = 0$ (left), $x = 0.125$, $x = 0.25$, $x = 0.375$, $x = 0.5$, $x = 1$ (right)).

The activity data at 60 bar (Figure SI 11.72) are comparable to the activity data at 20 bar. The cobalt-containing catalysts reached complete conversion at temperatures between 250 and 300 °C and a selectivity to hydrocarbons of C₁ to C₄ of 100 % at 275 °C. Only the pure cobalt catalyst has reached a complete conversion already at 225 °C and demonstrated no activity loss over the complete run. Contrarily, the pure cobalt catalyst showed a continuous activity increase, which was related to some structural changes during catalysis.

An additional activation was observed for the pure copper catalyst at 380 °C by a pronounced CO₂ formation (Figure SI 11.73). The oxygen balance should give clear picture, what happened, but unfortunately the water content in the gas effluent could not be determined during the catalytic tests. Therefore, an oxygen balance cannot be calculated. Nevertheless, the afterwards increased conversion activity of CO at 200 °C gives evidence that the catalyst was completely activated. The observed activation could be a result of increased strong metal–support interactions (SMSI) by enhanced zinc oxide reduction due to the high temperature and strong reducing gas phase¹⁵⁴.

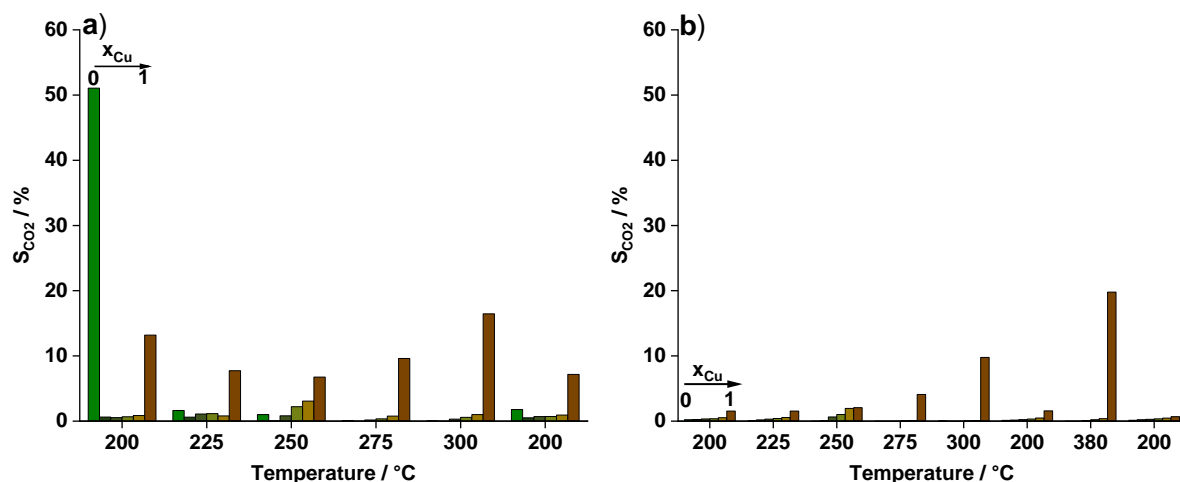


Figure SI 11.73: Temperature-dependent selectivity to CO₂ at a) 20 bar and b) 60 bar of 100 mg of the prepared catalysts diluted with an equal mass of silica carbide at 20 bar, H₂:CO = 4 and with a GHSV around 2800 h⁻¹. The copper amount ($x = n_{Cu} / (n_{Cu} + n_{Co})^{-1}$) increases from left to the right of each bar set ($x = 0$ (left), $x = 0.125$, $x = 0.25$, $x = 0.375$, $x = 0.5$, $x = 1$ (right)).

11.10.2.3

Comparison of selected activity data

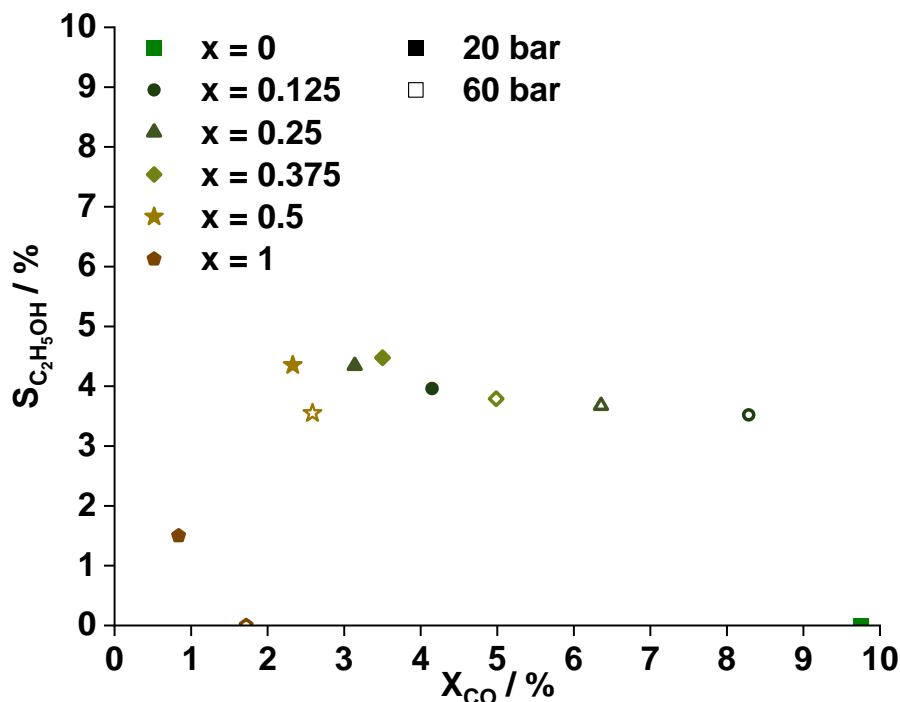


Figure SI 11.74: Ethanol selectivity over the CO conversion at 200 °C after temperature treatment (second run of 200 °C) of 20 bar (complete coloured) and 60 bar (inner white) with $H_2:CO = 4$ and a GHSV around 2800 h^{-1} for the prepared CuCo catalysts in comparison to the monometallic Co- and Cu-reference catalysts.

Ethanol was found to be the main alcohol product of cobalt-containing catalysts. Therefore, the selectivity over the conversion is shown in Figure SI 11.74. The conversion of the binary catalysts increased, as more cobalt the catalyst contained. The selectivity of ethanol was quite similar ($\approx 3.6\%$) for the copper-rich binary catalysts ($x = 0.5 - 0.25$). Both values result in an increased ethanol yield, as higher the conversion was determined, ergo as more cobalt the binary catalyst contained. The highest ethanol yield of 0.29 % at 20 bar and 200 °C was reached by the cobalt rich $x = 0.125$ Cu-Co catalyst. The low yield demonstrates the predominant hydrocarbon formation at these conditions. This finding is in alignment of earlier reported literature of CuCoCr catalysts, where the alcohol selectivity increased with the copper content if it exceeded about 50 % at reaction conditions of: 290 °C, 60 bar, $H_2:CO = 2$, GHSV= 4000 h^{-1} ²⁶⁸.

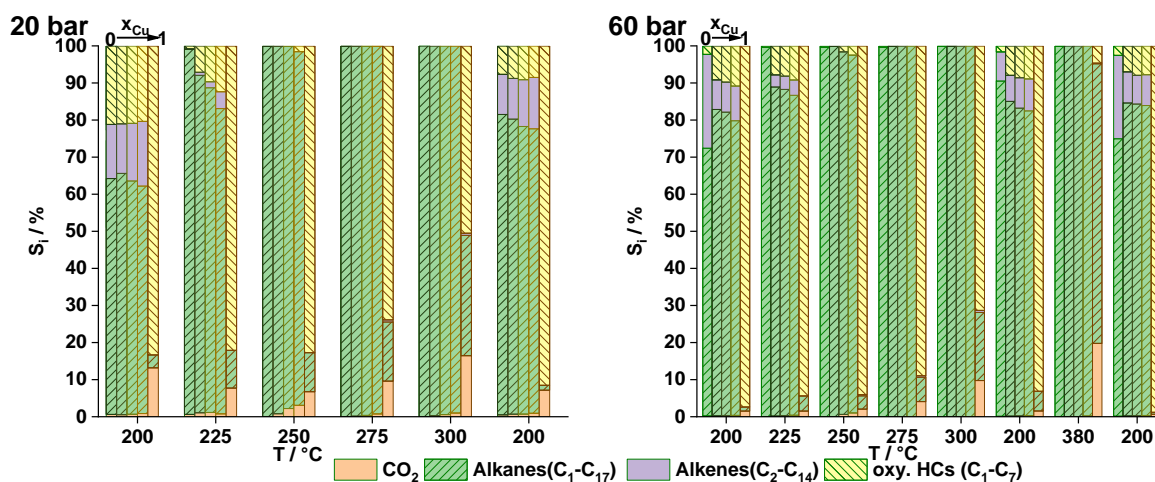


Figure SI 11.75: Product distribution of the investigated catalysts as a function of the temperature and pressure (for 20 bar left graph and for 60 bar right graph) during CO hydrogenation with $H_2:CO = 4$ and a GHSV around $2800 h^{-1}$. The copper content ($x = n_{Cu} / (n_{Cu} + n_{Co})^{-1}$) increase from left to the right of each bar set ($x = 0$ (left), $x = 0.125$, $x = 0.25$, $x = 0.375$, $x = 0.5$, $x = 1$ (right)). The selectivity are shown for CO_2 (bottom), alkanes including isomers for C_1 to C_{17} (green with lines to left bottom), alkenes including isomers for C_2 to C_{14} (purple) and oxygenated hydrocarbons including alcohols and aldehydes, ketones, and esters for C_1 to C_7 (yellow, with lines to right bottom).

The product selectivity distinguishing the hydrocarbon classes by alkanes, alkenes and oxygenated hydrocarbons are shown in Figure SI 11.75. The graphs visualize that the oxygenated products, including alcohols, are formed at temperatures below $250\text{ }^\circ\text{C}$ for cobalt-containing catalysts. The pure copper reference catalyst synthesized over the complete temperature range methanol (4.6 % - 99 % depending on temperature at 60 bar). Therefore, it could be expected that the methanol formation in a binary CuCo catalyst would favour the formation of other alcohols. The oxygenated products were found to vary in the range of 0 % to 21.1 %. The highest value was reached by the Cu-Co catalyst with $x = 0.125$ at $200\text{ }^\circ\text{C}$ and 20 bar right after activation. However, the results of the catalytic investigation demonstrate that besides the cobalt reference catalyst the mixed CuCo catalyst predominantly formed alkanes. The temperature-dependent selectivity distribution would result in the question if higher alcohol formation with the selected process conditions could be enhanced at lower temperatures than $200\text{ }^\circ\text{C}$. Regarding the activated state of the pure cobalt catalyst ($x = 0$) and the increased selectivity of the Cu-Co catalysts after catalyst activation at $200\text{ }^\circ\text{C}$, one could assume, that CoO catalyses higher alcohol synthesis rather than metallic cobalt. This should be scope of following investigations.

11.10.3 Characterization of the spent catalysts after passivation in air

The spent catalysts were recovered from the reactor and the diluent, SiC, was separated from the catalyst by sieving, because of its higher particle size ($>125\ \mu\text{m}$ vs. $d_{\text{catalyst}} = 38\text{-}125\ \mu\text{m}$).

The full XRD pattern of all spent catalysts are shown in the main text in Figure 8.5 a). After catalysis, all samples contained a spinel phase. In case of the copper reference catalyst, the formed water as a byproduct of hydrocarbon formation could have enhanced the spinel segregation and crystallization⁸⁷. Copper is highly active in CO hydrogenation to methanol¹⁴. The observed crystalline spinel segregated over the reaction process should not result in catalyst deactivation, contrarily, it stabilizes the metal particles. This assumption, is confirmed by the enhanced conversion rate and methanol selectivity, demonstrated in the main text in Figure 8.4 at 200 °C before and after the treatment at 380 °C. However, all spent samples contained fractions of the reduced metals as a result of sinter effects. Only the cobalt reference catalyst contained diffraction reflections around $2\theta = 10^\circ$, which are assumed to be somehow crystalline waxes, as they were observed in reported investigations²⁸⁷.

The IR spectroscopy (Figure SI 11.76), as well as the elemental analysis (Figure SI 11.77) and TG analysis (Figure SI 11.78) confirmed the assumed coke formation. From the elemental analysis the carbon amount was determined to 30 wt%, which is in accordance with the mass loss of around 28 % determined by TG. Because of the reoxidation, observed in TG analysis for the copper-containing catalysts, the missing 2 % of the mass loss in TG can be related to an overlay carbon burn off and reoxidation of the cobalt. The mass increase as a result of oxidation was determined to around 10 % for the cobalt-containing catalysts and to around 5 % for the copper reference catalyst.

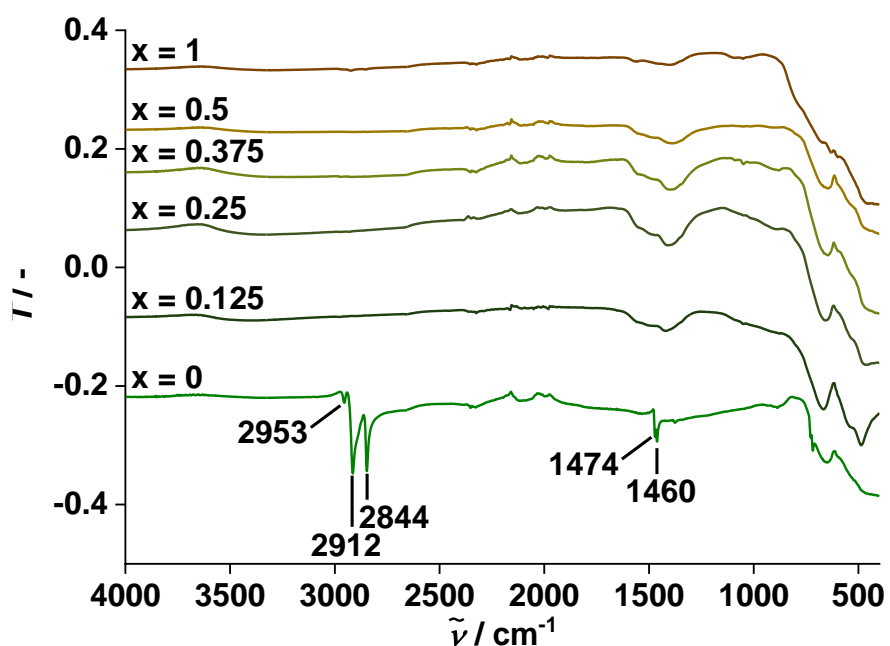


Figure SI 11.76: Infrared spectroscopy of the spent catalysts after CO hydrogenation at 20 bar / 60 bar and 200 °C – 380 °C after passivation at room temperature with air. The cobalt–copper ratio is described by: $x = n_{\text{Cu}} / (n_{\text{Cu}} + n_{\text{Co}})$.

The IR spectroscopy of the spent samples (Figure SI 11.76) showed some C–H stretching and bending modes around 2900 cm^{-1} and 1470 cm^{-1} . These modes are explained in the main text. The spectroscopic analysis gave evidence of coke formation in the pure cobalt catalyst. Therefore, a C and H analysis of the spent samples was carried out (Figure SI 11.77).

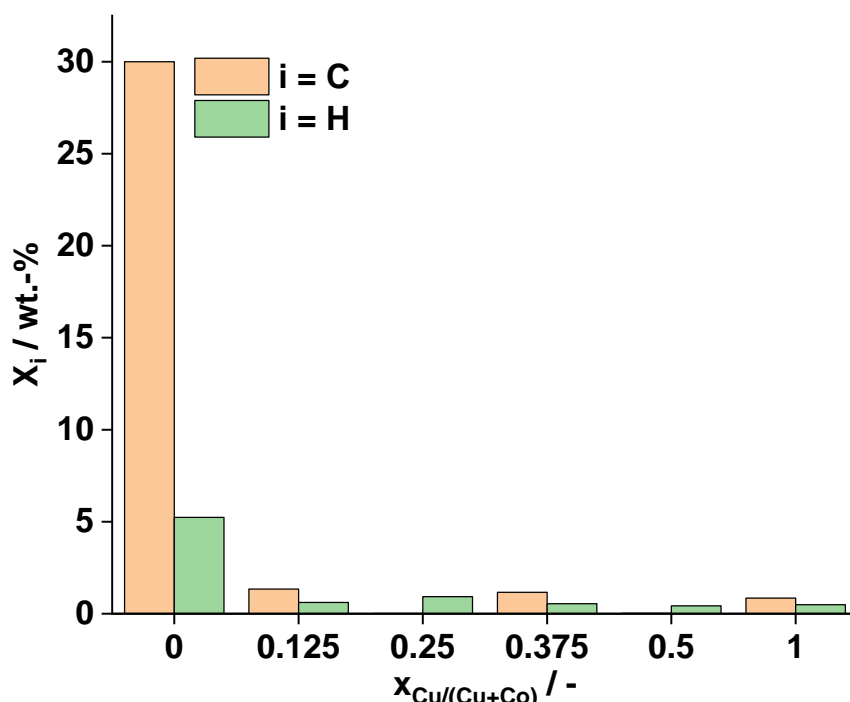


Figure SI 11.77: C, H analysis of the spent catalysts after CO hydrogenation at 20 bar/60 bar and 200 °C – 380 °C after passivation at room temperature with air. The cobalt–copper ratio is described as: $x = n_{Cu} (n_{Cu} + n_{Co})^{-1}$.

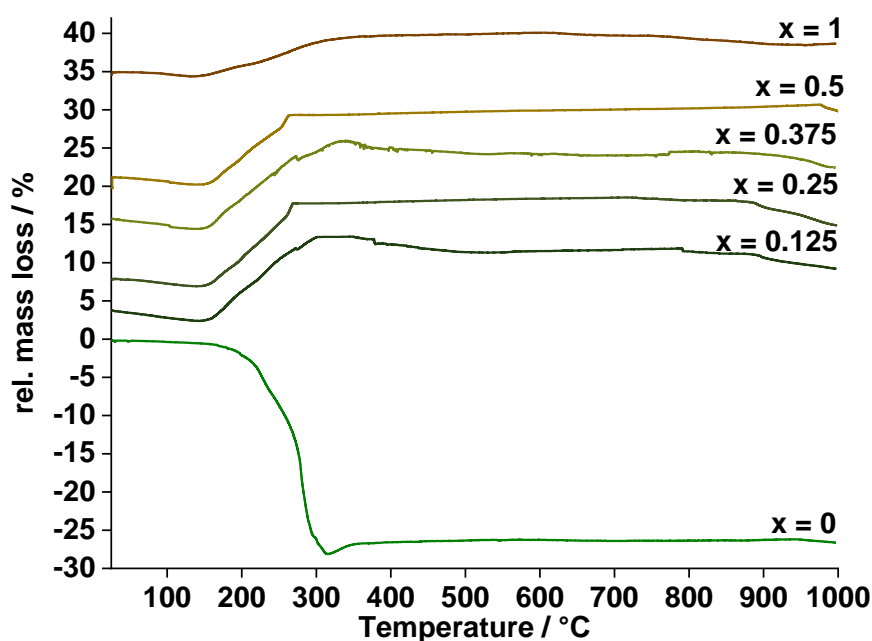


Figure SI 11.78: Thermogravimetric analysis of the spent catalysts after CO hydrogenation at 20 bar/60 bar and 200 °C – 380 °C after passivation at room temperature with air. The cobalt–copper ratio is described by: $x = n_{Cu} (n_{Cu} + n_{Co})^{-1}$. TG analysis was performed up to 1000 °C with heating ramp of 4 °C min⁻¹ in synthetic air.

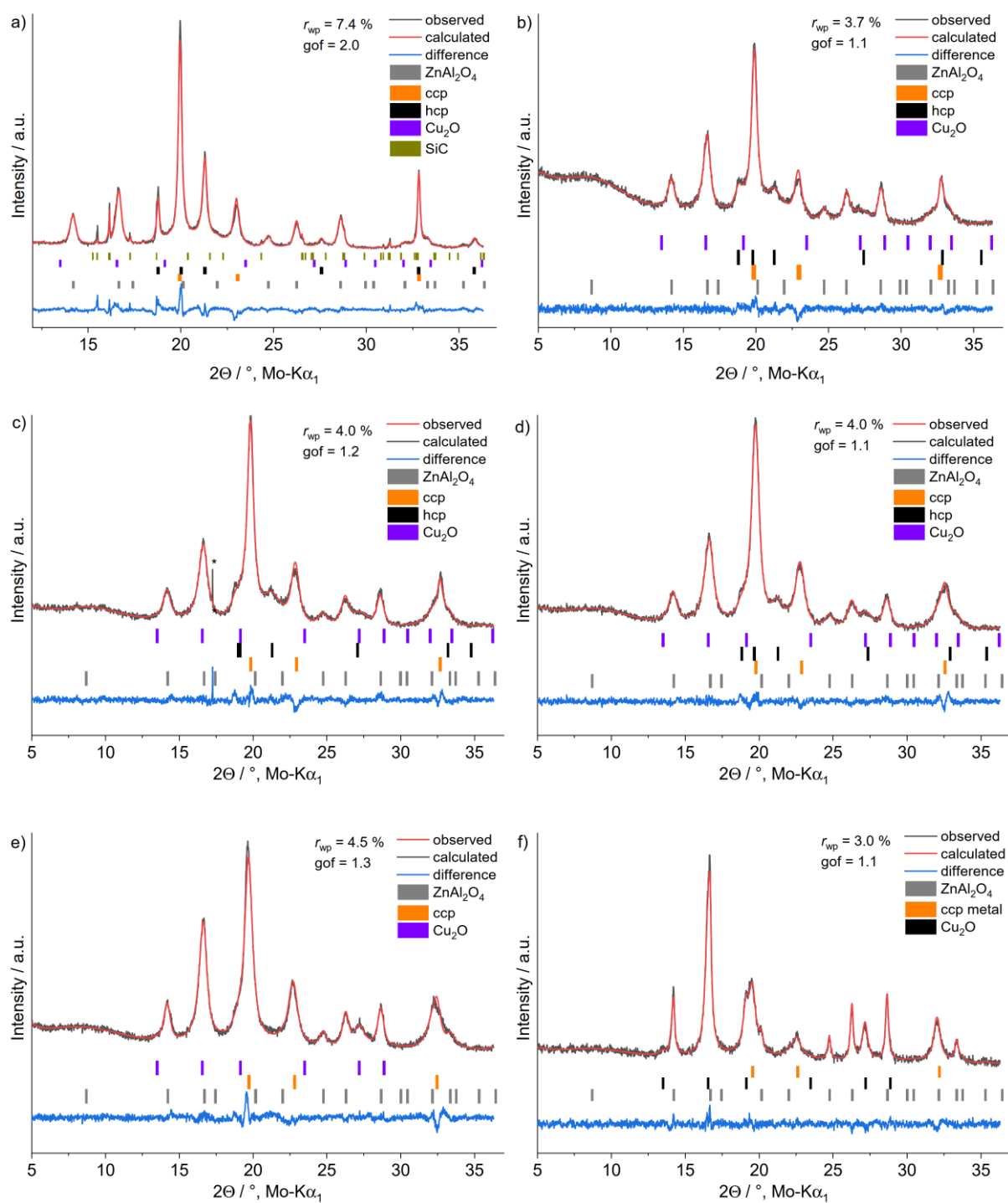


Figure SI 11.79: The difference plots for the Rietveld refinements of all spent catalysts with $x = 0, 0.125, 0.25, 0.375, 0.5$ and 1 are shown in a)-f) respectively. The signal in c) marked with an asterisk is likely an artefact due to the extremely narrow half width. In a) the fitted range is smaller to omit the unidentified reflections at 9.8 and $10.9^\circ 2\theta$ from the calculation of the r -value (weighted profile r -factor, r_{wp}) and goodness of fit (gof).

12 Publications

Peer reviewed publications

1. L. Pandit, A. Boubnov, G. Behrendt, B. Mockenhaupt, C. Chowdhury, J. Jelic, A.-L. Hansen, E. Saraçi, E.-J. Ras, M. Behrens, F. Studt, J.-D. Grunwaldt, *ChemCatChem* 2021, 13, 4120.
2. G. Behrendt, B. Mockenhaupt, N. Prinz, M. Zobel, E.-J. Ras, M. Behrens, *ChemCatChem* 2022, 14, e202200299.
3. Mockenhaupt, B., Özcan, F., Dalebout, R., Mangelsen, S., Machowski, T., de Jongh, P.E. and Behrens, M. (2022), Cu-Co/ZnAl₂O₄ Catalysts for CO Conversion to Higher Alcohols Synthesized from Co-Precipitated Hydrotalcite Precursors. *Chemie Ingenieur Technik*, 94: 1784-1797. DOI: 10.1002/cite.202200171.
4. Benjamin Mockenhaupt, Philipp Schwiderowski, Jelena Jelic, Felix Studt, Martin Muhler, and Malte Behrens, *The Journal of Physical Chemistry C* 2023 127 (7), 3497-3505, DOI: 10.1021/acs.jpcc.2c08823
5. Mockenhaupt, B., Wied, J. K., Mangelsen, S., Schürmann, U., Kienle, L., auf der Günne, J. S., and Behrens, M. (2023). Phase evolution, speciation and solubility limit of aluminium doping in zinc oxide catalyst supports synthesized via co-precipitated hydrozincite precursors. *Dalton Transactions*, 52(16), 5321-5335. DOI: 10.1039/D3DT00253E.

Poster and Oral presentations

1. F. Özcan, B. Mockenhaupt, K. Friedel Ortega, M. Behrens, **Insights into the Activity of Ga/Ni Intermetallic Compounds as CO₂ Hydrogenation Catalysts Derived from Layered Double Hydroxides**, 52. *Jahrestreffen Deutscher Katalytiker, Weimar, Germany*, 2019.
2. Andreas Hüttner, Fatih Özcan, Benjamin Mockenhaupt, Gereon Behrendt, Malte Behrens, **Malachite-based precursors for alcohol synthesis from CO_x**, 52. *Jahrestreffen Deutscher Katalytiker, Weimar, Germany*, 2019.
3. Benjamin Mockenhaupt, Fatih Özcan, Remco Dalebout, Thomas Machowski, Klaus Friedel Ortega, Petra E. de Jongh, Malte Behrens, **Cu-Co/ZnO/Al₂O₃ Catalysts for CO Conversion to Higher Alcohols synthesized from co-precipitated LDH precursors**, *EuropaCat 2019, Aachen, Germany*, 2019.

4. Fatih Özcan, Benjamin Mockenhaupt, Remco Dalebout, Klaus Friedel Ortega, Petra E. de Jongh, Malte Behrens, **Co-precipitated Ga-Ni Metal Catalysts for CO₂ Conversion**, *EuropaCat 2019*, Aachen, Germany, 2019.
5. Benjamin Mockenhaupt, Fatih Özcan, K. Friedel Ortega, Malte Behrens, **Synthesis and Characterization of Bimetallic Ni_xGa_y catalysts for Methanol Synthesis from Carbon Dioxide**, *3rd European Summer School on Catalyst Preparation*, Vogüé, France, 2019.
6. Benjamin Mockenhaupt, Fatih Özcan, Remco Dalebout, Thomas Machowski, Klaus Friedel Ortega, Petra E. de Jongh, Malte Behrens, **Cu-Co/ZnO/Al₂O₃ Catalysts for CO Conversion to Higher Alcohols synthesized from co-precipitated LDH precursors**, *CENIDE Celebration*, Essen, Germany, 2019
7. Benjamin Mockenhaupt, Gereon Behrendt, Lakshmi Pandit, Oleg Prymak, Jil Gieser, Alexey Boubnov, Erisa Saraçi, Jan-Dierk Grunwaldt, and Malte Behrens, **Malachite- and Layered Double Hydroxide-based Catalyst Precursors for Methanol Synthesis from CO₂-rich Synthesis Gas**, *17th International Congress on Catalysis*, Abstract-book, USA, 2020
8. B. Mockenhaupt, F. Özcan, T. Machowski, K. Friedel Ortega, M. Behrens, **Cu-Co/ZnO/Al₂O₃ Catalysts for CO Conversion to Higher Alcohols synthesized from co-precipitated LDH precursors**, *CENIDE*, Essen, Germany, 2020
9. B. Mockenhaupt, J. K. Wied, L. Kampermann, **Characterization of aluminium and gallium doped zinc oxide regarding the electronic promotion, as a support for a model methanol catalyst**, *20. Vortragstagung für Anorganische Chemie 2020*, Online, Germany, 2020
10. B. Mockenhaupt, K. Friedel Ortega, M. Behrens, **Aluminium and gallium doped zinc oxides as a model of the electronic promotion in the copper/zinc oxide/aluminium oxide methanol catalyst**, *54. Jahrestreffen Deutscher Katalytiker*, Online conference, Germany, 2021.

11. B. Mockenhaupt, M. Behrens, **Zinc oxide promoted nickel catalysts in the reverse water gas shift reaction**, *55. Jahrestreffen Deutscher Katalytiker*, Weimar, Germany, 2022.

Student works

The following student work was performed at the University of Duisburg-Essen in the group of Prof. Behrens in the context of the presented thesis. Benjamin Mockenhaupt participated in the definition of research questions, the planning of experiments with appropriate analytics, the evaluation and interpretation and the supporting the preparation of a scientific report.

Hongxiao Xiang, **Raman-Spektroskopie von verschiedenen Festkörpern sowohl als Pulver als auch in Suspension**, Practical Course (12/2019 – 02/2020)

13 Curriculum vitae

Der Lebenslauf ist in der Online-Version aus Gründen des Datenschutzes nicht enthalten.

13 Curriculum vitae

Der Lebenslauf ist in der Online-Version aus Gründen des Datenschutzes nicht enthalten.

13 Curriculum vitae

Der Lebenslauf ist in der Online-Version aus Gründen des Datenschutzes nicht enthalten.

13 Curriculum vitae

Der Lebenslauf ist in der Online-Version aus Gründen des Datenschutzes nicht enthalten.

14 Declaration of Authorship (Eidesstattliche Erklärung)

Ich versichere, dass ich die Arbeit mit dem Titel: „On the promotion effect of trivalent cations on zinc oxide and their influence on catalyst activity“ selbstständig verfasst und ohne fremde Hilfe und ohne Benutzung anderer als der angegebenen Quellen angefertigt habe und dass die Arbeit in gleicher oder ähnlicher Form noch keiner anderen Prüfungsbehörde vorgelegen hat und von dieser als Teil einer Prüfungsleistung angenommen wurde. Alle Ausführungen, die wörtlich oder sinngemäß übernommen wurden, sind als solche gekennzeichnet.

Essen, den 04.09.2023 _____

Benjamin Mockenhaupt